Proceedings of the Workshop on Identification and Control of Flexible Space Structures

Volume I

G. Rodriguez
Editor

April 1, 1985

NASA

National Aeronautics and
Space Administration

Jet Propulsion Laboratory
California Institute of Technology
Pasadena, California

All Blank Pages

Intentionally Left Blank

To Keep Document Continuity

N-155-538

Proceedings of the Workshop on Identification and Control of Flexible Space Structures

Volume I

G. Rodriguez
Editor

NASA

National Aeronautics and
Space Administration

Jet Propulsion Laboratory
California Institute of Technology
Pasadena, California

N-155-538

ABSTRACT

These proceedings report the results of a workshop on identification and control of flexible space structures held in San Diego, CA, July 4-6, 1984. The workshop was co-sponsored by the Jet Propulsion Laboratory and the NASA Langley Research Center, and preceded the 1984 American Control Conference held at the same location. The main objectives of the workshop were to provide a forum to exchange ideas in exploring the most advanced modeling, estimation, identification and control methodologies to flexible space structures. The workshop responded to the rapidly growing interest within NASA in large space systems (space station, platforms, antennas, flight experiments) currently under design. The workshop consisted of surveys, tutorials, contributed papers, and discussion sessions in the following general areas: missions of current interest - space platforms, antennas, and flight experiments; control/structure interactions modeling, integrated design and optimization, control and stabilization, and shape control; uncertainty management - parameter identification, model error estimation/compensation, and adaptive control; and experimental evaluation - ground laboratory demonstrations and flight experiment designs. Papers and lectures on these topics were presented at a total of fourteen sessions, including three panel discussions.

TABLE OF CONTENTS

VOLUME I

vii

NASA SPACE CONTROLS RESEARCH & TECHNOLOGY PROGRAM

D. E. McIver and **R. W. Key**
NASA Headquarters
Washington, D C 20546

NASA TECHNICAL ORGANIZATION

The Office of Aeronautics and Space Technology is one of the four major technical offices that comprise NASA.

The Office of Space Science and Applications administers programs that are directed towards using space-based or related techniques to further understanding of the total universe and to apply that understanding to practical applications in such areas as Astrophysics, Solar System exploration, Earth Sciences, Life Sciences, Communications and Information Systems.

The Office of Space Flight administers the programs for all U.S. civil launch capability, plus Spacelab development and operations.

The Office of Space Tracking & Data Systems administers the programs that operate and maintain a world-wide network of facilities for data acquisition, processing, and ground to spacecraft communications for all NASA missions.

OAST has primary responsibility within NASA for conducting space research and technology development to support commercial and military as well as NASA space interests.

OAST ORGANIZATION

OAST has the expertise that has been developed within NASA to do space research and technology development. The objective of this R&T effort is to provide understanding, new opportunities, technical options, and extended capabilities which support the needs and requirements of commercial, military, and NASA missions. The breadth of OAST's program spans numerous disciplines in the fields of both aeronautics and astronautics.

One of the principal goals of the space R&T effort is to advance new technology options to a sufficient level of maturity that demonstrates critical function/characteristic of a technique and/or component. Then only some modest level of low risk engineering development and testing is necessary to taylor this base technology for specific mission applications.

1

NASA ORGANIZATION

ADMINISTRATOR
DEPUTY ADMINISTRATOR

STAFF OFFICES

ASSOCIATE ADMINISTRATOR FOR SPACE SCIENCE AND APPLICATIONS
- JET PROPULSION LABORATORY
- GODDARD SPACE FLIGHT CENTER

ASSOCIATE ADMINISTRATOR FOR AERONAUTICS AND SPACE TECHNOLOGY
- AMES RESEARCH CENTER
- LANGLEY RESEARCH CENTER
- LEWIS RESEARCH CENTER

ASSOCIATE ADMINISTRATOR FOR SPACE FLIGHT
- LYNDON B JOHNSON SPACE CENTER
- JOHN F KENNEDY SPACE CENTER
- GEORGE C MARSHALL SPACE FLIGHT CENTER
- NATIONAL SPACE TECHNOLOGY LABORATORIES

ASSOCIATE ADMINISTRATOR FOR SPACE TRACKING & DATA SYSTEMS
- ASSOCIATE ADMINISTRATOR FOR MANAGEMENT

OFFICE OF AERONAUTICS AND SPACE TECHNOLOGY
TECHNICAL LINE MANAGEMENT ORGANIZATION

ASSOCIATE ADMINISTRATOR
DEPUTY ASSOCIATE ADMINISTRATOR
ASSISTANT ASSOCIATE ADMINISTRATOR

AEROSPACE RESEARCH DIVISION

FLUID & THERMAL PHYSICS
- COMPUTATIONAL FLUID DYNAMICS
- VISCOUS FLOW CONTROL
- EXPERIMENTAL AERODYNAMICS
- FLUID MECHANICS OF TURBOMACHINERY
- COMBUSTION & HEAT TRANSFER
- TEST TECHNIQUES
- AEROTHERMODYNAMICS

MATERIALS & STRUCTURES
- ADVANCED MATERIAL CONCEPTS
- LIFE PREDICTION
- COMPOSITES
- AEROELASTICITY
- STRUCTURES & DYNAMICS
- ANALYSIS & SYNTHESIS

CONTROLS & HUMAN FACTORS
- CONTROL THEORY & ANALYSIS
- FLIGHT CRUCIAL AIRCRAFT CONTROLS & GUIDANCE
- SPACECRAFT CONTROLS & GUIDANCE
- FLIGHT MANAGEMENT
- FLIGHT SIMULATION TECHNOLOGY
- SPACE HUMAN FACTORS

COMPUTER SCIENCE & APPLICATIONS
- ELECTRONICS
- SENSORS
- COMMUNICATIONS
- COMPUTER SCIENCE
- AUTOMATION
- COMPUTATIONAL FACILITIES
- DATA SYSTEMS

AERONAUTICAL SYSTEMS DIVISION

HIGH PERFORMANCE AIRCRAFT
- FIGHTER AIRCRAFT & MISSILES
- POWERED LIFT (V/STOL) AIRCRAFT
- HYPERSONIC VEHICLES
- HIGH PERFORMANCE FLIGHT RESEARCH

SUBSONIC AIRCRAFT
- AVIATION SAFETY
- AIRCRAFT FLIGHT DYNAMICS
- AIRCRAFT OPERATING SYSTEMS
- LAMINAR FLOW CONTROL
- ADVANCED COMPOSITE SYSTEMS
- SYSTEMS INTEGRATION STUDIES

ROTORCRAFT
- AERODYNAMICS & ACOUSTICS
- STRUCTURAL DYNAMICS
- OPERATING PROBLEMS
- GUIDANCE & CONTROL
- FLIGHT RESEARCH

PROPULSION
- TURBOMACHINERY COMPONENTS & INSTRUMENTATION
- COMBUSTORS
- INLETS DUCTS & NOZZLES
- POWER TRANSFER
- ENGINE DYNAMICS & CONTROL
- INTERMITTENT COMBUSTION ENGINES
- AUTOMOTIVE STIRLINGS & GAS TURBINES

ENERGY SYSTEMS
- WIND ENERGY TECHNOLOGY
- TERRESTRIAL FUEL CELL SYSTEMS
- ELECTRIC & HYBRID VEHICLE RESEARCH
- CONSERVATION TECHNOLOGY
- PHOTOVOLTAIC APPLICATIONS

SPACE SYSTEMS DIVISION

TRANSPORTATION SYSTEMS
- SYSTEMS ANALYSIS
- ORBITER EXPERIMENT PROGRAM
- ADVANCED CHEMICAL PROPULSION
  EARTH TO ORBIT
  ONBOARD
  ORBITAL TRANSFER

SPACECRAFT SYSTEMS
- SYSTEMS ANALYSIS
- SPACECRAFT TECHNOLOGY EXPERIMENTS

SYSTEMS TECHNOLOGY
- SPACELAB PAYLOADS
- LONG DURATION EXPOSURE FACILITY
- ION AUXILIARY PROPULSION SYSTEMS

SPACE STATION SYSTEMS
- SYSTEMS ANALYSIS
- OPERATIONS
- CREW/LIFE SUPPORT

SPACE ENERGY CONVERSION
- ADVANCED ENERGETICS
- ELECTRIC PROPULSION
- PHOTOVOLTAIC ENERGY CONVERSION
- THERMAL TO ELECTRIC CONVERSION
- POWER SYSTEMS MANAGEMENT & DISTRIBUTION

2

CONTROL TECHNOLOGY NEEDS

The OAST Space Controls Research and Technology Development Program is providing the advanced control technologies that will significantly improve performance, endurance, operational efficiency, and mission capability for future spacecraft. This program has evolved from the technology needs that have been identified by numerous studies done by NASA as well as outside organizations. These studies found a recurring set of control technology deficiencies in the areas listed in the illustration below. The needs listed have been recognized as universal in almost every application area. Developing the control technologies that can overcome these problems will be pivotal in enabling or enhancing most future missions capabilities, particularly those requiring large space structures.

SPACE CONTROLS RESEARCH
AND TECHNOLOGY

OBJECTIVE: DEVELOP CONTROLS TECHNOLOGY THAT WILL
EXPAND CONTROL CAPABILITY AND IMPROVE
CONTROL PERFORMANCE FOR FUTURE SPACE SYSTEMS

SOLAR POWER SATELLITES						
	LARGE EARTH ORBITING ANTENNAS					
		SPACE TRANSPORTATION SYSTEMS				
			SPACE STATION			
79	80	81	82	83	84	85
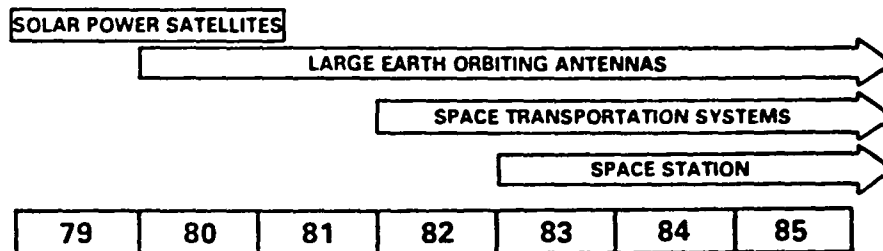
- UNCERTAINTY MANAGEMENT

- CONTROL AND STABILIZATION OF FLEXIBLE STRUCTURES

- ADVANCED MODELING TECHNIQUES

- ADVANCED HARDWARE AND SOFTWARE

- GROUND AND FLIGHT VALIDATION

AREAS OF CONTROLS R&T EMPHASIS

The Controls Research and Technology Program builds upon the expertise and experience NASA has gained from past missions as well as the state-of-the-art advances that are being made outside of NASA. The major program elements shown below span a broad spectrum of new and innovative solution approaches to several critical technological challenges that arise in the design of control systems for large space structures. These program elements each represent a category of control techniques which address the specific technology needs cited previously.

Various techniques of adaptive control and systems identification provide capability for uncertainty management. Some aspects of distributed control and systems identification provide new high fidelity modeling and estimation techniques that are necessary to describe and determine a physical system's characteristics. Additionally, distributed control approaches provide a number of techniques for controlling systems with distributed architecture and/or significant distributed mass/stiffness. Control sensors, actuators, and computer development activities are producing the unique advanced hardware and software required to implement new control techniques. Test and verification efforts are seeking to establish a technology evaluation methodology for determining both component and system level performance capability.

SPACE CONTROLS
RESEARCH AND TECHNOLOGY

MAJOR PROGRAM ELEMENTS

- ADAPTIVE CONTROL
- SYSTEMS IDENTIFICATION
- DISTRIBUTED CONTROL
- CONTROL SENSORS, ACTUATORS, COMPUTERS
- TEST AND VERIFICATION

ADAPTIVE CONTROL TECHNOLOGY

Future spacecraft control systems must be capable of operating physical plants over an increasingly larger range of dynamical properties. Engineering studies and practical experience from previous missions has shown that single operating point control system designs will not provide sufficient spacecraft control capability to meet the mission objectives of nearly all proposed large structure missions. Control instability can occur when these spacecraft experience large variations in their dynamical characteristics during operation. These changes in dynamical characteristics are a consequence of one or more of the following events; (1) structural modification of the physical plant; (2) failure of a system component; or (3) changes in the operating environment. Adaptive control techniques provide the necessary capability for accommodating these changes. Some of the specific operational capabilities that are being developed in the controls R&T program are listed below.

ADAPTIVE CONTROL

OBJECTIVE:

TO DEVELOP ALGORITHMS AND CONCEPTS FOR PRECISION AUTONOMOUS GUIDANCE AND CONTROL OF SYSTEMS WHICH HAVE TIME VARYING DYNAMICAL CHARACTERISTICS

- CONFIGURATION AND OPERATIONS ADAPTABLE
- ADAPTIVE COMPENSATION TO FAULTS
- ADAPTIVE GUIDANCE FOR OPTIMAL FLIGHT MANAGEMENT
- UNMODELED DYNAMICS ADAPTIVE

The need for developing a system identification functional capability is evident from several considerations. The changes in a physical system's characteristics, such as those stated in the discussion on adaptive control, must first be identified before any adaptive control based modifications can be effected. There are also basic operations like attitude control, thrust vector control, etc., that would benefit in both performance and economy by having real-time knowledge of system flight parameters such as center of mass, center of pressure, and total system momentum. Highly accurate shape and configuration metrology is required by missions, such as high frequency antennas, which require precision surface control. Structural dynamics identification is a critical function for accomplishing vibration control of systems which have significant structural flexibility. Also, exacting system characterization in the space environment is required to confirm the accuracy of ground based simulations and to aid in the development of the analytical tools used for predicting in-space behavior. Several approaches are under development in the R&T Program which provide the capability for identification of the control critical parameters implied by the above list of considerations. Some of the specific research and development targets are shown in the figure below.

SYSTEMS IDENTIFICATION

OBJECTIVE:
TO DEVELOP REAL-TIME TECHNIQUES FOR IDENTIFYING UNKNOWN/UNCERTAIN CONTROL CRITICAL PARAMETERS

- MASS PROPERTIES TRACKING TECHNIQUES

- SHAPE/CONFIGURATION DETERMINATION

- FLIGHT DYNAMICS IDENTIFICATION

DISTRIBUTED CONTROL TECHNOLOGY

Distributed control is a category of control techniques which at their root, all address the same basic problem of controlling spatially distributed mass. This mass distribution can have one or both of two forms; (1) a continuum of mass with elastic characteristics which impact control performance, (2) a modular collection of several rigid and/or flexible hinge connected bodies whose relative positions and rates must be controlled in a coordinated fashion. To effectively control and stabilize a system which fits either of these descriptions, some form of distributed control is required. The simplest implementation of distributed control would be a single sensor and actuator control loop closed around physical plant that behaves elastically (more than rigidly), and a controller plant model based upon some estimate of the plants distributed mass/stiffness characteristics (modal models can provide this description of the elastic characteristics). Even though this implementation would have some capability for controlling the flexible dynamics of the system, it would not provide the full performance capability that can be realized from also distributing several sensors and actuators throughout the structure. This later implementation of distributed sensing and actuation along with a distributed parameter control model is the area of most emphasis within the R&T Program. The search for an effective and efficient modeling methodology is also receiving much attention.

DISTRIBUTED CONTROL

OBJECTIVE:

TO DEVELOP TECHNIQUES FOR MODELING AND CONCEPTS FOR CONTROLLING SYSTEMS WHICH HAVE DISTRIBUTED ARCHITECTURE AND/OR DISTRIBUTED MASS AND STIFFNESS

- CONTROL-DRIVEN STRUCTURAL MODELING METHODOLOGY

- MODULAR SYSTEMS CONTROL TECHNIQUES

- FLEXIBLE STRUCTURE CONTROL AND STABILIZATION TECHNIQUES

The advanced control and guidance components/hardware now under development will be critical to the performance achieved when control concepts such as distributed and adaptive control are implemented. New hardware concepts such as a multi-target optical position sensor are pivotal for making the measurements required for shape determination of large precision surfaces.

Every high performance spacecraft control system could benefit from improved attitude rate information. A rotation sensor concept based on counter rotating laser pulses in a fiber optics coil is being developed to provide this improved measurement capability. More importantly (especially for long planetary missions), such a device would have no moving parts or inherent wear out mechanisms thus its operational life is expected to exceed 10 years.

Because launch mass is a prime driver of mission cost, finding new ways of providing essential functions with less hardware is an important problem. An actuator concept using a single spun-mass for combined momentum and energy storage is being developed. Also being studied is the feasibility of incorporating magnetic type bearings in such a device, which could greatly extend its operational life.

CONTROL
SENSORS — ACTUATORS — COMPUTER

OBJECTIVE:
TO DEVELOP THE NEW AND UNIQUE CONTROL SYSTEM HARDWARE NEEDED TO IMPLEMENT NEW CONTROL CONCEPTS

- 10 Hz BANDWIDTH MULTI-TARGET OPTICAL POSITION SENSOR

- FIBER OPTICS ROTATION SENSOR WITH 10 YEAR OPERATING LIFE

- LONG LIFE INTEGRATED MOMENTUM/ENERGY STORAGE ACTUATOR

One of the most difficult aspects of developing these new technologies is establishing effective ground test experiments which clearly demonstrate flight readiness and worthiness. For large structures this problem is compounded by the fact that full scale test models are very expensive to build and house, and perhaps impossible to use for performance testing since their dynamic behavior on the ground is heavily influenced by Earths gravity. A conspicuous void currently exists in our knowledge of the correlation between ground based simulations/experiments and in-space behavior. This problem is the focus of much debate and its resolution does not appear imminent. There is however, an effort under way within NASA to expand current efforts and to establish a large space structure dynamics and control technology evaluation program that will develop new simulation and test methodologies for determining both component and system level performance. While there is still much to be learned from analytical simulations and ground based experiments it is anticipated that the final step in the technology verification will have to come from in-space testing.

TEST AND VERIFICATION

OBJECTIVE:

TO DEVELOP NEW ANALYTICAL AND EXPERIMENTAL METHODS TO EVALUATE AND VERIFY CONTROL TECHNIQUE CAPABILITY AND PERFORMANCE

- CLOSED TREE TOPOLOGY FLEXIBLE BODY SIMULATION TOOLS
- GROUND BASED DYNAMICS AND CONTROL EXPERIMENT TECHNIQUES
- IN-SPACE EXPERIMENT METHODS FOR EVALUATING CONTROL/STRUCTURE DYNAMIC BEHAVIOR

ADVANCED CONTROL TECHNOLOGY INTEGRATION

Most missions require some combination of the advanced control technologies that have been described. A careful blend of these technologies can provide control system performance that is adaptable, robust, autonomous, fault tolerant, etc.. The diagram below illustrates how these technologies can be functionally integrated into a traditional control loop to provide such high performance capabilities. The systems identification function provides the real-time knowledge of plant characteristics which greatly influence control performance, such as flexibility, mass properties, external disturbances (shown as process noise in the diagram), sensor/actuator dynamics, etc.. This information is then available for updating the controller plant model and/or may also serve as the data base from which the adaptive control function can make decisions. Depending on the technique used, the adaptive control function could take action to modify the physical plant, sensor and actuator operation, and control laws, or any combination of these in order to achieve the desired control performance. Distributed control is integrated with this diagram in any combination of the following three ways; (1) the controller plant model is based upon a distributed mass/stiffness description of the physical structure; (2) the sensing and/or actuaction is spatially distributed throughout the structure; or (3) multiple individual control loops, such as the one illustrated, could be stacked on top of each other in a modular fashion coming out of the paper.

SPACE CONTROLS RESEARCH AND TECHNOLOGY
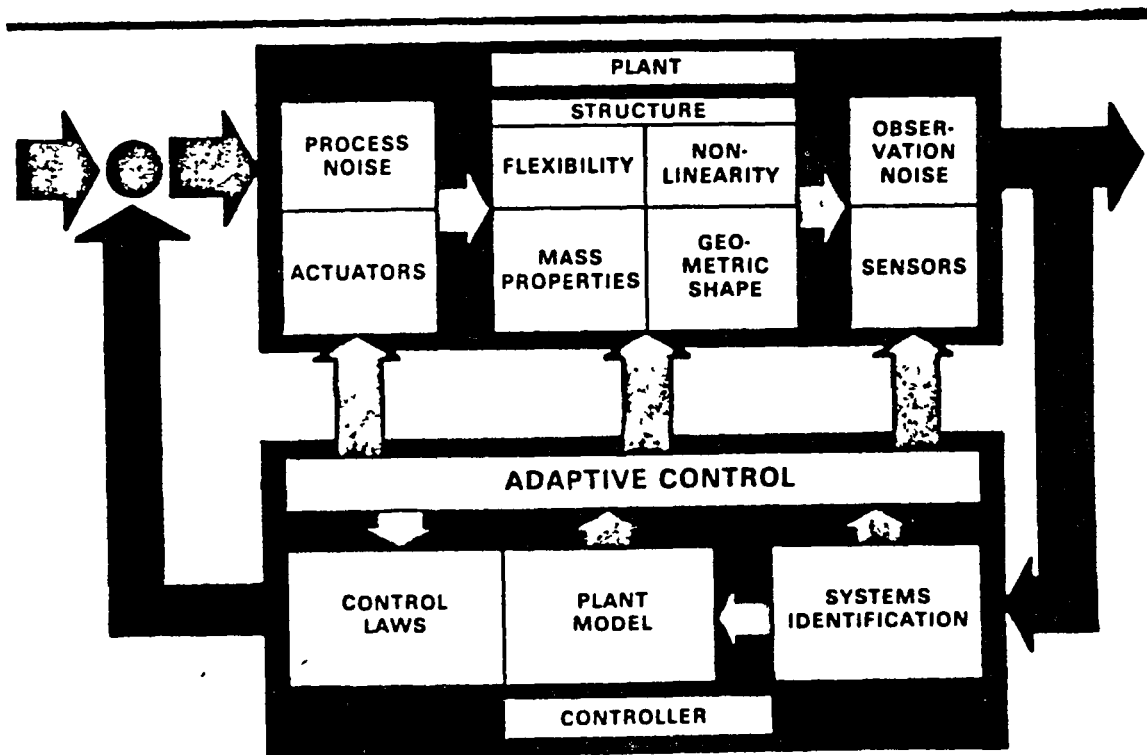
NASA   OAST   NASA HQ RT84 911 (3)
                            2 6 84

10

ADVANCED CONTROL TECHNOLOGY APPLICATIONS

A prime consideration in maturing these technologies is insuring timely availability for incorporation into the missions that lie ahead. The final stage of development for the advanced control techniques discussed herein will only occur after considerable mission experience has been gained and used to temper the original objectives set forth in the present program.

SPACE CONTROLS RESEARCH AND TECHNOLOGY
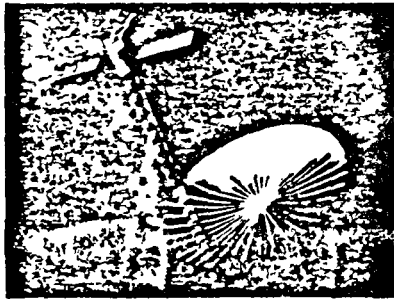
GOAL

TIMELY PROVISION OF NEW CONCEPTS AND ADVANCED CONTROLS TECHNOLOGY FOR SPACE TRANSPORTATION, EARTH ORBITING AND PLANETARY SPACECRAFT APPLICATIONS

RESEARCH AND TECHNOLOGY THRUSTS

- DISTRIBUTED CONTROL FOR LARGE SPACE SYSTEMS
- ADVANCED ANALYTICAL MODELING
- FAULT TOLERANCE/MANAGEMENT
- CONTROL SENSORS, ACTUATORS, AND RELATED INSTRUMENTATION
- SYNERGETIC SPACEFLIGHT SYSTEMS GN&C
- STS CONTROL ENVELOPE EXPANSION METHODOLGY
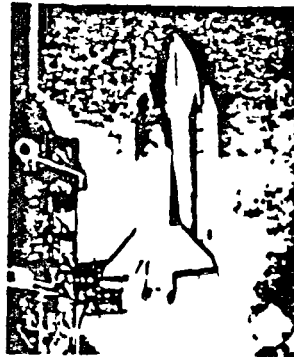
NASA

OAST
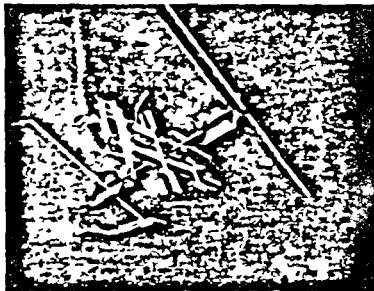
GOAL

PROVIDE A STRONG CONTROLS TECHNOLOGY BASE TO SUPPORT THE DEVELOPMENT OF BOTH THE INITIAL AND THE EVOLUTIONARY SPACE STATION

RESEARCH AND TECHNOLOGY THRUSTS

- ADAPTIVE CONTROL FOR DEPLOYMENT AND OPERATIONS
- FLIGHT DYNAMICS SYSTEM IDENTIFICATION
- MULTIPLE PAYLOAD CONTROL AND STABILIZATION
- INTEGRATED ENERGY STORAGE AND MOMENTUM MANAGEMENT
- SPACE TRAFFIC RENDEZVOUS AND DOCKING CONTROL

NASA

OAST

AFWAL CONTROL TECHNOLOGY PROGRAMS

V. O. Hoehne
Air Force Wright Aeronautical Laboratories
Wright Patterson Air Force Base, OH 45433

ABSTRACT

The space-oriented control technology programs underway in the Air Force Wright Aeronautical Laboratories (AFWAL) predominantly are being done in the Flight Control and Structures and Dynamics Division of the Flight Dynamics Laboratory. The nature of these programs extend from Basic Research (6.1) performed in-house to Exploratory Development (6.2) and Advanced Development (6.3) programs done under contract. The objective of this paper is to overview only those programs that are applicable to flexible large space structures. Sufficient information about each program will be provided for the reader to understand the objective of the program, the approach used to perform the study, and the final payoff expected. The names of the people involved in the program are provided along with their organizational symbol and telephone number. Through contacting these people, information to any level of detail desired can be acquired.

In general, the spacecraft control activity in the Flight Dynamics Laboratory is interdisciplinary, bringing together activities in structures, structural dynamics and control. This is very important since the large flexible structures to be controlled have many physical factors that influence the final controllability of the vehicle. Factors such as rigidity of both

13

structural elements and joints, damping inherent in both the material as well as discrete dampers located throughout the structure, and the band width of both sensors and actuators used to sense motion and control it are examples of those physical factors that are interdisciplinary and influence control.

The Flight Dynamic Laboratory spacecraft control program is not complete within itself, rather, it augments work already underway and planned at NASA, Air Force Space Technology Center, and other organizations by addressing issues needed by those missions that have a military goal. The work being done relies heavily on the expertise of the Laboratory gained through activities associated with developing technology for advanced aircraft. This is possible because the closer technology is to basic research, the more generic it becomes, having application to both aircraft and spacecraft with relatively minor changes in the given conditions.

INTRODUCTION

Traditionally, the AFWAL Flight Dynamics Laboratory has been involved in advancing the technology for controlling military aircraft and tactical missiles since its formation. Considerable experience has been gained in areas of technology that not only includes control, but also the structural and dynamic characteristics of the vehicle that impact the control of the vehicle. Some of this experience is generic and with minimal modifications can be applied to the development of technology for space vehicles. Hence, when it became obvious that the military use of space would require technological advancements, and some of these were in areas where experience existed, programs were inititated first in the Structures and Dynamics Division of the Laboratory and later in the Flight Control Division. Although not perfect as

yet, our approach to the technology is interdisciplinary in nature. In it we bring together the structures technology that deals with the strength and elasticity of the structure with the structural dynamics technology that defines the dynamic response of the structure to both operational and environmental loads and also with the controls technology that defines both the algorithms and the system for controlling this dynamic structure. We feel this interdisciplinary approach is essential to successfully controlling space structures because strength, flexibility, and control are inseparable in these structures. Recognizing also that as the structure becomes larger, it becomes more flexible since rigidity is related to weight and weight must be kept within practical bounds. These considerations place greater demands on the control system since many of the missions planned for spacecraft require very precise aiming, shaping, and vibrational or jitter limiting. Additional considerations that require the interdisciplinary approach for military operations include the need for autonomous operation and high reliability.

Many spacecraft to date have been designed and built as one-of-a-kind research or operational vehicles. If space is to be used as an effective support for the military, the devices that are used will need to be produced in more-than-one quantities with standards established to increase reliability and limit cost. This requires that design techniques be shared and standards be developed. Using the experience base on which to build and the somewhat uniqueness of the military need as the driver, the AFWAL Flight Dynamics Laboratory has programs both underway and planned that are directed toward providing a technology base to meet future military needs. Care is being taken to not duplicate work done by NASA or other governmental agencies in DoD. Our work is what we call "full spectrum" - it includes Basic Research in-house efforts as well Exploratory Development and Advanced Development contracted efforts.

The purpose of this paper is to overview the work underway in the AFWAL community that is applicable to the control of flexible spacecraft. The information here does not cover work being done in other laboratories of the Air Force. Neither does it cover work being done in AFWAL that is applicable to spacecraft such as the Advanced Military Spaceflight Capability (AMSC) and Transatmospheric Vehicle (TAV). Work applicable to such vehicles is felt to fall outside the scope of this workshop.

In the following descriptions of programs, an attempt is made to provide sufficient information for the reader to gain an understanding of what is being done, how it is being approached, and what the payoff is if successful. In addition, and most important, the people working the area and responsible for contracts in AFWAL are listed with their telephone numbers to simplify contacting them. Discussions are important to us; differences of opinion and reinforcement of opinion need to be brought forth. This is the business of this workshop.

The following descriptions start with programs that are in-house Basic Research in both the Flight Control and Structures and Dynamics Divisions. Following this are contracted Exploratory Development programs in both these Divisions with the last program description being of an Advanced Development program in only the Structures and Dynamics Division.

IN-HOUSE SPACE-ORIENTED CONTROL ACTIVITIES

All of the in-house control activities to be reviewed are oriented toward application in space. They are fundamental Basic Research studies and, as such, are actually generic in nature and can apply to many control problems. Orienting them toward space only means that the test problems used and the application jargon applied are spacecraft oriented with weights, frequencies,

band widths, etc. being those common to flexible space structures and their control systems rather than to aircraft. All of the work overviewed is supported by the Air Force Office of Scientific Research.

Reduced Order Control Theory

In general, the high frequency dynamics of large, flexible space structures are not well know with the order of the dynamics too large to design an effective control system. Methods are needed to control the low frequency modes without exciting the high frequency dynamics inherent in the structure. This is the objective of this study; it has been underway since 1982.

For study purposes, a reduced order model is used as a "design model" while a full order model is used as an "evaluation model". The approach used is a frequency-shaped linear quadratic Gaussian (LQG) methodology that makes it possible to apply less control energy to the high frequency modes and more to the low frequency modes to better regulate or control all modes. This is done by choosing the quadratic state and control weighting in the LQG methodology as functions of frequency. If the standard LQG methodology is used, it can apply equally to the whole dynamic spectrum possibly causing the control gains to spill over into the high frequency modes causing instabilities. Weighting prevents this.

The study approach that has been used is to examine the step-by-step application of this frequency-shaped LQG methodology to better understand the reduced-order control design theory. As work progresses, the payoffs and costs of the methodology are documented so that guidelines can be developed for choosing the frequency dependent quadratic state and control weightings. To aid in understanding the meanings of these weightings, they are being

interpreted in terms of classical control concepts. For example: it has been shown that shaping the state weighting is the same as using a dynamic compensator in the feedback loop; also shaping the control weighting is the same as using a roll-off filter in the feed forward loop. The major cost of using this method is the additional states required in the design model. For simple systems, this is no problem because the additional hardware needed for implementation is simple and increase in computational burden are minimal. For realistic space structures, however, the addition of states could require that some design states must be discarded for a realistic control design thus leading to loss in model information.

The researchers working this area are Drs. Siva Banda and Hsi-Han Yeh and Capt. Brett Ridgely of AFWAL/FIGC. Their telephone numbers are Area Code 513, 476-9077, 9083, and 9078 respectively. Their past and future publications are noted in References 1, 2, and 3.

Robustness of Multivariable Control Systems

In large space structures, there are a number of uncertainties that can impact the control system because they can't be anticipated and modelled during the control system design process. These uncertainties can be either in the spacecraft or plant that is being modelled or the environment in which the plant operates. Examples of these include plant parameter variations due to manufacturing, assembling and deploying in space; spacecraft dynamics either not modelled at all or not modelled well; on-board disturbances from power sources; structural deformations from unmodelled solar radiation gradients; space dust impact; sensor errors, etc. Robustness of the control system refers to the property of the closed-loop control system that allows it to tolerate these uncertainties without losing stability of the plant nor

allowing a degradation in plant performance. The objective of our program is to develop the technological fundamentals that will support the design of a robust multivariable control system. This includes the development of the tools to analyze and synthesis the control system and the techniques for applying these tools to the design process. The primary military need for robustness of the control system is the ability to operate autonomously, i.e., without continual monitoring by and adjusting through a network of satellite ground stations.

The robustness concept is not new. Classical controls engineers have been concerned with it since the beginning of control theory. Rather than calling it robustness, they called it feedback and used it to reduce the sensitivity of the system to both plant and operational variations. There is both stability robustness and performance robustness of a system – the AFWAL work has concentrated on stability robustness. This work uses singular values to analyze and test the robustness of the system. Several singular value robustness tests can be used; they are not equivalent and they do not imply that the resulting system is a practical system. These robustness tests are very conservative, which is related to the structure of the uncertainty. To reduce the conservatism of the test, norm-bounded test procedures are now being used to account for the structure of the uncertainty. This work is continuing; upon completion it will be applied to a practical structural space system.

The researchers working this area in AFWAL are the same ones noted above in the Reduced Order Control Theory section. Past publications in this area are listed as References 5-7.

Vibration Control of Flexible Space Structures

The objective of this Basic Research program is to design the structure

and its control system of a large space satellite to either eliminate structural vibration or reduce it to a desired level within a reasonable time span. Both active and passive means for vibrational control are being considered. The computation issues being addressed include the accurate dynamics modeling of the structure, modeling disturbances, the optimization of the structure for vibration resistance, and the development of control algorithms for large order systems. A matter of prime importance is the integration of a large order structural optimization with the algorithms for a closed-loop control system so that both can be used to effectively control the large order system. Arrangements are now being made to use the CRAY computer to support this work.

The payoff of this work will be the analysis techniques for synthesizing the algorithms for large order systems. An example of a system that will benefit from this work is space-based lasers where significant vibration or jitter reductions are required as well as precise pointing, slewing, and focusing.
The optimization of such a system using both active and passive means not only improves system effectiveness but also reduces the control input required.
The ability to solve linear optimal regulator problems of 100 state variables with between 50 to 100 actuators now exists in this program. This structural dynamics capability generates the state and control weighting matrices to solve either infinite time control problems, finite time control problems or control saturation problems.

The researchers working this area are Dr. V. B. Venkayya and Ms. V. A. Tischler, AFWAL/FIBR. Their telephone number is (513) 255-6992. Their publications are noted as References 8-10.

CONTRACTED SPACE-ORIENTED CONTROL ACTIVITIES

The work overviewed in this section both Exploratory Development (6.2) and

Advanced Development (6.3) programs which are now or soon will be under

contract. Even though many of the technical details of the work discussed is

generic in nature and can apply to a variety of systems, the emphasis here will

be on the application to large space structures. One program overviewed -

VCOSS I - has been completed; but since it forms the foundation for a follow-on

program - VCOSS II - it is included for completeness. The financial support

for the Exploratory Development programs is AFWAL; financial support for the

Advanced Development is AFSC/DL.

Large Space Structures Pointing and Shape Control

The Department of Defense has sponsored considerable work directed at

developing the analytical tools and techniques for understanding the dynamics

and control of large flexible space structures. These efforts have resulted in

a number of uncoordinated reports from a number of studies that include the

DARPA-funded ACOSS and AFWAL-funded VCOSS programs. Coupling this to the

extensive NASA technology activities in this same technology area indicates

that a rather large body of technical results exist that deals with the control

of flexible space structures. This program is directed toward bringing

together this state of knowledge in an orderly controls study to establish

procedures and tools for the preliminary design of control systems for flexible

space structures that have stringent slewing, pointing, shaping, and

vibrational control specifications.

The thrust of the program is to develop control algorithms for a large

space antenna of a type that could be used for surveillance or reconnaissance.

The structural design of the antenna was left to the contractor with the

requirements that it be realistic and that it meet the operational and accuracy requirements established by AFWAL. These requirements are rather arbitrary, being established primarily to test the control design so that (a) useable results for a range of spacecraft configurations would result and (b) the maturity and completeness of the state of the art of technology developments in areas of dynamics and control could be determined. In the program, the contractor is required to mathematically model the structure and structural dynamics of the antenna resulting from both the vehicle motions and the environmental disturbances, model these motions and disturbances, and develop algorithms for simultaneously slewing, pointing, shaping and vibrationally damping the structure. Using the noted foundation information, trade-off studies will be made to evaluate actuators and sensors to accomplish the control actions. These studies may lead to the establishment of performance specifications for control system hardware that are needed to control large flexible structures in space that exceed existing hardware capabilities. Other tradeoff studies to be done will examine the influence of disturbance extremes and the passive damping on control design using data from the PACOSS program. Application of robustness concepts will be included as well as an attempt to define an optimal control scheme for the antenna structure being studied.

The resulting program is 31 months long; it started in September 1983. General Dynamics, Convair Division is the prime contractor with H. R. Textron subcontracting to them. Figure 1 summarizes General Dynamics' viewpoint of the objective of the program. Although not accurate, the antenna shape shown is the type of antenna that has been modelled by them for study. The development of that model will be presented by John Sesak, Program Manager in the Control of Large Antennas session of the Workshop.[11] Figure 2 diagrammatically

describes the program. There are four tasks: model definition, control algorithms, tradeoff studies and documentation. The first task is being completed now: it prepares the structural definition of the antenna, its dynamic characteristics, and the mathematical models of the disturbances that result from the mission and environment. The second task will define the control system componentry and element placement and develop the candidate operational algorithms to meet the needs of the mission. The third task examines the influence of structural and control system variables on performance, seeking an optimal mix of passive and active control. The final task documents the results of the study. Figure 3 diagrammatically shows the interaction of the four elements of control being studied. This figure emphasized the significant interaction between pointing and vibrational control in a large flexible antenna structure such as this. For example, when the structure line of sight is changed, stopping this slewing motion - or using pointing control - causes the structure to vibrate due to the change in momentum of its members.

The AFWAL Project Engineer of this program is Capt Brett Ridgely, (513) 476-9078.

The Application of Robust Control Technology

to Large Space Antennas

This program is a new Exploratory Development program soon to be under contract to the Honeywell Systems Research Center. The objective of the program is to apply robust control technology to the large RF antenna being studied under the Large Space Structures Pointing and Shape Control program described above. The contractor will use the structural dynamics characteristics of the antenna model, the disturbance characteristics, and the

control requirements for slewing, pointing, shaping, and vibrationally controlling the model that General Dynamics has developed under Task 1 of that program (See Figure 2). This robust control program will provide practical analysis and design techniques for applying robust control techniques to a large space antenna. It will address critical issues of model reduction for robust control design for achieving performance and stability robustness, and for making control law simplification for design implementation.

The start of the program is keyed to the completion of Task 1 of the previously described program. The program period is 14 months in length so that the study results can fold back into the large space structures program before Task 3 of that program is complete.

The Project Engineer for this program is Dr. S. S. Banda, AFWAL/FIGC, (513) 476-9077.

Vibrational Control of Space Structures (VCOSS)

The VCOSS program consists of two efforts: VCOSS I having the above title and VCOSS II titled "Large Space Structure Vibrational Control". Although VCOSS I was completed in mid-1983, its results form the foundation for VCOSS II requiring that it be overviewed along with VCOSS II.

VCOSS I used the Draper Model 2 as a study configuration. Two contractors performed parallel studies: Lockheed Missiles and Space Company, Inc. and the Space and Technology Group of TRW. The objective of these studies was to apply modern control techniques and state-of-the-art sensor and actuator hardware concepts to actively control the vibration of the Draper Model 2 and compare the line-of-sight error and cost to a passive, stiffness oriented design. Inherent in this objective is the assessment of the characteristics of sensors and actuators, the placing them on the structure to gain their greatest

benefit, and the evaluation of the resulting mass loading on the structure.

As expected, the study results from each each contractor differed somewhat in specifics because they used different sensor/actuator suites, but they agreed in general. Both showed significant reductions in line-of-sight error through a closed-loop active control system. Both also showed that the power required and weight added by the active control system were a cost factor to be considered during preliminary design. As an example of the results, the control system hardware chosen by TRW for their control system design is summarized in Figure 4 and the locations of only the control devices are shown in Figure 5.

Both contractors differed in the number and type of sensors and actuators used and their location on the study structure. VCOSS A by LMSC used HAC/LAC hardware implementation[12] and VCOSS B by TRW used momentum exchange and truss damping control hardware[13]. Both selected hardware as well as sensor and processor hardware that was compatible with their control implementation. Actually these differences added value to this Exploratory Development program in that they illustrated that different implementation techniques and analysis philosophies can be used to control a flexible structure. The overriding conclusion common to both was that much larger reductions in LOS error can be achieved through rather simple active control systems than can be achieved by structural stiffening. The AFWAL Project Engineer on the VCOSS I study was Mr. Jerome Pearson, AFWAL/FIBG, (513) 255-5236.

To test the conclusions achieved during VCOSS I, a program was planned that would compare the predicted to the measured influence of active control on a realistic space structure. This program is now under contract to the TRW Spacecraft Engineering Division and is called Large Space Structure Vibration

Control - VCOSS II. The test model to be used is the Astromast suspended arrangement located at the NASA Marshall Space Flight Center. It includes the mast and an offset feed parabolic antenna (Figure 6). The Astromast has the same design as the masts flown on Voyager and Mariner Satellites. Although Figure 6 shows the mast suspended by a cable from a tripod with the Advanced Gimbal System (AGS) below the mast, the most current test configuration inverts this arrangement suspending the mast from the AGS rather than from the cable - a change that simplifies the dynamics of the mast. The objectives of VCOSS II are twofold: 1) to develop and optimize the sensor and actuator combinations for application to a test structure, and 2) to assess the adequacy of the analytical models for control system design by comparing experimental results to analytical predictions.

The issues to be addressed during this program are those that are common to the design of either a spacecraft or a test arrangement. These include the technique to be used for the test, sensor sensitivity and saturation, actuator, nonlinearities such as friction, etc. (Figure 7). The payoff of this type of test program is that is should verify the analysis and modelling techniques used, showing ways to improve our ability to model the structure and develop control algorithms. In the long run, this should yield greater control accuracy for flexible large space structures contributing to the design of lower-weight structures. The AFWAL Project Engineer for the VCOSS II program is Maj Hugh Briggs, (513) 255-2543.

<u>Passive and Active Control of Space Structures (PACOSS)</u>

PACOSS is the only Advanced Development (6.3) program to be overviewed. The objective of the program is to generically demonstrate dynamic dimensional control - or damping - in a large flexible space structure. The contractor for

the program is Martin-Marietta Denver Aerospace. The approach to the program is to design for subwavelength structural precision two 60-foot long flexible trusses having different levels of damping. These are fabricated in three 20-foot long sections having aluminum primary beam elements. The selective use of plexiglas tube diagonal members and discrete dampers in the five lowest truss bays provide the different levels of damping. The various damping levels that can be tested include low damped and high damped configuration both with and without discrete dampers. This allows four different levels of damping for the tests without control.[14] The intent is to design a control system configured to the structures with different levels of damping and evaluate the performance versus weight and power required for control to yield a measure of merit with and without the various levels of damping. First, however, before a control system is designed, the two trusses with the different levels of damping will be thoroughly tested to determine whether the calculated results of damping are achieved.

It is expected that a 90-percent reduction in jitter and a 50-percent reduction in settling time can be achieved through damping. For an optical satellite, this would provide a faster retarget time and a shortened time on target with decreased system complexity (Figure 8).

In summary, the PACOSS program is studying a low frequency, large flexible precision space structure with closely spaced structural dynamic modes. The program will develop the maximum feasible damping without control for this structure. Testing will be performed on the uncontrolled configuration to determine the structural response with various levels of damping to a vibratory disturbance. The tested configuration will then be used as the basis for designing an optimal mix of passive and active control (Figure 9). During the

27

period of February 27-29, 1984, the AFWAL sponsored the Vibration Damping Workshop at Long Beach, CA. During this Workshop, the state-of-the-art of structural damping were discussed as well as the status of Air Force funded contracts on the Damping Design Guide, PACOSS and Reliability of Satellite Equipment in a Vibroaconstic Environment (RELSAT) were reviewed.

The AFWAL Project Engineer for the PACOSS program is Dr. Lynn Rogers, AFWAL/FIBA, (513) 255-5664.

SUMMARY

The foregoing is an overview of the AFWAL activities that are relevant to the workshop topic of identification and control of flexible space structures. The method of carrying out this work is interdisciplinary with the Flight Control and Structures and Dynamics Divisions working closely together on the various technology efforts. The work is supported or funded by all three of the areas worked by AFWAL: Basic Research, Exploratory Development and Advanced Development. Hence, the work covers the spectrum from the very fundamental analytic research level to the fabrication and testing of large structures. No attempt has been made to present details of the work being done; rather, only sufficient information is provided to tell the reader the who, what and why of each program. In all cases, the people performing and/or managing the work are cited along with their AFWAL symbol and telephone number. Contacting them will provide details to whatever depth the reader desires.

Not all the space-oriented dynamics and control work in AFWAL has been overviewed. Work is either in planning or underway on technologies applicable to the control of vehicles categorized under the Advanced Military Spaceflight Capability (AMSC) activity and the Transatmospheric Vehicle (TAV). This work differs from that overviewed because the structures are more rigid and some of

the vehicles are planned to be manned. Air data sensor work has been supported in the past and is planned for future support to measure real gas densities in the region near the outer reaches of the atmosphere for use in control system gain computations for maneuvering of an AMSC/TAV. Linear actuator development for application to either large space structures or AMSC-type spacecraft is also underway. If information is desired on any of the work not overviewed, contact the author at AFWAL/FIGC, (513) 476-1075.

REFERENCES

1. D. B. Ridgely, S. S. Banda and D. V. Palmer, "Reduced Order Control Design Benefits and Costs of Frequency-Shaped LQG Methodology" AIAA Guidance and Control Conference, Gatlinburg, TN, 15-17 August 1983.

2. S. S. Banda, D. B. Ridgely and H. H. Yeh, "Robustness of Reduced Order Control ", Fourth VPI and SV/AIAA Symposium on Dynamics and Control of Large Structures", Blacksburg, VA, 6-8 June 1983.

3. S. S. Banda, D. B. Ridgely, H. H. Yeh, and D. V. Palmer, "Design and Robustness Analysis of Reduced Order Controllers for Large Flexible Space Vehicles", AGARD Symposium on Guidance and Control Techniques for Advanced Space Vehicles", Florence, Italy, 27-30 September 1983.

4. H. H. Yeh, D. B. Ridgely and S. S. Banda, "Nonconservative Evaluation of Uniform Stability Margins of multivariable Systems", AIAA Guidance and Control Conference, Seattle, WA, 20-22 August 1984.

5. R. K. Yedaralli, S. S. Banda and D. B. Ridgely, "Time Domain Analysis of Stability Robustness of Large Scale LQG Regulators", AIAA Guidance and Control Conference, Gatlinburg, TN, 15-17 August 1983.

6. H. H. Yeh, S. S. Banda and D. B. Ridgely, "Stability Robustness Measures Utilizing Structural Information", American Control Conference, San Diego, CA, 6-8 June 1984.

7. H. H. Yeh, S. S. Banda, and D. B. Ridgely, "Regions of Stability for Gain or Phase Variations in Multivariable Systems," submitted to 23rd Control Design Conference, Las Vegas, NV, 12-14 Dec 84.

8. D. F. Miller, B. R. Todd, W. R. Wells and V. B. Venkayya, "Structural Vibration Suppression: A Problem in Combined Structural and Control Optimization", SECTAM-XII Conference, Calaway Gardens, GA, May 10-11, 1984.

9. V. B. Venkayya and V. A Tischler, "Frequency Control and the Effect on the Dynamics Response of Flexible Structures" AIAA/ASME/ASCE/AHS Structures, Structural Dynamics and Materials Conference, Palm Springs CA, 14-18 May 84.

10. N. S. Khot and V. B. Venkayya, "Structural Modifications to Reduce LOS Error in Space Structures" AIAA/ASME/ASCE/AHS Structures, Structural Dynamics and Materials Conference, Palm Springs, CA, May 14-18, 1984.

11. J. Sesak, "Model Development for Spacecraft Pointing and Shape Control", Workshop on Identification and Control of Flexible Space Structures, San Diego, CA, June 4-6, 1984.

12. Vibration Control of Space Structures - VCOSS A: High and Low-Authority Hardware Implementations, AFWAL-TR-83-3074, Lockheed Missiles and Space Company, Inc., July 1983.

13. Vibration Control of Space Structures - VCOSS B: Momentum Exchange and Truss Damping, AFWAL-TR-83-3075, TRW Space and Technology Group, July 1983.

14. C. W. White and G. Morosow, "Passive and Active Control of Space Structures", Vibration Damping Workshop, Long Beach, CA February 27-29, 1984.
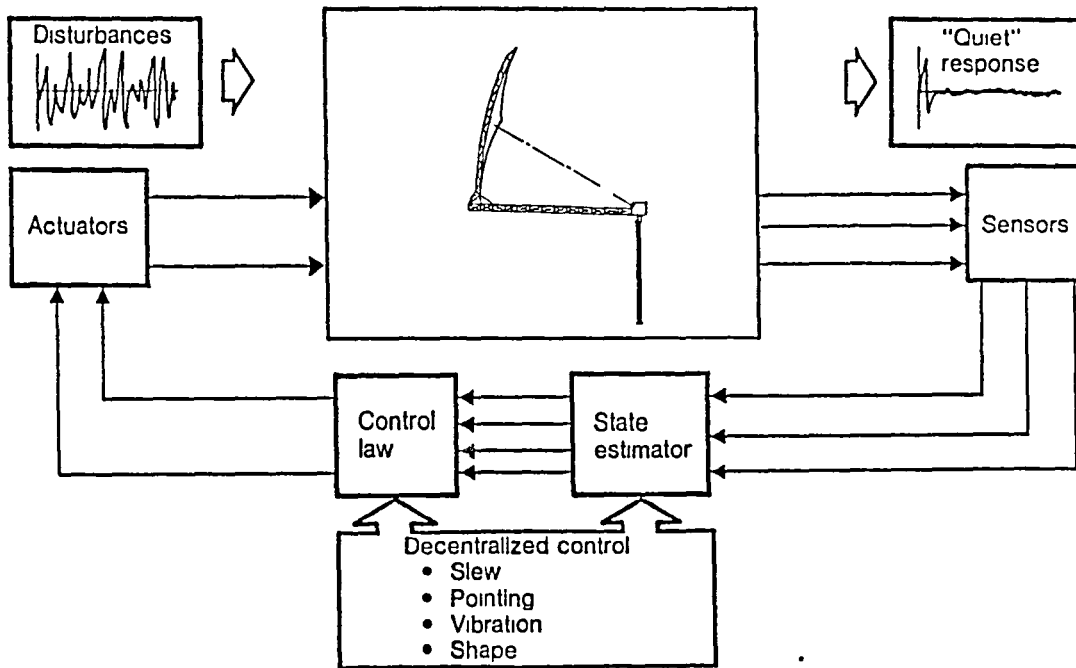
Figure 1. Large Spacecraft Pointing and Shape Control Program Objective
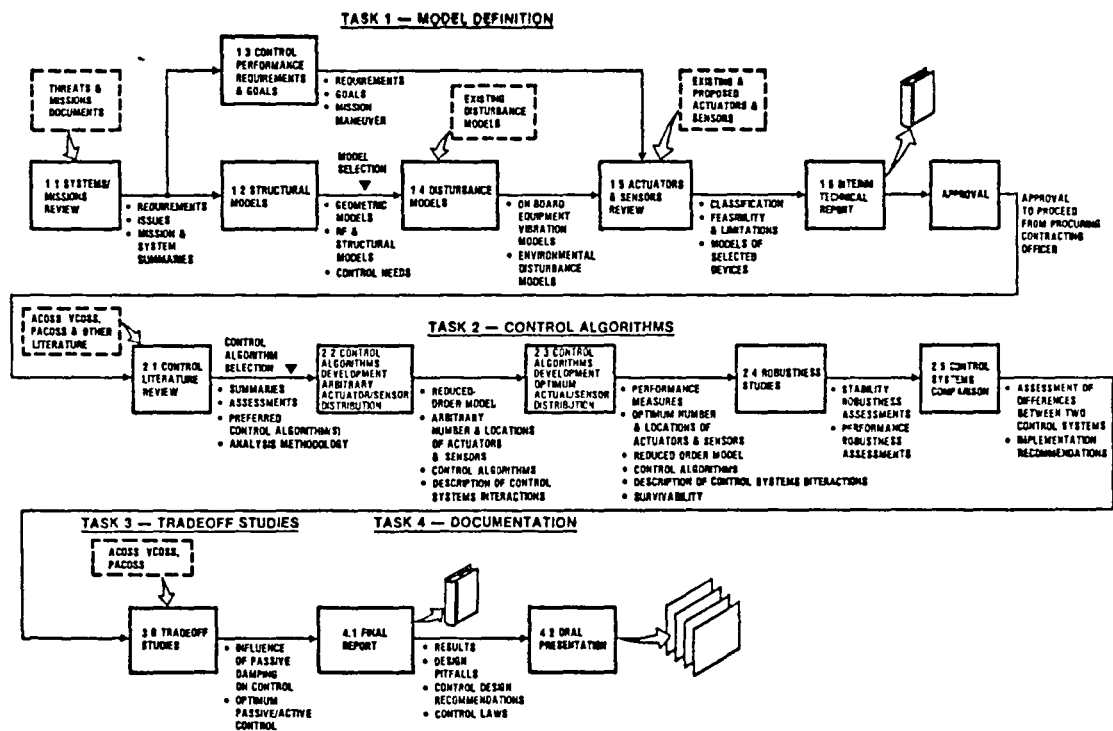
Figure 2. Overall Study Plan for Program
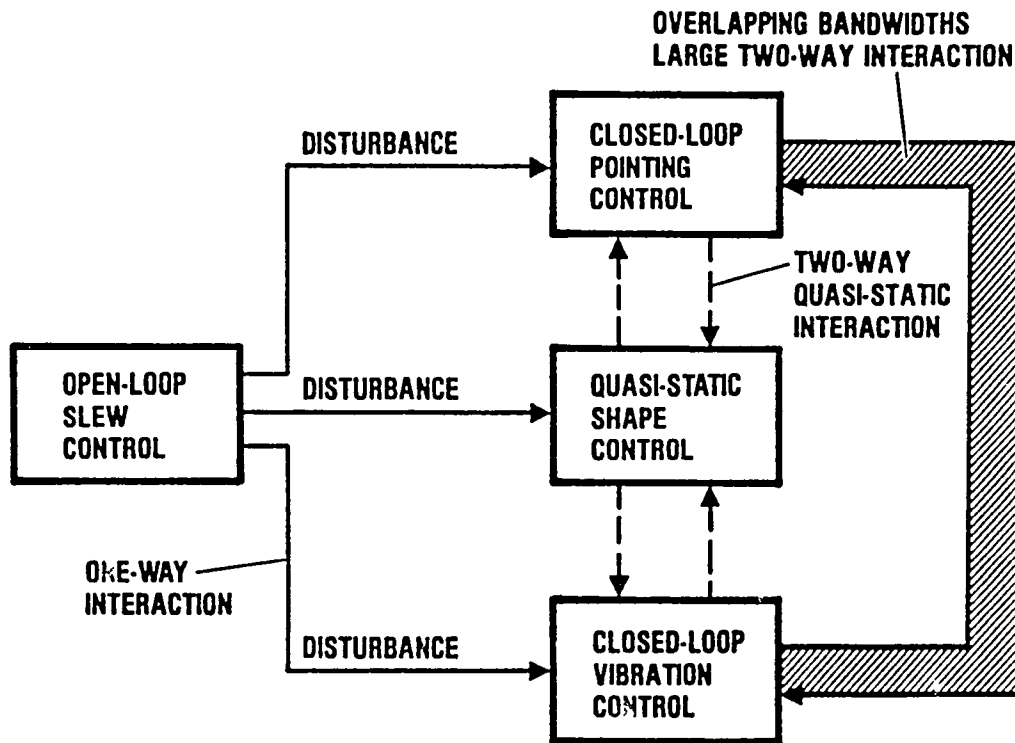
Figure 3. Control Subsystem Interaction for LSS

RESULTS - TRW

SUMMARY OF SELECTED HARDWARE

CONTROL APPROACH	TYPE OF ACTUATOR	NO. REQD	TYPE OF SENSOR	NO REQD	TYPE OF ELECTRONICS	NO. REQD
TRUSS DAMPENING	ELECTROMAGNETIC (KIMCO LA20-26)	12	ELONGATION (TRW F 0 INTER- FEROMETER)	12	HYBRID	12
MOMENTUM EXCHANGE	ELECTROMAGNETIC (KIMCO LA40-52)	8	ACCELEROMETER (SUNDSTRAND QA-2000)	8	ANALOG	8
ISOLATION CONTROL	ELECTROMAGNETIC (KIMCO LA 20 26)	8	ANGULAR DISPLACEMENT (TRW TAS)	8	MICROPROCESSOR	1
			ACCELEROMETER (SUNDSTRAND QA-2000)	4		

Figure 4. VCOSS I Results - Control System Hardware

33

RESULTS - TRW

CONTROL DEVICE LOCATIONS

9 - STRUCTURE ISOLATOR
    CONTROLS
12 - TRUSS DAMPENING
    CONTROLS
8 - MOMENTIUM EXCHANGE
    DEVICES

CONTROLLED
STRUCTURE

SOLAR
PANELS

CONTROL
DIRECTIONS

EQUIPMENT SECTION
(DIRTY BOX)
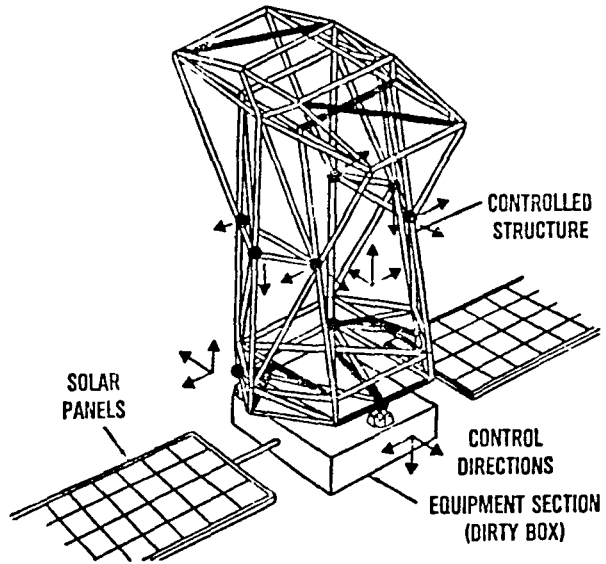
Figure 5. VCOSS I Results - Control Device Locations

VCOSS II MODIFICATION

TRIPOD
AIR BEARINGS

3 DOF ANGULAR RATE SIGNALS
3 DOF TRANSLATION SIGNALS
4 INSTRUMENT STATUS CHECKS

CONSTANT TENSION
CABLE

① 3 AXIS ACCELS
   AND RATE GYROS
② 3 AXIS RATE GYROS
③ 3 AXIS ACCELS
④ TRANSLATIONAL
   ACTUATOR
⑤ AZIMUTH ROTATION
   BASE PLATE

3 DOF ANGULAR RATE
SIGNALS

3 INSTRUMENT STATUS
CHECKS

PARABOLIC ANTENNA

3 GIMBAL ACTUATOR
SIGNALS

3 INSTRUMENT STATUS
CHECKS

ENGINEERING AGS

AZIMUTH ACTUATOR

HP 9845C   COSMEC
              1

SYSTEM CONSOLE
POWER SUPPLY
GIMBAL TORQUER AMPS
SYSTEM HEALTH MONITOR

3 DOF TRANSLATION SIGNALS
1 INSTRUMENT STATUS CHECK

AIR BEARINGS

Figure 6. VCOSS II - Program Test Setup

34

- **TECHNICAL ISSUES**
  - LAB TESTING TECHNIQUES
  - SENSOR SENSITIVITY AND SATURATION
  - ACTUATOR STICTION
  - SENSOR / ACTUATOR / STRUCTURE INTERACTIONS
  - CONTROL ALGORITHMS

- **PAYOFFS**
  - LAB CONFIRMATION OF ANALYTIC STUDIES
  - IMPROVED DYNAMIC MODELING
  - IMPROVED CONTROL ALGORITHMS
  - LIGHTER SPACE STRUCTURES
  - GREATER ALIGNMENT ACCURACY

- **GROWTH POTENTIAL**
  - SPACE SHUTTLE TEST
  - DISTRIBUTED CONTROL OF RELECTING SURFACES
  - IMPROVED ADAPTIVE CONTROL ALGORITHMS

Figure 7. VCOSS II – Program Specifics
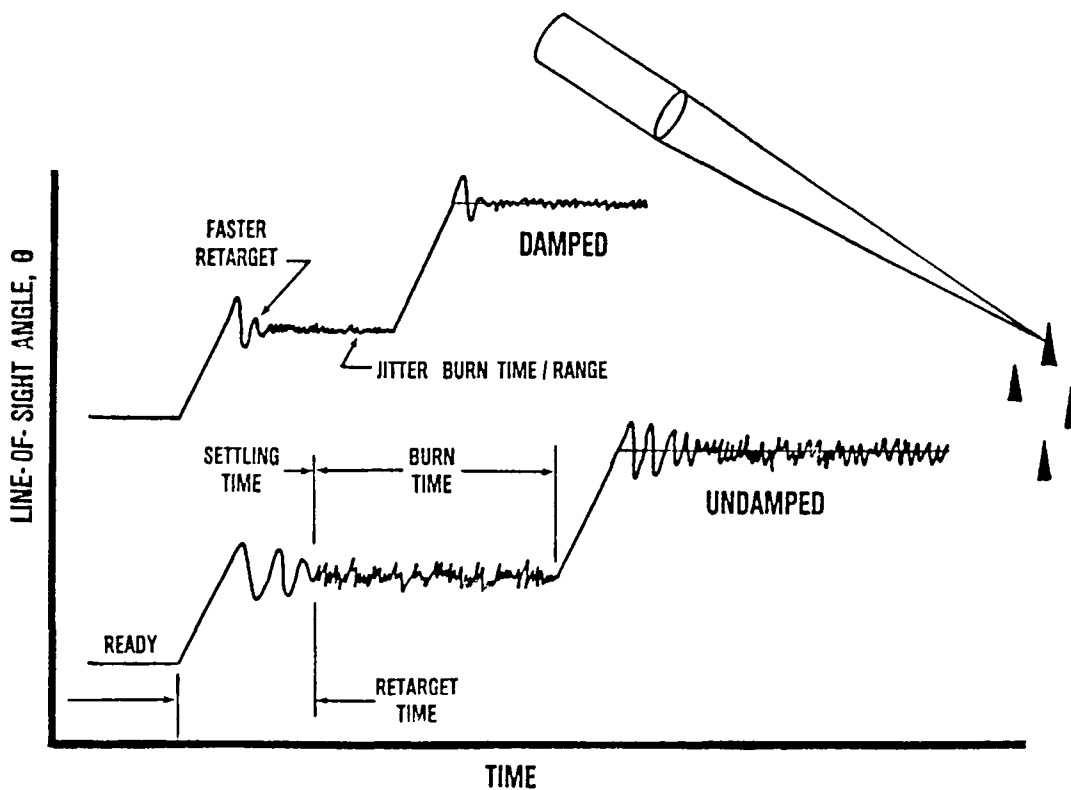
Figure 8. Payoff of Damping

35

- ADDRESS LOW FREQUENCY, CLOSELY SPACED MODES OF LARGE FLEXIBLE PRECISION SPACE STRUCTURE

- DEVELOP MAX PASSIVE DAMPING FEASIBLE

- SELECT OPTIMUM MIX OF PASSIVE AND ACTIVE CONTROL

- TEST FOR IDENTIFICATION, TRANSIENT AND JITTER

Figure 9. Summary of PACOSS Program

MULTIVARIABLE CONTROL OF A SOFT COUPLED SPACE STATION

J. W. Sunkel
NASA Johnson Space Center
Houston, TX 77058

A. F. Hotz
Purdue University
West Lafayette, IN 47907

Abstract

The paper discusses a multivariable controller design for a control configured space station concept. The space station concept is novel in that mechanical filters (soft couplers) are used to reduce structural interaction between adjacent modules. The primary objective of this study is to provide stability augmentation to the soft coupled configuration. The control objective is achieved by a state feedback compensator design. To obtain the desired feedback gains, a modified LQR technique is developed which provides prescribed close-loop frequencies and damping ratios.

Introduction

One prevailing concept of Space Station is that of a collection of individual modules linked by docking tunnels. An abundance of available solar power makes large solar arrays attractive as a power source. As the capability grows there will be a need for satellite servicing facilities, propellant storage tanks, orbital transfer vehicle hangars, construction sites, payloads dedicated to materials processing and other structural entities requiring attachment to the Space Station.

It is difficult to predict the size, shape, or form that will evolve throughout this growth process. Predicting changes in the structural dynamics of the complete configuration, after the rigid attachment of a new module, will be extremely difficult. Furthermore, due to the absence of high strength requirements, the resulting flexible body dynamics will include many bending modes within the frequency spectrum required for rigid body control.

The concept of a control configured spce station was developed to deal with this interaction. The concept uses mechanical filters for decoupling those degrees of freedom requiring control from structural bending dynamics, thereby simplifying the dynamics model required for control system design. A deailed development of this concept is presented in Reference 1.

This paper presents a possible control system design for providing stability augmentation and shape control to the Space Station.

Space Station Model

The aerospace community has been studying the construction of a permanently manned Space Station for some time. Studies at the Johnson Space Center have considered several Space Station candidates. The configuration considered here is modular. Under this concept, an initial Shuttle launch would deliver a "power module", consisting of large solar arrays deployed at the ends of two long booms. These booms are attached to a core module that contains batteries, power conditioning equipment, a reaction control system and thermal control system. Subsequent launches would add "habitat modules" which serve as multi-purpose crew quarters, laboratories and command post. Later flights would then bring propellant storage tanks, OTV hangers and other similar facilities.

The five body configuration shown in Figure 1 was chosen as a baseline for this study. This is the same model used in Reference 1.

As shown in Figure 1, the habitat modules and solar arrays are connected to the central power module by "soft couplers". The soft coupled connection points act as filters which prevent significant coupling of bending modes between adjacent modules. The soft coupling concept is illustrated by a simple example in Appendix A.

Each soft coupled joint has six springs which allow relative translational and rotational motion between adjacent modules. With four soft joints, each having six "spring constants", there are exactly as many coupler design parameters as there are coupled cluster bending modes; i.e. 24 for our case. (The word "cluster" is used here to signify a collection of individual modules linked by soft couplers.) For the present study, the flex properties of the individual modules and solar panels have been neglected. Using a symmetrical Space Station model and imposing symmetry constraints on the coupler devices, however, reduces the number of independent spring constants to 12. A detailed description of the approach used to obtain the coupler spring constants is given in Ref. 2. The approach taken obtained a set of coupler spring constants compatible with specified properties of the coupled cluster mode frequencies. The choice of

a frequency interval in which to place the coupled cluster mode frequencies is based on the following considerations

1. An adequate (about two octaves) gap in the frequency spectrum between the highest cluster mode frequency and the lowest free-free mode frequency of any module. For example, a first free-free mode frequency of 2.0 Hz would define 0.5 Hz as the upper bound for cluster modes.

2. A lower bound set by maximum deflections allowed due to attitude change maneuvers, reboost accelerations, and docking impulses.

3. A "reasonable" frequency interval between the cluster modes. For example, if the upper bound is 0.5 Hz and we can tolerate a first cluster mode of 0.05 Hz (based on item 2), then the interval $0.05 \leq \omega \leq 0.5$ Hz would define the frequency cluster interval.

Based on the above considerations, Ref. 1 proposes a cluster mode frequency spectrum in the interval $.02 \leq \omega \leq .3$ Hz. It is felt that this interval should provide adequate separation between the cluster mode frequencies and the lowest free-free modes of the Space Station core modules. It has also been assumed that the solar array support structure is fairly rigid and that the lowest free-free bending mode is well above the cluster mode frequencies.

It is likely some solar array low frequency blanket modes may fall within the cluster mode interval. This situation is of some concern. While it is unlikely that these modes would contain sufficient energy to induce motion at the core modules, they may be subject to excitation by the control system during maneuvers or stability augmentation. Possible remedies include stiffening the solar arrays through structural bracing or possibly a reduction in the cluster mode frequencies.

Space Station Control Model

As outlined in the previous section, the baseline Space Station model consists of five rigid bodies connected by soft coupler springs. Referring to Figure 1, bodies 1 and 3 are combination crew habitat/command/laboratory modules which are both softly connected to body 5. Bodies 2 and 4 represent solar arrays which are softly connected to the booms. We have assumed that the soft connectors between body 5 and bodies 1 and 3 are identical. Likewise, the connectors between body 5 and bodies 2 and 4 are identical.

The mass properties and geometric properties of the Space Station model are given in Table 1.

The rigid and oscillatory motion of the Space Station is characterized by 30 separate modes. The mode frequencies which resulted from the coupler spring design process described above are summarized in Table 2.

As previously mentioned, it is assumed that the structural bending dynamics of the individual modules and solar panels are beyond the soft-coupler passband. This remains to be verified, particularly as far as the solar panels are concerned.

The equations of motion are written for each body with respect to a coordinate system located at the center of gravity of the entire configuration. The coordinate system is shown in Figure 1. In this study we are primarily interested in the relative motion between the modules. From Table 2 it is clear that the cluster frequencies are small compared to an orbiter period, hence we have assumed the coordinate system to be fixed in intertial space and have ignored terms due to orbital motion. The resulting equations of motion for each body are given in Appendix B.

Space Station Control System

Routine Space Station operation will require multi-functional controllers capable of such tasks as attitude control, stabilization, shape control and station keeping. Though each of these control tasks suggests an autonomic control system structure, such designs are operationally burdensome and assume sensor and hardware prodigality. Furthermore, control designers attempting integrated controller designs are often faced with contradicting design requirements dictated by multi-control task specifications or by hardware considerations.

The primary control functions required for the Space Station configuration described herein are attitude control for the entire soft-coupled cluster and stabilization of all cluster modes. However, restrictions in the number and placement of control effectors on the structure, and, in particular, the inability to locate effectors on the solar panels, preclude the ability to simultaneously maneuver the structure and provide damping forces to the cluster modes[1]. From an operational viewpoint then, possible slew strategies include a concatenation of small maneuvers of moderate slew rate interrupted by intervals of stability augmentation or maneuvers with small slew rates that reserve stability augmentation until the maneuver is complete. Figure 2 illustrates a possible controller structure. The design strategy considered here separates the stability augmentation task from that of attitude control; moreover, the controller design presented here is confined to only the stability augmentation system.

Effector/Sensor Considerations

The achievable performance of the stability augmentation system is greatly influenced by the type, number and location of the control effectors and sensors. These considerations are often quantified in terms of the system observatility and controllability characteristics. If the motion of all the model states can be detected by the sensors

38

and the energy in each state can be altered by the control effectors then the system is said to be completely observable and completely controllable. Though these concepts are fundamental to the controller design, they are not always a design degree of freedom. The configuration of the physical system often defines the allowable locations of sensor/effector hardware and thus determines the controllability and observability characteristics of the system.

For the Space Station configuration considered here, it is doubtful that the solar panels (due to their fragile composition) could sustain direct application of control forces. Hence, the panels must be controlled by effectors on the core modules. It is assumed that all control effectors are confined to bodies 1, 3 and 5. Moreover, it is assumed that only torque effectors (CMG's along all 3 axes) are available and their placement is such that the resultant control forces are torques about the c.g.'s of bodies 1, 3 and 5.[2]

Though it is unlikely that control effectors would be located on the solar panels it is not unreasonable to assume that sensor packages (accelerometers and rate gyros) could be attached to the support structure.[3] Here we assume that the rates and displacements at the c.g. of each body (module) may be measured or derived. The location of all sensors and effectors are shown in Figure 3. Using this sensor/effector configuration, the cluster dynamics for the entire configuration is completely observable, however, only 16 of the 24 cluster modes are controllable. Table 3 details the controllability properties that result from this effector configuration.

It should be noted that the proposed sensor/effector configuration is preliminary and makes no claim of optimality or frugality. Practical considerations such as sensor/effector dynamics, component failure, etc. were not included in this study and may suggest a different configuration.

STABILITY AUGMENTATION SYSTEM DESIGN

Requirements and Objectives

The use of mechanical filters as a coupling mechanism between the Space Station and components significantly reduces the controller design requirements by allowing precise modeling definition of the structure in the frequency region where control authority is required and by preventing significant structural interaction between the components. Hence highly complex controllers incorporating spillover suppression schemes (3-5) and other such devices for coping with modeling error, control limitation and excitation transmission are unnecessary.

As discussed in the earlier sections, the soft-coupled design concept allows substantial freedom in designing the frequency spectrum of the structure. Intelligent exploitation of this freedom permits a frequency spectrum consisting of a finite set of well defined low frequency modes well separated from an infinite set of lessor defined higher frequency modes. The low frequency set results from the spring-mass dynamics (cluster modes) and defines the frequency region of required control influence. The higher frequency set results from the structural bending dynamics of the cluster modules. Since the cluster mode shapes are determinate, and assumed to be acceptable, then the crux of the stabilization problem is to add active damping to the cluster modes. Furthermore, damping of the relative motion between the cluster modules requires that the control frequencies lie within the frequency spectrum of the soft-couplers. This requirement can be achieved by damping the cluster modes while leaving their frequency unchanged. The mechanical filters shape the roll-off characteristics of the controller and prevent transmission of any high frequency controller residuals to the modules (see Figure 4).

In summary, the primary conmtroller requirement of this study is to provide stability augmentation to the Space Station structure. The controller design objective is to add damping to the cluster modes without altering their frequency spectrum.

Techniques

The settings for most control designs are dictated by the system model, environment, control objectives and hardware limitations. Because these settings vary greatly, the straightforward application of many of the available multivariable control design techniques often result in unsatisfactory controllers.

Modal Dashpot (6-7) or Pole Placement (8-11) methods often result in prohibitively high gain controllers or in controllers that exhibit unsatisfactory transient responses. Such undesirable controller by-products are explicitly addressed in Linear Quadratic Synthesis techniques (12-13) were the desired responses and control characteristics

---

[1]The incorporation of electromechanical actuators in the soft coupler devices would eliminate this malady. However, the availability of such devices is not assumed here.

[2]This could be achieved by either a single CMG at the c.g. or by an appropriately distributed set about the c.g.

[3]It is assumed that very little bending occurs in the solar panels support structure and that the sensor information contains only the rigid body dynamics of the panels.

are reflected in tne weighting matrices of a cost functional. Unfortunately, determination of the proper weighting matrices to satisfy the control objectives here is difficult. Ref. (14) describes a procedure for computing the required state weighting matrix corresponding to a prescribed set of closed loop eigenvalues, given the control weighting matrix. The procedure as posed though, does not allow arbitrary eigenvalue assignment for all controllable modes. Ref. (15) generalizes the technique of (14) and allows complete eigenstructure assignment. The procedure employed here reformulates the procedure in modal corrdinates.[4] The modified LQR procedure computes tne proper weighting on each mode to yield the desired closed loop modal frequencies and damping ratios given the control penalty for each actuator. Clearly the ability to prescribe closed loop frequencies and damping ratios is beneficial to satisfy the control objectives discussed earlier.

Control Model and Controller Formulation

Linear Quadratic techniques generally result in high bandwidth controllers. In fact, the frequency response of LQ controllers not incorporating frequency shaping techniques is determined by the actuator response characteristics. However, here the mechanical filters confine the controller bandwidth to the frequency region of the cluster modes and insure isolation of the higher frequency modes from any controller residuals.

We consider then the linear, time-invariant control model,

$$\dot{X}_c = A_c X_c + B_c U$$

$$Y_c = X_c$$

where X_c and U are vectors and A_c and B_c are matrices defining the cluster dynamics (see Appendix B).

Using the transformation,

$$X_c = T Z_c$$

where T is the modal matrix of the system in the state vector form, the transformed model becomes,

$$\dot{Z}_c = \Lambda_c Z_c + B_c U$$

$$Y_c = T Z_c$$

where

$$\Lambda_c = \text{diag}\left\{ \begin{bmatrix} 0 & 1 \\ -\omega_1^2 & -2\zeta_1\omega_1 \end{bmatrix}, \cdots, \begin{bmatrix} 0 & 1 \\ -\omega_n^2 & -2\zeta_n\omega_n \end{bmatrix} \right\}, \quad \bar{B}_c = T^{-1}B_c$$

and $Z_c^T = \begin{bmatrix} \eta_1, \dot{\eta}_1, \eta_2, \dot{\eta}_2, \cdot, \eta_n, \dot{\eta}_n \end{bmatrix}^T$

---

[4]This coordinate system is not to be confused with diagonal form which is often called "modal coordinates". The modal coordinate system is defined in a later section.

Here we note that the open loop modal frequency and damping ratio terms for each mode (ω_i, ζ_i) are explicit in the transformed equations and that the modal state vector consists of modal displacement, η, and modal velocity, $\dot{\eta}$.

We seek a control law,

$$U = \bar{G} Z_c = \bar{G} T^{-1} X_c$$

to provide damping to the cluster modes without altering the cluster mode frequencies. Alternately, we desire a set of feedback gains, $\bar{G}$, that yield a prescribed set of closed loop modal frequencies, ω_d, and damping ratios, ζ_d.

It is well known that LQR techniques result in a constant gain control law,

$$U = GX$$

which minimizes the cost functional,

$$J = \frac{1}{2} \int_0^\infty (Y_c^T Q Y_c + U^T R U) \, dt$$

where,

$$\dot{X} = AX + Bu$$

$$Y = CX$$

and the weighting matrices Q & R reflect the desired closed loop response characteristics. As noted earlier, though, the quantitative relationship between the closed loop eigenvalues and the elements of Q and R is not clear.

Appendix C develops simple relationships between the modal state weighting elements and the desired closed loop modal properties.

In particular, consider the cost functional,

$$J = \frac{1}{2} \int_0^\infty (Z_c^T \bar{Q} Z_c + U^T R U) \, dt$$

where,

$$Z_c^T = \begin{bmatrix} \eta_1, \dot{\eta}_1, \ldots, \eta_n, \dot{\eta}_n \end{bmatrix}, \quad R = \text{diag}\begin{bmatrix} r_1, \ldots, r_n \end{bmatrix},$$

$r_i \epsilon R$ = the control penalty on the ith effector and $\bar{Q} = \text{diag}[q_{d1}, q_{v1}, \ldots, q_{dn}, q_{vn}], (q_{dj}, q_{vi}) = $ weighting on the modal displacement and modal velocity for the ith mode. The desired closed loop modal damping, δ_{di}, and desired closed loop modal frequency, ω_{di}, for the ith mode is obtained by penalizing the modal displacement and modal velocity states of the ith mode by,

$$q_{d_i} = \frac{\omega_{d_i}^4 - \omega_i^4}{h_{ii}}$$

40

and

$$q_{v_i} = \frac{2(\omega_i{}^2 - \omega_{d_i}{}^2) + 4(\zeta_{d_i}^2 \omega_{d_i}^2 - \zeta_i^2 \omega_i^2)}{h_{ii}}$$

where $h_{ii} \in \bar{B} R^{-1} \bar{B}^T$ as described in Appendix C.

Since it is desired that $\omega_{d_i} = \omega_i$ for each mode and if we assume that the soft couplers provide no appreciable damping to the structure, $\zeta_i = 0.$, the weighting terms reduce to,

$$q_{d_i} = 0$$

and

$$q_{v_i} = 4 \zeta_{d_i}^2 \omega_i{}^2 / h_{ii}$$

The above weighting will obtain the desired frequency and damping ratio for the ith mode. The gain matrix and new system matrix are computed as shown in Appendix C. The procedure is repeated for each mode and the feedback gain matrices are summed to yield the final result. This procedure obtaining the total feedback gain is detailed in (14).

The resulting controller, in physical coordiantes,

$$u = GX_c$$

yields the desired closed loop characteristics.

Controller Sensitivity

In recent years the design of controllers tolerant to uncertainties in the system model has been the subject of intense research [16-20]. Model uncertainty can generally be subdivided into two classes, structured and unstructured [19]. The uncertainties considered here are highly structured and easily parameterized. Specifically, it is clear that deviations in the soft-coupler properties will occur (aging, heating/cooling, etc) and cause variations in the open loop modal frequencies. Though it is unlikely that these variations will be large, small deviations in the open loop frequencies may result in large changes in the closed loop system frequencies. Clearly, the incurrence of the control frequencies beyond the passband of the soft-couplers is of concern.

It is well known that LQ controlleres using full state feedback exhibit good robustness properties [21-22].

The following Lemma presents simple expressions that result from the LQR design procedure relating variations of the closed loop modal frequencies and damping ratios to deviations in the open loop modal frequencies.

Lemma

If the open loop frequency of the ith mode, ω_i', deviates from the nominal value, ω_i, by,

$$\omega_i' = (1 + K) \omega_i \;, \; K > -1.0$$

then the corresponding variations in the closed loop modal frequency, ω_{cLi}, and damping ratio, ζ_{cLi}, for the ith mode are given by,

$$\omega_{cLi} = (1 + K) \omega_i$$

$$\zeta_{cLi} = \zeta_{NCL}/(1+K), \; NCL = \text{NOMINAL CLOSED LOOP}$$

Proof

From the Appendix C, it is shown that the closed loop characteristic equation for the ith mode is given by,

$$s^4 + (2\omega_i'^2 - 4\zeta_i^2 \omega_i'^2 - q_{v_i} h_{ii}) s^2 + (\omega_i'^4 + q_{d_i} h_{ii}) = 0. \quad ①$$

If we assume,

$$\zeta_i = 0, \text{ and define } \omega_{cL_i} = \omega_i \quad ②$$

where ω_i is the nominal open loop frequency,

then,

$q_{d_i} = 0$ and $q_{v_i} = 4 \zeta_{NCL_i}^2 \omega_i{}^2$ where ζ_{NCL_i} is the specified nominal closed loop damping ratio.

Let,

$$\omega_i' = (1 + K) \omega_i \; , \; K > -1 \quad ③$$

and using ② & ③ in ① yields,

$$s^4 + \{ 2 (1 + K)^2 \omega_i{}^2 - 4\zeta_{NCL_i}^2 \omega_i{}^2 \} s^2 + \{(1 + K)^4 \omega_i{}^4\} = 0. \quad ④$$

Factoring ④ yields,

$$(s^2 + 2\zeta_{NCL_i} \omega_i s + \omega_i{}^2 (1 + K)^2)(s^2 - 2\zeta_{NCL_i} \omega_i s + \omega_i{}^2 (1 + K)^2)$$

from which,

$$\omega_{cL_i} = (1 + K) \omega_i \text{ and } \zeta_{cL_i} = \frac{\zeta_{NCL_i}}{1+K}$$

Some Results and Simulations

This section presents some time reponses for the feedback design summarized in Table 4. As we are interested only in the performance of the stability augmentation system, the rigid body modes were deleted. Hence all motions are with respect to the c.g. of the entire configuration fixed in space. It is recognized that most disturbances to the Space Station will excite both the rigid body modes and the structural modes and that significant interaction between the rigid body motion and the stability augmentation system will occur.

The Space Station is subjected to an artificial disturbance from which every mode is excited by the same amount. The modal excitation is achieved by initializing each modal state (displacement and

41

velocity) to unity. This is equivalent to initializing each physical state (displacement and velocity at the c.g. of each body) to the amount given by,

$$X(0) = TZ(0)$$

where X and Z are the state vectors in physical coordinates and modal coordinates respectively and T is the modal matrix.

The intent here is to present the response of the system to a disturbance that is "rich" in modal excitation energy and in particular to show the effect of the uncontrollable modes on the motion of each body. It is clear that the presence of any uncontrolled modes in the responses will result in some undamped motion. Figures 5 thru 7 show undamped displacement motion along the X-axis for habitat module 1 and both undamped rotational and displacement motion in several directions for the solar panels. Similar responses (not shown) show some undamped motion for the remaining bodies. Figures 8 thru 10 and others not shown, however, indicate that all other motions of the habitat modules and the power module are well damped. In fact, the results show that the only undamped motion of modules 1, 3 & 5 (the habitat modules and power module) are X (displacement along the X-axis) and X. In contrast, all solar panel motions are undamped. This was expected since many of the uncontrollable modes contain solar panel motion.

Figures 11 thru 13 are typical of the control input histories observed for all CMG's. The results show that all control gyro motions are well behaved.

As the magnitude and shape of any response is dependent on the power spectrum of the input or disturbance and initial conditions, the results presented here give only a qualitative flavor of the response characteristics of the closed-loop system.[5]

Responses to shuttle docking, attitude maneuvers, CMG desaturation and other such "realistic" disturbances will provide more conclusive information on the suitability of the effector configuration used here and provide valuable insight to the amount of active damping required to yield acceptable magnitudes and durations of response.

---

[5] It is clear that several of the responses have "large" magnitudes. It should be noted that the initial conditions for these cases were proportionally "large" in magnitude.

Summary and Conclusions

A multivariable control system has been developed for a control-configured Space Station. Responses of the closed-loop system show that disturbances "rich" in modal excitation energy may cause unacceptable motion of the solar panels, but indicate sufficient control authority for the power module and habitat modules. Further studies are needed to determine the necessary damping requirements to yield acceptable responses and to provide additional insight for control effector placement. Several possible solutions are delineated below:

o Include the inherent structural damping which would exist at the soft coupled joints. A value of .005 for the damping ratio will be used here.

o Add active damping at the soft coupled joints. We feel certain that dampers will be needed to stabilize the solar panels. They may be beneficial in the other joints as well. Values of damping ratio in the order of .7 will be used to model active damping. It should be noted that inserting dampers will tend to diminish the vibration filtering properties of the soft couplers.

In addition, we are presently developing flexible models of the booms and solar arrays. Additional testing will be conducted with the flexible Space Station to study, in particular, the filter properties of the soft couplers.

Acknowledgement

References

1. Peters, W. H. and Sunkel, J. W., "Attitude Control and Stability of a Space Station". presented at the AAS Annual Rocky Mountain G&C Conf., Feb. 5-9, 1983, Keystone, CO.

2. Private communication with Dr. D. Glandorf, LEMSCO, Houston, TX.

3. Lin, J. G., "Three Steps to Alleviate Control & Observation Spillover Problems of Large Space Structures", Proceedings of 19th IEEE Conference on Decisio and Control, Albuquerque, NM., Dec. 1980 p.p. 438-444.

4. Sesak, J. R., Likens, P. and Coradetti, T., "Flexible Spacecraft Control by Model Error Sensitivity Suppression", The Journal of the Astronautical Sciences, Vol. XXVII, No. 2, p.p. 131-156, April-June 1979.

5. Gupta, N. K., "Frequency-Shaped Cost Functionals: Extension of Linear-Quadratic-Gaussian Design Methods", Journal of Guidance and Control, Nov.-Dec. 1980, p.p. 529-535.

6. Canavin, J. R., "The Control of Spacecraft Vibrations Using Multivariable Output Feedback", Paper 78-1419, AIAA/AAS Conf., Palo, Alto, CA, August 7-9, 1978.

7. Preston, R. B. and Lin, J. G., "Pareto Optimal Vibration Damping of Large Space Structures with Modal Dashpots", Proceedings of 1980 JACC, August 198, Paper FP1-C.

8. Wonham, W. M., "On Pole Assignment of Multi-input Controllable Linear Systems", IEEE Trans. Auto. Control, AC-12, p.p. 660-665.

9. Davison, E. J. and Wang, S. H., "On Pole Assignment in Linear Multi-variable Systems Using Output Feedbac", IEEE Trans. Auto. Control, Vol. AC-20, p.p. 516-518, 1975.

10. Porter, B. Eigenvalve Assignment in Linear Multivariable Systems by Output Feedback", Int, Journal of Control, Vol. 25, No. 3, p.p. 483-490, 1977.

11. Davison, E. J. and Chow, S. G., "An Algorithm for the Assignment of Closed Loop Poles Using Output Feedback in Large Linear Multivariable Systems", IEEE Trans. Auto. Control, Vol AC-18, p.p. 74-75, Feb. 1973.

12. Anderson, B. D. O. and Moore, J. B., "Linear Optimal Control", Englewood Cliffs, NJ, Prentice Hall, 1972.

13. Kwakernaak, H. and Sivan, R., "Linear Optimal Control Systems", New York: Wiley, 1972.

14. Solhem, O. A., "Design of Optimal Control Systems with Presceibed Eigenvalues", Int. Journal of Control, 1972, Vol. 15, No. 2, p.p. 143-160.

15. Eastman, W. L. and Bossi, T. J., "On the Geometric Structure of the Linear Quadratic Regulator and Specification of Eigenvalues and Eigenvectors," Proceeding of IEEE Conference on Decision Control, December 1982.

16. Safonov, M. G., "Stability and Robustness of Multivariable Feedback Systems", Cambridge MA: MIT Press, 1980.

17. Tehtomaki, N. A., Sandell, N. R., and Athans, M., "Robustness results in Linear-Quadratic Gaussian Based Multivariable Control Desings", IEEE Transaction on Automatic Control, Vol. AC-26 No. 1 Februray 1981.

18. Safonov, M. G. Lamb, A. J., and Hastman, G. L., "Feedback Properties of Multivariable System: The role and use of the Return Difference Matrix", IEEE Transaction on Automatic Control, Vol. AC-26, No. 1, Feb. 1981.

19. Doyle, J. C. and Stein, G., "Multivariable Feedback Design· Concept for a Closial/Modern Synthesis, "IEEE, Translations on Automatic Control, Vol. AC-26 No. 1.

20. Yedavalli, R. K., and Skelton, R. E., "Controller Design for Parameter Sensitivity Reduction in Liear Regulators", Optional Control Applications and Method, Vol. 3, 221-240, 1982.

21. Safonov, M. G., and Athans, "Gain and Phase Margin for Mithiloop LQG Regulators, "IEEE Transactions on Automatic Control, Vol. AC-22, No. 2, April 1977.

22. Doyle, J. C., "Guaranteed Margin for LQG Regulators," IEEE Transactions on Automatic Control, Vol. AC-23, No. 4, Aug. 1978.
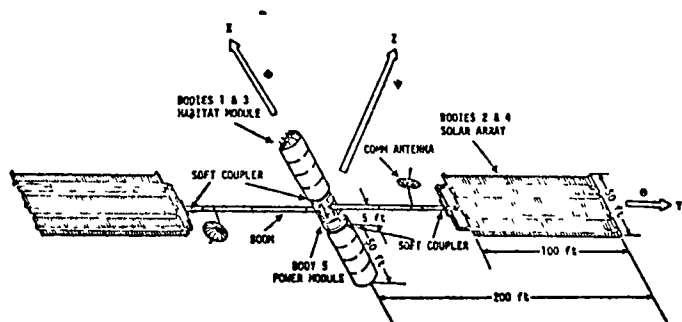
Figure 1. Control Configured Space Station
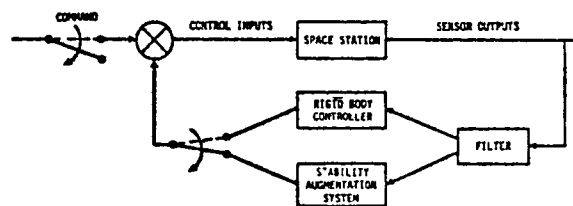
Figure 2. Space Station Control System
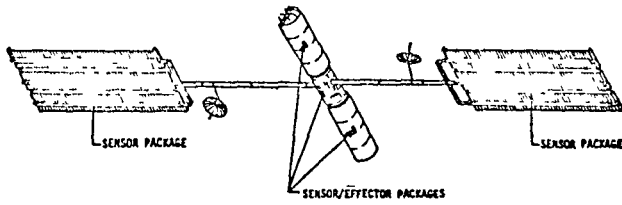
Figure 3. Sensor / Effector Configuration
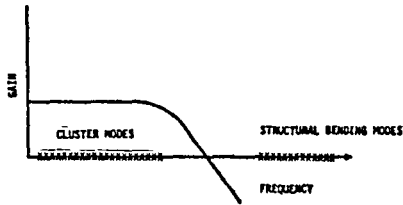
Figure 4. Mechanical Filter
Characteristics
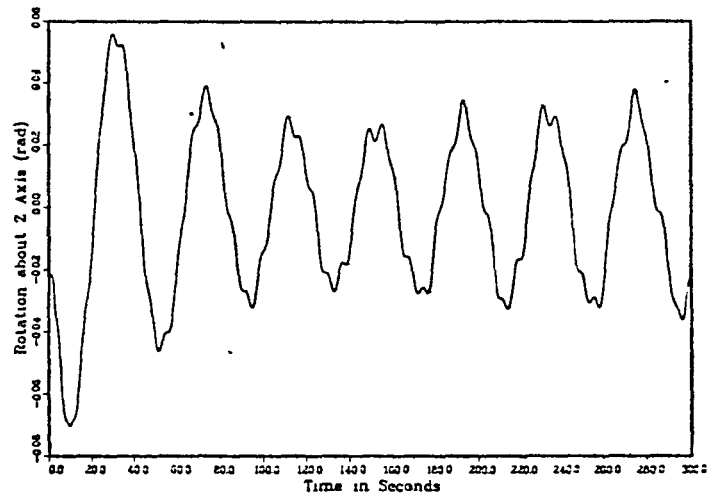
Figure 6. Body 2 - Solar Panel
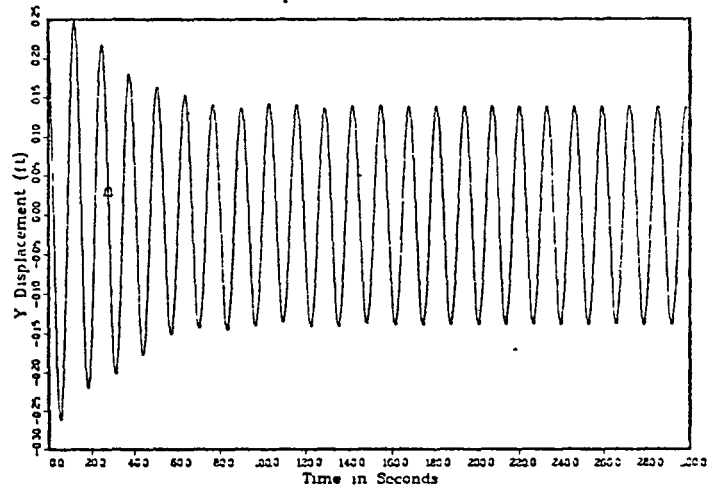
Figure 7. Body 4 - Solar Panel
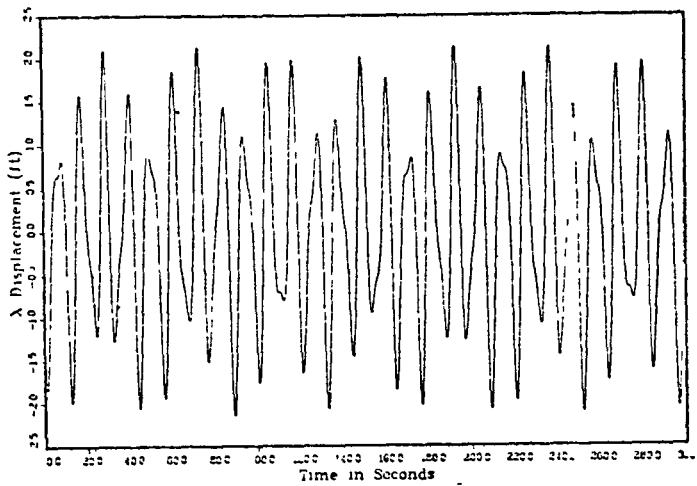
Figure 5. Body 1 - Habitat Module
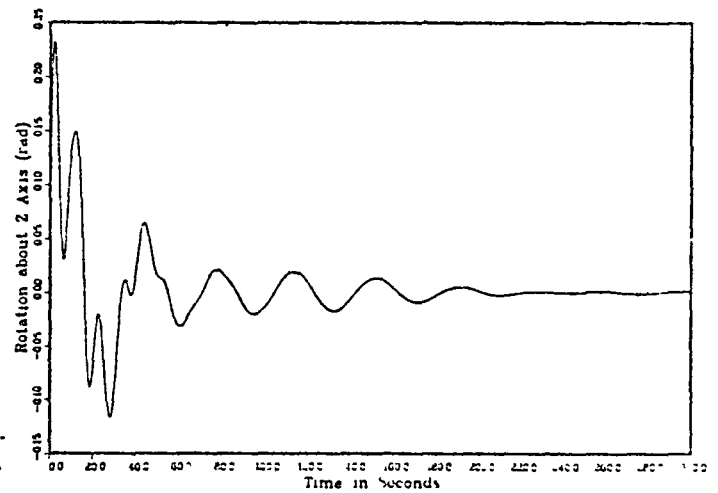
Figure 8. Body 1 - Habitat Module

44
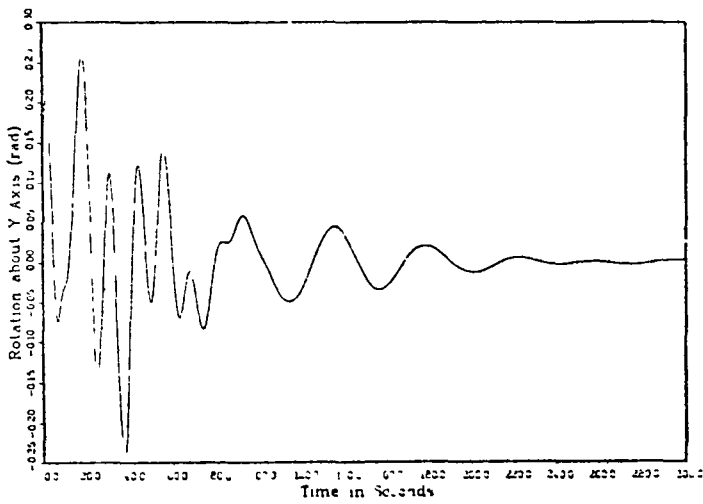
Figure 9. Body 3 - Habitat Module
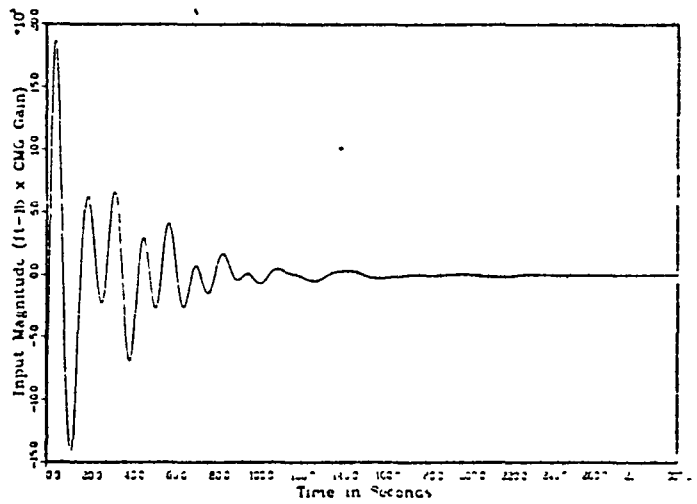
Figure 12. Body 2 - Y-Axis CMG
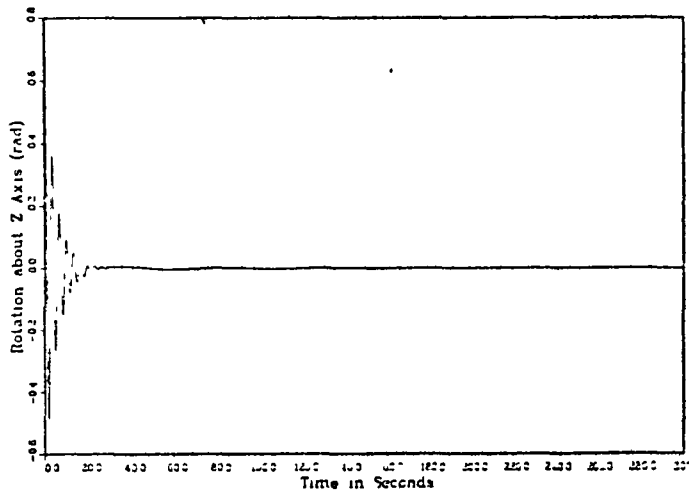
Figure 10. Body 5 - Power Module
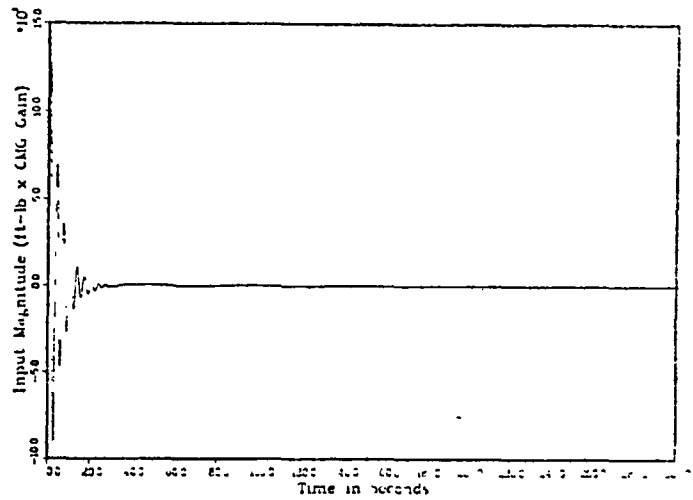
Figure 13. Body 3 - Z-Axis CMG
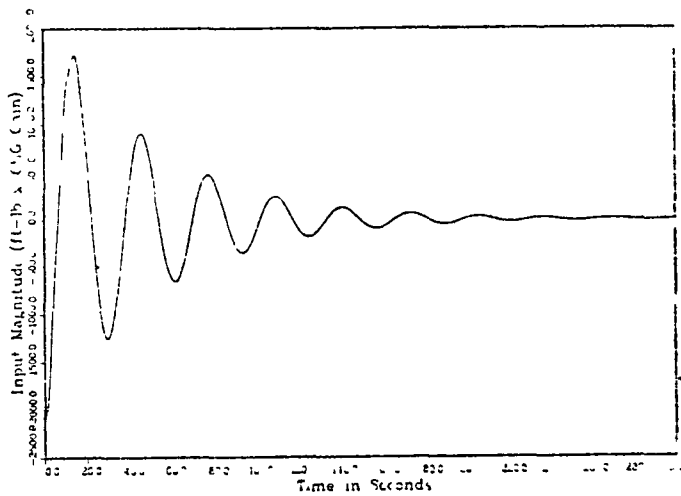
Figure 11. Body 1 - X-Axis CMG

45

TABLE I

MASS AND GEOMETRIC DATA

Parameter	Habitat Module	Solar Array	Power Module
Weight (lbs)	45,000	1,800	45,000
Ixx (slug-ft2)	68,534	46,621	34,207
Iyy (slug-ft2)	325, 651	11,655	28,789
Izz (slug-ft2	325,651	58,277	28,789
Diameter (ft)	14		14
Height (ft)	50		10
Length (ft)		100	
Width (ft)		50	-

TABLE II

MODES AND FREQUENCIES

Mode	Frequency (rad)	Mode	Frequency
1	0 0	16	0.4654
2	0.0	17	0 4832
3	0 0	18	0 4834
4	0 0	19	0 533
5	0 0	20	0 5331
5	0.0	21	0 5546
7	0.1228	22	0 5760
8	0 1355	23	0 5912
9	0.1533	24	0 6887
10	0 1549	25	0 9345
11	0 1738	26	0 9832
12	0.1924	27	0 9986
13	0.1998	28	1.1096
14	0 2215	29	1 1681
15	0 2247	30	1.9377

TABLE 3

CONTROLLABILITY PROPERTIES

Controllable Modes

4, 5, 6, 7, 8, 10, 11, 12, 13, 14, 16, 17, 20, 23, 24, 26, 28, 29, 30

Uncontrollable Modes

1, 2, 3, 9, 15, 18, 19, 21, 22, 25, 27

TABLE 4

FEEDBACK DESIGN SUMMARY

Effector weighting   R = Identify matrix

Desired Damping ratio (ith mode) $\zeta d_i = .1$, all controllable modes*

Desired Frequency (ith mode) $\omega d_i = \omega$, all modes

Computed (modal) state weighting   (Weighting on controllable modes)

Closed Loop System Obtained

Mode	Frequency (rad/sec)	Damping ratio
1	0	0.
2	0.	0
3	0	0
4	0.	0
5	0.	0.
6	0	0
7	1233	0941
8	.1354	.0998
9	.1537	0
10	.1541	0 940
11	.1738	0998
12	.1923	.0999
13	.1998	0999
14	2215	.0991
15	.2246	0.
16	.4653	0999
17	.4910	0895
18	.4833	0
19	.5330	0
20	.5456	0895
21	.5545	0
22	.5759	0.
23	.5911	0999
24	.6898	.0969
25	.9344	0
26	.9814	0969
27	.9986	0
28	1 109	0999
29	1.168	0999
30	1 937	0999

*The design procedure outlined in the proceeding
section will exactly obtain the desired closed
loop modal properties, a slightly different
approach was taken here to reduce computational
time This accounts for the differences in the
obtained frequencies and damping ratios from
those specified

APPENDIX A

The concept of soft coupling between adjacent substructures is illustrated by a simple example, which could be viewed as the coupling that might exist between the first longitudinal modes of two like "spacecraft" connected via a docking tunnel. The purpose of this illustration is to demonstrate the trend for migration of modal resonance frequencies to lower values as more modules are connected, and to demonstrate the decoupling properties of a mechanical filter (relatively weak spring) connection as compared with a more rigid connection. The model chosen for this example is two equal masses connected by a single linear spring (with spring constant K) and motion is considered only along the axis of the spring. Two such "spacecraft" are then connected together via a spring with spring constant K_c and the coupled dynamics are examined for three cases; namely (a) tethered ($K_c \rightarrow o$), (b) rigidly attached ($K_c \rightarrow \infty$), and (c) soft coupled ($K_c < K/2$). The model configuration with applicable degrees of freedom identified is shown in Fig. 1.
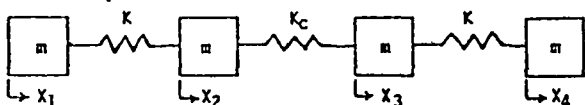
Fig. 1 - Example Model Definition

Defining a new set of coordinates representing linear combinations of the physical coordinates depicted in Fig. 1, we have $X_{ij} \underline{\Delta} X_i - X_j$ and $\bar{X} = X_1 + X_2 + X_3 + X_4$. The equations of motion in hybrid coordinates are easily obtained from Fig. 1 by inspection to be

$$
\left.
\begin{array}{l}
m\ddot{X}_1 = + KX_{21} + 0 \quad + 0 \\
m\ddot{X}_2 = - KX_{21} + K_cX_{32} + 0 \\
m\ddot{X}_3 = + 0 \quad - K_cX_{32} + KX_{43} \\
m\ddot{X}_4 = + 0 \quad + 0 \quad - KX_{43}
\end{array}
\right\}
\quad (1)
$$

By executing the following steps, equation (1) is transformed into equation (2) below.

- normalize to mass m and define $K/m = \omega^2$
- add (-1) times each row to each succeeding row
- form a fourth equation as the sum of equations (1)
- take Laplace transform
- collect terms and put in matrix format

$$
\begin{bmatrix}
s^2 + 2\omega^2 & -\omega_c^2 & 0 & 0 \\
-\omega^2 & s^2 + 2\omega_c^2 & -\omega^2 & 0 \\
0 & -\omega_c^2 & s^2 + 2\omega^2 & 0 \\
0 & 0 & 0 & s^2
\end{bmatrix}
\begin{bmatrix}
X_{21} \\
X_{32} \\
X_{43} \\
\bar{X}
\end{bmatrix}
= 0 \quad (2)
$$

The trivial solution to the characteristic equation from (2); i.e., $s^2 = 0$, represents the rigid body mode where all masses are translating in unison. The coupled vibrational mode frequencies are embodied in the determinant of the upper 3 x 3 given by

$$(s^2 + 2\omega^2)[s^4 + 2(\omega^2 + \omega_c^2)s^2 + 2\omega^2\omega_c^2] = 0 \quad (3).$$

Equation (3) identifies one vibrational mode with frequency $\sqrt{2}\omega$, that is independent of the coupler spring constant which is implicit in ω_c. The next step is to identify the impact of ω_c, as a parameter, on the frequencies of the two remaining vibrational modes defined by the terms inside the square bracket. Since the bracketed polynomial is quadratic in s^2 we apply the quadratic formula to obtain the solutions

$$s^2 = -\omega^2 - \omega_c^2 \pm \omega^2 \sqrt{1 + \left(\frac{\omega_c}{\omega}\right)^4} \quad (4)$$

The case (a) solutions ($\omega_c \rightarrow 0$) are:

$$s^2 = 0 \; ; \; -2\omega^2 \quad (5)$$

This provides one additional rigid body mode, as would be expected, p one additional vibrational mode at $\sqrt{2}\omega$, which would also be expected The case (b) solutions ($\omega_c \gg \omega$) are:

$$s^2 = -\omega^2 \; ; \; -(\omega^2 + 2\omega_c^2) \quad (6)$$

We now have a mode with frequency ω, that is <u>30 percent lower</u> than the lowest vibrational mode for the tethered case. The other mode is at a frequency only slightly higher than the very large high frequency $\sqrt{2}\omega_c$ These solutions demonstrate the potential for a downward migration of modal resonance frequencies when two bodies are rigidly attached and th extreme alteration of dynamics for the components. This satisfies the first objective of our example.

The final and most interesting condition is case (c), where K_c is finit and small but nonzero. By way of definition we decree that small means $\omega_c < \omega/2$. In this case the term modifying unity beneath the radical in equation (4) is 0.0625 or less and the approximation $(1 + a)^m = 1 + ma$ is valid, so that equation (4) reduces to

$$s^2 \approx -\omega^2 - \omega_c^2 \pm \omega^2 \left[1 + \frac{1}{2}\left(\frac{\omega_c}{\omega}\right)^4 \right] \quad (7)$$

The term modifying unity in the bracketed quantity of equation (7) is 3.125 percent or less for our example so that the approximate case (c) solutions are.

$$s^2 \approx -\omega_c^2 \; ; \; - (2\omega^2 + \omega_c^2) \quad (8)$$

The approximate solutions (8) become even more exact as the ratio ω_c/ω shrinks below 0.5.

The solutions (8) represent the soft coupled condition where the two substructures are connected via a mechanical filter. They differ from the case (a) solutions in that the additional rigid body mode of case (a) has become the low frequency vibrational mode at frequency ω_c, and the coupled vibrational mode shifted upward in frequency by only 6.0 percent or less, indicating minimal impact on those dynamics. The case (c) solutions differ from the case (b) solutions in that the coupling mode frequency shifted down below the lowest case (b) vibrational mode frequency, ω, by <u>exactly one octave</u>, and the same low frequency vibrational mode for case (b) moved upward in frequency from ω to $\sqrt{2\omega^2 + \omega_c^2}$, slightly greater than a <u>40 percent increase</u>. Both of these effects are desirable in order to provide frequency separation between the dynamics <u>requiring control</u> (i.e., the rigid body freedoms of each substructure) and the substructure vibrational dynamics. In this example, comparing ratios between the lowest cluster mode frequency and next highest component vibrational frequency for cases (b) and (c), the ratio goes from 0.707 for the rigid coupled case to 0 3535 for the <u>soft coupled</u> case This additional octave of frequency separation has the dual primary benefits of (a) lowering the frequency of vibrational dynamics <u>requiring control</u>, such that they are more compatible with reference frame mode control, and (b) enabling rolloff filter attenuation of the higher frequency vibrational dynamics. This completes the second objective of the example

APPENDIX B

EQUATONS OF MOTION

The equations of motion for each body are presented below. The ith set describes the translational and rotational motion at the c.g. of the ith body with respect to the c.g. of the entire configuration.

47

BODY 1

$$m_1 \ddot{X}_1 + K_{X_1}(X_1 - X_5) = F_{X_1}$$

$$m_1 \ddot{Y}_1 + K_{Y_1}(Y_1 - Y_5 - \ell_1\psi_1 - \ell_3\psi_5) = F_{Y_1}$$

$$m_1 \ddot{Z}_1 + K_{Z_1}(Z_1 - Z_5 + \ell_1\theta_1 + \ell_3\theta_5) = F_{Z_1}$$

$$I_{X_1} \ddot{\phi}_1 + K_{\phi_1}(\phi_1 - \phi_5) = L_1$$

$$I_{Y_1} \ddot{\theta}_1 + K_{\theta_1}(\theta_1 - \theta_5) + \ell_1 K_{Z_1}(Z_1 - Z_5 + \ell_1\theta_1 + \ell_3\theta_5) = M_1$$

$$I_{Z_1} \ddot{\psi}_1 + K_{\psi_1}(\psi_1 - \psi_5) - \ell_1 K_{Y_1}(Y_1 - Y_5 - \ell_1\psi_1 - \ell_3\psi_5) = N_1$$

BODY 2

$$m_2 \ddot{X}_2 + K_{X_2}(X_2 - X_5 + \ell_2\psi_2 + \ell_1\psi_5) = F_{X_2}$$

$$m_2 \ddot{Y}_2 + K_{Y_2}(Y_2 - Y_5) = F_{Y_2}$$

$$m_2 \ddot{Z}_2 + K_{Z_2}(Z_2 - Z_5 - \ell_2\phi_2 - \ell_4\phi_5) = F_{Z_2}$$

$$I_{X_2} \ddot{\phi}_2 + K_{\phi_2}(\phi_2 - \phi_5) - \ell_2 K_{Z_2}(Z_2 - Z_5 - \ell_2\phi_2 + \ell_4\phi_5) = L_2$$

$$I_{Y_2} \ddot{\theta}_2 + K_{\theta_2}(\theta_2 - \theta_5) = M_2$$

$$I_{Z_2} \ddot{\psi}_2 + K_{\psi_2}(\psi_2 - \psi_5) + \ell_2 K_{X_2}(X_2 - X_5 + \ell_2\psi_2 + \ell_4\psi_5) = N_2$$

BODY 3

$$m_1 \ddot{X}_3 + K_{X_1}(X_3 - X_5) = F_{X_3}$$

$$m_1 \ddot{Y}_3 + K_{Y_1}(Y_3 - Y_5 + \ell_1\psi_3 + \ell_3\psi_5) = F_{Y_3}$$

$$m_1 \ddot{Z}_3 + K_{Z_1}(Z_3 - Z_5 - \ell_1\theta_3 - \ell_3\theta_5) = F_{Z_3}$$

$$I_{X_1} \ddot{\phi}_3 + K_{\phi_1}(\phi_3 - \phi_5) = L_3$$

$$I_{Y_1} \ddot{\theta}_3 + K_{\theta_1}(\theta_3 - \theta_5) - \ell_1 K_{Z_1}(Z_3 - Z_5 - \ell_1\theta_3 - \ell_3\theta_5) = M_3$$

$$I_{Z_1} \ddot{\psi}_3 + K_{\psi_1}(\psi_3 - \psi_5) + \ell_1 K_{Y_1}(Y_3 - Y_5 + \ell_1\psi_3 + \ell_3\psi_5) = N_3$$

BODY 4

$$m_2 \ddot{X}_4 + K_{X_2}(X_4 - X_5 - \ell_2\psi_4 - \ell_4\psi_5) = F_{X_4}$$

$$m_2 \ddot{Y}_4 + K_{Y_2}(Y_4 - Y_5) = F_{Y_4}$$

$$m_2 \ddot{Z}_4 + K_{Z_2}(Z_4 - Z_5 + \ell_2\phi_4 + \ell_4\phi_5) = F_{Z_4}$$

$$I_{X_2} \ddot{\phi}_4 + K_{\phi_2}(\phi_4 - \phi_5) + \ell_2 K_{Z_2}(Z_4 - Z_5 + \ell_2\phi_4 + \ell_4\phi_5) = L_4$$

$$I_{Y_2} \ddot{\theta}_4 + K_{\theta_2}(\theta_4 - \theta_5) = M_4$$

$$I_{Z_2} \ddot{\psi}_4 + K_{\psi_2}(\psi_4 - \psi_5) - \ell_2 K_{X_2}(X_4 - X_5 - \ell_2\psi_4 - \ell_4\psi_5) = N_4$$

BODY 5

$$m_5 \ddot{X}_5 - K_{X_1}(X_1 + X_3 - 2X_5) - K_{X_2}(X_2 + X_4 - 2X_5 + \ell_2\psi_2 - \ell_2\psi_4) = F_{X_5}$$

$$m_5 \ddot{Y}_5 - K_{Y_1}(Y_1 + Y_3 - 2Y_5 - \ell_1\psi_1 + \ell_1\psi_3) - K_{Y_2}(Y_2 + Y_4 - 2Y_5) = F_{Y_5}$$

$$m_5 \ddot{Z}_5 - K_{Z_1}(Z_1 + Z_3 - 2Z_5 + \ell_1\theta_1 - \ell_1\theta_3) - K_{Z_2}(Z_2 + Z_4 - 2Z_5 - \ell_2\phi_2 + \ell_2\phi_4) = F_{Z_5}$$

$$I_{X_5} \ddot{\phi}_5 - K_{\phi_1}(\phi_1 + \phi_3 - 2\phi_5) - K_{\phi_2}(\phi_2 + \phi_4 - 2\phi_5)$$
$$+ \ell_4 K_{Z_2}(Z_4 - Z_2 + \ell_2\phi_2 + \ell_2\phi_4 + 2\ell_4\phi_5) = L_5$$

$$I_{Y_5} \ddot{\theta}_5 - K_{\theta_1}(\theta_1 + \theta_3 - 2\theta_5) - K_{\theta_2}(\theta_2 - 2\theta_5 + \theta_4)$$
$$+ \ell_3 K_{Z_1}(Z_1 - Z_3 + \ell_1\theta_1 + \ell_1\theta_3 + 2\ell_3\theta_5) = M_5$$

$$I_{Z_5} \ddot{\psi}_5 - K_{\psi_1}(\psi_1 + \psi_3 - 2\psi_5) - K_{\psi_2}(\psi_2 + \psi_4 - 2\psi_5)$$
$$+ \ell_3 K_{Y_1}(Y_3 - Y_1 + \ell_1\psi_1 + \ell_1\psi_3 + 2\ell_3\psi_5) + \ell_4 K_{X_2}(X_2 - X_4 + \ell_2\psi_2 + \ell_2\psi_4 + 2\ell_4\psi_5) = N_5$$

Where:

$I_{X_i}, I_{Y_i}, I_{Z_i}$ - Principle axis inertias of component i

X_i, Y_i, Z_i - Body coordinates

ϕ_i, θ_i, ψ_i - Angular displacements (roll, pitch, and yaw, respectively)

$K_{X_1}, K_{Y_1}, K_{Z_1}$ - Spring constants between Body 1 and Body 5 (Body 3 and Body 5)

$K_{\phi_1}, K_{\theta_1}, K_{\psi_1}$

$K_{X_2}, K_{Y_2}, K_{Z_2}$ - Spring constants between Body 2 and Body 5

$K_{\phi_2}, K_{\theta_2}, K_{\psi_2}$ - (Body 4 and Body 5)

$F_{X_2}, F_{Y_2}, F_{Z_2}$ - Transition forces due to RCS jets

L_i, M_i, N_i - Torques due to CMGs

The complete coupled 3-axis equations of motion emphasize the simplicity of the dynamics model of a Space Station that utilizes the soft coupling approach to isolate superfluous degrees of freedom. These equations are of the general form

$$\ddot{Z}(t) + KZ(t) = F(t) \qquad (B.1)$$

Choosing

$$X(t) = \left[Z(t)^T, \ \dot{Z}(t)^T \right]^T$$

transforms the Space Station model into the state space form

$$\dot{X}(t) = AX(t) + BU(t)$$

48

where

X (t) = 60 X 1   state space vector

U (t) = 30 X 1   control input vector

A   = 60 X 60 constant coefficient matrix

B   = 60 X 30 constant coefficient matrix

and the matrices A and B have the following form:

$$A = \begin{bmatrix} 0 & \vdots & I \\ \text{-----} & \vdots & \text{-----} \\ \text{Elements of} & \vdots & \\ K \text{ in} & \vdots & 0 \\ \text{Eq. } \underline{B\ 1} & \vdots & \end{bmatrix}$$

$$B = \begin{bmatrix} 0 \\ \text{-----} \\ \text{Elements of } F(t) \\ \text{in Eq. } \underline{B\ 1} \end{bmatrix}$$

The output vector for the system is

Y (t)   =   C X (t)

where

Y (t)   =   r X 1 output vector where r is a function of the number of sensors

C   =   r X 60 constant coefficient matrix

APPENDIX C

As in [14], consider the plant model in physical coordinates,

$$X = AX + BU, \quad Y = CX$$

and a quadratic cost functional,

$$J = \tfrac{1}{2} \int_0^T (X^T QX + U^T RU)\ dt, \quad Q = C^T Q_y C.$$

The well known solution to this optimal control problem is given by,

Control law   U = GX

Control Gain $G = -R^{-1}B^T S$

Ricatti Equ. $\dot{S} + SA + A^T S - SBR^{-1}B^T S + Q = 0$

This solution results by   solving the Euler-Lagrange equations,

$$1 \quad \begin{bmatrix} \dot{X} \\ \dot{\lambda} \end{bmatrix} = \begin{bmatrix} A & \vdots & -BR^{-1}B^T \\ -Q & \vdots & -A^T \end{bmatrix} \begin{bmatrix} X \\ \lambda \end{bmatrix} = F \begin{bmatrix} X \\ \lambda \end{bmatrix}$$

where the relation,

$$\lambda = SX$$

is assumed.

A transformation to "true" modal coordinates yields,

$$Z = \Lambda Z + \bar{B}u, \quad y = CTZ, \quad X = TZ.$$

where

$$\Lambda = \text{diag} \left\{ \begin{bmatrix} 0 & 1 \\ -w_1^2 & -2\zeta_1 W_1 \end{bmatrix}, \dots, \begin{bmatrix} 0 & 1 \\ -w_n^2 & -2\zeta_n W_n \end{bmatrix} \right\}$$

$$T^{-1}B = \bar{B} = \begin{bmatrix} 0 & ---- & 0 \\ b_{11} & & b_{1m} \\ 0 & ---- & 0 \\ b_{21} & & b_{2m} \\ 0 & ---- & 0 \\ b_{n1} & & b_{nm} \end{bmatrix}$$

for a structural dynamic system.

The cost functional becomes,

$$J = \tfrac{1}{2} \int_0^T (Z^T \bar{Q} Z + U^T RU)\ dt, \quad \bar{Q} = T^T QT$$

and the Euler-Lagrange equations,

$$2 \quad \begin{bmatrix} \dot{Z} \\ \dot{P} \end{bmatrix} = \begin{bmatrix} \Lambda & -H \\ -\bar{Q} & -\Lambda^T \end{bmatrix} \begin{bmatrix} Z \\ P \end{bmatrix} = \tilde{F} \begin{bmatrix} Z \\ P \end{bmatrix}, \quad H = T^{-1}BR^{-1}\{T^{-1}B\}^T$$

Similarly, the control law is given by,

$$U = \bar{G}Z, \quad P = \bar{S}Z, \quad \bar{G} = -R^{-1}\{T^{-1}B\}^T \bar{S}$$

and $\dot{\bar{S}} + \bar{S}\Lambda + \Lambda^{T}\bar{S} - \bar{S}T^{-1}BR^{-1}\{T^{-1}B\}^T \bar{S} + \bar{Q} = 0$

Clearly,

$$|sI-F| = |sI-\tilde{F}|$$

where s is the Laplace transform variable. Using the transformation,

$$\begin{bmatrix} I & 0 \\ -\bar{Q}(sI-\Lambda)^{-1} & I \end{bmatrix} \cdot [sI - \tilde{F}] \quad \text{gives}$$

$$|sI-\tilde{F}| = \begin{vmatrix} sI - \Lambda & \vdots & H \\ 0 & \vdots & sI + \Lambda^T - \bar{Q}(sI-\Lambda)^{-1}H \end{vmatrix}$$

$$= |sI-\Lambda||sI+\Lambda^T-\bar{Q}(sI-\Lambda)^{-1}H|$$

It is easy to show that if only the jth mode is weighted,

$$\bar{Q}_j = \begin{bmatrix} 0_0 & & & \\ & q_{d_j} & & \\ & & q_{v_j} & \\ & & & 0_0 \end{bmatrix}$$

q_{d_j} = weight on modal displacement state for the jth mode

q_{v_j} = weight modal velocity state for the jth mode

then,

$$|sI + \lambda^T \bar{Q}(sI-\Lambda)^{-1}H| = \begin{vmatrix} s & -\omega_1^2 \\ 1 & s-2\zeta_1\omega_1 \end{vmatrix}$$

$$\begin{vmatrix} s & (-q_{d_j} h_{jj})/\Delta - \omega_j^2 \\ 1 & s - 2\zeta_j\omega_j - (s\,q_{v_j}\,h_{jj})/\Delta \end{vmatrix} \cdot \begin{vmatrix} s & -\omega_n^2 \\ 1 & s-2\zeta_n\omega_n \end{vmatrix}$$

$$= \left\{ \prod_{\substack{i=1 \\ i \neq j}}^{n} (s^2-2\zeta_i\omega_i s + \omega_i^2) \right\} \cdot$$

$$\left\{ s^2-2\zeta_j\omega_j s + \omega_j^2 + q_{d_j} h_{jj}/\Delta - s^2 q_{v_j} h_{jj}/\Delta \right\}$$

where h_{jj} $\in H$ is the jth diagonal term of H and

$$\Delta = s^2 + 2\zeta_j\omega_j s + \omega_j^2.$$

Finally, the characteristic equation may be written

$$|sI - \Lambda||sI + \Lambda^T - \bar{Q}(sI - \Lambda)^{-1}H| =$$

$$\left\{ \prod_{\substack{i=1 \\ i \neq j}}^{n} (s^2-2\zeta_i\omega_i s+\omega_i^2)(s^2+2\zeta_i\omega_i s+\omega_i^2) \right\}$$

$$X \left\{ (s^2-2\zeta_j\omega_j s+\omega_j^2)(s^2 + 2\zeta_j\omega_j s+\omega_j^2) + q_{d_j} h_{jj} - s^2 q_{v_j} h_{jj} \right\} = 0$$

Expanding only that part involving h & q yields,

$$s^4 + (2\omega_j^2 - 4\zeta_j^2\omega_j^2 - q_{v_j} h_{jj})s^2 + (\omega_j^4 + q_{d_j} h_{jj})$$

The desired characteristic equation for the jth mode can be written as,

$$(s^2 + 2\zeta_d \omega_d s + \omega_d^2)_j (s^2 - 2\zeta_d\omega_d s+\omega_d^2)_j = s^4 + (2\omega_d^2 - 4\zeta_d^2\omega_j^2)s^2 + \omega_d^4$$

Equating terms of equal powers in s and solving for q_{d_j}, q_{v_j} yields,

$$q_{d_j} = (\omega_d^4 - \omega_j^4) / h_{jj}$$

and

$$q_{v_j} = \{2(\omega_j^2 - \omega_d^2) + 4(\zeta_j^2\omega_d^2 - \zeta_j^2\omega_j^2)\}/h_{jj}$$

where

$\omega_j, \zeta_j \triangleq$ open loop frequency and damping ratio respectively

$\bar{\omega}_d, \zeta_d \triangleq$ desired closed loop frequency and damping ratio respectively

The gain is computed by,

$$G_i = \bar{G}_i T^{-1} \qquad \bar{G}_i = -R^{-1} \bar{B} \bar{S}_j$$

where

$$\dot{\bar{S}}_j = -\bar{S}_j \Lambda_c - \Lambda_c \bar{S}_j + \bar{S}_j \bar{B} R^{-1} \bar{B}^T \bar{S}_j + Q_j = 0$$

The matrix, $\tilde{A} = A + BG_i$ represents the new system matrix. The procedure is then repeated for the next mode (using $\tilde{A}$ in place of A). The recursive nature of this procedure is clear.

The total gain matrix results by summing the gain matrices obtained at each iteration,

$$G = G_1 + G_2 + \ldots + G_i + \ldots G_n.$$

50

A DUAL SPIN SPACE STATION DESIGN

M. A. Paluszek[1]
Charles Stark Draper Laboratory
Cambridge, MA 02139

ABSTRACT

A dual spin space station design is described in this paper. The space station has a cylindrical solar array that is spun to provide both gyroscopic stiffness to the space station and to stiffen the array structure. The platform is spun at the orbital angular rate. The space station is designed to have gravity gradient and aerodynamic restoring torques. An active control system is used to stabilize the station and store excess angular momentum until it can be removed from the station by magnetic torquers.

I. INTRODUCTION

Most space station configurations to date have consisted of modular cores and large planar solar panels. Active control systems are necessary to stabilize such stations, a task made more difficult by the very low vibration frequencies of the solar panels.

An alternative is a dual spin configuration, one of several that have gyroscopic stiffness due to stored angular momentum. The proposed dual spin configuration developed at Draper is illustrated in Figure 1.

The various habitat, service, command and laboratory modules are sandwiched between two solar arrays. The solar arrays are spun to provide gyroscopic stiffness to the station and to increase the vibration frequencies of the arrays. An active control system is used to stabilize the station and eliminate any attitude offsets due to steady-state torques. Excess momentum is removed by magnetic torquers located in the core.

II. OVERALL DESIGN

The proposed dual spin space station has two cylindrical solar arrays which are spun to provide gyroscopic stiffness. The core platform rotates at orbit rate about the spin axis and is earth pointing. The platform consists of a hub along the pitch or spin axis and service modules which attach to the hub and point radially. Other modules are attached to these service modules and to the hub.

---

1   Technical Staff, Charles Stark Draper Laboratory.

This particular design has four hangars. Two hangars and fuel storage depots for the Orbit Transfer Vehicles (OTV) are attached to the hub directly. Two Orbit Maneuvering Vehicle (OMV) hangars are attached to the service modules. The array hubs have tunnels that connect to the core of the station and the outer hub to which the solar arrays are attached.

The minimum operational station can be orbited in eight shuttle flights. The first two flights carry the solar arrays which are assembled on orbit. The next flight brings up the central service module that serves as the hub. The remaining flights deliver the two service modules, a habitat module, a laboratory module and the magnetic torquers. At this time the arrays are spun up and the system becomes operational.

The station is built up from the minimum configuration by connecting modules to the twenty-six ports on the service modules. If more modules are desired, additional service modules or docking adaptors can be attached. The Orbiter docks at docking hatches located at either end of the space station along the spin axis. This is done to reduce the disturbances produced by an attached Orbiter and to maintain a stabilizing gravity gradient torque.   .

The product of array diameter and length gives the effective area receiving solar radiation. The other half will receive the flux from the earth's reflected radiance which is $\approx$ 1/3 the solar flux. This increases the power available by 33%, somewhat offsetting the disadvantage of the additional solar cell area. If more power is needed, additional solar arrays can be attached to the ends of the station above or below the existing arrays.

Radii for the solar arrays have been chosen to be 30 m and the height 16 m. The arrays rotate at 16.43 RPM to provide sufficient stored angular momentum. The primary radial supports are 4 trusses. Trusses behind the array provide circumferential support. The array was designed to have a despun lowest natural frequency of .11 Hz which is 4 times the nutation frequency of the station. The next four modes have frequencies of .14 Hz, .14 Hz, .15 Hz and .19 Hz. The first torsional mode has a frequency in excess of .31 Hz. The vibration frequencies of the arrays are $\approx$ 10 percent higher when the arrays are spinning due to the centrifugal forces on the arrays. A solar array is illustrated in Figure 2.

The spun solar array does not track the sun; therefore it is desirable to put the station in an orbit in the ecliptic plane to maximize the available power. However, because of the J_2 term in the earth's gravitational potential, the orbit plane will oscillate about this plane [3] causing the incidence angle to vary as a function of time. The power available over an orbit, divided by the the solar flux per unit area, will vary as illustrated in Figure 3. The long term variation is due to the orbit precession. The short term is due to the orbit of the earth about the sun. The range is from .48 to .63 of the total (uneclipsed) solar flux.

III. THE EQUATIONS OF MOTION FOR THE DUAL SPIN SPACE STATION

The equations of motion for a dual spin space station under the influence of the gravity gradient and aerodynamic disturbing torques are:

$$I \cdot \dot{\omega} + \omega x I \cdot \omega + j J_r \dot{\Omega}_r + i \omega_z J_r \Omega_r - k \omega_x J_r \Omega_r + \omega x J \cdot \Omega + J \cdot \dot{\Omega}$$
$$= 3 \mu R x I \cdot R/R^5 + (1/2) \rho C_D V^2 r x u$$

$$J_r (\dot{\Omega}_r + \dot{\omega}_y) = T_r$$
$$J_1 (\dot{\Omega}_1 + \dot{\omega}_x) = T_1$$
$$J_2 (\dot{\Omega}_2 + \dot{\omega}_y) = T_2$$
$$J_3 (\dot{\Omega}_3 + \dot{\omega}_z) = T_3$$

(1)

i, j and k are unit vectors in the body axis system. j is along the spin axis, which is normal to the orbit plane. k points to the center of the earth and i completes the right handed system. I is the total inertia matrix of the station, J is a diagonal matrix whose elements are the polar moments of inertia of the reaction wheels and Ω is the vector of their rates. T_r is the motor torque on the solar array and T_1, T_2 and T_3 are the motor torques on the reaction wheels. u is the unit velocity vector in body axis and r is the vector from the center of mass to the center of pressure. The angular momentum stored in the solar array $= J_r \Omega_r$, the product of the array rate and inertia. $J_r \Omega_r$ is positive if it rotates in the same direction as the station platform does in its orbit. The radius and angular velocity vectors are:

$$R = \psi_y R i - \psi_x R j - R k$$

$$\omega = (\dot{\psi}_x - \dot{\theta} \psi_z) i + (\dot{\psi}_z - \dot{\theta}) j + (\dot{\psi}_z + \dot{\theta} \psi_x) k$$

(2)

For small eccentricity:

$$d\theta/dt \approx n[1 + 2e\cos nt]$$

$$R \approx a[1 - e\cos nt]$$

(3)

where t is the time since periapsis passage, a is the semimajor axis and n is the mean orbital rate.

The equations of motion can be linearized by assuming that only the solar array angular velocity is a large quantity. Orbit eccentricity is small; therefore:

$$e^2 \approx 0$$

$$\mu/R^3 \approx n^2$$

(4)

The angular momentum stored in the reaction wheels is assumed to be negligible. The linearized equations of motion are:

53

$$I_x(\ddot{\psi}_x - n\dot{\psi}_z) + I_{xy}(\ddot{\psi}_y - \ddot{\theta}) + I_{xz}(\ddot{\psi}_z + n\dot{\psi}_x) + I_{yz}(n^2 - 2n\dot{\psi}_y)$$
$$- (n\dot{\psi}_z + n^2\psi_x)(I_z - I_y) + I_{xz}(n^2\psi_z - n\dot{\psi}_x) + H(\dot{\psi}_z + n\psi_x) \tag{5}$$
$$= 3n^2(-I_{yz} + \psi_x(I_z - I_y) + \psi_y I_{xy}) + T_x + 2n^2 I_{xy} e \sin nt$$

$$I_{xy}(\ddot{\psi}_x - n\dot{\psi}_z) + I_y(\ddot{\psi}_y - \ddot{\theta}) + I_{yz}(\ddot{\psi}_z + n\dot{\psi}_x)$$
$$- I_{xy}(n\dot{\psi}_z + n^2\psi_x) - I_{yz}(n^2\psi_z - n\dot{\psi}_x) \tag{6}$$
$$= 3n^2(-I_{xz} - \psi_y(I_x - I_z) + \psi_x I_{xy}) + T_y + 2n^2 I_y e \sin nt$$

$$I_{xz}(\ddot{\psi}_x - n\dot{\psi}_z) + I_{yz}(\ddot{\psi}_y - \ddot{\theta}) + I_z(\ddot{\psi}_z + n\dot{\psi}_x) - I_{xy}(n^2 - 2n\dot{\psi}_y)$$
$$+ (n^2\psi_z - n\dot{\psi}_x)(I_y - I_x) + I_{xz}(n^2\psi_x + n\dot{\psi}_z) - H(\dot{\psi}_x - n\psi_z) \tag{7}$$
$$= -3n^2(\psi_x I_{xz} + \psi_y I_{yz}) + T_z + 2n^2 I_{yz} e \sin nt$$

IV. OPEN LOOP DYNAMICS

One of the advantages of a spinning spacecraft is that it is gyroscopically stiff. The stored angular momentum will cause the vehicle to oscillate about its initial position when it is disturbed. This stiffness applies only to the axes transverse to the spin axis.

Gravity gradient torques, torques due to the angular rate of the platform, aerodynamic torques and energy dissipation must be considered when determining the passive stability of the station. All four are dependent on the space station configuration and make the arrangement of the masses within the station of critical importance.

The three torque sources produce both steady-state torques and attitude dependent torques. The steady state torques are:

$$T_x = -4n^2 I_{yz}$$
$$T_y = 3n^2 I_{xz} - \gamma_z \tag{8}$$
$$T_z = n^2 I_{xy} + \gamma_y$$

γ is the aerodynamic torque vector on the station in station body axes. These torques, together with the attitude stiffness, will determine what the offset angle of the station from Local Vertical Local Horizontal coordinates will be. Clearly, it is desirable to have all of the parameters in these equations as small as possible. The first and third equations have contributions from both the gravity gradient torque and the orbit rate.

The magnitude of the desired angular momentum is based on the maximum desired steady state error due to the secular disturbing torques. The necessary angular momentum is approximately:

$$H = 2T/n\Delta\theta \tag{9}$$

which is found by eliminating the cross product terms in the inertia matrix and solving algebraically for the step response. $\Delta\theta$ is the maximum

allowable attitude error. H is limited by the requirements of building an array to hold the angular momentum as well as the limits on the nutation frequency. If H is large relative to the transverse inertias the nutation frequency may be close to the structural frequencies of the rotor causing undesirable interaction.

Gravity gradient and aerodynamic torques also can provide stiffness to the station. This is most important about the pitch axis since this axis does not have any gyroscopic stiffness. The attitude-dependent torques due to the gravity gradient and aerodynamics are:

$$T_x = \psi_y(I_{xy} - \gamma_y) - \psi_z\gamma_z$$
$$T_y = \psi_y(I_z - I_x + \gamma_x) + \psi_x I_{xy} \qquad\qquad (10)$$
$$T_z = - \psi_x I_{xy} - \psi_y I_{yz}$$

Terms which are much smaller than the angular momentum terms have been ignored. If $\gamma_x < 0$ it will contribute to pitch stiffness as will the gravity gradient term if $I_x > I_z$. Module placement is critical in achieving both gravity gradient stiffness and in keeping the cross product terms low. The effect of the other terms is not as obvious. For example, the first equation has a $\psi_z\gamma_z$ term. As it turns out this term is destabilizing. A simple model will suffice to demonstrate this. Assume that there are no cross coupling terms in the inertia matrix and that $I_x = I_z$. The characteristic equation for the roll-yaw axis, with angular momentum h stored about the pitch axis is:

$$(s^2 + nH)(s^2 + nH) + sH(sH + G_z) = 0 \qquad\qquad (11)$$

$H = h/I$ and $G_z = \gamma_z/I$. For small values of G_z this can be factored into two second order polynomials:

$$(s^2 + (G_z/H)s + n^2)(s^2 - (G_z/H)s + H^2) = 0 \qquad\qquad (12)$$

For any value of $G_z \neq 0$ the roll-yaw axis motion will be unstable.

The cross product of inertia terms produce similar effects and lead to the slow divergence of the station attitude. Modules should be placed so as to keep both the cross product terms in the platform inertia matrix and the destabilizing aerodynamics terms as small as possible.

The inertia matrices of the space station without and with the Orbiter are:

$$\begin{bmatrix} 67.4 & -0.065 & 0.58 \\ -0.065 & 37.8 & 0.0 \\ 0.58 & 0.0 & 45.7 \end{bmatrix} \qquad \begin{bmatrix} 143.4 & 0.86 & 0.57 \\ 0.86 & 47.2 & -0.02 \\ 0.57 & -0.02 & 139.5 \end{bmatrix} \times 10^6 \text{ kg-m}^2$$

respectively. The center of mass coordinates are:

$$[\; 0 \quad 0 \quad 0\;] \qquad\qquad [\; .077 \quad -9.6 \quad -.003\;]\; m$$

55

The eigenvalues of the attitude motion for these configurations will not all be in the left half plane. The eigenvalues without and with the Orbiter are:

$$-1.1 \times 10^{-7} \qquad \pm i.18 \qquad -1.0 \times 10^{-7} \pm i.0726$$
$$1.1 \times 10^{-7} \qquad \pm i.00111 \qquad -1.6 \times 10^{-8} \pm i.0011$$
$$0.0 \qquad \pm i.00159 \qquad 9.0 \times 10^{-8} \pm i.00073$$

The first is primarily associated with the nutation mode, the second with the orbit mode and the third with the pitch gravity gradient mode. The reduction in frequency in the nutation and pitch mode when the Orbiter is attached is due to the much larger transverse inertias. The real parts are very small and will result in a very slow divergence from the initial attitude. This analysis excludes the effects of energy dissipation due to spacecraft dynamics. There will be energy dissipation in both the core and the solar arrays. The dissipation in the core will be due to the motion of fluids, structural damping and other forms of mechanical motion. Dissipation in the rotor will be due primarily to structural damping, which is very small. Analysis by Iorillo [1] indicates that the dissipation in the core will have to be greater than .1 of that in the rotor for asymptotic stability. If passive stability is desired, and the platform damping is inadequate, passive dampers may be added to the plaform [6].

V. THE AUTOMATIC CONTROL SYSTEM

An automatic control system has been designed to stabilize the space station and to compensate for steady-state torques. The system also provides angular momentum storage to temporarily store the angular momentum buildup due to secular torques.

The station has three reaction wheels, one for each axis. The solar array motors are also used as actuators for the pitch axis. The pitch control effort is partitioned between the solar array and reaction wheel by means of second order filters in the control loop. This is done to prevent the solar array from reacting to high frequency excitations.

Since the number of states is small, and the system is multivariable a linear quadratic regulator was designed for the system. The system equations are augmented with equations for the integrals of the attitude angles to permit integral feedback to prevent attitude offsets from steady-state torques. The results of the LQ analysis indicate that it is not necessary to provide full state feedback to all the actuators. Since the cross coupling terms between the spin and transverse axes are small, elimination of the gains that feedback the roll/yaw states to the pitch actuators and the pitch states to the roll/yaw actuators are not needed, except for the roll rate feedback to pitch. Setting these gains, which are small relative to the other gains, to zero does not destabilize the closed loop system. However, stability margins will be affected by removing the cross coupling gains from the feedback.

Any one of the actuators is sufficient to stabilize the system if all of the states are available to each of the actuators. The station can have up to three actuator failures and still maintain a stable attitude, although it will not be possible to attain all the performance of the complete system. For example, only one actuator is needed on the transverse axis to achieve roll/yaw stability. However, the integral control action on the transverse axis without the actuator is very weak.

Reaction control jets would be used as a backup in case of the failure of all the momentum exchange devices and the motors that drive the solar arrays.

A block diagram of the proposed automatic control system is given in Figure 4.

VI. THE MOMENTUM DESATURATION LAW

Steady state disturbance torques will result in the buildup of angular momentum in the momentum wheels on a space station. It will be necessary to periodically desaturate the momentum wheels to prevent excessive momentum buildup. The change in angular momentum produced by a magnetic torquer is:

$$dh/dt = T_m = D_m \times B_e \tag{13}$$

where B_e is the earth's magnetic field vector, D_m is the dipole moment of the coils and T_m is the resulting torque due to the magnetic torquers. One method is to use magnetic torquers. The equations for the change in angular momentum are:

$$
\begin{aligned}
dh_x/dt &= NA(I_z B_y - I_y B_z) = T_x \\
dh_y/dt &= NA(I_z B_x - I_x B_z) = T_y \\
dh_z/dt &= NA(I_x B_y - I_y B_x) = T_z
\end{aligned}
\tag{14}
$$

D_m has been replaced by $NA(iI_x + jI_y + kI_z)$ where N is the number of turns of wire in the coil, I is the current and A is the area of the coil. The coils are each assumed to have the same area, number of turns of wire and resistance. The power consumed by the coils is:

$$P = R(I_x^2 + I_y^2 + I_z^2) \tag{15}$$

At time $t = 0$ the excess angular momentum is:

$$h = h_o + \Delta h \tag{16}$$

Δh is the expected change in angular momentum due to the action of secular torques over the period of time t_f. The control law is designed to reduce h to zero in a fixed time t_f. The Hamiltonian for this system is:

$$H = NA(\lambda_x T_x + \lambda_y T_y + \lambda_z T_z)$$
$$+ w((\tau_x - T_x)^2 + (\tau_y - T_y)^2 + (\tau_z - T_z)^2) \qquad (17)$$
$$+ R(I_x^2 + I_y^2 + I_z^2)$$

The λ's are the Lagrange multipliers, and the τ's are the average torque desired. The τ's are equal to the expected values of the steady-state torques. w is the weight that is placed on deviations from these values. The control laws are found by taking the partial derivatives of the Hamiltonian with respect to the controls and setting them equal to zero. The control laws that result are:

$$I_x = NA(\lambda_y B_z - \lambda_z B_y + 2w(B_y \tau_z - B_z \tau_y))/D$$
$$I_y = NA(\lambda_z B_x - \lambda_x B_z + 2w(B_z \tau_x - B_x \tau_x))/D \qquad (18)$$
$$I_z = NA(\lambda_x B_y - \lambda_y B_x + 2w(B_x \tau_y - B_y \tau_x))/D$$

where

$$D = 2wNAB^2 + 2R \qquad (19)$$

λ_x, λ_y and λ_z are constants since the derivative of the Hamiltonian with respect to h is zero. The λ's can be found by substituting the control laws into the equations of motion and integrating from $t = 0$ to $t = t_f$ and finding λ such that $\Delta h = h_o$. It is necessary to solve the following three equations simultaneously

$$h = h_o + \Delta h = \begin{matrix} \lambda_x a_{xx} + \lambda_y a_{xy} + \lambda_z a_{yz} \\ \lambda_x a_{xy} + \lambda_y a_{yy} + \lambda_z a_{yz} + Z \\ \lambda_x a_{xz} + \lambda_y a_{yz} + \lambda_z a_{zz} \end{matrix} \qquad (20)$$

where, for example:

$$a_{xy} = (NA)^2 \int_0^{t_f} B_x B_y dt/D \qquad (21)$$

and

$$z_x = w(NA)^2 \int_0^{t_f} [B_z(B_x \tau_z - B_z \tau_x) + B_y(B_x \tau_y - B_y \tau_x)]/D dt \qquad (22)$$

λ is to be calculated based on the previous period's B. t_f is set equal to the period of the orbit, which is long enough to include the major variations in the earth's magnetic field. Δh can be estimated from Equation (8). The magnetic torquer law wraps around the momentum exchange loop.

It is not necessary to store the measured values of the magnetic field. The a matrix can be integrated as measurements are taken so that only nine numbers need be stored.

The desaturation torques over one orbit with $w = 0$ and $w = 10000$ are shown is Figure 5. In the latter case the maximum torques are much nearer

the average of -2.2 N-m. The penalty is an average power consumption of 501 watts as opposed to the power optimal (w = 0) solution of 150 watts.

VII. SIMULATION RESULTS

The simulation described in this paper is for a Space Shuttle Orbiter docking with the space station. The simulation starts 1000 seconds before the Orbiter docks with the station and ends 4600 seconds after docking. The space station is acted upon by several different types of disturbing torques. The aerodynamic torques have a steady state component and an oscillatory component at twice the orbital frequency due to atmospheric density variations. The gravity gradient torque has a steady state component due to the cross product terms in the inertia matrix. Both will vary linearly as the space station oscillates in attitude. Disturbance torques due to crew motion have frequency components that range from 0 to 5 Hz. The magnitude of these torques is much larger than the gravity gradient or aerodynamic torques. An action as innocuous as a sneeze can produce a force of up to 100 N. Docking of the Orbiter produces torques due to both the impact and the change in inertia of the station.

The simulation program [2] includes nonlinear gravity gradient and aerodynamics models. The atmospheric density model is the 1971 Jacchia model. The space station motion is modeled with nonlinear equations but does not include the effects of flexibility. The crew disturbance model is based on Skylab experimental data [4]. It is assumed that there are 6 crew members on board the station. The model accounts for module placement, crew station orientation and crew motion. In this case the astronauts are all working at consoles which have been oriented to reduce the disturbance torques on the station. Actuator and sensor dynamics are not included in this simulation.

The control laws operate at first under a set of gains designed for the station without the Orbiter. When the Orbiter docks, a second set of gains designed for the new mass properties is used. This assumes that the new mass properties are known. The system is not stable if the original set of gains is used.

The magnetic torquers were designed to produce a maximum torque of 2.2 N-m with a maximum power dissipation of 25 watts [5] when the Earth's magnetic field is .4 gauss. The radii of the coils was set at 5.0 m. Each coil has a mass of 3000 kg.

The disturbance torques during the simulation are illustrated in Figure 6. The docking torque has been truncated so as not to obscure the other torques. Its value is 46000 N-m. The maximum torques produced by the reaction wheels was 9, 18 and 10 N-m for the roll, pitch and yaw axis. The maximum torque produced by the solar array motor was 20 N-m. Resulting attitude behavior is illustrated in Figure 7. The angular rates of the pitch actuators are illustrated in Figure 8. The steady state buildup of momentum due to offset torques is eliminated by the magnetic torquers on the average over one orbit.

VIII. SYSTEM IDENTIFICATION

The control laws in this paper assume knowledge of the mass and aerodynamic properties of the space station. This may not be the case in practice since the mass properties will vary greatly as fuel is consumed, crew members move about and other vehicles are launched and recovered. Errors in mass property estimates could lead to instabilities.

The mass properties of the station could be determined by keeping track of the positions of the crew members and large pieces of moveable equipment including vehicles that are docked to the station, monitoring propellant consumption and fluid flow. Even with good bookkeeping, a system identification algorithm may be needed to check for errors.

Determining the aerodynamic properties is far more complicated due to the complex nature of the aerodynamic interaction and the time variation of the atmospheric density. Determination of the station aerodynamics may be simplified by flying a satellite in the same orbit as the station, away from the station environment, and measuring the atmospheric density, thus eliminating one unknown from the calculations. The aerodynamics will still be a complicated function of attitude though less so in designs, such as this one, where the aerodynamic surface is dominated by one or two simple shapes.

IX. SUMMARY AND CONCLUSIONS

A dual spin space station design with an active control system is demonstrated in this paper. The space station is designed to take advantage of environmental torques and the stored angular momentum to achieve near passive stability. Passive stability requires the addition of dampers to the platform. The active control system, uses three reaction wheels and the solar array motors to control the system. The pitch control effort is partitioned by frequency between the rotor and reaction wheel. Magnetic torquers are used to reduce steady state disturbing torques and desaturate the rotor. Simulation testing demonstrates the validity of this concept.

X. ACKNOWLEDGEMENT

LIST OF REFERENCES

1. Iorillo, A.J., "Nutation Damping Dynamics of Axisymmetric Rotor Stabilized Satellites," ASME Winter Meeting, Chicago, Nov. 1965.

2. Eyles, D., Malchow, H., Paluszek, M., Users's Guide to the Space Station Simulator, CSDL-R-1673, Cambridge, MA, September 1983.

3. Solar Cell Array Design Handbook Jet Propulsion Laboratory, Vol. 1, JPL-SP-43-38.

4. Kullas, M.C., Handbook on Astronaut Crew Motion Disturbances for Control System Design, Martin Marietta Aerospace, NASA Reference Publication 1025, May 1979.

5. Paluszek, M.A., "Resistojets for Space Station Altitude and Attitude Control," CSDL-R-1660, Cambridge, MA, August 1983.

6. Kaplan, M. H., Modern Spacecraft Dynamics and Control, John Wiley & Sons New York 1976 pp 109 - 112.
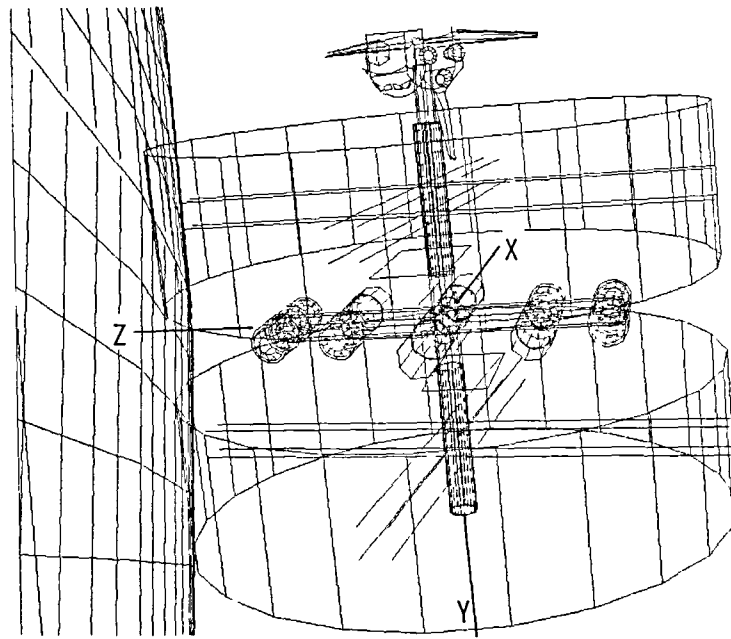
Figure 1. The Dual Spin Space Station with a Docked Orbiter
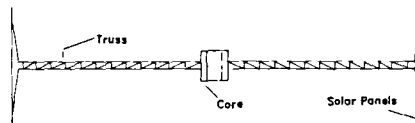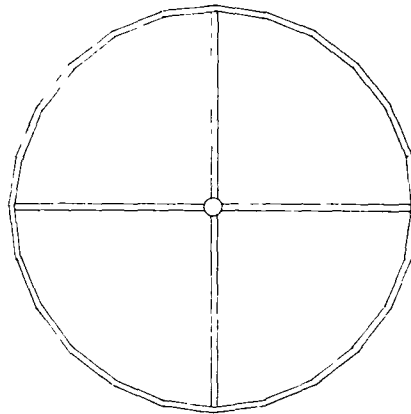
Figure 2. The Solar Array
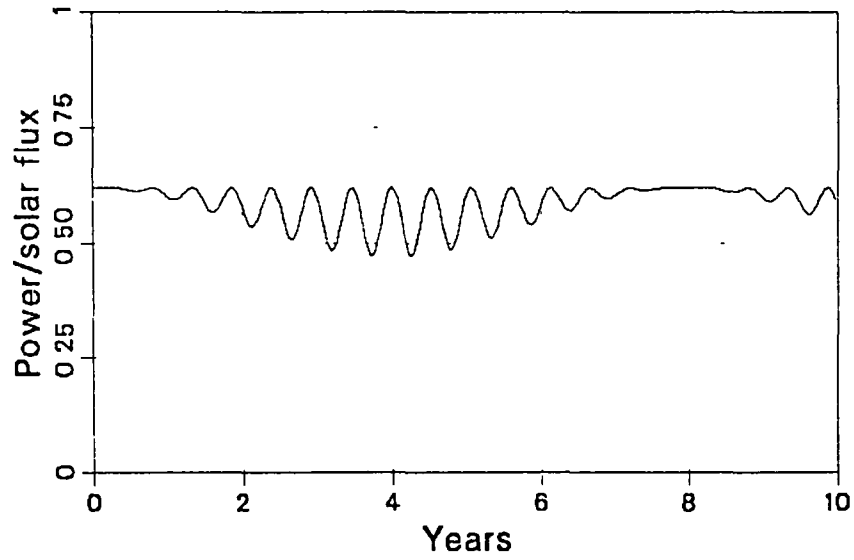
Figure 3. The Average Power Over One Orbit as a Function of Time
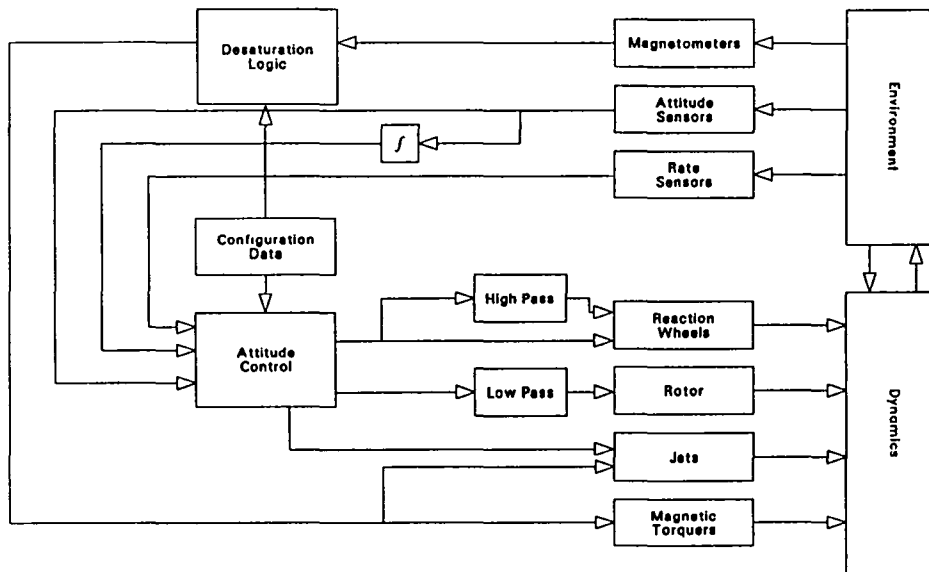
Figure 4. The Automatic Control System
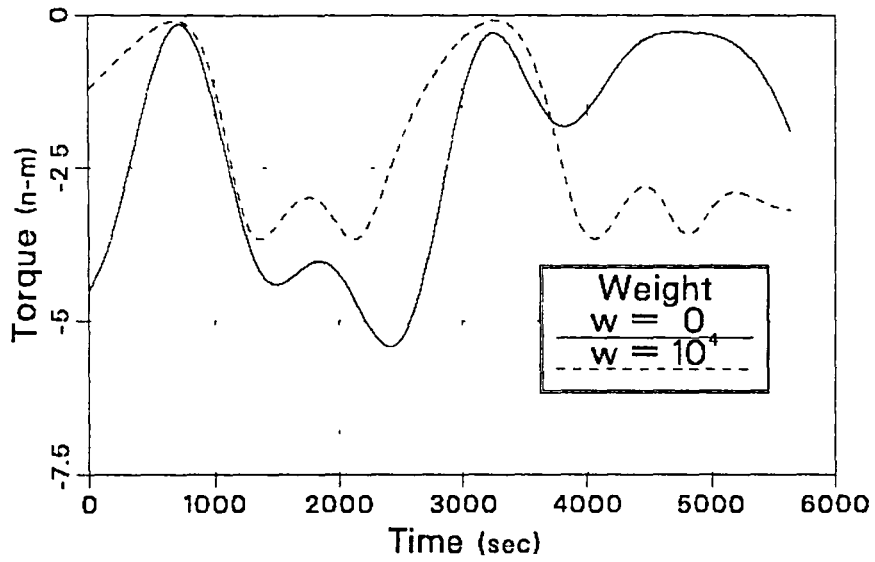
Figure 5. Magnetic Torquer Desaturation Torques in Pitch for w = 0 and w = 10000
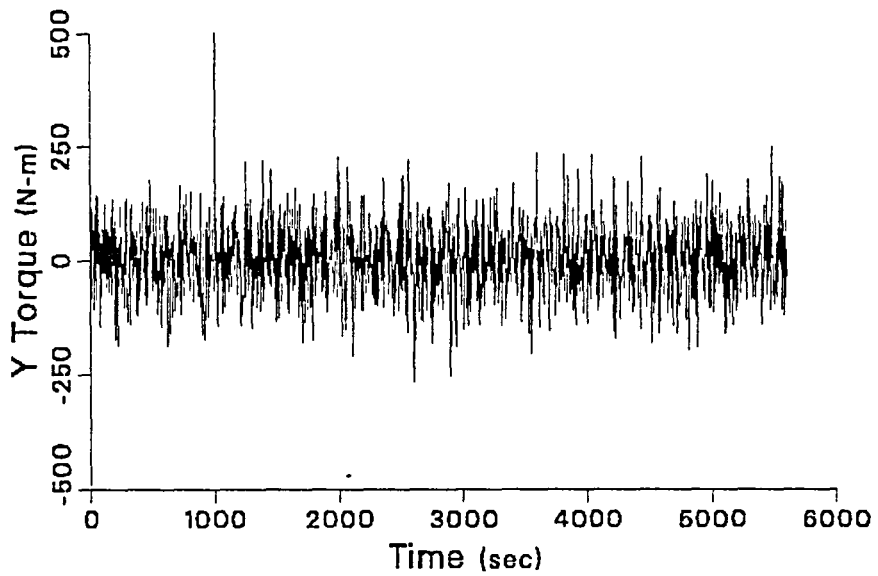
Figure 6. Crew, Docking, Aerodynamic and Gravity Gradient Disturbing Torques about the Pitch Axis
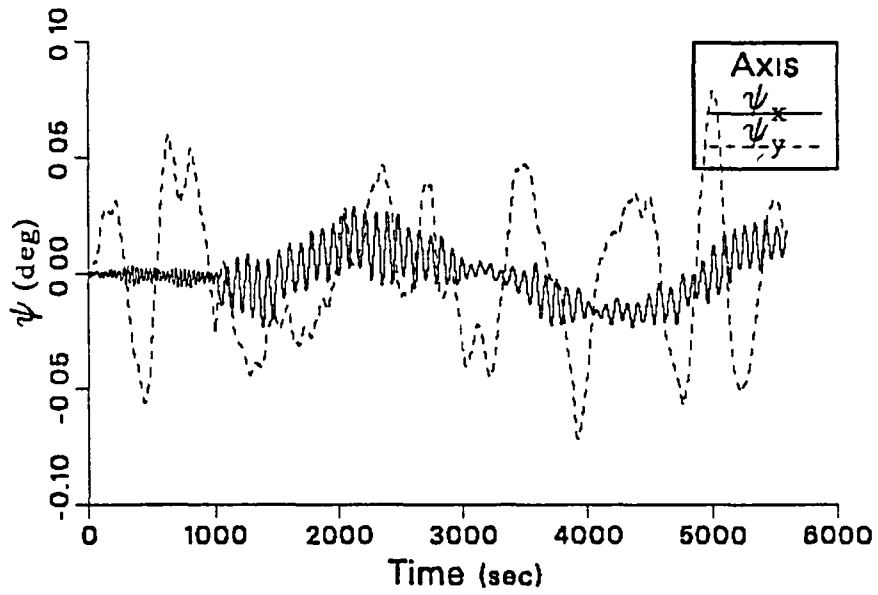
Figure 7. Space Station Attitude
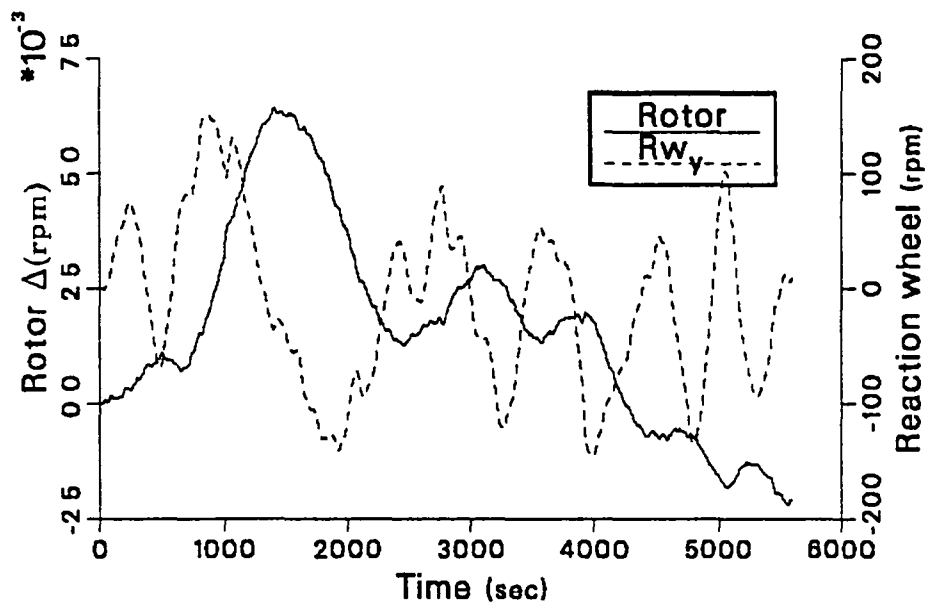
Figure 8. Solar Array and Pitch Reaction Wheel Rates

AUTOMATIC ASSEMBLY OF SPACE STATIONS

P. K. C. Wang*
University of California
Los Angeles, CA 90024

.

ABSTRACT

A basic problem in the automatic assembly of space stations is the determi-
nation of guidance laws for the terminal rendez-vous and docking of two structur-
al components or modules.   This problem involves the feedback control of both
the relative attitude and translational motion of the modules. Here, a suitable
matnematical model based on rigid body dynamics is used for this study.   First,
the basic requirements, physical constraints and difficulties associated with the
control problem are discussed.   Then, an approach which bypasses some of the
difficulties is proposed.   A nonlinear guidance law satisfying the basic require-
ments is derived.   This is followed by a discussion of the implementation re-
quirements.   The performance of the resulting feedback control system with rigid
and flexible structural components is studied by means of computer simulation.

I INTRODUCTION

In the construction of large space stations and platforms such as the pro-
posed Advanced Science and Applications Space Platform (ASASP) [1],geostationary
platforms [2], and the Space Operations Center (SOC) [3], the structural compo-
nents are placed into an Earth orbit by a sequence of orbiter flights and then
assembled in a systematic manner.   The assembly could be achieved either manual-
ly,semi-automatically, or automatically.   In an actual operation, semi-automatic
or automatic assembly is preferred since it greatly reduces the necessary train-
ing and task of the assembly crew.   In the automatic assembly process, the fol-
lowing basic steps may be taken: (1) Initiation Stage: A basic structural com-
ponent or module (eg. the power module) is placed into the desired orbit.   This
unit should possess a self-contained control system for regulating its attitude
(2) Orbital Rendez-vous Stage: A second structural component or module is placed
in the vicinity of the first module.   This module should also contain a control
system for regulating its attitude for maneuvering itself toward the initial
basic target module. (3) Terminal Rendez-vous and Docking Stage: The first and
second modules approach each other at a small relative speed and with an appro-
priate relative attitude until the attachment devices touch.   Then, a rigid con-
nection between the two modules is made.   This process may be achieved automati-
cally.   (4) Steps (2) and (3) are repeated for the remaining structural com-

---

ponents of the space station.

The problem of automatic assembly in space has been studied by Legostaev and Raushenbach. Specific schemes for automatic orbital rendez-vous and docking of the Russian satellite pairs Kosmos-186 and 188, and Kosmos-212 and 213 are described in [4]. Various problems associated with the rendez-vous and docking of space vehicles such as the Apollo,Gemini,Skylab and space shuttle vehicles have been discussed in references [5]-[9].

In this paper, our attention is focused on the basic problem of deriving guidance laws for the automatic terminal rendezvous and docking of two modules. This problem involves the automatic control of both the relative attitude and translational motion of the modules. The results may also be applied to the automatic rendez-vous and docking between a space shuttle vehicle and a space station. The problem of deriving guidance laws for the automatic orbital rendez-vous of two modules (regarded as point masses) will be discussed elsewhere [10].

We begin with the development of a suitable mathematical model for the terminal rendez-vous and docking of two modules. Then the basic requirements and difficulties associated with the control problem are discussed. An approach which bypasses some of the difficulties is proposed and a nonlinear guidance law which satisfies the basic requirements is derived. This is followed by a discussion of the implementation requirements. The performance of the resulting feedback control system with both rigid and flexible structural components is studied by means of computer simulation.

II MATHEMATICAL MODEL

Figure 1 shows the two modules to be assembled. We assume that both modules are rigid bodies, each containing a rigid docking reference platform. The structural flexibility effects of the modules may be included in the model by regarding them as inertial parameter perturbations. To describe the module motions, we introduce Cartesian coordinate systems (x_1,y_1,z_1) and (x_2,y_2,z_2) with origins at the mass centers of the first and second modules respectively. Their axes are along the respective principal axes of inertia. The docking reference platforms are described by the simplexes Π_1 and Π_2 given by $\Pi_i = Co\{p_{i1},p_{i2},p_{i3}\}$, i= 1,2, the convex hull of the reference point triplet $\{p_{i1},p_{i2},p_{i3}\}$. The reference point p_{ij} is specified by the vector S^i_j relative to the (x_i,y_i,z_i)-coordinate system, or by the vector r^i_j relative to the inertial (X,Y,Z)-coordinate system.

Let $B_0 = \{e_X,e_Y,e_Z\}$ and $B_i = \{e_{xi},e_{yi},e_{zi}\}$ denote the orthonormal basis for the fixed (X,Y,Z) and moving (x_i,y_i,z_i) coordinate systems respectively, and $[v]_i$ denote the representation of a vector v with respect to basis B_i. Then the basis vectors in B_0 and B_i are related by a linear transformation C defined by

$$e_{xi} = C\,e_X, \quad e_{yi} = C\,e_Y, \quad e_{zi} = C\,e_Z, \quad i=1,2, \tag{1}$$

whose representation with respect to basis $\mathcal{B}_0$ is given by the direction cosine matrix:

$$
C(\underline{q}_i) = \begin{bmatrix}
q_{i1}^2 - q_{i2}^2 - q_{i3}^2 + q_{i4}^2 & 2(q_{i1}q_{i2} + q_{i3}q_{i4}) & 2(q_{i1}q_{i3} - q_{i2}q_{i4}) \\
2(q_{i1}q_{i2} - q_{i3}q_{i4}) & -q_{i1}^2 + q_{i2}^2 - q_{i3}^2 + q_{i4}^2 & 2(q_{i2}q_{i3} + q_{i1}q_{i4}) \\
2(q_{i1}q_{i3} + q_{i2}q_{i4}) & 2(q_{i2}q_{i3} - q_{i1}q_{i4}) & -q_{i1}^2 - q_{i2}^2 + q_{i3}^2 + q_{i4}^2
\end{bmatrix}, \quad (2)
$$

where $\underline{q}_i = (q_{i1}, q_{i2}, q_{i3}, q_{i4})^T$ denotes the Euler quaternion with q_{ij} being the Euler symmetric parameters [11]-[14] defined by

$$
q_{ij} = \varepsilon_{ij} \sin(\phi_i/2), \quad j=1,2,3; \quad q_{i4} = \cos(\phi_i/2), \tag{3}
$$

where ϕ_i is the principal angle and the ε_{ij}'s are the components of the principal vector of rotation $\underline{\ell}_i$ defined by

$$
\underline{\ell}_i = \varepsilon_{i1}\underline{e}_X + \varepsilon_{i2}\underline{e}_Y + \varepsilon_{i3}\underline{e}_Z = \varepsilon_{i1}\underline{e}_{xi} + \varepsilon_{i2}\underline{e}_{yi} + \varepsilon_{i3}\underline{e}_{zi}. \tag{4}
$$

The Euler symmetric parameters q_{ij} satisfy the constraint:

$$
\sum_{j=1}^{4} q_{ij}^2 = 1, \quad i=1,2. \tag{5}
$$

The time derivative of q_{ij} is related to the angular velocity $\underline{\omega}_i = \omega_{ix}\underline{e}_{xi} + \omega_{iy}\underline{e}_{yi} + \omega_{iz}\underline{e}_{zi}$ of the moving coordinate system (x_i, y_i, z_i) relative to the inertial frame (X,Y,Z) by

$$
d\underline{q}_i/dt = \Omega([\underline{\omega}_i]_i)\underline{q}_i, \quad i=1,2, \tag{6}
$$

where $[\underline{\omega}_i]_i = (\omega_{ix}, \omega_{iy}, \omega_{iz})^T$ and

$$
\Omega([\underline{\omega}_i]_i) = \frac{1}{2} \begin{bmatrix}
0 & \omega_{iz} & -\omega_{iy} & \omega_{ix} \\
-\omega_{iz} & 0 & \omega_{ix} & \omega_{iy} \\
\omega_{iy} & -\omega_{ix} & 0 & \omega_{iz} \\
-\omega_{ix} & -\omega_{iy} & -\omega_{iz} & 0
\end{bmatrix}. \tag{7}
$$

We note that since $\Omega([\underline{\omega}_i]_i)$ is skew-symmetric, system (6) is Euclidean-norm invariant, i.e. $\|\underline{q}_i(t)\|^2 = \underline{q}_i(t)^T\underline{q}_i(t) = $ constant for all t. For Euler symmetric parameters, the initial condition $\underline{q}_i(0)$ satisfies $\|\underline{q}_i(0)\| = 1$.

The angular velocities of the two modules are governed by the following Euler's moment equations:

$$\frac{d}{dt}(I_i \cdot \underline{\omega}_i) + \underline{\omega}_i \times (I_i \cdot \underline{\omega}_1) = \underline{\tau}_{ci}, \quad i=1,2, \tag{8}$$

where I_i and $\underline{\tau}_{ci}$ are the tensor of inertia and control torque associated with the i-th module respectively, and differentiation is taken with respect to the moving body frame (x_i, y_i, z_i). Equation (8) has the following representation with respect to basis B_1:

$$\frac{d}{dt}\begin{bmatrix} \omega_{ix} \\ \omega_{iy} \\ \omega_{iz} \end{bmatrix} = - \begin{bmatrix} I_{i1}\omega_{iy}\omega_{iz} \\ I_{i2}\omega_{ix}\omega_{iz} \\ I_{i3}\omega_{ix}\omega_{iy} \end{bmatrix} + \begin{bmatrix} \tau_{cix}/I_{ix} \\ \tau_{ciy}/I_{iy} \\ \tau_{ciz}/I_{iz} \end{bmatrix}, \quad i=1,2, \tag{9}$$

where

$$I_{i1} = (I_{iz}-I_{iy})/I_{ix}, \quad I_{i2} = (I_{ix}-I_{iz})/I_{iy}, \quad I_{i3} = (I_{iy}-I_{ix})/I_{iz}, \tag{10}$$

where I_{ix}, I_{iy} and I_{iz} are the principal moments of inertia of the i-th module.

The equation for $\underline{\rho}$ (relative translation of the mass centers) relative to the moving coordinate system (x_1, y_1, z_1) is given by

$$\frac{d^2\underline{\rho}}{dt^2} + \frac{d\underline{\omega}_1}{dt} \times \underline{\rho} + 2\underline{\omega}_1 \times \frac{d\underline{\rho}}{dt} + \underline{\omega}_1 \times (\underline{\omega}_1 \times \underline{\rho}) = \underline{F}_{c2}/M_2 - \underline{F}_{c1}/M_1 + \underline{F}_{g2}/M_2 - \underline{F}_{g1}/M_1, \tag{11}$$

where F_{gi} and F_{ci} are the gravitational and control forces acting on the i-th module respectively, and differentiation is taken with respect to the moving coordinate system (x_1, y_1, z_1). Equation (11) has the following representation with respect to basis B_1:

$$\frac{d^2}{dt^2}\begin{bmatrix} \rho_{x1} \\ \rho_{y1} \\ \rho_{z1} \end{bmatrix} + \begin{bmatrix} 0 & \rho_{z1} & -\rho_{y1} \\ -\rho_{z1} & 0 & \rho_{x1} \\ \rho_{y1} & -\rho_{x1} & 0 \end{bmatrix} \frac{d}{dt}\begin{bmatrix} \omega_{1x} \\ \omega_{1y} \\ \omega_{1z} \end{bmatrix} + 2B_1([\underline{\omega}_1]_1) \frac{d}{dt}\begin{bmatrix} \rho_{x1} \\ \rho_{y1} \\ \rho_{z1} \end{bmatrix} + B_2([\underline{\omega}_1]_1)\begin{bmatrix} \rho_{x1} \\ \rho_{y1} \\ \rho_{z1} \end{bmatrix}$$

$$= \begin{bmatrix} (\underline{F}_{g2}/M_2 - \underline{F}_{g1}/M_1)_{x1} \\ (F_{g2}/M_2 - F_{g1}/M_1)_{y1} \\ (F_{g2}/M_2 - F_{g1}/M_1)_{z1} \end{bmatrix} + \begin{bmatrix} u_{x1} \\ u_{y1} \\ u_{z1} \end{bmatrix}, \tag{12}$$

where $\underline{\rho} = \rho_{x1}\underline{e}_{x1} + \rho_{y1}\underline{e}_{y1} + \rho_{z1}\underline{e}_{z1}$,

$$B_1([\underline{\omega}_1]_1) = \begin{bmatrix} 0 & -\omega_{1z} & \omega_{1y} \\ \omega_{1z} & 0 & -\omega_{1x} \\ -\omega_{1y} & \omega_{1x} & 0 \end{bmatrix}, \quad B_2([\underline{\omega}_1]_1) = \begin{bmatrix} -\omega_{1y}^2-\omega_{1z}^2 & \omega_{1x}\omega_{1y} & \omega_{1x}\omega_{1z} \\ \omega_{1x}\omega_{1y} & -\omega_{1x}^2-\omega_{1z}^2 & \omega_{1y}\omega_{1z} \\ \omega_{1x}\omega_{1z} & \omega_{1y}\omega_{1z} & -\omega_{1x}^2-\omega_{1y}^2 \end{bmatrix},$$

$$(13)$$

where $(\underline{F}_{g2}/M_2 - \underline{F}_{g1}/M_1)_{k1}$ (resp. u_{k1}), k=x,y,z, denote the components of $(\underline{F}_{g2}/M_2 - \underline{F}_{g1}/M_1)$ (resp. $(\underline{F}_{c2}/M_2 - \underline{F}_{c1}/M_1)$) with respect to basis $\mathcal{B}_1$. Using (9) to eliminate the term $d[\underline{\omega}_1]_1/dt$ in (12) gives:

$$\frac{d^2}{dt^2}\begin{bmatrix} \rho_{x1} \\ \rho_{y1} \\ \rho_{z1} \end{bmatrix} + 2B_1([\underline{\omega}_1]_1)\frac{d}{dt}\begin{bmatrix} \rho_{x1} \\ \rho_{y1} \\ \rho_{z1} \end{bmatrix} + \{B_2([\underline{\omega}_1]_1) + B_3([\underline{\omega}_1]_1)\}\begin{bmatrix} \rho_{x1} \\ \rho_{y1} \\ \rho_{z1} \end{bmatrix}$$

$$= \begin{bmatrix} (\underline{F}_{g2}/M_2 - \underline{F}_{g1}/M_1)_{x1} \\ (\underline{F}_{g2}/M_2 - \underline{F}_{g1}/M_1)_{y1} \\ (\underline{F}_{g2}/M_2 - \underline{F}_{g1}/M_1)_{z1} \end{bmatrix} - \begin{bmatrix} 0 & \rho_{z1} & -\rho_{y1} \\ -\rho_{z1} & 0 & \rho_{x1} \\ \rho_{y1} & -\rho_{x1} & 0 \end{bmatrix}\begin{bmatrix} \tau_{c1x}/I_{1x} \\ \tau_{c1y}/I_{1y} \\ \tau_{c1z}/I_{1z} \end{bmatrix} + \begin{bmatrix} u_{x1} \\ u_{y1} \\ u_{z1} \end{bmatrix}, \quad (14)$$

where

$$B_3([\underline{\omega}_i]_i) = \begin{bmatrix} 0 & I_{i3}\omega_{ix}\omega_{iy} & -I_{i2}\omega_{ix}\omega_{iz} \\ -I_{i3}\omega_{ix}\omega_{iy} & 0 & I_{i1}\omega_{iy}\omega_{iz} \\ I_{i2}\omega_{ix}\omega_{iz} & -I_{i1}\omega_{iy}\omega_{iz} & 0 \end{bmatrix}, \quad i=1,2. \quad (15)$$

Assuming a central Newtonian gravitational force field, the gravitational force acting on the i-th module is given by

$$\underline{F}_{gi} = -\mu M_i \underline{R}_i/r_i^3, \qquad i=1,2, \qquad (16)$$

where μ is the geocentric gravitational constant (the product of the gravitational constant and the mass of the Earth); $\underline{R}_i$ is the vector specifying the position of the mass center of the i-th module relative to the inertial frame; and $r_i = \|\underline{R}_i\|$, the Euclidean length of $\underline{R}_i$. Let $\underline{e}_y \triangleq \underline{R}_1/r_1$. We can write

$$\underline{R}_1 = r_1\underline{e}_y = r_1(c_{y,x1}\underline{e}_{x1}+c_{y,y1}\underline{e}_{y1}+c_{y,z1}\underline{e}_{z1}), \quad \underline{R}_2 = \underline{R}_1 + \underline{\rho}, \quad (17)$$

71

where $c_{y,a}$ denotes the direction cosine or inner product between the unit vectors $\underline{e}_y$ and $\underline{e}_a$, $a=x1,y1,z1$. Using the fact that during terminal rendez-vous, $r_1/r_2 \simeq 1$, the components of $(\underline{F}_{g2}/M_2 - \underline{F}_{g1}/M_1)$ in (14) can be written as:

$$(\underline{F}_{g2}/M_2 - \underline{F}_{g1}/M_1)_{x1} = \omega_o^2\{r_1 c_{y,x1}-(r_1/r_2)^3(\rho_{x1}+r_1 c_{y,x1})\} \simeq -\omega_o^2 \rho_{x1},$$

$$(\underline{F}_{g2}/M_2 - \underline{F}_{g1}/M_1)_{y1} = \omega_o^2\{r_1 c_{y,y1}-(r_1/r_2)^3(\rho_{y1}+r_1 c_{y,y1})\} \simeq -\omega_o^2 \rho_{y1}, \qquad (18)$$

$$(\underline{F}_{g2}/M_2 - \underline{F}_{g1}/M_1)_{z1} = \omega_o^2\{r_1 c_{y,z1}-(r_1/r_2)^3(\rho_{z1}+r_1 c_{y,z1})\} \simeq -\omega_o^2 \rho_{z1},$$

where $\omega_o=\sqrt{\mu/r_1}$ is the orbital angular speed of the modules about the origin of the inertial frame (X,Y,Z).

Now, we consider the system output variables corresponding to those quantities which can be directly measured or estimated. Besides the measurable quantities $[\underline{\omega}_i]_1$ and q_i, $i=1,2$, it is also possible to determine $\underline{d}_j$ (the vector directed from the docking reference point $\underline{p}_{1j}$ to $\underline{p}_{2j}$) by optical methods. From Fig.1, we have the relations:

$$\underline{d}_j = \underline{R}_2 + \underline{S}_j^2 - \underline{R}_1 - \underline{S}_j^1 = \underline{\rho} + \underline{S}_j^2 - \underline{S}_j^1, \qquad j=1,2,3, \qquad (19)$$

where $\underline{\rho}=\underline{R}_2-\underline{R}_1$. The vectors $\underline{S}_j^i,\underline{\rho}$ and $\underline{d}_j$ can be expressed in terms of the basis vectors $\{\underline{e}_X,\underline{e}_Y,\underline{e}_Z\}$ and $\{\underline{e}_{x1},\underline{e}_{y1},\underline{e}_{z1}\}$ as follows:

$$\underline{S}_j^1 = s_{j1X}\underline{e}_X + s_{j1Y}\underline{e}_Y + s_{j1Z}\underline{e}_Z = s_{jix}\underline{e}_{xi} + s_{jiy}\underline{e}_{yi} + s_{jiz}\underline{e}_{zi},$$

$$\underline{\rho} = \rho_X\underline{e}_X + \rho_Y\underline{e}_Y + \rho_Z\underline{e}_Z = \rho_{xi}\underline{e}_{xi} + \rho_{yi}\underline{e}_{yi} + \rho_{zi}\underline{e}_{zi}, \qquad (20)$$

$$\underline{d}_j = d_{jX}\underline{e}_X + d_{jY}\underline{e}_Y + d_{jZ}\underline{e}_Z = d_{jx1}\underline{e}_{xi} + d_{jyi}\underline{e}_{yi} + d_{jzi}\underline{e}_{zi},$$

$$i=1,2; \; j=1,2,3.$$

The vector components corresponding to the fixed and moving coordinate systems are related by

$$\begin{bmatrix} s_{j1X} \\ s_{j1Y} \\ s_{j1Z} \end{bmatrix} = C(\underline{q}_1)\begin{bmatrix} s_{jix} \\ s_{j1y} \\ s_{jiz} \end{bmatrix}, \; \begin{bmatrix} \rho_X \\ \rho_Y \\ \rho_Z \end{bmatrix} = C(\underline{q}_i)\begin{bmatrix} \rho_{xi} \\ \rho_{yi} \\ \rho_{zi} \end{bmatrix}, \; \begin{bmatrix} d_{jX} \\ d_{jY} \\ d_{jZ} \end{bmatrix} = C(\underline{q}_i)\begin{bmatrix} d_{jx1} \\ d_{jyi} \\ d_{jzi} \end{bmatrix}, \qquad (21)$$

$$i=1,2; \; j=1,2,3,$$

where $C(\underline{q}_i)$ is given by (2). For each fixed time t, equation (19) has a representation with respect to basis $B_0=\{\underline{e}_X,\underline{e}_Y,\underline{e}_Z\}$:

$$\begin{bmatrix} d_{jX}(t) \\ d_{jY}(t) \\ d_{jZ}(t) \end{bmatrix} = \begin{bmatrix} s_{j2X}(t) \\ s_{j2Y}(t) \\ s_{j2Z}(t) \end{bmatrix} - \begin{bmatrix} s_{j1X}(t) \\ s_{j1Y}(t) \\ s_{j1Z}(t) \end{bmatrix} + \begin{bmatrix} \rho_X(t) \\ \rho_Y(t) \\ \rho_Z(t) \end{bmatrix}, \tag{22}$$

which, in view of (21), can be rewritten as

$$\begin{bmatrix} d_{jx1}(t) \\ d_{jy1}(t) \\ d_{jz1}(t) \end{bmatrix} = C(\underline{q}_1(t))^T C(\underline{q}_2(t)) \begin{bmatrix} s_{j2x} \\ s_{j2y} \\ s_{j2z} \end{bmatrix} - \begin{bmatrix} s_{j1x} \\ s_{j1y} \\ s_{j1z} \end{bmatrix} + \begin{bmatrix} \rho_{x1}(t) \\ \rho_{y1}(t) \\ \rho_{z1}(t) \end{bmatrix}. \tag{23}$$

Since the docking reference platforms are assumed to be rigidly attached to the modules, the column vectors $[\underline{S}_j^i]_i = (s_{jix}, s_{jiy}, s_{jiz})^T$, $i=1,2$; $j=1,2,3$ are known fixed quantities, and they are independent of t. Thus, $[\underline{\rho}(t)]_1 = (\rho_{x1}(t), \rho_{y1}(t), \rho_{z1}(t))^T$ can be determined from the measured quantities $[\underline{d}_j(t)]_1 = (d_{jx1}(t), d_{jy1}(t), d_{jy1}(t))^T$, $\underline{q}_1(t)$ and $\underline{q}_2(t)$ by using relation (23).

From (19), we also have

$$\underline{\dot{d}}_j = \underline{\dot{d}}_j\big|_1 + \underline{\omega}_1 \times \underline{d}_j = (\underline{\dot{\rho}}\big|_1 + \underline{\omega}_1 \times \underline{\rho}) + (\underline{\dot{S}}_j^2\big|_2 + \underline{\omega}_2 \times \underline{S}_j^2) - (\underline{\dot{S}}_j^1\big|_1 + \underline{\omega}_1 \times \underline{S}_j^1), \tag{24}$$

where $\underline{\dot{d}}_j$ and $\underline{\dot{d}}_j\big|_i$ denote the time rates-of-change of $\underline{d}_j$ with respect to the inertial and moving (x_i,y_i,z_i)-coordinate systems respectively. From the assumption that the modules and docking reference platforms are rigid bodies, $\underline{\dot{S}}_j^2\big|_2$, $\underline{\dot{S}}_j^1\big|_1=\underline{0}$. Consequently,

$$\underline{\dot{d}}_j\big|_1 = \underline{\dot{\rho}}\big|_1 + \underline{\omega}_1 \times (\underline{\rho} - \underline{d}_j - \underline{S}_j^1) + \underline{\omega}_2 \times \underline{S}_j^2 = \underline{\dot{\rho}}\big|_1 + (\underline{\omega}_2 - \underline{\omega}_1) \times \underline{S}_j^2. \tag{25}$$

The above equation has the following representation with respect to basis B_1:

$$\begin{bmatrix} \dot{d}_{jx1} \\ \dot{d}_{jy1} \\ \dot{d}_{jz1} \end{bmatrix} = \begin{bmatrix} \dot{\rho}_{x1} \\ \dot{\rho}_{y1} \\ \dot{\rho}_{z1} \end{bmatrix} + C(\underline{q}_1)^T C(\underline{q}_2) \begin{bmatrix} \omega_{2y}s_{j2z} - \omega_{2z}s_{j2y} \\ \omega_{2z}s_{j2x} - \omega_{2x}s_{j2z} \\ \omega_{2x}s_{j2y} - \omega_{2y}s_{j2x} \end{bmatrix} - \begin{bmatrix} \omega_{1y}[\underline{S}_j^2]_{1z} - \omega_{1z}[\underline{S}_j^2]_{1y} \\ \omega_{1z}[\underline{S}_j^2]_{1x} - \omega_{1x}[\underline{S}_j^2]_{1z} \\ \omega_{1x}[\underline{S}_j^2]_{1y} - \omega_{1y}[\underline{S}_j^2]_{1x} \end{bmatrix}, \tag{26}$$

where $[\underline{S}_j^2]_1 = ([\underline{S}_j^2]_{1x}, [\underline{S}_j^2]_{1y}, [\underline{S}_j^2]_{1z})^T = C(\underline{q}_1)^T C(\underline{q}_2)(s_{j2x}, s_{j2y}, s_{j2z})^T$. Using (26), $[\underline{\rho}(t)]_1 = (\rho_{x1}(t), \rho_{y1}(t), \rho_{z1}(t))^T$ can be determined from the measured quantities

$[\underline{d}_j(t)]_1 = (d_{jx1}(t), d_{jy1}(t), d_{jz1}(t))^T$, $\underline{q}_1(t), \underline{q}_2(t), [\underline{\omega}_1(t)]_1$ and $[\underline{\omega}_2(t)]_2$.

Thus, the complete mathematical model for terminal rendez-vous is given by differential equations (6),(9) and (14) along with output equations (23) and (26). The output variables are $[\underline{\omega}_1]_1$, $\underline{q}_1$, i=1,2; $[\underline{d}_j]_1$ and $[\underline{\dot{d}}_j|_1]_1$, j=1,2,3.

III. BASIC REQUIREMENTS

Before discussing the problem of deriving suitable guidance laws for terminal rendez-vous, we first consider a few basic requirements, physical constraints and difficulties associated with the problem.

(i) During terminal rendez-vous, the maneuvers of the two modules must be collision-free. Moreover, they should have a certain margin of safety. Let $\Gamma_i(t)$ denote the closed bounded spatial domain in $\mathbb{R}^3$ occupied by the i-th module at time t. The collision-free requirement implies that $\Gamma_1(t) \cap \Gamma_2(t)$ must be an empty set for all t in the terminal rendez-vous period $[0, t_T]$. In general, $\Gamma_1(t)$ and $\Gamma_2(t)$ are nonconvex. We may introduce a margin of safety by imposing a more stringent requirement that $Co(\Gamma_1(t)) \cap Co(\Gamma_2(t))$ be empty for all $t \in [0, t_T]$. Of course, in this case, the docking reference platforms Π_1 should be contained in the boundary of $Co(\Gamma_1(t))$.

(ii) It is evident from (14) that the relative translational motion of the mass centers of the two modules referenced with respect to the moving coordinate system (x_1, y_1, z_1) depends on the angular velocity $\underline{\omega}_1$ and the control torque $\underline{\tau}_c^1$. From the control viewpoint, it is highly desirable to minimize the effect of this coupling so that the relative translational and rotational motions of the two modules can be controlled almost independently.

(iii) It is desirable to have the docking reference platforms Π_1 and Π_2 approaching each other in a smooth non-oscillatory manner during the final approach. This can be fulfilled by requiring $\|\underline{d}_j(\cdot)\|$ to be a smooth strictly monotone decreasing function of t over some subinterval $[t', t_T] \subseteq [0, t_T]$, and $\|\underline{d}_j(t)\| \to 0$ as $t \to t_T$. Here, we assume that the corresponding docking reference points of the two modules can be matched exactly. Thus, it is possible to have $\underline{d}_j = \underline{0}$, j=1,2,3 simultaneously.

(iv) At the initiation of the terminal rendez-vous stage, it is desirable to orient the modules so that their docking reference platforms face each other. Moreover, they remain facing each other throughout the terminal rendez-vous period. Thus, the corresponding docking reference points p_{1j} and p_{2j}, j=1,2,3, are exposed to each other optically so that $\underline{d}_j(t)$ can be measured at any time $t \in [0, t_T]$.

(v) The complete guidance control system for terminal rendez-vous should be on-board the modules so that no ground assistance is required. This implies that the guidance laws should depend only on module-based sensor output data, and that they should be sufficiently simple so as to permit on-board real-time implementation.

Evidently, the inclusion of the foregoing requirements and constraints associated with terminal rendez-vous leads to a formidable control problem. A basic difficulty is that the characterization of the class of controls $\underline{F}_{c1} = \underline{F}_{c1}(t)$,

$\tau^i_{-c} = \tau^i_{-c}(t)$, i=1,2, which generate the collision-free maneuvers and monotone approach cannot be readily determined.   In contrast to the usual attitude control problem for a single rigid body in which the natural physical quantities such as energy and momentum play an important role in the derivation of suitable guidance laws, the variables to be controlled here (i.e. $\underline{d}_j(t)$) are not natural physical quantities.   In what follows, we propose an approach which bypasses some of the above mentioned difficulties.

IV. PROPOSED APPROACH

The basic idea is to decompose the terminal rendez-vous and docking into three phases:

(i) <u>Acquisition Phase</u>: At the initiation of terminal rendez-vous,appropriate attitude maneuvers are introduced so that the docking reference platforms of the two modules face each other.   This permits the determination of the vectors $\underline{d}_j(t)$ by optical methods.   The task can be achieved by simple attitude maneuvers involving one or both modules using optical or infrared sensors.   We shall not discuss this relatively simple automatic acquisition problem here.

(ii) <u>Reference Platform Alignment Phase</u>: To avoid the possibility of collision between the two modules to be assembled, an attitude maneuver involving one or both modules is introduced when they are sufficiently far apart.   The objective is to align the docking reference platforms so that

$$\underline{d}_1(t_1) = \underline{d}_2(t_1) = \underline{d}_3(t_1) \quad \text{and} \quad \underline{d}_1(t_1) \times \underline{n}_1(t_1) = \underline{0} \tag{27}$$

at some time $t_1 > 0$, where $\underline{n}_1$ denotes the unit normal vector associated with Π_1 directed to the exterior of the i-th module.   The above condition implies that the platforms are parallel to each other and that the corresponding docking reference points directly face each other.   Moreover, we require that the time rate-of-change of $\underline{d}_j$ relative to the (x_1, y_1, z_1)-coordinate system satisfies

$$\underline{\dot{d}}_j \big|_1 (t_1) = \underline{0}, \quad j=1,2,3. \tag{28}$$

The above condition, in view of (25), implies

$$\underline{\dot{\rho}} \big|_1 (t_1) = [(\underline{\omega}_1 - \underline{\omega}_2) \times \underline{S}^2_j](t_1), \quad j=1,2,3. \tag{29}$$

(iii) <u>Final Approach Phase</u>: The objective of this phase is to control the two modules in such a way that condition (27) is maintained at all times during the final approach.   Moreover, $\|\underline{d}_j(t)\|$ decreases monotonically toward zero and at a specified time $t_T > 0$, we require

$$\|\underline{d}_j(t_T)\| \leqslant \varepsilon_1, \qquad \|\underline{\dot{d}}_j\big|_1(t_T)\| \leqslant \varepsilon_2, \tag{30}$$

where ε_1 and ε_2 are specified nonnegative numbers.

V. GUIDANCE LAW

Assuming that the docking reference platforms face each other initially, the problem is to derive appropriate feedback controls such that conditions (27) and (28) (resp.(30)) are satisfied for the alignment phase (resp. the final approach phase). Here, we assume that module 2 contains a control system for regulating its attitude about a desired orientation with respect to the inertial frame, independent of the motion of module 1. The attitude of module 2 may vary with time due to both internal and external disturbances and changes in the desired module attitude. This assumption is also applicable to the terminal rendezvous and docking of a space shuttle vehicle (identified with module 1) with a space station (identified with module 2). The problem reduces to finding a terminal guidance law for module 1 with a moving target corresponding to the docking reference platform Π_2 of module 2. Since the future motion of module 2 is not known in advance, useful guidance laws cannot be derived by solving an optimal tracking problem involving an integral cost functional. In what follows, we shall derive a terminal guidance law for both the alignment and final approach phases which only depends on the instantaneous states of both modules.

A. Attitude Control

First, we consider the rotational motion of module 1 described by (6),(7), (9) and (10). Let $\underline{\omega}_1^d(t)$ and $\underline{q}_1^d(t)$ denote respectively the desired $\underline{\omega}_1$ and $\underline{q}_1$ at time t. Evidently, we may set $\underline{\omega}_1^d(t) = \underline{\omega}_2(t)$ for $t > 0$. The quantity $\underline{q}_1^d(t)$ is determined by requiring the docking reference platforms Π_1 and Π_2 to be parallel, with their respective reference points $\underline{p}_j^i$ directly opposite each other as shown in Fig.2. Thus, we have

$$\underline{\rho}^d - \underline{\tilde{S}}_j^1 = \underline{d}_j^d - \underline{S}_j^2 , \qquad j=1,2,3. \tag{31}$$

For the alignment phase, we set $\underline{d}_j^d = \underline{d}^d$, $j=1,2,3$, where $\underline{d}^d$ is a vector which is normal to the plane containing Π_2, and its length is sufficiently large for ensuring collision-free maneuvers. For the final approach phase, we set $\underline{d}_j^d = \underline{d}^d$ with small $\|\underline{d}^d\|$. Let $\tilde{B}_1(t) = \{\underline{\tilde{e}}_{x1}(t), \underline{\tilde{e}}_{y1}(t), \underline{\tilde{e}}_{z1}(t)\}$ denote the basis corresponding to the desired orientation of the principal axes of module 1 at time t; $\underline{d}^d(t) = d_X^d(t)\underline{e}_X + d_Y^d(t)\underline{e}_Y + d_Z^d(t)\underline{e}_Z$, and $\underline{\tilde{\rho}}^d(t) = \tilde{\rho}_{x1}^d(t)\underline{\tilde{e}}_{x1}(t) + \tilde{\rho}_{y1}^d(t)\underline{\tilde{e}}_{y1}(t) + \tilde{\rho}_{z1}^d(t)\underline{\tilde{e}}_{z1}(t)$. Since $[\underline{\tilde{S}}_j^1]_0 = C(\underline{q}_1^d(t))[\underline{S}_j^1]_1$, (31) has the following representation:

$$\underline{w}_j(t) \triangleq \begin{bmatrix} d_X^d(t) \\ d_Y^d(t) \\ d_Z^d(t) \end{bmatrix} - C(\underline{q}_2(t)) \begin{bmatrix} s_{j2x} \\ s_{j2y} \\ s_{j2z} \end{bmatrix} = C(\underline{q}_1^d(t)) \left\{ \begin{bmatrix} \tilde{\rho}_{x1}^d(t) \\ \tilde{\rho}_{y1}^d(t) \\ \tilde{\rho}_{z1}^d(t) \end{bmatrix} - \begin{bmatrix} s_{j1x} \\ s_{j1y} \\ s_{j1z} \end{bmatrix} \right\} , \quad j=1,2,3. \tag{32}$$

Setting j=1,2 in (32), we have

$$\Delta\underline{w}(t) = \underline{w}_1(t) - \underline{w}_2(t) = C(\underline{q}_1^d(t))\Delta\underline{S}_1, \tag{33}$$

where $\Delta\underline{w}$ and $\Delta\underline{S}_1$ are known quantities given by

$$\Delta \underline{S}_i = \begin{bmatrix} s_{2ix} \\ s_{2iy} \\ s_{2iz} \end{bmatrix} - \begin{bmatrix} s_{1ix} \\ s_{1iy} \\ s_{1iz} \end{bmatrix} , \quad i=1,2; \quad \Delta \underline{w}(t) = C(\underline{q}_2(t)) \Delta \underline{S}_2. \tag{34}$$

Note that $\Delta \underline{S}_i$ is a constant vector representing the edge of Π_i joining the docking reference points $\underline{p}_2^i$ and $\underline{p}_1^i$. The desired quaternion for module 1 at time t is a vector $\underline{q}_1^d(t)$ with unit norm satisfying (33). It has the following explicit form:

$$\underline{q}_1^d = (\eta_1 \sin(\Phi/2), \eta_2 \sin(\Phi/2), \eta_3 \sin(\Phi/2), \cos(\Phi/2))^T, \tag{35}$$

where

$$(\eta_1, \eta_2, \eta_3)^T = (\Delta \underline{w} \times \Delta \underline{S}_1) / \| \Delta \underline{w} \times \Delta \underline{S}_1 \| ; \tag{36}$$

$$\sin(\Phi/2) = \pm \left\{ \frac{\| \Delta \underline{w} \|^2 - (\Delta \underline{S}_1)^T \Delta \underline{w}}{2 \| \Delta \underline{w} \|^2} \right\}^{\frac{1}{2}}, \quad \text{(+ if } \Phi/2 \text{ is in the first or second quadrant, and } - \text{ otherwise);}$$

$$\cos(\Phi/2) = \pm \left\{ \frac{\| \Delta \underline{w} \|^2 + (\Delta \underline{S}_1)^T \Delta \underline{w}}{2 \| \Delta \underline{w} \|^2} \right\}^{\frac{1}{2}}, \quad \text{(+ if } \Phi/2 \text{ is in the first or fourth quadrant, and } - \text{ otherwise).}$$

To derive an attitude control law for module 1, we introduce a nonlinear transformation $\underline{z}_1 = \underline{z}_1(\underline{q}_1)$ defined by

$$\underline{z}_1(\underline{q}_1) = (q_{11}/q_{14}, q_{12}/q_{14}, q_{13}/q_{14})^T. \tag{37}$$

The vector $\underline{z}_1(\underline{q}_1)$ corresponds to the so-called Gibbs vector or Cayley-Rodriguez parameters [14]-[16]. It can be verified that the evolution of $\underline{z}_1$ with time is governed by the following equation:

$$2 d\underline{z}_1/dt = \{(\underline{z}_1^T [\underline{\omega}_1]_1)[I] - B_1([\underline{\omega}_1]_1)\} \underline{z}_1 + [\underline{\omega}_1]_1, \tag{38}$$

where [I] is the 3×3 identity matrix, and B_1 is given in (13). Let $\underline{z}_1^d = (q_{11}^d/q_{14}^d, q_{12}^d/q_{14}^d, q_{13}^d/q_{14}^d)^T$. We introduce the deviations:

$$[\Delta \underline{\omega}_1]_1 \overset{\Delta}{=} [\underline{\omega}_1^d]_1 - [\underline{\omega}_1]_1, \quad \Delta \underline{z}_1 \overset{\Delta}{=} \underline{z}_1^d - \underline{z}_1(\underline{q}_1). \tag{39}$$

These deviations satisfy the following equations:

$$d[\Delta \underline{\omega}_1]_1/dt = \frac{1}{2} \Pi_1 \{A([\Delta \underline{\omega}_1]_1) - 2A([\underline{\omega}_1^d]_1)\}[\Delta \underline{\omega}_1]_1 - \Pi_{p1}^{-1} [\underline{\tau}_{c1}]_1 + \underline{f}_d, \tag{40}$$

where $\underline{f}_d = d[\underline{\omega}_1^d]_1/dt + \Pi_1 A([\underline{\omega}_1^d]_1)[\underline{\omega}_1^d]_1/2,$

77

$$A([\underline{\omega}_1]_1) = \begin{bmatrix} 0 & \omega_{1z} & \omega_{1y} \\ \omega_{1z} & 0 & \omega_{1x} \\ \omega_{1y} & \omega_{1x} & 0 \end{bmatrix}, \quad \Pi_{p1} = \begin{bmatrix} I_{1x} & & \bigcirc \\ & I_{1y} & \\ \bigcirc & & I_{1z} \end{bmatrix}, \quad \Pi_1 = \begin{bmatrix} I_{i1} & & \bigcirc \\ & I_{i2} & \\ \bigcirc & & I_{i3} \end{bmatrix},$$

$$i = 1, 2, \qquad (41)$$

$$2d(\Delta\underline{z}_1)/dt = \{(\underline{z}_1^d - \Delta\underline{z}_1)(\underline{z}_1^d - \Delta\underline{z}_1)^T + [I]\}[\Delta\underline{\omega}_1]_1 + \{(\underline{z}_1^d - \Delta\underline{z}_1)^T[\underline{\omega}_1^d]_1[I]$$

$$+ \underline{z}_1^d[\underline{\omega}_1^d]_1^T - B_1([\underline{\omega}_1^d]_1)\}\Delta\underline{z}_1 - B_1([\Delta\underline{\omega}_1]_1)(\underline{z}_1^d - \Delta\underline{z}_1) + 2\underline{h}^d, \qquad (42)$$

where

$$\underline{h}^d \overset{\Delta}{=} d\underline{z}_1^d/dt + \{(B_1([\underline{\omega}_1^d]_1) - (\underline{z}_1^d)^T[\underline{\omega}_1^d]_1[I])\underline{z}_1^d - [\underline{\omega}_1^d]_1\}/2. \qquad (43)$$

We shall use (40) and (42) to derive an attitude control law $\underline{\tau}_{c1}$ such that $\|([\Delta\underline{\omega}_1(t)]_1, \Delta\underline{z}_1(t))\| \to 0$ as $t \to \infty$.

Consider the following positive definite function of $([\Delta\underline{\omega}_1]_1, \Delta\underline{z}_1)$ defined on $\mathbb{R}^6$:

$$V_1 = [\Delta\underline{\omega}_1]_1^T \Pi_{p1}^2 [\Delta\underline{\omega}_1]_1 + k_{p1}(\Delta\underline{z}_1)^T \Delta\underline{z}_1, \qquad (44)$$

where k_{p1} is a positive constant. By direct computation, the rate-of-change of V_1 with respect to t along any trajectory of (40) and (42) is given by

$$dV_1/dt = 2[\Delta\underline{\omega}_1]_1^T \Pi_{p1}^2 \{\underline{f}_d - \Pi_1 A([\underline{\omega}_1^d]_1)[\Delta\underline{\omega}_1]_1 + k_{p1}\Pi_{p1}^{-2}((\underline{z}_1^d - \Delta\underline{z}_1)(\underline{z}_1^d - \Delta\underline{z}_1)^T + [I])\Delta\underline{z}_1/2$$

$$- \Pi_{p1}^{-1}[\underline{\tau}_{c1}]_1\} + k_{p1}\{2(\underline{h}^d)^T \Delta\underline{z}_1 + (\underline{z}_1^d - \Delta\underline{z}_1)^T[\underline{\omega}_1^d]_1(\Delta\underline{z}_1)^T \Delta\underline{z}_1$$

$$+ ((\Delta\underline{z}_1)^T[\underline{\omega}_1^d]_1)((\underline{z}_1^d)^T \Delta\underline{z}_1) - (\underline{z}_1^d)^T B_1([\Delta\underline{\omega}_1]_1)\Delta\underline{z}_1\}. \qquad (45)$$

We wish to choose a feedback control $[\underline{\tau}_{c1}]_1$ such that $dV_1(t)/dt$ is nonpositive for all $t \geqslant 0$. A possible choice is given by

$$\Pi_{p1}^{-1}[\underline{\tau}_{c1}]_1 = \underline{f}_d + \{K_1 - \Pi_1 A([\underline{\omega}_1^d]_1) + k_{p1}\gamma_1[I]\}[\Delta\underline{\omega}_1]_1$$

$$+ k_{p1}\Pi_{p1}^{-2}\{(\underline{z}_1^d - \Delta\underline{z}_1)(\underline{z}_1^d - \Delta\underline{z}_1)^T + [I]\}\Delta\underline{z}_1/2, \qquad (46)$$

where

$$\gamma_1 = \frac{[2\underline{h}^d + (\underline{z}_1^d - \Delta\underline{z}_1)^T[\underline{\omega}_1^d]_1\Delta\underline{z}_1 + ((\Delta\underline{z}_1)^T[\underline{\omega}_1^d]_1)\underline{z}_1^d + B_1([\Delta\underline{\omega}_1]_1)\underline{z}_1^d]^T\Delta\underline{z}_1}{2[(I_{1x}\Delta\omega_{1x})^2 + (I_{1y}\Delta\omega_{1y})^2 + (I_{1z}\Delta\omega_{1z})^2]} \qquad (47)$$

78

and K_1 is a feedback gain matrix with positive diagonal elements:

$$K_1 = \begin{bmatrix} k_{1x} & & \bigcirc \\ & k_{1y} & \\ \bigcirc & & k_{1z} \end{bmatrix}. \tag{48}$$

With the above control law, dV_1/dt reduces to

$$dV_1/dt = -2[k_{1x}(I_{1x}\Delta\omega_{1x})^2 + k_{1y}(I_{1y}\Delta\omega_{1y})^2 + k_{1z}(I_{1z}\Delta\omega_{1z})^2] \leqslant 0, \tag{49}$$

and the corresponding equations for $\Delta\underline{z}_1$ and $[\Delta\underline{\omega}_1]_1$ are given by (42) and

$$\begin{aligned} d[\Delta\underline{\omega}_1]_1/dt &= \{\Pi_1 A([\Delta\underline{\omega}_1]_1)/2 - K_1 - k_{p1}\gamma_1[I]\}[\Delta\underline{\omega}_1]_1 \\ &\quad + k_{p1}\Pi_{p1}^{-2}\{(\underline{z}_1^d - \Delta\underline{z}_1)(\underline{z}^d - \Delta\underline{z})^T + [I]\}\Delta\underline{z}_1/2. \end{aligned} \tag{50}$$

Note that when the attitude of module 2 varies with time, system (42) and (50) is nonautonomous.

Evidently, (49) implies that for the feedback control system,

$$\| ([\Delta\underline{\omega}_1(t)]_1, \Delta\underline{z}_1(t)) \|^2 \leqslant \frac{\max\{k_{p1}, I_{1x}^2, I_{1y}^2, I_{1z}^2\}}{\min\{k_{p1}, I_{1x}^2, I_{1y}^2, I_{1z}^2\}} \| ([\Delta\underline{\omega}_1(0)]_1, \Delta\underline{z}_1(0)) \|^2 \tag{51}$$

for all $t \geqslant 0$. Moreover, $dV_1/dt = 0$ if and only if $[\Delta\underline{\omega}_1]_1 = \underline{0}$. Since $(\underline{z}_1^d - \Delta\underline{z}_1)(\underline{z}_1^d - \Delta\underline{z}_1)^T + [I]$ is positive definite on $\mathbb{R}^3$ for all $(\underline{z}_1^d - \Delta\underline{z}_1)$, when $[\Delta\underline{\omega}_1]_1 = \underline{0}$, the right-hand-side of (50) is equal to $\underline{0}$ if and only if $\Delta\underline{z}_1 = \underline{0}$. Consequently, the set $\mathscr{E} = \{([\Delta\underline{\omega}_1]_1, \Delta\underline{z}_1) \in \mathbb{R}^6 : [\Delta\underline{\omega}_1]_1 = \underline{0}\}$ contains only the origin as an equilibrium state. Assuming that the rotational motion of module 2 is stable, there exists a positive constant c such that $\| ([\underline{\omega}_1^d(t)]_1, \underline{z}_1^d(t)) \| \leqslant c$ for all $t \geqslant 0$. Then, on any compact subset of $\mathbb{R}^6$, the right-hand-sides of (42) and (50) are bounded in norm for all $t \geqslant 0$. We can deduce from LaSalle's Invariance Principle for nonautonomous systems [17],[18] that all trajectories $([\Delta\underline{\omega}_1(t)]_1, \Delta\underline{z}_1(t))$ of (42) and (50) tend to $\mathscr{E}$ as $t \to \infty$. However, we cannot conclude that $([\Delta\underline{\omega}_1(t)]_1, \Delta\underline{z}_1(t)) \to \underline{0}$ as $t \to \infty$. Now, if we impose the stronger assumption that the attitude control system of module 2 has the property that $[\underline{\omega}_2(t)]_2 \to \underline{0}$ and $\underline{q}_2(t) \to \underline{q}_2^\infty$ (a constant vector) as $t \to \infty$, the system (42),(50) is asymptotic to the following autonomous system:

$$\begin{aligned} d[\Delta\underline{\omega}_1]_1/dt &= \{\Pi_1 A([\Delta\underline{\omega}_1]_1)/2 - K_1 - k_{p1}\gamma_1^\infty[I]\}[\Delta\underline{\omega}_1]_1 \\ &\quad + k_{p1}\Pi_{p1}^{-2}\{(\underline{z}_{1\infty}^d - \Delta\underline{z}_1)(\underline{z}_{1\infty}^d - \Delta\underline{z}_1)^T + [I]\}\Delta\underline{z}_1/2, \end{aligned} \tag{52}$$

$$2d(\Delta\underline{z})/dt = \{(\underline{z}_{1\infty}^d - \Delta\underline{z}_1)(\underline{z}_{1\infty}^d - \Delta\underline{z}_1)^T + [I]\} [\Delta\underline{\omega}_1]_1 - B_1([\Delta\underline{\omega}_1]_1)(\underline{z}_{1\infty}^d - \Delta\underline{z}_1),$$

where $\underline{z}_{1\infty}^d = (q_{21}^\infty/q_{24}^\infty, q_{22}^\infty/q_{24}^\infty, q_{23}^\infty/q_{24}^\infty)^T$, and

$$\gamma_1^\infty = -\frac{(\underline{z}_{1\infty}^d)^T B_1([\Delta\underline{\omega}_1]_1)\Delta\underline{z}_1}{2[(I_{1x}\Delta\omega_{1x})^2 + (I_{1y}\Delta\omega_{1y})^2 + (I_{1z}\Delta\omega_{1z})^2]} . \tag{53}$$

It follows from a result of Yoshizawa [19],[20] that all trajectories of (42), (50) tend to the largest invariant set M of (52) in $\mathscr{E}$. Since $M = \{\underline{0}\}$, $([\Delta\underline{\omega}_1(t)]_1, \Delta\underline{z}_1(t)) \to \underline{0}$ as $t \to \infty$.

Alternatively, we may add the following term $\Pi_{p1}^{-1}[\underline{\tau}_{c1}]_1$ to the control law (46):

$$\Pi_{p1}^{-1}[\underline{\tau}_{c1}]_1 = k_{p1}[\Delta\underline{\omega}_1(t)]_1(\Delta\underline{z}_1)^T(\Delta\underline{z}_1)/\{2[\Delta\underline{\omega}_1(t)]_1^T\Pi_{p1}^2[\Delta\underline{\omega}_1(t)]_1\} , \tag{54}$$

where k_{p1} is a positive constant. Then,

$$dV_1/dt = -2[k_{1x}(I_{1x}\Delta\omega_{1x})^2 + k_{1y}(I_{1y}\Delta\omega_{1y})^2 + k_{1z}(I_{1z}\Delta\omega_{1z})^2] - k_{p1}(\Delta\underline{z}_1)^T\Delta\underline{z}_1$$

$$\leqslant -2\delta V_1, \tag{55}$$

where $\delta = \min\{k_{1x}, k_{1y}, k_{1z}, k_{p1}/(2k_{p1})\}$. Hence, we have

$$V_1(t) \leqslant V_1(0)\exp\{-2\delta t\}, \quad t \geqslant 0, \tag{56}$$

which implies that $\|([\Delta\underline{\omega}_1(t)]_1, \Delta\underline{z}_1(t))\| \to 0$ as $t \to \infty$. However, the form of (54) is undesirable, since it is singular at the origin $(\Delta\underline{\omega}_1, \Delta\underline{z}_1) = \underline{0}$.

Finally, in the special case where $\underline{z}_1^d = \underline{0}$ and $[\underline{\omega}_1^d]_1 = \underline{0}$, the control law given by (46) reduces to

$$\Pi_{p1}^{-1}[\underline{\tau}_{c1}]_1 = K_1[\Delta\underline{\omega}_1]_1 + k_{p1}(1 + (\Delta\underline{z}_1)^T\Delta\underline{z}_1)\Pi_{p1}^{-2}\Delta\underline{z}_1/2, \tag{57}$$

which is essentially the same result as that given in [14], although the above expression has a simpler form.

B. Relative Translational Motion Control

Now, we shall derive a control law for the translational motion of module 1 relative to module 2. Let $\underline{\rho}^d(t)$ (resp. $\underline{\rho}(t)$) denote the vector originating from the desired (resp. actual) position of the mass center of module 1, and pointing to the mass center of module 2 at time t as shown in Fig.3. As in Figure 2, the desired location for Π_1 is determined by requiring Π_1 and Π_2 to be parallel, with their respective reference points $\underline{p}_j^i$ directly opposite each other such that (31) is satisfied for $\underline{d}_j^d = \underline{d}^d$, j=1,2,3. We define

$$\Delta \underline{\rho}(t) = \underline{\rho}^d(t) - \underline{\rho}(t), \tag{58}$$

where

$$\underline{\rho}(t) = \underline{R}_2(t) - \underline{R}_1(t). \tag{59}$$

Using the fact that

$$\frac{d\underline{\rho}^d}{dt} = \frac{d\underline{\rho}^d}{dt}\Big|_2 + \underline{\omega}_2 \times \underline{\rho}^d = \underline{\omega}_2 \times \underline{\rho}^d \ , \qquad \frac{d\Delta\underline{\rho}}{dt} = \frac{d\Delta\underline{\rho}}{dt}\Big|_1 + \underline{\omega}_1 \times \Delta\underline{\rho}, \tag{60}$$

where $d(\cdot)/dt$ and $[d(\cdot)/dt]\big|_i$ denote the time rates-of-change with respect to the inertial and moving (x_i, y_i, z_i)-coordinate systems respectively, we can obtain the following equation for $\Delta\underline{\rho}$:

$$\frac{d^2\Delta\underline{\rho}}{dt^2}\Big|_1 + 2\underline{\omega}_1 \times \frac{d\Delta\underline{\rho}}{dt}\Big|_1 + \frac{d\underline{\omega}_1}{dt} \times \Delta\underline{\rho} + \underline{\omega}_1 \times (\underline{\omega}_1 \times \Delta\underline{\rho}) = \frac{d\underline{\omega}_2}{dt} \times \underline{\rho}^d + \underline{\omega}_2 \times (\underline{\omega}_2 \times \underline{\rho}^d)$$

$$-\underline{F}_{g2}/M_2 + \underline{F}_{g1}/M_1 - \underline{F}_{c2}/M_2 + \underline{F}_{c1}/M_1. \tag{61}$$

The above equation has the following representation with respect to basis B_1:

$$[\Delta\underline{\ddot{\rho}}]_1 + 2B_1([\underline{\omega}_1]_1)[\Delta\underline{\dot{\rho}}]_1 + \{B_2([\underline{\omega}_1]_1) + B_3([\underline{\omega}_1]_1) + \omega_o^2[I]\} \ [\Delta\underline{\rho}]_1$$

$$-B_1([\Delta\underline{\rho}]_1)\Pi_{p1}^{-1} [\underline{\tau}_{c1}]_1 = C(\underline{q}_1)^T C(\underline{q}_2) \{(B_2([\underline{\omega}_2]_2) + B_3([\underline{\omega}_2]_2) + \omega_o^2[I])[\underline{\rho}^d]_2$$

$$- B_1([\underline{\rho}^d]_2)\Pi_{p2}^{-1} [\underline{\tau}_{c2}]_2\} - [\underline{u}]_1, \tag{62}$$

where $\Delta\underline{\rho} = \Delta\rho_{x1}\underline{e}_{x1} + \Delta\rho_{y1}\underline{e}_{y1} + \Delta\rho_{z1}\underline{e}_{z1}$, $\underline{\rho}^d = \rho_{x2}^d\underline{e}_{x2} + \rho_{y2}^d\underline{e}_{y2} + \rho_{z2}^d\underline{e}_{z2}$, $[\Delta\underline{\rho}]_1 = (\Delta\rho_{x1}, \Delta\rho_{y1}, \Delta\rho_{z1})^T$, $[\Delta\underline{\dot{\rho}}]_1 = (d\Delta\rho_{x1}/dt, d\Delta\rho_{y1}/dt, d\Delta\rho_{z1}/dt)^T$, $[\Delta\underline{\ddot{\rho}}]_1 = (d^2\Delta\rho_{x1}/dt^2, d^2\Delta\rho_{y1}/dt^2, d^2\Delta\rho_{z1}/dt^2)^T$, $[\underline{\rho}^d]_2 = (\rho_{x2}^d, \rho_{y2}^d, \rho_{z2}^d)^T$, $[\underline{u}]_1 = (u_{x1}, u_{y1}, u_{z1})^T$, and

$$B_1([\Delta\underline{\rho}]_1) = \begin{bmatrix} 0 & -\Delta\rho_{z1} & \Delta\rho_{y1} \\ \Delta\rho_{z1} & 0 & -\Delta\rho_{x1} \\ -\Delta\rho_{y1} & \Delta\rho_{x1} & 0 \end{bmatrix}. \tag{63}$$

The matrices B_j, $j=1,2,3$, are defined in (13) and (15). We shall use (61) to derive a control law $[\underline{u}]_1$ for module 1 such that $\|([\Delta\underline{\rho}(t)]_1, [\Delta\underline{\dot{\rho}}(t)]_1)\| \to 0$ as $t \to \infty$.

Here, we consider the following positive definite function of $([\Delta\underline{\rho}]_1, [\Delta\underline{\dot{\rho}}]_1)$ on $\mathbb{R}^6$:

81

$$V_2 = k_{\rho 0}\omega_o^2 [\Delta\underline{\rho}]_1^T [\Delta\underline{\rho}]_1 + [\Delta\underline{\dot{\rho}}]_1^T [\Delta\underline{\dot{\rho}}]_1 \; , \quad k_{\rho 0} > 1. \tag{64}$$

The time rate-of-change of V_2 along any trajectory of (61) is given by

$$dV_2/dt = 2[\Delta\underline{\rho}]_1^T (-\{B_2([\underline{\omega}_1]_1) + B_3([\underline{\omega}_1]_1) - (k_{\rho 0}-1)\omega_o^2 [I]\}[\Delta\underline{\rho}]_1 + C(\underline{q}_1)^T C(\underline{q}_2)\{(B_2([\underline{\omega}_2]_2)$$

$$+ B_3([\underline{\omega}_2]_2) - \omega_o^2 [I])[\underline{\rho}^d]_2 - B_1([\underline{\rho}^d]_2)\Pi_{p2}^{-1}[\underline{\tau}_{c2}]_2\} + B_1([\Delta\underline{\rho}]_1\Pi_{p1}^{-1}[\underline{\tau}_{c1}]_1 - [\underline{u}]_1). \tag{65}$$

If we set

$$[\underline{u}]_1 = -\{B_2([\underline{\omega}_1]_1) + B_3([\underline{\omega}_1]_1) - (k_{\rho 0}-1)\omega_o^2 [I]\}[\Delta\underline{\rho}]_1 + C^T(\underline{q}_1)C(\underline{q}_2)\{(B_2([\underline{\omega}_2]_2) + B_3([\underline{\omega}_2]_2)$$

$$+ \omega_o^2 [I])[\underline{\rho}^d]_2 - B_1([\underline{\rho}^d]_2)\Pi_{p2}^{-1}[\underline{\tau}_{c2}]_2\} + B_1([\Delta\underline{\rho}]_1)\Pi_{p1}^{-1}[\underline{\tau}_{c1}]_1$$

$$+ (k_{\rho 1}[I] - 2B_1([\underline{\omega}_1]_1))[\Delta\underline{\dot{\rho}}]_1 \tag{66}$$

with $k_{\rho 1}$ being a positive constant, then dV_2/dt reduces to

$$dV_2/dt = -2[\Delta\underline{\dot{\rho}}]_1^T \{k_{\rho 1}[I] - 2B_1([\underline{\omega}_1]_1)\}[\Delta\underline{\dot{\rho}}]_1 = -2k_{\rho 1}[\Delta\underline{\dot{\rho}}]_1^T [\Delta\underline{\dot{\rho}}]_1 \le 0, \tag{67}$$

and $[\Delta\underline{\rho}]_1$ is governed by the following linear time-invariant differential equation:

$$[\Delta\underline{\ddot{\rho}}]_1 + k_{\rho 1}[\Delta\underline{\dot{\rho}}]_1 + k_{\rho 0}\omega_o^2 [\Delta\underline{\rho}]_1 = \underline{0}. \tag{68}$$

It is apparent that the above equation for $[\Delta\underline{\rho}]_1$ is decoupled from the equations for $[\Delta\underline{\omega}_1]_1$ and $\Delta\underline{z}_1$ given by (42) and (50). Furthermore, the control law given by (66) involves partial cancellation of the terms in (62). Therefore it is of importance to consider the effect of imperfect cancellation on the system behavior. The imperfect cancellation may be caused by inaccurate knowledge of the model parameters and state variables, and actuator saturation. We model this imperfection by introducing persistent disturbances $\underline{N}$ in (68) as follows.

$$[\Delta\underline{\ddot{\rho}}]_1 + k_{\rho 1}[\Delta\underline{\dot{\rho}}]_1 + k_{\rho 0}\omega_o^2 [\Delta\underline{\rho}]_1 = N(t, [\Delta\underline{\rho}]_1, [\Delta\underline{\dot{\rho}}]_1) \tag{69}$$

We require that the zero state of (68) be stable under persistent disturbances [21],[22], i.e. given any $\varepsilon > 0$, there exist two positive numbers $\delta_1(\varepsilon)$ and $\delta_2(\varepsilon)$ such that if

$$\| ([\Delta\underline{\rho}(0)]_1, [\Delta\underline{\dot{\rho}}(0)]_1) \| < \delta_1(\varepsilon),$$

$$\|\underline{N}(t, [\Delta\underline{\rho}]_1, [\Delta\underline{\dot{\rho}}]_1)\| \le \delta_2(\varepsilon) \text{ for all } \|([\Delta\underline{\rho}]_1, [\Delta\underline{\dot{\rho}}]_1)\| \le \varepsilon \text{ and } t > 0,$$

then the corresponding solutions of the perturbed system (69) satisfy

$$\| ([\Delta \underline{\rho}(t)]_1, [\Delta \underline{\dot{\rho}}(t)]_1) \| \leq \varepsilon \quad \text{for all } t \geq 0.$$

It can be readily shown that the zero state of (69) is stable under persistent disturbances for any $k_{\rho 1} > 0$. By taking $k_{\rho 1}$ sufficiently large so that all the poles of system (68) are negative real, each component of $[\Delta \underline{\rho}(t)]_1$ becomes a strictly monotone decreasing function for $t \geq 0$ and initial condition $[\Delta \underline{\rho}(0)]_1 > \underline{0}$ and $[\Delta \underline{\dot{\rho}}(0)]_1 \leq \underline{0}$.

Finally, we consider the deviation of the output variable $\underline{d}_j$ from its desired value $\underline{d}_j^d$ obtained from (31) and (23):

$$[\Delta \underline{d}_j]_1 \triangleq [\underline{d}_j^d]_1 - [\underline{d}_j]_1 = \{[I] - C(\underline{q}_1)^T C(\underline{q}_1^d)\}[\underline{s}_j^1]_1 + [\Delta \underline{\rho}]_1, \quad j=1,2,3. \tag{70}$$

Suppose that during the final approach phase, the attitude control law given by (46) maintains $\underline{q}_1(t) \simeq \underline{q}_1^d(t)$. Then $[\Delta \underline{d}_j(t)]_1 \simeq [\Delta \underline{\rho}(t)]_1$, $j=1,2,3$. Thus, the monotonicity of the components of $[\Delta \underline{\rho}(t)]_1$ implies that the components of $[\Delta \underline{d}_j(t)]_1$ are essentially monotone.

It is apparent from control laws (46) and (66) that their implementation requires the knowledge of $[\underline{\omega}_1(t)]_1$, $\underline{z}_1(t)$ (or $\underline{q}_1(t)$), $[\underline{\rho}(t)]_1$, $[\underline{\dot{\rho}}(t)]_1$, and the desired quantities $[\underline{\omega}_1^d(t)]_1$, $\underline{z}_1^d(t)$ (or $\underline{q}_1^d(t)$), $[\underline{\rho}^d(t)]_1$ and $[\underline{\dot{\rho}}^d(t)]_1$. The quantities $[\underline{\omega}_1(t)]_1$ and $\underline{z}_1(t)$ (or $\underline{q}_1(t)$) can be measured or estimated on-board module i. Knowing $[\underline{\omega}_2(t)]_2$ and $\underline{q}_2(t)$, we can determine $\underline{q}_1^d(t)$ from (35), and $[\underline{\omega}_1^d(t)]_1$ from

$$[\underline{\omega}_1^d(t)]_1 = C(\underline{q}_1(t))^T C(\underline{q}_2(t))[\underline{\omega}_2(t)]_2. \tag{71}$$

Moreover, $[\underline{d}^d(t)]_2$ can be determined from the orientation of Π_2. Thus, $[\underline{\rho}^d(t)]_1$ can be calculated from (31) or

$$[\underline{\rho}^d(t)]_1 = C(\underline{q}_1(t))^T \{C(\underline{q}_1^d(t))[\underline{s}_j^1]_1 + C(\underline{q}_2(t))([\underline{d}^d(t)]_2 - [\underline{s}_j^2]_2)\}. \tag{72}$$

From the measured quantities $[\underline{d}_j(t)]_1$ and $[\underline{\dot{d}}_j(t)]_1$, we can determine $[\underline{\rho}(t)]_1$ and $[\underline{\dot{\rho}}(t)]_1$ from (23) and (26) respectively. Finally, since $\underline{\dot{d}}_j^d|_1(t)=\underline{0}$, we have from (25) that

$$[\underline{\dot{\rho}}^d(t)]_1 = [(\underline{\omega}_1^d(t) - \underline{\omega}_2(t)) \times \underline{s}_j^2]_1 = \underline{0}. \tag{73}$$

Figure 4 shows a block diagram of the proposed automatic terminal rendez-vous control system.

VI. SIMULATION STUDY

The main objective of this simulation study is to determine the performance of the proposed feedback control system for automatic terminal rendez-vous in the presence of actuator saturation and inertial parameter variations induced by

vibrations of the flexible structural components. Here, we assume that module 2 utilizes the following control law for regulating its attitude about a fixed desired orientation with respect to the inertial frame:

$$\Pi_p^{-1} [\underline{\tau}_{c2}]_2 = -\{K_2 + k_{p2}\gamma_2[I]\}[\underline{\omega}_2]_2 + k_{p2}\Pi_{p2}^{-2}\{(\underline{z}_2^d - \Delta\underline{z}_2)(\underline{z}_2^d - \Delta\underline{z}_2)^T + [I]\}\Delta\underline{z}_2/2$$

$$\tag{74}$$

with $\underline{z}_2^d = (q_{21}^d/q_{24}^d, q_{22}^d/q_{24}^d, q_{23}^d/q_{24}^d)^T$, $\underline{z}_2 = (q_{21}/q_{24}, q_{22}/q_{24}, q_{23}/q_{24})$, $\Delta\underline{z} = \underline{z}_2^d - \underline{z}_2$,

$$\gamma_2 = \frac{(\underline{z}_2^d)^T B_1([\underline{\omega}_2]_2) \Delta\underline{z}_2}{2[(I_{2x}\omega_{2x})^2 + (I_{2y}\omega_{2y})^2 + (I_{2z}\omega_{2z})^2]} \quad, \tag{75}$$

where $k_{p2} > 0$; K_2 is a positive definite diagonal feedback gain matrix, and $\underline{q}_2^d = (q_{21}^d, q_{22}^d, q_{23}^d, q_{24}^d)^T$ is a constant vector corresponding to the desired quaternion for module 2. The above control law is a special case of (46) with $[\underline{\omega}_2^d]_2 = \underline{0}$ and $\underline{z}_2^d$ a constant vector. Table 1 gives the values of various parameters for modules 1 and 2 in the simulation study. These values correspond to those of a space shuttle (module 1) and a typical space station (module 2). Figure 5 shows the motion of module 2 with initial conditions $[\underline{\omega}_2(0)]_2 \neq [\underline{\omega}_2^d]_2 = \underline{0}$ and $\underline{q}_2(0) \neq \underline{q}_2^d$. It can be seen that $[\underline{\omega}_2(t)]_2$ and $\underline{q}_2(t)$ asymptotically approach their desired values as t increases. To determine the effect of vibrations of the flexible structural components of the space station (module 2), we let $I_{2z} = I_{2zo}(1 + \alpha_f \sin \omega_f t)$, where I_{2zo} corresponds to the nominal value of I_{2z} given in Table 1. The parameters in control law (74) are fixed at their nominal values given in Table 1. Computer simulation showed that the inertial parameter perturbations have negligible effect on the dynamic behavior of the attitude control system provided that the perturbed inertia tensor remains positive definite. Figure 6 shows a typical result for $\alpha_f = 0.95$ and $\omega_f = 0.5$ radian/sec. Comparing this result with that shown in Fig.5, it is evident that the corresponding trajectories of the perturbed and unperturbed systems are almost identical. Obviously, to minimize the effects of flexible structure vibrations, the docking platforms should be attached to the relatively rigid portion of the space station. It should be noted that for the large values of I_{1x}, I_{1y} and I_{1z} given in Table 1, the term involving γ_2 in (74) is small as compared to the remaining terms. Therefore it can be dropped for simplifying the control law. Computer simulation showed that dropping the abovementioned term has negligible effect on the feedback control system's dynamical behavior.

To simulate the reference platform alignment phase, we set $[\underline{d}^d]_2 = (5,0,0)^T$ (meters). Figure 7 shows a typical motion of module 1. The corresponding variations of $\|\underline{d}_j(t)\|$, $[\underline{\tau}_{c1}(t)]_1$, and $[\underline{u}(t)]_1$ with time t are shown in Fig.8. The results show that $\|\underline{d}_j(t)\|$, $j=1,2,3$ tend to their desired value $\|\underline{d}^d\| = 5$ as t increases. At t=150 seconds, $\underline{d}^d$ is changed to $(0.1,0,0)^T$ for the final approach phase. The subsequent time-domain variations of $\|\underline{d}_j(t)\|$, $[\underline{\tau}_{c1}(t)]_1$ and $[\underline{u}(t)]_1$ are shown in Fig.9. The feedback gains k_{p0} and k_{p1} have been readjusted so that each $\|\underline{d}_j(\cdot)\|$ is a strictly monotone decreasing function of t. It should be noted that for the purpose of reducing the computation time in simulation, the

feedback gains k_{p0}, k_{p1} and k_{p2} have been set at high values. This causes a fast system response but very high peak values of the control variables. This situation can be avoided by relaxing the system response time.

To determine the effect of actuator saturation on the system behavior, amplitude limits are imposed on each component of the feedback controls $[\underline{\tau}_{cl}]_1$ and $[\underline{u}]_1$ in the simulation study. The results show that for the chosen feedback gain values, the behavior of the system trajectories does not differ appreciably from that without actuator saturation if the saturation time duration is within 25% of the transient time duration. A typical result is shown in Fig.10.

VII. CONCLUDING REMARKS

In this work, we used a mathematical model based on rigid body dynamics to develop a guidance law for automatic terminal rendez-vous. The resulting attitude control system is found to be highly robust with respect to inertial parameter variations. This suggests that the proposed attitude control law may be applicable to modules with flexible structural components. In this development, the controls are assumed to be active at all times. In practical situations where thrusters are used, the controls are on-off in nature. We may modify the present model for the case with on-off controls by introducing a relay with deadzone in each control channel. The development of guidance laws for automatic terminal rendez-vous based on the modified model is being made at this time. The results will be reported in the near future.

Finally, in the automatic assembly of space stations, we may utilize the developed guidance law in the construction of self-contained control modules which can be attached to the structural components to be assembled. These control modules serve as basic tools in the automatic assembly process.

ACKNOWLEDGMENTS

TABLE 1

Parameter	Module 1 (i=1)	Module 2 (i=2)
I_{ix} (kg.m^2)	1.164723×10^6	1.10472×10^4
I_{iy}	2.35767×10^5	1.10472×10^4
I_{iz}	1.22723×10^6	1.68772×10^4
$(s_{1ix}, s_{1iy}, s_{1iz})$ (m.)	$(10,1,0)$	$(-30,1,0)$
$(s_{2ix}, s_{2iy}, s_{2iz})$	$(10,0,1)$	$(-30,0,1)$
$(s_{3ix}, s_{3iy}, s_{3iz})$	$(10,0,-1)$	$(-30,0,-1)$

$$\omega_o = \sqrt{\mu/r_1^3} = 0.6747 \times 10^{-3} \text{ rad./sec.}$$

REFERENCES

[1]   J. White and F. Runge, "Advanced Science and Applications Space Platform," in Large Space Systems Technology - 1980, Vol.I, System Technology, NASA CP-2168, p.133.

[2]   G.R. Stone, "Structural Requirements and Technology Needs of Geostationary Platforms," in Large Space System Technology - 1980, Vol.I, System Technology, NASA CP-2168, p.149.

[3]   C. Covington, et al., "Space Operations Center - A Concept Analysis," NASA Johnson Space Center Report No. JSC-16277, Nov. 1979.

[4]   V.P. Legostaev and B.V. Raushenbach, "Automatic Assembly in Space," Kosmicheskie Issledovaniya, Vol.7, No.6, pp.803-813, Nov.-Dec. 1969 (English Translation: Cosmic Research, Vol.7, Nov.-Dec. 1969, pp.723-731)

[5]   N.V. Petersen (Editor), Advances in the Astronautical Sciences, Space Rendez-vous, Rescue and Recovery, Vol.16, Pt.1 Am. Astronautical Soc. 1963.

[6]   D. Chiarappa, "Analysis and Design of Space Vehicle Flight Control Systems," Vol.VIII, Rendez-vous and Docking, NASA Contractor Report, NASA CR-827, July, 1967.

[7]   E.P. Blanchard, et al., "Space Shuttle Vehicle Automatic Docking Study," NASA Contractor Report, NASA CR-115248, Oct. 1971.

[8]   J. Wohl, "Space Tug Automatic Docking Control Study," NASA Contractor Report, NASA CR-120578, October 1974.

[9]   Bendix Corp. Guidance Systems Div. "Space Construction Base Control System," Final Report, NASA CR-161288, Oct. 1978.

[10]   P.K.C. Wang, "Nonlinear Guidance Laws for Orbital Rendez-vous," in preparation.

[11]   Sir W.R. Hamilton, Elements of Quaternions, Longmans,Green and Co. London, 1866.

[12]   E.T. Whittaker, A Treatise on the Analytical Dynamics of Particles and Rigid Bodies, Cambridge Univ. Press, Cambridge, 1961.

[13]   J.R. Wertz (Ed.), Spacecraft Attitude Determination and Control, D. Reidel Pub. Co., Boston, 1980.

[14]   R.E. Mortensen, "On Systems for Automatic Control of the Rotation of a Rigid Body," Electronics Research Lab., Series No.63, Issue No.23, Univ. of Calif. Berkeley, Nov. 27, 1963.

[15]   A. Cayley, "On the Motion of Rotation of a Solid Body," Cambridge Math. J., Vol.II, No.1843, pp.224-232. Reprinted in The Collected Papers of Arthur Cayley, Vol.I, Cambridge Univ. Press, Cambridge, 1899, pp.28-35.

[16]   J.W. Gibbs and E.B. Wilson, Vector Analysis, Scribner, N.Y. 1901.

[17]   J.P. La Salle, "An Invariance Principle in the Theory of Stability," in Differential Equations and Dynamical Systems, Acad. Press, N.Y. 1967, pp.277-286.

[18] J.P. La Salle, "Stability Theory for Ordinary Differential Equations," J. Diff. Equations, Vol.4, 1968, pp.57-65.

[19] T. Yoshizawa, "Asymptotic Behavior of Solutions of a System of Ordinary Differential Equations," Contrib. Diff. Eqs., Vol.1, 1963, pp.371-387.

[20] T, Yoshizawa, "Stability Theory of Liapunov's Second Method," Publication No.9, The Math. Soc. of Japan, Tokyo, 1966.

[21] J. La Salle and S. Lefschetz, Stability by Liapunov's Direct Method with Applications, Academic Press, N.Y. 1961.

[22] N.N. Krasovskii, Stability of Motion, Stanford Univ. Press, Stanford, 1963 (Translated by J.L. Brenner).
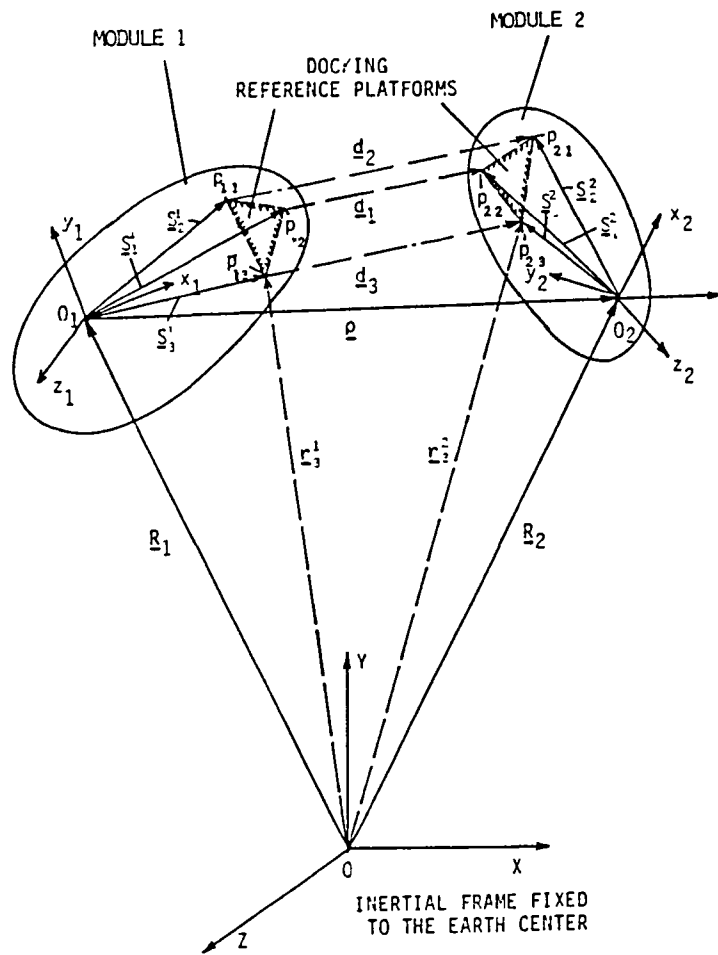
Fig.1 Sketch of the modules to be assembled.
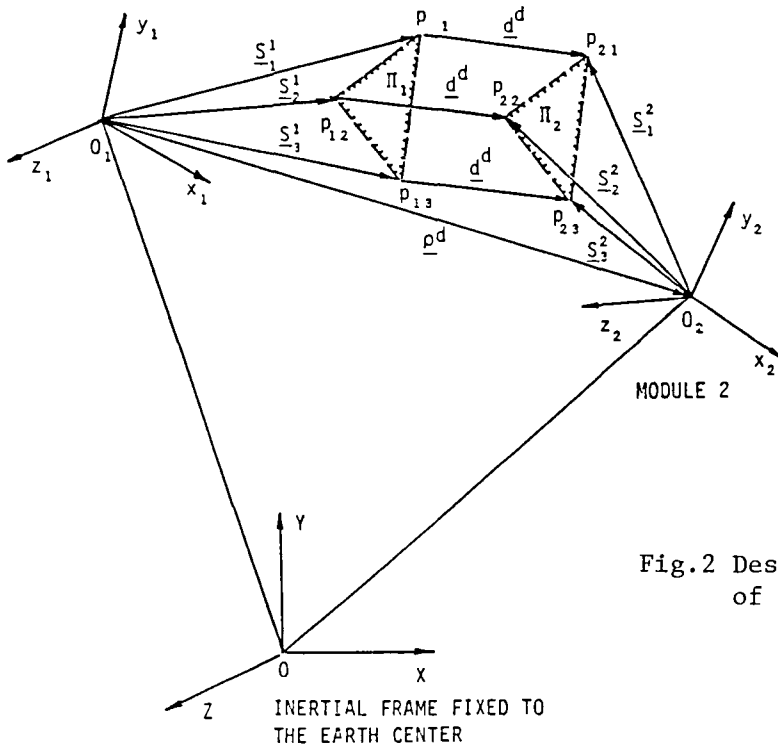
DESIRED ATTITUDE AND
LOCATION OF MODULE 1

Fig.2 Desired attitude and location
of module 1.
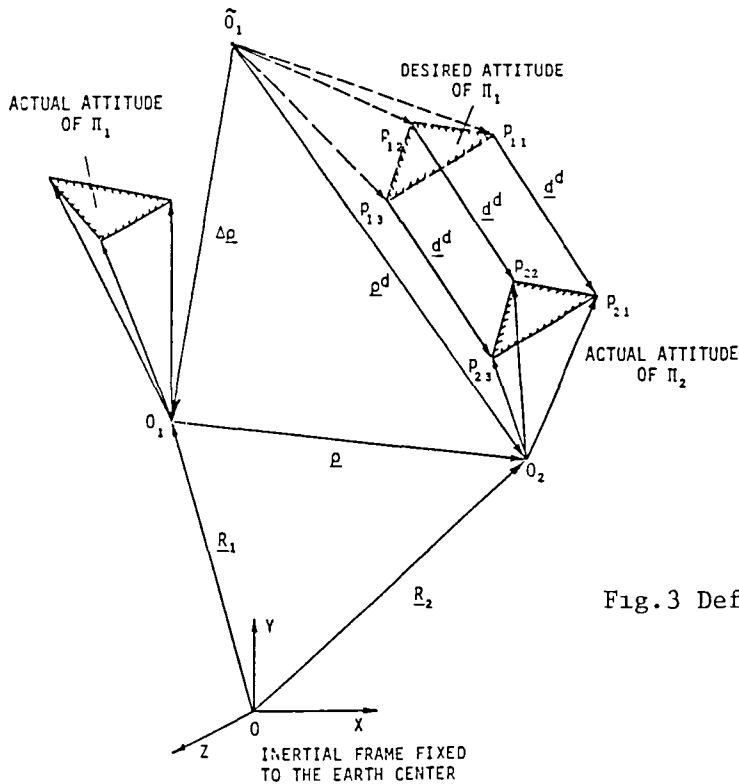
Fig.3 Definition of increment $\Delta\underline{\rho}$.

TRANSFOR-
MATION
Eq (37)

$\underline{z}_1$ $[\underline{\omega}_1]_1$

COMPUTATION

q_1^d (Eq.(35))

$[\underline{\omega}_1^d]_1$ (Eq (71))

$[\underline{\rho}^d]_1$ (Eq.(72))

DEVIATIONS.

$[\Delta\underline{\omega}_1]_1$, $\Delta\underline{z}_1$,

$[\Delta\underline{\rho}]_1$, $[\Delta\underline{\dot{\rho}}]_1$

ATTITUDE
CONTROL
LAW
(Eq 46)

$[\Delta\underline{\omega}_1]_1$,
$\Delta\underline{z}_1,\underline{z}_1^d$,
$[\underline{\omega}_1^d]$

$[\underline{\tau}_{c1}]_1$

MODULE 1
ROTATIONAL
MOTION

$[\rho^d]_1$

$[\Delta\underline{\rho}]_1$

$[\Delta\underline{\dot{\rho}}]_1$

RELATIVE
TRANSLATIONAL
MOTION
CONTROL LAW
(Eq.66)

$[\underline{u}]_1$

RELATIVE
TRANSLATIONAL
MOTION

TRANSFOR-
MATIONS
Eq (23)
&
Eq (26)

$\underline{0}$

$\underline{q}_2^d$

ATTITUDE
CONTROL
LAW

$[\underline{\tau}_{c2}]_2$

MODULE 2
ROTATIONAL
MOTION

$[\underline{d}_j]_1$

$[\underline{\dot{d}}_j]_1$

j=1,2,3

ON-BOARD
DATA
PROCESSING

SELF-CONTAINED ATTITUDE CONTROL SYSTEM

OUTPUT

$[\underline{\omega}_1]_1$

$\underline{q}_1$

$[\underline{d}_1]_1$
$[\underline{d}_2]_1$
$[\underline{d}_3]_1$
$[\underline{\dot{d}}_1]_1$
$[\underline{\dot{d}}_2]_1$
$[\underline{\dot{d}}_3]_1$

$[\underline{\omega}_2]_2$

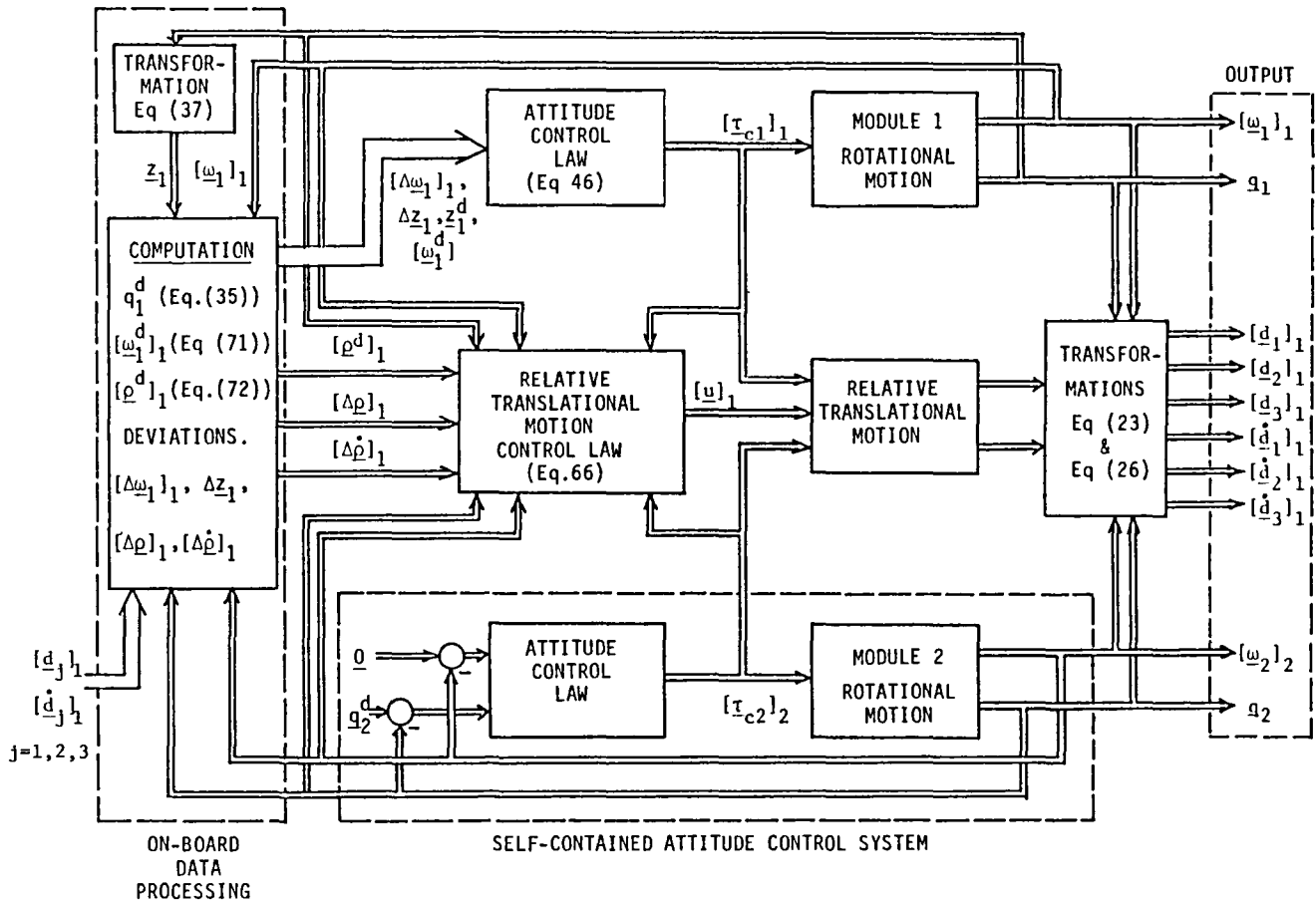$\underline{q}_2$

Fig.4 Block diagram of the proposed automatic terminal rendez-
vous control system.

89

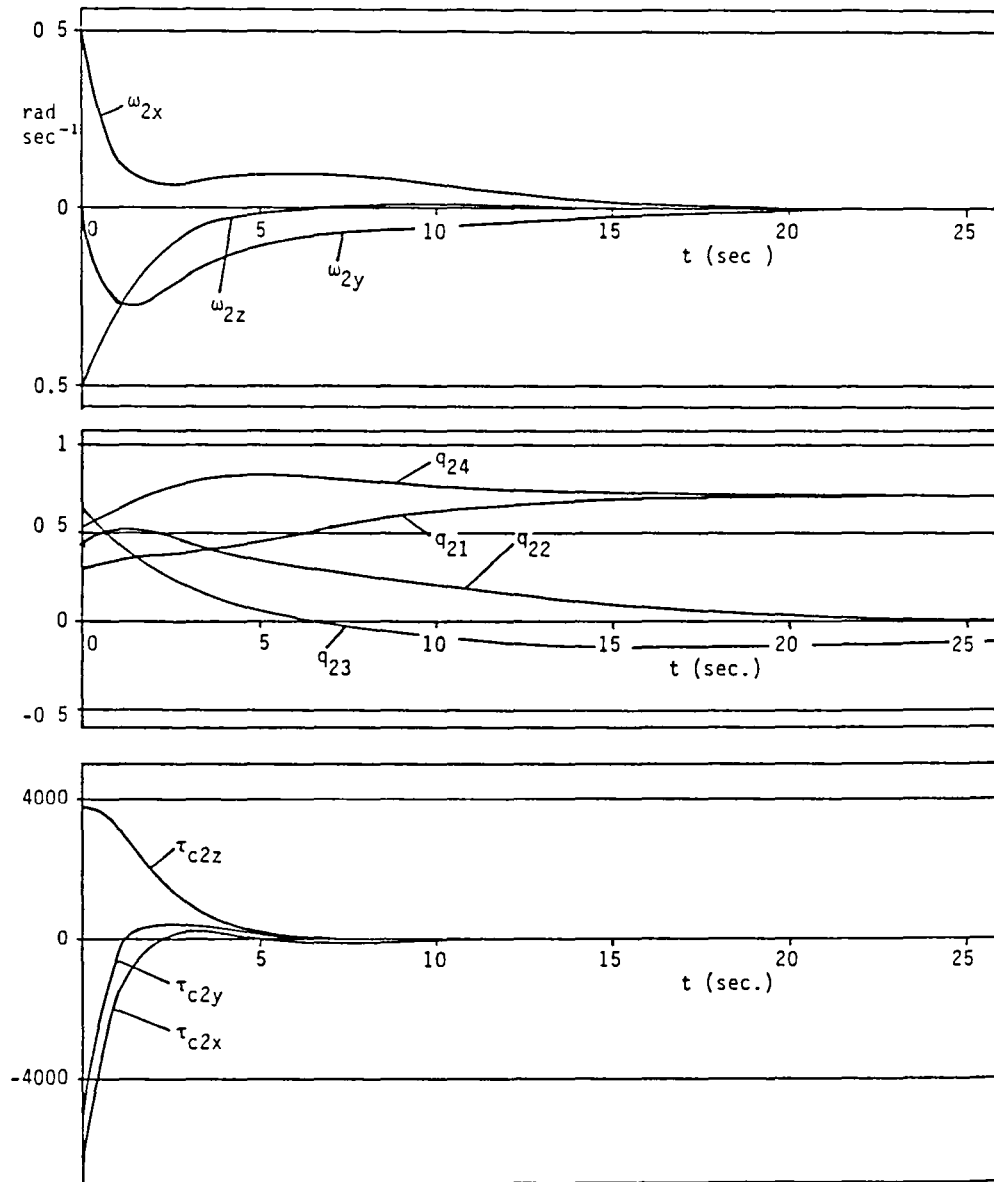Fig.5 Time-domain trajectories of module 2 with attitude control law (74) and initial conditions: $[\underline{\omega}_2(0)]_2 = (0.5,0,-0.5)^T$ rad./sec., $[\underline{\omega}_2^d]_2 = \underline{0}$,

$\underline{q}_2(0) = (\sqrt{0.1},\sqrt{0.2},\sqrt{0.4},\sqrt{0.3})^T$, $\underline{q}_2^d = (1/\sqrt{2},0,0,1/\sqrt{2})^T$;

and feedback gains: $k_{2x} = k_{2y} = k_{2z} = 1.0$ and $k_{p2} = 5 \times 10^7$.
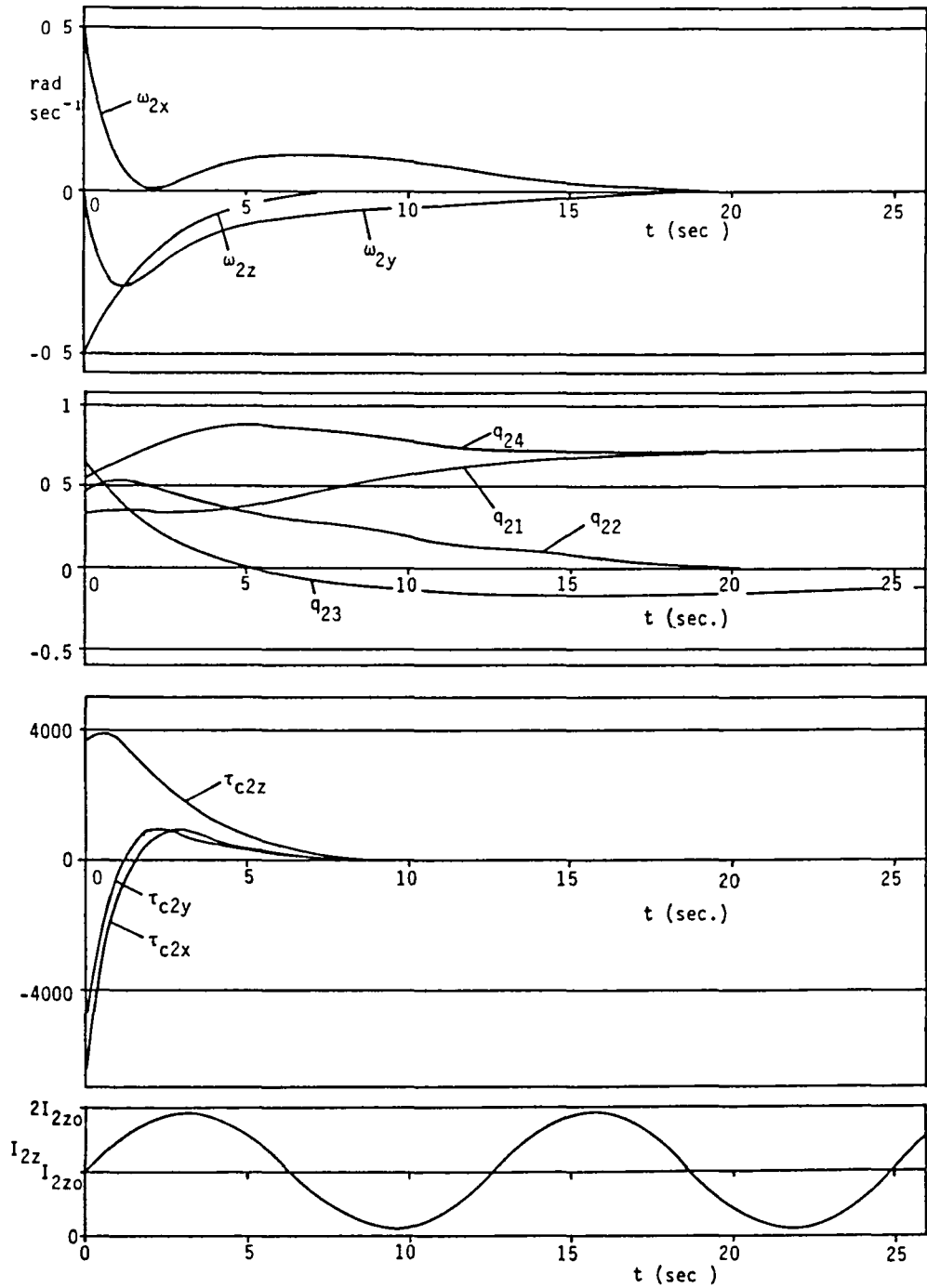
Fig.6 Time-domain trajectories of module 2 with attitude control
law (74),initial conditions and feedback gains given in
Fig.7, and with perturbed $I_{2z}(t)=1.68772\times10^4(1+0.95\sin(t/2))$
$(kg.m^2.)$
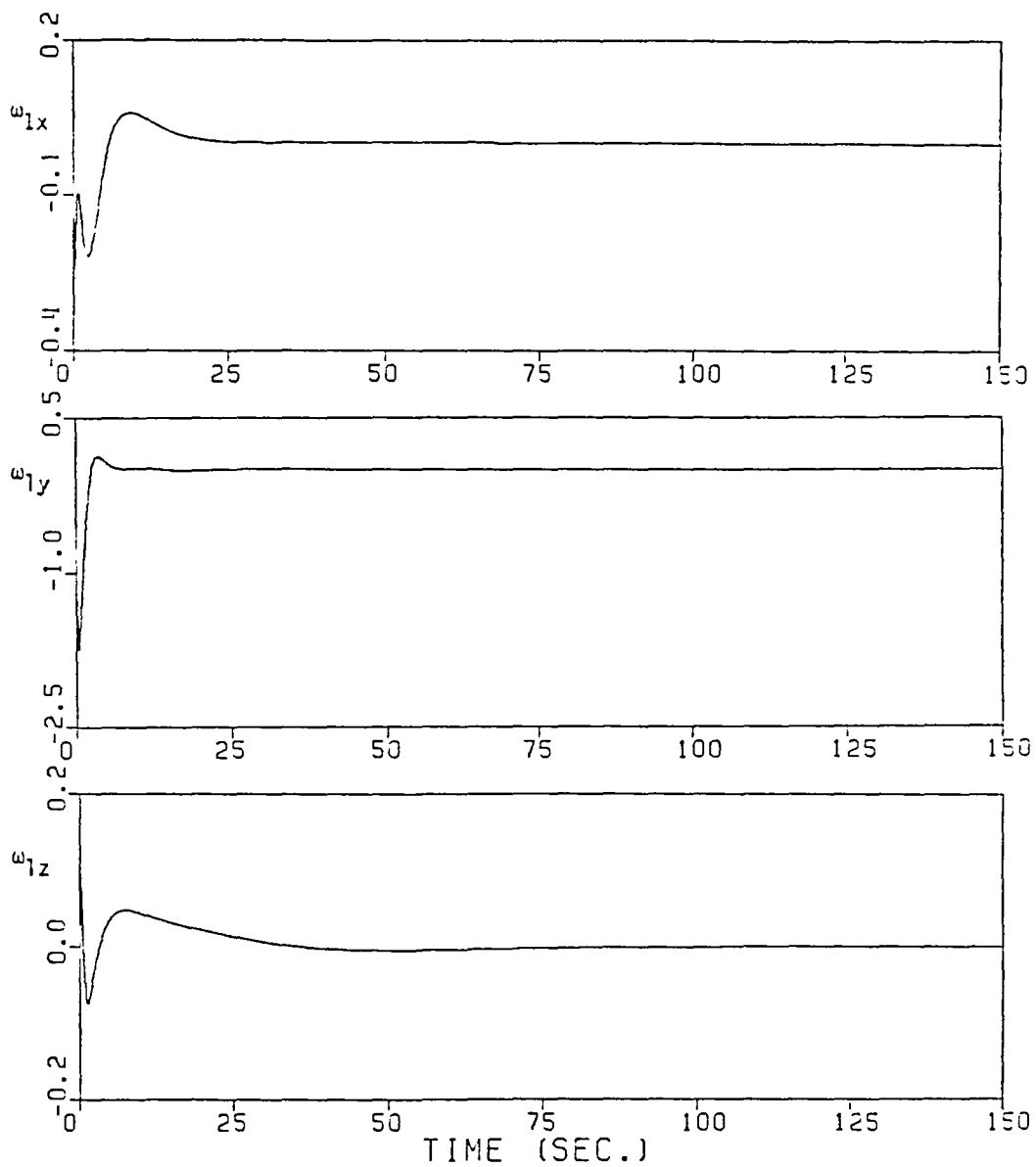
Fig.7 Time-domain trajectories of module 1 with initial
conditions: $[\underline{\omega}_1(0)]_1 = (-0.2, 0. 0.2)^T$ rad./sec.;
$\underline{q}_1 \cdot (\sqrt{0.3}, \sqrt{0.4}, \sqrt{0.2}, \sqrt{0.1})^T$ and feedback gains $k_{1x} = k_{1y} = k_{1z} = 1.0$, $k_{p1} = 10^{11}$.

Fig.7a Time-domain trajectories of $[\underline{\omega}_1(t)]_1$.

Fig.7b Time-domain trajectories of $\underline{q}_1(t)$.

93

Fig.8a Time-domain behavior of $\|\underline{d}_j(t)\|$, j=1,2,3 corresponding to motions of modules 1 and 2 shown in Figures 7 and 5, and initial conditions for relative translation given by $[\underline{\rho}(0)]_1 = (50,0,5)^T$m., $[\underline{\dot{\rho}}(0)]_1 = (0,-5,0)^T$m./sec.,and feedback gains: $k_{\rho 0} = 2.2 \times 10^6$ and $k_{\rho 1} = 40$.
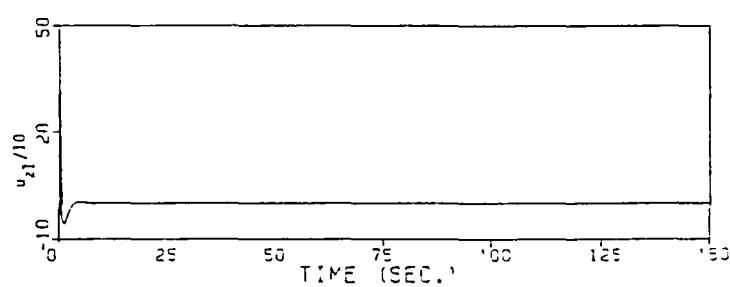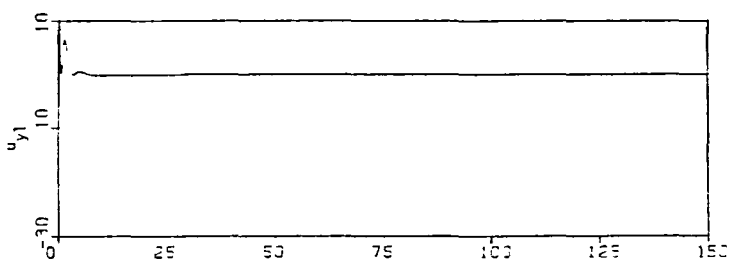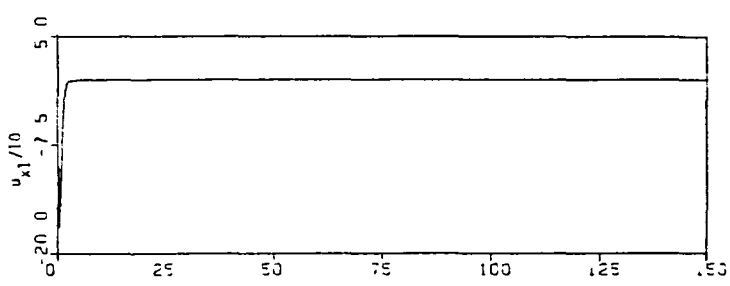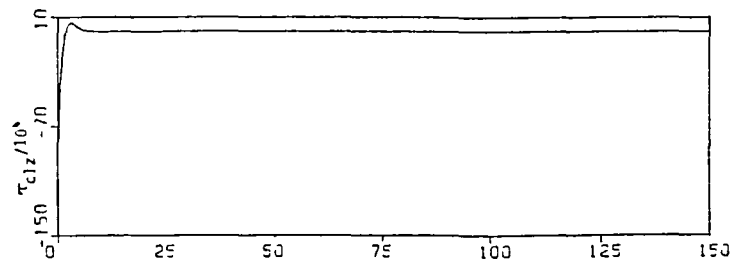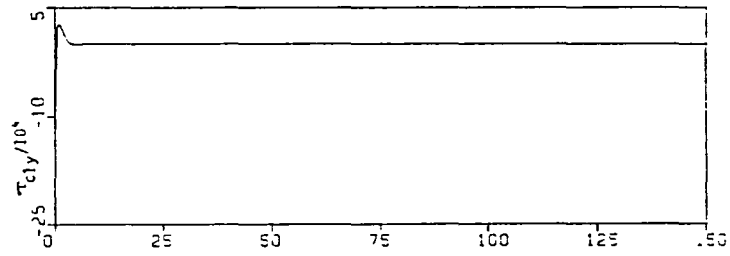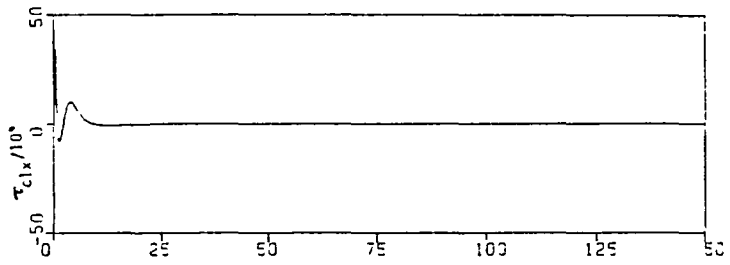
Fig.8b Time-domain behavior of $[\underline{\tau}_{cl}(t)]_1$.

Fig.8c Time-domain behavior of $[\underline{u}(t)]_1$.

TIME (SEC.)

95
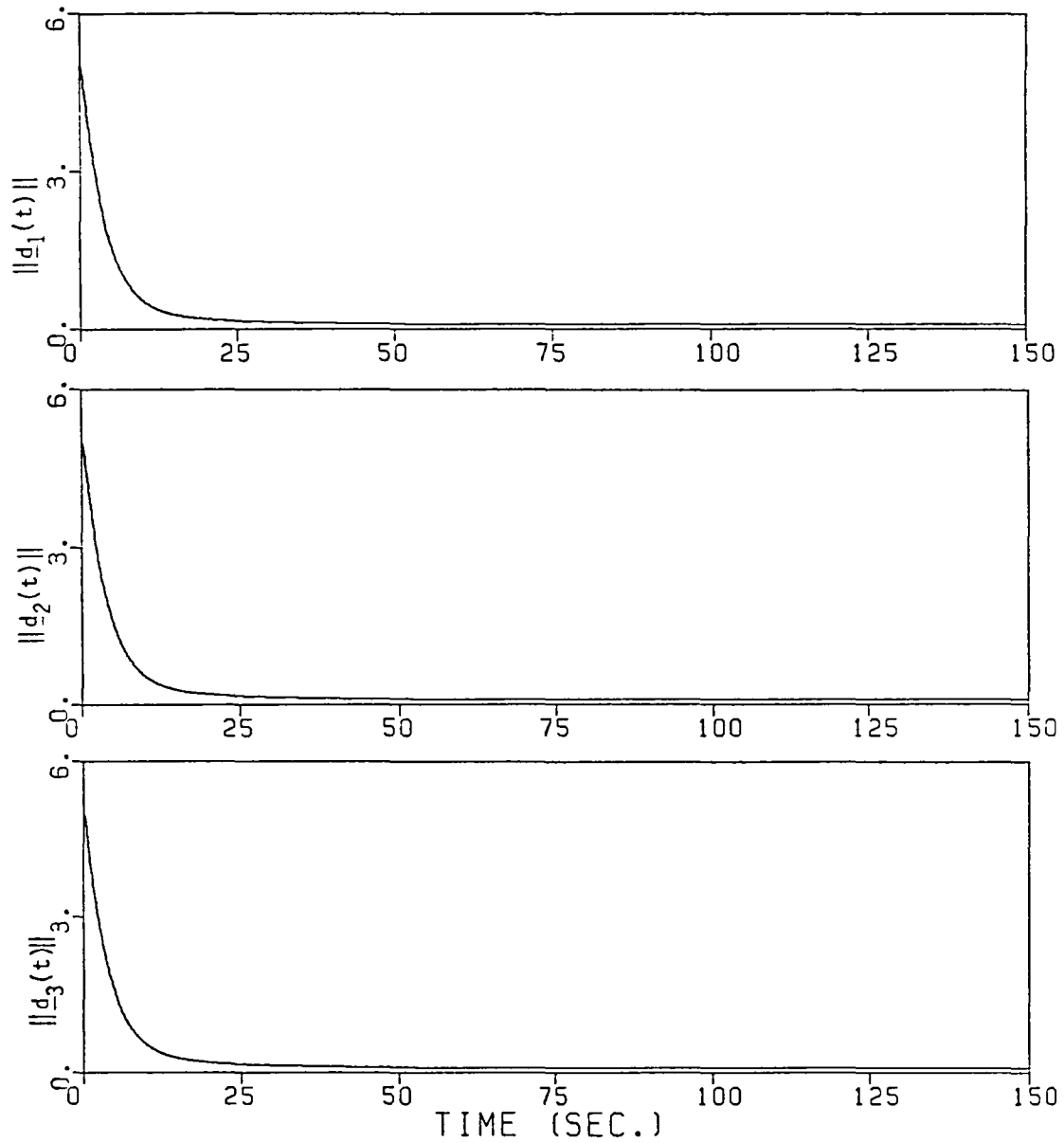
Fig.9a Time-domain behavior of $\|\underline{d}_j(t)\|$, j=1,2,3 for the final
approach phase of modules 1 and 2 with feedback gains
$k_{\rho 0} = 2.2 \times 10^6$, $k_{\rho 1} = 4$, and $\underline{d}^d = (0.1,0,0)^T$.
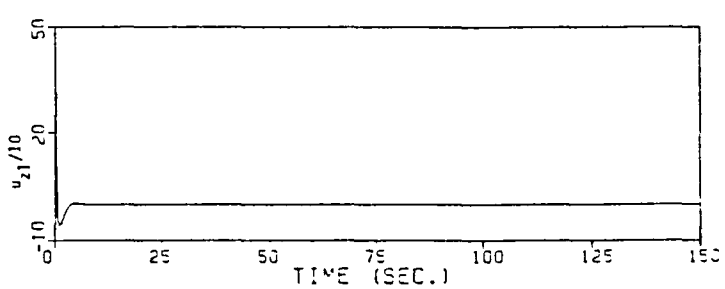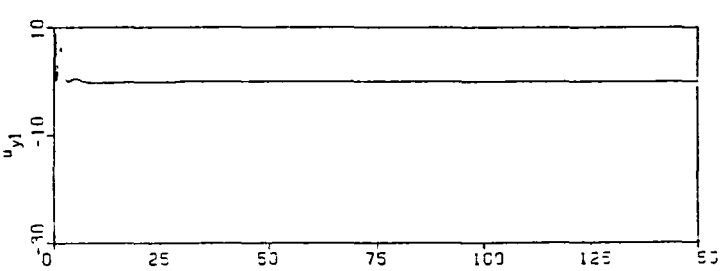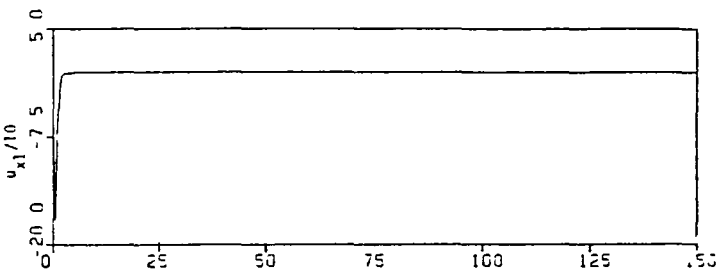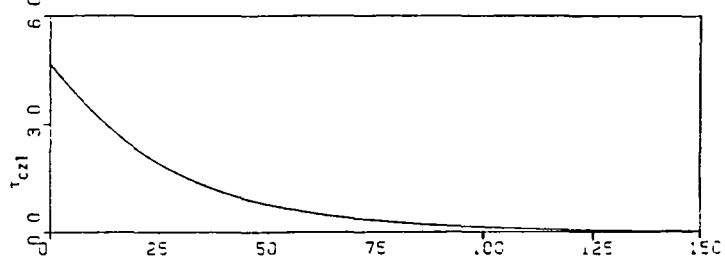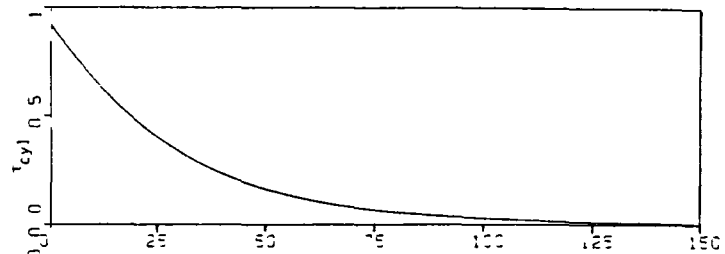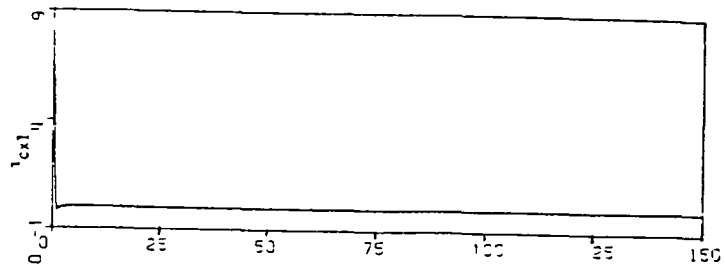
Fig.9b Time-domain behavior
of $[\underline{\tau}_{c1}(t)]_1$.

Fig.9c Time-domain behavior
of $[\underline{u}(t)]_1$.

97
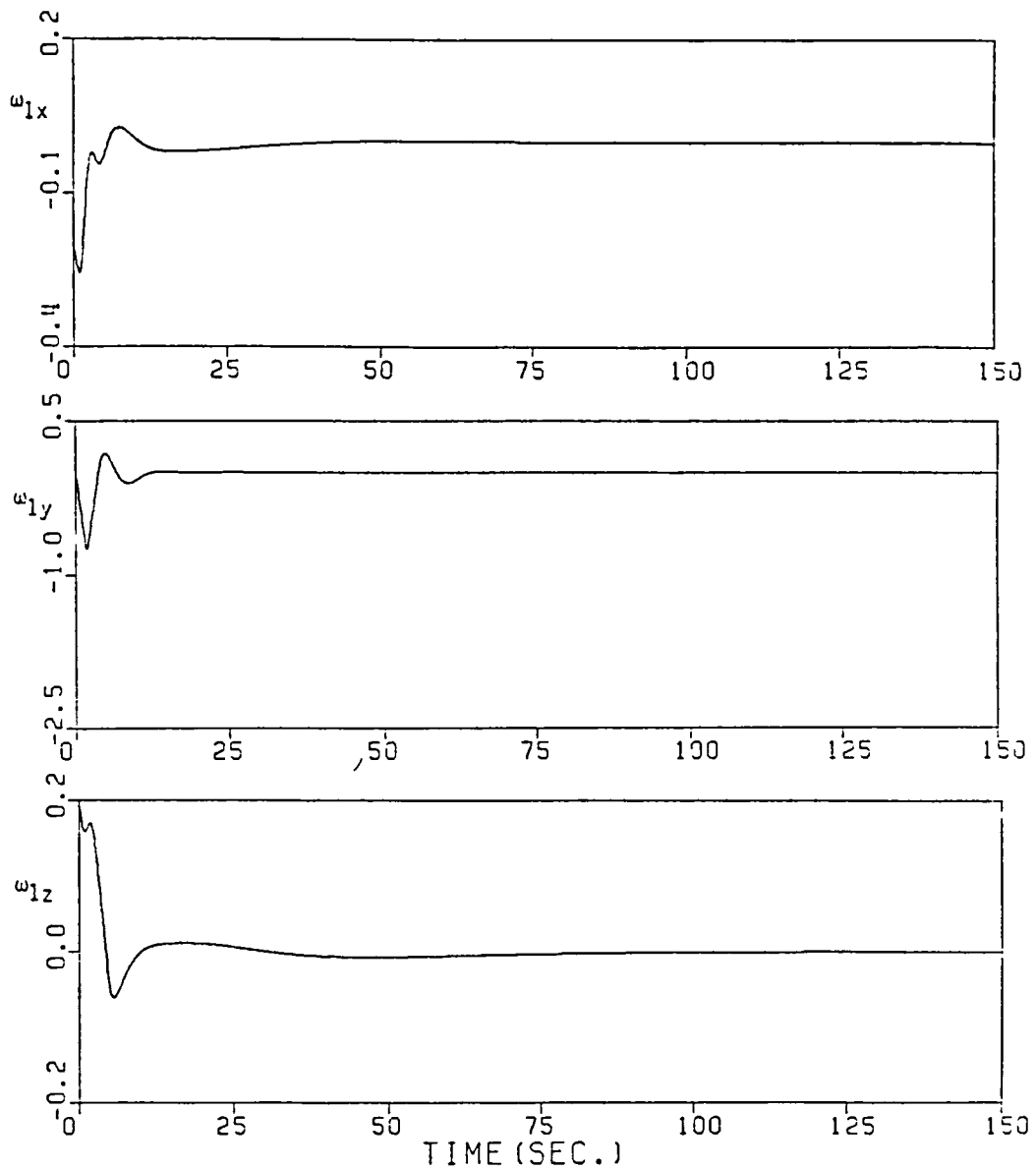
Fig.10 Time-domain trajectories of module 1 with actuator
saturation: $|\tau_{c1k}| \leqslant 10^5, k=x,y,z;$ and with initial
conditions and feedback gains identical to those
given in Fig.7.

Fig.10a Time-domain trajectories of $[\underline{\omega}_1(t)]_1$.
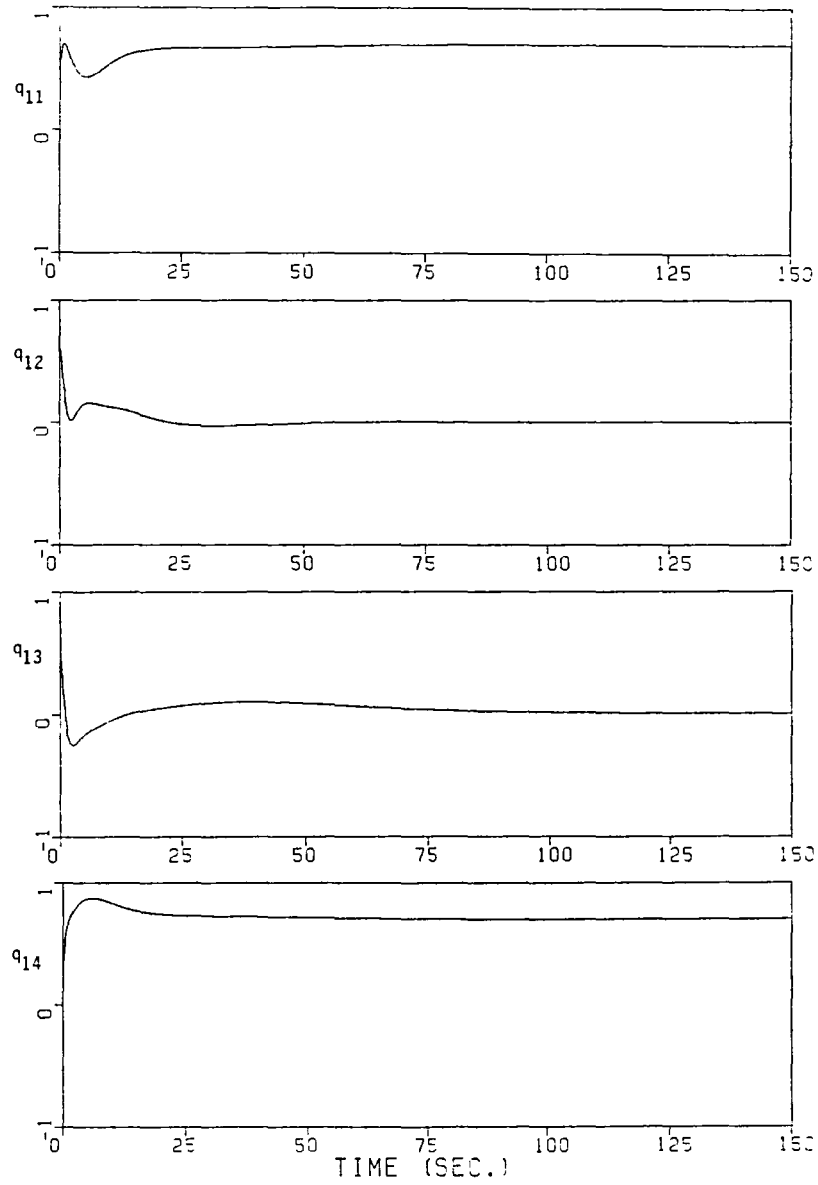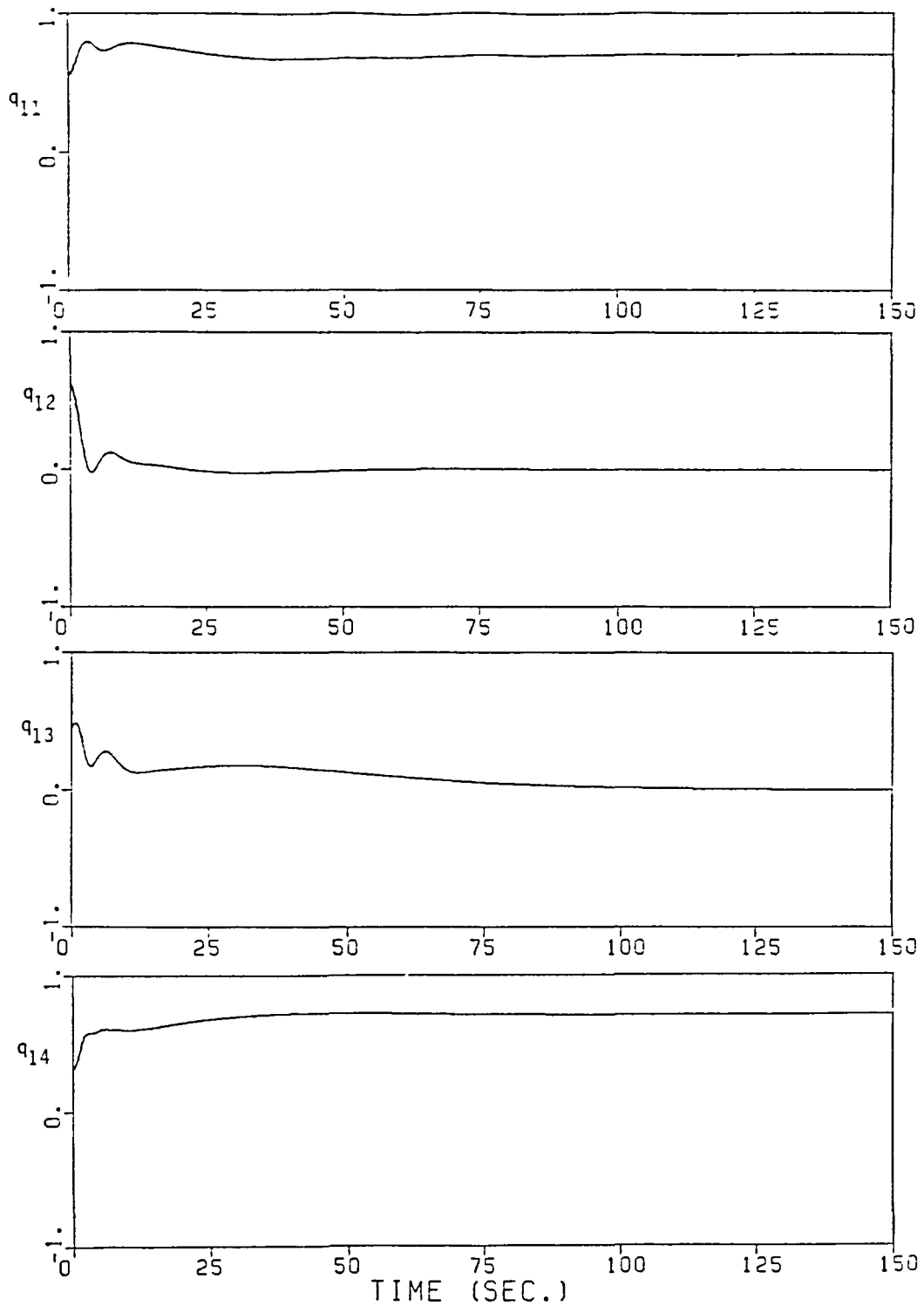
Fig.10b Time-domain trajectories of $\underline{q}_1(t)$.

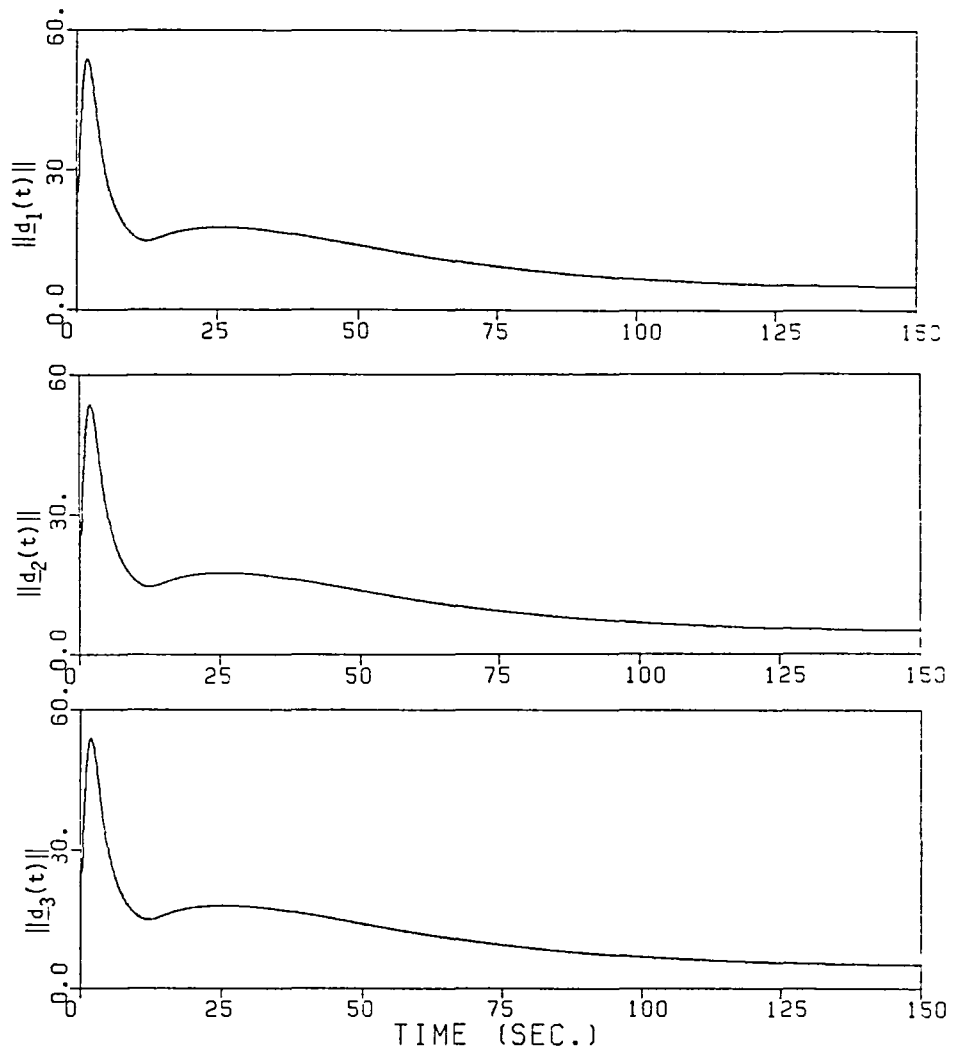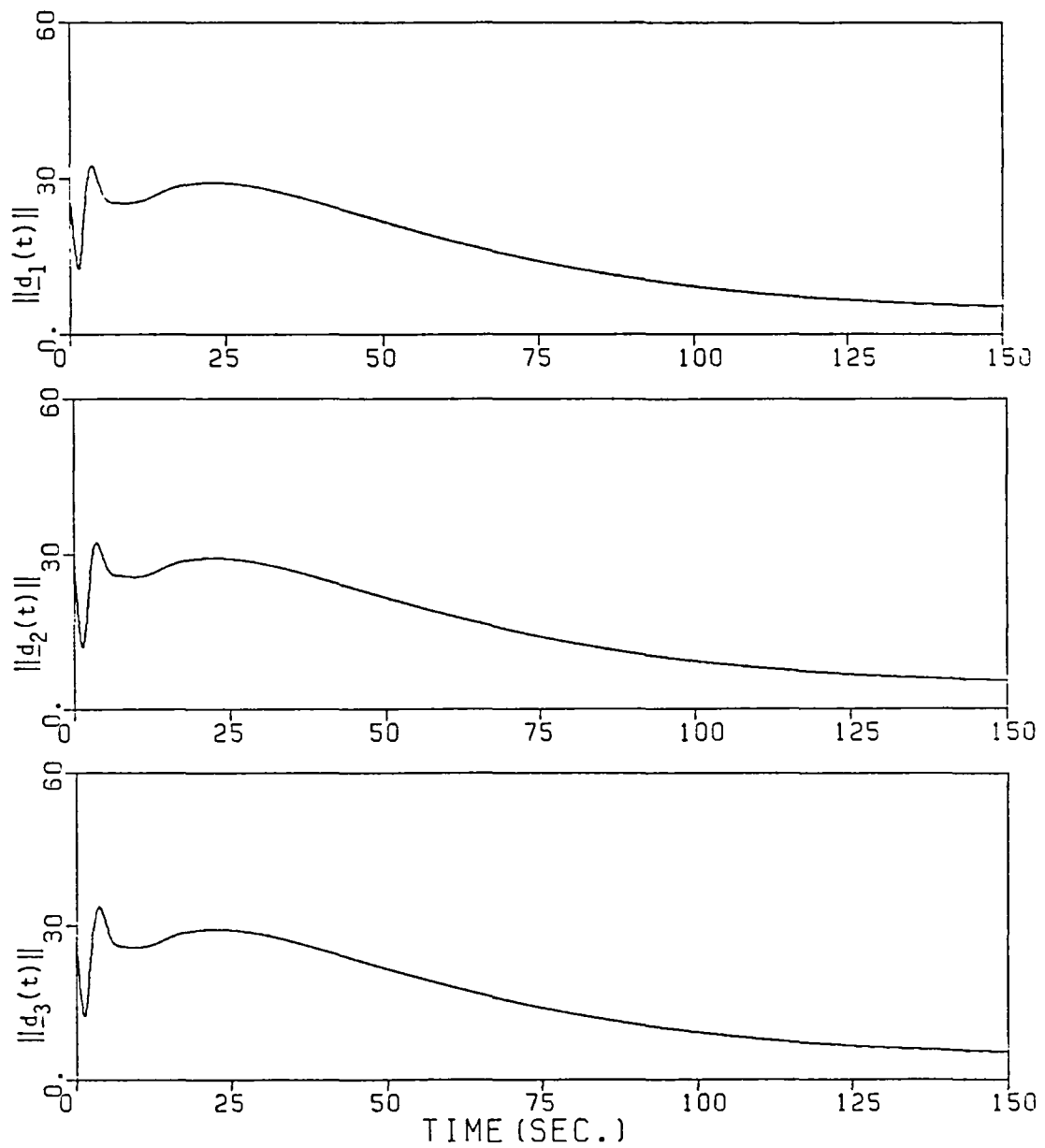Fig.10c Time-domain behavior of $\|\underline{d}_j(t)\|$, j=1,2,3 corresponding
to motions of modules 1 and 2 shown in Figures 10a
and 10b.
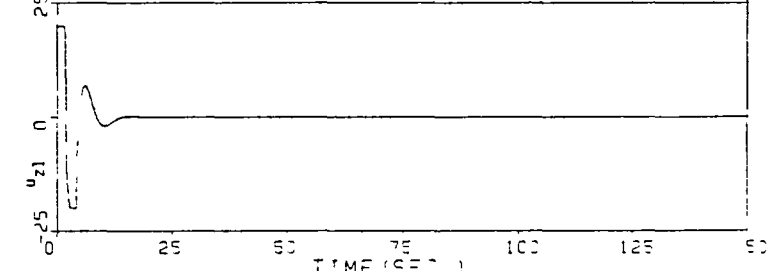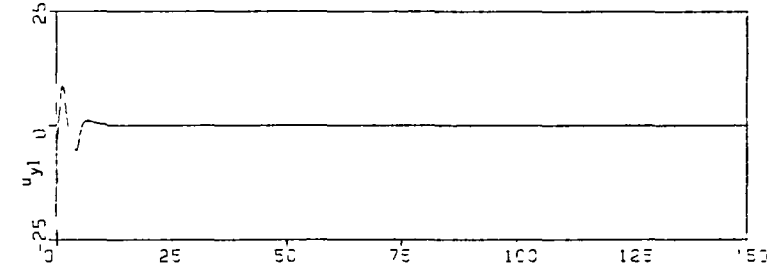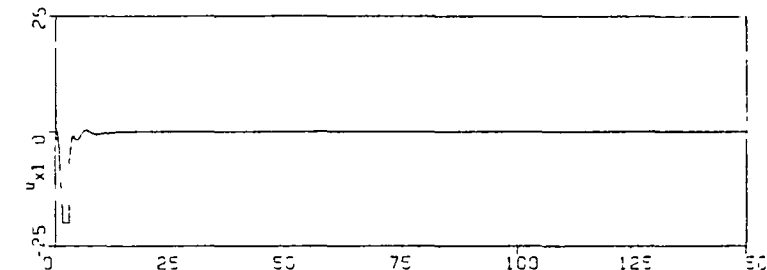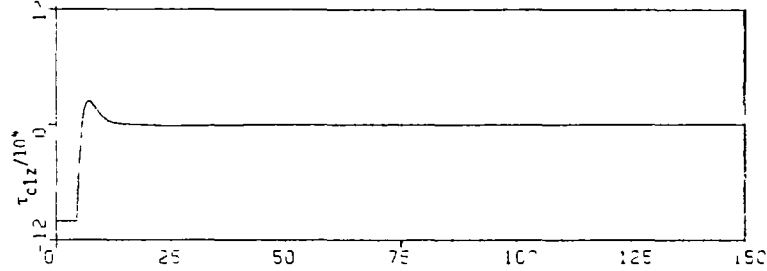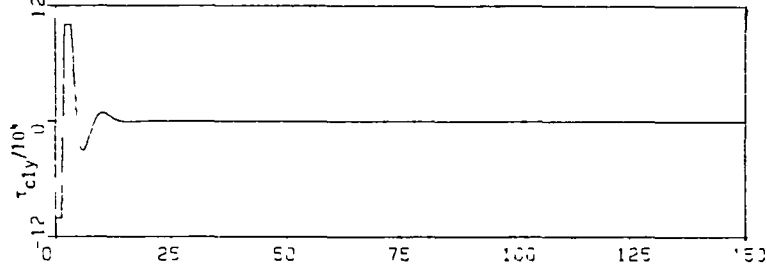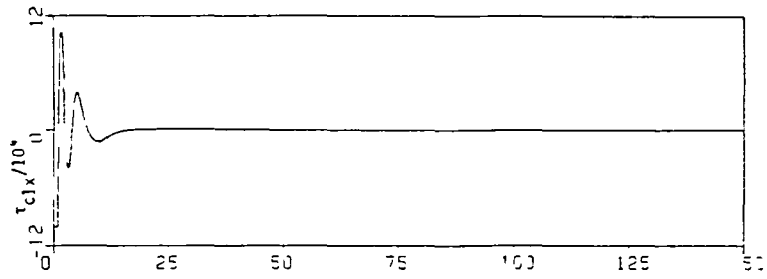
Fig.10d Time-domain behavior of $[\underline{\tau}_{c1}(t)]_1$.

Fig.10e Time-domain behavior of $[\underline{u}(t)]_1$, $|u_{k1}| < 20$, $k=x,y,z$.

TIME (SEC.)

101

SPACE STATION DYNAMIC MODELING, DISTURBANCE ACCOMMODATION, AND ADAPTIVE CONTROL

S. J. Wang, C. H. Ih, Y. H. Lin, and E. Mettler
Jet Propulsion Laboratory
California Institute of Technology
Pasadena, CA 91109

ABSTRACT

The space station is a large space structure with a unique operational environment. Dynamic disturbances of many orders of magnitude greater than those of conventional spacecraft will be routine for the space station. Accurate knowledge of inflight structural dynamics and disturbances will be lacking. System identification will reduce uncertainties. To deal with the remaining model errors and time varying elements, adaptive control may be required. Dynamic models for two space station configurations are derived. Space shuttle docking disturbances and their effects on the station and solar panels are quantified. Simulation results reveal that hard shuttle docking can cause solar panel buckling. Soft docking and berthing can substantially reduce structural loads at the expense of large shuttle and station attitude excursions. To achieve safe and routine operations, it is found that pre-docking shuttle momentum reduction is necessary. A direct model reference adaptive control is synthesized and evaluated with respect to the station model parameter errors and plant dynamics truncations. Both the rigid body and the flexible modes are treated. Preliminary simulation results show that convergence of the adaptive algorithm can be achieved in 100 seconds with reasonable performance even during shuttle hard docking operations in which station mass and inertia are instantaneously changed by more than 100 percent.

I. INTRODUCTION

After the Space Shuttle, the next major space endeavor will be a permanent manned space station. The launching of an initial space station is planned for the early 1990's. To the control technologists, this will provide new opportunities and challenges in the design of a complex space structure.

By virtue of its mission and function, the space station will be a large space structure with a very unique operational environment. Dynamic disturbances of many orders of magnitude greater than those encountered by the conventional spacecraft will be routine for space stations. Disturbance isolation and vibration suppression for the large solar panels, radiators, and payloads will be necessary. Methodologies for control systems that evolve with the station, from initial build-up to its full operation, will be required. Accurate knowledge of inflight structural dynamics, disturbances, and interactions between major system components will be lacking. System identification and state estimation will be able to reduce uncertainties but cannot eliminate them. Robust control designs can desensitize the effects of these uncertainties. Adaptive control incorporated with model switching will be able to deal with, and minimize the effects of parameter errors, unmodeled dynamics, and the time varying elements of the station due to operations including vehicle docking and berthing, crew motion, and assembly, etc. Fig. 1 shows the space station operational environment and control issues. In a broader context, Ref. 1, consisting of eleven articles, discussed key technologies and problems in all major station subsystems.

This paper deals with some of the issues stated above including the development of space station dynamic models; quantitative assessment of shuttle docking contact dynamics, solar panel interactions, and ways for reducing docking loads; and adaptive control techniques for space stations. Simulations of hard and soft docking dynamics reveal a critical design parameter. A concept of plant augmentation is proposed. Incorporating this augmentation with adaptive control algorithms, our initial generic investigation shows promising results. A fast convergence rate has been observed for all simulated adaptive control cases. Further investigation of this approach with more practical hardware implementation considerations is the subject of continuing research.

In Section II of this report, two space station configurations and their mass properties are described. Dynamic models for these configurations are developed in Section III. Docking dynamics and adaptive control are treated along with numerical results in Sections IV and V. Conclusions are summarized in Section VI.

POINTING/STABILITY
- SYSTEM POINTING   1° ~ 2°
- SYSTEM JITTER   0.1° ~ 0.2°
- PAYLOAD STABILITY   0.1 ~ 1 sec
- ACTIVE VIBRATION DAMPING
- MODULAR/DISTRIBUTED CONTROL TECHNIQUES

DISTURBANCES
- SHUTTLE DOCKING 0.02-0.20 g (PANEL BUCKLE)
- MAN-PUSH OFF 4-10 m
- REBOOST
- SOFT DOCKING TECHNOLOGY
- DISTURBANCE ESTIMATION AND ISOLATION

GROWTH AND CONFIGURATION CHANGE ACCOMMODATION CONTROL
- MODULAR RECONFIGURABLE CONTROL
- ADAPTIVE CONTROL/GAIN SWITCHING
- FAILURE DETERMINATION AND CONTROL
- AUTONOMOUS MASS PROPERTY MANAGEMENT

USER/PAYLOAD ACCOMMODATION AND CONTROL
- MULTI DOF CONTROLLED DISTURBANCE DECOUPLING
- CLOSE FORMATION FLIGHT TECHNIQUES
- BASE MOTION COMPENSATION
- JITTER SUPPRESSION CONTROL

SYSTEM IDENTIFICATION AND DYNAMIC PARAMETER ESTIMATION
- IDENTIFICATION OF
  - MASS PROPERTIES
  - DISTURBANCES
  - DYNAMICS
  - C.P. AND C.M. OF MAJOR COMPONENTS

RENDEZVOUS/DOCKING/TRAFFIC CONTROL
- OPERATIONAL SAFETY/CONTAMINATION
- DOCKING SENSOR TECHNOLOGY
- AUTOMATIC DOCKING METHODOLOGY AND CONTROL LAWS

Fig. 1. Space station operational environment and control issues

II. CONFIGURATIONS AND MASS PROPERTIES

During the last year, several space station configurations have been developed. Two of them are of particular interest, the two-panel and four-panel planar configurations These configurations were developed by the NASA Task Force and they are discussed in detail in this paper.

A. Four- Panel Planar Configuration [2,3]

Referring to Fig. 2, the four-panel planar configuration is a balanced symmetric design. This design consists of four solar panels with split resource modules, each one associated with two 100 ft by 50 ft solar panels and two 70 ft by 20 ft radiators.

The main structure of the station measures 280 feet in length and it supports two resource modules, several pressurized modules, a 30-foot service truss, and payloads. The pressurized modules are sized 22 ft in length by 14 ft in diameter and are determined by the space shuttle payload bay size.

The station has a ground weight of 223,000 lbs, and moments of inertia of $I_{xx} = 1.49 \times 10^7$, $I_{yy} = 3.37 \times 10^6$, and $I_{zz} = 1.63 \times 10^7$ slug-ft^2. The center of mass is nearly at the center of the structure, or X = -1.235 ft, Y = Z = 0.

The solar panels are hinged to rotate about the roll (X) and pitch (Y) axes for solar inertial pointing; the radiators are also hinged for articulation, and the core or the bus of the station is pointed to the nadir direction.

Due to the large size and the flexibility, the solar panels are the dominant factor for the flexible body dynamics.

B. Two-Panel Configuration

The two-panel configuration shown in Fig. 3 is one of the earlier concepts and much attention was focused on it at the earlier stage of this work due to its structural simplicity. The system dynamics is dominated by the two very large solar panels. The panels are sized to 250 ft by 40 ft each and weigh 4000 lbs each on the ground.

This configuration has only one radiator panel of 50 ft by 10 ft in size and a main bus structure, several pressurized modules, a berthing truss and payloads. The entire station weighs 134,000 lbs. The moments of inertia are $I_{xx} = 8.75 \times 10^0$, $I_{yy} = 1.58 \times 10^6$, and $I_{zz} = 8.60 \times 10^6$ slug-ft^2. Due to the asymmetric design, the products of inertia are quite high, $I_{xy} = -9.57 \times 10^4$, $I_{yz} = -4.89 \times 10^4$, and $I_{xz} = 5.18 \times 10^4$ slug-ft^2. With the selection of the reference coordinates as shown in Fig. 3, the center of mass has a high bias of X = 27, Y = -2.3, and Z = 5 ft.

Fig. 2 Four-panel planar configuration

106

TELEOPERATOR MANEUVERING SYSTEM

22' x 14 DIA HABITAT

250' x 40'
4000 LBS
SOLAR ARRAY PANEL

S/C BUS & RESOURCE
35' x 10' DIA 36500 LBS

RMS

LAB

FREE FLYER

50' x 10' 2500 LBS
RADIATOR

Z
NADIR

LOGISTICS

30' BERTH TRUSS

ORBIT NORMAL

X

TANKS

Y

400 km ORBIT
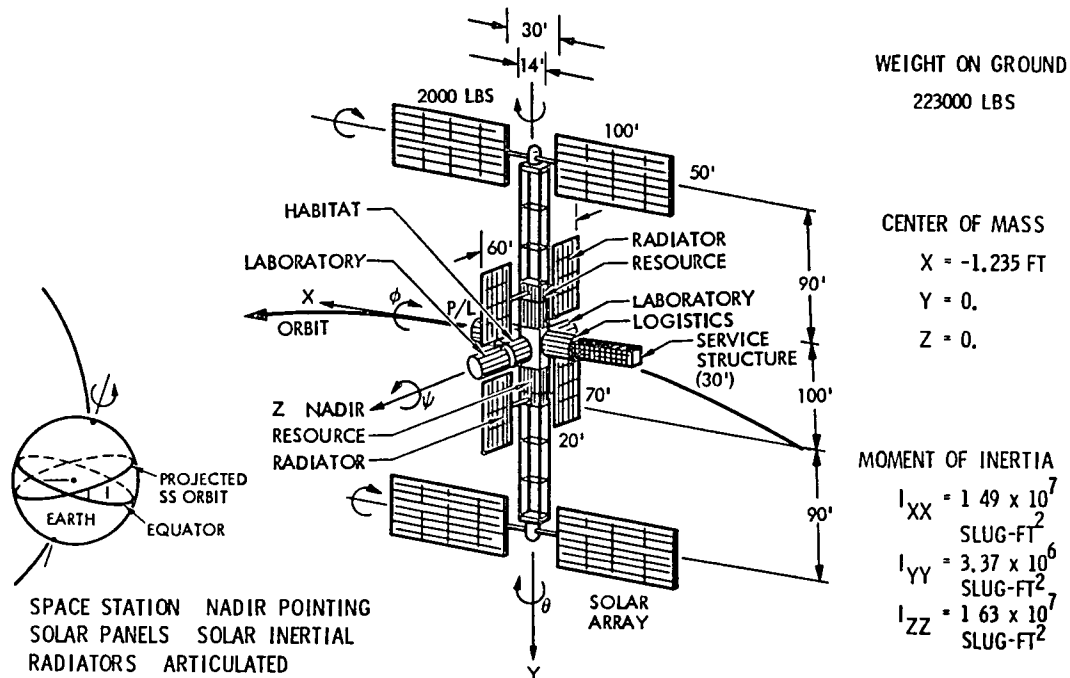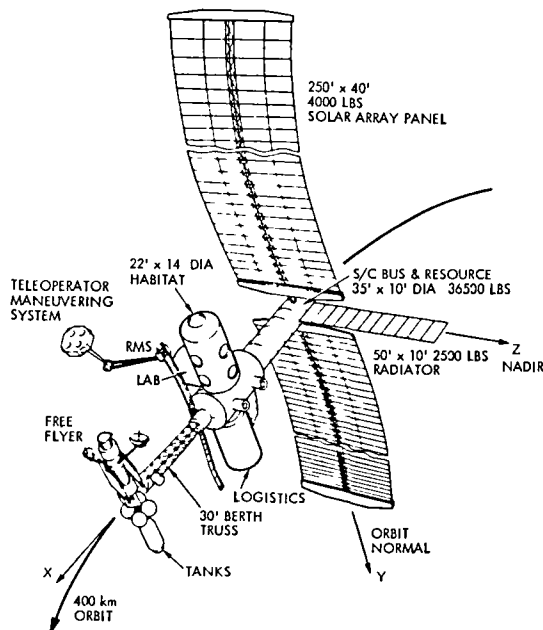
WEIGHT ON GROUND
134000 LBS

CENTER OF MASS

X = 27 FT

Y = -2.3 FT

Z = 5.0 FT

MOMENT OF INERTIA

I_{XX} = 8.75 x 10^6 SLUG-FT^2

I_{YY} = 1.58 x 10^6 SLUG-FT^2

I_{ZZ} = 8.60 x 10^6 SLUG-FT^2

I_{XY} = -9.57 x 10^4 SLUG-FT^2

I_{YZ} = -4.89 x 10^4 SLUG-FT^2

I_{XZ} = 5.18 x 10^4 SLUG-FT^2

Fig. 3 Two-panel baseline configuration

Note that the lighter weight of this station compared with that of the four-panel configuration is due to the fact that fewer modules were considered for this configuration rather than the structural differences between the two concepts.

III. DYNAMIC MODELS

Three dynamic models have been developed for the two configurations, i.e., a distributed parameter model and a finite-element model for the four-panel concept, and a low degree-of-freedom (DOF) finite-element model for the two-panel concept.

A. Distributed Parameter Model for the Four-Panel Configuration

This model is developed for the purpose of in-depth analysis and performance evaluation. Dynamics in the full three dimensional space including the elastic body motions, interbody coupling, and orbital effects are derived, discretized, and truncated to a finite dimensional model. The four solar array panels and the radiator panels are modeled as uniformly distributed flexible plates. The panels are attached to the main station structure through flexible booms and multi-axis hinges. The main structure is treated as a rigid body that supports all the panels and modules.

The detailed derivation of this model is presented in a companion paper, Ref. 4.

B. Finite-Element Model for the Four-Panel Configuration

The distributed parameter model is intended for performance evaluation and analysis of higher order effects where lower order models will not have enough resolution. However, high order models are more costly and time consuming for data generation. Models of lower order are valuable for their simplicity and useful for first order analysis with fast turnaround time. The finite-element models were developed for this purpose.

Referring to Fig. 4, the main or backbone structure is modeled as two flexible beams which are rigidly attached to the core body. The solar panels are treated as flexible beams attached to the ends of the main structure. Two payloads, assumed rigid for simplicity, are hinge connected to the core body. To keep the model to a tractable size, the beams are assumed torsionally stiff, and hence, only bending angles and the associated deflections are modeled.

Let $Z_1, ..., Z_7$ be the out-of-plane linear deformations at the various locations of the beams; $\Theta_1, ..., \Theta_7$ be the corresponding bending angles in the pitch or Y-axis direction; $\phi_2, \phi_4,$ and ϕ_6 be the bending angles in the roll or X-axis direction; and $\gamma_{8x}, \gamma_{8y}, \gamma_{9x}, \gamma_{9y}$ be the payload inertial attitude angles and $\gamma'_{8x}, \gamma'_{8y}, \gamma'_{9x}$ and γ'_{9y} be the corresponding hinge angles. Since the beams are assumed torsionally stiff, the following constraints apply,

$$\Theta_2 = \Theta_6 = \Theta_4 \qquad\qquad\qquad\qquad (III.1)$$
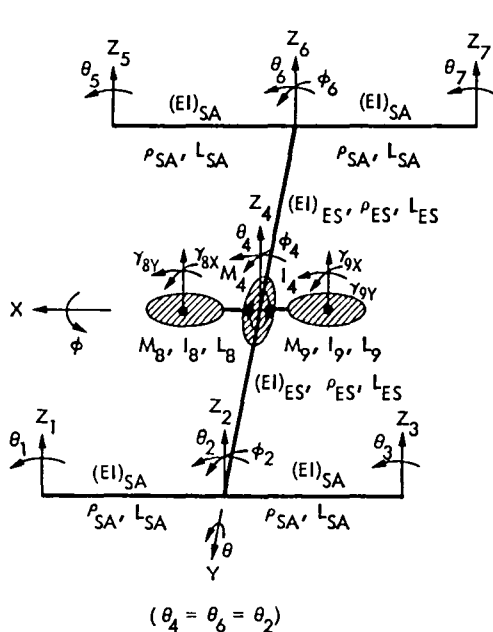
MODEL PARAMETERS

- **SOLAR ARRAYS**
  $(EI)_{SA} = 9.48 \times 10^6$ LB-FT^2
  $L_{SA} = 115$ FT
  $\rho_{SA} = 0.541$ SLUG/FT
- **MAIN STRUCTURE**
  $(EI)_{ES} = 9.48 \times 10^7$ LB-FT^2
  $L_{ES} = 140$ FT
  $\rho_{ES} = 1.048$ SLUG/FT
- **CORE STATION**
  $M_4 = 4165.35$ SLUGS
  $I_{4XX} = 3.869 \times 10^6$ SLUG-FT^2
  $I_{4YY} = 1.343 \times 10^6$ SLUG-FT^2
- **PAYLOADS**
  $M_8 = M_9 = 994.72$ SLUGS
  $L_8 = L_9 = 18$ ft
  $I_{8XS} = I_{9XS} = 2.437 \times 10^4$ SLUG-FT^2
  $I_{8YS} = I_{9YS} = 5.637 \times 10^4$ SLUG-FT^2

Fig. 4   19-DOF finite-element model for the four-panel
planar configurations

108

With Eq. (III.1), and the fact that the linear displacements of the payloads are functions of the hinge angles, etc., the model can be represented with 19 dynamical variables.

The model parameters including mass, inertia, physical dimensions, and flexural rigidities are specified in Fig. 4.

B.1 The Stiffness Matrix

To obtain the stiffness matrix by using finite-element technique [5], one starts by dividing the structure into a finite number of elements, the properties of each element are then determined. The properties of the entire structure are obtained by superimposing those of the elements at the associated nodes. The deflected beam shapes can be described by a set of cubic Hermitian polynomials. The stiffness coefficients are obtained by integrating the product of the flexural rigidity and the second spatial derivatives of the two related shape functions over the entire length of the beam segment.

Consider, for instance, the panel -- the uniform beam identified by Z_1, Θ_1, Z_2, Θ_2, the stiffness matrix will be

$$
\begin{bmatrix} F_1 \\ T_{1\theta} \\ F_2 \\ T_{2\theta} \end{bmatrix} = \frac{2(EI)_s}{L_s^3} \begin{bmatrix} 6 & 3L_s & -6 & 3L_s \\ 3L_s & 2L_s^2 & -3L_s & L_s^2 \\ -6 & -3L_s & 6 & -3L_s \\ 3L_s & L_s^2 & -3L_s & 2L_s^2 \end{bmatrix} \begin{bmatrix} Z_1 \\ \theta_1 \\ Z_2 \\ \theta_2 \end{bmatrix} \tag{III.2}
$$

The stiffness matrix for the adjoining panel is similarly obtained. By adding the element stiffness at the joining point, the stiffness matrix for these combined panels is,

$$
\begin{bmatrix} F_1 \\ T_{1\theta} \\ F_2 \\ T_{2\theta} \\ F_3 \\ T_{3\theta} \end{bmatrix} = \frac{2(EI)_s}{L_s^3} \begin{bmatrix} 6 & 3L_s & -6 & 3L_s & 0 & 0 \\ 3L_s & 2L_s^2 & -3L_s & L_s^2 & 0 & 0 \\ -6 & -3L_s & 12 & 0 & -6 & 3L_s \\ 3L_s & L_s^2 & 0 & 4L_s^2 & -3L_s & L_s^2 \\ 0 & 0 & -6 & -3L_s & 6 & -3L_s \\ 0 & 0 & 3L_s & L_s^2 & -3L_s & 2L_s^2 \end{bmatrix} \begin{bmatrix} Z_1 \\ \theta_1 \\ Z_2 \\ \theta_2 \\ Z_3 \\ \theta_3 \end{bmatrix} \tag{III.3}
$$

The stiffness matrix for the other two adjoining solar panels and that for the main structure are obtained similarly. Combining these stiffness matrices, in a similar manner to (III.3) and using constraints (III.1), the following relation is obtained,

$$F_S = K_S Z_S \tag{III.4}$$

where the force and displacement vectors are defined as follows:

$$F_S = (F_1, T_{1\theta}, F_3, T_{3\theta}, F_2, T_{2\phi}, F_4, T_{4\theta}, T_{4\phi}, F_6, T_{6\phi}, F_5, T_{5\theta}, F_7, T_{7\theta})^T \tag{III.5}$$

and

$$Z_S = (Z_1, \theta_1, Z_3, \theta_3, Z_2, \phi_2, Z_4, \theta_4, \phi_4, Z_6, \phi_6, Z_5, \theta_5, Z_7, \theta_7)^T \tag{III.6}$$

and the stiffness matrix K_S is

$$
K_S =
\begin{bmatrix}
6\alpha & 3l_s\alpha & 0 & 0 & 6\alpha & 0 & 0 & 3l_s\alpha & 0 & 0 & 0 & 0 & 0 & 0 & 0 \\
3l_s\alpha & 2l_s^2\alpha & 0 & 0 & 3l_s\alpha & 0 & 0 & l_s^2\alpha & 0 & 0 & 0 & 0 & 0 & 0 & 0 \\
0 & 0 & 6\alpha & 3l_s\alpha & 6\alpha & 0 & 0 & 3l_s\alpha & 0 & 0 & 0 & 0 & 0 & 0 & 0 \\
0 & 0 & 3l_s\alpha & 2l_s^2\alpha & 3l_s\alpha & 0 & 0 & l_s^2\alpha & 0 & 0 & 0 & 0 & 0 & 0 & 0 \\
6\alpha & 3l_s\alpha & 6\alpha & 3l_s\alpha & 12\alpha+6\beta & 3l_e\beta & 6\beta & 0 & 3l_e\beta & 0 & 0 & 0 & 0 & 0 & 0 \\
0 & 0 & 0 & 0 & 3l_e\beta & 2l_e^2\beta & 3l_e\beta & 0 & l_e^2\beta & 0 & 0 & 0 & 0 & 0 & 0 \\
0 & 0 & 0 & 0 & 6\beta & 3l_e\beta & 12\beta & 0 & 0 & -6\beta & 3l_e\beta & 0 & 0 & 0 & 0 \\
3l_s\alpha & l_s^2\alpha & 3l_s\alpha & l_s^2\alpha & 0 & 0 & 0 & 8l_s^2\alpha & 0 & 0 & 0 & 3l_s\alpha & l_s^2\alpha & 3l_s\alpha & l_s^2\alpha \\
0 & 0 & 0 & 0 & 3l_e\beta & l_e^2\beta & 0 & 0 & 4l_e^2\beta & 3l_e\beta & l_e^2\beta & 0 & 0 & 0 & 0 \\
0 & 0 & 0 & 0 & 0 & 0 & 6\beta & 0 & 3l_e\beta & 12\alpha+6\beta & 3l_e\beta & 6\alpha & 3l_s\alpha & 6\alpha & 3l_s\alpha \\
0 & 0 & 0 & 0 & 0 & 0 & 3l_e\beta & 0 & l_e^2\beta & 3l_e\beta & 2l_e^2\beta & 0 & 0 & 0 & 0 \\
0 & 0 & 0 & 0 & 0 & 0 & 0 & 3l_s\alpha & 0 & 6\alpha & 0 & 6\alpha & 3l_s\alpha & 0 & 0 \\
0 & 0 & 0 & 0 & 0 & 0 & 0 & l_s^2\alpha & 0 & 3l_s\alpha & 0 & 3l_s\alpha & 2l_s^2\alpha & 0 & 0 \\
0 & 0 & 0 & 0 & 0 & 0 & 0 & 3l_s\alpha & 0 & 6\alpha & 0 & 0 & 0 & 6\alpha & 3l_s\alpha \\
0 & 0 & 0 & 0 & 0 & 0 & 0 & l_s^2\alpha & 0 & 3l_s\alpha & 0 & 0 & 0 & 3l_s\alpha & 2l_s^2\alpha
\end{bmatrix}
\tag{III.7}
$$

where $\alpha = \dfrac{2(EI)_s}{L_s^3}$ and $\beta = \dfrac{2(EI)_e}{L_e^3}$.

110

B.2 The Consistent-Mass Matrix

The consistent-mass matrix is the mass matrix for the distributed mass of the flexible structure. The term consistent signifies that this matrix is obtained using the same shape functions as those used for deriving the stiffness matrix.

By following a similar approach for obtaining the stiffness matrix, the following relation is obtained,

$$F_S = M_{SC} \ddot{Z}_S \tag{III.8}$$

where F_S and Z_S are defined in (III.5) and (III.6), and the consistent-mass matrix M_{SC} is,

$$M_{SC} = \begin{bmatrix}
156a & 22L_sa & 0 & 0 & 54a & 0 & 0 & 13L_sa & 0 & 0 & 0 & 0 & 0 & 0 & 0 \\
22L_sa & 4L_s^2a & 0 & 0 & 13L_sa & 0 & 0 & 3L_s^2a & 0 & 0 & 0 & 0 & 0 & 0 & 0 \\
0 & 0 & 156a & 22L_sa & 54a & 0 & 0 & 13L_sa & 0 & 0 & 0 & 0 & 0 & 0 & 0 \\
0 & 0 & 22L_sa & 4L_s^2a & 13L_sa & 0 & 0 & 3L_s^2a & 0 & 0 & 0 & 0 & 0 & 0 & 0 \\
54a & 13L_sa & 54a & 13L_sa & 312a+156b & 22L_eb & 54b & 0 & 13L_eb & 0 & 0 & 0 & 0 & 0 & 0 \\
0 & 0 & 0 & 0 & 22L_eb & 4L_e^2b & 13L_eb & 0 & 3L_e^2b & 0 & 0 & 0 & 0 & 0 & 0 \\
0 & 0 & 0 & 0 & 54b & 13L_eb & 312b & 0 & 0 & 54b & 13L_eb & 0 & 0 & 0 & 0 \\
13L_sa & 3L_s^2a & 13L_sa & 3L_s^2a & 0 & 0 & 0 & 16L_s^2a & 0 & 0 & 0 & 13L_sa & 3L_s^2a & 13L_sa & 3L_s^2a \\
0 & 0 & 0 & 0 & 13L_eb & 3L_e^2b & 0 & 0 & 8L_e^2b & 13L_eb & 3L_e^2b & 0 & 0 & 0 & 0 \\
0 & 0 & 0 & 0 & 0 & 0 & 54b & 0 & 13L_eb & 156b+312a & 22L_eb & 54a & 13L_sa & 54a & 13L_sa \\
0 & 0 & 0 & 0 & 0 & 0 & 13L_eb & 0 & 3L_e^2b & 22L_eb & 4L_e^2b & 0 & 0 & 0 & 0 \\
0 & 0 & 0 & 0 & 0 & 0 & 0 & 13L_sa & 0 & 54a & 0 & 156a & 22L_sa & 0 & 0 \\
0 & 0 & 0 & 0 & 0 & 0 & 0 & 3L_s^2a & 0 & 13L_sa & 0 & 22L_sa & 4L_s^2a & 0 & 0 \\
0 & 0 & 0 & 0 & 0 & 0 & 0 & 13L_sa & 0 & 54a & 0 & 0 & 0 & 156a & 22L_sa \\
0 & 0 & 0 & 0 & 0 & 0 & 0 & 3L_s^2a & 0 & 13L_sa & 0 & 0 & 0 & 22L_sa & 4L_s^2a
\end{bmatrix} \tag{III.9}$$

where $\quad a = \dfrac{\rho_s L_s}{420} \quad$ and $\quad b = \dfrac{\rho_e L_e}{420}$.

111

B.3 The Lumped-Mass Matrix

M_{SC} accounts for the distributed mass for the flexible structure but not the lumped mass associated with the rigid bodies. Let M_{SD} be the lumped-mass matrix for the station excluding the payloads, then

$$M_{SD} = \text{diag } (0,0,0,0,0,0,M_4,I_{4yy},I_{4xx},0,0,0,0,0,0) \tag{III.10}$$

The total mass matrix, excluding payloads, is

$$M_S = M_{SC} + M_{SD} \tag{III.11}$$

The corresponding dynamic equation due to mass and inertia is

$$F_S = M_S \ddot{Z}_S \tag{III.12}$$

B.4 Payload Dynamics and Hinge Torque Model

The dynamic model for the payloads, bodies 8 and 9, and the hinge coordinates are shown in Fig. 5.

To include the payload dynamics and the dynamic interactions between the payloads and the station, the following expressions are obtained using Lagrangian approach:

$$F_4 - (M_8 + M_9)\ddot{Z}_4 + (M_8 L_8 - M_9 L_9)\ddot{\Theta}_4 + M_8 L_{8b}\ddot{\gamma}'_{8y} - M_9 L_{9b}\ddot{\gamma}'_{9y} \tag{III.13}$$

$$\begin{aligned} T_{4\Theta} + (M_8 L_8 - M_9 L_9)\ddot{Z}_4 - (I_{8ys} + M_8 L_8^2 + I_{9ys} + M_9 L_9^2)\ddot{\Theta}_4 \\ - (I_{8ys} + M_8 L_{8a} L_{8b} + M_8 L_{8b}^2)\ddot{\gamma}'_{8y} - (I_{9ys} + M_9 L_{9a} L_{9b} + M_9 L_{9b}^2)\ddot{\gamma}'_{9y} \end{aligned} \tag{III.14}$$

$$T_{4\phi} - (I_{8xs} + I_{9xs})\ddot{\phi}_4 - I_{8xs}\ddot{\gamma}'_{8x} - I_{9xs}\ddot{\gamma}'_{9x} \tag{III.15}$$

Equations (III.13), (III.14), and (III 15) are used to replace F_4, $T_{4\Theta}$, and $T_{4\phi}$ in (III.12).

The torques applied at the payload hinges are,

$$T_{8x} = I_{8xs}\ddot{\phi}_4 + I_{8xs}\ddot{\gamma}'_{8x} \tag{III.16}$$

$$T_{9x} = I_{9xs}\ddot{\phi}_4 + I_{9xs}\ddot{\gamma}'_{9x} \tag{III.17}$$

$$T_{8y} = -M_8 L_{8b}\ddot{Z}_4 + (I_{8ys} + M_8 L_{8a} L_{8b} + M_8 L_{8b}^2)\ddot{\Theta}_4 + (I_{8ys} + M_8 L_{8b}^2)\ddot{\gamma}'_{8y} \tag{III.18}$$

$$T_{9y} = M_9 L_{9b}\ddot{Z}_4 + (I_{9ys} + M_9 L_{9a} L_{9b} + M_9 L_{9b}^2)\ddot{\Theta}_4 + (I_{9ys} + M_9 L_{9b}^2)\ddot{\gamma}'_{9y} \tag{III.19}$$

112
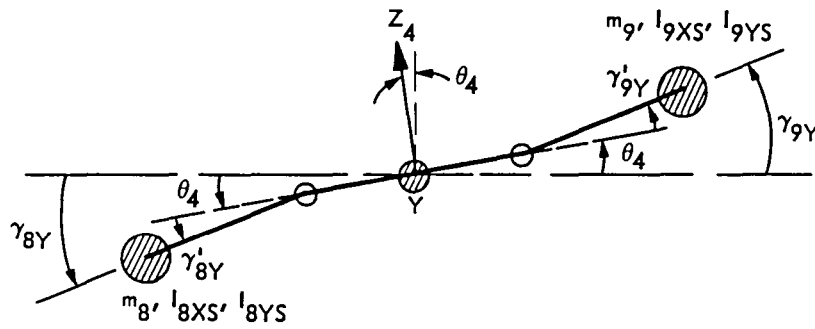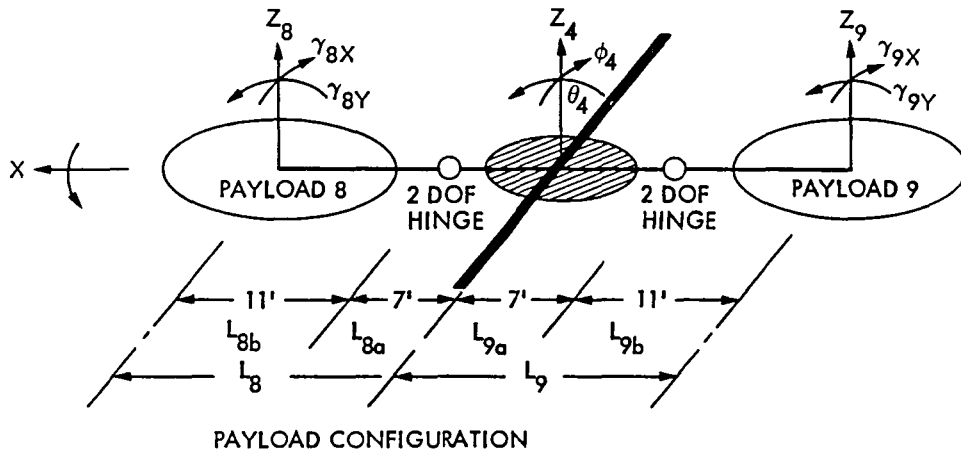
$$\gamma'_{8X} = \gamma_{8X} - \phi_4 = \text{HINGE ANGLE FOR "PAYLOAD 8" ABOUT X-AXIS}$$

$$\gamma'_{8Y} = \gamma_{8Y} - \theta_4 = \text{HINGE ANGLE FOR "PAYLOAD 8" ABOUT Y-AXIS}$$

$$\gamma'_{9X} = \gamma_{9X} - \phi_4 = \text{HINGE ANGLE FOR "PAYLOAD 9" ABOUT X-AXIS}$$

$$\gamma'_{9Y} = \gamma_{9Y} - \theta_4 = \text{HINGE ANGLE FOR "PAYLOAD 9" ABOUT Y-AXIS}$$

Fig. 5 Payload dynamics and hinge coordinates

B.5 Equations of Motion

Let $F_p = (T_{8x}, T_{9x}, T_{8y}, T_{9y})^T$ and $Z_p = (\gamma'_{8x}, \gamma'_{9x}, \gamma'_{8y}, \gamma'_{9y})^T$ be the payload forcing and displacement vectors, the corresponding vectors for the system can be partitioned as follows,

$$F = \begin{bmatrix} F_s \\ --- \\ F_p \end{bmatrix} \quad \text{and} \quad Z = \begin{bmatrix} Z_s \\ --- \\ Z_p \end{bmatrix} \tag{III.20}$$

The system mass matrix becomes,

$$M = M_C + M_D \tag{III.21}$$

where

$$M_C = \begin{bmatrix} M_{SC} & 0_{15x4} \\ \hline 0_{4x15} & 0_{4x4} \end{bmatrix} \tag{III.22}$$

and

$$M_D = \begin{bmatrix} M_{SD} + M'_{SD} & M_{PSD}^T \\ \hline M_{PSD} & M_{PD} \end{bmatrix} \tag{III.23}$$

M_{SC} is defined in (III 9) and M_{SD} in (III.10), and M'_{SD}, M_{PD}, M_{PSD} are,

$$M'_{SD} = \begin{bmatrix} 0_{6x6} & & 0_{6x3} & & 0_{6x6} \\ \hline & m_8+m_9 & m_9L_9-m_8L_8 & 0 & \\ 0_{3x6} & m_9L_9-m_8L_8 & m_8L_8^2+m_9L_9^2+I_{8YS}+I_{9YS} & 0 & 0_{3x6} \\ & 0 & 0 & I_{8YS}+I_{9YS} & \\ \hline 0_{6x6} & & 0_{6x3} & & 0_{6x6} \end{bmatrix} \tag{III.24}$$

$$M_{PD} = \begin{bmatrix} I_{8XS} & 0 & 0 & 0 \\ 0 & I_{9XS} & 0 & 0 \\ 0 & 0 & I_{8YS}+m_8L_{8b}^2 & 0 \\ 0 & 0 & 0 & I_{9YS}+m_9L_{9b}^2 \end{bmatrix} \tag{III.25}$$

114

$$M_{PSD} = \begin{bmatrix} & 0 & 0 & I_{8XS} & \\ & 0 & 0 & I_{9XS} & \\ 0_{4x6} & & & & 0_{4x6} \\ & -m_8 L_{8b} & I_{8YS} + m_8 L_{8a} L_{8b} + m_8 L_{8b}^2 & 0 & \\ & m_9 L_{9b} & I_{9YS} + m_9 L_{9a} L_{9b} + m_9 L_{9b}^2 & 0 & \end{bmatrix} \qquad \text{(III.26)}$$

The system stiffness matrix is

$$K = \begin{bmatrix} K_s & 0_{15x4} \\ 0_{4x15} & 0_{4x4} \end{bmatrix} \qquad \text{(III.27)}$$

where K_s is defined in (III.7).

The equation of motion is

$$M\ddot{Z} + KZ = F \qquad \text{(III.28)}$$

B.6 Modal Coordinates and Modal Properties

Let $\eta(t)$, Λ, and Φ be the modal amplitude vector, eigenvalue matrix, and eigenvector matrix, respectively. Let $Z(t) = \Phi\eta(t)$, substitute this into (III.28) and premultiply (III.28) by Φ^T, then $\Phi^T M \Phi = I$ and $\Phi^T K \Phi = \Lambda$, one has the following dynamical equation in modal form,

$$\ddot{\eta} + \Lambda\eta = \Phi^T F \qquad \text{(III.29)}$$

where $\Lambda = \text{diag}(\omega_1^2, \dots, \omega_{19}^2)$. Adding damping terms, (III.29) becomes,

$$\ddot{\eta} + \text{diag}(2\zeta_1 \omega_1, \dots, 2\zeta_{19}\omega_{19})\dot{\eta} + \text{diag}(\omega_1^2, \dots, \omega_{19}^2)\eta = \Phi^T F \qquad \text{(III.30)}$$

The corresponding damped dynamical equation in physical coordinates can be obtained through transformation. Let D be the damping factor matrix, one has

115

$$D = \phi^{-T} \text{diag} (2\zeta_1 \omega_1, \quad , 2\zeta_{19} \omega_{19})\phi^{-1} \qquad \text{(III.31)}$$

and the equation of motion becomes,

$$M\ddot{Z} + D\dot{Z} + KZ = F \qquad \text{(III.32)}$$

For the purpose of control, let B and C be the control influence matrix and measurement distribution matrix, respectively. The system equations in physical and model coordinates are, respectively,

$$M\ddot{Z} + D\dot{Z} + KZ = BU \qquad \text{(III.33a)}$$

$$Y = C(\alpha Z + \dot{Z}) \qquad \text{(III.33b)}$$

and

$$\ddot{\eta} + \text{diag} (2\zeta_1 \omega_1, \ldots , 2\zeta_{19} \omega_{19}) \dot{\eta} + \text{diag} (\omega_1^2, \ldots , \omega_{19}^2) \eta = \phi^T BU \qquad \text{(III.34a)}$$

$$Y = C (\alpha\phi\eta + \phi\dot{\eta}) \qquad \text{(III.34b)}$$

To obtain the modal properties, i.e., to determine the eigenvalues and eigenvectors, for the open loop system, one can either free the hinges for the payloads, or clamp them. For the latter case, a 15-coordinate system is resulted with 12 flexible modes and 3 rigid body modes. For the former case, however, a 19-coordinate system is resulted since the payloads are considered rigid bodies and the hinges are freed, it ends up with 4 additional rigid or zero frequency modes. Since this does not yield additional information, only the clamped-hinge case is considered in this paper.

The modal frequencies and mode shapes for the four-panel planar configuration with clamped-hinge case are shown in Fig. 6. These modes are divided into three groups. The first bending group consists of 6 modes with frequencies ranging from 0.115 Hz to 0.302 Hz. These modes are formed with the first symmetric or antisymmetric bending of the three major structures, i.e., the two solar panel pairs and the main structure The second bending group is caused by the second symmetric or the antisymmetric bending of the three major structures. The frequencies for this group are much higher than those of the first group, and range from 1.67 Hz to 2 34 Hz The third group consists of three rigid body modes with zero frequency

The structural and mass parameters used for generating these modes are shown in Fig. 4. The flexural rigidity $(EI)_s = 9.48 \times 10^6$ lb-ft^2 has been used for the solar panels and a value of an order of magnitude higher has been used for the main structure.

MODE 4
$\omega_4 = 0.11526$ Hz

MODE 5
$\omega_5 = 0.16961$ Hz

MODE 6
$\omega_6 = 0.17794$ Hz

MODE 7
$\omega_7 = 0.21767$ Hz

MODE 8
$\omega_8 = 0.28061$ Hz

MODE 9
$\omega_9 = 0.30205$ Hz

(a) First bending group

MODE 10
$\omega_{10} = 1.6663$ Hz

MODE 11
$\omega_{11} = 1.6714$ Hz

MODE 12
$\omega_{12} = 1.7533$ Hz

MODE 13
$\omega_{13} = 1.7638$ Hz

MODE 14
$\omega_{14} = 2.3364$ Hz

MODE 15
$\omega_{15} = 2.3389$ Hz

(b) Second bending group

MODE 1
$\omega_1 = 0$

MODE 2
$\omega_2 = 0$

MODE 3
$\omega_3 = 0$
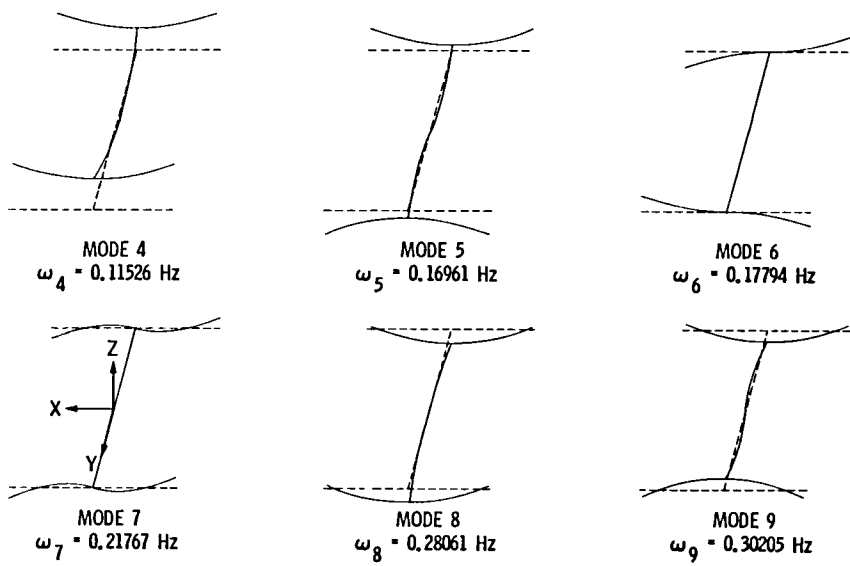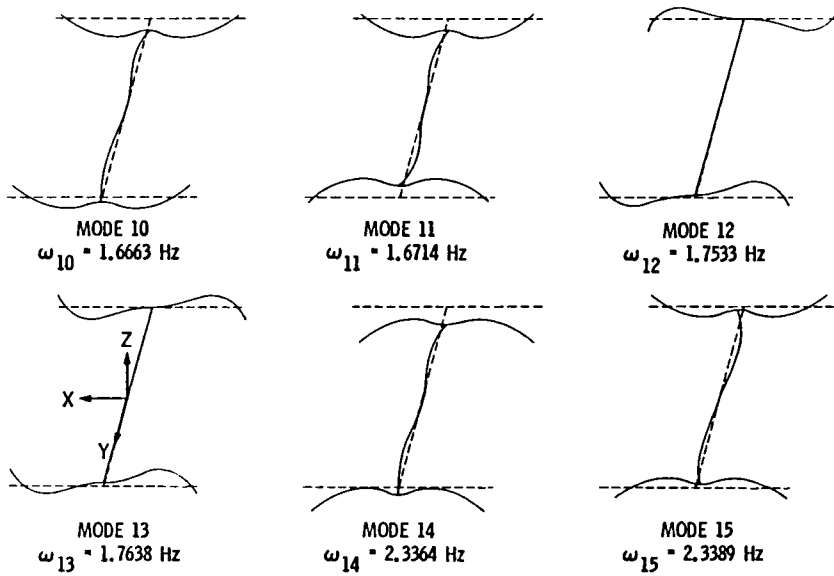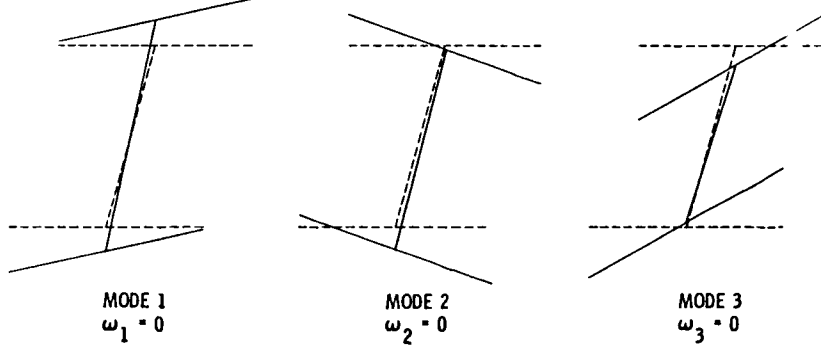
(c) Rigid body modes

Fig. 6 Four-Panel space station modal properties

117

C. Finite-Element Model for the Two-Panel Configuration

The finite-element model for the two-panel configuration is a low order system. It consists of only 6 dynamical variables, 3 out-of-plane translation (Z-direction) and 3 rotations about the X-axis as shown in Fig. 7. Two flexible beams of 250 feet long each are used to model the two solar panels. The bus and the modules are modeled as a rigid core body located at the joint of the panels as shown in Fig. 7.
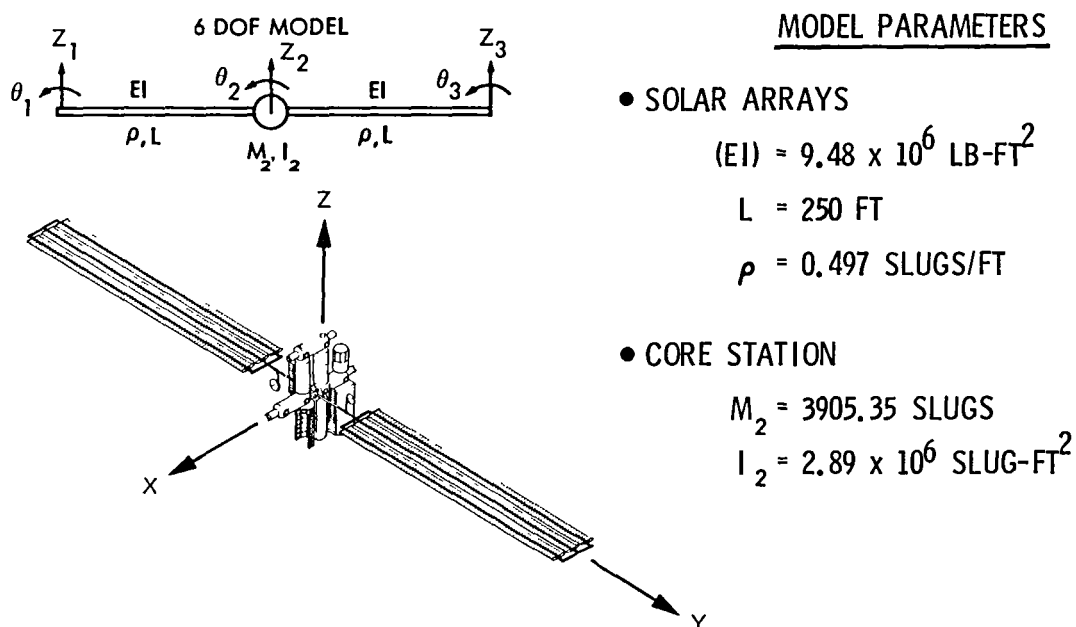
Fig. 7. Finite-element model for the two-panel configuration

The equation of motion in both the physical coordinates and modal coordinates are the same as (III.33) and (III.34), respectively, except that there are only 6 coordinates here. For this case,

$$Z = (Z_1, \Theta_1, Z_2, \Theta_2, Z_3, \Theta_3)^T \tag{III.35a}$$

$$\eta = (\eta_1, \eta_2, \eta_3, \eta_4, \eta_5, \eta_6)^T \tag{III.35b}$$

$$\Lambda = \text{diag}(\omega_1^2, \omega_2^2, \omega_3^2, \omega_4^2, \omega_5^2, \omega_6^2) \tag{III.35c}$$

118

The stiffness matrix K and the consistent-mass matrix M_c are, respectively,

$$K = \frac{2EI}{L^3} \begin{bmatrix} 6 & 3L & -6 & 3L & 0 & 0 \\ 3L & 2L^2 & -3L & L^2 & 0 & 0 \\ -6 & -3L & 12 & 0 & -6 & 3L \\ 3L & L^2 & 0 & 4L^2 & -3L & L^2 \\ 0 & 0 & -6 & -3L & 6 & -3L \\ 0 & 0 & 3L & L^2 & -3L & 2L^2 \end{bmatrix}$$

(III.36)

$$M_C = \frac{\rho L}{420} \begin{bmatrix} 156 & 22L & 54 & -13L & 0 & 0 \\ 22L & 4L^2 & 13L & -3L^2 & 0 & 0 \\ 54 & 13L & 312 & 0 & 54 & -13L \\ -13L & -3L^2 & 0 & 8L^2 & 13L & -3L^2 \\ 0 & 0 & 54 & 13L^2 & 156 & -22L \\ 0 & 0 & -13L & -3L^2 & -22L & 4L^2 \end{bmatrix}$$

(III.37)

The lumped-mass matrix is

$$M_D = \text{diag}(0, 0, M_2, I_2, 0, 0)$$

(III.38)

The system mass matrix is

$$M = M_C + M_D$$

(III.39)

Using the same solar panel structural properties of the four-panel configuration, i.e., $(EI) = 9.48 \times 10^6$ lb-ft^2, and other panel parameters of Fig. 7, modal properties of this configuration are obtained as shown in Fig. 8. Due to the very large panel size, the fundamental frequency of this model is 0.04 Hz, much less than that of the four-panel model. Of the 6 modes, there are two zero-frequency rigid body rotation and translation modes, two first bending modes – symmetric and antisymmetric, and two second bending modes. The largest modal frequency of this model is 0.39 Hz.

MODE 1
RIGID BODY ROTATION
$\omega_1 = 0$

MODE 3
1ST SYMMETRIC BENDING
$\omega_3 = 0.040$ Hz

MODE 5
2ND SYMMETRIC BENDING
$\omega_5 = 0.3885$ Hz

MODE 2
RIGID BODY TRANSLATION
$\omega_2 = 0$

MODE 4
1ST ANTISYMMETRIC BENDING
$\omega_4 = 0.0637$ Hz

MODE 6
2ND ANTISYMMETRIC BENDING
$\omega_6 = 0.3947$ Hz

Fig. 8 Modal properties for the two-panel configuration model

D. Frequency Characterization of Space Station Dynamical Systems

With the availability of these space station models, the frequency characteristics of the various dynamical systems in the space station environment are identified as shown in Fig. 9.
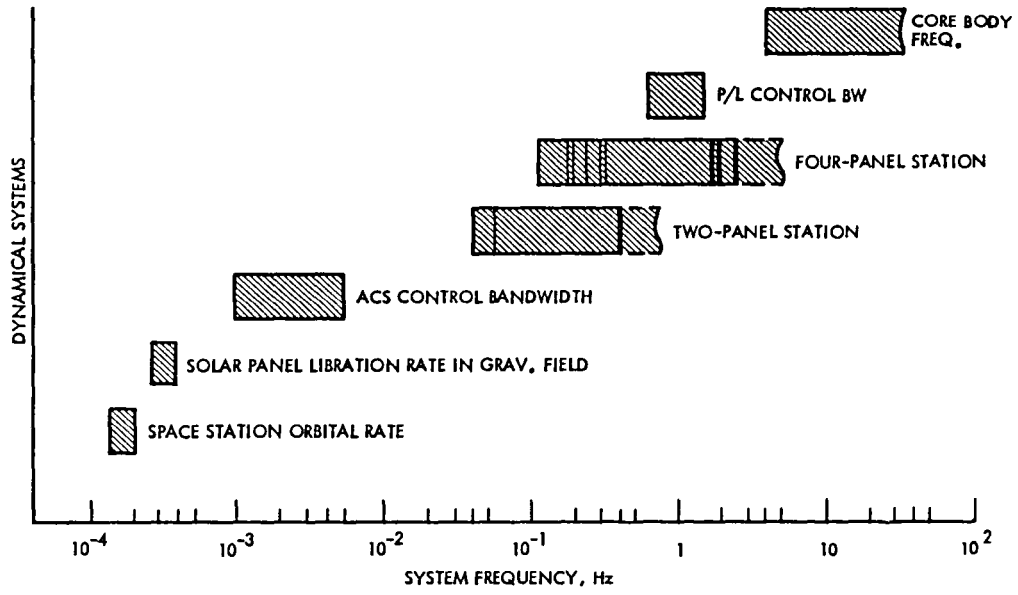
Fig. 9 Frequency characteristics of space station dynamical systems

120

For a nominal orbital altitude of 400 km, the orbital period is 92.61 minutes and the orbital rate is 1.8×10^{-4} Hz rate. For an altitude close to 400 km, the orbital rate will be inside the shaded narrow region in Fig. 9. The solar panel libration frequency for quasi-solar-inertial pointing [6] will be twice the orbital rate as shown in Fig. 9. A low bandwidth attitude control system for the space station will have a bandwidth in the range of 0.001 Hz to 0.005 Hz. The two-panel low DOF model and the four-panel finite-element model are shown in Fig. 9 with their modeled frequencies identified by vertical lines. The dashed regions extending the modeled modes represent the modal spectra that are not included in the models. The payload attitude control systems for a range of applications will have a bandwidth in a range centered at 1 Hz. The core body including the pressurized modules should have structural frequencies above 9 Hz. The figure indicates that the spectral separations of the orbital rate, the attitude controllers, and the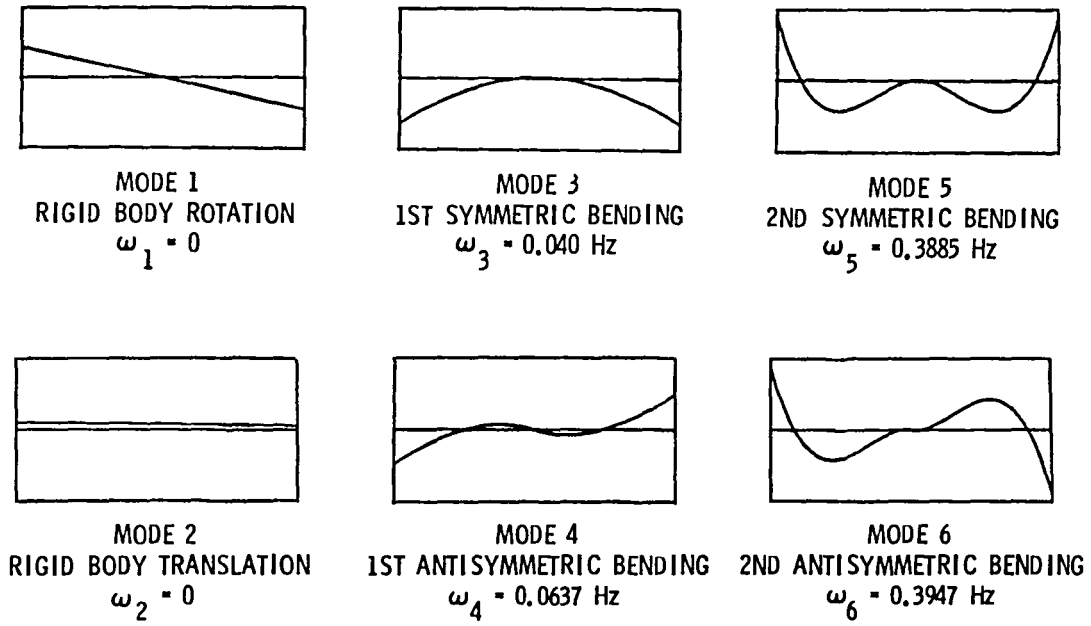 low frequency modes of the station structure are reasonable. However, the same cannot be said about the structural modes and the payload controls. For instance, the payload bandwidth falls between the modes of the first and the second bending groups. This result strongly suggests that decoupling control of the payload is required.

IV. DYNAMIC INTERACTION AND DISTURBANCE ACCOMMODATION

Crew motion, reboost, and vehicle docking disturbances are the major disturbance sources. These will also cause changes of mass property. Crew motion will cause a shift of the center of mass, reboost will result in gradual mass reduction, and vehicle docking will spontaneously increase mass and inertia of the system. From the point of view of time varying effect and the level of disturbances, space shuttle docking is by far the most significant source of disturbance. In this paper, only the shuttle docking effects are discussed.

A. Shuttle Reaction Control Subsystem Residual Rates

The shuttle Reaction Control Subsystem (RCS) consists of two major parts, the primary (PRCS) and the vernier (VRCS) subsystems. There are a total of 44 thrusters, 38 of them are associated with the PRCS, each has a nominal thrust level of 870 lbs; and the other 6 are associated with the VRCS with a thrust level of 24 lbs each. Phase plane control laws are employed to determine when actuations are needed and jet select logics are used to determine what thrusters are to turn on. The states of the system are estimated by a two-stage state estimator with a dual cycle time of 80 ms and 160 ms. Fig. 10 shows the phase plane control law switching curves and parameters.

PRCS is normally employed for ΔV change, attitude maneuvers, and coarse attitude control; and the VRCS is for fine attitude control. Since shuttle docking requires maneuvers, PRCS must be used. Due to the high thrust level of the PRCS, and with several jets used at the same time to maintain attitude and approach rate while maneuvering, large residual rates result. The best achievable (minimum) residual rates, i.e., rates obtained under ideal conditions, are $\Delta V = 0.05$ ft/sec and $\Delta \omega = 0.20$ deg/sec. However, these minimum rates are difficult to realize under nominal operational conditions and much higher rates are expected. These expected rates are on the order of $\Delta V = 0.50$ ft/sec and $\Delta \omega = 1.00$ deg/sec.
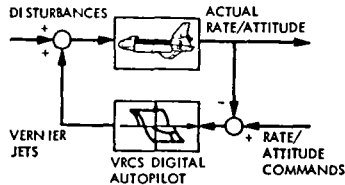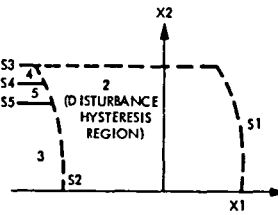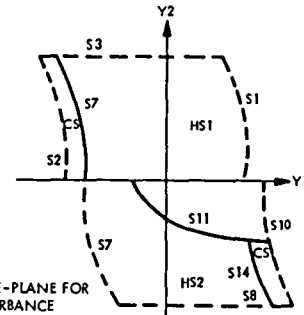
Fig. 10 Shuttle Reaction Control Subsystem and residual rates

The following assumptions are made:

1) Throughout the docking period, the space station attitude control system will maintain operational on attitude hold mode.

2) Just prior to the contact, the shuttle RCS should be set at passive mode, i.e., no thrusters should be allowed to fire.

3) Once contact is made, latching is assumed, i.e., no separation is allowed in the analysis.

B. Shuttle Hard Docking

Hard docking is a rather idealized condition. Under this condition, the shuttle momentum is transferred to the space station for a brief period of time, Δt. At the end of Δt, the station and the shuttle are moving together as one integrated body. The initial momentum of the shuttle is determined by the shuttle mass, $M_s = 7.81 \times 10^3$ slugs (2.52×10^5 lbs) and inertia, $I_s = 7.54 \times 10^6$ slug-ft^2, and the shuttle residual rate ΔV and $\Delta \omega$ (see Fig. 10). The final velocities are, of course, determined by the system mass and inertia.

122

Dynamics for hard shuttle docking using the low order finite-element model (two-panel configuration) was conducted for the best achievable rates case. Two of the plotted time histories are shown in Fig. 11. The results show that the station bus attitude will have a 2.72° excursion along with relative solar panel bending of 1° and tip swing of 12.6 feet. The greatest concern is the dynamic loads at the solar panels. A relative panel tip acceleration of as much as 0.02 g resulted, and a load analysis for a panel design derived from Ref. 7 indicates that the panel longerons will buckle. Even before any design margin is applied, this size panel will not stand more than 0.006 g of relative acceleration load.
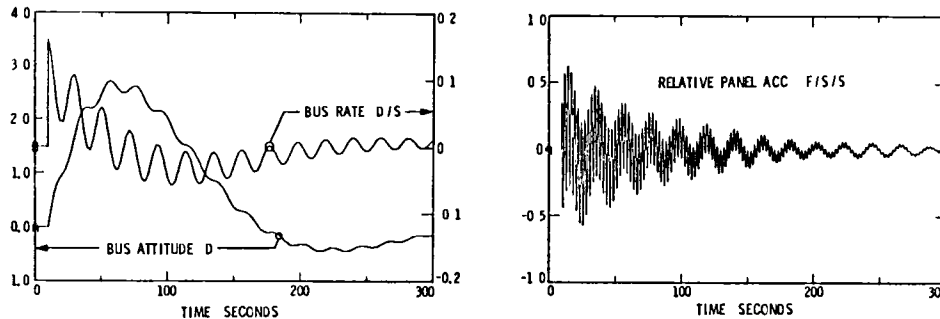
ΔV = 0.05 FT/SEC

Δω = 0.20 DEG/SEC

SHUTTLE COASTING BEFORE CONTACT

STATION CONTROL BW = 0.005 Hz

- LARGE BUS ATTITUDE EXCURSION (2.72°)
- HIGH PANEL TIP ACC. (0.020 G REL.) -- PANEL TO BUCKLE
  EVEN WITH BEST ACHIEVABLE SHUTTLE RESIDUAL RATE

Fig. 11 Shuttle and space station hard docking dynamics for
best achieveable shuttle residual rates

From these simulated results, one can conclude that hard docking is unacceptable even for the best achievable residual rates.

C. Shuttle Soft Docking

Since hard docking is no longer a viable option, soft docking or berthing concepts are the most likely alternatives. Fig. 12 shows the concept and design of soft docking. Consider two body systems that are coupled by a set of angular and rectilinear spring and damper devices. Let M_s and I_s be the shuttle mass and inertia, and M_2 and I_2 be the mass and inertia for the station. The values of the spring constants and damping factors can be computed using the equations shown in Fig. 12 by specifying the natural frequencies and damping ratios for the docking devices.
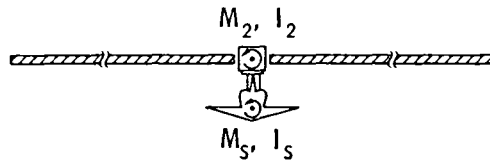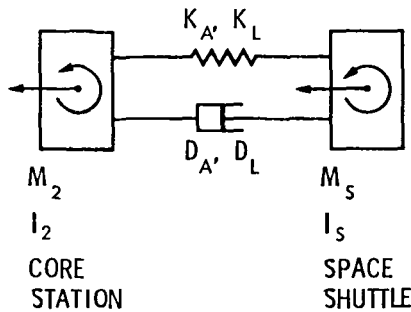
DOCKING SYSTEM PARAMETERS

• ANGULAR STIFFNESS AND DAMPING

$$K_A = \omega_A^2 \left(\frac{I_2 I_s}{I_2 + I_s}\right) \quad \text{FT-LB/RAD}$$

$$D_A = 2\zeta_A\omega_A \left(\frac{I_2 I_s}{I_2 + I_s}\right) \quad \text{FT-LB/RAD/SEC}$$

• LINEAR STIFFNESS AND DAMPING

$$K_L = \omega_L^2 \left(\frac{M_2 M_s}{M_2 + M_s}\right) \quad \text{LB/FT}$$

$$D_L = 2\zeta_L\omega_L \left(\frac{M_2 M_s}{M_2 + M_s}\right) \quad \text{LB/FT/SEC}$$

• MASS AND INERTIA

$I_2 = 2.89 \times 10^6$ SLUG-FT^2

$I_s = 7.54 \times 10^6$ SLUG-FT^2

$M_2 = 3.91 \times 10^3$ SLUGS $(1.26 \times 10^5$ LBS$)$

$M_s = 7.82 \times 10^3$ SLUGS $(2.52 \times 10^5$ LBS$)$

Fig. 12 Soft docking design and system parameters

A number of cases have been considered and simulated. Table 1 shows the parameters of 9 design cases. Cases 1 to 4 apply to rotational soft coupling only. Our analysis shows that, under the assumptions made on the relevant system parameters, the major disturbance responses are due to residual angular rate rather than linear rate. Table 2 shows that the relative panel tip load has dropped to 0.0046 g with soft docking design Case 3 from 0.020 g of the hard docking case. However, further improvement from soft angular coupling is no longer possible as indicated by Case 4 in Table 2. Additional improvement can be achieved by adding linear soft coupling. For instance, in Case 6 which has the same angular soft coupling of Case 3, the linear soft coupling has further reduced the load to 0.0011 g.

Table 1. Soft Docking Parameters

CASE NO	ζ -	f_A Hz	τ_A Sec	K_A FT-LB/RAD	D_A FT-LB/RAD/SEC	f_L Hz	τ_L Sec	K_L LB/FT	D_L LB/FT/SEC	ΔV FT/SEC	$\Delta\omega$ RAD/SEC
1	.707	1.000	225	8.25×10^7	$1\ 86\times10^7$	DO NOT APPLY (Rotational Soft Compliance Only)				05	20
2	.707	010	22.5	$8\ 25\times10^3$	$1\ 86\times10^5$					05	.20
3	.707	.003	75.0	742	$5\ 57\times10^4$					05	.20
4	.707	002	112 6	330	$3\ 71\times10^4$					05	20
5	.707	003	75.0	742	5.57×10^4	10	2.25	$1\ 028\times10^3$	$2\ 313\times10^3$	05	.20
6	.707	003	75 0	742	$5\ 57\times10^4$	03	7 50	92 49	$6\ 938\times10^2$	05	20
7	707	010	22 5	$8\ 25\times10^3$	$1\ 86\times10^5$	03	7 50	92 49	$6\ 938\times10^2$	05	20
8	707	.003	75.0	742	5.57×10^4	.03	7 50	92 49	$6\ 938\times10^2$	.50	1 00
9	707	.010	22.5	8.25×10^3	$1\ 86\times10^5$	03	7 50	92 49	$6\ 938\times10^2$	50	1 00

Table 2. Simulated Docking Dynamics

CRITICAL DYNAMIC PROPERTIES		HARD	SOFT								
			1	2	3	4	5	6	7	8	9
Bus Attitude Excursion	Deg	2.72	2 47	2 57	1 46	1 04	1.45	1 45	2.54	7 27	12.80
Habit Module Acc	g	.017	.020	.0007	.0005	.0005	.00013	8.1×10^{-5}	.00022	.00051	0012
Relative Panel Bending Angle	Deg	.985	.914	.272	.177	.165	.139	.124	238	.977	1.54
Relative Panel Tip Swing	Feet	12 6	11.5	11.5	6.58	4 74	6.54	6.49	11.4	33 2	58 0
Relative Panel Tip Acc.	g	.020	.020	0053	.0046	.0045	.002	0011	.002	.0086	013
Shuttle Attitude Excursion	Deg	2.72	2 38	4.86	13.53	19.6	13.5	13.5	4 82	67.6	24.2
Linear Docking Displacement	Inch	0	-	-	-	-	.44	1.48	1.48	14.76	14 76
Combined Disp., 2mD Compl. Table	Inch						8.69	9.73	3.42	44.74	24 34

Fig. 13 shows the time history of docking dynamics for Case 6. The core station excursion has reduced to 1.46° in addition to the load reduction from hard docking. The shuttle excursion has increased to 13.5°.
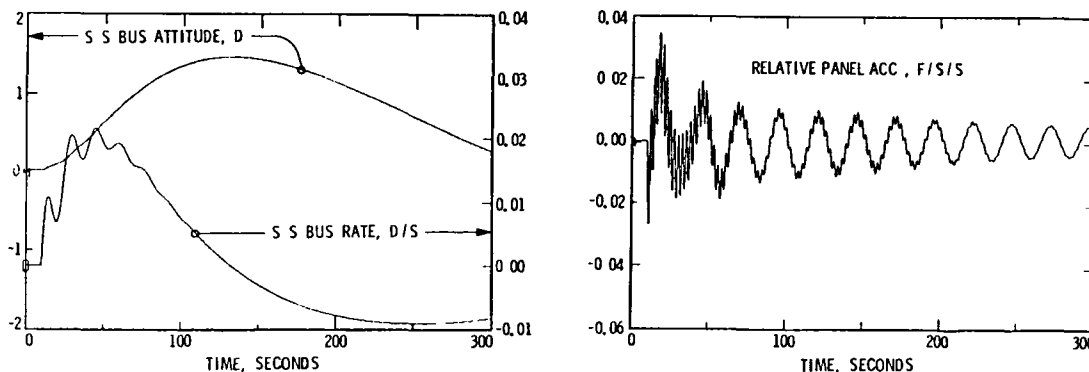
ΔV = 0.05 FT/SEC K_A = 742 FT-LB/RAD K_L = 92.49 LB/FT
$\Delta \omega$ = 0.20 DEG/SEC D_A = 5.57 x 10⁴ FT-LB/RAD/SEC D_L = 693.8 LB/FT/SEC
ζ = 0.707 f_A = 0.003 Hz f_L = 0.03 Hz
   τ_A = 75 SEC τ_L = 7.5 SEC

• REDUCED BUS ATTITUDE EXCURSION (1.46°)
• REDUCED TIP ACC. TO RELATIVE SAFE LEVEL (0.0011 g REL.)
• LARGE SHUTTLE ATTITUDE EXCURSION (13.5°)

Fig. 13 Dynamic responses of soft docking with best achievable residual rates (Case 6)

The above results were obtained with the best achievable shuttle approach rates as was done with the hard docking case. The real test is what if the expected rates are applied. Fig. 14 shows the results of the soft docking Case 8 which employs the same soft coupling devices of Case 6 but with higher approach rates. The bus attitude excursion has increased to 7.27° and the shuttle attitude excursion has

125

reached 68°. These excursions are so high that operational safety of the station is in doubt. In addition, the dynamic load has increased to 0.0086 g, although this is much lower than that of the hard docking case with lower residual rates, it still exceeds the load capacity of the large panels.

Now, it has been demonstrated that soft docking or berthing alone will not be sufficient to solve this problem. The excessive momentum of the docking vehicle must be removed to a low level before docking occurs. This can be achieved by a number of options:
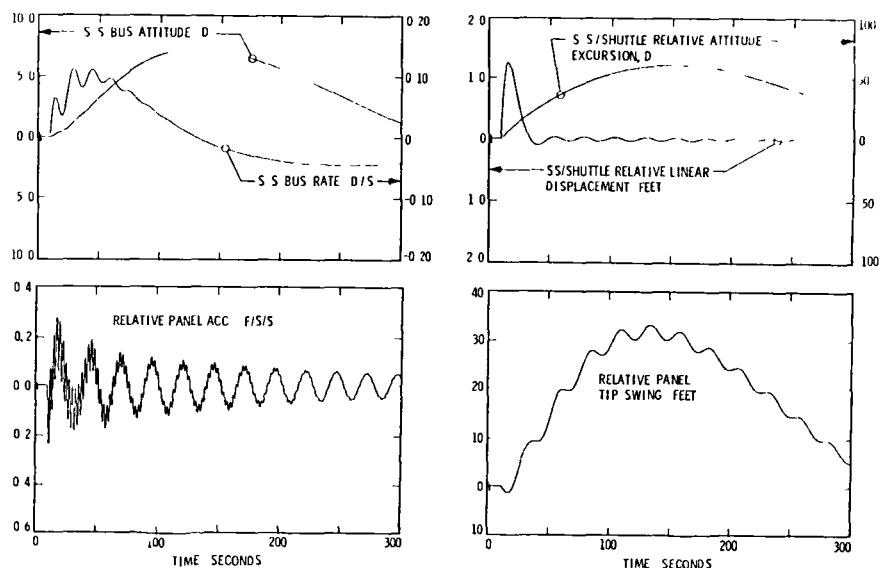
$\Delta V = 0.50$ FT / SEC
$\Delta \omega = 1.00$ DEG / SEC

OTHER DOCKING PARAMETERS
ARE SAME TO CASE 6

- VERY HIGH BUS ATTITUDE EXCURSION (7.27°)
- EXTREMELY HIGH SHUTTLE ATTITUDE EXCURSION (67.6°)
- PANEL LOAD (0.0086 g) EXCEEDS ALLOWABLE RANGE

Fig. 14   Dynamic responses of soft docking with expected approaching rates (Case 8)

1) Augment the space shuttle with additional vernier thrusters so that refined rate adjustments can be achieved with higher resolution impulses.

2) Attach an External Momentum Exchange System to the docking vehicle before the docking phase starts, the excessive momentum can be removed before docking with the space station occurs. Such an intermediate system may be loosely coupled to the station and contain its own ACS.

126

V. ADAPTIVE CONTROL APPLICATION FOR SPACE STATION

The space station is a large flexible space structure. As such, it suffers the same drawbacks as other large space structures. This has to do with the large size, the flexibility, and the way it is built and deployed. The size and flexibility prevent it from comprehensive ground measurement and test, which implies that preflight knowledge of the spacecraft dynamics will be imprecise. Inflight system identification will enhance our knowledge on flight dynamics but it cannot totally eliminate the model parameter uncertainties. Structural flexibility means infinite dimensional dynamics. Model truncation is inevitable. With current technology, only a relatively small number of states can be handled in control design and state estimation. Previous studies, for instance, control of large space antennas, have concluded that destabilization can occur when the parameters of a design model deviate from those of the actual plant by a significant amount [8]. In addition to parameter uncertainties and unmodeled dynamics, there are other problems, including time varying elements of the system. Shuttle docking can cause an instantaneous change of mass of more than 100% accompanied by a high intensity shock load. Station assembly, launching and retrieving of satellites, etc., will all contribute to disturbance and model parameter variations. A viable control system must be capable of coping with these time varying conditions, and living with dynamic uncertainties.

Robust adaptive control system provides a potential solution for this problem. Since the late 1970's, much progress has been made in adaptive control theory, some representative works are described in Refs. 9-15. However, there are still many formidable problems that require intense research efforts. One of the problems which is most pertinent to large space structures is the unmodeled dynamics. As pointed out in Ref. 16, all of the algorithms tested in that work have failed to maintain stability at the presence of unmodeled dynamics. More recently, robustness has been a major concern. Improvement in stability has been made for some special situations [17-20]. Theoretically, flexible space structures are ideal for adaptive control applications. However, due to the difficulties caused by model parameter uncertainties and model truncations, some progress has only been made more recently [19,21,22].

The purpose of this work is to develop and evaluate generic adaptive control techniques for space stations. The emphasis here is to treat both rigid body modes and flexible body dynamics, poorly known and truncated plant, and time varying effects.

A. Problem Formulation

Let x_p be the N_p-dimensional plant states, u_p and y_p are the M-dimensional plant inputs and outputs, respectively. Let A_p, B_p, and C_p be the state, control influence, and measurement distribution matrices of appropriate dimensions. The controlled station can be represented by the following state space model,

$$\dot{x}_p = A_p x_p + B_p u_p \qquad (V.1)$$

$$y_p = C_p x_p \qquad (V.2)$$

Consider model reference adaptive control. Let x_m be the N_m-dimensional model states, and u_m, y_m, A_m, B_m, and C_m are similarly defined. The reference model is,

$$\dot{x}_m = A_m x_m + B_m u_m \tag{V.3}$$

$$y_m = C_m x_m \tag{V.4}$$

Assume that the system (A_p, B_p, C_p) is controllable and observable, and the reference system (A_m, B_m, C_m) is asymptotically stable. For large flexible space systems, it is necessary to assume that

$$N_p \gg N_m \tag{V.5}$$

Define the output error, e_y, as

$$e_y = y_m - y_p \tag{V.6}$$

The design objective is, without complete knowledge of the plant, to design an adaptive mechanism so that an adaptive control input is obtained such that

$$\lim_{t \to \infty} e_y = 0. \tag{V.7}$$

B. Control Architecture

Referring to Fig. 7, the most rigid location on the station is its core on which inertial sensors, accelerometers and actuators are located. CMG's (Control Moment Gyro) are assumed and are effective only for antisymmetric modes; their controllability for the symmetric modes are essentially zero. To gain controllability and to compensate for vibrations of the large flexible panel structure, reaction wheels at the tips of the panels are postulated. Accelerometers and vibration sensors for relative attitude and rate measurement are also placed at the panel tips. Although the panel tips are far from ideal for locating hardware components, the choice is nil. For translational control, force actuators are required at the bus.

With the above control architectural design, the control input and output vectors are defined as follows:

$$
u_p = \begin{bmatrix} u_{p1} \\ u_{p2} \\ u_{p3} \\ u_{p4} \end{bmatrix} = \begin{bmatrix} \text{wheel torque at left panel tip} \\ \text{force at central bus} \\ \text{wheel torque at central bus} \\ \text{wheel torque at right panel tip} \end{bmatrix} \tag{V.8}
$$

128

and

$$y_p = \begin{bmatrix} y_{p1} \\ y_{p2} \\ y_{p3} \\ y_{p4} \end{bmatrix} = \begin{bmatrix} \alpha\Theta_{p1} + \dot{\Theta}_{p1} \\ \alpha Z_{p2} + \dot{Z}_{p2} \\ \alpha\Theta_{p2} + \dot{\Theta}_{p2} \\ \alpha\Theta_{p3} + \dot{\Theta}_{p3} \end{bmatrix} \qquad (V.9)$$

consider the dynamic model for the two-panel configuration. Let η_p be the modal amplitude vector, the plant state vector x_p is defined as,

$$x_p = \begin{bmatrix} \eta_p \\ -- \\ \dot{\eta}_p \end{bmatrix} \qquad (V.10)$$

The corresponding A_p, B_p, and C_p matrices are,

$$A_p = \left[\begin{array}{cc|cc} \multicolumn{2}{c|}{0_{6x6}} & \multicolumn{2}{c}{I_{6x6}} \\ \hline -\omega_{p1}^2 & 0 & -2\zeta_{p1}\omega_{p1} & 0 \\ & \ddots & & \ddots \\ 0 & -\omega_{p6}^2 & 0 & -2\zeta_{p6}\omega_{p6} \end{array} \right] \qquad (V.11)$$

$$B_p = \begin{bmatrix} 0 \\ --- \\ \Phi_p^T B \end{bmatrix} \qquad (V.12)$$

$$C_p = \left[\begin{array}{c|c} \alpha C\Phi_p & C\Phi_p \end{array} \right] \qquad (V.13)$$

where $C^T = B$, and

$$B = \begin{bmatrix} 0 & 0 & 0 & 0 \\ 1 & 0 & 0 & 0 \\ 0 & 1 & 0 & 0 \\ 0 & 0 & 1 & 0 \\ 0 & 0 & 0 & 0 \\ 0 & 0 & 0 & 1 \end{bmatrix} \qquad (V.14)$$

In (V.12 & V.13), Φ_p is the mode shape matrix for the plant. ω_{pk} and ζ_{pk}, in (V.11), are the modal frequency and damping ratio, respectively.

C. Adaptive Algorithm

The adaptive algorithm that is focused at this time is an extension of that developed in Refs. 21-23, in which the problems of large flexible space structures are addressed directly. Following the work of Sobel et al. [23], the plant control input vector $u_p(t)$ is a linear combination of the output errors e_y, reference model states x_m, and reference model input commands u_m,

$$u_p(t) = K_e(t)e_y(t) + K_x(t)x_m(t) + K_u(t)u_m(t) = K(t)r(t) \qquad (V.15)$$

where

$$r = \begin{bmatrix} e_y \\ x_m \\ u_m \end{bmatrix} \quad \text{and} \quad K(t) = \begin{bmatrix} K_e(t) & K_x(t) & K_u(t) \end{bmatrix} \qquad (V.16)$$

the gain $K(t)$ is a combination of proportional gain, $K_p(t)$, and integral gain, $K_I(t)$,

$$K(t) = K_p(t) + K_I(t) \qquad (V.17)$$

where K_p and K_I are, in part, proportional to the quadratic output errors, i.e.,

$$K_p(t) = e_y(t)r^T(t) \ \overline{T} \qquad (V.18)$$

$$\dot{K}_I(t) = e_y(t)r^T(t) \ T \qquad (V.19)$$

where T and $\overline{T}$ are gain weighting matrices to be chosen by the designer.

Let P be a $N_p \times N_p$ symmetric positive definite matrix, $\tilde{K}$ an unspecified $M \times (2M + N_m)$ constant gain matrix, and S a $M \times M$ nonsingular matrix. By choosing a Lyapunov function as follows,

$$V(e_x, K_I) = e_x^T(t)Pe_x(t) + tr [S(K_I - \tilde{K}) \ T^{-1} \ (K_I - \tilde{K})^T S^T] \qquad (V.20)$$

where

$$e_x(t) = x_p^*(t) - x_p(t) \qquad (V.21)$$

130

and $x_p^*(t)$ is an ideal trajectory, then it is found that [23] the system is asymptotically stable if T is positive definite, $\overline{T}$ is positive semidefinite, $PB_p = C_p^T(S^TS)$ and P is chosen such that there exists a $\tilde{K}_e$ such that $P(A_p-B_p\tilde{K}_eC_p) + (A_p-B_p\tilde{K}_eC_p)^TP$ is negative definite. A weaker condition corresponding to requiring that the input-output transfer function $C_p(sI-A_p+B_p\tilde{K}_eC_p)^{-1}B_p$ be positive real for the existence of a gain matrix $\tilde{K}_e$ is also possible by selecting $\overline{T}$ to satisfy a certain condition [22].

One of the simplest structures is a flexible beam. In Ref. 22, this adaptive algorithm was specialized to the case of a simply supported beam. With the measurement type similar to (V.9), it has been shown that if $\alpha < (min(\lambda_k))^{1/2} = \omega_{min}$ and $\alpha \leq min \ (\zeta\omega_{min}, \ \omega_{min}/\zeta)$, then the output error, e_y, vanishes asymptotically. However, for a beam with more general boundary conditions, such as a free-free beam or a space structure, these conditions can no longer be realized since these structures have zero frequency rigid body modes.

Zero frequency rigid body modes are unstable modes. Our simulation results show that this adaptive algorithm has failed to yield stable states or outputs.

D. Adaptive Controller with Plant Augmentation

To solve this unstable rigid body mode problem, a method termed plant augmentation is proposed here. The plant augmentation is accomplished by introducing an inner control loop to the plant.

Consider the equation of motion, before the damping term is added,

$$M\ddot{Z}_p + KZ_p = Bu_p - K_{IL}Z_p \tag{V.22}$$

Where K_{IL} is the inner loop control gain matrix. By rewriting (V.22) as follows,

$$M\ddot{Z}_p + (K + K_{IL})\ Z_p = Bu_p \tag{V.23}$$

one can see that the modal characteristics of the plant have been altered due to K_{IL} By choosing the values and structure of K_{IL}, the rigid body modes will no longer have zero frequencies. As a result of this plant characteristic change, a stable adaptive control system can be realized. It is important to note that to design such an inner loop, one does not require accurate knowledge of the plant This is because the inner loop controller can be made very robust by choosing the loop only at the location where the controllability is the highest for the rigid body modes. Furthermore, the exact values of the augmented rigid mode frequencies are not important; what is important is that they are different from zero. Looking from another point of view, the stability of the adaptive system has been improved by the highly robust inner control loop. Fig. 15 shows a block diagram of the system.

Consider again the two-panel station, the location at which the rigid modes are affected is the central bus. K_{IL} is selected as,

$$K_{IL} = \text{diag} (0,0,K_{z2}, K_{\Theta2}, 0,0) \qquad (V.24)$$

the natural frequencies for the rigid modes can be estimated as follows,

$$\omega_{z2} \cong (K_{z2}/M_2)^{1/2} \qquad (V.25)$$

$$\omega_{\Theta2} \cong (K_{\Theta2}/I_2)^{1/2} \qquad (V.26)$$

Knowing the values of M_2 and I_2, the selection of ω_{z2} and $\omega_{\Theta2}$ will determine the values of K_{z2} and $K_{\Theta2}$.
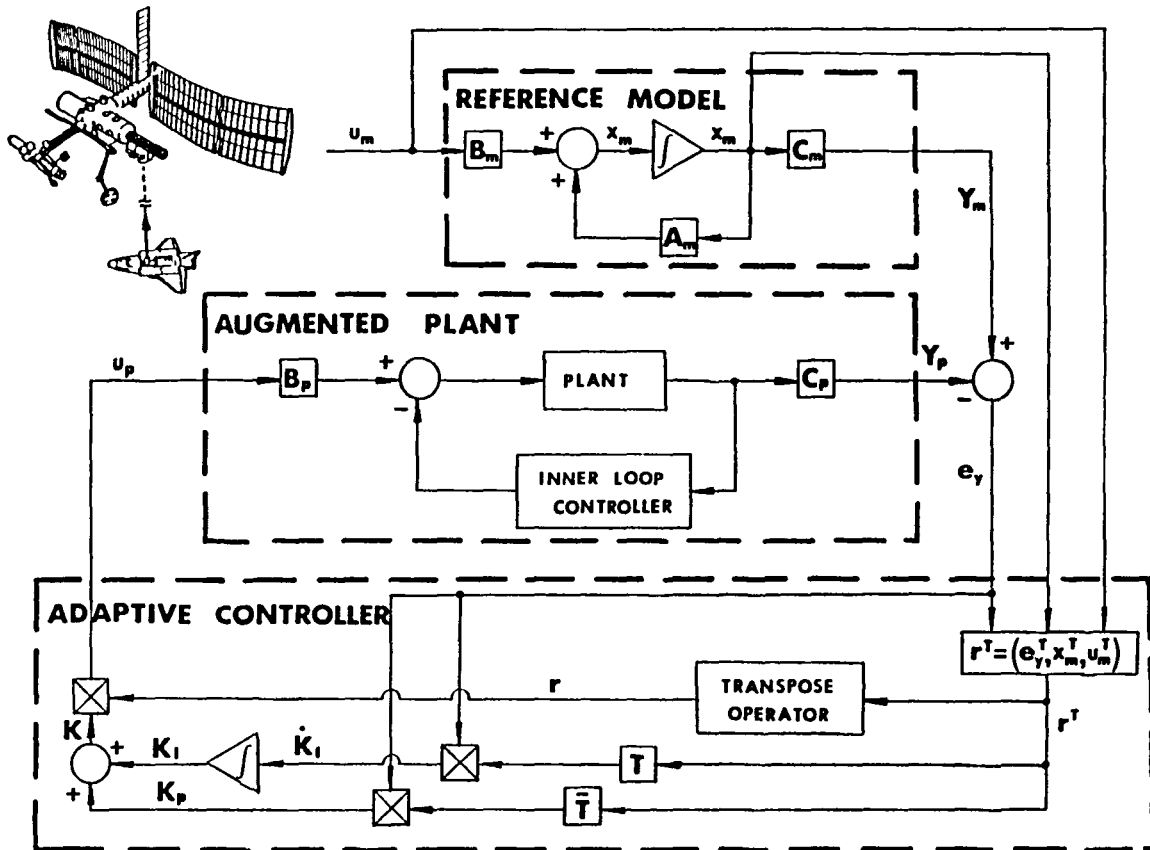
Fig. 15 Space station adaptive control system block diagram

E. Simulation Results

Consider the plant for the two-panel station. The model has 12 states X_p, 4 control actuators u_p and 4 measured outputs y_p as defined in (V.10), (V.8), and (V.9), respectively. The corresponding system matrices A_p, B_p, and C_p are specified by

132

(V.11) to (V.14). Plant augmentation has caused changes of modal frequencies from those shown in Fig. 8 to: $f_{p1} = 0.01163$, $f_{p2} = 0.039$, $f_{p3} = 0.0656$, $f_{p4} = 0.1684$, $f_{p5} = 0.3892$, and $f_{p6} = 0.3947$, all in Hz. The modal dampings are assumed to be .5% for all modes. The mode shape matrix Φ_p is,

$$
\Phi_p = \begin{bmatrix}
-.921E-1 & .128 & -.922E-1 & .144E-1 & .178 & .178 \\
.382E-3 & -.704E-3 & .705E-3 & -.264E-3 & -.544E-2 & -.549E-2 \\
.382E-9 & .177E-3 & .641E-8 & -.158E-1 & .185E-2 & .226E-5 \\
.332E-3 & -.745E-8 & -.465E-3 & -.959E-9 & .135E-6 & -.117E-3 \\
.921E-1 & .128 & .922E-1 & .144E-1 & .178 & -.177 \\
.382E-3 & .704E-3 & .705E-3 & .264E-3 & .546E-2 & -.548E-2
\end{bmatrix} \quad \text{(V.27)}
$$

To evaluate the performance of the controller, the reference model is selected to have lower order, significantly different model parameter, and high damping. The model consists of 4 modes or 8 states, 4 inputs u_m, and 4 outputs y_m with the system matrices defined as follows,

$$
A_m = \left[
\begin{array}{c:c}
0_{4x4} & I_{4x4} \\
\hdashline
\begin{matrix} -\omega^2_{m1} & & \\ & \ddots & \\ & & -\omega^2_{m4} \end{matrix} & \begin{matrix} -2\zeta_{m1}\omega_{m1} & & \\ & \ddots & \\ & & -2\zeta_{m4}\omega_{m4} \end{matrix}
\end{array}
\right] \quad \text{(V.28)}
$$

$$
B_m = \begin{bmatrix} 0 \\ \hdashline \Phi_m^T B \end{bmatrix} \quad \text{(V.29)}
$$

$$
C_m = \left[\alpha C\Phi_m \; \vdots \; C\Phi_m \right] \quad \text{(V.30)}
$$

where B and C are shown in Section V.B. The natural frequencies are: $f_{m1} = 0.02$, $f_{m2} = 0.03$, $f_{m3} = 0.04$, $f_{m4} = 0.06$Hz. The modal damping $\zeta_{mk} = 0.707$ for all modes. The position to rate measurement weighting factor $\alpha = 0.2$ and the gain weighting matrices $T = \overline{T} = \text{diag}$ $(2.5x10^9, 2.5x10^9, 2.5x10^{11}, 2.5x10^9, 1000, 1000, 1000, 1000, 1000, 1000, 1000, 1000, 400, 400, 400, 400)$ are used.

133

E.1 Adaptive Regulator Control with Initial Transient

The purpose of this simulation is to evaluate the convergence property of the adaptive controller for attitude hold and vibration suppression under very large initial transient conditions. The initial conditions for the plant are:

$$
\begin{array}{ll}
Z_{p1} = -3.699 \text{ ft} & \dot{Z}_{p1} = -0.877 \text{ ft/sec} \\[1.5em]
\theta_{p1} = 0.860 \text{ deg} & \dot{\theta}_{p1} = 0.336 \text{ deg/sec} \\[1.5em]
Z_{p2} = 0.345 \text{ ft} & \dot{Z}_{p2} = 0.035 \text{ ft/sec} \\[1.5em]
\theta_{p2} = 0.937 \text{ deg} & \dot{\theta}_{p2} = 0.037 \text{ deg/sec} \\[1.5em]
Z_{p3} = 4.071 \text{ ft} & \dot{Z}_{p3} = 1.045 \text{ ft/sec} \\[1.5em]
\theta_{p3} = 0.723 \text{ deg} & \dot{\theta}_{p3} = 0.387 \text{ deg/sec}
\end{array}
\tag{V.31}
$$

The corresponding initial conditions in the modal coordinates are obtained through the following transformation,

$$
\begin{aligned}
\eta_p &= \Phi_p^{-1} Z_p \\[1em]
\dot{\eta}_p &= \Phi_p^{-1} \dot{Z}_p
\end{aligned}
\tag{V.32}
$$

The initial conditions for the reference model are,

$$
\begin{aligned}
\eta_{mi} &= 0.9 \, \eta_{pi} \\[1em]
\dot{\eta}_{mi} &= 0.9 \, \dot{\eta}_{pi}
\end{aligned}
\tag{V.33}
$$

for $i = 1, \ldots, 4$.

The initial states given in (V.31) were taken from shuttle hard docking simulation. These data correspond to the space station response at 10 seconds after docking contact was made.

The simulation results for the plant and model physical states are shown in Fig. 16. These results show that the plant follows the model closely despite the truncation and parameter errors. The results also indicate that the system converges within 100 seconds from the transient start.

(a) Plant and model translational state responses
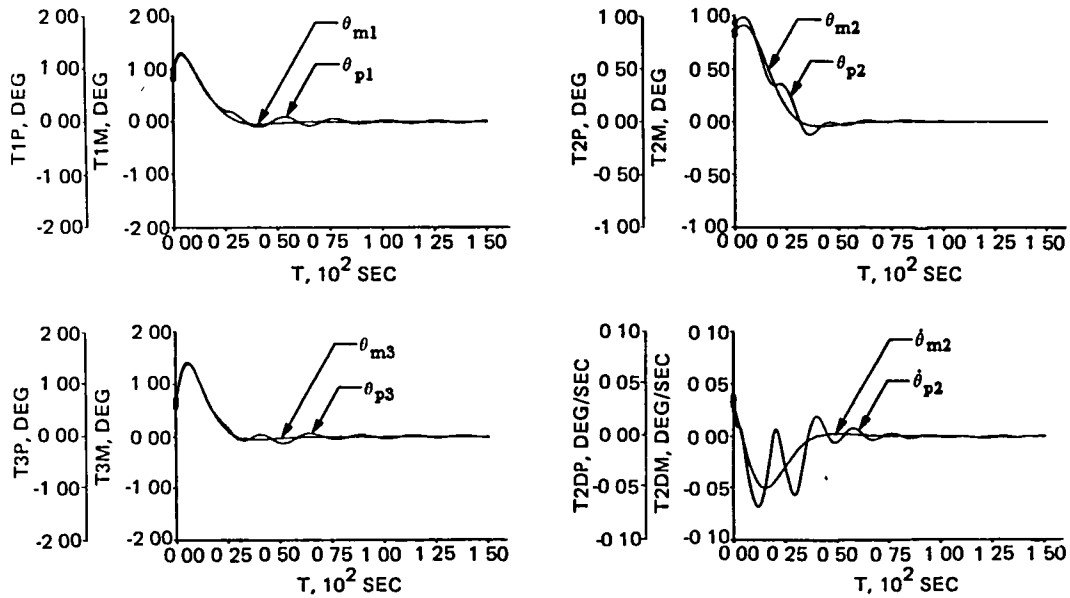
(b) Plant and model rotational state responses
Fig. 16 Adaptive regulator control simulation with initial transient

135

E.2 Adaptive Control During Shuttle Docking

Perhaps the most stressful test to a controller is a dynamically significant event which happens without warning. This may include major component failures, vehicle collisions, etc. Accompanying these events, there may be high dynamic disturbances, configuration and mass property changes. Control system stability under these conditions is critically important to continued operation and safety of the station.

This simulation is designed to test the controller performance and stability under these conditions using shuttle hard docking dynamics. Shuttle hard docking will cause instant mass property change of more than 100%, and disturbance high enough to cause solar panels to buckle. To simulate the unexpected nature of the problem, no model switching and model disturbance input were employed.

The dynamic responses for the plant physical variables under the same adaptive controller of V.E.1 are shown in Fig. 17. Of course, the model states in this case are the null states. The results show that the plant states converge to the model states well within 100 seconds.
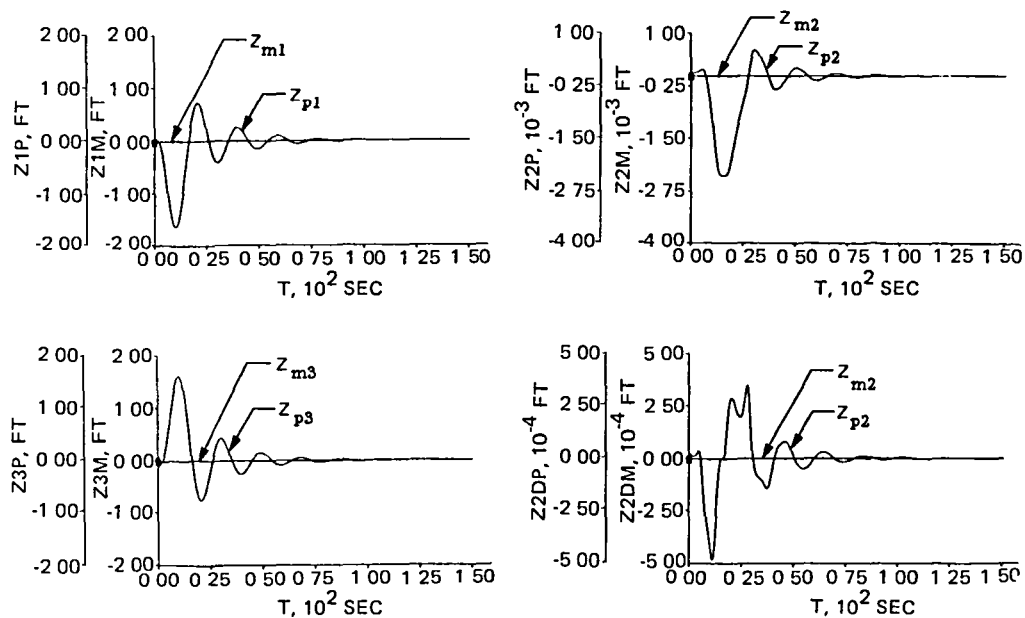
• PLANT OUTPUTS CONVERGE TO THE ZERO STATE WELL WITHIN 100 SECONDS IN THE PRESENCE OF TRUNCATION, PARAMETER ERRORS, AND INSTANTANEOUS CHANGE OF MASS AND INERTIA BY MORE THAN 100%

(a) Plant and model translational state responses

136
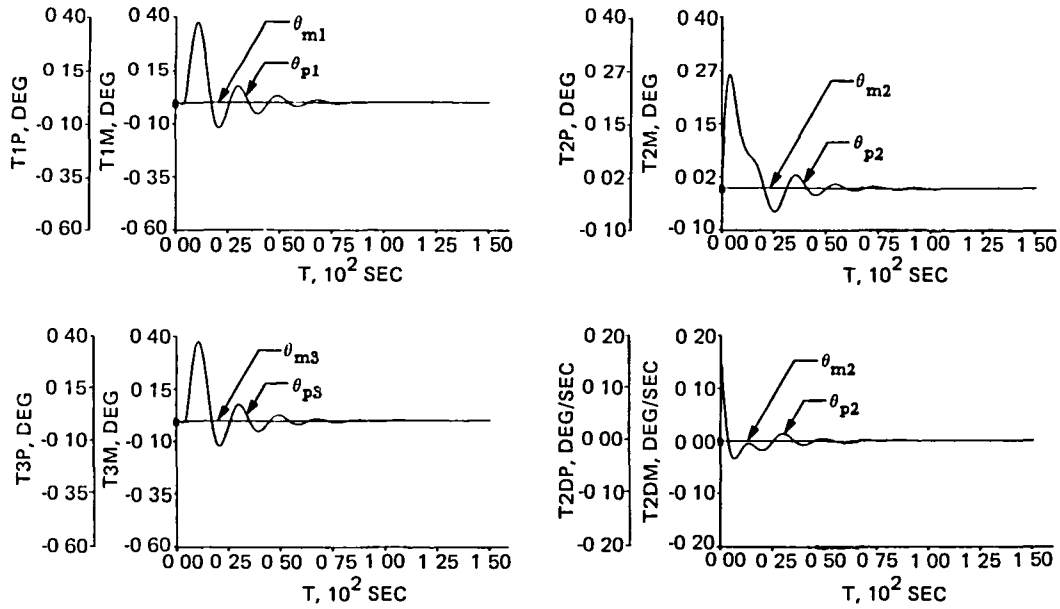
(b) Plant and model rotational state responses

Fig. 17 Adaptive control simulation during shuttle docking

F. Discussion

The generic adaptive control conditions evaluated here reflect key operational properties of an initial space station. However, there are many practical issues that require further investigation. These problems include external plant disturbances, measurement noise, nonlinear effects including actuator saturation or gain limiting, and effects of time delays in the control system. Also of particular interest are methods of improving controller robustness, effects of model switching, parameter update, and model excitation.

VI. CONCLUSIONS

1. Hard docking disturbances can cause solar panels to buckle

2. Acceptable performance can be obtained with soft docking designs provided that shuttle residual rates do not exceed the best achievable values (ΔV = 0.05 ft/sec, $\Delta\omega$ = 0.20 deg/sec).

3. Soft docking with the expected shuttle approach rate (ΔV = 0.50 ft/sec, $\Delta\omega$ = 1.0 deg/sec) may threaten safety due to excessive shuttle and space station attitude excursion.

4. Berthing may not be the solution, the real issue is finding the means to take out shuttle momentum.

137

5. Fast convergent rate has been observed with the adaptive control system in the presence of truncated and poorly known dynamics and instant change of system mass property of more than 100%.

6. The proposed inner-loop plant augmentation method as part of the adaptive system has improved the system convergence significantly and stabilized the rigid body modes.

7. The study results show promising potential applications of adaptive control to space stations.

VII. REFERENCES

1. Olstad, W. B., et al, A series of eleven articles on Space Station Technologies, Astronautics and Aeronautics, March 1983, pp. 28-68.

2. "Workshop Briefing, Study Task No. 9--Berthing", NASA Space Station Task Force Concept Development Group, Dec. 5-9, 1983.

3. Craig, Mark, "Workshop Briefing, Study Task No. 11--Configuration and Controllability Status," Dec. 16, 1983.

4. Hamidi, M. and S. J. Wang, "Parameter Models for Space Stations," Paper presented at the Workshop on Identification and Control of Flexible Space Structures, June 4-6, 1984, San Diego, CA.

5 Clough, R. W. and J. Penzien, Dynamics of Structures, McGraw-Hill, New York, N.Y., 1975.

6. Juang, J. N. and S. J. Wang, "An Investigation of Quasi-Inertial Attitude Control for a Solar Power Satellite," Space Solar Power Review, Vol. 3, pp. 337-352, 1982.

7. Garba, J. A., D. A. Kudija, B. Zeldin, and E. N. Costogue, "Parametric Study of Two Planar High Power Flexible Solar Array Concepts," JPL Publication 78-95, Dec. 15, 1978.

8. Wang, S. J. and J. M. Cameron, "Dynamics and Control of a Large Space Antenna," Journal of Guidance, Control, and Dynamics, Vol. 7, No. 1, Jan.-Feb. 1984, pp. 69-76.

9. Monopoli, R. V., "Model reference adaptive control with an augmented error signal,"IEEE Trans. on Automatic Control, Vol. AC-19, Oct. 1974, pp. 474-485.

10. Goodwin, G. C., P. J. Ramadge and P. E. Caines, "Discrete time multivariable adaptive control", IEEE Trans. on Automatic Control, Vol. AC-25, No. 3, June 1980, pp. 449-456.

11. Narendra, K. S. and L. S. Valavani, "Direct and indirect adaptive control," Automatica, Vol. 15, No. 6, Nov. 1979, pp. 653-664.

12. Morse, A. S., "Global stability of parameter adaptive control systems," IEEE Trans. on Automatic Control, Vol. AC-25, No. 3, June 1980, pp. 433-439.

13. Landau, I. D. and H. M. Silveira, "A Stability Theorem with Applications to Adaptive Control," IEEE Trans. on Automatic Control, Vol. AC-24, April 1979, pp. 305-312.

14. Narendra, K. S., Y. H. Lin, and L. S. Valavani, "Stable adaptive controller design -- Part II: proof of stability," IEEE Trans. on Automatic Control, Vol. AC-25, No. 3, June 1980, pp. 440-448.

15. Landau, I.D., "Adaptive Control - Actual Status and Trends," Paper presented at Workshop on Identification and Control of Flexible Space Structures, June 4-6, 1984, San Diego, CA.

16. Rohrs, C. E., L. Valavani, M. Athans, and G. Stein, "Robustness of adaptive control algorithms in the presence of unmodeled dynamics," Proc. of 21st IEEE Conf. on Decision and Control, Dec. 1982, pp. 3-11.

17. Narendra, K. S. and A. M. Annaswamy, "Robust Adaptive Control," Paper presented at Workshop on Identification and Control of Flexible Space Structures, June 4-6, 1984, San Diego, CA.

18. Ioannou, P., "Robust Adaptive Control," Proc. of 1984 American Control Conference, June 6-8, San Diego, CA., pp. 1574-1578.

19. Bar-Kana, I. and H. Kaufman, "Low-Order Model Reference Direct Multivariable Adaptive Control," Proc. of 1984 American Control Conference, June 6-8, San Diego, CA., pp. 1259-1264.

20. Rohr, C. E. and K. Shortelle, "Conditioning a Plant for Frequency Selective Adaptive Control with Improved Robustness," Proc. of 1984 American Control Conference, June 6-8, San Diego, CA., pp. 1579-1583.

21. Balas, M. J., H. Kaufman, and J. Wen, "Stable Direct Adaptive Control of Linear Infinite-Dimensional Systems Using a Command Generator Tracker Approach," Paper presented at Workshop on Identification and Control of Flexible Space Structures, June 4-6, 1984, San Diego, CA.

22. Bar-Kana, I. H. Kaufman, and M. Balas, "Model Reference Adaptive Control of Large Structural Systems," Journal of Guidance, Control, and Dynamics, Vol. 6, No. 2, March-April, 1983, pp. 112-118.

23. Sobel, K., H. Kaufman, and L. Mabius, "Implicit Adaptive Control Systems for a class of Multi-Input, Multi-Output Systems," IEEE Trans. on Aerospace and Electronics Systems, Vol. AES-18, No. 5, Sept. 1982, pp. 576-590.

DYNAMIC PERFORMANCE OF SEVERAL
LARGE ANTENNA CONCEPTS

G. C. Andersen and **L. B. Garrett**
NASA Langley Research Center
Hampton, VA 23665

R. E. Calleson
Kentron International
Hampton, VA 23665

ABSTRACT

Four antenna concepts--the box truss, tetrahedral truss, wrap-radial rib, and hoop and column antenna are examined for their dynamic performance when subjected to an operational environment. Space applications for the concepts are numerous; however, the Land Mobile Satellite System (LMSS) was chosen as a baseline study and its operational constraints are applied to each concept (i.e. surface accuracy requirements, slew rates, settling time, etc.) The dynamic response of each concept is examined in terms of structural displacement and structural damping effects. From the dynamic responses, the necessity of a control system for vibrational displacement reduction is examined along with a comparison of the relative merits of each antenna concept.

I. INTRODUCTION

Large space structures have one common characteristic--flexibility. This single characteristic has initiated many man-hours of study and research into the effects on mission performance and the controllability of these effects. Currently, these large flexible space structures consist primarily of antennas ranging from tens to hundreds of meters in diameter, with a wide variety of space applications. Consequently, the behavior of these structures, when subjected to external forces such as those required for attitude control, often significantly impacts the ability to achieve the mission objectives.

For comparison of the various antenna concepts, the Land Mobile Satellite System (LMSS) mission has been examined for baseline technical requirements. The structural concepts analyzed have numerous additional applications such as microwave radiometer antennas and Earth observation platforms. A LMSS is capable of providing mobile communications for commercial and government applications in the continental United States and Canada as an augmentation to existing and planned land mobile terrestrial systems. The satellite system would provide "narrow band" telecommunications services such as mobile radio, telephone, dispatch, safety, and special radio services[1] and thin-route fixed telephone and data services in the 806 to 890 MHz band.

Four different large antenna structural concepts are examined. The first three antenna concepts (55 meters in diameter) include two lattice truss-structures, the box-truss and tetrahedral-truss antenna, and a cantilever-beam structure, the wrap-radial rib antenna. All are parabolic offset-fed systems with a focal length of 82.5 meters (focal length/diameter (f/d) = 1.5). The remaining antenna concept (122 meters in diameter) is a tension-stabilized hoop and column structure which forms a center-fed, quad-aperture system with an effective aperture of 55 meters and an effective f/d of 1.5. Finite-element models of these structural concepts are shown in Figure 1.

The antennas are subjected to external forces which could be experienced in an operational environment; in this case, the dynamic responses of the individual antenna structural configurations are examined to quantify structural errors such as decenter, defocus, RMS surface roughness, and angular rocking. Performance comparisons of the individual concepts and their ability to meet LMSS mission requirements are assessed. From these comparisons, the necessity for and extent of active control is determined. In the examination of the effects from various external forces, a range of material damping ratios from 0.2 percent to 2.0 percent is used parametrically to simulate the variability in manufacturing of the structural members.

II. STRUCTURAL CONCEPTS

The antenna concepts all vary in the type and number of secondary subsystems attached to each system. These subsystems include components such as telemetry packages, control jets, reaction wheels, and other components necessary to complete an autonomous spacecraft. To determine the dynamic characteristics of the basic individual antennas, the subsystems which would tend to mask the dynamic characteristics were removed from each concept. However, the mass of the communications feed and solar arrays, located at the end of the feed mast of each antenna, were included in the analysis to provide a better representation of an antenna structure. The same mass (1500 kg) was assigned to each concept. This resulted in structural and mass models that are directly comparable from concept to concept.

Summary data for each structural concept are shown in Figure 2. The structural mass includes the structural members, joints, and reflective mesh. The total spacecraft mass is the structural mass in addition to the 1500 kg added mass. The design and sizing of the structural members of the various concepts for sufficient static-load-carrying capabilities, from such sources as gravity gradient, aerodynamic drag, and thermal-induced loads, were analyzed previously for the LMSS.[2] For the tetrahedral truss concept, the graphite/epoxy dish members were designed with a bending stiffness of 6500 N-m^2, while the mast, also comprised of graphite/epoxy members, was designed with a bending stiffness of 3.9×10^7 N-m^2. The feed mast for the radial rib antenna was designed with a bending stiffness of 3.6×10^7 N-m^2. Each of the 24 ribs of the radial rib antenna was designed with an approximate bending

stiffness of 2.2×10^5 N-m^2, based on the varying cross-section. However, the thin-ply cantilever rib will not support its own weight under a one-g bending load due to its low bending strength.

The mast of the hoop column was designed with a large bending stiffness of 7.5×10^7 N-m^2, while the hoop itself will support a 1.5×10^6 N load which results in a bending stiffness of 5.5×10^4 N-m^2. The tension members were sized to a 1.25 ratio of maximum allowable member stress to maximum experienced tensile stresses. The horizontal folding members of the box truss were designed to a bending stiffness of 8200 N-m^2 which would support a 1000 N compressive load. The vertical members are square-finned tubes and were sized using data from a previous study.[3] The box truss dish mast used the identical graphite/epoxy structural members as those of the dish.

III. DYNAMIC ANALYSIS METHODOLOGY

Modal Analysis

The dynamic response synthesis and analysis are performed utilizing the Interactive Design and Evaluation of Advanced Spacecraft (IDEAS) system.[4] This system allows the user to create a finite-element model and perform numerous types of analyses, including modal analyses, with the use of the finite-element Structural Analysis Program (SAP), and dynamic response analyses. Another analysis program, Engineering Analysis Language (EAL), was also used for confirmation of the results.[5] The intent of this is to obtain independent confirmation of the modal analysis and subsequent dynamic response results using more than one program. The modal analysis utilizes the eigenvalue/eigenvector determination technique for the extraction of the modal frequencies and mode shapes. This method calculates the eigenvalues and eigenvectors of the undamped free vibration equation,

$$[M]\ddot{x} + [K]x = 0 \qquad (1)$$

and the resulting eigenvalue/eigenvector equation,

$$[K][\emptyset] = Wn^2 [M][\emptyset] \qquad (2)$$

where [K] and [M] are the global stiffness and mass matrices, respectively, associated with the finite-element model. Wn^2 and [$\emptyset$] are the eigenvalues and eigenvectors (or modal frequencies and mode shapes), respectively, associated with the free vibration of the model. These values were determined using a subspace iterative technique.

Each structural concept was subjected to this type of modal analysis to determine the first four modal frequencies and corresponding mode shapes. The results of the modal analysis are shown in Figures 3-7. Both the SAP and EAL modal analysis of the radial rib antenna are shown (Figs. 5 and 6) to demonstrate the modal analysis capabilities, including accuracy, of the

simpler SAP model. The results illustrate the flexible nature of all the various large antenna concepts. However, one antenna concept, the box truss antenna, produced significantly higher modal frequencies than the three remaining concepts. This is due to the relatively stiff nature of the mast and reflecting dish. The three other configurations all had a lowest natural frequency on the order of 0.1 to 0.35 Hz, while the box truss was an order-of-magnitude higher. These low frequencies, which result from low structural stiffness, will result in higher vibrational amplitudes.

The major spacecraft substructures contributing to the low frequencies can be determined from the mode shapes for the various frequencies. (The mode shapes shown are magnified to better illustrate their relative shapes.) For the hoop and column, radial rib, and tetrahedral truss antennas, the first modes are due to the flexible nature of the communications feed mast. The dish movement contributes only to the higher natural frequencies. It is apparent that the lower frequencies of the particular structure will dominate the dynamic response analysis; therefore, the need and possible control of these lower modes must be examined.

Application Of External Force And Structural Damping

The dynamic response of the various models depend entirely on the results of the modal analysis, the internal damping, and the external forces experienced by the structural concepts. The latter two are incorporated in the analysis through the use of the following equations which defines the dynamic response of the structure:

$$[\ddot{q}] + 2\rho W n[\dot{q}] + W n^2 [q] = [\phi]^T [f] \tag{3}$$

$$[y] = [\phi][q] \tag{4}$$

The [q] and [y] matrices represent the generalized and true nodal displacements of the finite-element models at a particular instant in time. The external force and internal forces are represented by [f] and ρ, respectively. The external forces are applied at the desired nodal locations in the form of a forcing function dependent on the mission slew and slew rate requirements. The structural damping ratio, which varies with the natural frequency of the structure, currently can only be determined accurately through the use of experimentation. Therefore, a range of damping coefficients is examined. The solution of the above second-order differential equation in terms of the generalized deflection is performed using an iterative technique based on the modal displacement and the modal velocity.

Operational Force Requirements

The external dynamic forces experienced by the four antenna concepts are based upon slew and slew rates somewhat larger than the original mission requirements to demonstrate the dynamic merits or disadvantages of each

structural concept. Three conditions were examined: two slew rates, 0.1 deg/sec and 1.0 deg/sec, and a maximum nodal deflection condition, each with a 20-degree slew. Slewing is accomplished by thrusters located at the LMSS feed position to produce large moment arms and operate in a bang-coast-bang firing scheme. Two thrusting directions were examined, one parallel and one perpendicular to the plane of symmetry of the spacecraft (in the case of the hoop column antenna, only one thrust direction was chosen due to the symmetrical nature of the antenna). A firing sequence was chosen for each thrust direction to produce the maximum nodal deflections, thus establishing an upper limit on the possible magnitudes of the modal deflections for each antenna concept. The firing duration was chosen to be half of the natural period of the dominant mode corresponding to the direction of thrust. The coast duration was chosen to be an integer multiple of the natural period to produce an approximate 20-degree slew. The various spacecraft moments of inertial along with the various moment arms led to the differing firing sequences. In the case of the box truss antenna, the firing sequence to produce maximum nodal deflections was found to be identical to that used to obtain the 1.0-deg/sec slew. All of the firing sequences used to meet the slewing requirements are shown in Figure 8. A thruster force of 300 Newtons is needed for the higher slew rate and was used for the lower rate to provide a worst-case dynamic response. The dynamic response scales linearly with the thruster force.

The internal damping ratio applied parametrically to each antenna concept has a range of 0.2 percent to 2.0 percent and was chosen as representative of the current values for candidate materials. Due to the lack of other damping mechanisms present on Earth, such as air damping, only energy dissipation due to material damping is present. The variation of the damping ratios with the natural frequencies was not taken into account due to the lack of adequate experimental data on the subject. Therefore, the same damping ratio was used for all the natural frequencies; however, the range studied appears adequate to cover variations due to materials and natural frequencies.

IV. ANTENNA CONCEPTS DYNAMIC RESPONSES

Structural Accuracy Requirements

Each of the antenna concepts was subjected to forces that would be experienced during an operational mission. The dynamic response of the various structural concepts is examined in terms of antenna structural requirements to meet the operational mission needs. These structural requirements are based on the electromagnetic performance requirements of the mission; decenter, defocus, angular rocking, and RMS surface roughness (illustrated in Fig. 9). These mission criteria are then compared to the same parameters generated from the dynamic response analysis. Since the antenna concepts under examination have a wide variety of space applications, a specific mission, the Land Mobile Satellite System (LMSS), was chosen as a

baseline study to demonstrate the relative merits and disadvantages of each concept.

The LMSS satellite would be placed in geosynchronous orbit over the continental United States and would require a pointing accuracy of $\pm$0.1 degrees absolute with a peak directivity loss of no more than 0.1 dB. The pointing requirement is comprised of two components, angular rocking and decenter. Angular rocking refers to the rocking motion of the dish, while decenter is the lateral movement of the communications feed with respect to the center of the dish. The peak directivity loss requirement is a function of the operation wavelength (λ) (37.0 cm for the LMSS mission). The electromagnetic performance requirements of defocus and RMS surface roughness contribute to directivity losses. Defocus is the deviation in position of the dish relative to the feed along the focal line. RMS surface roughness is a measure of the surface deviation from the idealized parabolic shape. The structural accuracy tolerances for RMS surface roughness, defocus, decenter, and angular rocking, are on the order of λ/16 (2.3 cm), λ/2 (18.5 cm), 12.3 cm, and 6×10^{-4} radians, respectively.[6] Each of these quantities is determined using the dynamic loads program in IDEAS at various time points after the maneuver to obtain the spacecraft's dynamic configuration. At each particular time point, the nodal displacements of the dish and the feed are calculated. From the dish nodal displacements, a best-fit parabola is formed to represent the new dish shape, which in turn, is used for the calculation of the RMS surface accuracy, defocus, and angular rocking.

Dynamic Analysis Results

The maximum vibrational responses of the different antenna concepts, in terms of the structural accuracy tolerances, are listed in Figures 10-13 for the different firing sequences. The thrusters were fired in two different directions and only nodal deflections occurring after the firing sequence were examined. These dynamic responses are all based on a damping ratio of 0.2 percent, which would provide the worst possible dynamic response of each of the cases tested. The settling time shown is based upon the time required for the antenna structure to fall within that particular accuracy tolerance set forth for the LMSS mission. From the results of this analytical test, the relative merits and disadvantages of the individual concepts are readily apparent.

All of the antenna concepts were well within the RMS surface roughness requirement of 2.3 cm demonstrating the ability of the four concepts to retain a basic parabolic dish surface. In the case of the tetrahedral truss antenna (Fig. 10) the structure failed to meet two of the four accuracy requirements, decenter and angular rocking. The angular rocking surpassed the LMSS requirements in all but one test case, but the subsequent settling time is minimal. This is due to a contribution of only the higher modes to the dish rocking. However, decenter error far exceeds the requirements and the settling time is well beyond a reasonable limit. This large error is due to the first two modes of the structural concept, which basically deal with only

lateral translation of the dish and the feed. Thrust in the parallel direction excited the first mode which is a translational displacement in this direction. This resulted in the extreme values for decenter. The second mode, excited by the perpendicular thrust direction, dealt primarily with dish rotation about the focal line with only minor dish translation. This led to lower values for decenter error. The defocus error of the antenna was well within the requirements due to the primarily in-plane lateral movement of the antenna dish. The dynamic response of the antenna to the two firing sequences resulted in a smaller response for the 1.0 deg/sec slew than for the 0.1 deg/sec slew. This is due to the ratio of the longer thrust duration to natural period for the higher slew rate which, near the end of the firing sequence, produced a force in the direction opposite to the motion of the nodal vibration response. Therefore, the maximum possible nodal deflection (which corresponds to an intermediate slew rate between 0.1 deg/sec and 1.0 deg/sec) was determined to provide an upper limit. Examination of this upper limit revealed that the displacements far exceed acceptable values for angular rocking and decenter. However, it retained its accuracy in terms of defocus and RMS surface roughness.

The radial rib antenna (Fig. 11) exhibited very different response characteristics to those of the tetrahedral truss antenna. The results presented were determined using two different programs, IDEAS and EAL. Only results pertaining to pointing could be determined from EAL. These results are presented as a confirmation of those obtained from IDEAS. The EAL modal analysis resulted in a mast truss structure mode (mode 2) that did not appear in the SAP analysis due to the simple modeling of the mast as a singular beam element with similar properties. However, the absence of this mode in the IDEAS analysis did not have a major effect on the results. The EAL modes dealing with pure rib movement (modes 4-6) had lower frequencies due to the ability to better model the lenticular shape of the ribs. This is a possible explanation for the discrepancies in the results between IDEAS and EAL. In addition, the simple modeling of the dish-mast connection in the IDEAS finite-element model contributed to the discrepancies. From these results, the angular rocking and defocus tolerances were exceeded by the vibrational response of the radial rib antenna. The angular rocking of the dish far exceeded the LMSS requirements and the settling time is very large due to the slight structural damping. The large error due to perpendicular thrust is a result of the first vibrational mode of the antenna which is excited by this thrust direction. For thrust in the direction parallel to the plane of symmetry, the angular rocking is due to excitation of the second and third modes. The defocus error, which is based on the movement of the entire dish in a direction along its focal line, exceeds the accuracy tolerance only when the thrust is applied in this direction. This is due to excitation of the second mode which is the only mode of those examined which deals with the out-of-plane translation of the entire dish. The decenter error, which dominated the dynamic response of the tetrahedral truss, easily met the requirements. As in the case of the tetrahedral truss antenna, a larger dynamic response was obtained with the smaller slew rate. This again due to the ratio of the longer thrust duration to natural period for the 1.0 deg/sec slew. When this

antenna concept was subjected to a firing sequence that resulted in the maximum dynamic response, it was well outside reasonable limits for angular rocking in both thrust directions and defocus for the parallel thrust direction case. The decenter and RMS surface roughness requirements remained within the LMSS tolerance.

The dynamic response of the hoop column antenna (Fig. 12) met most of the mission requirements. (The results were obtained using EAL due to the inability to create a working SAP/IDEAS model.) Angular rocking, resulting from the first and third modes, was the only parameter to exceed the displacement requirements. The subsequent settling time for the 0.1 deg/sec slew was within reasonable limits. For the maximum response case, however, the angular rocking had a much larger settling time. The slew rate of 1.0 deg/sec produced smaller angular rocking which is, again, due to the long thrust duration and the chosen coast time. In the case of decenter, the antenna's mode shapes appear to produce a large error, however, the mode shape is only relative and the displacements are severely exaggerated. Consequently, the decenter error is sufficiently small to meet the accuracy requirements. In terms of defocus, the antenna performed adequately.

Of all four of the antenna concepts, the box truss (Fig. 13) is the only concept to remain well within all the structural accuracy tolerances when subjected to the operational environment and a firing scheme that would produce maximum nodal deflections. This is due to the relatively high modal frequencies inherent in this type of truss structure and the structural rigidity of the feed mast.

Concept Dynamic Response Comparisons

Each individual antenna concept has its own merits and disadvantages in terms of its dynamic performance when subjected to loads incurred during an operational mission. Figure 14 is a comparison of the four antenna concepts in terms of ability to meet the mission requirements. The rankings are based upon the results obtained with 0.2 percent damping which probably best represents the actual structural characteristics. The concepts are ranked according to how well each met the displacement accuracy requirements or the resulting settling time. Each accuracy requirement has equal importance in the evaluation of antenna performance and a comparison of antenna concepts in terms of differing requirements has not been attempted. The box truss antenna far exceeded the other concepts in terms of dynamic response and the ability to retain its predesigned shape and, therefore, must be taken into consideration for future space missions.

The next most successful antenna concept was the hoop-column antenna which failed to meet only one of the requirements, angular rocking. Due to the value of the lowest modal frequency and the relatively small angular rocking error, this antenna is an excellent candidate for vibrational control through increased structural damping.

The tetrahedral truss antenna follows in terms of dynamic performance and the ability to meet mission requirements. This concept failed to meet two requirements adequately, decenter and angular rocking. The extreme magnitudes of the decenter error negates the use of increased damping as a control measure. Use of this antenna concept would require either an active control system for structural accuracy control or a redesigning of the feed mast, which was the cause of the two lowest modal frequencies which resulted in the high response amplitudes.

For the radial rib antenna, which exhibited the worst response, the flexible mast supporting the feed contributed greatly to the low structural rigidity observed. This high flexibility must be actively controlled or a redesigning of the feed mast structure is required. A redesign of the mast structure would probably not result in a major difference due to the "L" shaped nature of the feed mast required for this antenna concept. The ribs also have a low modal frequency which cannot be effected greatly by rib redesign due to the rib length requirements and mass limitations.

Structural Damping Eeffects On Dynamic Results

An alternative to active control of vibrational response is through the use of increased structural damping. Structural damping (or internal damping) is the only passive mechanism available for internal energy dissipation which is responsible for the vibratory action of the structure. To examine the effects of structural damping on the maximum nodal deflections and the resulting settling time, damping ratios ranging from 0.2 percent and 2.0 percent were examined. Example results for the feed nodal deflection of each concept with damping ratios of 0.2 percent and 2.0 percent are shown in Figures 15 and 16. As would be expected, the maximum nodal deflections decreased with increased damping ratios as did the resulting settling time. The major effect of a structural damping increase is on the settling time, which closely obeyed the exponential decay law for a damped oscillatory system with the natural frequency being that of the lowest mode that was excited.

In terms of the structural accuracy tolerances, the errors of the individual concepts would all decrease with the increased damping ratio. An example of structural damping effects on the accuracy errors and the corresponding settling time, for the case of decenter error exhibited by the tetrahedral truss antenna, is shown in Figure 17. The results are representative of the responses of all the concepts to varying structural damping. The increase in damping had only minor effects on the deflections; however, a marked decrease in the settling times did occur. Therefore, manufacturing the concepts for increased structural damping could be effectively used in controlling structural accuracy in terms of settling time for the accuracy tolerances that were exceeded by a reasonable limit. In the case of large errors, an increase in structural damping to 2.0 percent will not satisfy the LMSS requirements and other methods for suppression of the dynamic response must be examined.

CONCLUSIONS

Large antenna conceptual designs were evaluated in terms of their dynamic response to applied forces representative of those encountered during mission operation. The LMSS mission was selected for the baseline technical requirements. The antenna's vibrational responses were evaluated for decenter, RMS surface roughness, defocus, and angular rocking error and then ranked accordingly. The effects of increased structural damping were examined as a possible means for vibration suppression and reducing settling time. The box truss antenna exhibited excellent response characteristics in meeting the LMSS mission requirements and far out performed the other three concepts. The three remaining concepts, the hoop-column, tetrahedral truss, and radial rib antenna, either require increased structural damping or active controls for vibrational response suppression.

REFERENCES

1. Golder, C. T.; Lackey, J. A.; and Spear, E.: "Configuration Development of the Land Mobile Satellite System (LMSS) Spacecraft," Large Space Systems Technology, 1981, Williams J. Boyer, compiler, NASA CP-2215, Part 2, 1982, pp. 717-760.

2. Garrett, L. B. and Ferebee, M. J.: "Comparative Analysis of Large Antenna Spacecraft Using the Ideas System," AIAA Paper No. 83-0798-CP, 1983.

3. Brook, A. L.; Coyer, J. V.; Gardner, W. J.; and Mihora, D. J.: "Conceptual Design and Analysis of a Large Antenna Utilizing Electroelastic Management," NASA CR-3522, February 1982.

4. Whetstone, W. D.: "EISI-EAL Engineering Analysis Language Reference Manual," Engineering Information Systems, Incorporated, July 1983.

5. Akle, Wade: "Requirements for a Mobile Communications Satellite System," CR-168105, TRW, Inc., Volume 3, Contract NAS3-23257, March 1983.
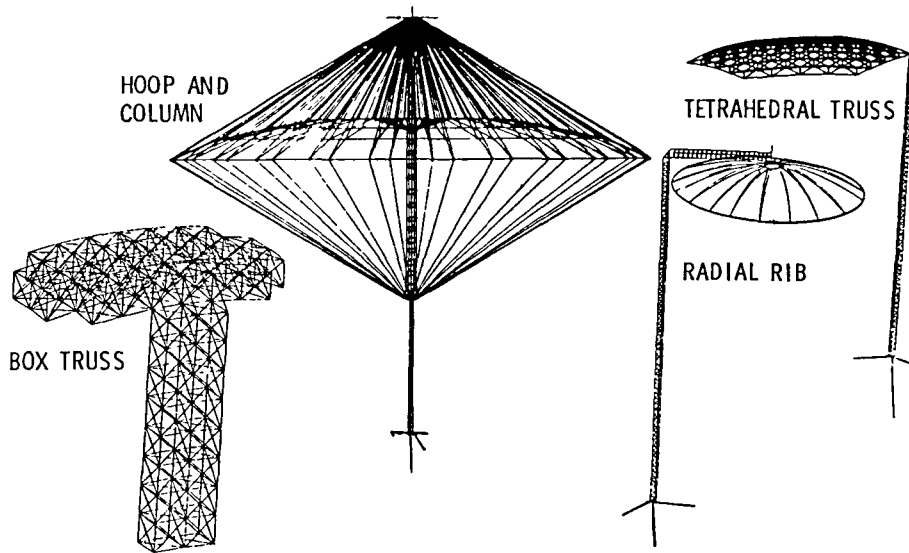
Figure 1. Antenna Structural Concepts
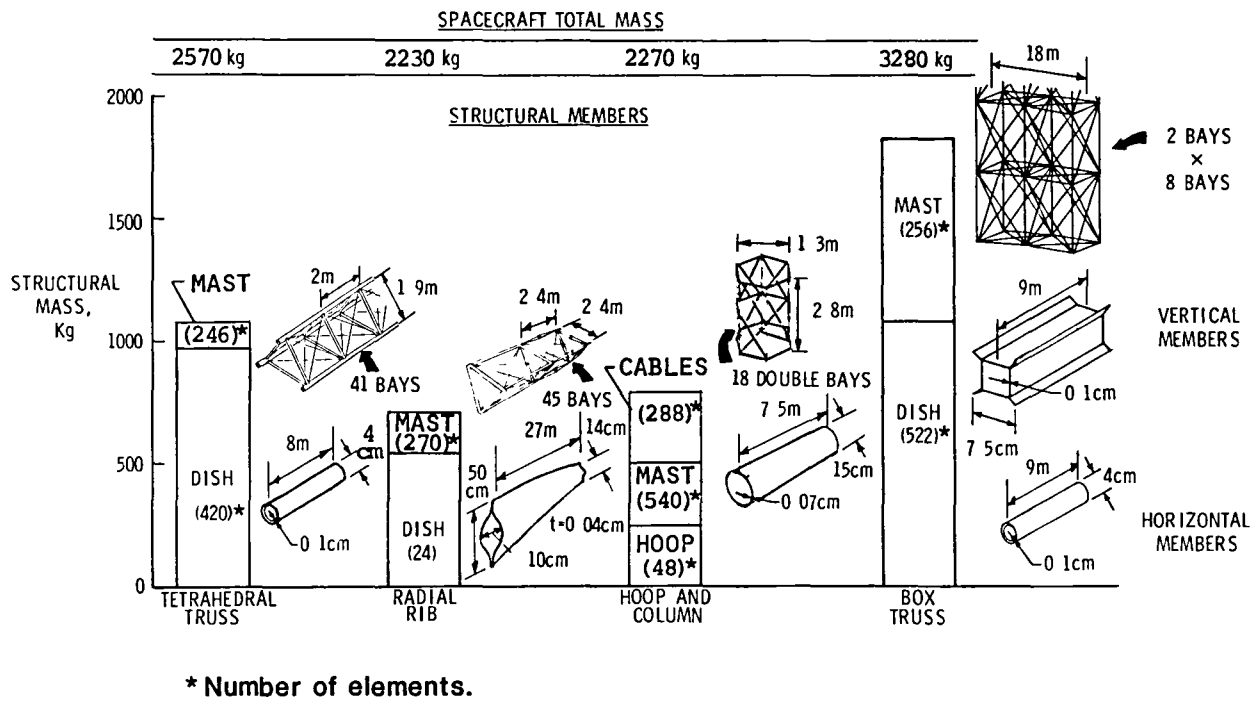
Figure 2. LMSS Mass and Structural Data
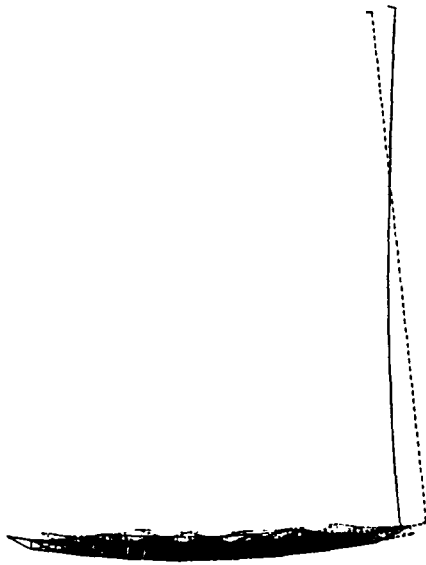
Mode 1

Frequency 0.09732 Hz
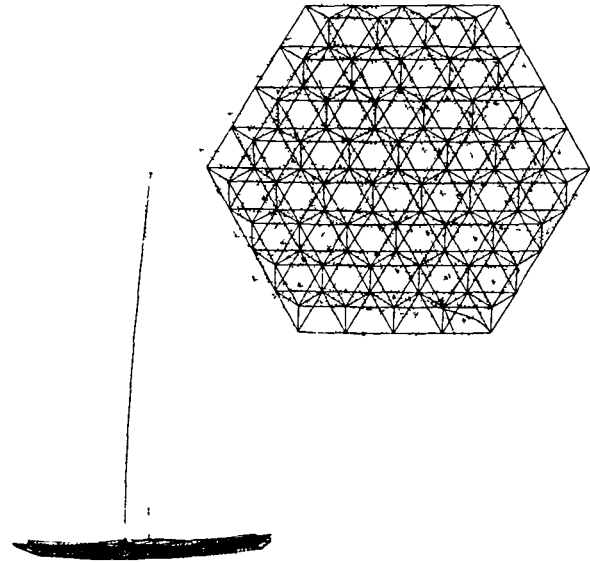
Mode 2

Frequency 0.1434 Hz
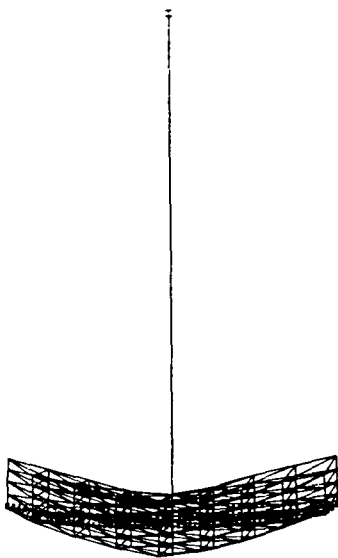
Mode 3

Frequency 1.243 Hz
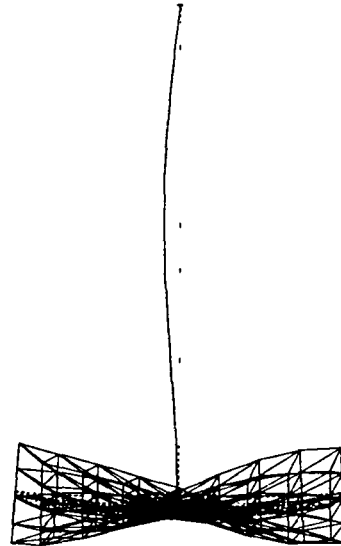
Mode 4

Frequency 2.226 Hz

Figure 3. Tetrahedral Truss Antenna Mode Shapes
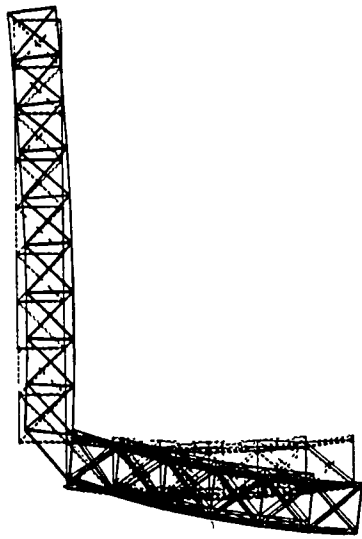
Mode 1
Frequency 1.365 Hz
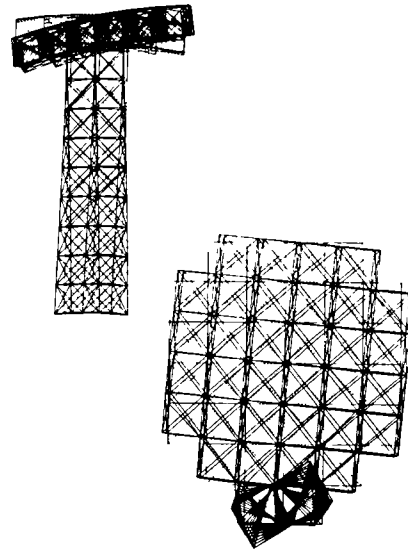
Mode 2
Frequency 1.771 Hz
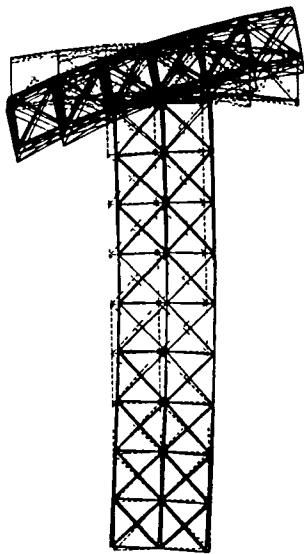
Mode 3
Frequency 2.562 Hz
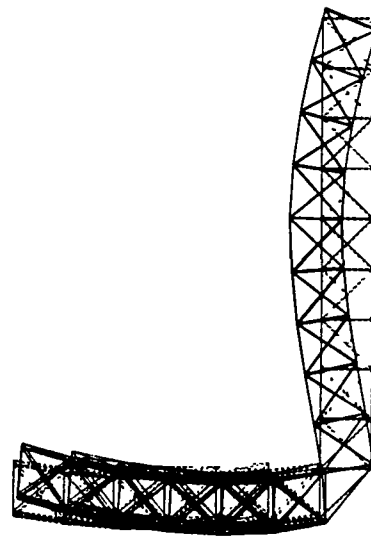
Mode 4
Frequency 5.140 Hz

Figure 4. Box Truss Antenna Mode Shapes
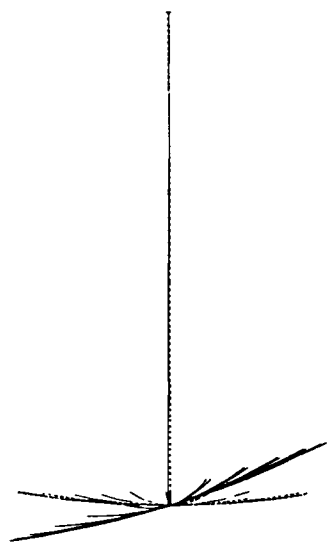
Mode 1

Frequency 0.1183 Hz
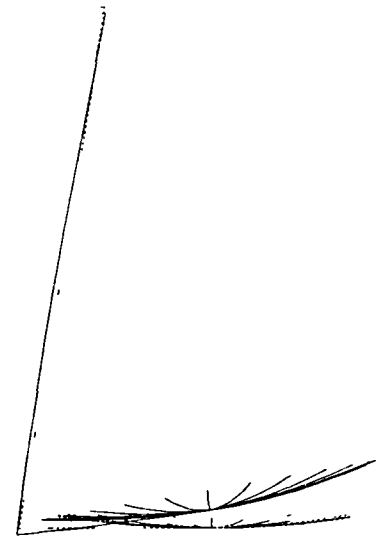
Mode 2

Frequency 0.2123 Hz
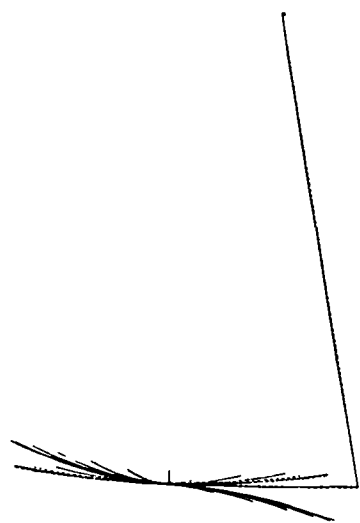
Mode 3

Frequency 0.5360 Hz
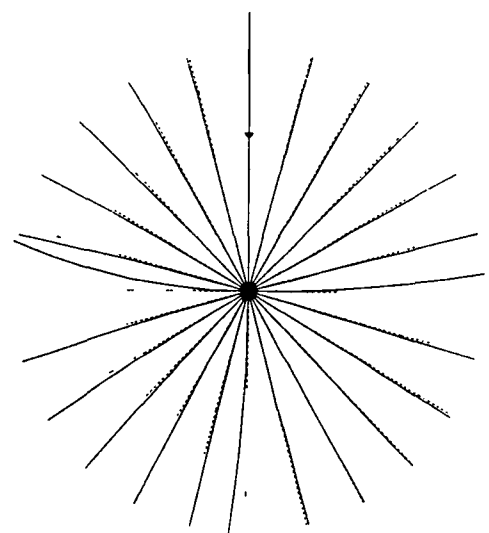
Mode 4

Frequency 0.5470 Hz

Figure 5.   Radial Rib Antenna Mode Shapes
IDEAS Generated
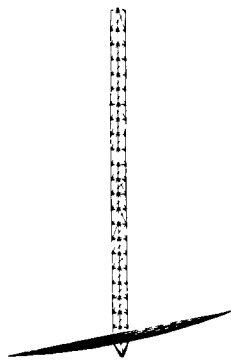
Mode 1
Frequency 0.09363 Hz
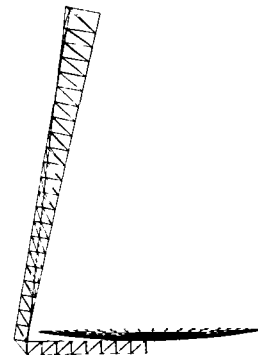
Mode 2
Frequency 0.1621 Hz
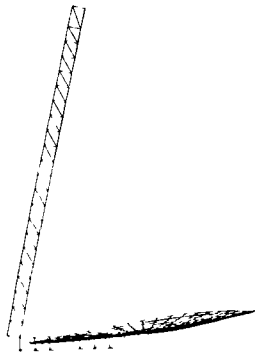
Mode 3
Frequency 0.2578 Hz
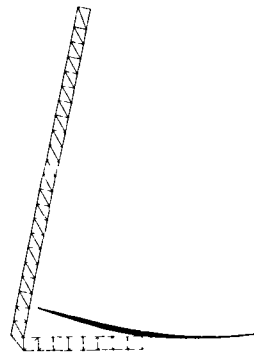
Mode 4
Frequency 0.3395 Hz
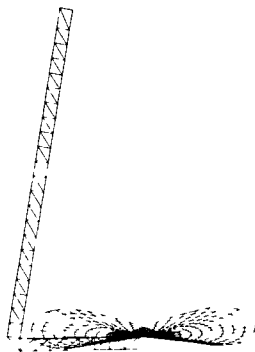
Mode 5
Frequency 0.3730 Hz
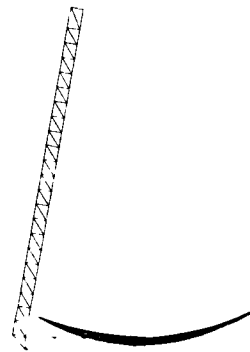
Mode 6
Frequency 0.4384 Hz

Figure 6. Radial Rib Antenna Mode Shapes
EAL Generated

Mode 1
Frequency 0.3658 Hz

Mode 2
Frequency 0.3659 Hz

Mode 3
Frequency 0.5091 Hz

Mode 4
Frequency 0.9111 Hz

Mode 5
Frequency 1.104 Hz

Mode 6
Frequency 1.106 Hz
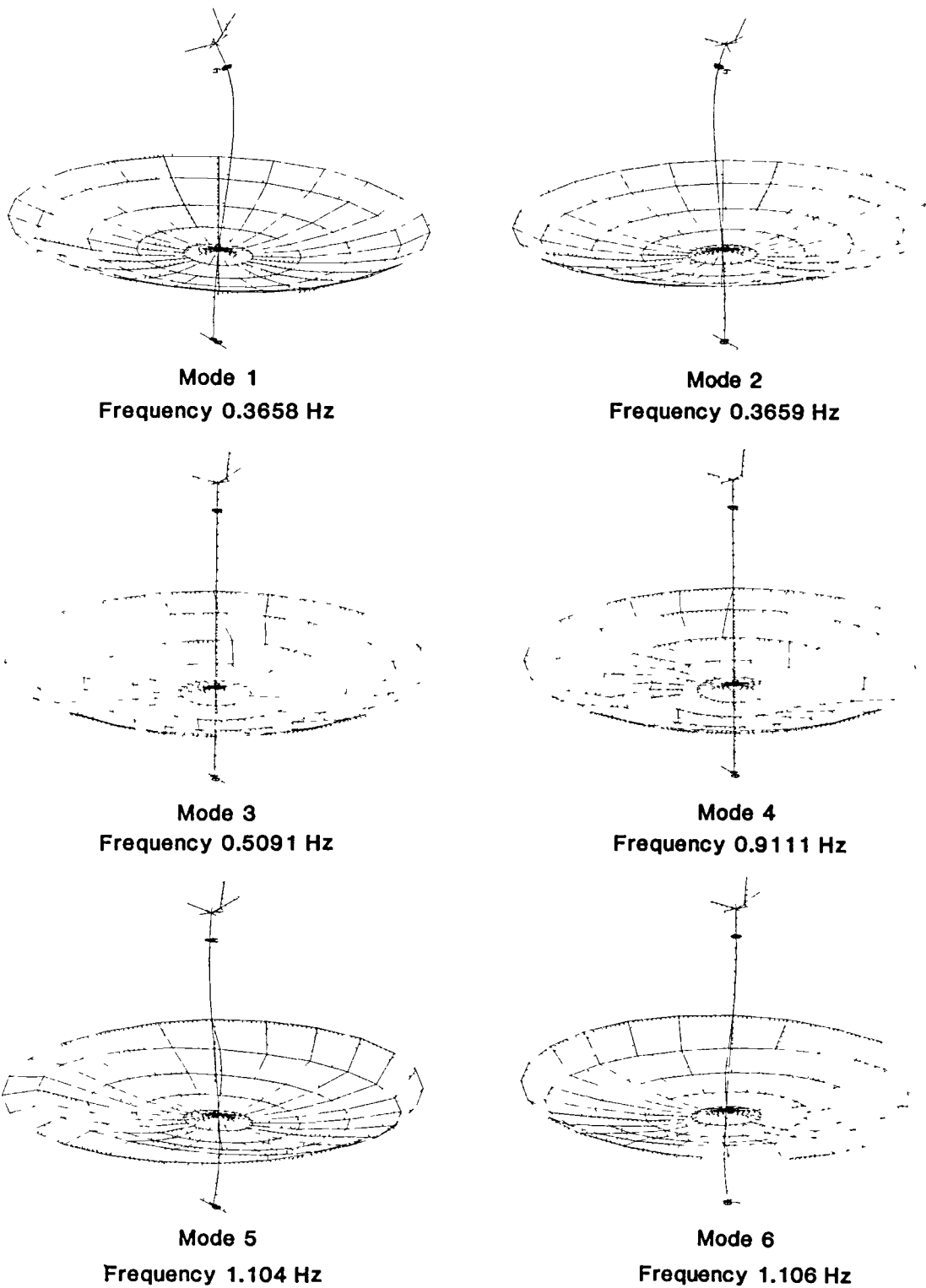
Figure 7. Hoop Column Antenna Mode Shapes

	Positive 300-N Thrust Duration (sec)	Coast Duration (sec)	Negative 300-N Thrust Duration (sec)
0.1 DEG/SEC SLEW			
BOX TRUSS	1.5	199.1	1.5
TETRAHEDRAL TRUSS	0.9	199.7	0.9
RADIAL RIB	0.9	199.7	0.9
HOOP COLUMN	0.55	200.1	0.55
1.0 DEG/SEC SLEW			
BOX TRUSS	15.2	4.9	15.2
TETRAHEDRAL TRUSS	8.9	11.2	8.9
RADIAL RIB	8.9	11.2	8.9
HOOP COLUMN	5.5	14.2	5.5
MAXIMUM NODAL DEFLECTION			
BOX TRUSS	Same as 1.0 deg/sec slew		
TETRAHEDRAL TRUSS			
Parallel thrust (0.66 deg/sec slew)	5.14	20.6	5.14
Perpendicular thrust (0.45 deg/sec slew)	3.49	41.8	3.49
RADIAL RIB			
Parallel thrust (0.29 deg/sec slew)	2.36	65.9	2.36
Perpendicular thrust (0.52 deg/sec slew)	4.23	33.8	4.23
HOOP COLUMN			
Parallel thrust (0.17 deg/sec slew)	1.37	68.4	1.37

Figure 8. Thrust Sequence for Required Slew Rates and Maximum Nodal Deflection
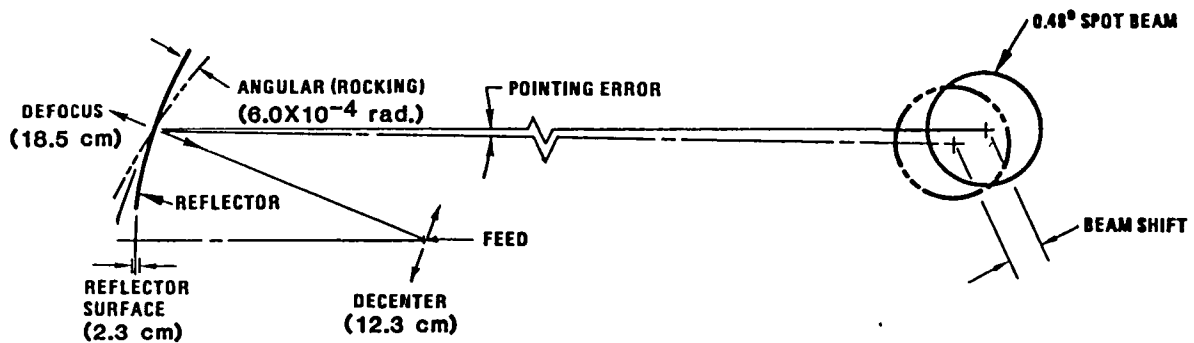
Figure 9. Antenna Accuracy Requirements

Accuracy Tolerance	1.0 DEG/SEC SLEW		0.1 DEG/SEC SLEW		MAXIMUM DEFLECTION	
	Parallel thrust	Perpendicular thrust	Parallel thrust	Perpendicular thrust	Parallel trusts	Perpendicular thrust
Rocking (10^{-4} rad.)	-1.747	8.636	6.942	-6.173	26.28	29.92
Settling time (sec.)	N/A	202	119	16	1200	892
Decenter (cm)	13.98	11.91	55.18	8.65	208.0	41.95
Settling time (sec.)	105	N/A	1220	N/A	2312	681
Defocus (cm)	-.529	.0046	1.95	-.0051	7.03	-.0222
Settling time (sec.)	N/A	N/A	N/A	N/A	N/A	N/A
RMS Roughness (cm)	.0073	.0098	.0219	.0052	.0811	.0026
Settling Time (sec.)	N/A	N/A	N/A	N/A	N/A	N/A

Figure 10. Tetrahedral Truss Antenna Dynamic Response

Accuracy Tolerance	1.0 DEG/SEC SLEW				0.1 DEG/SEC SLEW				MAXIMUM DEFLECTION	
	Parallel thrust		Perpendicular thrust		Parallel thrust		Perpendicular thrust		Parallel thrust	Perpendicular thrust
	IDEAS	EAL	IDEAS	EAL	IDEAS	EAL	IDEAS	EAL	IDEAS	IDEAS
Rocking (10^{-4} rad.)	11.12	20.45	24.45	46.45	17.91	17.23	37.4	44.5	39.86	179.4
Settling time (sec.)	231	592	945	1739	410	395	1231	1348	710	2286
Decenter (cm)	.59	.78	.16	.52	.97	.69	.24	.34	2.09	1.17
Settling time (sec.)	N/A	N/A	N/A	N/A	N/A	N/A	N/A	N/A	N/A	N/A
Defocus (cm)	-18.6		6.9E-4		-30.2		6.9E-4		-58.7A	-8.7E-4
Settling time (sec.)	2.0		N/A		184		N/A		433	N/A
RMS Roughness (cm)	.0673		.0357		.099		.055		.212	.262
Settling time (sec.)	N/A		N/A		N/A		N/A		N/A	N/A

Figure 11. Radial Rib Antenna Dynamic Response

Accuracy Tolerance	1.0 DEG/SEC SLEW Parallel thrust	0.1 DEG/SEC SLEW Parallel thrust	MAXIMUM DEFLECTION Parallel thrust
Rocking (10^{-4} rad.)	0.295	8.30	16.3
Settling time (sec)	N/A	71	217
Decenter (cm)	0.074	2.07	4.06
Settling time (sec)	N/A	N/A	N/A
Defocus (cm)	0.11	3.30	6.30
Settling time (sec)	N/A	N/A	N/A

Figure 12. Hoop Column Antenna Dynamic Response

Accuracy Tolerance	1.0 DEG/SEC SLEW		0.1 DEG/SEC SLEW		MAXIMUM DEFLECTION	
	Parallel thrust	Perpendicular thrust	Parallel thrust	Perpendicular thrust	Parallel thrust	Perpendicular thrust
Rocking (10^{-4} rad.)	.6308	.2507	.3774	.619	.6300	.2507
Settling time (sec.)	N/A	N/A	N/A	N/A	N/A	N/A
Decenter (cm)	.11	.0698	.0416	.0712	.11	.0698
Settling Time (sec.)	N/A	N/A	N/A	N/A	N/A	N/A
Defocus (cm)	-.041	-2.5E-6	-.0298	1.3E-6	-.041	-2.5E-6
Settling time (sec.)	N/A	N/A	N/A	N/A	N/A	N/A
RMS Roughness (cm)	.0037	.0078	.0019	.0048	.0037	.0078
Settling time (sec.)	N/A	N/A	N/A	N/A	N/A	N/A

Figure 13. Box Truss Antenna Dynamic Response

ANTENNA CONCEPTS DYNAMIC RESPONSE PERFORMANCE*

	Decenter	Defocus	RMS Roughness	Angular Rocking
Tetrahedral Truss	0	2	2	1
Box Truss	2	2	2	2
Radial Rib	2	0	2	0
Hoop Column	2	2	2	1

Legend: 0 - Does not meet requirements.

1 - Met requirements within satisfactory settling time.

2 - Met requirements with zero settling time.

*Structural damping is 0.2%

Figure 14.

TETRAHEDRAL TRUSS
(Parallel Thrust)

DISPLACEMENT (M) vs time

0.6, 0.2, -0.2, -0.6 ; 0, 50, 100

Slew Rate: 1.0 deg/sec   Damping. 0.2%

0.6, 0.2, -0.2, -0.6 ; 0, 50, 100

Slew Rate: 1.0 deg/sec   Damping: 2.0%

0.3, 0.1, -0.1, -0.3 ; 0, 100, 200, 300, 400

Slew Rate: 0.1 deg/sec   Damping. 0.2%

0.15, 0.05, -0.05, -0.15 ; 0, 100, 200, 300, 400

TIME (SEC)

Slew Rate: 0.1 deg/sec   Damping. 2.0%

BOX TRUSS
(Parallel Thrust)

DISPLACEMENT (M) vs time

0.6, 0.2, -0.2, -0.6 ; 0, 50, 100

Slew Rate: 1.0 deg/sec   Damping: 0.2%

$X10^{-3}$

0.6, 0.1, -0.4 ; 0, 50, 100

Slew Rate: 1.0 deg/sec   Damping: 2.0%

$X10^{-3}$

0.4, -0.1, -0.6 ; 0, 100, 200, 300, 400

Slew Rate: 0.1 deg/sec   Damping. 0.2%

$X10^{-3}$

0.4, 0.0, -0.4 ; 0, 100, 200, 300, 400

TIME (SEC)

Slew Rate: 0.1 deg/sec   Damping: 2.0%

Figure 15.   Feed Nodal Deflections

161
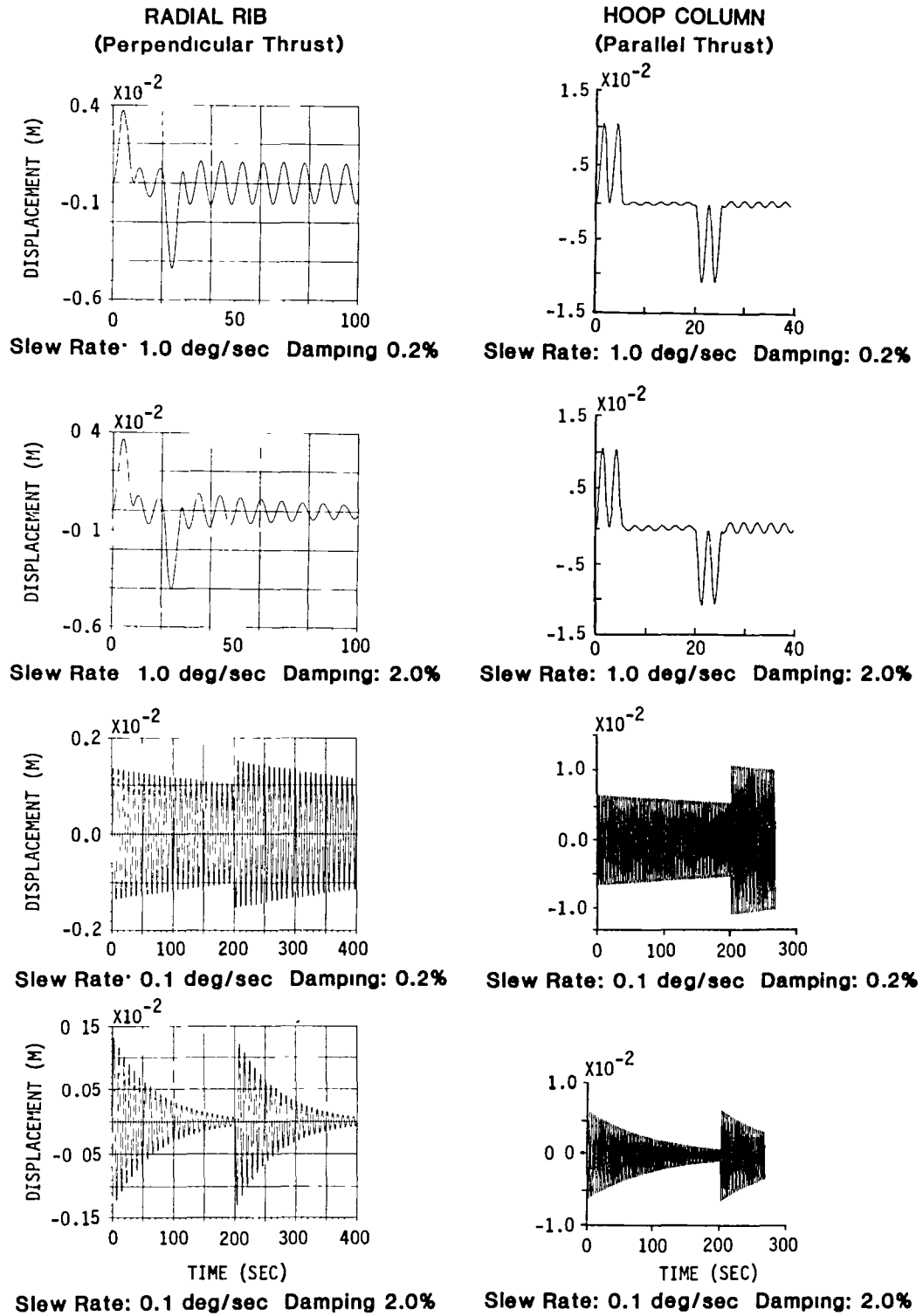
Figure 16. Feed Nodal Deflections

162
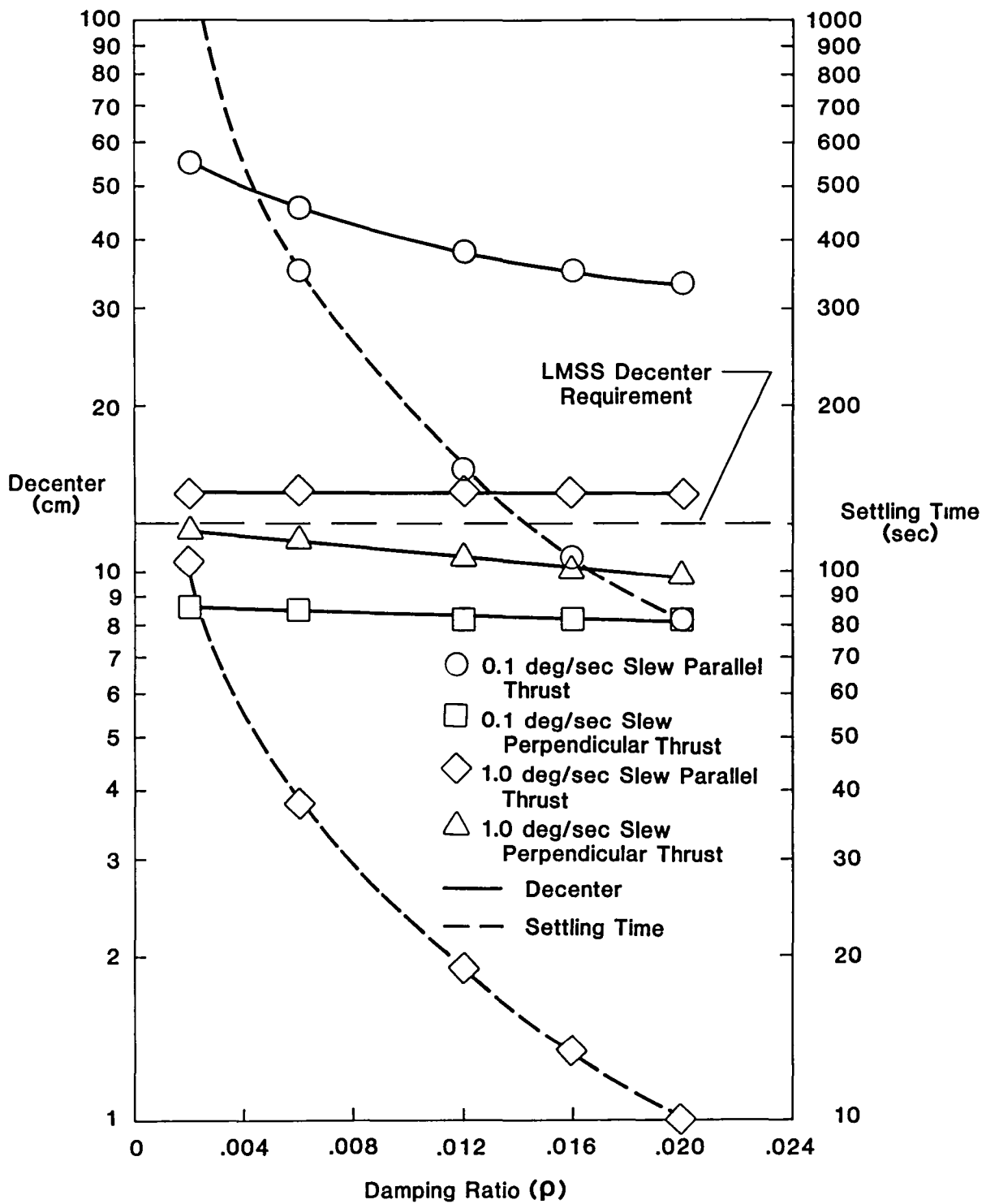
Figure 17. Damping Effects on Tetrahedral Truss Dynamic Response

ANTENNA POINTING OF LARGE FLEXIBLE TELECOMMUNICATIONS SPACECRAFT

B. Govin and **A. Bousquet**
MATRA, Space Branch, BP n°1
78146 Velizy, France

ABSTRACT

This paper presents some results obtained during the investigation of attitude control problems for large flexible telecommunications spacecraft. A typical S/C configuration is described and modeled by modal data derived from a finite element analysis.The effect of structural flexibility on radio-frequency sensor is analyzed. Model reduction using modal gain considerations is applied. Two control concepts are investigated : separate central body and antenna pointing control using direct feedback laws, centralized control using modal observer and optimal control.
Performances of each concept are assessed and conclusions about the algorithm implementation are drawn.

1. INTRODUCTION

The structures that are now proposed for communication satellites include large solar arrays and large deployable antennas and masts. Furthermore, increasing antenna size and power, and sometimes political constraints, lead to higher requirements for the antenna pointing accuracy (few hundredths of a degree). For the achievement of these objectives, the problem of interaction between the spacecraft structure and control has a very high significance.

Distributed attitude control concepts become more and more attractive : each antenna beam could be pointed independently through antenna pointing mechanisms (APM) and radio-frequency sensors (RFS), the main body attitude orientation being measured by means of infra-red observation (IRES)[1] .

This paper presents the analysis and design of attitude control system for a large flexible telecommunications spacecraft during high level thrust North-South station-keeping (NSSK) . The following configuration of sensors and actuators is considered :

- Infra-red earth sensor (about roll and pitch), yaw rate integrating gyro (RIG) and three-axis bipropellant reaction control system on the central body ;

- RFS and antenna pointing mechanisms for antenna beam control.

The objective of the study is to determine what level of performance one could achieve with two different classes of control design ; these are :

- Separate antenna beam pointing and central body attitude control using direct output feedback laws.

- Centralized control concept using state estimation and feedback making use of all sensor outputs and control informations.

Satellite configuration and dynamic modeling are first dealt with. Interactions between structural deformations and R.F detection are discussed. Order reduction methods are applied to get simplified models. The two different classes of controller are then studied. Performance evaluations and critical assessments of implementation problems are finally discussed.

II. SATELLITE CONFIGURATION AND MODELING

The satellite configuration comprises mainly (see figure 1) :

- a rigid central body in which are located the infra-red earth sensor, the gyros, the antenna horns and the thrusters,

- one large flexible antenna (10 m diameter) with typical mode frequencies of 3 Hz,

- a flexible antenna support (typical frequency 0.1 Hz) clamped to the central body,

- two long flexible solar arrays (30 m x 1.6 m) with 0.1 Hz bending mode frequencies,

- an APM providing a two-axis orientation of the antenna with a range of ± 2.0 degrees.

The typical mass properties are the following :

. S/C mass   :   1800 Kg
. S/C inertiae : I_x = $1.4 \ 10^5$ Kg.m^2
                   I_y = $1.5 \ 10^4$ Kg.m^2
                   I_z = $1.6 \ 10^5$ Kg.m^2

. antenna inertia   =   250 Kg.m^2

A Full NASTRAN free-free model is derived for the spacecraft, corresponding to one orientation of the solar arrays and antenna. This model is well adapted to some distributed control design but a non-linear model with several S/C configurations must be used for the performance evaluation. In the NASTRAN model, the APM is modeled as a linear stiffness.
It uses the classical transformation :

$$x = \phi \, q \qquad (1)$$

on the linear system :

$$m\ddot{x} + kx = F \qquad (2)$$

where m is the mass matrix, k the stiffness matrix, F a vector representing forces acting on the structure, x the vector of mass-element translations and rotations, ϕ the modal matrix the columns of which are the mode shapes and q the vector of mode amplitude. The equation (2) becomes :

$$M \ (q + \Omega^2 q) = \phi^T F = \phi^T B_A u \qquad (3)$$

where $\Omega^2 = \text{diag} \ (\omega_i^2)$ and ω_i is the frequency of the i-th mode ; $M = \text{diag} \ (M_i)$ and M_i is the generalized weight of the i-th mode ; u is the control vector with a dimension equal to the number of actuators ; B_A is a matrix specifying the actuator load on the structure. A sensor measurement vector is defined by :

$$y = H_p u + H_v \dot{u} \qquad (4)$$

where the matrices H_p and H_v are determined by the position (H_p) or velocity (H_v) sensor location and measurement axes. Defining the state vector x of the system by :

$$x = (q \dot{q})^T \qquad (5)$$

Equations 3 and 4 can be represented in state-space notation as

$$\dot{x} = Ax + Bu \qquad (6)$$
$$y = Cx \qquad (7)$$

where

$$A = \begin{pmatrix} 0 & I \\ -\Omega^2 & 0 \end{pmatrix} \qquad (8)$$

$$B = \begin{pmatrix} 0 \\ M^{-1} \phi^T B_A \end{pmatrix} \qquad (9)$$

and

$$C = (H_p \phi \quad H_v \phi) \qquad (10)$$

The system described by Equations (6) and (7) is in a canonical form and is, in theory, of infinite dimension.

The following table gives the NASTRAN outputs in terms of mode frequency and generalized mass.

Mode	Frequency, Hz	G M. kg x 10^{-3}	Description
1-6	0		Rigid Body Modes
7	0589	0900	Solar array — first sym bending
8	0619	0256	Large antenna — first lateral trans
9	1329	0107	Large antenna & solar array — pitch
10	1346	00885	Large antenna — roll
11	1361	1843	Solar array — 1st anti-torsion
12	1368	0614	Large antenna pitch — sol array & 1st sym torsion
13	1791	1096	Solar array — 1st anti-bending ant roll
14	2205	0268	Large antenna pitch & lat trans
15	3528	0899	Solar array — 2nd sym bending
16	4465	0633	Solar array — 2nd anti bending
17	5747	0992	Solar array — 2nd anti-torsion
18	5747	0991	Solar array — 2nd sym torsion
19	7362	1046	Solar array — 1st in plane bending
20	7668	0367	Astro mast bending — spacecraft roll
21	9694	0908	Solar array — 3rd sym bend
22	1.152	0498	Solar array — 3rd anti-bend
23	1 188	0609	Astro mast bending — spacecraft pitch
24	1 224	0679	Solar array — 3rd anti torsion
25	1 224	0684	Solar array — 3rd sym torsion
26	1 375	0320	Astro mast bending — spacecraft roll

TABLE 1 —   EIGENFREQUENCIES OF THE S/C MODEL

III. ACTUATOR AND SENSOR MODELS

Only APM and RFS models are briefly described here. The selected APM motor is a stepping motor commanded in a continuous or quasi-continuous (microstepping) way. The following model has been used :
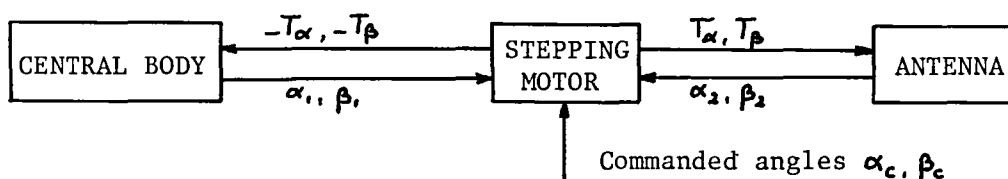
Figure 2 : APM motor model.

with :

$$
\begin{cases}
T_\alpha = T_0 \; \sin \dfrac{\pi}{2\Delta\theta} \left(\alpha_1 - \alpha_2 - \alpha_c \right) \\[2mm]
T_\beta = T_0 \; \sin \dfrac{\pi}{2\Delta\theta} \left(\beta_1 - \beta_2 - \beta_c \right)
\end{cases}
\tag{11}
$$

where T_α , T_β are the applied torques, T_0 the holding torque, $\Delta\theta$ the step amplitude, α_1 , α_2 , β_1 , β_2 the actual rotations at stator and rotor modes and α_c and β_c the commanded positions.

The RFS considered here is of the amplitude comparison monopulse type. The measurement of the Earth beacon direction is given by the mismatching of the 4 horns placed in the focal plane of the diffraction spot. The effects producing RFS outputs are :

i)   the relative translations between horns and reflector

ii)   the rotation of the reflector

iii) the rotations of the horns (negligible)

iv)   the reflector flexible modes.

As an approximation, the reflector flexible modes are not taken into account here.

170
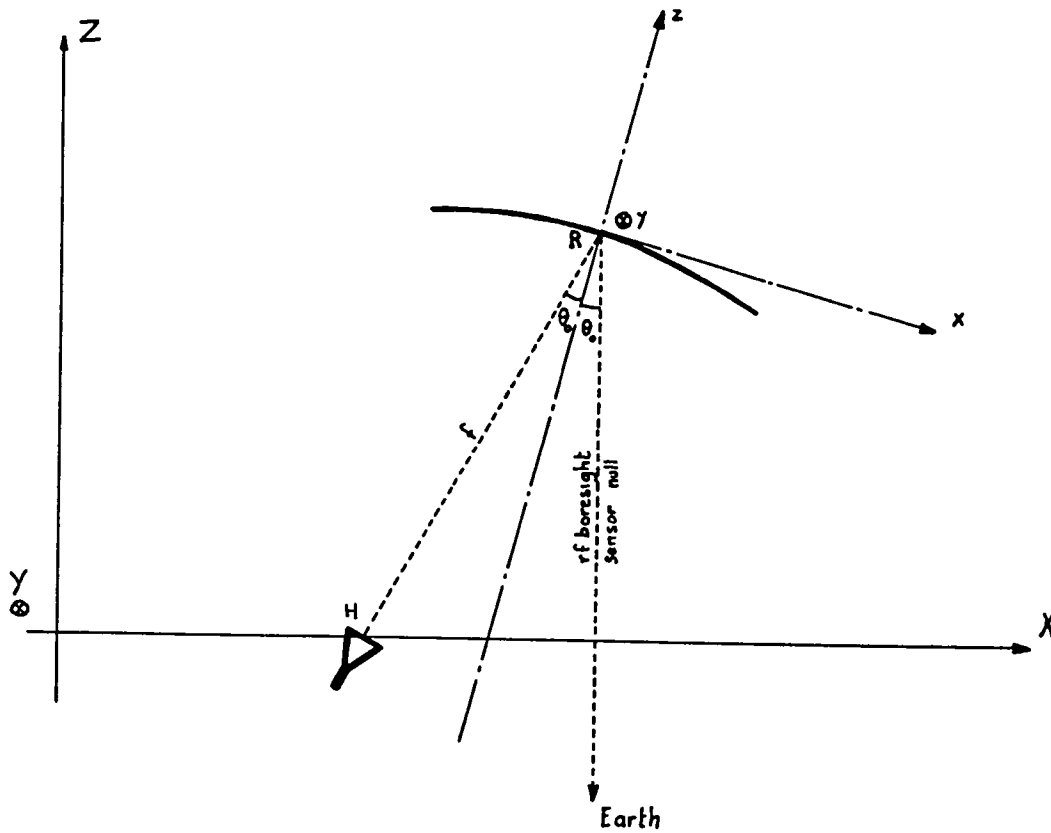
Figure 3 : REFLECTOR/HORN LOCATION IN S/C REFERENCES

The figure 3 gives the references and notations for computing the effect (i) and (ii) :

. X, Y, Z is the satellite reference set

. x, y, z is the RFS reference set

. R is the vertex of the reflector

. H is the horn location

. θ_0 is the rotation around y axis (parallel to Y axis) which defines the RFS reference

. f is the focal length .

171

With these notations, the RFS outputs (α_{RFS}, β_{RFS}) with respect to rigid body rotations (α_o, β_o), relative horn/reflector translations (ΔX, ΔY) and reflector rotations (θ_X, θ_Z) are :

$$
\begin{cases}
\alpha_{RFS} = \alpha_o & -\dfrac{\Delta X}{f} + 2\cos^2\theta_o \cdot \theta_x - \sin 2\theta_o\, \theta_z \\
\beta_{RFS} = \beta_o & + (\Delta X \cos^2\theta_o - \Delta Z \sin 2\theta_o)/f\cos^2\theta_o + 2\theta_y
\end{cases}
\tag{12}
$$

$\underbrace{\hspace{3cm}}_{\text{rigid body}}$ $\underbrace{\hspace{7cm}}_{\text{flexibility effects}}$

assuming the beam deviation factor equal to one. The distributed nature of the RFS is well described by equations (12).

IV. CONTROL REQUIREMENTS AND MODEL REDUCTION

The control system must be designed using the antenna beam angles with respect to the earth reference system as performance measurements (allocated pointing error : 0.05 deg, 3σ). For the central body, the allocated pointing error is 0.1 deg (3 σ). The disturbance models are derived from the thruster configuration used for station-keeping maneuver.
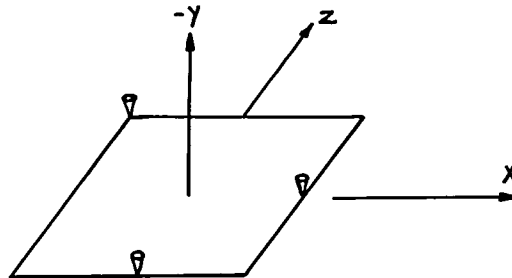
Figure 4 :   THRUSTER CONFIGURATION DURING STATION KEEPING
(Using off-modulation).

Plume effect, thrust uncertainty and misalignment, and center-of-mass shift produce unbalance torques of about 1 Nm (x,z). Uncertainty is assumed to be 20 % of this value.

The selected model reduction principle is then the following :

- from the expected disturbances and control requirements the control bandwidth is determined on simplified models.

- the model is truncated to include all frequencies up to some multiple of the control bandwidth (max. frequency : 3 Hz)

- modal gain considerations are then used : modes which contribute little in all the input/output transfer functions are neglected.
  By the way, modes which are not excitable or which are not observable are discarded.

- however, modes which may be unstable are not discarded even though they have low modal gains (modes 22,26).

It is clear that this procedure must be tested after controller design on a complete validation model. From the modal gain considerations, the mode clas- sification is shown in table 2 for the RFS/APM loops (roll and pitch transfer functions). Finally modes 7, 11, 17, 18, 21, 24 have been discarded.
17 modes are retained for the control analysis. Furthermore control about pitch axis can be decoupled and a further reduction is done for state feedback (section 5) :

. 4 modes are retained inside the control bandwidth using pitch measurements and torques on central body and antenna (5,9,12,14).

. 5 modes are retained for roll/yaw control (4,6,8,10,13).

	RANK	FLEXIBLE MODE NUMBER	FREQUENCY ω_1 (Hz)	MODAL GAIN
ROLL	1	10	0.13	$7.73 \cdot 10^{-6}$
	2	13	0.18	$7.77 \cdot 10^{-7}$
	3	8	0.062	$9.99 \cdot 10^{-8}$
	4	16	0.45	$6.76 \cdot 10^{-8}$
	5	20	0.77	$3.10 \cdot 10^{-8}$
	6	26	1.37	$-2.14 \cdot 10^{-8}$
	7	22	1.15	$-1.63 \cdot 10^{-9}$
PITCH	1	9	0.13	$7.98 \cdot 10^{-6}$
	2	12	0.14	$9.83 \cdot 10^{-7}$
	3	14	0.22	$8.32 \cdot 10^{-7}$
	4	23	1.19	$1.66 \cdot 10^{-7}$
	5	25	1.22	$1.13 \cdot 10^{-9}$
	6	15	0.35	$3.33 \cdot 10^{-10}$
	7	18	0.57	$2.12 \cdot 10^{-10}$

TABLE 2 : DOMINANT MODES IN RFS/APM LOOPS

(Using modal gain considerations)

V. SEPARATE LOOPS USING DIRECT OUTPUT FEEDBACK

A simple approach using independent mono-variable control loops has been first tested (see figure 5). A minimum mode excitation from central body control is achieved by CAUER filtering (see figure 6). On the contrary, because of the high accuracy required on the antenna beam pointing, this loop needs a large bandwidth. However it can be seen on the root locus for RFS/APM roll loop, (figure 7) that the loop bandwidth is limited by the presence of flexible mode 26 (astromast bending) which may become unstable. Furthermore, weakly damped oscillations appear in the closed loop response (as a classical drawback of the direct output feedback technique).

Consequently, poor antenna pointing performances are obtained (see figure 8). It is clear that the use of additional actuators and sensors would improve antenna pointing performances but this is beyond the scope of this paper.

VI. CENTRALIZED APPROACH USING STATE ESTIMATION AND FEEDBACK

The objective is now, using the same set of actuators and sensors, to develop modal control algorithm to assess the performances which could be achieved. Basically, a LQG control is selected by minimizing a quadratic performance index :

$$J = \lim_{T \to \infty} \frac{1}{T} \int_0^T \left(X^T F X + U^T G U \right) dt \tag{13}$$

for the system evolution $\dot{X} = AX + BU$, where F and G are state and control weighting matrices. The control U is given by :

$$U = -K\hat{X} \tag{14}$$

where
$$K = G^{-1} B^T P \tag{15}$$

$$0 = PA + A^T P + F - PBG^{-1} B^T P \tag{16}$$

$\hat{X}$ is the estimate of the controlled state through the observer :

$$\dot{\hat{X}} = A\hat{X} + BU + L (Y - C\hat{X}) \tag{17}$$
$$Y = CX \tag{18}$$

where
$$L = SC^T R^{-1} \tag{19}$$

$$0 = AS + SA^T - SC^T R^{-1} CS + Q \tag{20}$$

R and Q are measurement and process noise covariance matrices.

However extension of standard LQG design using frequency-shaped cost functionals (ref. [2]) enables spillover and disturbances reduction (see figure 9).

As an illustration, let us consider a high control weighting at high frequencies to reduce spillover :

$$G(j\omega) = \frac{\omega^2 + \omega_0^2}{\omega_0^2} \, G \tag{21}$$

we now define a new vector $\bar{U}$ by :

$$\dot{U} + \omega_0 U = \omega_0 \bar{U} \tag{22}$$

the performance index can be written in the form :

$$J = \lim_{T \to \infty} \frac{1}{T} \int_0^T \left(X^T F X + \bar{U}^T B \bar{U} \right) \, dt \tag{23}$$

the feedback control law will be :

$$\bar{U} = C_1 X + C_2 U \tag{24}$$

and therefore :

$$\dot{U} + \omega_0 (1 - C_2) \, U = \omega_0 C_1 X \tag{25}$$

$$U = \omega_0 \left[sI + \omega_0 (1 - C_2) \right]^{-1} C_1 X \tag{26}$$

In the same way, consider that we want to attenuate modes higher than ω_0 in the sensor measurement Y. Let $\bar{Y}$ be the filtered measurement :

$$\bar{Y} = \frac{\omega_0}{s + \omega_0} \, Y \tag{27}$$

Equation (27) makes us consider an additional state equation

$$\dot{Z} = -\omega_0 Z + \omega_0 C X \tag{28}$$

The original measurement equation Y = CX has become $\bar{Y}$ = Z for the augmented state representation :

$$\begin{cases} \dot{X} = A X + B U \\ \dot{Z} = -\omega_0 Z + \omega_0 C X \end{cases} \tag{29}$$

176

the corresponding asymptotic observer will have the form :

$$\begin{cases} \dot{\hat{X}} = A\hat{X} + BU + L_1 \ (\overline{Y} - \hat{Z}) \\ \dot{\hat{Z}} = -\omega_o\hat{Z} + \omega_o C\hat{X} + L_2 \ (\overline{Y}-\hat{Z}) \end{cases} \qquad (30)$$

VII. NUMERICAL RESULTS AND CONCLUSION

A 10 order observer including spillover filtering has been deve-
loped using 2 inputs and 2 outputs for central body and antenna
beam control around pitch axis. Simulation test runs gave a
number of interesting results (see typical output in figure 10) :

. due to the optimal control, the stability margins are very good,

. robustness is good for the controlled modes and no performances
  degradation is observed when the frequency of the modes is
  changed by 20 %,

. in the nominal case (with a microstepping motor for the APM)
  the performances are :
  - for central body pointing   roll = 0.048 deg
                                           pitch = 0.050 deg
                                           yaw   = 0.155 deg

  - for antenna pointing   roll = 0.040 deg
                                           pitch = 0.045 deg

. as concerns equipment, it appears that the use of gyros for roll
  and pitch measurement would give significantly better results ;
  the continuous feature of the APM is very interesting since it
  does not constitute a mode excitation source.

Implementation on a microprocessor (TI SBP 9989) has been analyzed
Briefly, for control algorithm involving 4 modes for each axis,
total computation time of 50 msec has been found (using fix

double-word arithmetic). This allows sampling frequency up to
12 Hz which is compatible with the control bandwidth used in vali-
dation examples.
In conclusion, state feedback techniques associated with frequency
shaping filters have been tested for the antenna beam control
(through RFS and APM) and central body attitude control. These
techniques enable performance improvement of typically 0.05 deg
at antenna level. Computation load is reasonable. Further works
will be necessary to fully validate this concept with a complete
non-linear model taking into account modal parameter dispersions
and S/C configuration changes. For that, there is a need of
further development of modeling and model reduction techniques
and of ground and flight test methods.

Acknowlegments :

This paper is based on work performed under the sponsorship and
technical direction of the International Telecommunications
Satellite Organization (INTELSAT). Any views expressed are not
necessarily those of INTELSAT.

References :

[1] A. BOUSQUET, JC. AMIEUX, B. GOVIN, R. HAVAS, G. MULLER
    "Integrated Attitude Detection and Estimation System"
    Final Report, INTELSAT Contract n° INTEL-129, Oct. 1983

[2] N.K. GUPTA
    "Frequency-Shaped Cost Functionals : Extensions of Linear
     Quadratic Gaussian Design Methods"
    AIAA Journal of Guidance, Control and Dynamics,
    Nov./Dec. 1980 - pp 529-535.
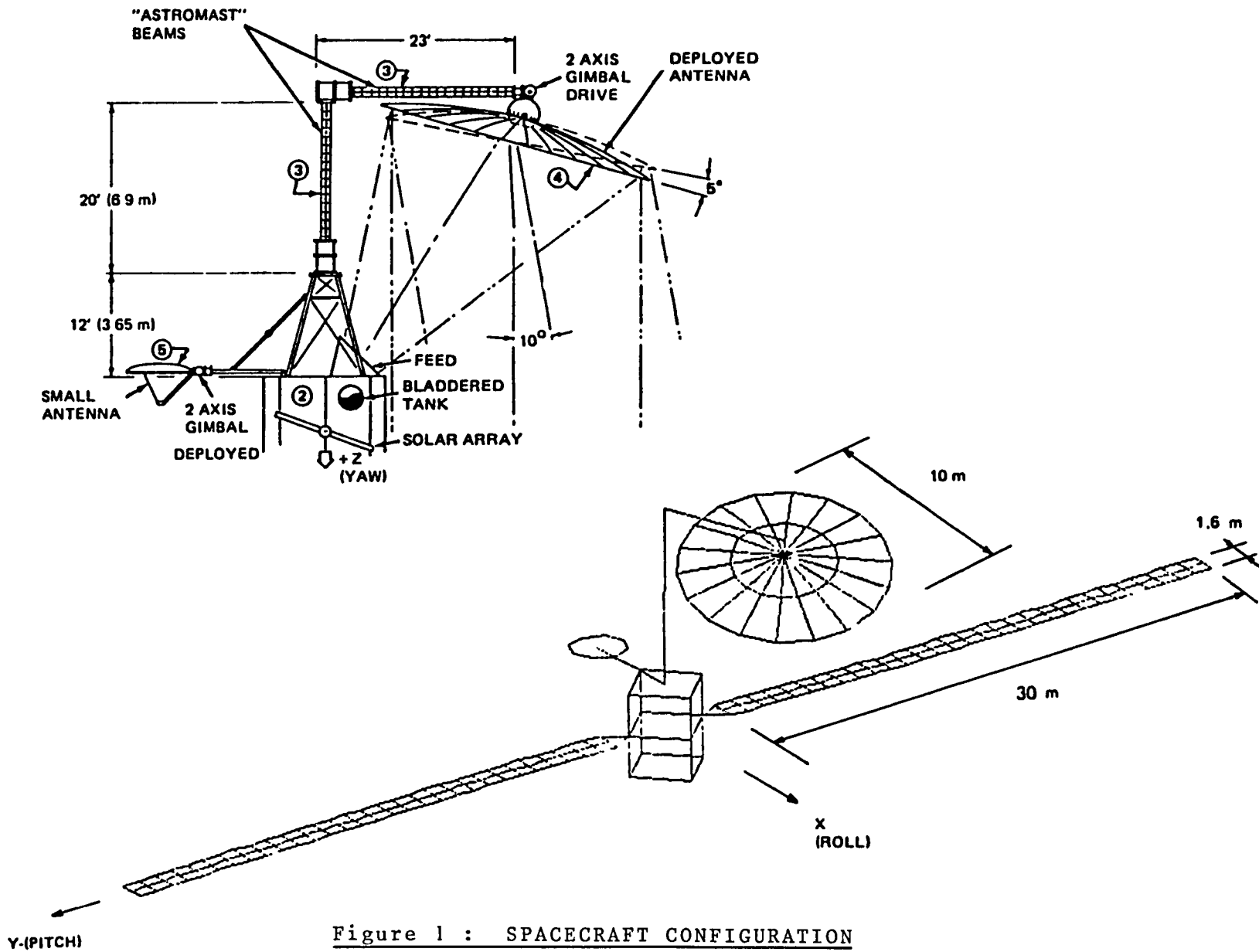
Figure 1 : SPACECRAFT CONFIGURATION
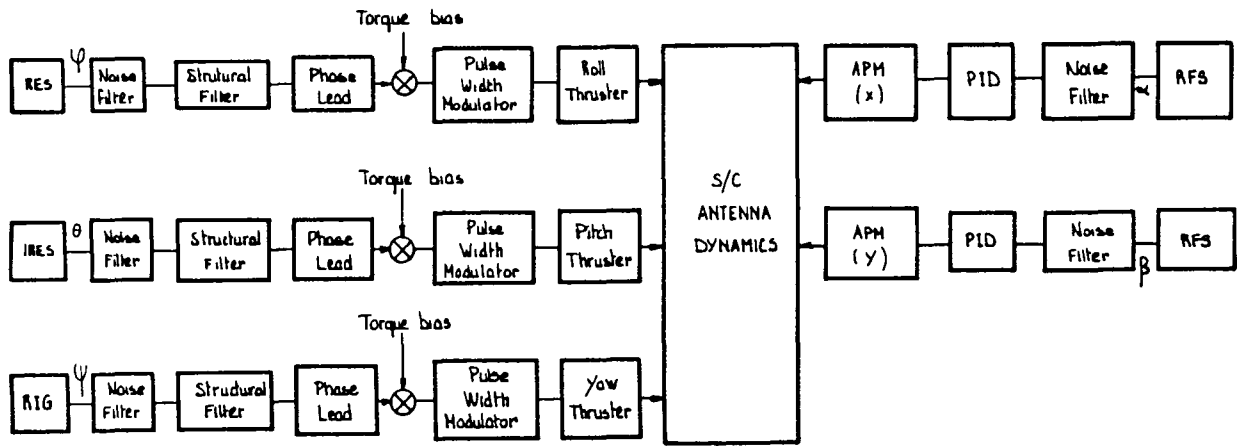
Figure 5 : 1st CONTROL CONCEPT: SEPARATE BODY ATTITUDE AND
ANTENNA BEAM CONTROL LOOPS
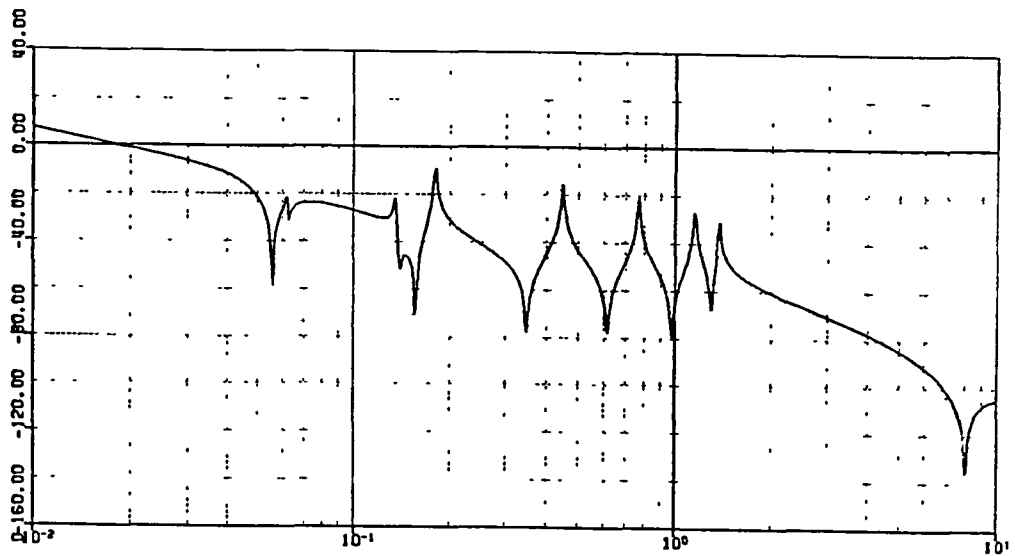
Figure 6 : CENTRAL BODY TRANSFER FUNCTION USING P.D NETWORK
AND CAUER FILTERING (1st control concept)

k = 0,100,200,... ,1000
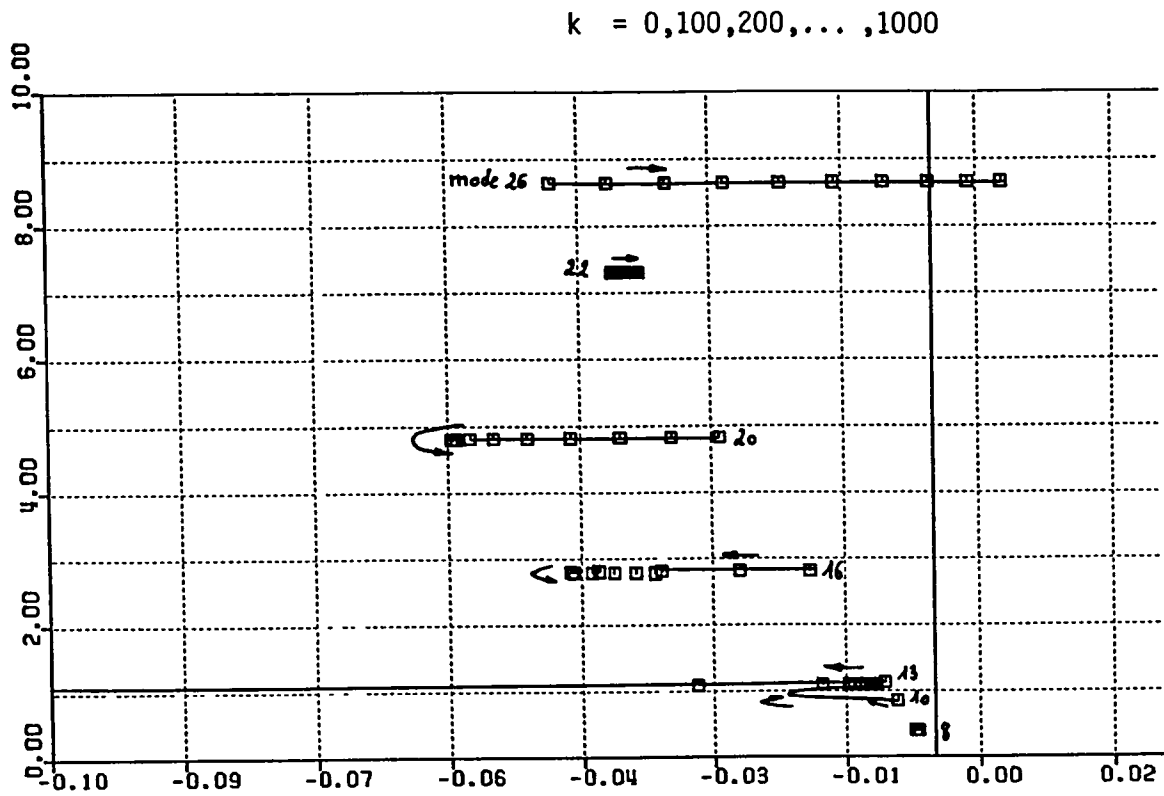
Figure 7 : ROOT LOCUS FOR RFS/APM ROLL LOOP BY CHANGING
LOOP STIFFNESS (1st control concept)
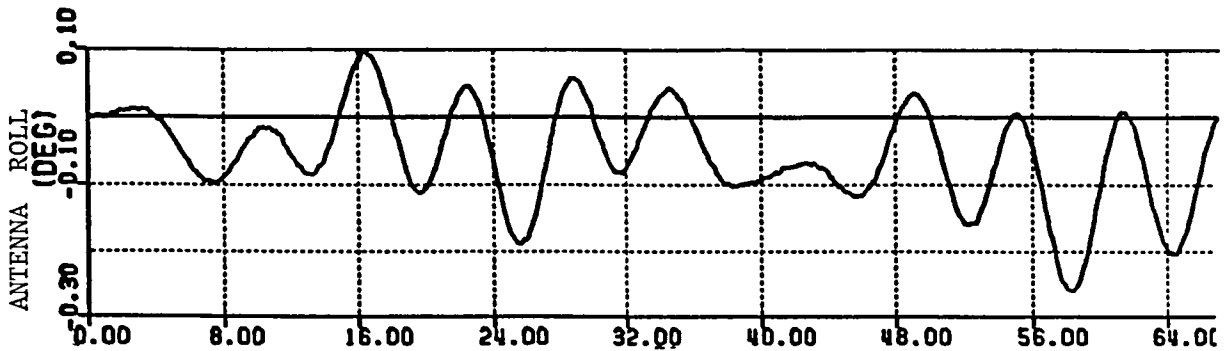
Figure 8 : SIMULATION RESULTS OF 1st CONTROL CONCEPT :
ANTENNA ROLL DEPOINTING
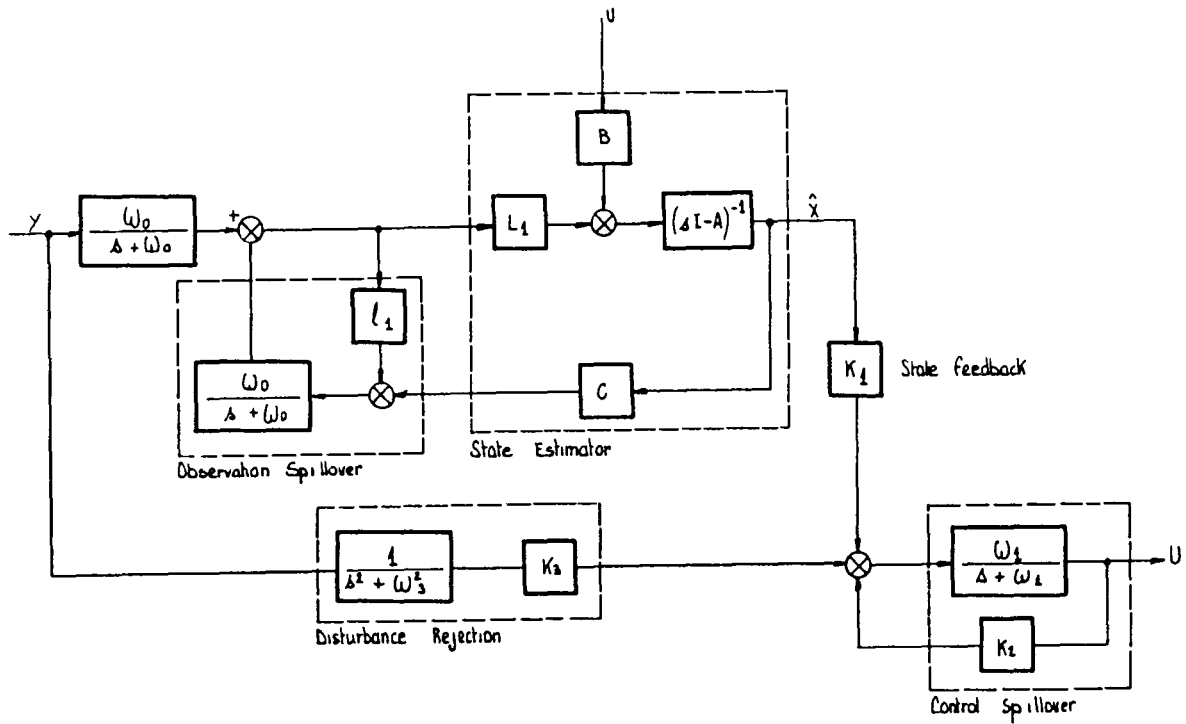
Figure 9 : 2nd CONTROL CONCEPT : STATE ESTIMATION AND FEEDBACK USING
FREQUENCY-SHAPED TECHNIQUES
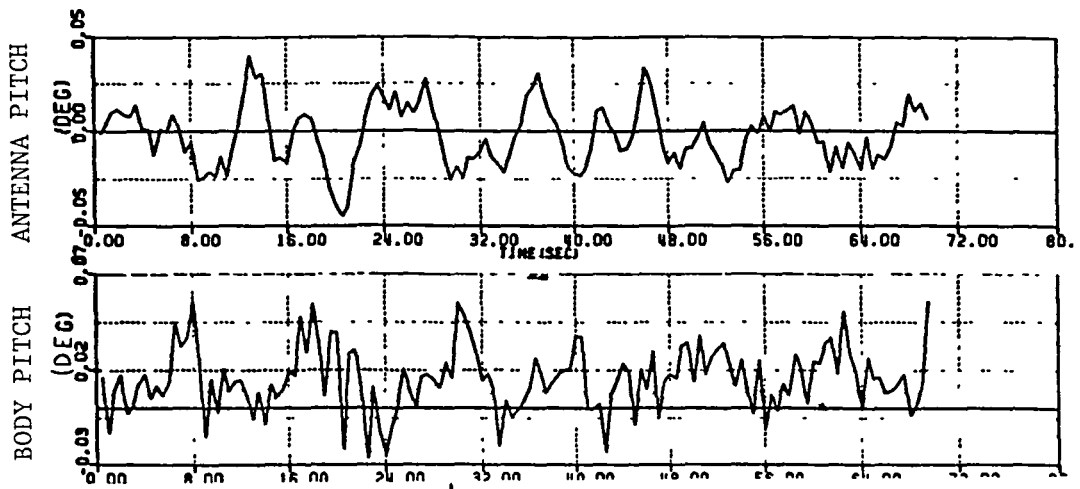
Figure 10 : 2nd CONTROL CONCEPT SIMULATION RESULTS : ANTENNA AND
CENTRAL BODY PITCH ATTITUDE.

182

DESIGN AND EVALUATION OF CONTROL SYSTEMS FOR LARGE COMMUNICATIONS SATELLITES

M. E. Steiber
Communications Research Centre
Ottawa, Canada

ABSTRACT

Control techniques for future large flexible spacecraft are being developed in a joint industry, university and government research project. Control design and analysis are supported by a comprehensive CAD system. The proposed Operational Mobile Communications Satellite (OMSAT) featuring a 44 m offset fed antenna is used as target application. A reduced version of a high fidelity dynamics model of the satellite serves as a benchmark system. Requirements for satellite attitude control and communications beam pointing are defined. The following control methods are applied to the system: standard linear optimal regulator (LOR) with Luenberger observer, LOR/observer with selective spill-over suppression, frequency shaped LOR, LOR with closed-loop order reduction by cost decoupling, and Robust Servomechanism. The design results are compared.

1. Introduction

Several spacecraft missions under consideration in Canada will require the application of large space structure technology Of particular interest to the Department of Communications (DOC) is the Operational Mobile Communications Satellite (OMSAT), proposed for the mid 1990's [1]. This geostationary satellite, originally planned as a joint U.S.-Canada project, would provide mobile communications service in the 800 MHz band throughout Canada and the 50 United States. The mission requires 106 communication beams and a large reflector to generate beam patterns small enough for reasonable beam separation and frequency reuse [2]. The beams of 0 5 degrees width require pointing accurate to 0 05 degrees. In a configuration tradeoff study [3], the spacecraft configuration shown in Fig 1 was selected from 34 candidates as the baseline for the OMSAT mission. It features an offset-fed antenna configuration with a 44 m diameter reflector, a 70 m angled support tower and a 38 m solar array delivering 8.2 kW of power. The spacecraft mass is in the order of 3500 kg, with the center of mass located outside the physical structure.

The engineering challenges to design, build and test such a spacecraft are quite significant and dynamics and control has been identified as a critical area [4]. A joint industry, university and government research project led by the Communications Research Centre (CRC – a DOC lab) undertakes to develop the attitude and orbit control techniques required for this class of spacecraft [5]. This paper summarizes some aspects of this joint effort. A Computer-Aided Design (CAD) system, used for development, evaluation and verification of control techniques, is described in Section 2. A benchmark spacecraft dynamics model and benchmark control design requirements are defined in Section 3. A preliminary comparison of several control methods applied to the benchmark case is presented in Section 4

2. Computer-Aided Control Design System

A comprehensive Computer-Aided Control Design System has been implemented at CRC in Ottawa in collaboration with Ruhr University, Bochum, F R.G. This system essentially is the KEDDC

package developed under coordination of Schmid [6] at Lehrstuhl ESR (Prof. Unbehauen) of Ruhr University. It serves not only as an efficient tool for control system analysis conducted at CRC but is intended to also play a role as an interface and stimulus for the communication between the various research groups within industry, universities and CRC.

Fig 2 provides a block diagram of the main components of the CAD system and their interfaces with the applications environment specific to large space structures projects. The major components are a set of interactive non real-time programs for system and signal analysis, a database, an extensive program library and, to be implemented in the near future, real-time programs interfacing with experimental hardware.

The package supports a wide variety of operations for system manipulation and analysis, control system synthesis, simulation and signal processing. The methods are essentially limited to finite dimensional linear systems. Systems may be represented in any of the 10 different forms shown in Fig.3 and transformed with ease between time domain, state space and frequency domain. The choice of system descriptions includes deterministic and stochastic input/output signals, continuous and discrete time transfer matrices, continuous and discrete state space representations, as well as matrix fraction descriptions.

The users interact with KEDDC through a command driven dialog and can perform operations in arbitrary sequence, accessing the implemented methods and algorithms like tools in a toolbox. Menu and help facilities normally enable even casual users to master the system without reference to manuals A KEDDC session does not require any pre-planning or programming as forgotten steps can be interlaced in the dialog at any time, such that a "hang-up" cannot occur. The solution of common subtasks is usually supported by a number of numerical options in order to ensure efficient and accurate solution of high order problems (e.g. 13 numerical options for the solution of stationary Riccati equations).

Access to a common database improves the communication between research groups working on a common project and ensures that individual developments are based on common grounds In particular, access by all users to high order models, system order reduction and control design procedures can help to improve the interfacing between dynamic analysis and control design (Fig. 2) KEDDC also forms a common software base reducing the duplication of program development. Methods developed during this project are also being applied to studies on flexible manipulators and the Space Station. However, the idea of using KEDDC as a common forum for the exchange of data and software is only slowly gaining acceptance in industry and at universities participating in the project, mainly because remote users face the inconvenience of limited data transmission rates, and the necessity to familiarize with another computer system.

KEDDC is organized as an open system, parts of which may be added, updated or removed at any time This unlimited extendability is of particular importance in an applied R&D environment with on-going development of new programs and methods The development of non real-time programs presently focusses on methods for the reduction of the order of open- and closed-loop systems. As indicated in Fig 2, program development is supported by the program library which contains about 1000 routines for basic mathematical functions (LINPACK, EISPACK, polynomial operations etc), control engineering, database management and graphics. Program development may take place on other than the target machine as the numerical library programs are portable. Implementation of existing real-time programs on state-of-the-art hardware will allow immediate implementation of control algorithms, on-line system identification and adaptive control (Schmid [7]) of ground based hardware experiments, which are in preparation (Hughes [8]).

3. Benchmark Dynamics Model and Control Requirements

One objective of the control studies is to explore the interaction between control systems and space structures with uncertain and unmodelled dynamics. A second objective is to develop robust control techniques for this class of systems. The 'strawman' chosen for this study is the OMSAT of Fig.1, because the spacecraft design has progressed to a level of detail which permitted the development of a realistic and coherent dynamics model with much attention to detail.

Fig.4 shows the various stages of the modelling and model order reduction process. Finite element dynamic models of the three flexible substructures (solar array, tower and reflector) were developed separately (Hughes [9], Brouillette [10]). Data for the reflector was interpolated from data provided by JPL on 15m and 55m wrap-rib designs. After eliminating some flexible modes from the array and reflector models on the basis of a combined modal momentum and frequency criterion, the flexible substructure models and the rigid spacecraft bus model were combined into an overall spacecraft model with 65 flexible vehicle modes and 8 rigid body modes (Hughes [9]).

The equations describing small motions of the spacecraft can be represented in the following form:

$$\dot{x} = Ax + Bu + Hw \qquad (1)$$

where u denotes the control inputs and w denotes disturbance inputs. When the motion of the system (1) is described in undamped modal coordinates, the state vector x contains the amplitude and velocity associated with each mode and A assumes the form

$$A = \begin{bmatrix} 0 & I \\ -\Omega^2 & -(D+G) \end{bmatrix} \qquad (2)$$

with

I : identity matrix
$\Omega = \text{diag}(\omega_i)$, ω_i = frequency of ith mode
D : damping matrix (non diagonal)
G : gyroscopic matrix (non diagonal)

The control objective is accurate attitude and communications beam pointing. Analysis of the ray geometry etc. leads to the definition of a performance output vector

$$z = Px \qquad (3)$$

where P is a performance distribution matrix describing how much the excitation of each state contributes to the elements of the beam pointing error. The control objective is expressed by the cost functional

$$V = \int_0^{\infty} z^T Q z \, dt \qquad (4)$$

where Q is a positive definite weighting matrix for the error components (e.g., roll, pitch and yaw error). This cost functional is used in the further reduction of the model order by Modal Cost Analysis, (Skelton, Hughes, Hablani [11], [12], [13]). The total cost V_f for all flexible modes is the sum of the cost V_i of the individual flexible modes :

$$V_f = \sum_{flex\ modes} V_i \qquad (5)$$

185

If the structure is lightly damped (D assumed diagonal) and if there is no stored momentum ($G = 0$), the cost V_i of mode i depends only on its own characteristics. For unity impulsive type inputs, the cost of each flexible mode is:

$$V_i = \frac{p_i^T Q p_i + \omega_i^2 p_{m+i}^T Q p_{m+i}}{4\varsigma_i \omega_i^3} \|b_{m+i}\|^2 \tag{6}$$

with

$$p_i = i^{th} \text{ column of } P$$

$$b_i = i^{th} \text{ row of } B$$

$$m = \text{total number of modes}$$

$$\varsigma_i = \frac{1}{2\omega_i} D_{ii}$$

In a relatively simple expression, (6) states to what degree the following modal characteristics influence the modal cost: modal frequency ω_i, modal damping ratio ς_i, the importance of each mode in the performance output (p_i) and the degree to which each flexible mode is excited (b_i). Modal cost of rigid body modes is not defined ("∞") in this sense

The 11 most significant modes account for 97 percent of the total cost of all 65 flexible modes of this model Fig 5 shows their frequencies and respective cost. A reduced model containing (besides rigid body modes) only these 11 flexible modes was chosen as benchmark model for control studies.

For the control benchmark case, the spacecraft is assumed to be in a conventional N-S stationkeeping maneuver. Attitude control during stationkeeping has been identified as a critical operation during recent analysis of the Demonstration MSAT mission, due to large unknown torques caused by thrust level uncertainties The control objective is to maintain attitude control and beam pointing during the stationkeeping maneuver Stationkeeping itself is assumed to be controlled by a strategy independent of attitude control and hence the three translational spacecraft rigid body modes, describing the orbital kinematics, are deleted from the model. Fig 6 shows the baseline actuator configuration with three reaction wheels and four thrusters located at the spacecraft bus, four thrusters at the tower tip and two reflector gimbal torquers. During stationkeeping a thruster based control system is assumed with the reaction wheels locked at zero speed. For the control studies, 22 N bipropellant thrusters were baselined in order to explore the implications of relatively high thrust levels on the structure, although electric propulsion is considered a more viable option, especially for stationkeeping.

For control design, the following simplifying assumptions are made: the 8 nonlinear (one way) thrusters are combined to form 5 equivalent independent, linear actuators. (An approximately linear thruster characteristic may be obtained by Pulse Width Modulation or Pulse Frequency Modulation although some excitation of high frequency modes will be concomitant with this technique) Further, sensors with ideal characteristics are assumed to provide the following measurements. spacecraft bus attitude and angular rate about three axes, two reflector gimbal angles, and the relative displacement between spacecraft bus and tower tip in two directions. The sensor output y is described by

$$y = Cx \tag{7}$$

The 10 outputs were chosen from a larger set, considering the feasibility of the sensor implementation and the spectral condition of the system output matrix C

Thus, the benchmark control model described by eq (1) and (6), has 7 control inputs, 10 measured outputs, 5 rigid body modes, and 11 flexible modes and is completely controllable and observable

Sensors and actuators located at the spacecraft bus and reflector hub, respectively, are mechanically connected by rigid mounts. However, sensors and actuators are not dual $(B \neq C^T; CB > 0)$.

The requirements for the control system are:

1) stabilization of attitude and communications beam in presence of uncertain and unmodelled plant dynamics,

2) regulation of attitude and beam against environmental disturbances and thruster inbalances, and

3) spacecraft rigid body response time constants in the order of magnitude of the lowest spacecraft flexible mode. (The absolute value of the closed-loop eigenvalues associated with one or more rigid vehicle modes shall be larger than the frequency [rad/s] of the lowest frequency elastic mode.)

Although it has not been shown yet that the last requirement is a necessity for the OMSAT mission it is considered important for this study in order to ensure that interaction between control system and structure occurs.

4. Preliminary Comparison of Control Techniques

A number of methods have been suggested in the literature to solve the generic space structure controls problem and most current methods were summarized by Balas [14]. Kosut, Salzwedel and Emami-Naeini [15] present a comparison of five control techniques applied to a tetrahedral truss structure. Under this project, so far the following control techniques were applied to the OMSAT benchmark:

1) standard linear optimal regulator (LOR) with Luenberger observer,

2) LOR/observer with selective spill-over suppression,

3) LOR/observer with frequency shaping,

4) LOR with closed-loop system reduction by cost decoupling,

5) Robust Servomechanism (optimal dynamic output feedback).

Work on a comparison of these techniques only has started, and the results presented here are preliminary. All methods with the exception of 5 initially are applied without consideration of the requirement 2) for disturbance rejection. The undisturbed spacecraft model $(w = 0)$ is decomposed into a controlled subsystem, a secondary subsystem and a residual subsystem as shown in (8), with the subscripts c,s,r denoting controlled, secondary and residual respectively:

$$\begin{bmatrix} \dot{x}_c \\ \dot{x}_s \\ \dot{x}_r \end{bmatrix} = \begin{bmatrix} A_{cc} & A_{cs} & A_{cr} \\ A_{sc} & A_{ss} & A_{sr} \\ A_{rc} & A_{rs} & A_{rr} \end{bmatrix} \begin{bmatrix} x_c \\ x_s \\ x_r \end{bmatrix} + \begin{bmatrix} B_c \\ B_s \\ B_r \end{bmatrix} u \qquad (8)$$

$$y = [C_c C_s C_r] \begin{bmatrix} x_c \\ x_s \\ x_r \end{bmatrix} \qquad (9)$$

$$z_c = P_c x_c \qquad (10)$$

For all methods except 4), this decomposition is just a rearrangement of the modes of the modal representation (1) The dimensions of the sub-state vectors x_c, x_s, x_r and the order of the subsystems are denoted n_c, n_s, and n_r respectively. The control systems are designed on the basis of the controlled subsystem, and in some cases with additional information about the secondary subsystem. The residual subsystem comprises all known plant dynamics not used for control system design. The minimum numbers of controlled and secondary states required to design a control system which fulfils the requirements 1) and 3) are used as criteria for comparison of the control methods. For all design cases, the minimum n_c and n_s are summarized in Table 1, together with the following additional criteria: the minimum number of flexible modes required to be included in the controlled subsystem, m_c, order and stability of the feedback compensator system and the maximum relative perturbation Δ of the plant modal frequencies tolerated by the control system (as implicitly defined by $\Omega_{perturbed} = (1 - \Delta)\Omega$).

LOR and Luenberger observer

This design method yields a feedback compensator of the form

$$u(s) = -F(sI - A_c + EC_c + B_cF)^{-1}Ey(s) \tag{11}$$

with

E : observer gain matrix
F : controller gain matrix
s : Laplace variable

No secondary system is considered in this method. With well known procedures (e.g. see [16]), E is designed such that $A_c - EC_c$ has desirable eigenvalues and F is determined such that the control law $u = -Fx_c$ minimizes the cost functional

$$J = \int_0^\infty (z_c^T Q z_c + \rho u^T u)e^{2\alpha t}dt \tag{12}$$

with

ρ : scalar relative cost factor
α : exponential weighting factor

The location of closed-loop eigenvalues is controlled by ρ and α and chosen to fulfil requirement 3) For design case 1a the controlled flexible modes are selected according to their modal cost (Fig.5) and inclusion of 10 flexible modes into the controlled subsystem is required to obtain a satisfactory control system with this design procedure ($n_c = 30, m_c = 10$). In design case 1b the flexible modes to be included in the controlled subsystem are selected by ascending frequency. Only the nine lowest frequency modes need to be considered to obtain a satisfactory result. This indicates that modes with low open-loop modal cost may still be important for control design, as in this case the mode at 1.02 rad/s (Fig.5) Other observations are that, for this particular design, the compensator system (11) is unstable (Johnson [17]) and that the closed-loop system is very susceptible to perturbations of the plant dynamics A change of less than one percent in the modal frequencies is sufficient to cause instability.

LOR/observer with selective spill-over suppression

The spill-over suppression techniques applied here was suggested by Yuan [18] and an essentially similar method is described by Kissel and Lin [19]. It yields a compensator of the form (11) with E and F having particular properties. For observation spill-over suppression (design case 2a in Table 1),

188

F is determined on the basis of (12) as described above while the observer gain matrix E is chosen such that C_s is in its null space:

$$E = E_O T_O \tag{13}$$

with

$$T_O C_s = 0 \tag{14}$$

By this choice of E, the observation spill-over term is nulled for the secondary subsystem, which may only contain a limited number of flexible modes for a nontrivial transformation T_O to exist $(n_s < dimension(y))$. Accurate knowledge of the mode shape of these few selected modes is required in order to compute T_O, while the modal frequencies do not need to be known. Application of this method in conjunction with full order Luenberger observer design is appealing, because it makes use of the available design freedom without restricting free pole placement.

However, two difficulties are encountered in the benchmark case: although one would expect to be able to suppress spill-over from 4 secondary modes because there are 10 measured outputs, the pair $\{T_O C_c, A_{cc}\}$ becomes unobservable when attempting to suppress more than two modes. The compensator with spill-over suppression for two modes fails to stabilize the system even in absence of any residual plant dynamics $(n_r = 0)$, because the controlled and secondary (suppressed) modes of the system are lightly coupled through the off-diagonal elements of the damping matrix D. This problem possibly could be overcome by transformation of the system to damped gyroscopic natural modal coordinates (Vigneron [20], Meirovitch [21]). The problem indicates however, that the suppression technique is not very robust because the coupling through damping is extremely light. Stored momentum aboard the spacecraft would significantly increase the coupling between flexible modes in non-gyroscopic coordinates.

In a dual manner, the method may also be applied to suppress control spill-over (design case 2b). The control feedback gain matrix F of the compensator (11) is chosen to be of the form

$$F = T_C F_C \tag{15}$$

with

$$B_s T_C = 0 \tag{16}$$

In the application of this method to the benchmark similar problems as for observation spill-over suppression become apparent. The pair $\{B_C T_C, A_{cc}\}$ becomes uncontrollable when trying to suppress spill-over from more than one mode. The closed-loop system is unstable in presence of the suppressed mode, without any residual modes. The combination of control and observation spill-over suppression for one mode (case 2c) yields a compensator which stabilizes the closed-loop system in presence of the suppressed mode, but fails to stabilize the system when residual modes are included in the plant dynamics.

LQR/observer with frequency shaping

The extension of the LQG method to include frequency-shaped weighting matrices in the cost functional is described by Gupta [22]. In the application to the OMSAT benchmark problem, the following cost functional is used to optimize the controller:

$$J = \int_{-\infty}^{\infty} [x_c^*(j\omega) G^*(j\omega) P_c^T Q P_c G(j\omega) x_c(j\omega) + \rho u^*(j\omega) u(j\omega)] d\omega \tag{17}$$

where * denotes conjugate transpose, ω is frequency and $G(j\omega)$ is a n_c by n_c frequency shaping matrix of the following form:

$$G = \text{diag}(g_i)$$

$$g_i = \begin{cases} \frac{\omega_i}{j\omega+\omega_i} & \forall i = 1...\frac{n_c}{2} \\ \\ 0 & \forall i = \frac{n_c}{2}+1 \ .n_c \end{cases} \qquad (18)$$

This diagonal form is chosen, because relative and combined weighting of the states according to the control objective is already performed by $P_c^T Q P_c$. The zero elements correspond to beam pointing rate terms which have zero weight. The resulting compensator is of the form of (11) but with additional dynamics in the state-feedback controller.

$$F = F(s) = F_F \begin{bmatrix} I \\ ---- \\ G_F(s) \end{bmatrix} \qquad (19)$$

where F_F is a constant state-feedback matrix computed for an appended system with state vector $\begin{bmatrix} x_c \\ q \end{bmatrix}$ and $q(s) = G_F(s)x_c(s)$. Since the beam error rate has no weight in the performance index, the order of the compensator is $\frac{3}{2}n_c$. The order increases significantly when higher order frequency shaping functions are used. In the particular benchmark design case (#3 in Table 1), this method did not yield any improvements over the standard LQR/observer design and the compensator obtained was open-loop unstable.

Closed-Loop System Reduction by Cost Decoupling

This method is a direct extension of Skelton's [19] concept of cost decoupled coordinates to closed-loop systems. To the author's knowledge this extension was presented for the first time by West-Vukovich and Hughes in [24].

For a system of the form (1) the loop is closed by optimal state feedback. The closed-loop system then is transformed to so-called cost decoupled coordinates. In this coordinate system, the cost, as defined by the cost functional of the optimal regulator problem, for regulation upon initial conditions or impulsive disturbances, is the sum of independent cost elements which are a function of the characteristics of each particular state only. The transformation to cost decoupled coordinates is found from the solution to the attendant Riccati equation and the expected value of initial conditions or impulsive disturbances. The closed-loop cost for each state of the transformed system is evaluated and the states with high cost are combined to the controlled subsystem of (8) while the states with low cost form the secondary subsystem. No residual system is considered ($n_r = 0$). Optimal state feedback for the controlled subsystem forms the final controller and may be obtained by truncation of the state feedback gain matrix for the transformed full order system:

$$u = -F_D T_D^T x_c \qquad (20)$$

with

$\qquad F_D$. state-feedback matrix of controlled subsystem in cost decoupled coordinates
$\qquad T_D$ · orthogonal transformation from cost decoupled coordinates to original coordinates.

This approach is still under investigation and, so far, no observer was included in the design The ideal state-feedback control system, however, suffers from control and observation spill-over in the presence of the secondary subsystem The results given in Table 1 (case 4) were obtained for a case

similar, but not identical to the benchmark. Spill-over effects lead to closed-loop instability when the number of controlled states n_c is less than 15.

Robust Servomechanism

This approach developed by Davison [25],[26] optimizes a general dynamical compensator system in order to synthesize a control law. The application of this method to the OMSAT problem is described by Davison [27] and results in a generalized PID type controller and servocompensator of the following form:

$$u = -K_1(y - y_{ref}) - sK_2y - \frac{K_3}{s}(y - y_{ref}) \qquad (21)$$

with

K_i : constant gain matrices

y_{ref} : (filtered) reference input

The compensator gain matrices K_i are determined without reference to any secondary subsystem ($n_s = 0$) However, the measured output required for implementation of this compensator is different than the sensor complement provided in the benchmark model and may include elastic deformation rate signals. The results listed in Table 1 (case 5) were obtained in a design not aimed at the benchmark requirements and violating requirement 3) by an order of magnitude.This design, however, achieves rejection of low frequency disturbances and is robust in the sense of [25].

Table 1

Preliminary Comparison of 5 Control Design Methods applied to the OMSAT Benchmark

Case	Method	n_c	m_c	n_s	Comp. Order	Comp. Stable[a]	Δ
1a	LQR - Modes by Modal Cost	30	10	0	30	no	
1b	LQR - Modes by Frequency	28	9	0	28	no	.009
2a,2b,2c	Spill-over Suppression	*fails to stabilize system*					
3	Frequency Shaping	28	9	0	42	no	.007
4	Closed-Loop Reduction[b]	15	—	17	15[c]		
5	Robust Servomechanism[d]	18	4[e]	0	9[f]	yes	

Remarks.

a: Compensator open-loop stability

b: The case considered here is similar but not identical to the benchmark; the design only approximately fulfils the rigid-body response time requirement.

c: Assumes full-order observer which was not included in this particular design.

d: This design requires other measurements than provided in the benchmark model and violates the rigid-body response time requirement by an order of magnitude.

e: Actual (i e not minimum) number of flexible modes included for design; other results indicate that only as few as one mode may be required to obtain stable design with this method.

f: Assumes availability of rate output signals.

5. Observations, Conclusions and Direction of Further Work

The CAD system KEDDC has been found a very efficient and versatile, almost indispensable tool for the reliable analysis of high-order systems. Its architecture and user interface are particularly well suited for an applied R&D environment.

During the application of several control techniques to a large space structure benchmark problem, it was observed that LQ type methods may require (unrealistically) accurate plant modelling approximately two frequency decades beyond the closed-loop system bandwidth. Modal cost was found not to be a reliable indicator for the importance of flexible modes for control design. The spill-over suppression technique applied failed in presence of weak coupling between flexible modes, e g. due to damping. In the benchmark case, frequency shaping of the cost functional does not result in any improvement over standard LQ methods. Observer based compensators frequently were open-loop unstable. Closed-loop order reduction and the Robust Servomechanism appear promising but have to be investigated more thoroughly before a conclusive comparison can be made.

The criteria used here for comparison are related to the model order required for a given control design method and system performance requirements. However, they appear insufficient to draw strong conclusions, in particular in presence of very small design and model error margins. Other criteria have to be consulted (e.g. those suggested by Kosut et al. [15], Yuan [28] and Davison [29]). A basic problem in comparing control methods on a benchmark case is, however, that the methods are not being directly compared, but rather only particular designs obtained with those methods.

Acknowledgements

The author wishes to thank A.H. Reynaud of CRC for support and encouragement, J. de La-fontaine of DREO, Drs. P.C. Hughes, G. West-Vukovich, G. Sincarsin of DYNACON Enterprises Ltd., Dr. E J Davison of the University of Toronto and Dr. J. S.-C. Yuan of SPAR Aerospace Ltd. for their contributions to this project. Last but not least, the author thanks Dr. C. Schmid and U. Keuchel of Ruhr University for their open minded and active cooperation in the exchange of software.

References

[1] Franklin, C.A , Breithaupt, R.W., "The Canadian Mobile Satellite Program", Pacific Telecommunications Conference, January 8-11, 1984, Honolulu, Hawaii.

[2] Spar Aerospace Ltd , "MSAT Spacecraft Conceptual Design Studies - Executive Summary", November 1981, DOC-CR-SP-81-047B*

[3] Barker, H.F. Jones, A.F , Ravindran, R , Yuan, J. S.-C., "Study on Control of Large Spacecraft - Final Report", May 1981, DOC-CR-SP-81-013*

[4] Naderi F., et al, "Land Mobile Satellite Service (LMSS): A Conceptual System Design and Identification of the Critical Technologies" JPL, February, 1982 N82-28325

[5] Reynaud, A.H , Barker, H.F., Hughes, P.C., "Attitude and Communications Beam Control System for Third Generation Spacecraft", Second Canadian Conference on Astronautics, Ottawa, Nov. 30-Dec. 1, 1982.

[6] Schmid, C., "KEDDC - A Computer Aided Analysis and Design Package for Control Systems", 1982 American Control Conference, Arlington, VA, June 14-16, 1982

[7] Schmid, C , "CAD of Adaptive Systems Using KEDDC", IFAC Symposium on Computer-Aided Design of Control Systems, Zürich, Switzerland, August 29-31, 1979.

[8] Hughes, P.C , "Laboratory Demonstration of Control Techniques for Third Generation Spacecraft - Executive Summary (83-84)", March 1984, DOC-CR-84-011*

[9] Hughes, P C., "Development of Dynamics Models and Control System Design for Third Generation Spacecraft - Executive Summary", August 1982, DOC-CR-SP-056*

[10] Brouillette, M., "Normal Mode Analysis of 8.2 kW MSAT Arrays", Spar Structural Mechanics Report, Spar Aerospace Ltd , January 1982.

[11] Hughes, P.C. and Skelton, R E., "Model Truncation for Flexible Spacecraft," J. Guidance and Control, Vol 4, No. 3, May-June 1981, pp. 291-297.

[12] Skelton, R.E. and Hughes, P.C., "Modal Cost Analysis for Linear Matrix-Second-Order Systems," J. Dynamic Systems Measurement and Control, Vol. 102, Sept. 1980, pp. 151-158

[13] Skelton, R.E., Hughes, P.C. and Hablani, H.B., "Order Reduction for Models of Space Structures Using Modal Cost Analysis," J. Guidance, Control, and Dynamics, Vol. 5, No. 4. July-August, 1982, pp. 351-357.

[14] Balas, M.J , "Some Trends in Large Space Structure Control Theory: Fondest Hopes; Wildest Dreams", IEEE Transactions on Automatic Control, Vol. AC-27 June 1982.

[15] Kosut, R L , Salzwedel, H., Emami-Naeini, A., "Robust Control of Flexible Spacecraft" Journal of Guidance and Control, Vol. 6. No. 2, March- April 1983, pp. 104-111.

[16] Kailath, T., "Linear Systems", Prentice Hall Inc., Englewood Cliffs, N.Y., 1980.

[17] Johnson, C.D., "State Variable Design Methods May Produce Unstable Feedback Controllers", International Journal of Control, Vol. 29, No. 4, 1979, pp. 607-619

[18] Yuan, J. S.-C., "Optimal Stationkeep and Attitude Control of Flexible Spacecraft", October 1982, DOC-CR-SP-82-064"*.

[19] Kissel, G J., and Lin, J.C., "Spill-over Prevention via Proper Synthesis/Placement of Actuators and Sensors", 1982 American Control Conference, Arlington, VA, June 14-16, 1982, Proceedings pp. 1213-1218, Vol. 3.

[20] Vigneron, F.R.,"Natural Modes and Real Modal Variables for Flexible Spacecraft", CRC Report No 1348, Department of Communications, Ottawa, Canada, November 1981 *

[21] Meirovitch, L., Baruh, H., "Optimal Control of Damped Flexible Gyroscopic Systems", J. Guidance and Control, Vol. 4, No. 2, March-April 1981, pp. 157-163

[22] Gupta, N.K., "Frequency-Shaped Cost Functionals: Extension of Linear-Quadratic-Gaussian Design Methods", Journal of Guidance and Control, Nov-Dec 1980, pp. 529-535.

[23] Skelton, R E., "Cost Decomposition of Linear Systems with Application to Model Reduction", Int. J. Control, Vol. 32, No. 6, 1980, pp. 1031-1055

[24] West-Vukovich, G., and Hughes, P.C., "Laboratory Demonstration of Control Techniques for Third Generation Spacecraft: Model Order Reduction (Part 1)", DOC-CR-84-012*, March 1984

[25] Davison, E J., "Robust Control of a Servomechanism Problem for Linear Time-Invariant Multivariable Systems", IEEE Trans. on Automatic Control, Vol. AC-21, No., 1, 1976, pp. 25-34

[26] Davison, E.J., Goldenberg, A., "Robust Control of a General Servomechanism Problem: The Servo-Compensator", Automatica, Vol. 11, 1975, pp. 461-471.

[27] Davison, E.J., "A Study on the Control of Third Generation Spacecraft", Workshop on Identification and Control of Large Space Structures, San Diego, CA., June 4-5, 1984.

[28] Yuan, J. S.-C., "Demonstration of Flexible Spacecraft Control Design Software and Techniques - Final Report", May 1984, DOC-CR-84-020*

[29] Davison, E J.,"Study of Control Techniques Applicable to Third-Generation Spacecraft – Part III", February 1984, DOC-CR-84-002 *

REFLECTOR 44.4 M DIA.

42.5 M DIA. APERTURE

REFLECTOR
GIMBAL

FEED ARRAY
4.7 x 9.2 M

BUS STRUCTURE

23.6 M

46.9 M

0.5 M DIA. ASTROMAST

38 M

SOLAR ARRAY
8.2 kW EOL

4 M
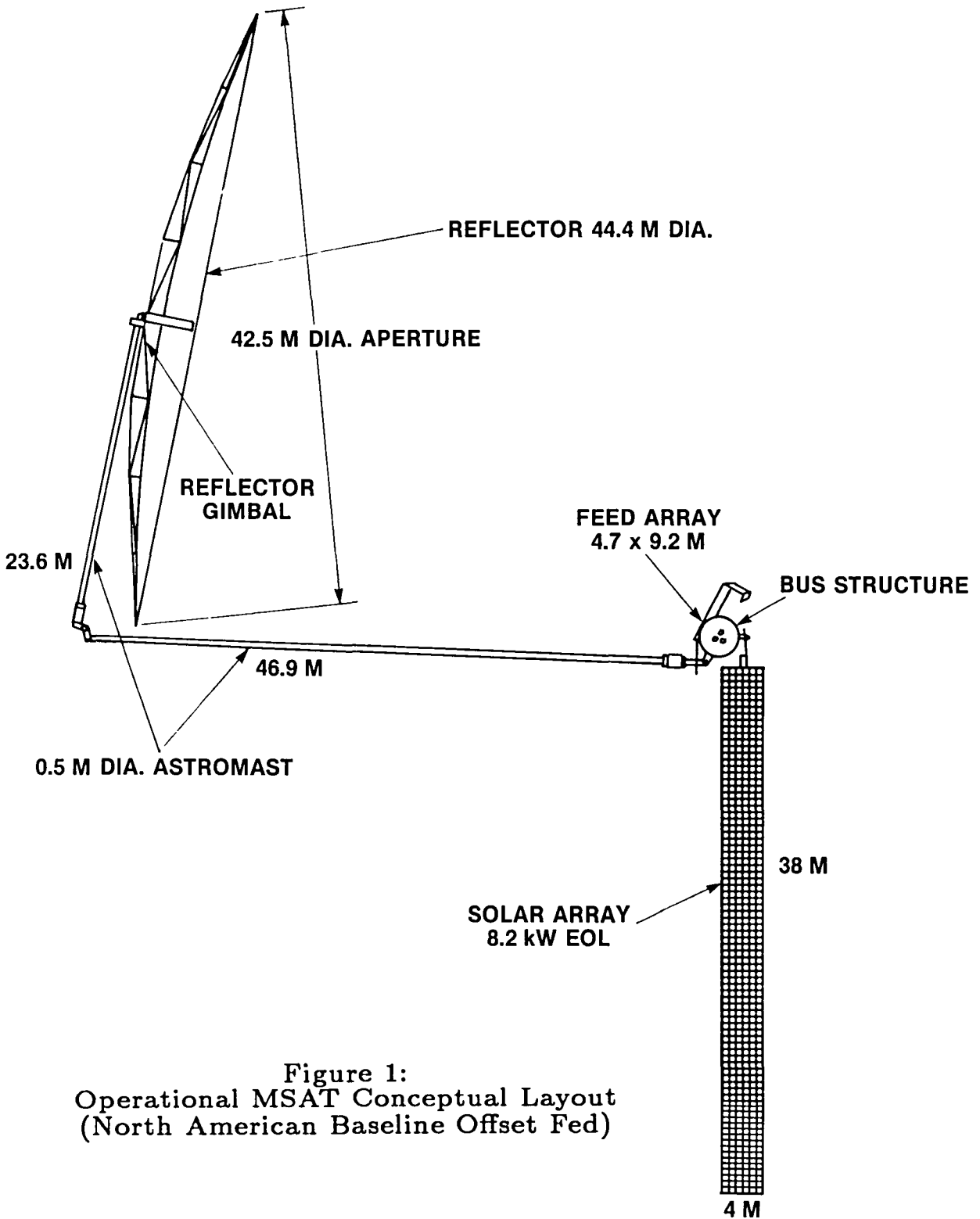
Figure 1:
Operational MSAT Conceptual Layout
(North American Baseline Offset Fed)
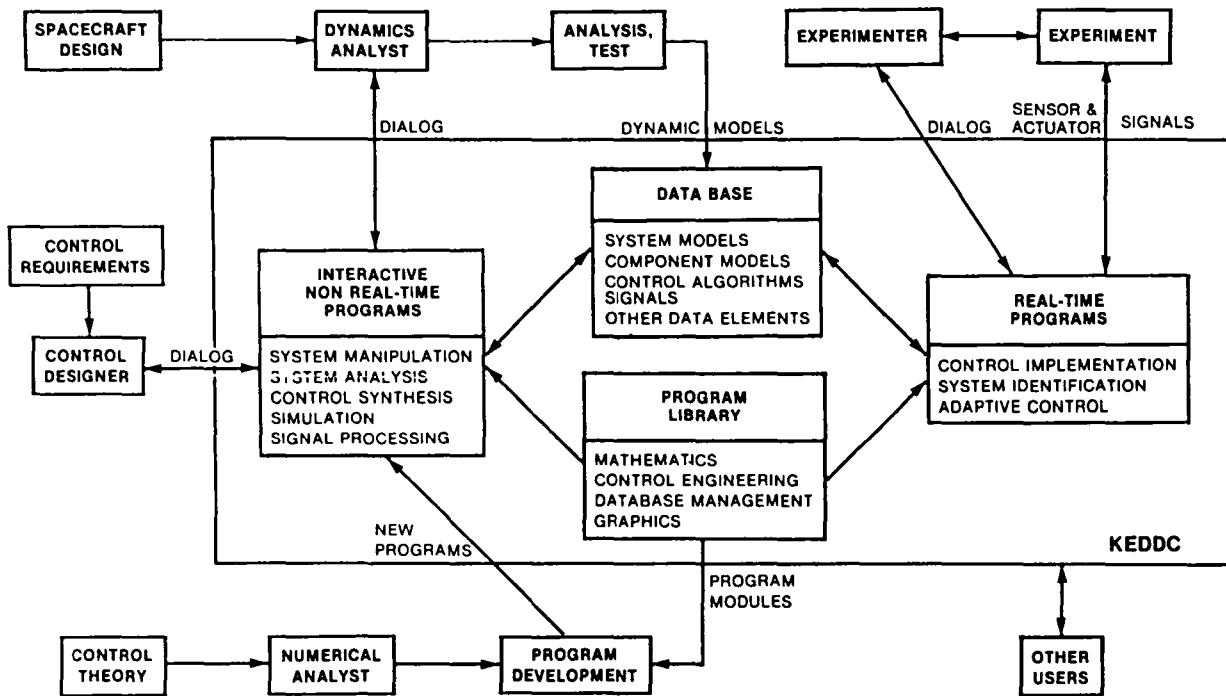
Figure 2: Computer-Aided Control Design System and Applications Environment

1 {u(i),y(i)} series of deterministic or stochastic signals
2 {R$_{xx}$(i),R$_{xy}$(i)} series of auto- or crosscorrelation values
3 {g(i)} discrete values of pulse responses
4 {h(i)} discrete values of step responses
5 {G$_{ik}$(s)} transfer function in s-domain
6 {G$_{ik}$(z)} transfer function in z-domain
7 {G$_{ik}$(jω)} discrete values of frequency responses
8 {A,B,C,D} matrices for continuous state space
9 {A',B',C',D'} matrices for discrete state space
10 {P,Q} polynomial matrices for MFD

Figure 3 System Description Forms and
Transformations Supported by KEDDC

Figure 4: OMSAT Dynamics Modelling

Figure 5:Cost and Frequency of Benchmark Model Elastic Modes
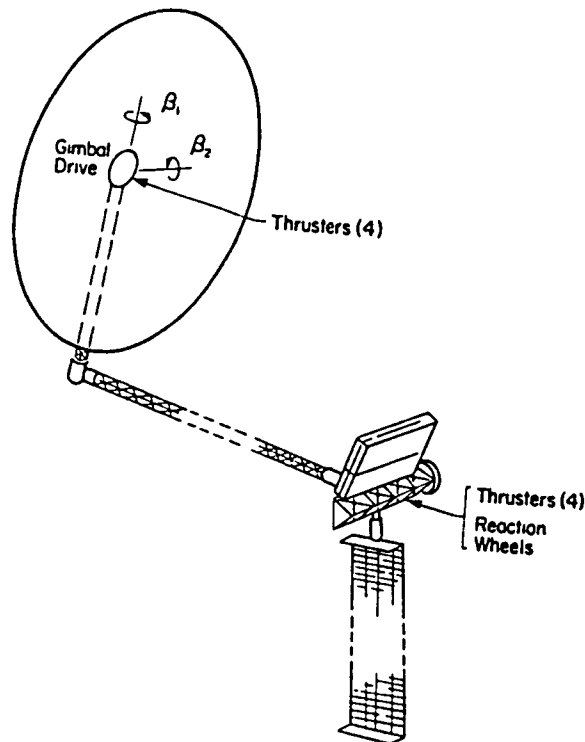
Figure 6: OMSAT Actuator Configuration

CONTROL OF LARGE ANTENNAS BASED ON ELECTROMAGNETIC PERFORMANCE CRITERIA

Y. H. Lin, M. Hamidi, and M. Manshadi
Jet Propulsion Laboratory
California Institute of Technology
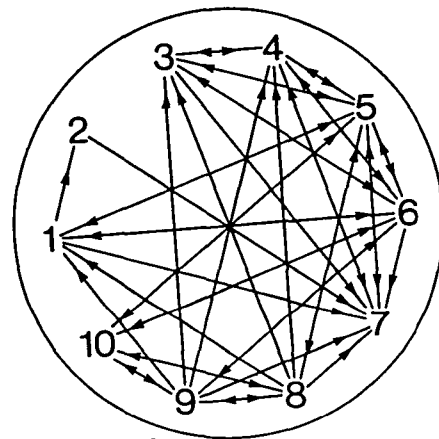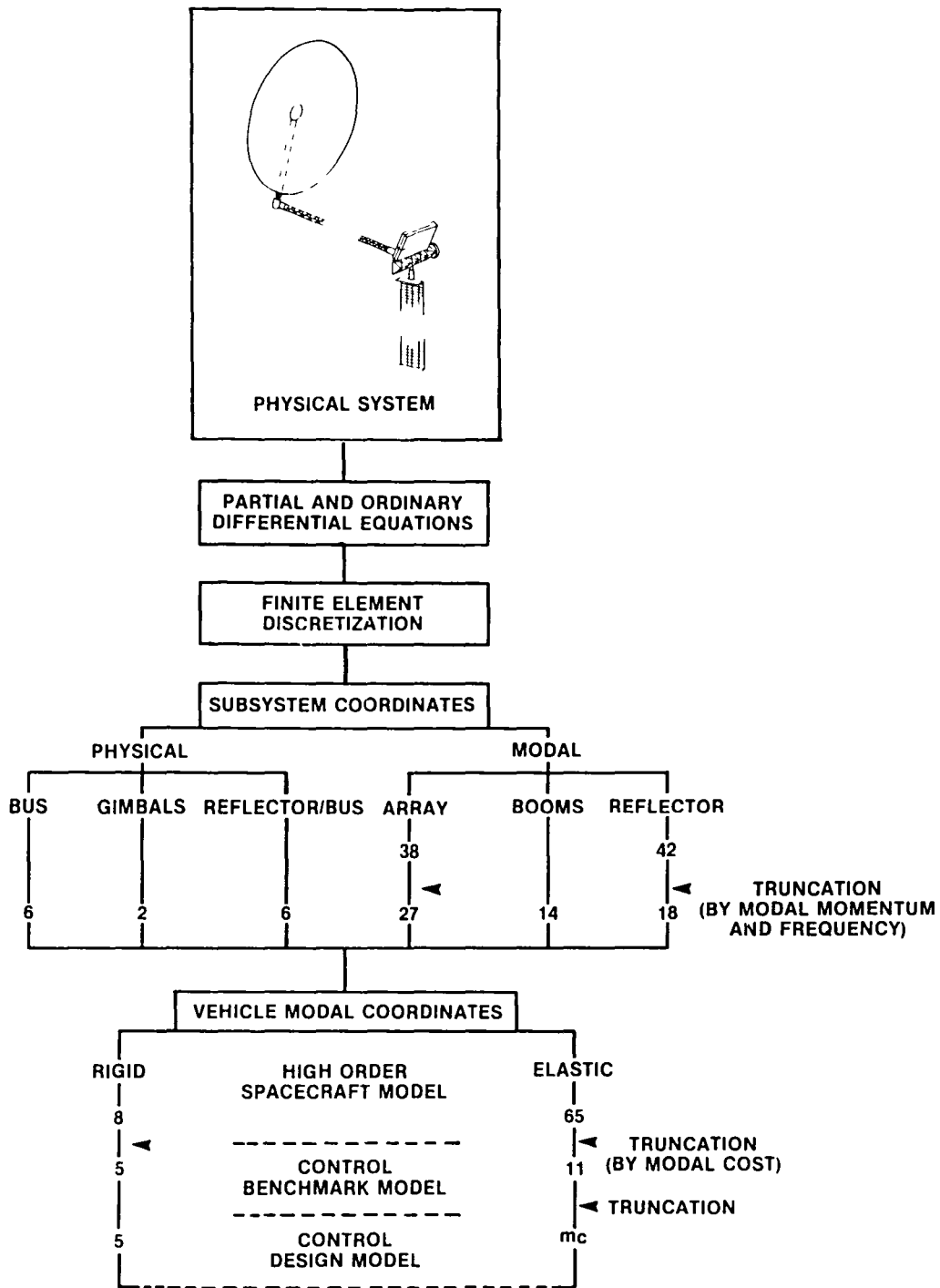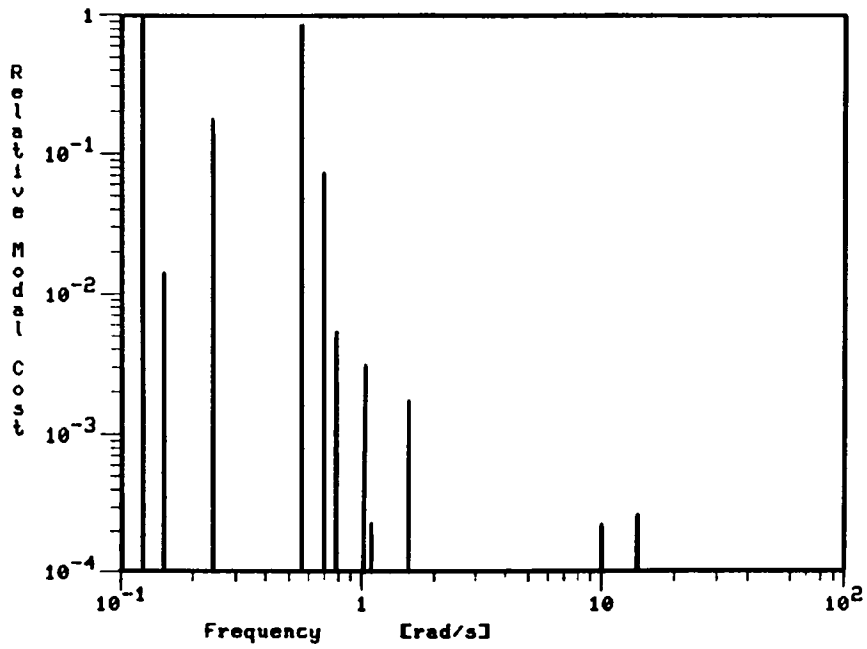Pasadena, CA 91109

I. INTRODUCTION

Large space antenna missions that have been studied recently at the Jet Propulsion Laboratory include Land Mobile Satellite System (LMSS) for communications, Surveillance Satellite System (SSS) for aircraft position determination, Very Long Baseline Interferometer (VLBI) for radio astronomy, and Large Deployable Reflector (LDR) for infrared through submillimeter astronomy.

LMSS is a multiple-beam communications mission, intended to provide telephone service to mobile users across the continental U.S. (Figure 1). Its operating frequency is between 806 and 890 MHz. The mission calls for a single shuttle launch in mid-90's. After the launch, the antenna will be transferred to and operated in a geostationary orbit.

One candidate for LMSS is the wrap-rib antenna shown in Figure 2. It consists of a 55-meter reflector dish and a spacecraft bus mounted with the antenna feed. The antenna dish and the spacecraft bus are connected by an L-shaped boom. The long leg of the boom is approximately 80 meters long and the short one 33 meters. The total system mass is 9695 lbs.

The same configuration has also been considered for the SSS mission which calls for a constellation of 4 or more large antennas to provide surveillance and data communication for 50,000 simultaneously airborne aircraft (Figure 3). To achieve desired position determination accuracy, a

highly inclined and highly eccentric 24 hours orbit is considered. The operating frequency for this system is in the range of 1030-1090 MHz.

The VLBI mission is mainly concerned with the astrophysical investigation of the nuclei of radiogalaxies and quasars. The concept has been demonstrated at centimeter wavelengths exploiting the longest baselines available on the surface of the Earth. Even at centimeter wavelengths, compact radio sources are found, requiring yet longer baselines to investigate their structure. To place an antenna in space will allow the smaller spatial structural details of the compact source to be explored (Figure 4). The orbiting antennas considered have sizes from 15 meters to 40 meters and observing frequencies of 1.7, 5, and 22 GHz. The orbiting antenna will be placed in an elliptical orbit with inclination of about 60°.

LDR is to be a dedicated astronomical observatory in space operating in the far infrared and submillimeter region of the spectrum where the Earth's atmosphere is nearly opaque. This is generally between 30μm and 1mm wavelength. Unique LDR observational capabilities include studies of star formation and planetary systems in our own and nearby galaxies and cosmological studies of the structure and evolution of the universe. The major elements of LDR (Figure 5) are the 20 meter segmented primary mirror, a 20-30 meter thermal shroud, the spacecraft bus, and two solar arrays. The total mass of the system is approximately 27,000 Kg, the orbit altitude about 750 Km, and the orbit inclination 28°.

The antenna control requirements for missions described above and other selected missions are summarized in Figure 6 for comparison. For communications and surveillance missions such as LMSS and SSS, the typical pointing accuracy required is about 0.1° and the surface RMS (root-mean-square) accuracy a few (5) mm. For VLBI, the surface accuracy requirement

THE LAND MOBILE SATELLITE SYSTEM
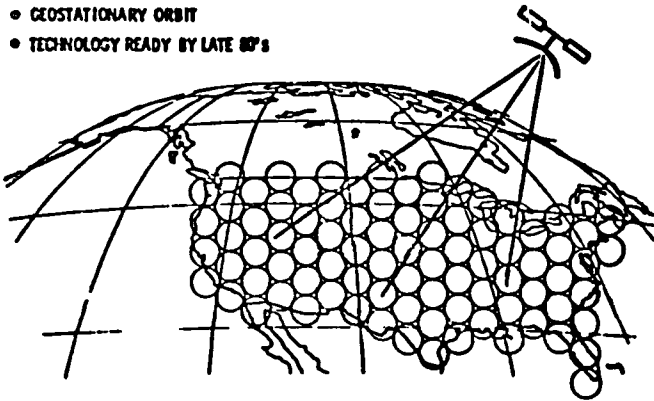
Fig. 1   LMSS Mission

TOTAL MASS   9615 LBS

MOMENTS OF INERTIA
$$I_x = 2.91 \times 10^6 \ \text{SLUG-FT}^2$$
$$I_y = 2.64 \times 10^6$$
$$I_z = 0.37 \times 10^6$$

PRODUCTS OF INERTIA
$$I_{xy} = -3.56 \times 10^3$$
$$I_{xz} = -4.22 \times 10^3$$
$$I_{yz} = 0.72 \times 10^6$$

ATS-6

THE SHUTTLE

55 METERS DIAMETER

DISH+RIB MASS = 1277 LBS

UPPER BOOM LENGTH = 33 CM MASS = 69 LBS

EARTH

MASS OF BUS = 7450 LBS

FOCAL LENGTH 82.5 METERS

LOWER BOOM LENGTH = 80 METERS MASS = 210 LBS

9 METERS DIAMETER
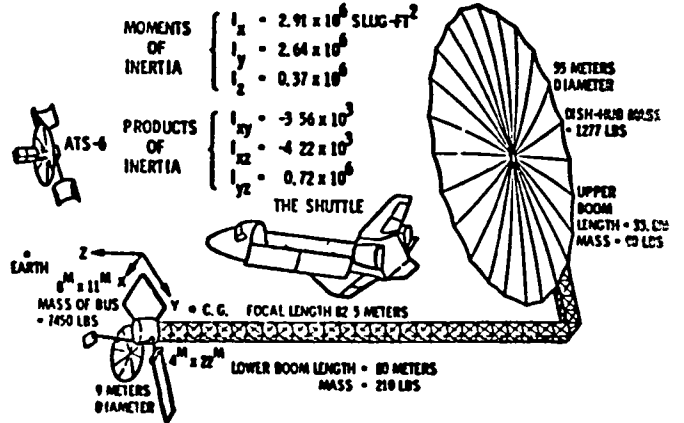
Fig. 2   Wrap-Rib LMSS Configuration and Mass Properties
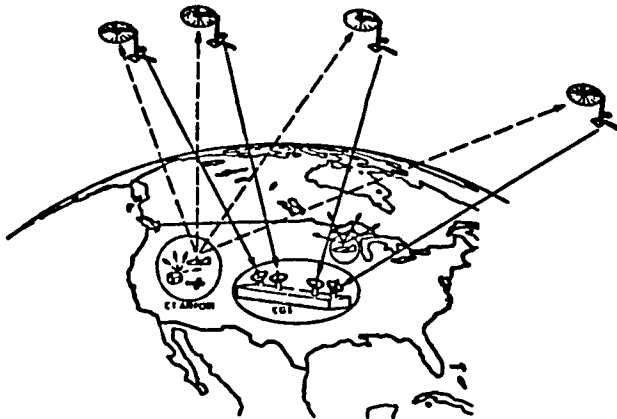
Fig. 3   Surveillance Satellite System Concept

TO CELESTIAL RADIO SOURCE

ORBITING ANTENNA

SIGNAL FROM SOURCE

GROUND ANTENNAS

EARTH

SCIENTIFIC CONCERNS OF VLBI

- QUASARS GALACTIC NUCLEII
- INTERSTELLAR MASERS
- RADIO STARS
- PULSARS
- INTERSTELLAR MEDIA
- ASTROMETRY
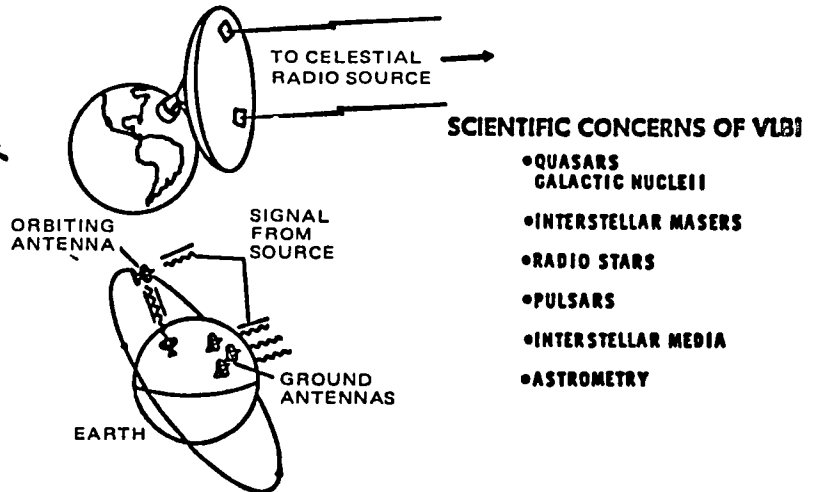
Fig. 4   Orbiting VLBI: Synthesizing Antennas Larger Than the Earth

Fig. 5   Large Deployable Reflector

SPACE TELESCOPE   SIRTF   MMS LANDSAT D   GALILEO VOYAGER   SEASAT VIKING

SURFACE ACCURACY, mm

RADIOMETERS

VLBI ODSRS-RF

COMMUNICATIONS

LDR ODSRS-OPTICAL
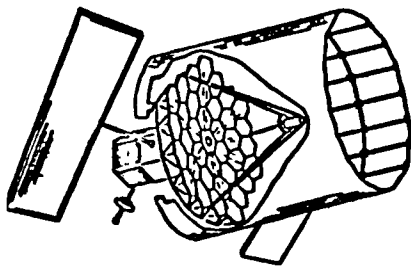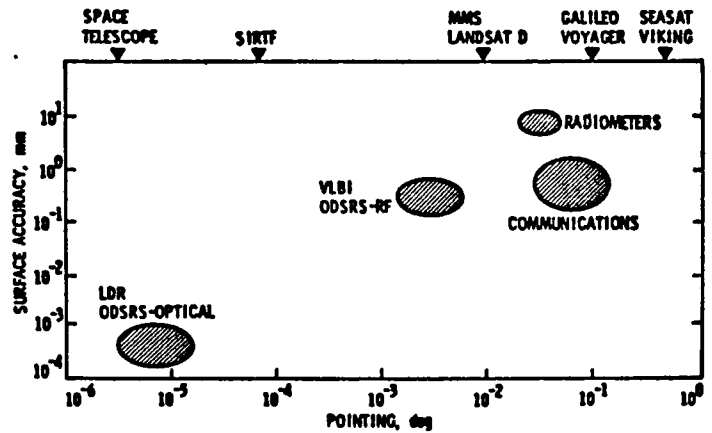
POINTING, deg

Fig. 6   Antenna Control Requirements

is slightly more stringent, and the pointing accuracy tighter by an order of magnitude. For LDR, the pointing accuracy is about 10^{-5} degree (0.04 arc second), similar to the one required for the Space Telescope. The RMS surface error, however, is in the sub-micron region.

The control of these large antennas has been studied and a hierarchy of control designs with increasing sophistication has been developed. The relative performance of the various control designs has also been evaluated[3].

Traditionally, control designs have been developed based on antenna dynamic models only and the antenna's electromagnetic (EM) information has not been used. Therefore, the control designs were aimed at the minimization of a performance index involving antenna vibration errors which were weighted in a heuristic manner.

However, antenna dynamic errors in the performance index can be weighted according to their relative importance to the electromagnetic (EM) performance as will be illustrated in this paper. The potential benefit of utilizing additional antenna electromagnetic information is that either a better EM performance will be achieved with the same amount of control effort, or the same EM performance will be achieved with less control effort, or both.

II. ANTENNA ELECTROMAGNETIC FIELD MODEL

Consider the reflector antenna shown in Figure 7. The reflector surface Σ is constructed by intersecting a circular cylinder with an arbitrary curved surface. The cylinder axis is taken as the z axis; the x-y plane is perpendicular to the z axis. The projection of Σ on the x-y plane is the circular region o with radius a. The feed is assumed to be located at some arbitrary point.

The far-field approximations for the scattered electric and magnetic fields of the offset-fed antenna are readily evaluated using a technique developed by Y. Rahmat-Samii and V. Galindo-Israel.[1] A brief summary of this technique is presented in the following paragraphs.
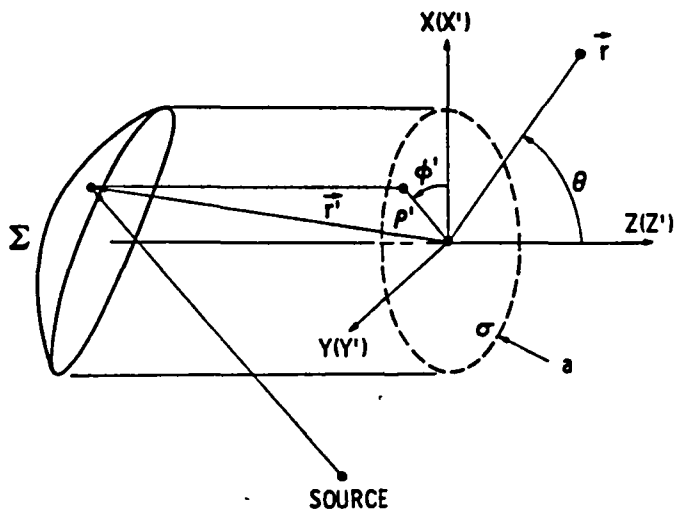
Fig. 7. Offset Shaped Reflector Antenna

The electromagnetic fields E and H are given by

$$\begin{cases} H = \nabla \times A \\ \\ E = \dfrac{1}{j\omega\varepsilon} \nabla \times H \end{cases}$$

A is the vector potential expressed as:

$$A = \int_{\Sigma} J \, \frac{e^{-jk|r-r'|}}{4\pi|r-r'|} \, ds'$$

203

where J is the induced current on the reflector surface due to the magnetic field H_s radiated by the source. It is given by[2]

$$J = 2\hat{n} \times H_s$$

where $\hat{n}$ is the unit vector normal to the reflectors surface and directed towards the positive direction of the z axis.

Introducing the far-field approximations in the expressions for E and H, one obtains[1]

$$\begin{cases} H = jk \frac{e^{-jkr}}{4\pi r} \ \left[T_\phi \, \hat{\theta} - T_\theta \, \hat{\phi} \right] + 0 \, r^{-2} \\[3em] E = -jk\eta \frac{e^{-jkr}}{4\pi r} \ \left[T_\theta \, \hat{\theta} + T_\phi \, \hat{\phi} \right] + 0 \, r^{-2} \end{cases}$$

where $\eta = \sqrt{\frac{\mu}{\varepsilon}}$, the parameters (r,θ,ϕ) are the coordinates of the observation point, $\hat{\theta}$ and $\hat{\phi}$ the unit vectors corresponding to θ and ϕ, and T the radiation integral given by

$$T = \int_\Sigma J(r') \, e^{jkr' \cdot \hat{r}} \, ds'$$

It has been found that the radiation integral provides a very accurate solution for predicting the far-field radiations of reflector antennas. The necessity of having an efficient technique for the evaluation of this integral stems from the fact that it has to be computed accurately each time the observation angles change. Moreover, the integrand of the radiation integral oscillates rapidly and thus makes the integration more strenuous, for large reflectors.

To circumvent the difficulties in the integration, the radiation integral is first expressed in terms of a summation of Fourier Transforms

of an "effective" aperture distribution

$$T = \sum_{p=0}^{p \to \infty} G_p (\theta) \int_0^{2\pi} \int_0^a Q_p(\rho',\phi') e^{jk\rho' B \cos(\Phi-\phi')} \rho' d\rho' d\phi'$$

where B and ϕ are functions of the observation angles θ and ϕ.

The Fourier Transform integrals are then expanded in terms of Jacobi-Bessel series by writing that

$$Q_p(as',\phi') = \sum_{n=0}^{+\infty} \sum_{m=0}^{+\infty} \left[{}_pC_{nm} \quad {}_pD_{nm} \right] \begin{bmatrix} \cos n\phi' \\ \sin n\phi' \end{bmatrix} F_m^n(s')$$

where F_m^n (.) are the modified Jacobi polynomials defined by

$$F_m^n(x) = \sqrt{2(n+2m+1)} \ P_m^n(1-2x^2) \ x^n$$

$$P_m^n(x) = \frac{(-1)^m 2^{-m}}{m!} (1-x)^{-n} \frac{d^m}{dx^m} \left[(1-x^2)^m (1-x)^n \right]$$

and the coefficients ${}_pC_{nm}$ and ${}_pD_{nm}$ are given by

$$\begin{Bmatrix} {}_pC_{nm} \\ {}_pC_{nm} \end{Bmatrix} = \frac{\varepsilon_n}{2\pi} \int_0^{2\pi} \int_0^1 Q_p(as',\phi') \begin{Bmatrix} \cos n\phi' \\ \sin n\phi' \end{Bmatrix} F_m^n(s') s' ds' d\phi'$$

$$\varepsilon_n = \begin{cases} 1 & n=0 \\ 2 & n\neq 0 \end{cases}$$

Finally, the radiation integral is expressed as

$$T = 2\pi a^2 \sum_{p=0}^{p \to \infty} G_p(\theta) \sum_{n=0}^{n \to \infty} \sum_{m=0}^{m \to \infty} j^n \left[{}_pC_{nm} \quad {}_pD_{nm} \right]$$

$$\begin{Bmatrix} \cos n\phi \\ \sin n\phi \end{Bmatrix} \sqrt{2(n+2m+1)} \cdot \frac{J_{n+2m+1}(kaB)}{kaB}$$

where J_n(.) indicates the Bessel function of order n, and $j = \sqrt{-1}$.

205

This method has several important features which may be summarized as follows:

1) Higher order coefficients $_pC_{nm}$ and $_pD_{nm}$ can be calculated from zero order coefficients $_0C_{nm}$ and $_0D_{nm}$ by use of recursion relations.

2) Once $_pC_{nm}$ and $_pD_{nm}$ are determined they can be used for all observation angles.

3) The numerical integrations involved in the computation of $_0C_{nm}$ and $_0D_{nm}$ do not contain the highly oscillatory Fourier Transform kernel of the original expression.

To illustrate the variation of the RF pattern of a reflector antenna as a function of its feed location, the far fields of a 55-m parabolic reflector antenna are plotted for four different feed locations: (1) Feed at focal point. (2) Feed displaced in the x direction with y and z constant. (3) Feed displaced in the y direction with x and z constant. (4) Feed displaced in the z direction with x and y constant. (Figures 8 through 11.)
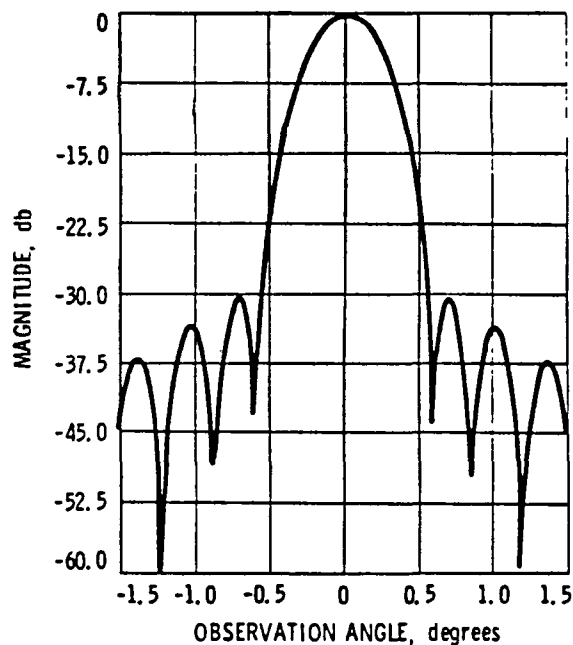
Fig. 8. Feed at Focal Point
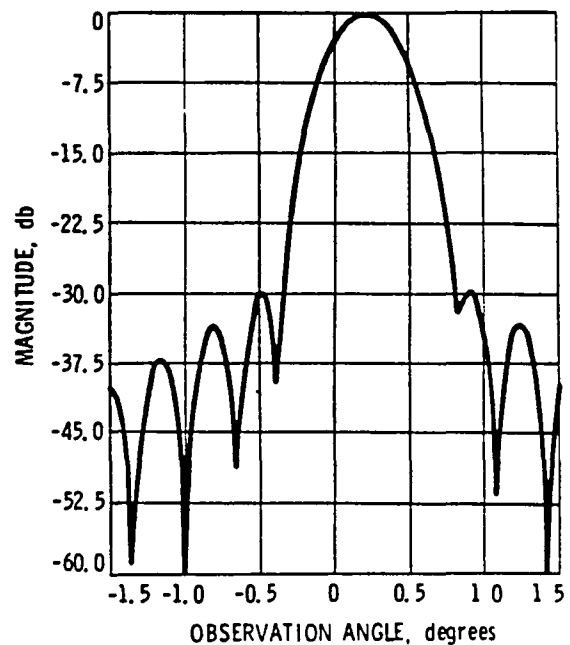
Fig. 9. Feed Displaced by 1 Wavelength in x Direction
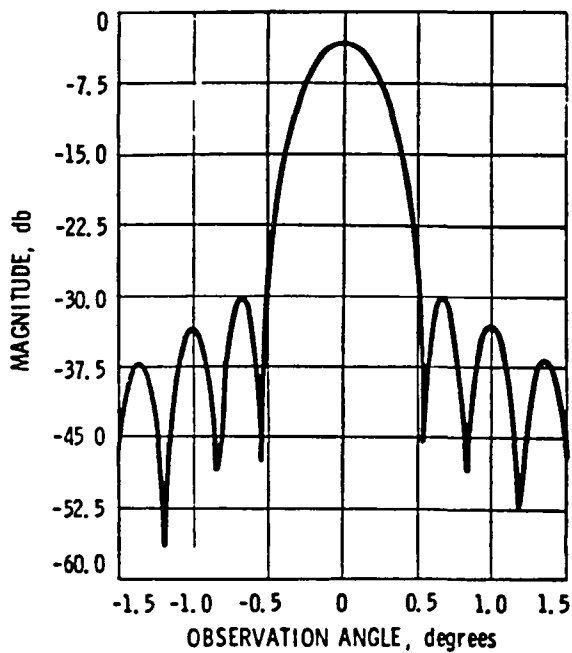
**Fig. 10 Feed Displaced by 1
Wavelength in y Direction**
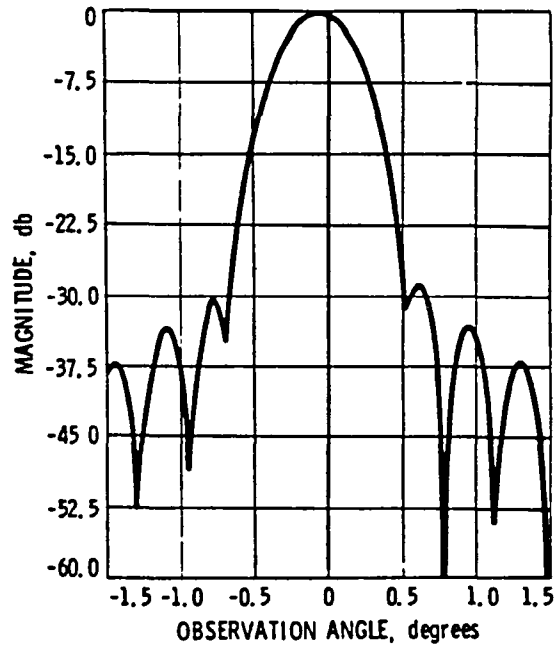
**Fig. 11 Feed Displaced by 1
Wavelength in z Direction**

As can be noticed, displacements along the x and y axes produce significant variations in the gain while displacements along the z axis have almost negligible effects. It can thus be observed that, to optimize the gain most of the effort should be concentrated on controlling the feed displacements along the x and y directions and that the control along the z direction can be relatively loose.

III. ANTENNA CONTROL MODEL

Let P be an EM performance parameter to be optimized (e.g., gain, bandwidth, magnitude of the electric or magnetic field). Let x_1, x_2, ... x_n be the independent variables whose variations affect P: $P = P(x_1, x_2, ... x_n)$; and let $x = (x_1 \; x_2 \; ... \; x_n)^T$. Suppose P assumes its optimal value at $x_0 = (x_{10} \; x_{20} \; ... \; x_{n0})^T$. Around this point P can be expressed as

$$P(x) = P(x_0) + \nabla P\big|_{x_0} \cdot \Delta x + \frac{1}{2} \Delta x^T H\big|_{x_0} \Delta x + ...$$

where P and H denote the gradient vector and the Hessian matrix of P with respect to x and $\Delta x = x - x_0$.

Since P is optimum at x_0

$$\nabla P\big|_{x_0} = 0$$

and $H|_{x_0}$ is positive definite or negative definite depending on whether P is minimum or maximum at x_0.

Hence, around the given point,

$$P(x) = P(x_0) + \frac{1}{2} \Delta x^T H\big|_{x_0} \Delta x + ...$$

and we can approach the optimum value of P by minimizing $|\frac{1}{2} \Delta x^T H \Delta x|$. Note that if this minimum reduces to zero we actually attain the optimum value of P. Note also that if $H > 0$,

$$\left|\frac{1}{2} \Delta x^T H \; \Delta x\right| = \frac{1}{2} \Delta x^T H \; \Delta x$$

and if $H < 0$,

$$\left|\frac{1}{2} \Delta x^T H \; \Delta x\right| = \frac{1}{2} \Delta x^T (-H) \; \Delta x$$

and that in both cases,

$$\left| \frac{1}{2} \Delta x^T H \Delta x \right| = \frac{1}{2} \Delta x^T A \Delta x$$

where A is a positive definite matrix.

The antenna is modeled by an equation of the form[3]

$$M\ddot{y} + Ky = Bu \qquad y(t_o) = y_o, \qquad \dot{y}(t_o) = \dot{y}_o$$

It is always possible to relate Δx to y by an equation of the form $\Delta x = Ty$. Hence, minimizing

$$\frac{1}{2} \Delta x^T A \Delta x$$

and reducing it to zero is equivalent to minimizing

$$\frac{1}{2} \int_0^\infty y^T T^T A Ty \, dt.$$

We can thus formulate a linear quadratic optimal control problem by writing: Minimize

$$J = \frac{1}{2} \int_0^\infty (y^T T^T A Ty + u^T Ru) \, dt$$

subject to

$$M\ddot{y} + Ky = Bu \qquad y(t_o) = y_o, \qquad \dot{y}(t_o) = \dot{y}_o$$

The term

$$\frac{1}{2} \int_0^\infty u^T Ru \, dt$$

where R is a positive definite matrix, is added to account for the restrictions in energy consumption for the control.

The rest of the procedure is classical. A damping term Dy is added to the equation, and the system is augmented by considering the state vector $W = (y \ \dot{y})^T$. This leads to the system

209

$$\dot{W} = \begin{pmatrix} 0 & I \\ -M^{-1}K & -M^{-1}D \end{pmatrix} W + \begin{pmatrix} 0 \\ M^{-1}B \end{pmatrix} u \triangleq FW + Gu$$

associated with the cost functional

$$J = \frac{1}{2} \int_0^\infty (W^T QW + u^T Ru)\ dt$$

where

$$Q \triangleq \begin{pmatrix} T^T AT & 0 \\ 0 & 0 \end{pmatrix}$$

The optimal control is given by

$$u(t) = -CW(t)$$

with

$$C = R^{-1}G^T K$$

where K is the positive definite solution of the Riccati equation

$$F^T K + K F + Q - K G^T R^{-1}G K = 0$$

IV. FEED-DISH MOTION COMPENSATION FOR A 55-M, WRAP-RIB, OFFSET-FED ANTENNA

To illustrate the application of the method, in the following we describe the design of an EM optimal controller for the 55-m, offset-fed, wrap-rib antenna considered in the LMSS study. The controller is designed to minimize the relative feed-dish motion of the antenna.

A schematic diagram of the antenna is given in Figure 12. It is composed of a 55-m diameter reflector dish, a massive feed array, and a long L-shaped boom connecting the dish and the feed. The antenna's operation frequency is 871 MHz which leads to the values of 1159.68λ for the dish's diameter and 239.6λ for its focal length (λ is the wavelength at 871 MHz).

Construction of the State Cost Matrix

Let r_0 be the vector from the center of gravity of the spacecraft's bus to the boom's elbow and r_1 the vector from the elbow to the center of gravity of the reflector's dish. The position of the feed is characterized by the vector.
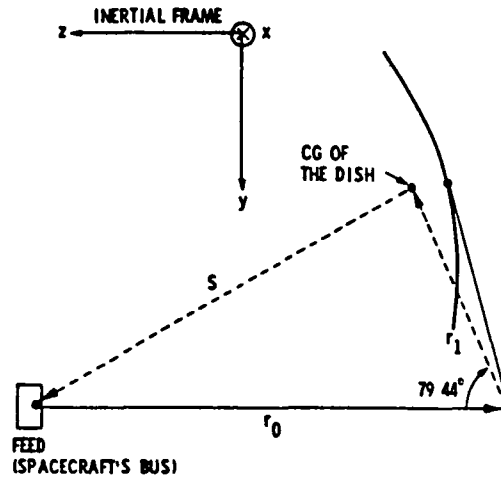
Figure 12. Schematic Diagram of the Antenna

$$S = (x \ y \ z)^T = - (r_0 + r_1)$$

Let $S_o = (x_o \ y_o \ z_o)^T$ be the position for which the electric field is maximized. For the neighborhood of this point

$$E = E(s_o + \nabla_s E|_s o \ . \ \Delta S + \frac{1}{2} \Delta a S^T H(s_o)\Delta S + \ldots = E(s_o) + \frac{1}{2} \Delta S^T H(s_o) \ \Delta S + \ldots$$

since

$$\nabla_s E|_{s_o} = 0.$$

The value of the electric field was evaluated using the algorithm described in the first section of this paper for different feed positions. The following Hessian matrix $H(s_o)$ was obtained through numerical differentiation of the electric field (as a function of feed position):

$$H(S_o) = \begin{pmatrix} -26.0966 & -.00344 & -.0076 \\ -.00344 & -24.231 & 6.396 \\ -.0076 & 6.396 & -1.96 \end{pmatrix}$$

211

To evaluate ΔS, we interpret the feed-dish motion by considering the feed and the lower boom, r_o, fixed and the dish, hence r_1, rotating about the coordinate axes. Thus,

$$\Delta s = -\Delta r_1$$

The antenna's distortions are supposed to be small. This leads to

$$\Delta r_1 = r_1 \times \Gamma$$

where

$$\Gamma = (\gamma_1 \ \gamma_2 \ \gamma_3)^T$$

designates the rotation of r_1 about the x, y and z axes of the inertial frame. Writing Δr_1 in a matrix form, we obtain

$$\Delta s = -D \ \Gamma$$

with

$$D = \begin{pmatrix} 0 & +c & -b \\ -c & 0 & +a \\ b & -a & 0 \end{pmatrix}$$

where a, b and c are the components of the vector r_1: $r_1 = (a \ b \ c)^T$.

Thus,

$$\Delta E = E - E(S_o) = \frac{1}{2} \Gamma^T D^T H D \Gamma \triangleq \frac{1}{2} \Gamma^T H' \Gamma$$

$$H' = D^T H D$$

E has a maximum at S_o. H is therefore negative definite and so is H'. Consequently, the state cost is given by

$$|\Delta E| = \frac{1}{2} \Gamma^T (-H') \Gamma$$

Antenna Model

The antenna is modeled by the linear system[3]

$$M\ddot{y} + Ky = Bu$$

where the state vector y has 12 components as follows: y_1 to y_3 represent

the attitude θ_x, θ_y, and θ_z of the spacecraft; y_4 to y_6 the rotations γ_1, γ_2, and γ_3; and y_7 to y_{12} the six most important modes of the reflector dish.

The state cost weighting matrix takes the form

$$Q_{ij} = -H'_{(i-3)(j-3)} \qquad 4 \leq i \leq 6, \qquad 4 \leq j \leq 6$$

$$Q_{ij} = 0 \qquad \text{elsewhere}$$

Optimal Feedback Computation and Simulation

The OPTSYS[4] program package was used to determine the optimal gain for the case where a three-dimensional control is applied at the spacecraft's bus. The choice of the control cost weighting matrix is explained in the following section.

V. CONTROLLER PERFORMANCE

The EM optimal controller described in the previous section was used to derive the antenna and extensive simulations were performed to analyze the antenna's structural and electromagnetic behavior. These results were also compared with their counterparts obtained through the use of an optimal controller whose design is based solely on geometrical consideratons.[3]

Since geometrical considerations for the control of antennas are needlessly stringent, an EM optimal controller must be able to achieve the same EM performance as a geometrically based controller, with much less control effort involved. The simulation results show that the EM controller did indeed achieve the same performance as the geometric controller using only 37% as much energy.

Figures 13-15 summarize the simulation results. All simulation runs

characterize the response of the system to an initial disturbance of 1° in γ_1. Figure 13 shows the time behavior of the feed-dish distance variation and the control effort $E_c = \int_o^t u^2(\sigma)d\sigma$ when the system is driven by a geometrically based optimal controller. The choice of the state and control cost weighting matrices is described in Ref. 3.
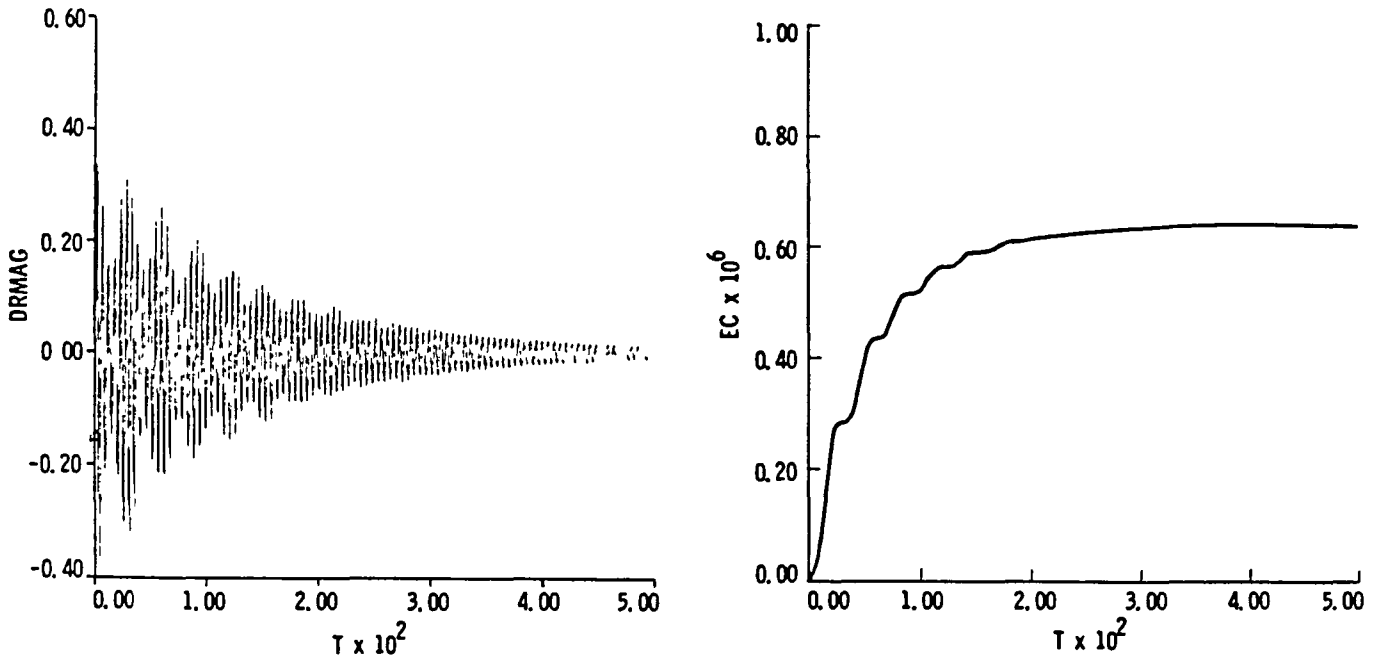
Figure 13. Variations of the Feed-Dish Distance and Control Energy (Geometric Controller).

Figure 14 shows the same two variables when the system is driven by an EM based optimal controller. The choice of the state cost weighting matrix was previously described. The control cost weighting matrix is chosen such as to result in the same RF performance as in the previous case. It should be noted that the control effort is only 37% of the value of the preceding case.

Figure 15 gives a comparison of the time history of the tilt angle (pointing angle) and the magnitude of the peak electric field of the antenna for the two controllers. As it can be noted, the RF controller

achieves the same performance as the geometric controller with only 37% as much energy.
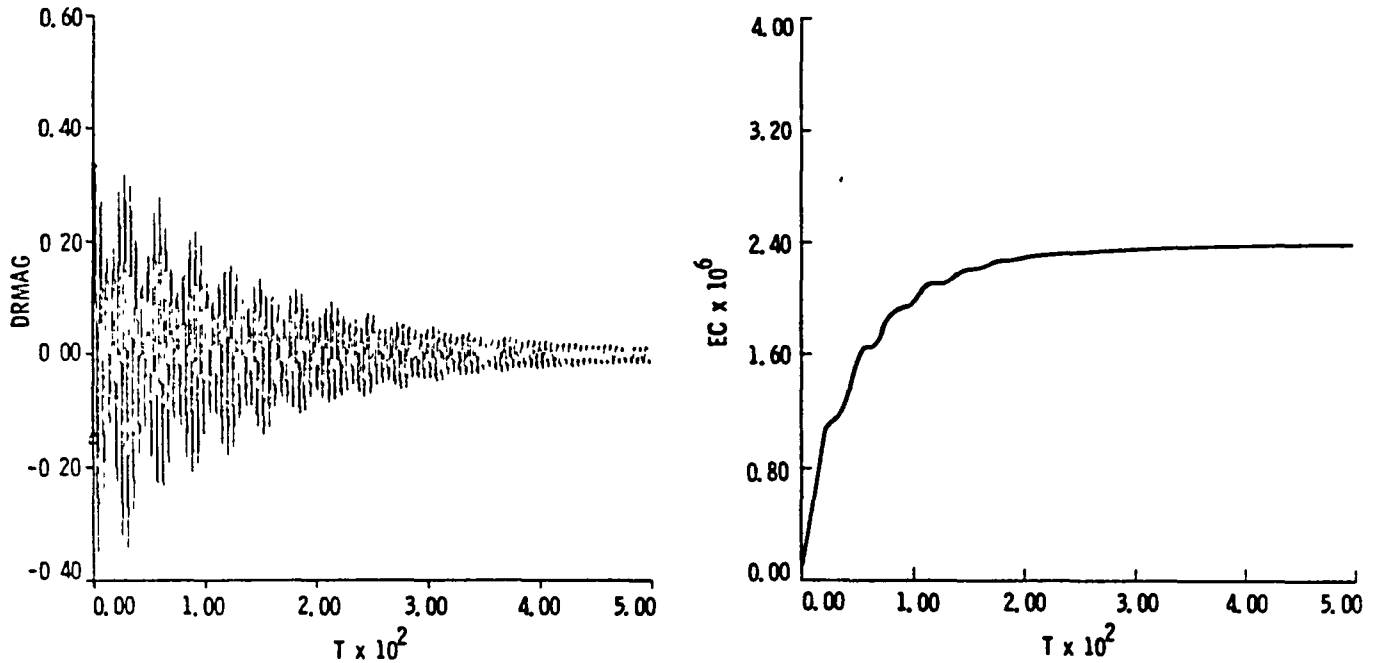
Figure 14. Variations of the Feed-Dish Distance and the Control Energy (EM Controller).

E_C = CONTROL ENERGY
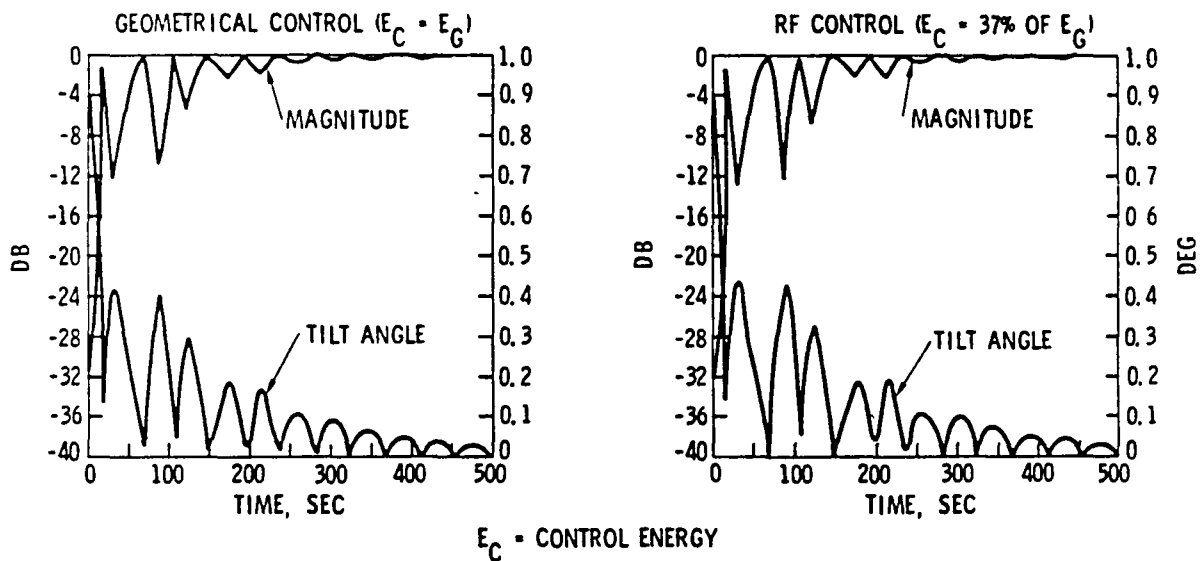
Figure 15. Comparison of the Tilt Angle and the Magnitude of the Electric Field.

VI. GENERALIZED ANTENNA CONTROL DESIGN BASED ON EM PERFORMANCE MODEL

To generalize the design of optimal controllers to take dish surface control under consideration, it is needed to compute the sensitivity of some EM characteristics such as gain, tilt angle (pointing), sidelobe level, etc. to the dish modal distortion.

Mathematical Model Relating the EM Pattern to Modal Distortion

In developing this model, both the structural model and the EM model of the reflector antenna are used. Generally for large space reflectors, the structural dynamics of the dish is modeled by equations of the form:

$$M\ddot{x} + Kx = u(t) \tag{1}$$

Where M is the mass matrix (Positive definite), K the stiffness matrix (Positive), and u(t) the control. x(t) describes the dish surface distortion. This system can be transformed into the canonical form:

$$\ddot{y} + \Omega^2 y = q(t) \tag{2}$$

with y and q defined by

$$x = \phi y$$
$$q = \phi^T u \tag{3}$$

where ϕ is the matrix of modal shapes such that

$$\phi^T M \phi = I \text{ (The identity matrix)} \tag{4}$$

and

$$\phi^T K \phi = \Omega^2 \tag{5}$$

Ω^2 is a diagonal matrix whose elements are the squares of the natural frequencies of the structure. The surface distortion of the dish is given by:

$$x = (\phi_1|\phi_2| \,\text{---}\, |\phi_N) \begin{pmatrix} y_1 \\ y_2 \\ \cdot \\ \cdot \\ y_N \end{pmatrix} \tag{6}$$

or

$$x = \sum_{i=1}^{N} y_i(t)\, \phi_i(r) \tag{7}$$

where the mode shapes $\phi_i(r)$ are known over the entire surface of the reflector and $y_i(t)$ are the modal amplitudes obtained from Eq. (2). When the dish surface is given by the finite element model, the modal shaped ϕ_i are known at a finite number of nodes of a mesh. Thus for node j the distortion is given by:

$$x_j = \sum_{i=1}^{N} y_i(t)\, \phi_i(r_j) \tag{8}$$

If the nominal surface is shown by $\tilde{x}$ the instantaneous surface shape at node j is given by:

$$s_j(t) = \tilde{x}_j + \sum_{i=1}^{N} y_i(t)\phi_i(r_j) \quad ; \quad j = 1, m \tag{9}$$

where m is the number of nodes of the finite element mesh.

To relate the reflector surface to the EM pattern, we should consider the EM model discussed in section II. If the surface Σ is described as

$$z' = f(x', y') \tag{10}$$

the unit vector normal to Σ is given by

217

$$\hat{n} = \frac{\vec{N}}{|N|} \qquad (11)$$

where

$$\vec{N} = - \frac{\partial f}{\partial x'} \hat{x} - \frac{\partial f}{\partial y'} \hat{y} + \hat{z} \qquad (12)$$

and

$$|N| = \sqrt{\left(\frac{\partial f}{\partial x'}\right)^2 + \left(\frac{\partial f}{\partial y'}\right)^2 + 1.} \qquad (13)$$

where $\hat{x}$, $\hat{y}$ and $\hat{z}$ denote the unit vectors along the x, y and z axes, respectively. Therefore, to be able to compute the electric and magnetic fields of the reflector, we must have the value of the surface $z' = f(x',y')$ and its derivatives with respect to x' and y' at points necessary for the compution of the integral yielding the potential vector A:

$$A = \int_{\Sigma} J \frac{e^{-jk|r-r'|}}{4\pi|r-r'|} ds'$$

When the surface is known only at some finite number of nodes (Eq. 9), it can be interpolated at any desired location (x_0, y_0) by fitting a bicubic spline function

$$z = \sum_{i=1}^{4} \sum_{j=1}^{4} C_{ij} (x'-x_0)^{(i-1)} \cdot (y'-y_0)^{(j-1)} \qquad (14)$$

to a number of nodal coordinates (minimum 16 points) in the vicinity of this point. The values of the surface and its derivatives are thus approximated over the entire reflector dish. The polynomial coefficients C_{ij} of Eq. (14) are computed by a least square fit method. The surface and its

derivatives at (x_0, y_0) are simply given by

$$z'(x_0, y_0) = C_{11}$$

$$\partial z'(x_0, y_0)/\partial x' = C_{21} \tag{15}$$

$$\partial z'(x_0, y_0)/\partial y' = C_{12}$$

Numerical Application

The 55 meter wrap-rib antenna was used again for numerical analysis. The feed is assumed to be at the focal point with an edge taper equal to -15 DB. The RF pattern of the non-distorted antenna is shown in Fig. (16). For this geometry the pattern is symmetric and its peak is normalized to zero DB. To show the effect of surface distortion on the RF pattern, modes 1, 2, and 15 of the dish were considered one at a time. Mode 1 is the so called skirt mode and causes the dish to rotate about the hub axis. The RF distortion for small amplitudes for this mode is insignificant, but for large amplitudes such as 100, the RF pattern is distorted as shown in Fig. (17). Mode 15 is the umbrella mode and even for an amplitude equal to 1, it causes the RF pattern to be distorted as shown in Fig. (18). Mode 2 represents a mostly nonsymmetric displacement of the reflector nodes and some rotation. Figure 19 shows two cuts of the RF pattern at $\Phi = 0^O$ and $\Phi = 90^O$. The cuts were evaluated for a mode 2 amplitude equal to 10.
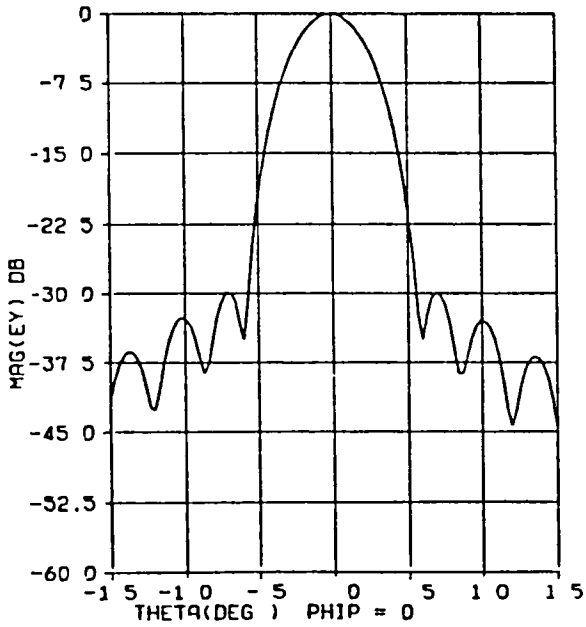
Fig. 16   Undistorted Antenna
Pattern

Fig. 17   Pattern Distortion When
Mode 1 Amplitude = 100

MODE=15   AMP=1 0

MODE=2   AMP 10

Fig. 18   Pattern Distortion When
Mode 15 Amplitude = 1.0
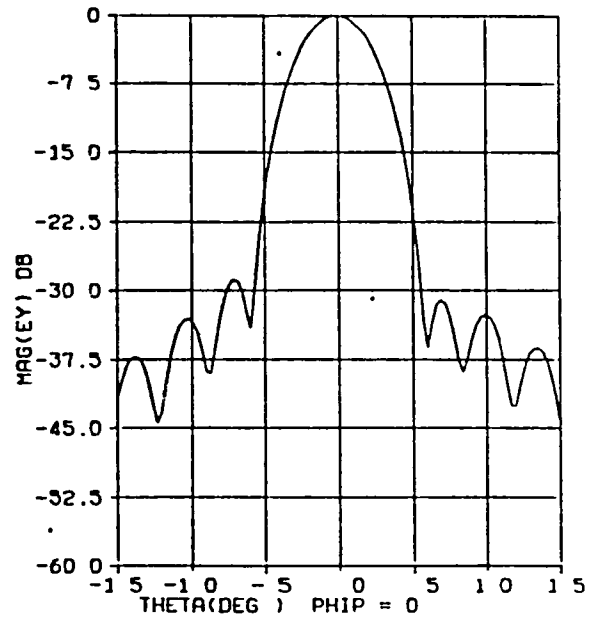
Fig. 19   Pattern Distortion When
Mode 2 Amplitude = 10

VII. CONTROLLER DESIGN FOR SHAPE COMPENSATION
OF THE 55 METER WRAP-RIB ANTENNA

The sensitivity matrix is formed by computing the second derivatives of the peak electric field with respect to the amplitudes of the most significant modes. If the modal amplitudes considered are shown by η_1, η_2 .... η_6, and the Peak Electric field by P, then the sensitivity matrix is defined as follows:

$$S^P_\eta = \begin{pmatrix} \dfrac{\partial^2 P}{\partial \eta_1^2} & \text{TRANSPOSED} & \\ & \text{OF LOWER HALF} & \\ \dfrac{\partial^2 P}{\partial \eta_1 \, \partial \eta_2} & \dfrac{\partial^2 P}{\partial \eta_2^2} & \\ \vdots & \vdots & \ddots \\ \dfrac{\partial^2 P}{\partial \eta_1 \, \partial \eta_6} & \dfrac{\partial^2 P}{\partial \eta_2 \, \partial \eta_6} & \cdots \cdots \dfrac{\partial^2 P}{\partial \eta_6^2} \end{pmatrix} \tag{16}$$

Each element of the sensitivity matrix is computed by tabulating the values of the peak electric field as a function of the corresponding modal amplitudes about $\eta_1 = \eta_2 = ... = \eta_6 = 0$ and then using the bi-cubic spline function to interpolate P. The second derivatives are then obtained from the spline coefficients.

EM Sensitivity Matrix

The Sensitivity Matrix is defined as the matrix of the second derivative of the peak electric field (P) with respect to the amplitude of

the distortion modes of the reflector (η_1, η_2,... η_6) c.f. Eq.(16). The peak electric field of the antenna is computed using the finite element model of the reflector. For the numerical differentiation of P and for the computation of the elements S_{ij} of the corresponding sensitivity matrix, P was computed over a 5 x 5 mesh corresponding to values of η_i and η_j about $\eta_i = \eta_j = 0$. This result was then used to interpolate P about $\eta_i = \eta_j = 0$ by bi-cubic spline functions according to the formula:

$$P(\eta_i, \eta_j) = \sum_{n=1}^{4} \sum_{m=1}^{4} C_{ij} \, \eta_i^{(i-1)} \, \eta_j^{(j-1)} \qquad (17)$$

The coefficients C_{ij} of the bi-cubic splines are computed by using the 25 values of $P(\eta_i, \eta_j)$ and its corresponding η_i and η_j in equation (17) and solving the system of 25 equations with 16 unknowns by a least square fit algorithm. The value of $P(\eta_i, \eta_j)$ and its first and second derivatives with respect to η_i and η_j are obtained as follows:

$$P(\eta_i, \eta_j) = C_{11} \qquad\qquad \frac{\partial^2 P}{\partial \eta_i \partial \eta_j} = C_{22}$$

$$\frac{\partial P}{\partial \eta_i} = C_{21} \qquad\qquad \frac{\partial^2 P}{\partial \eta_i^2} = 2\, C_{31} \qquad (18)$$

$$\frac{\partial P}{\partial \eta_j} = C_{12} \qquad\qquad \frac{\partial^2 P}{\partial \eta_j^2} = 2\, C_{13}$$

It was experienced that the off-diagonal terms of the sensitivity matrix are much smaller than the diagonal terms, therefore to reduce computational cost, only the diagonal terms were evaluated. The resulting sensitivity matrix is shown below:

$$
P = \begin{pmatrix}
-.243\text{x}10^{-3} & & & & & \\
& -.341\text{x}10^{-3} & & & 0 & \\
& & -.489\text{x}10^{-3} & & & \\
& & & -.24.23 & & \\
& 0 & & & -40.21 & \\
& & & & & -42.75
\end{pmatrix}
$$

Controller Design and Simulation for the Wrap-Rib Antenna

The performance of the control design based on the above sensitivity matrix was assessed through extensive simulations. The following simulation results illustrate the control performance. For the illustrative runs, the initial conditions for all state variables were set to zero except for the amplitude of Mode 15 which was set to 1. In Figure 20, the time history of the upper boom rotation angles (Y_4, Y_5, Y_6), the amplitudes of modes, 1, 2, 3, 15, 16, and 17 (Y_7 thru Y_{12}), the dish surface RMS error (RMS), the change in feed dish distance (DRMAG) and the control energy (EC) are shown.
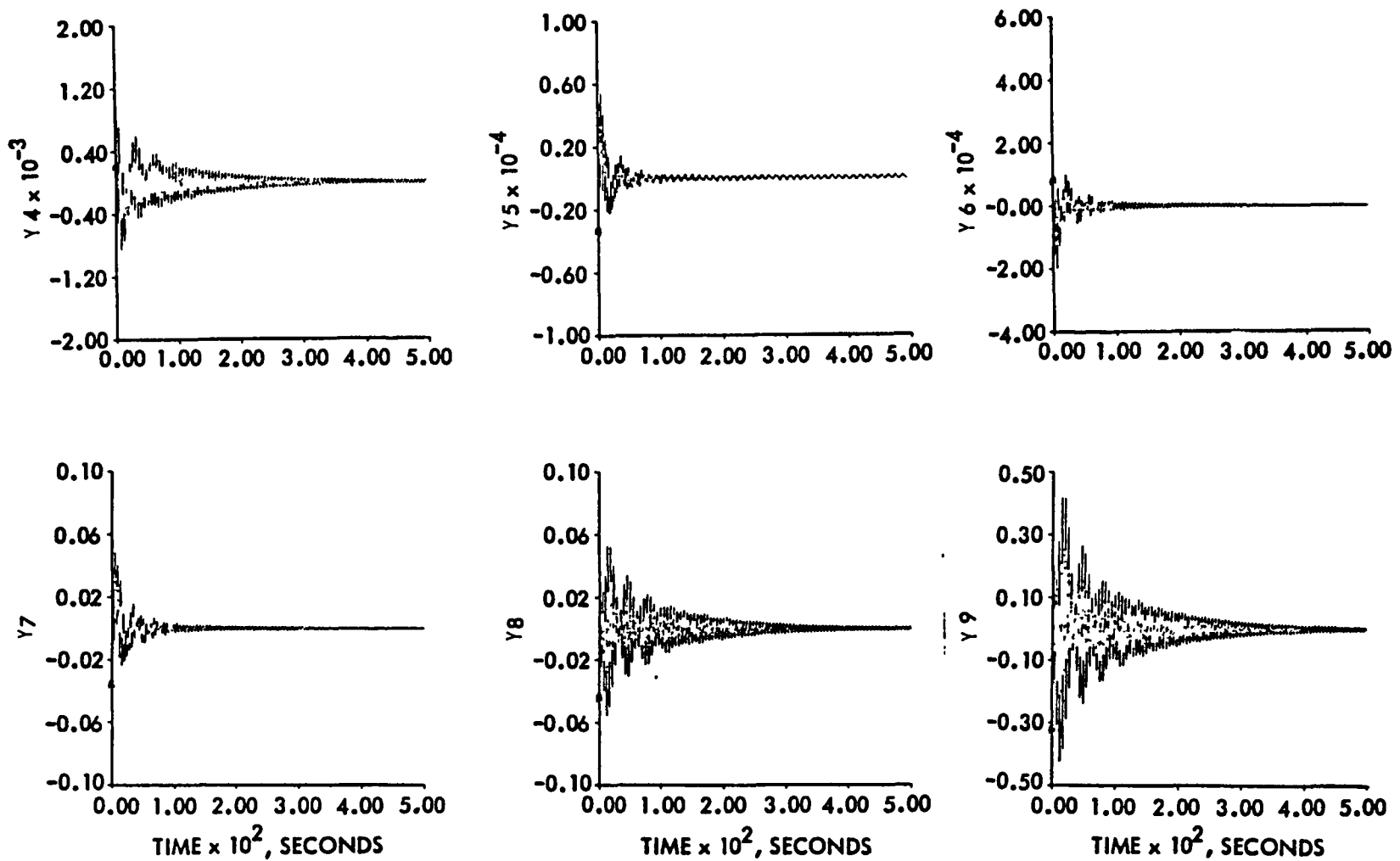
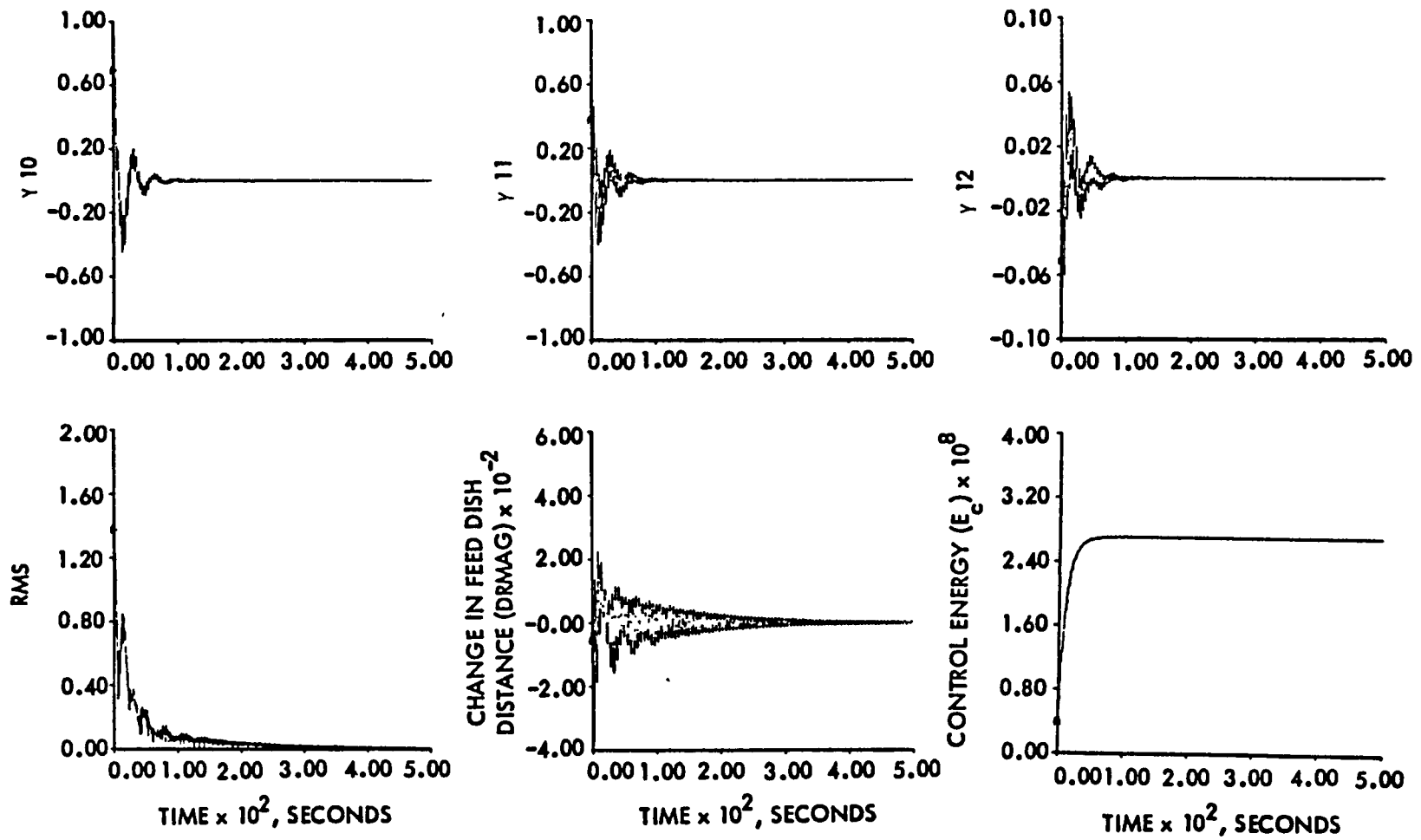Figure 20. Antenna control Performance Using EM Sensitivity Information

Figure 20. (Continued)

VIII. CONCLUSION

The EM performance of large flexible antennas is traditionally achieved by imposing stringent geometric restrictions on the structural distortions from a nominal optimum configuration. In this paper, we have presented an approach to alleviate the stringency of the geometrical criteria of satisfactory performance. The approach consists of generating a linear optimal control problem with quadratic cost functional where the cost functional is obtained from the EM characteristics of the antenna and the dynamic system constraint is given by the structural model of the antenna.

The method was applied to the feed-dish motion and shape vibration compensation for a 55-m wrap-rib, offset-fed antenna. From the time simulations, it was established that the EM based optimal controller is considerably more efficient than the traditional geometrical based controllers, in the sense that the same EM performance can be achieved with a much reduced control effort.

REFERENCES

1. J. Rahmat-Samii and V. Galindo-Israel, "Shaped Reflector Antenna Analysis Using the Jacobi-Bessel Series," IEEE Trans. Antenna and Propagation, Vol. AP-28, pp. 425-435, July 1980.

2. R. F. Harrington, <u>Time Harmonic Electromagnetic Fields</u>, McGraw-Hill Book Co., 1961.

3. J. M. Cameron, M. Hamidi, Y. H. Lin, and S. J. Wang, "Distributed Control of Large Space Antennas," JPL Publication 83-46, Proceedings of the Workshop on Applications of Distributed System Theory to the Control of Large Space Structures, July 14-16, 1982, Jet Propulsion Laboratory, Pasadena, CA.

4. A. E. Bryson, Jr., and W. E. Hall, Jr., "Optimal Control and Filter Synthesis by Eigenvector Decomposition," Stanford University, SUDAR #436, December 1971.

VIBRATION CONTROL EXPERIMENT DESIGN FOR THE 15-m HOOP/COLUMN ANTENNA

F. M. Ham and **D. C. Hyland**
Harris Government Aerospace Systems Division
Melbourne, FL 32902

ABSTRACT

A test program is designed for a ground-based vibration control experiment utilizing as the test article the 15-M Hoop/Column Antenna. Overall objectives of the designed ground-based test program include: the validation of Large Space Structure (LSS) control system techniques, the validation of LSS parameter identification techniques, the evaluation of actuator and sensor placement methodology and the validation of LSS computer models. Critical concerns in LSS Controls and Dynamics are: low frequency vibrational modes, close modal spacing, parameter uncertainties, controller software limitations, nonlinearities and coupling of modes through damping. Analytical results are presented which include compensator designs for varying compensator order.

I. INTRODUCTION

In the near future NASA plans to conduct a Large Space Antenna Flight Experiment. Preliminary efforts on shuttle attached experiments have been performed [1]. This endeavor represents an attempt to advance the design, development, test and evaluation of large, actively controlled space structures to a sufficient level for an effective transfer of resulting technology to mission programs. The goals of the program are (1) validate technologies necessary to implement active control of large structures, (2) to provide feedback to the mission community concerning risks, limitations, and related problems, and (3) to help guide future technological endeavors.

With the preceeding goals in mind, a logical first step is to consider a ground-based experiment, and the 15-M Hoop/Column Antenna is a very good choice for the test article. A prototype is currently being built under a contract by Harris Corporation. This structure is a deployable mesh reflector design for space communication applications.

The deployed configuration is shown in Figure 1. Figure 2 shows the
actual configuration for ground testing of the antenna. The structure
consists of a cable stiffened mesh reflective surface which is suspended
from the deployable hoop and is controlled by cables which attach to the
central mast. In addition to attitude (precision pointing) and slewing
control via multiple reaction control jets and momentum exchange
devices, it is possible to control the reflector surface by changing
tension in the control cords.

Configurations of the Hoop/Column antenna which are well in excess
of 100 meters have been studied for possible communications and science
missions. It is possible to package them in the Shuttle Bay, and the
associated structural weight will be a small fraction of the Shuttle
payload capacity.

NO GRAVITY COUNTERBALANCE SYSTEM IS
REQUIRED ONCE DEPLOYMENT IS COMPLETE

COUNTER
BALANCE
SYSTEM
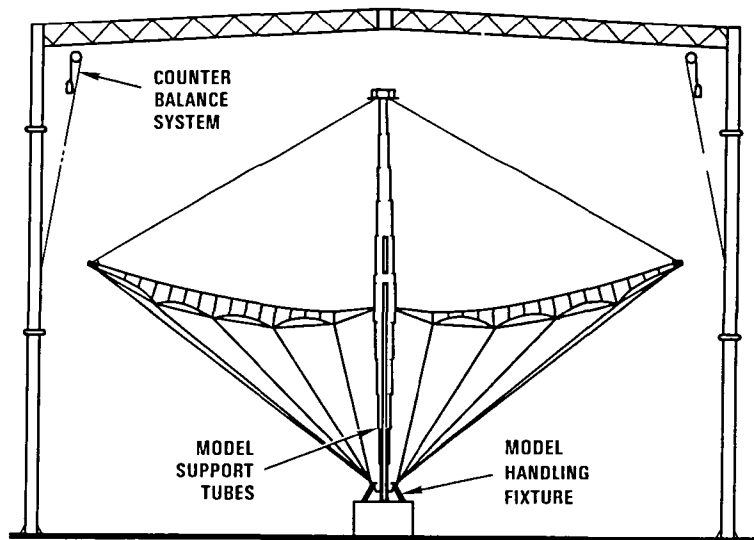
MODEL
SUPPORT
TUBES

MODEL
HANDLING
FIXTURE

Figure 1. 15-Meter H/C Model Deployed

An initial design concept has been developed and specific
objectives set forth [2]. The objectives of the ground-based experiment

SUPPORT CABLE

VOICE COIL ACTUATORS (X Y)

RATE GYROS (X Y)

SAMS CCD
ARRAY

TARGETS FOR SAMS MEASUREMENT
SYSTEM (1 TARGET EVERY 4TH GORE)

STRAIN GAUGES
(1 EVERY 2ND GORE)

PIEZOELECTRIC
TENSIONERS EVERY
2ND GORE (ALL CORDS ON
A GORE)

JACK SCREW POSITIONERS
EVERY 4TH GORE (MIDDLE
AND OUTER CORDS)

2 DISTURBANCE
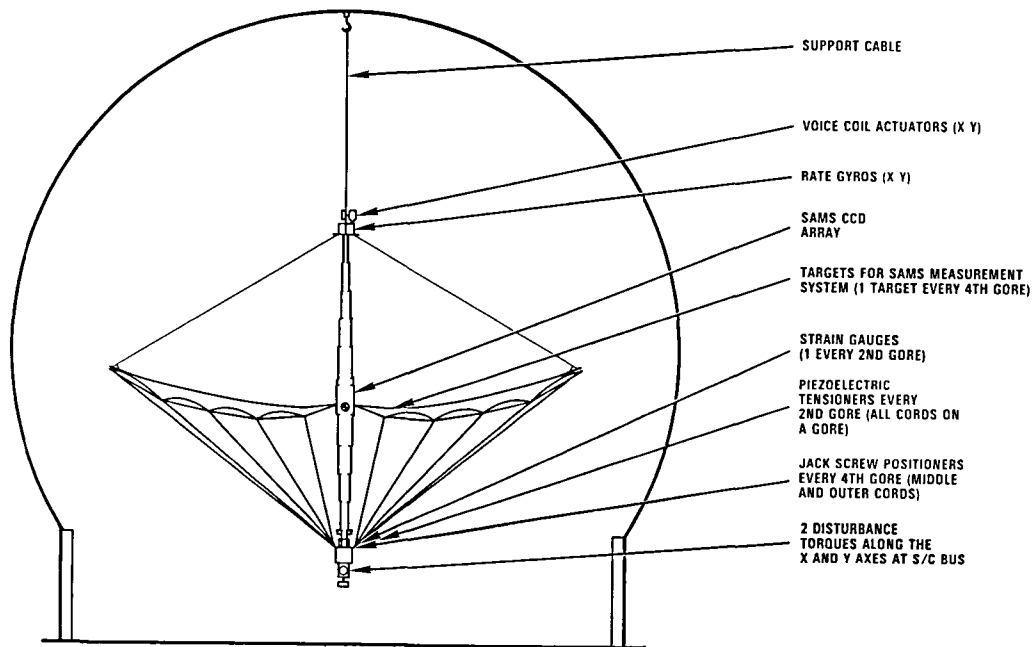TORQUES ALONG THE
X AND Y AXES AT S/C BUS

Figure 2.   15-Meter H/C Model Cable Suspended Configuration for
Ground Testing

include (1) verification of actuators and sensors used for attitude and shape
control, (2) establish traceability of ground testing to space testing, (3)
establish limitations imposed by processors, (4) establish adequacy of the
controller to control low frequency and closely spaced modes, (5) define a
complexity/performance tradeoff and (6) verification (and possible refinement) of
the analytical structural model of the antenna through parameter identification
(this would reduce risk in the flight experiment).

The ground-based experiment results should provide information which can be
utilized for an STS-attached flight experiment. Actuator and sensor placement
(and number) is a critical issue in performing the experiment. The ground-based
experiment configuration provides a logical first-cut at actuator/sensor placement
and number. Resulting data can be subsequently analyzed to refine the various
locations and number of devices on the structure to increase system performance,
and also provide input for an analysis of the tradeoffs between closed-loop
performance and controller complexity. In order to perform the flight experiment,
flight-qualified hardware must be developed. This includes actuators, sensors,

231

and all controller processing hardware. The ground-based experiment again can provide a baseline for that hardware. Performance of the prototypes can be assessed and refinements made prior to the flight experiment, providing low cost/low risk hardware. Verification and refinement of the analytical finite-element model for the structure can be accomplished through parameter identification. This can provide a more refined model of the structure for the flight experiment, possibly resulting in better performance.

II. EXPERIMENT DESIGN

A. Control Methodology

The control of large flexible space structures offers a number of challenging problems to be overcome. First of all, one must design a controller in the face of incomplete information, namely uncertainty in plant modeling. Secondly, since models of large flexible structures, such as large antennas, will be extremely large the order of the controller can not be the same as the plant order. In other words, it is necessary to design a dynamic controller whose order is prespecified in accordance with onboard software limitations and is, at the same time, robust in the face of modeling uncertainties. The answer to both of these problems can be found in the Maximum Entropy [3,4,5] and Optimal Projection [6,7] theories.

Given the dynamic system of equations

$$\dot{x}(t) = Ax(t) + Bu(t) + w_1(t) \tag{1}$$

where

$$x(t) = \begin{bmatrix} x_1(t) \\ x_2(t) \\ \cdot \\ \cdot \\ \cdot \\ x_N(t) \end{bmatrix} \tag{2}$$

is the state of the plant (in the antenna control problem this will be modal displacements and velocities) the output of the sensors is given by:

$$y(t) = Cx(t) + w_2(t) \tag{3}$$

where $y(t)$ is a vector of ℓ sensor outputs with measurement noise $w_2(t)$. Now, the optimal control problem consists of minimizing the quadratic functional of $x(t)$ and

$$E[J] = E\left[\int_0^\infty (x^T(t)\ R_1 x(t) + u^T(t)\ R_2 u(t))dt\right] \qquad (4)$$

$u(t)$ subject to the constraint equations given by Equation 1.

The standard theory works well if A, B and C are known precisely, but this will never be the case in an application such as the antenna control problem. One is always faced with residual modeling errors and actual physical changes in structural parameters. The Maximum Entropy approach to system modeling allows parameter uncertainties to be directly included in the overall design process by use of a stochastically parametered system model which incorporates the minimum of available parameter statistical information. The approach provides a mechanism whereby modeling uncertainties can be uniquely quantified and the controller design can be made robust.

Since implementation constraints are ever present in any system, the order of the controller (N_c) is fixed at the maximum order ($N_c \ll$ N) allowable, which is dictated by system software constraints. In order to arrive at an optimal control formulation under these conditions the Optimal Projection theory can be utilized. The optimal projection approach to reduced - order controller design involves direct solution of the optimality conditions for the problem of quadratically optimal fixed-form dynamic compensation. The basic design equations termed the "optimal projection equations" are first order necessary conditions of the optimization problem rendered in a highly simplified form. The design equation also incorporates parameter uncertainties as modeled under the maximum entropy approach. Convergent techniques for numerical solution of the design equations allows the acceptance of a large-order plant model and yet provides the quadratically optimal controller having a fixed dimension which is dictated by on-line computing capacity.

Therefore, the control design approach utilized consists of Maximum Entropy Modeling, and Optimal Projection. The Maximum Entropy modeling approach addresses the consequent need to acknowledge inescapable errors in the parameters of the structural model and to accept such uncertainties at their a priori levels. Optimal Projection addresses and resolves the following problem: given the plant model (structure, actuators, sensors) including modeling uncertainties as treated under the Maximum Entropy formulation, design the optimal dynamic controller whose order (number of dynamic degrees of freedom) is preassigned in accordance with on-line computing capacity. This approach produces a strictly optimal, fixed-order compensator and supersedes all ad hoc suboptimal reduction and/or controller order reduction procedures.

Due to the amount of computer time required for solution of the optimal projection equations, for large order systems, an approximate gain selection algorithm has been formulated. The method assumes diagonal-dominance of the matrices in the system equations, thus

yielding an algorithm which converges relatively fast. The analytical results presented later are a result of utilizing the approximate gain selection software.

B. Experiment Configuration

Two configurations were considered for a 15-meter model dynamic experiment, the based-fixed and pendulum. Both were reviewed for application in a dynamic controls test and it was decided that the pendulum (or cable suspended) configuration was superior for the reasons listed below:

- The cable suspended configuration possesses quasi rigid-body modes and thus allows the inclusion of pointing and retargeting in the experiment (limited to small angular motion).

- Better isolation from ground disturbances.

- Better definition of the system boundary condition. The support structure in the based-fixed configuration will interact with a number of structural modes. This will add uncertainty to the model.

A finite element model of the cable suspended configuration was developed to aid in the experiment design, and Table 1 gives the element description. Several simplifications were made for convenience in developing the finite element model. The surface is modeled by a single layer of membrane elements without details of the cord structure, and the finite element model contains twelve (12) gores, whereas the structure contains twenty-four (24) gores. Both simplifications have been correlated with detailed models in other investigations. Lower frequency modes will be represented accurately and high frequency modes will have similar characteristic shapes and frequency ranges. These approximations are reasonable at this stage in the experimental design. Detailed finite element models will be needed for correlation and final design of the control system.

One hundred (100) modes were computed using the finite element model. Modal density versus frequency is plotted in Figure 3. Mode shapes which illustrate the regimes shown in Figure 3 are plotted in Figures 4 through 6. The number of modes below a given frequency is plotted versus frequency in Figure 3. The mode at 2.4 Hz is a torsional kinematic mode where the mast rotation is balanced by the hoop.

The low quasi-rigid body modes place several restrictions on the experimental configuration.

Table 1. Finite Element Model Description

ANTENNA COMPONENT	TYPE ELEMENT	NO. OF ELEMENTS
Hoop Segment	beam	12
Mast Segment Bays	beam	7
Mast/Cord Interface	beam	48
Cords	stringer	348
● upper and lower hoop control ● surface backup structure		
Bungy (antenna suspension)	stringer	4
		419

N(ω) △ NUMBER OF MODAL FREQUENCIES BELOW ω

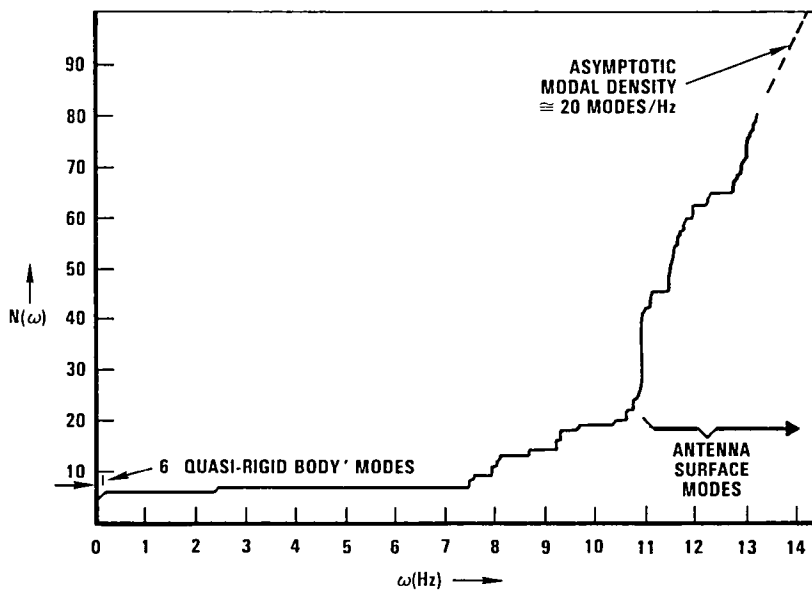
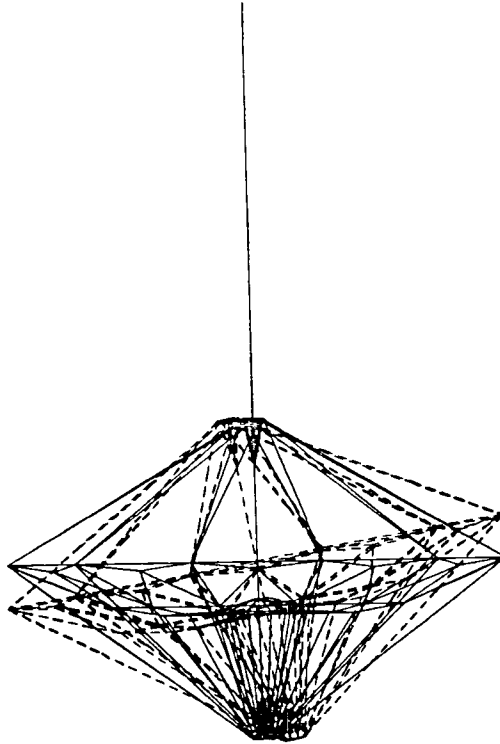Figure 3. 15-M Model Ground Test Configuration Mode - Count Versus Frequency

Figure 4. Mode 4: Quasi-Rigid Rotation (f = 0.163 Hz)
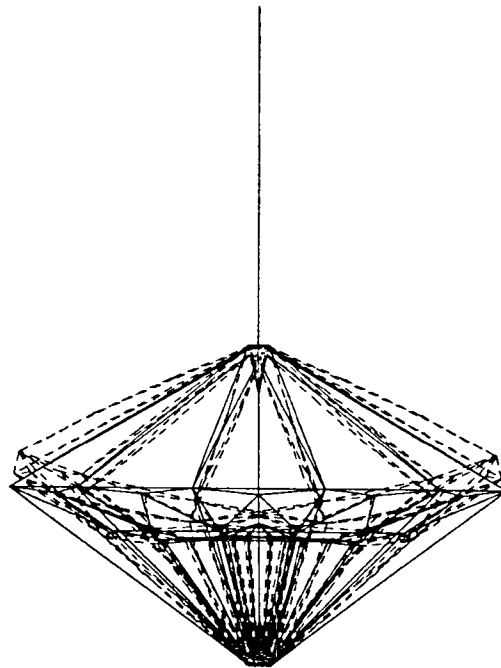
Figure 5. Mode 6: First Hoop Bending (f = 7.493 Hz)
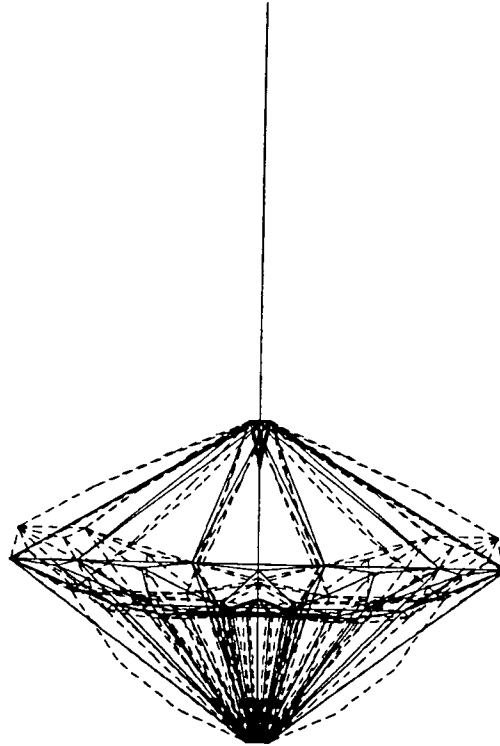
Figure 6. Mode 10: Higher-Order Hoop Bending (f = 8.029 Hz)

● Both inertial (absolute) and displacement (relative) sensors
  and actuators must be contained within the structure.

● Small external forces can produce large quasi-rigid
  displacement.

The first restriction is actually an advantage because the problems
of ground disturbances and compliance can be avoided. The second
indicates that significant efforts to control environmental disturbances
near the experiment will be required.

C. Disturbance Spectrum and Performance Metric

There are a number of requisites which a Large Space Structure
experiment must have to satisfy the objective given in the introduction

and ensure that it is meaningful to the LSS controls community. Review of literature from ACOSS [8,9,10] and other efforts on structural control indicates several pathologies typical of LSS control.

These are:

1. Controller Tasks: Retargeting, precision pointing, surface shaping, and vibration suppression.

2. Large number of closely spaced modes, i.e., a restriction in terms of damping bandwidth such as $\Delta\omega/2\eta\omega < 1.0$ is desired.

3. Disturbance spectrum should cover 100 modes.

4. Performance requirements which demand control of 20 to 30 modes.

The structural test configuration guarantees that item 1 above is satisfied. A disturbance spectrum which satisfied item 3 is shown in Figure 7. The spectrum is based on the same logic as the VCOSS I disturbance spectrum [11,12]. The 15 Hz half-power band covers more than 100 modes. As shown in Figure 2 the disturbance will be applied at the antenna base. The disturbance torques will be applied independently along the X and Y axes.

It is desirable to develop a performance index which will be indicative of the intended use of the structure. In this case the appropriate index should account for RF beam mispointing (Line of Sight, LOS error), wavefront error, and defocus error at the same time. This index must weight sufficient modes to satisfy item 4 above. Mispointing and defocus are linear functions of feed displacement. The effects of the surface distortion on wavefront error and beam dispersion are obtained by rather complex surface current integrals and can sometimes be simplified to generate optical expressions. Even a simplistic approach, using a best-fit parabola to fit the distortions, results in a non-linear relationship between reflector distortions and mispointing and defocus. In the small displacement limit, this relation can be linearized to form a linear transformation between the distortions and the mispointing and defocus. Also, the residual roughness can be separated from mispointing and defocus contributions by a linear transformation. Development of a performance metric, which exhibits several distinct parts, can be constructed as shown in Equation 5.

$$ J = E \left\{ W_1 \alpha_X^2 + W_2 \alpha_Y^2 + W_3 \delta^2 + W_4 r^2 + \rho u^T(t)\, u(t) \right\} \quad (5) $$

THE DASHED LINES FOLLOW THE MODAL DENSITY CURVE IN FIGURE 3
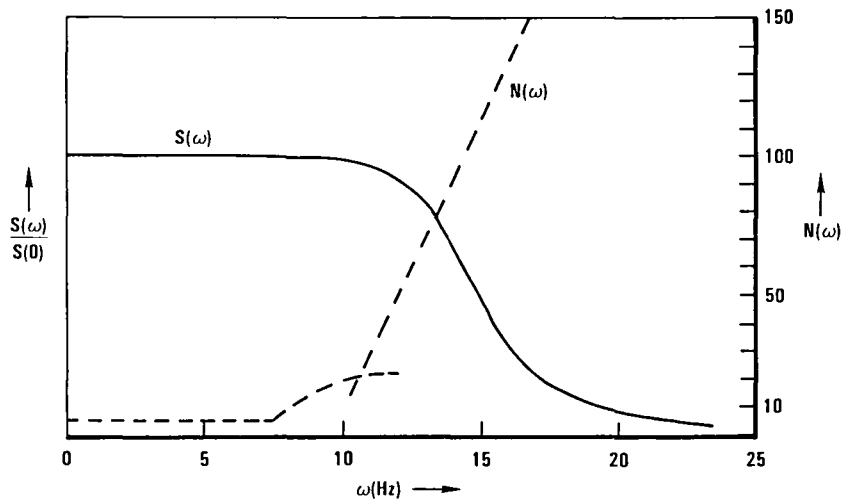

Figure 7. Suggested Broad-Band Disturbance Spectrum for 15-M Ground Test (Applied Independently Along X and Y axes)

where:

α_X = Angular Pointing Error About X
α_Y = Angular Pointing Error About Y
δ = Fractional Defocus
r = Surface Roughness
$u(t)$ = System Control Vector

and

W_1, W_2, W_3, W_4, and ρ are the respective weighting factors.

D. Actuator/Sensor Issues and Initial Design Methodology

Shown in Figure 8 are some guidelines for the determination of the number of actuators and sensors for the antenna system. Figure 2 shows the relative locations of the devices for the initial selection process, and Figure 9 details the actual types and bandwidths for the control problem. Again, this is a preliminary selection for types of devices and locations on the structure.

Figure 10 shows the initial design methodology, which includes assessment of the effects of actuator and sensor dynamics. Items 1-4 in Figure 10 deals with the basic problem of "how to get started" in the design. The problem faced in designing a control system is the following: Choice of an actuator/sensor configuration to optimize performance actually demands evaluation of closed-loop system performance, yet the control system design requires a complete model of the system including the actuator and sensor dynamics and placement. The complexity of the problem is increased due to the large number of possible hardware configurations and the difficulty, for large order structural models, of designing an acceptable control law for any one such hardware configuration. Figure 10 depicts an iterative method to establish an initial controller design.

E. Hardware Configuration

Figure 11 shows an overall hardware concept for the ground-based experiment utilizing the 15-M H/C Antenna in the pendulum configuration as the test article. This suggested control hardware configuration is the result of the preliminary steps of the design process depicted in Figure 10. The HP-6942A Multiprogrammer can be utilized to perform all A/D and D/A conversions as well as performing data handling. The control algorithm would be implemented on the HP 9836A Desktop Computer. This is a Motorola MC68000 microprocessor-based (16-bit) machine. The purpose of the external CPU is to assist in data handling and route data to off-line storage devices. After the completion of the experiment, stored data can be analyzed; performing parameter identification tests and correlating results with analytical predictions.

F. Suggested Test Sequence

In order to establish the validity of actuator and sensor modeling an initial open-loop test must be performed. This will verify transfer functions and noise models of the devices chosen for structural control. Before any additional testing is conducted a calibration

```
┌─────────────────────────┐                    ┌─────────────────────────┐
│ TOO FEW                 │                    │ TOO MANY                │
│                         │                    │                         │
│ ▪ POOR CONTROL          │                    │ ▪ EXCESSIVE COST.       │
│   REDUNDANCY            │                    │ ▪ HIGH NET FAILURE      │
│ ▪ PRECLUDES GRACEFUL    │                    │   RATE, EXCESSIVE       │
│   FAILURE MODES (EACH   │                    │   REPLACEMENT           │
│   CONTROL TASK          │                    │   FREQUENCY.            │
│   REQUIRES SOME         │   NO. OF SENSORS   │ ▪ PHYSICAL              │
│   REDUNDANCY.)          │   AND ACTUATORS    │   INTERFERENCE          │
│ ▪ DOES NOT              │                    │   WITH PAYLOAD          │
│   ACCOMODATE            │                    │   OPERATION             │
│   REASONABLE VARIETY    │                    │   (CROWDING).           │
│   OF CONTROL            │                    │ ▪ MASSIVE               │
│   APPROACHES.           │                    │   ELECTRICAL CABLE      │
│                         │                    │   BUNDLES               │
└─────────────────────────┘                    └─────────────────────────┘
```
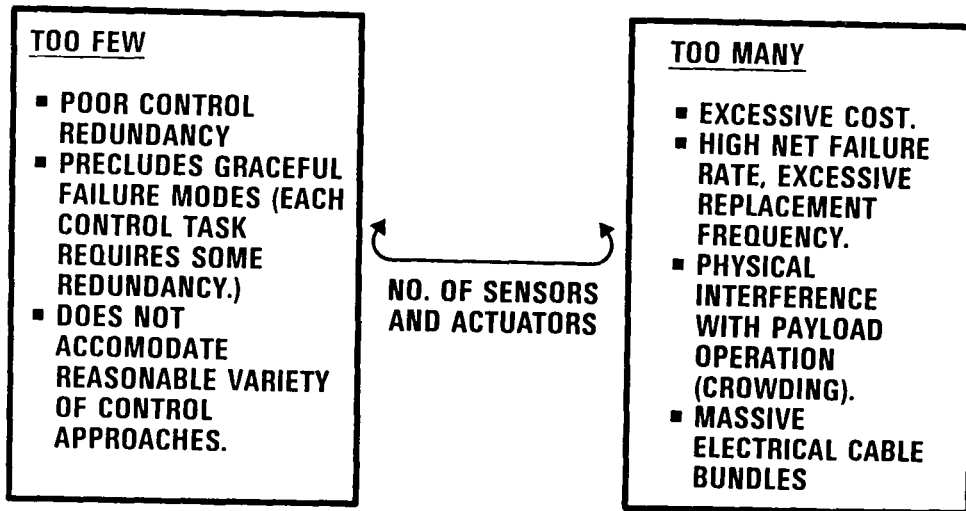
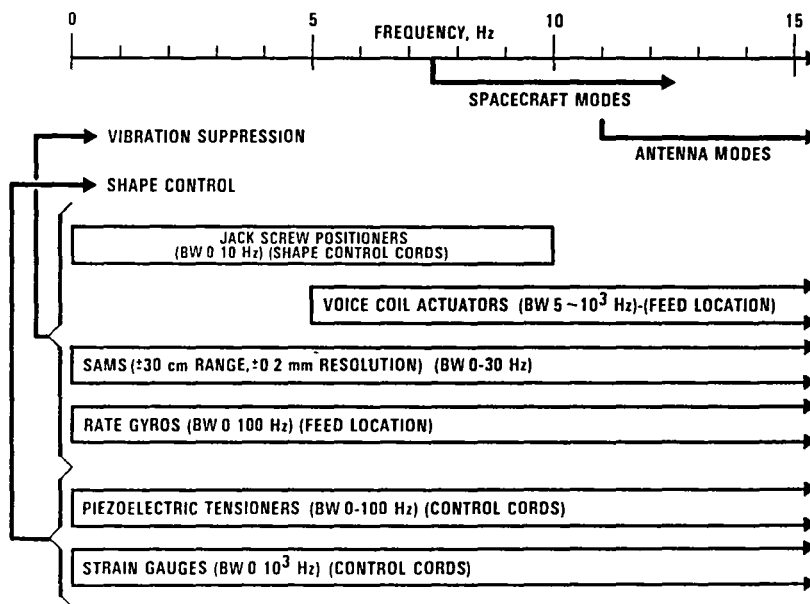Figure 8. Number of Sensors and Actuators (Some Guidelines)

Figure 9. Selection of Actuators and Sensors For Vibration
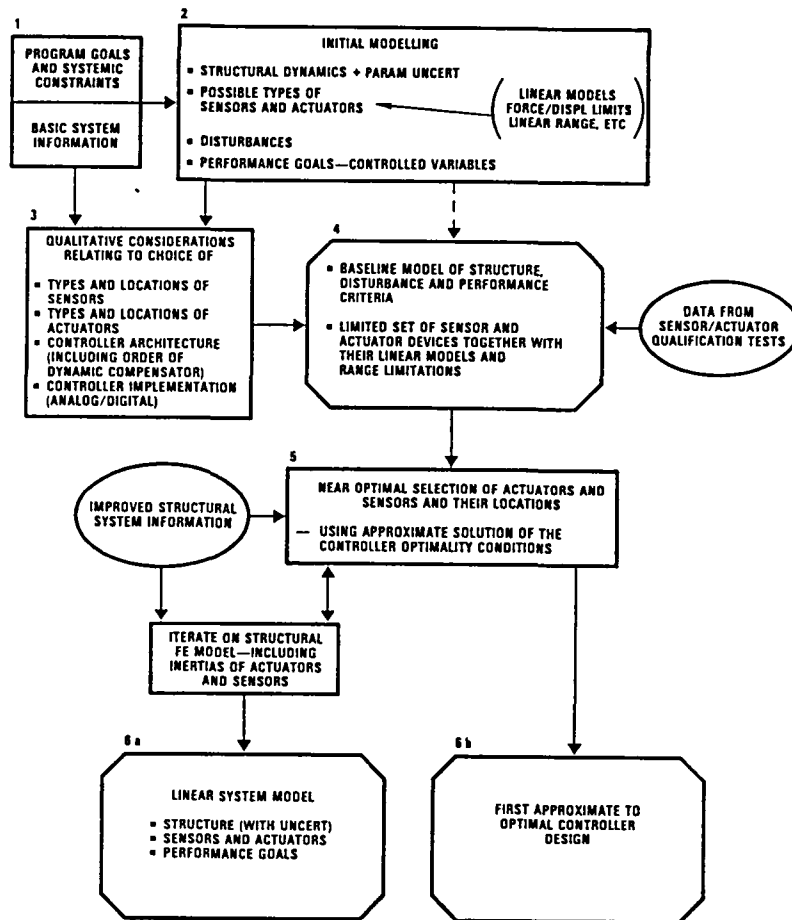Suppression and Shape Control (With Bandwidths).

241

Figure 10. Initial Design Methodology: Closed-Loop Modeling
and Sensor/Actuator/Control Logic Selection

procedure must be performed in order to compensate for the supporting
cable (see Figure 2) transmitted noise and acoustic disturbance. Listed
in Table 2 are the additional tests which should be performed to yield a
meaningful ground-based experiment. There are a number of parameter
identification algorithms which can be utilized, namely, (1) recursive
estimation (ARMA), (2) least-squares frequency domain methods (FFT), and
(3) the Ibrahim time domain method.
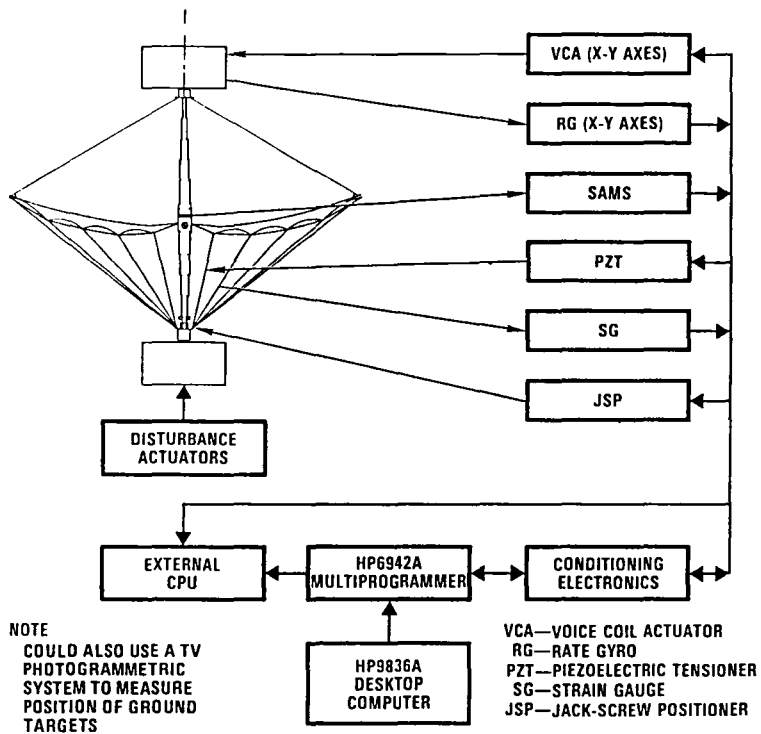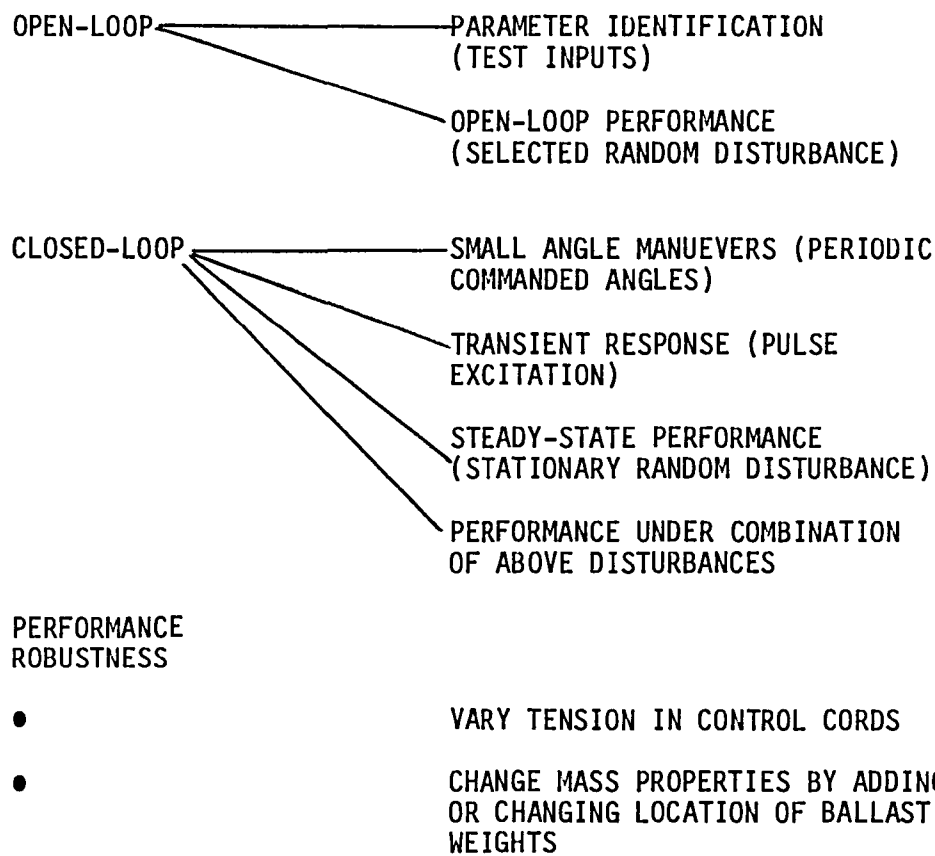
NOTE
COULD ALSO USE A TV
PHOTOGRAMMETRIC
SYSTEM TO MEASURE
POSITION OF GROUND
TARGETS

VCA—VOICE COIL ACTUATOR
RG—RATE GYRO
PZT—PIEZOELECTRIC TENSIONER
SG—STRAIN GAUGE
JSP—JACK-SCREW POSITIONER

Figure 11. Overall Experiment Hardware Concept

Table 2. Suggested Test Sequences

OPEN-LOOP ←————————————→ PARAMETER IDENTIFICATION
                         (TEST INPUTS)

                         OPEN-LOOP PERFORMANCE
                         (SELECTED RANDOM DISTURBANCE)

CLOSED-LOOP ←————————————→ SMALL ANGLE MANUEVERS (PERIODIC
                           COMMANDED ANGLES)

                           TRANSIENT RESPONSE (PULSE
                           EXCITATION)

                           STEADY-STATE PERFORMANCE
                           (STATIONARY RANDOM DISTURBANCE)

                           PERFORMANCE UNDER COMBINATION
                           OF ABOVE DISTURBANCES

PERFORMANCE
ROBUSTNESS

●   VARY TENSION IN CONTROL CORDS

●   CHANGE MASS PROPERTIES BY ADDING
                           OR CHANGING LOCATION OF BALLAST
                           WEIGHTS

244

III. Analytical Results

Preliminary analytical results are shown in Figures 12 and 13. The analysis includes twenty (20) modes of the system. The type of devices used and their placement on the structure are as follows:

Actuators

Piezoelectric Tensioners	-	Every Second Gore (All Cords on a Gore)
Jackscrew Positioners	-	Every Fourth Gore (Middle and Outer Cords)
Voice Coil Actuators	-	Two At Tip of Antenna (X-Y Axes)

Sensors

Strain Gauges	-	Every Second Gore (All Cords on a Gore)
Inertial Accelerometers*	-	Two at Tip of Antenna (X-Y Axes)
SAMS Measurement System	-	Receiver at Node 51 in Model
	-	Reflectors Every Fourth Gore at Tip and Middle of Gore

Disturbance

| 2 Disturbance Torques | - | Applied Independently Along the X and Y Axes at S/C Bus (1 lb RMS) |

Figure 12 essentially depicts the results obtained by use of Optimal Projection. The system cost is plotted as a function of the number of modes compensated. The dashed line at the top of the figure shows the open-loop cost, and the remaining curves were obtained by changing the control penalty (lower control penalty results in higher control authority).

For a control penalty of 10^6 the curve becomes flat at a point for compensation of only four modes. Therefore, a dynamic compensator design whose order is greater than $N_c = 8$ is not necessary, since this would not gain anything in the system in terms of system cost. Figure 13 shows a plot of the open and closed-loop poles for a control penalty of 10^6 and 5 modes compensated. The X's are the open-loops and the diamonds are the closed-loop poles.

*The inertial accelerometers are being used in lieu of the Rate Gyros.
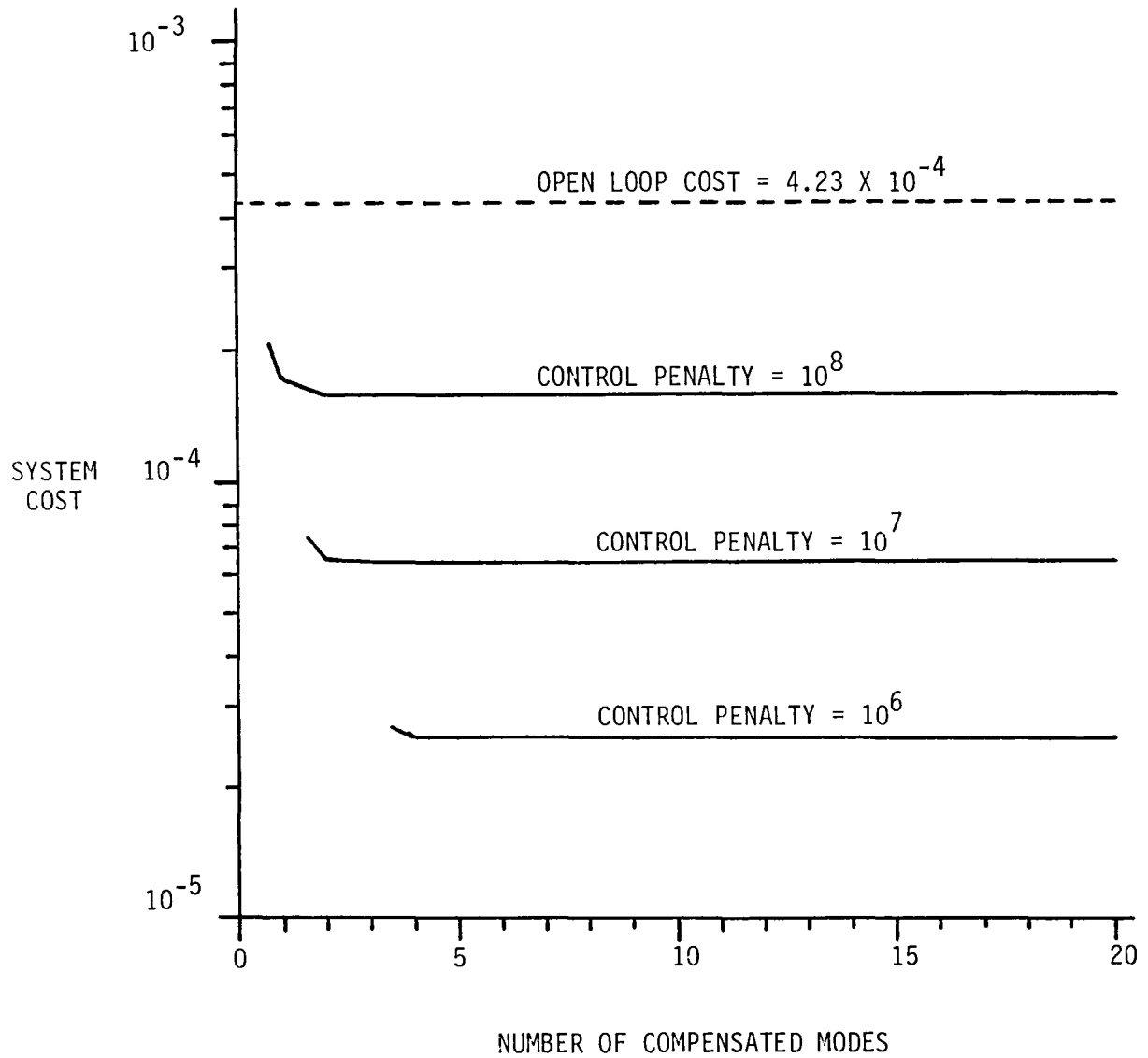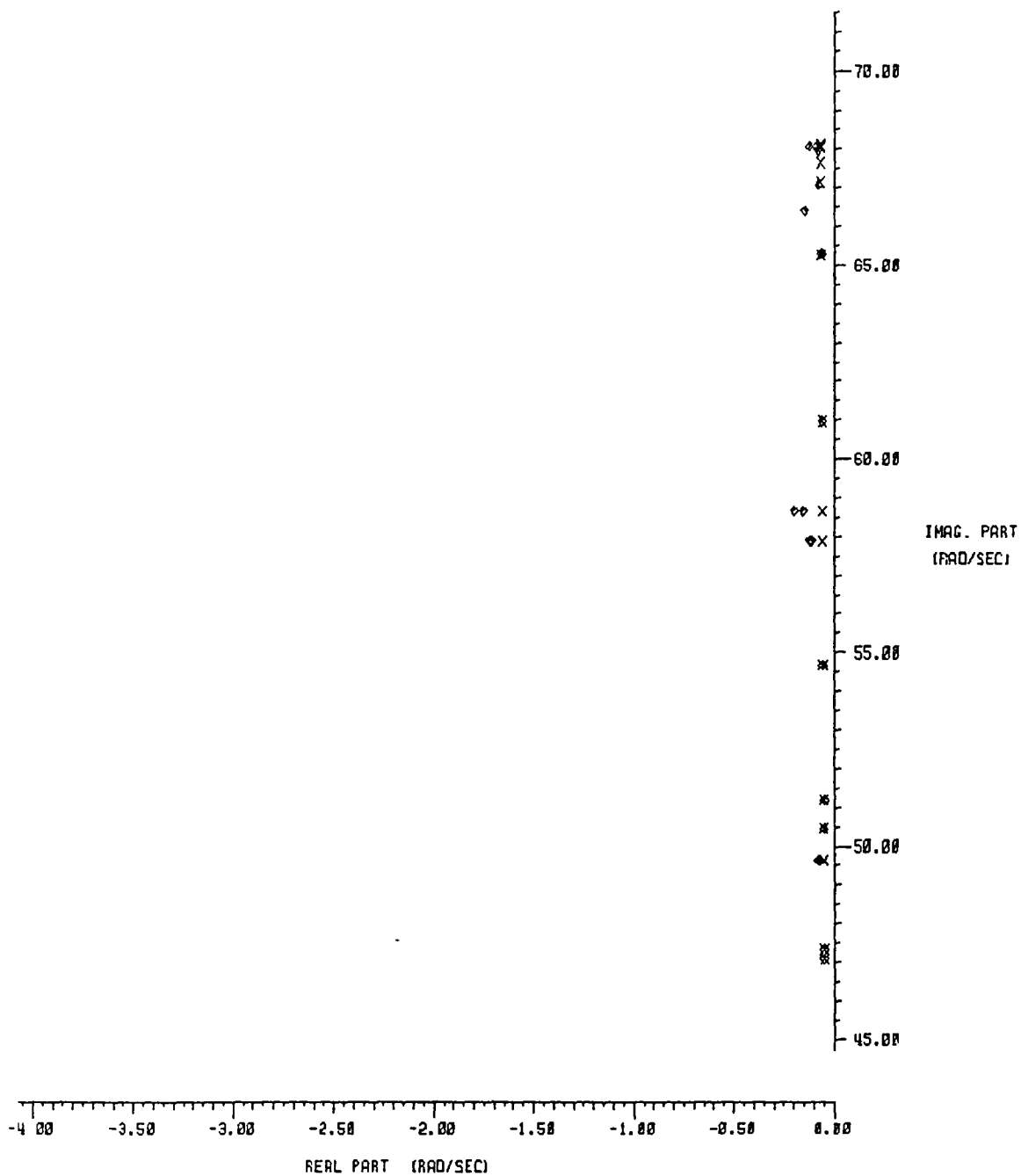
Figure 12. Preliminary Analytical Results

Figure 13. Open and Closed Loop Poles
(For ρ =10^6, and 5 Modes Compensated)

IV. Concluding Comments

The design of a ground-based vibration control experiment for a large space antenna (utilizing the 15-M Hoop/Column Model) has been outlined. This is a continuing effort and only preliminary results have been presented. Current activities include generating compensator designs of varying order for all of the system modes utilizing Optimal Projection. Sensor and actuator dynamics are included in the overall structural model with appropriate noise levels for the devices.

After finalization of the ground-based experiment, the next major step is to utilize the design to devise a flight experiment, which will be an STS-attached configuration. The deployment sequence for the 15-M Hoop/Column Antenna is shown in Figure 14.
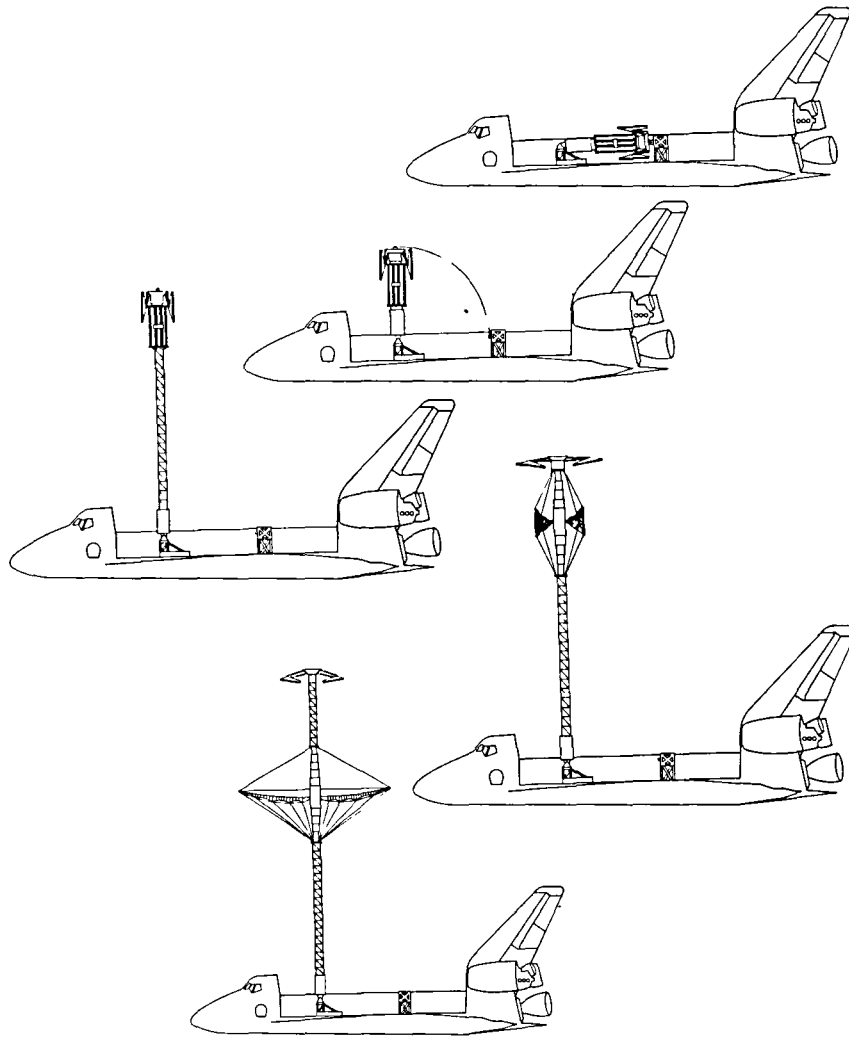
Figure 14.   Flight Experiment Deployment Sequence

V. References

1. "50-Meter Antenna Flight Experiment Study", Harris Corp., Vol. 1 (Hoop/Column Antenna), Vol.2 (Deployable Truss Structure (DTS)), Prepared for NASA Langley Research Center, May 20, 1983.

2. F.M. Ham, J.W. Shipley, and D.C. Hyland, "Design of a Large Space Structure Vibration Control Experiment", 2nd International Modal Analysis Conference, Orlando, Florida, February 6-9, 1984.

3. D.C. Hyland, "Active Control of Large Flexible Spacecraft: A New Design approach Based on Minimum Information Modeling of Parameter Uncertainties", VIP & SU/AIAA Symposium, June 1981.

4. D.C. Hyland, "Maximum Entropy Stochastic Approach to Control Design for Uncertain Structural Systems", No. 9475, ACC(IEEE), June 1982.

5. D.C. Hyland, "Minimum Information Modeling of Structural Systems with Uncertain Parameters", JPL Workshop on Applications of Distributed System Theory to the Control of Large Space Sturctures, 14-16 July 1982.

6. D.C. Hyland, "Optimality Conditions for Fixed-Order Dynamic Compensation of Flexible Spacecraft with Uncertain Parameters", No. 82-0312, AIAA Aerospace Sciences Meeting, January 1982.

7. D.C. Hyland and D.S. Bernstein, "Explicit Optimality Conditions for Fixed-Order Dynamic Compensation", 22nd IEEE Conference on Decision and Control, San Antonio, TX, Dec. 14-16, 1983.

8. "ACOSS Eight (Active Control of Space Structures)", Phase II, TRW, Sponsored by DARPA, No. 3654, RADC-TR-81-242, Sept. 1981.

9. "ACOSS Six (Active Control of Space Structures)", The Charles Stark Draper Lab. Inc., Sponsored by DARPA, No. 3654, RADC-TR-81-289, Oct. 1981.

10. "ACOSS-16 (Active Control of Space Structures)", Honeywell, Sponsored by DARPA, No. 3654, RADC-TR-82-225, Oct. 1982.

11. "Vibration Control of Space Structures - Final Technical Report", Prepared for Department of the Air Force, Air Force Systems Command, Aeronautical Systems Division, Wright-Patterson AFB, by Lockheed Missiles and Space Co. Inc., and Integrated Systems Inc., April 1983.

12. "Vibration Control of Space Structures - Final Technical Report", Prepared for Department of the Air Force, Air Force Systems Command, Aeronautical Systems Division, Wright-Patterson AFB, by TRW Space and Technology Group, May 15, 1983.

VI. Acknowledgements

A HARDWARE DEMONSTRATION OF DISTRIBUTED CONTROL FOR A FLEXIBLE OFFSET-FEED ANTENNA

D. B. Schaechter
Lockheed Palo Alto Research Laboratory
Palo Alto, CA 94304

N. C. Nguyen
Lockheed Missiles & Space Company
Sunnyvale, CA 94089

ABSTRACT

A fully instrumented hardware model of a flexible offset-feed antenna has been constructed for laboratory tests. Three rate gyros, four angular position laser sensors, and a set of ten distributed accelerometers are used to reconstruct the antenna state. Three control moment gyros are used to simultaneously orient the antenna, and to maintain a stable line of sight. This paper contains a description of the distributed antenna control system and experimental results.

INTRODUCTION

In recent years, there has been increasing interest in large space structures that require precise attitude control, pointing control, and figure control [1]. The advent of the NASA Space Shuttle has opened the way to launching deployable or erectable satellites which are an order of magnitude larger and more complex than previous satellites. This capability makes possible new applications in Earth sensing, communications, astrophysics, and detection and ranging of flight vehicles.

These spacecraft will require new techniques for vibration control. It will no longer be sufficient to design a stiff structure and control it as a rigid body. Large antennas and mirrors require that the damping and stiffness of the structure be augmented, that the dynamic disturbance inputs be minimized by careful design, that specific devices be applied to maintain surface figure accuracy, and that control forces during slewing be tailored to minimize elastic responses. This results in a growing need for testing of emerging control technologies on hardware simulations of complex space vehicles.

Recently, several hardware experiments have been assembled. These experiments include a hanging flexible beam at the Jet Propulsion Laboratory [2], a flexible beam at NASA Langley Research Center, a large cantilever beam at Lockheed, plates at

TRW and Lockheed, a two-dimensional truss structure at General Dynamics, a torsional pendulum and a flexible beam at Stanford University, a beam-like structure at Hughes, a three-dimensional truss at Lockheed, and the Lockheed TOYSAT structure control experiment [3]. The most ambitious experiment constructed thus far is the hardware simulation of the offset-feed antenna described in [4]. It is known as the Proof-of-Concept (POC) experiment, and is designed to validate the applicability of modern control theory to the control of flexible structures involving realistic space hardware. This paper will present an extension of the material documented in [4].
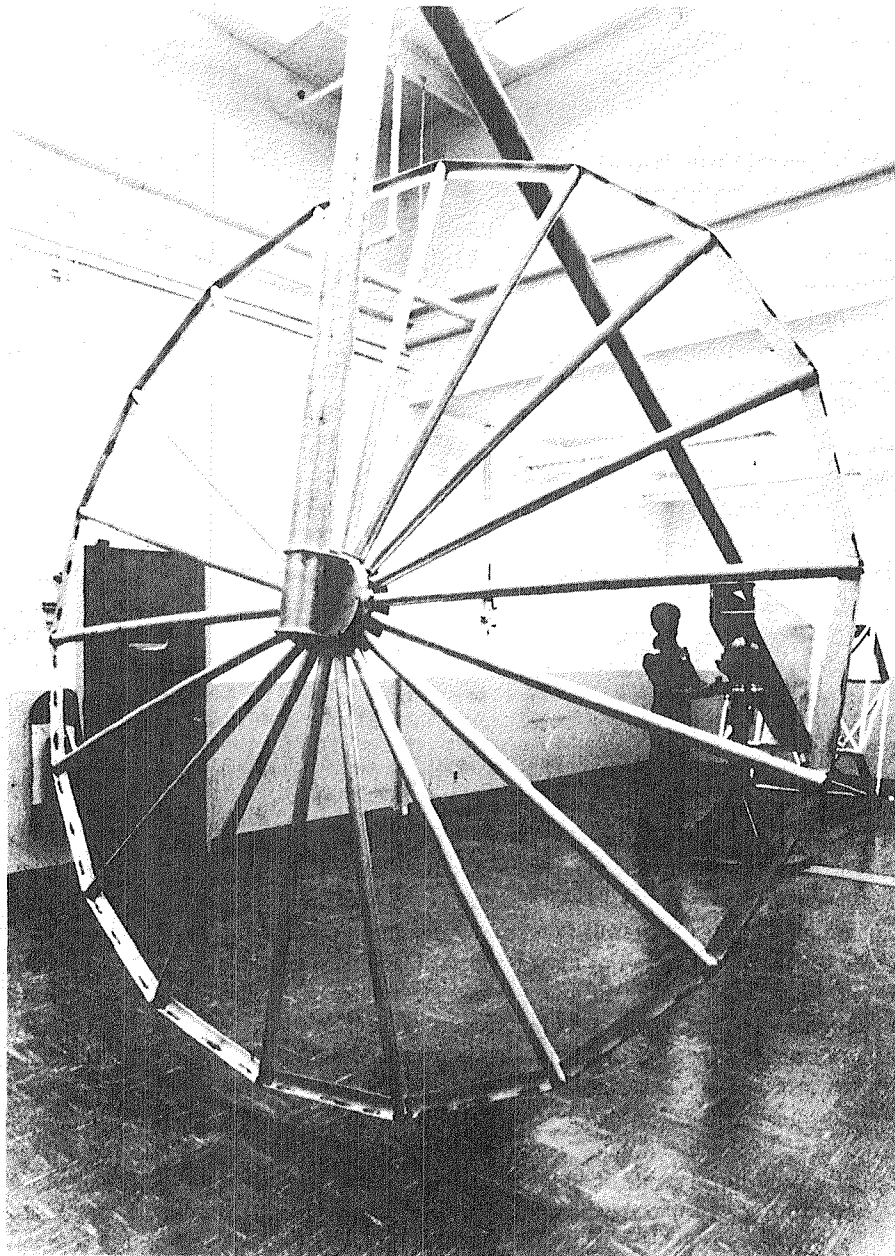

FIG. 1. Hardware Setup for POC Experiment.

254

HARDWARE SETUP

The hardware test bed shown in Figs. 1 and 2 is a version of an offset-feed antenna communications vehicle approximately thirty feet long, and weighing almost 600 lbs. A three-axis air bearing is used to provide support while allowing unrestricted attitude motion. Principal control actuation is provided by a cluster of three control-moment gyros (CMGs), each capable of as much as 100 ft-lbs of torque. Sensing is provided by three rate-gyros colocated with the CMGs, ten distributed accelerometers, and two laser attitude sensing devices. The control algorithms are carried out by a PDP-1145 digital computer augmented with a CSPI array processor.
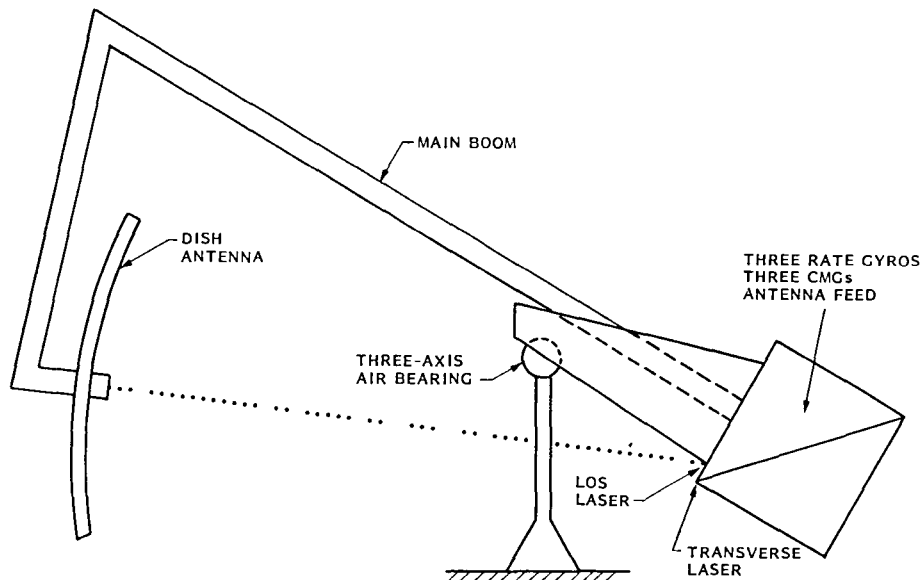

FIG. 2   Schematic of POC Test Specimen

ANTENNA MODEL

A modal model of the POC attitude and flexible body dynamics was derived from a finite element model of the structure. The POC posesses flexible modes in addition to the three rigid body rotation modes. A general description of these modes is contained in Table 1. In all of the experiments to date, the controller has contained the three rigid body modes as well as the five lowest frequency structural bending modes.

255

TABLE 1. Modal Characteristics of POC Specimen

| Mode Number | Experimental Results | | | Analytical Resonant Frequency (Hz) | Percent Difference, Analytical vs Experimental |
	Resonant Frequency (Hz)	Damping (% Viscous)	General Description		
1	1 50	0 27	1st Y bending	1 67	11 3
2	1 58	0 47	1st X bending	1 72	9 0
3	3 01	0 28	2nd X bending	3 28	8 9
4	5 07	0 18	Torsion	4 50	11 2
5	6 91	0 21	2nd Y bending	6 23	9 9
6	11 49	0 40	Combined X-Y bending	10 09	12 2
				10 72	6 7
7	13 02	1 30	X-boom bending and reflector rotation	12 11	7 0
8	14 24	0 58	X-boom bending, reflector Z bending	14 95	5 0
9	15 33	0 65	Boom and reflector Y bending	15 44	0 7
10	16 90	0 20	Reflector Z bending	16 36	3 2
11	16 98	0 32	Y-boom bending and ES torsion	17 29	1 9
12	17 61	0 32	Y-boom bending and ES bending		
13	19 10	0 10	Z Reflector bending	19 49	2 0
14	19 97	0 73	ES Y bending		

ESTIMATION AND CONTROL

Standard optimal estimation and optimal control techniques were first used to obtain controllers for the POC [4,5]. Optimal estimation is used to reconstruct estimates of the modal states from the available sensors on the POC, and the optimal controller uses the estimated states to alter the open loop dynamics. The three rate-gyros, the vertical and horizontal components of the line-of-sight and transverse lasers, and the ten accelerometers provide a total of seventeen measurements to the state estimator.

The dual to the state estimation problem is the control problem. The control objective is to trade the closed loop control performance against the amount of control which must be exerted by the three CMGs. The iterative control system design process proceeds as follows. First, an optimal estimator is implemented on the POC. The measure of how well the estimator is performing is the amount of the difference between the actual sensor outputs and the predicted sensor outputs. The predicted sensor outputs are based upon what ideal sensors would measure if the estimated state were the true state. A small difference indicates that the estimator is working well.

256

The next step is to introduce a weak feedback control system into the FOC. As greater confidence in the correctness of the closed loop dynamics is established, a gradual tightening of the control loop is made. [4] contains detailed results of the open loop and the closed loop tests performed on the FOC without the use of the accelerometers, and several of the anomalies that were encountered in these studies.

ACCELEROMETER MEASUREMENTS

The purpose of this current work is to develop and implement distributed estimation techniques for structural control. A distributed set of ten accelerometers is mounted on the FOC. Since the bandwidth of the accelerometers (>50 Hz) is much greater that the bandwidth of the rate gyros (10 Hz), the inclusion of accelerometer information in the state estimator will improve the reconstruction of the high frequency modes of the structure. Furthermore, since the accelerometers are spatially distribued across the structure, the numerical conditioning of the problem to "invert" the measurements to obtain the state estimates is improved. Again, improved state estimates will result.

The process by which acceleration measurements are included in the state estimation process is discussed below. First, the design begins with a continuous time system in state variable format:

$$\dot{x} = F\,x + G\,w_c \qquad\qquad (1)$$

$$z = H_1\,x + H_2\,\dot{x} + v_c$$

The continuous white noise sources w_c and v_c are uncorrelated, have zero means, and spectral densities Q_c and R_c respectively. The measurement vector has now been expanded to include measurements of the state and measurements of the time derivative of the state. (1) may be rewritten as:

$$\dot{x} = F\,x + G\,w_c \qquad\qquad (2)$$

$$z = H\,x + H\,G\,w_c + v_c$$

where $H = H_1 + H_2\,F$. The discrete time equivalent of (2) is given by:

$$x_{n+1} = \phi\,x_n + \Gamma w_d \qquad\qquad (3)$$

$$z_n = H\,x_n + H_2 G\,w_c + v_c$$

where the covariance of the process and measurement noises are given by:

$$Q_d = Q_c / T$$

$$R_d^* = (H_2 G Q_c G^T H_2 + R_c) / T$$

where T is the sample time. An examination of (3) reveals that the "process" and "measurement" noises are now correlated. One standard approach for handling correlated noise sources is to add "zero" to the first equation in (3) in a special way to "uncorrelate" these sources. The result is:

$$x_{n+1} = (\phi - L H) x_n - L z_n \qquad + \text{process noise} \qquad (4)$$

$$z_n = H x_n \qquad\qquad\qquad + \text{measurement noise}$$

where

$$Q_d^* = \Gamma Q_d \Gamma^T - T^2 \phi G Q_d G^T H_2^T R_d^{*-1} H_2 G Q_d G^T \phi^T \qquad (5)$$

$$R_d^* = H_2 G Q_d G^T H_2^T + R_d$$

$$L = T \phi G Q_d G^T H_2^T R_d^{*-1}$$

The transformed system in (4) and (5) may now be used for estimator design.

SIMULATION

Simulation of the behavior of the open loop system was performed by evaluating the filter performance with a seventeen mode evaluation model. This evaluation model consists of the eight controlled modes and the other structural modes of the POC. The state transition equation was augmented with the filter equation to yield the recursive equation:

$$\begin{bmatrix} x_{n+1} \\ \hat{x}_{n+1} \end{bmatrix} = \begin{bmatrix} \phi_F & 0 \\ K H_F & \phi - K H \end{bmatrix} \begin{bmatrix} x_n \\ \hat{x}_n \end{bmatrix} + \begin{bmatrix} \Gamma_d \\ 0 \end{bmatrix} d_n$$

with initial conditions $x(0) = x(0) = 0$. d_n is the amplitude of the disturbance force (chirp input) applied to the POC during the interval zero to four seconds. Γ_d is the disturbance distribution vector that represents the orientation and location of the disturbance force. ϕ_F and H_F are the transition and measurement matrices of the evaluation model. Dimensions of x and $\hat{x}$ are 34 by 1 and 16 by 1, respectively. The corresponding matrices, accordingly, take on the appropriate dimensions.

The initial simulation showed that the frequencies of two of the modes were slightly different from those observed in the real test. These values were subsequently adjusted by changing the
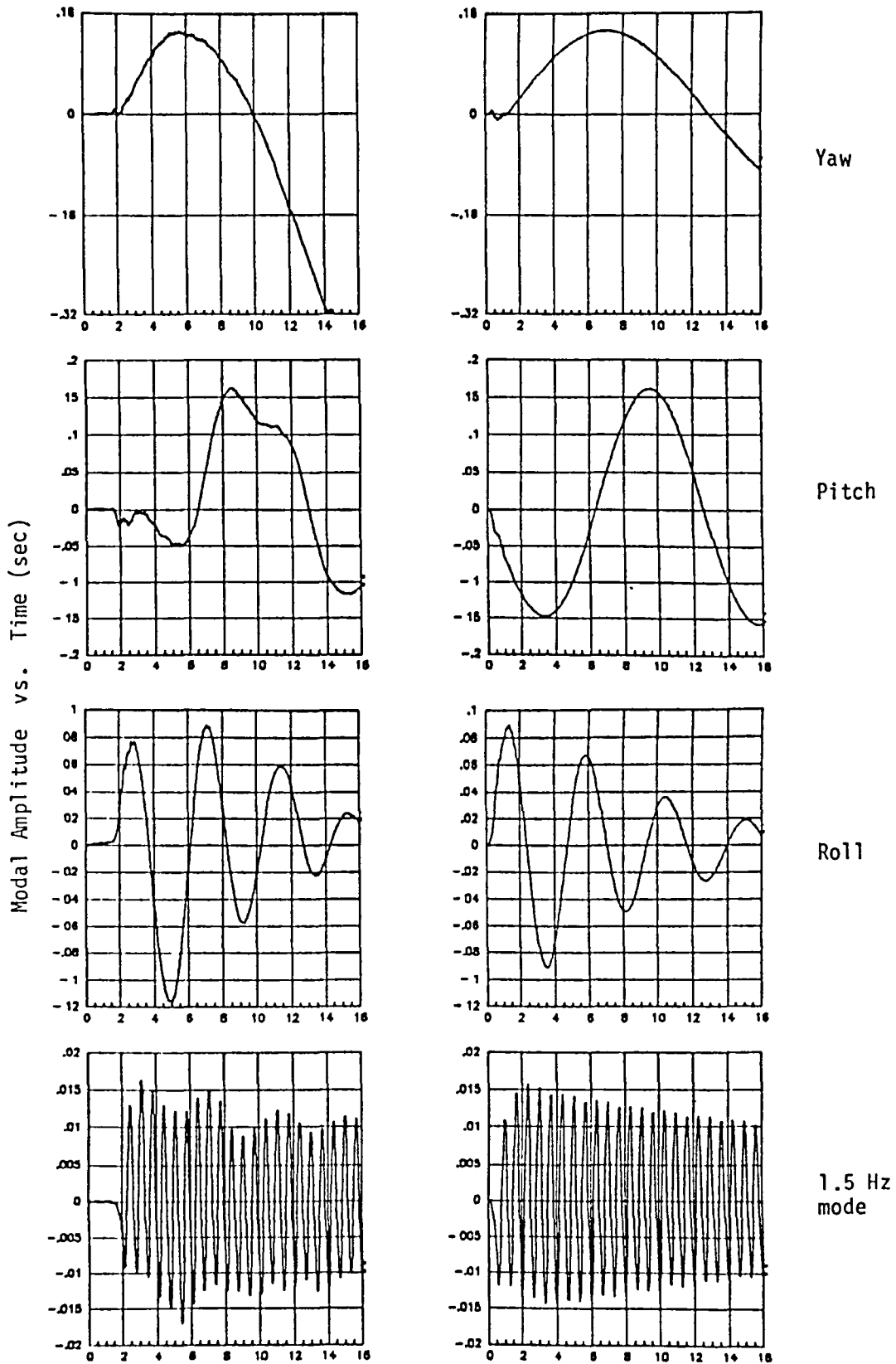
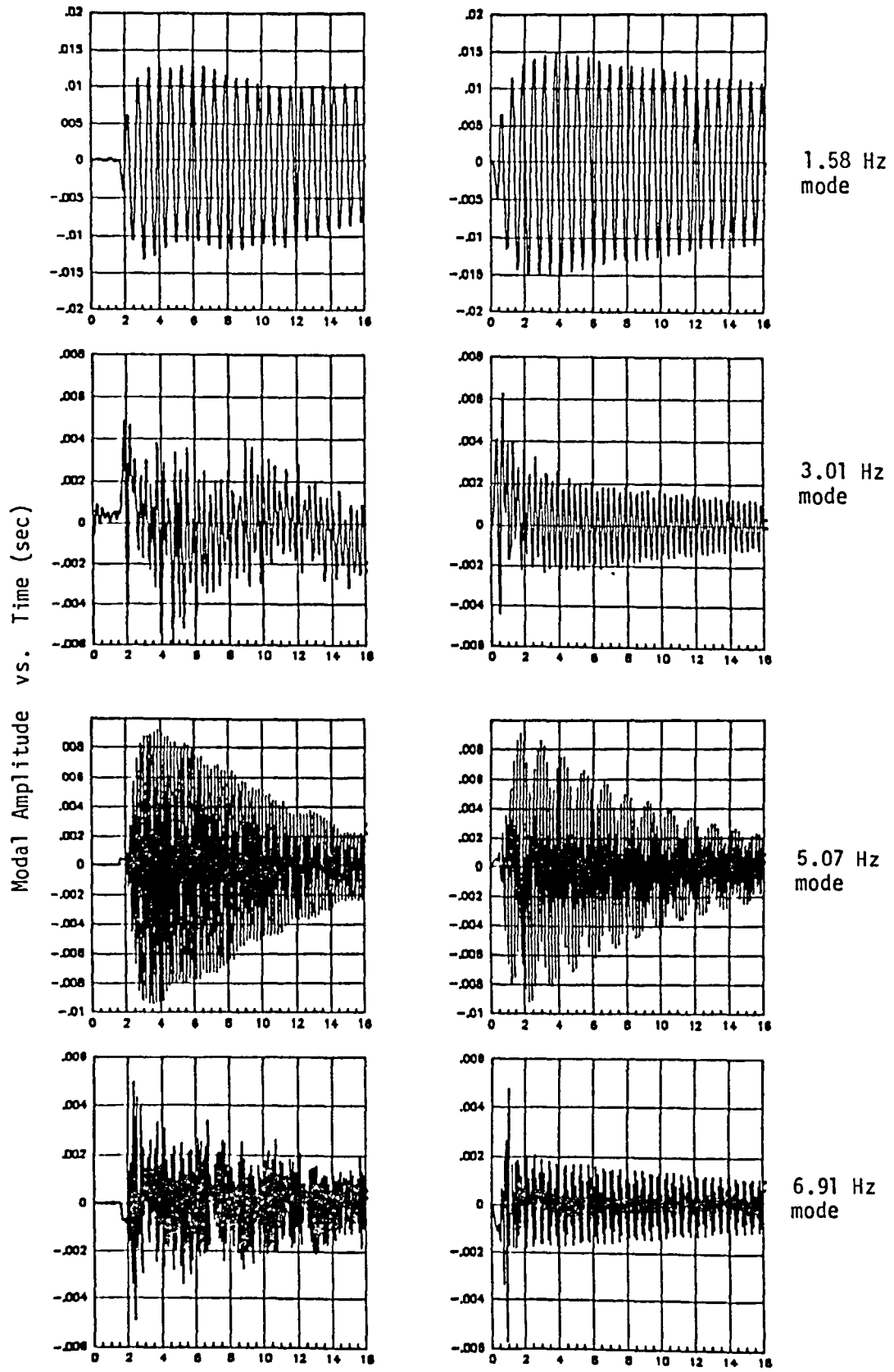Fig. 3   Open-loop state estimator outputs: actual test (left column) and simulation (right column)

Fig. 4   Open-loop state estimator outputs: actual test (left column) and simulation (right column)

corresponding elements of the system matrix F_F, the continuous time version of ϕ_F. Due to uncertainties in the orientation of the disturbance force, some of the elements of Γ_d were also scaled such that modal displacements and velocities obtained from the simulation agreed with the experimental results.

A comparison of the estimator outputs obtained in the laboratory, and the computer simulation outputs is shown in Figs. 3 and 4. Generally speaking, the simulation results agree quite well with the test results. The beat frequency appearing in the 5.07 Hz. mode is a result of plotting every fourth point of simulated data. When all the points are plotted, this feature disappears. It should also be noted that the disturbance force was applied to the POC and t=1.5 seconds in the laboratory, whereas in the simulation, the disturbance was applied at t=0 seconds.

EXPERMIMENTAL RESULTS

As with previous tests [4] the criterion used to guage the performance of the estimator is the closeness between the predicted sensor outputs based on the estimated states, and the true sensor outputs. The weights on the accelerometer error covariances in the optimal estimator performance index were selected so the contribution in the state estimator of the rate gyros and the accelerometers at the frequency of seven Hz were roughly equivalent. In this way, rate gyro information would be used primarily to reconstruct states associated with modes below seven Hz, and the accelerometers would produce major effects above seven Hz. The value of seven Hz was selected in part by consideration of the ten Hz bandwidth limit of the rate gyros, and in part by previous tests [4] which resulted in poorer than expected closed loop response of the seven Hz mode.

Fig. 5 contains the estimates of the full sixteenth order state vector composed of the modal rates and the corresponding modal amplitudes when accelerometer information is used. This sixteen second duration test was initiated by the introduction of a four second chirp external disturbance that was applied at t=0 to excite the structure. The set of four laser measurements, three rate gyros, and ten accelerometers were sampled and the state vector was updated at sixty-four Hz. Since the contribution of the accelerometer measurements begins at seven Hz, the time histories provide only a visual comparison that the state estimates are roughly the same as they were when no accelerometers were used. The true test of the performance of the estimator is contained in Figs. 6-10 where the estimated and actual sensor outpus are compared. The comparisons of the time histories of the lasers and gyros, and of the frequency transforms of the accelerometers indicate that the filter is performing well.
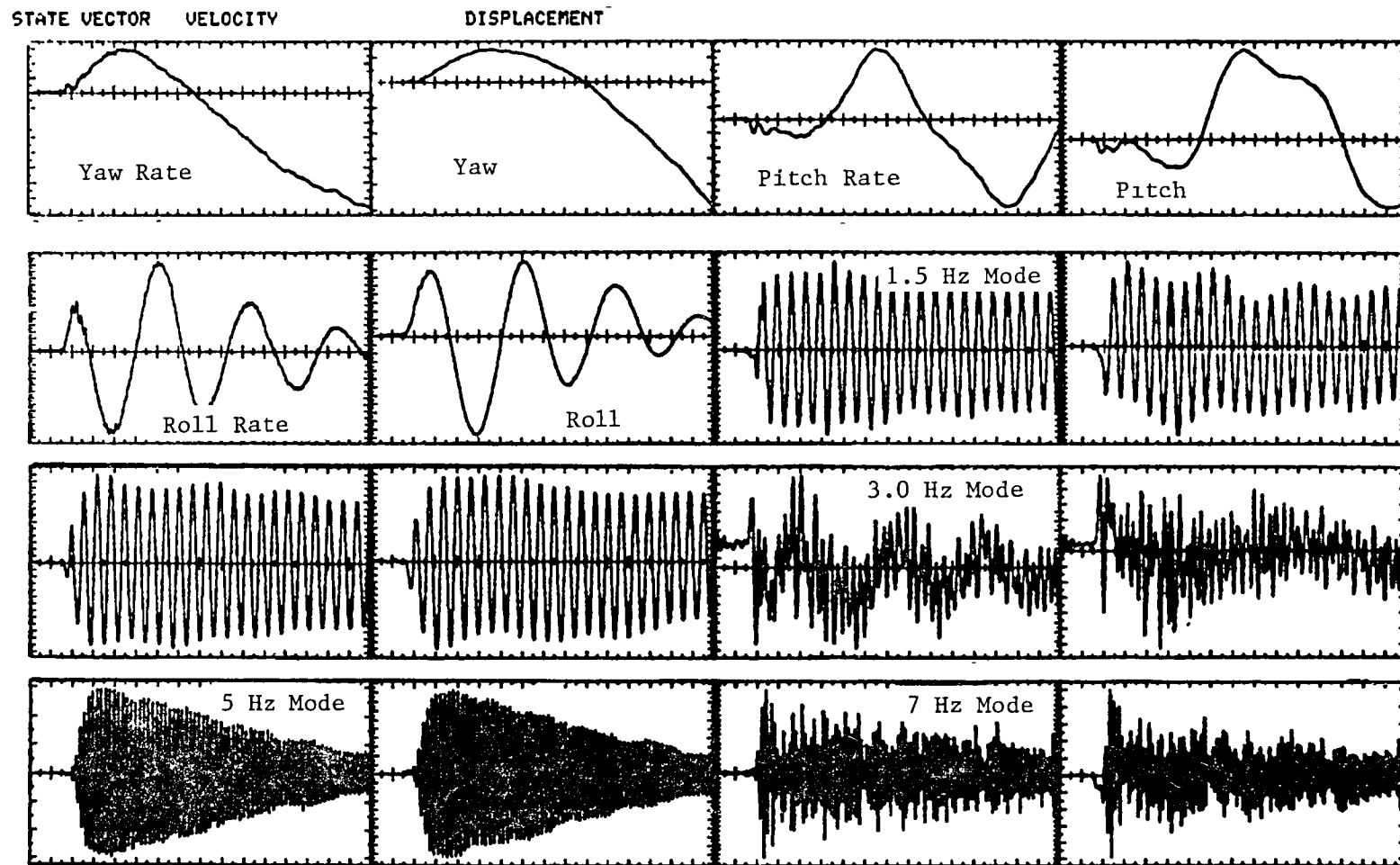
STATE VECTOR   VELOCITY   DISPLACEMENT

| Yaw Rate | Yaw | Pitch Rate | Pitch |

| Roll Rate | Roll | 1.5 Hz Mode | |

| | | 3.0 Hz Mode | |

| 5 Hz Mode | | 7 Hz Mode | |

Fig. 5   Estimated State Vector-(Timespan is 16 sec, chirp applied at t=2 sec)

Fig. 6 Actual vs. Predicted Laser Line-of-Sight

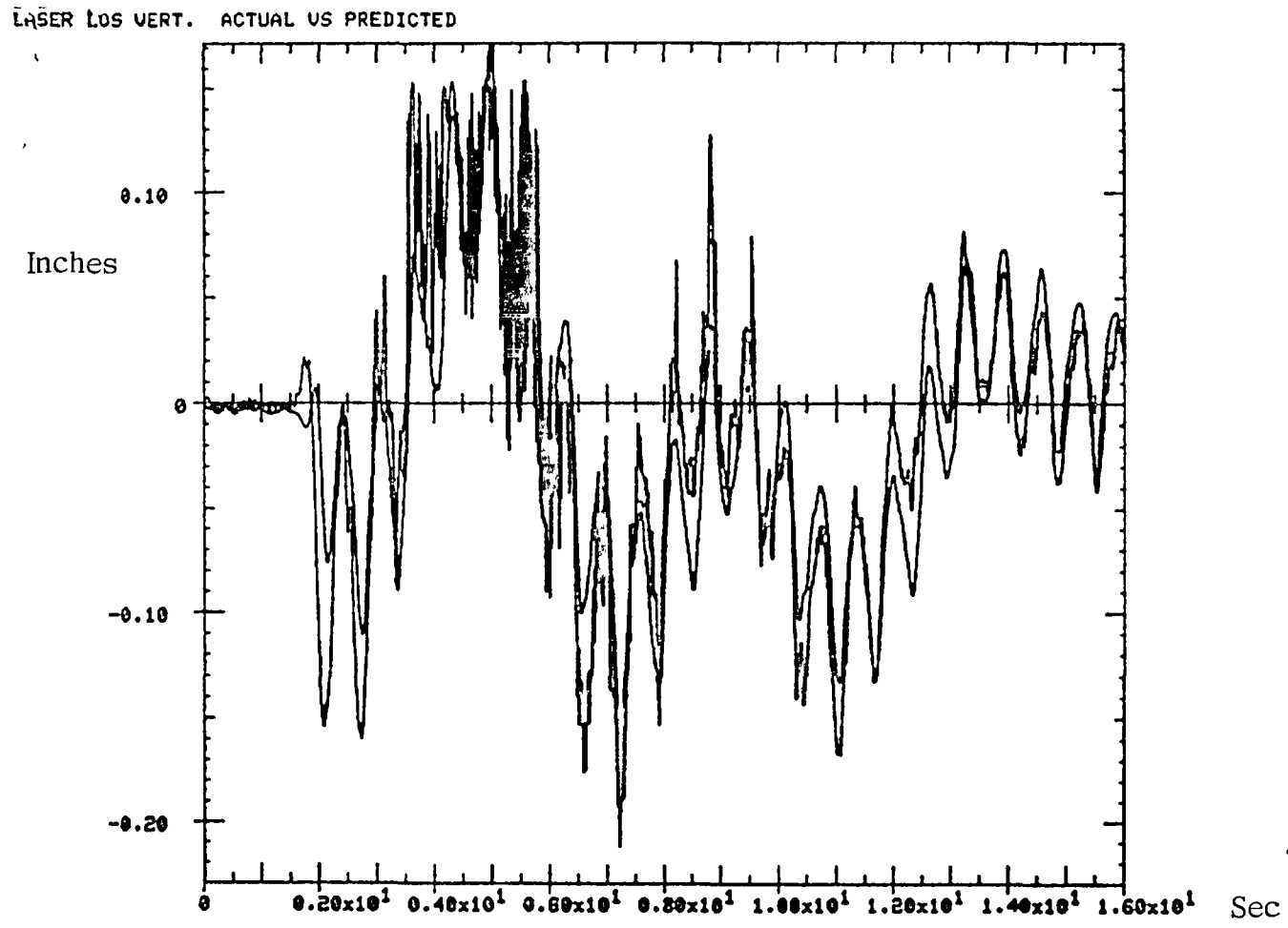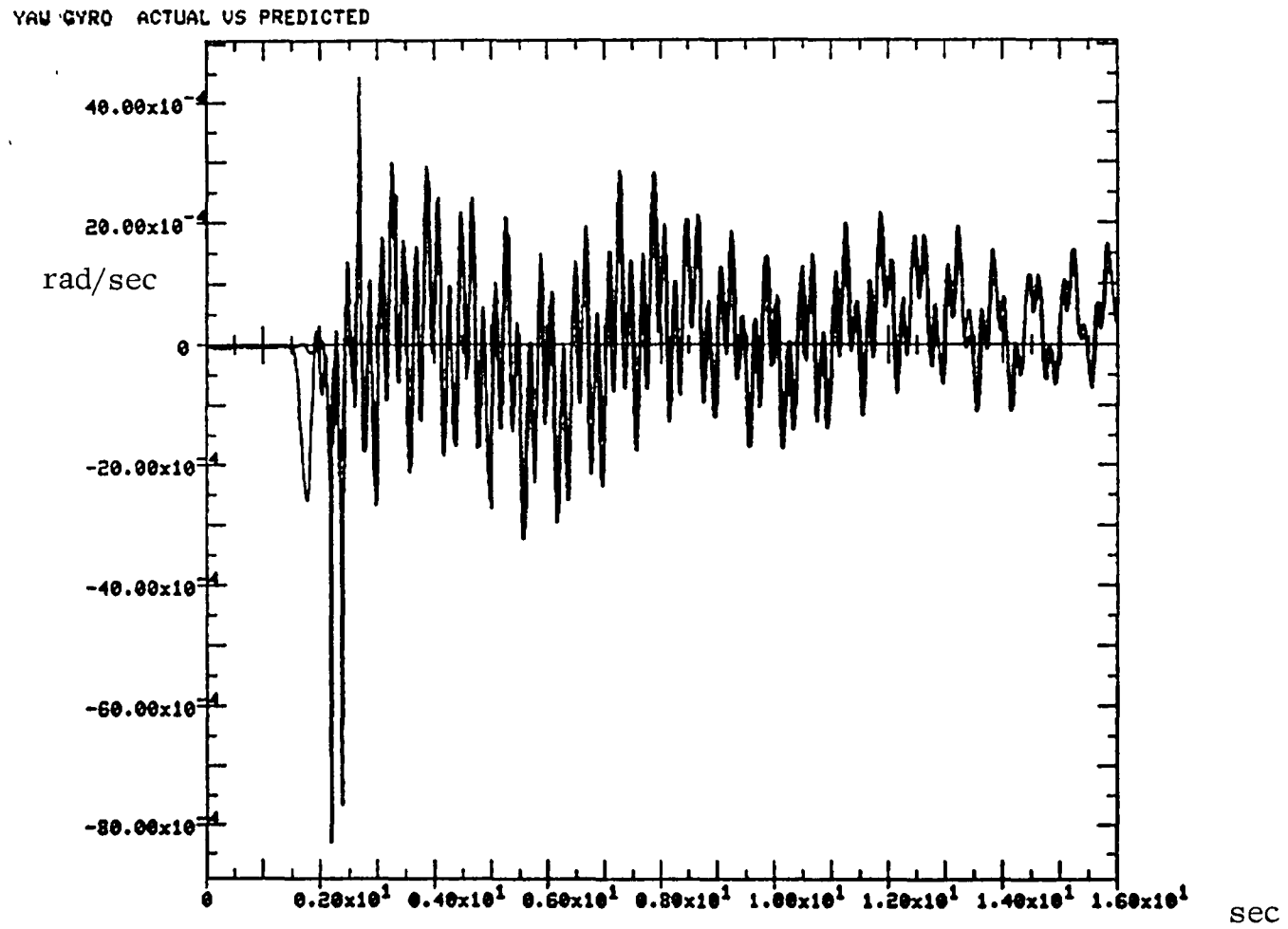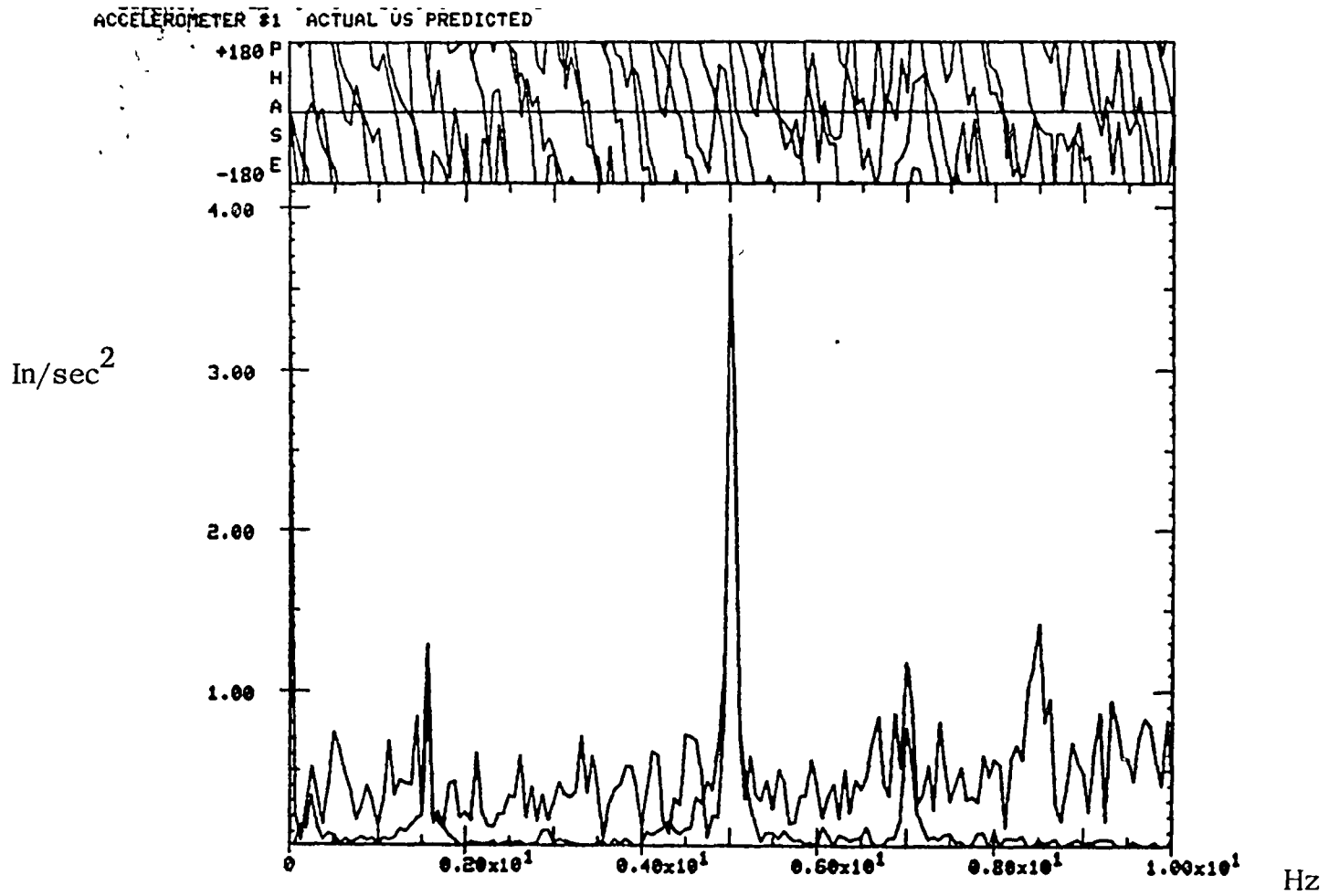YAU GYRO ACTUAL VS PREDICTED

Fig. 7 Actual vs. Predicted Yaw Gyro Output

Fig. 8   Transform of actual and predicted accelerometer outputs

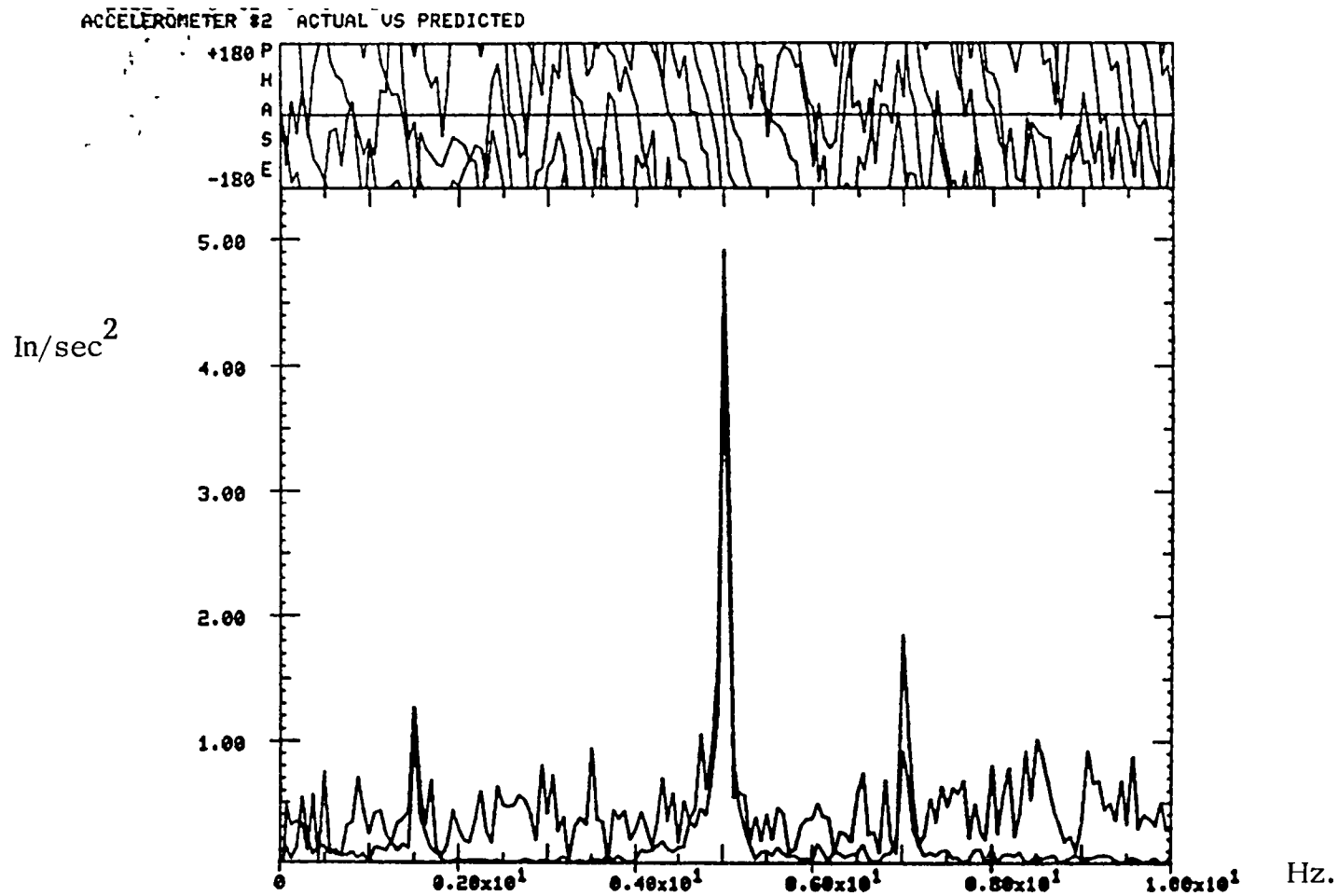ACCELEROMETER #2 ACTUAL VS PREDICTED

In/sec^2

Fig. 9   Transform of actual and predicted accelerometer outputs

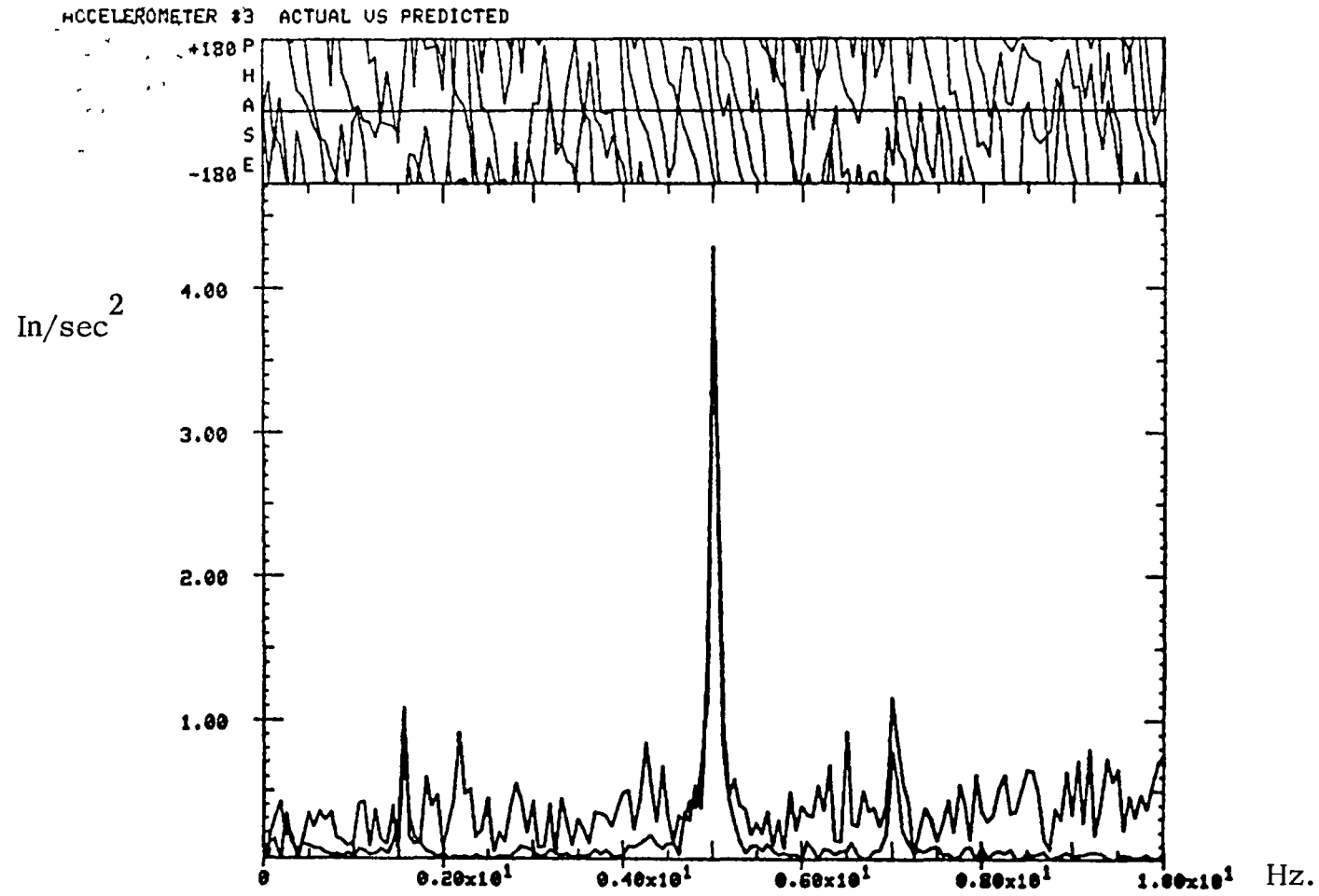ACCELEROMETER #3   ACTUAL VS PREDICTED

Fig.10 Transform of actual and predicted accelerometer outputs

CONCLUSIONS

The second testing phase of structural control algorithms on the POC test specimen has been successfully completed. Discrete time state estimators with accelerometer measurements have been derived. With a distributed set of sensors, the state vector associated with an eight mode model of the POC can be estimated accurately in real time. Digital simulation of this process has produced results that agree quite well with the experimental results. The estimator design step serves as the first stage in the two stage controller design process. The next step is to close the control loop around the POC with the estimated state vector. This second stage will employ distributed actuation in the form of pivoted proof-mass (PPM) actuators in conjunction with the distributed estimation.

REFERENCES

[1] BALAS, M.J., "Trends in Large Space Structures Control Theory: Fondest Hopes, Wildest Dreams", IEEE Transactions on Automatic Control, Vol AC-27, June 1982, pp. 535-552.

[2] SCHAECHTER, D.B., "Hardware Demonstration of Flexible Beam Control", AIAA Journal of Guidance and Control", Vol. 5, January-February, 1982, pp. 48-53.

[3] BREAKWELL, J.A. and CHAMBERS, G.J. "The TOYSAT Structural Control Experiment", The Journal of the Astronautical Sciences, Vol. 31, No. 3, July-September, 1983.

[4] BAULDRY, R.D., et al, "A Hardware Demonstration of Control for a Flexible Offset-Feed Antenna", The Journal of the Astronautical Sciences, Vol. 31, No. 3, July-September, 1983.

[5] BRYSON, A.E. and HO, Y.C., Applied Optimal Control, Blaisdell, Waltham Massachusetts, 1969.

CONTROL OF FLEXIBLE STRUCTURES

R. A. Russell
NASA Headquarters
Washington, DC 20546

RECOGNITION OF THE NEED

The requirements for future space missions indicate that many of these spacecraft will be large, flexible, and in some applications, require precision geometries. A technology program that addresses the issues associated with the structure/control interactions for these classes of spacecraft is required. The Ad Hoc Subcommittee on Controls/Structures Interaction of the Space Systems Technology Advisory Committee (SSTAC) recommended that NASA take an aggressive lead in defining and developing this technology to a state of flight readiness. This plan is the proposed NASA/OAST (Office of Aeronautics and Space Technology) response to that recommendation. A special thanks goes to Drs. J.F. Garibotti and K. Soosaar of the SSTAC Materials and Structures Subcommittee for their review and support during the development of this plan.

CONTROL OF FLEXIBLE STRUCTURES

RECOGNITION OF THE NEED

FEBRUARY 15, 1983
MILITARY SPACE SYSTEMS TECHNOLOGY MODEL

CONCEPTS:

"IN ONE-HALF OF THE TOP TEN PRIORITY (MMSTM MISSIONS) — STRUCTURES/CONTROLS INTERACTION REQUIRES ENABLING TECHNOLOGIES"

CONTROLS:

"AN ON-ORBIT PROOF-OF-CONCEPT DEMONSTRATION/FLIGHT EXPERIMENT IS PROBABLY THE MOST IMPORTANT PROGRAM NEEDED IN LARGE SPACE STRUCTURES CONTROL TECHNOLOGY DEVELOPMENT"

JUNE 9, 1983
SSTAC AD HOC SUBCOMMITTEE ON CONTROLS/STRUCTURE INTERACTION (CSI)

"FLIGHT-READINESS FOR THIS TECHNOLOGY (CSI) WILL REQUIRE A COORDINATED OVERALL DEVELOPMENT PROGRAM INCLUDING ANALYSIS AND DESIGN, GROUND TESTING, AND ON-ORBIT TESTING"

JUNE 30, 1983
ASEB WORKSHOP ON NASA'S SPACE RESEARCH AND TECHNOLOGY PROGRAM

"THE TESTING OF CONTROL SYSTEMS FOR LARGE, FLEXIBLE STRUCTURES WILL REQUIRE EMPHASIS IN THE COMING YEARS. BOTH GROUND AND TESTING IN-SPACE ARE NEEDED TO VERIFY THEORY AND ESTABLISH PERFORMANCE LIMITS"

NASA

OAST NASA HQ RT84 1268(1)
3-27-84

The control of flexible structures technology program will address analysis and design, ground testing, implementation (sensors, actuators, processors, etc.) and on-orbit testing to achieve a valid flight ready technology. The products of this program will be validated tools and approaches so that a practical implementation of this technology can be achieved.

ACKNOWLEDGEMENTS

The following NASA personnel contributed directly to the definition of this technology plan.

NASA HQ	LANGLEY RESEARCH CTR	JET PROPULSION LAB	MARSHALL SPACE FLT CTR
I. Abel	W. W. Anderson	J.A. Garba	R. Ryan
J. B. Dahlgren	M. F. Card	G. Rodriques	
R. A. Russell	A. Fontana	S. Szirmay	
S. L. Venneri	B.R. Hanks	A.F. Tolivar	
	L.W. Taylor	B.K. Wada	

CONTROL OF FLEXIBLE STRUCTURES

OBJECTIVE

- DEFINE A CONTROL OF FLEXIBLE STRUCTURES TECHNOLOGY PLAN THAT INCLUDES:

   - ANALYTICAL DEVELOPMENT

   - GROUND TESTING

   - IMPLEMENTATION (SENSORS, ACTUATORS, PROCESSORS, ETC.)

   - ON-ORBIT TESTING

NASA

One of the more significant design problems for all spacecraft is the need to stabilize the vehicle and to point it, or its sensors, with some prescribed accuracy. This is accomplished by a system of sensors, actuators, and associated electronics which combine to constitute the spacecraft control system. If the spacecraft can be treated as a rigid body, structural modes outside the bandwidth of the actuator, the design problem is greatly simplified. In the case of large flexible vehicles, where the bandwidth of the actuator may include many flexible modes, the assumption of rigidity is not valid. In addition to attitude and pointing control, flexible spacecraft will require several orders of magnitude of vibration suppression beyond what can be obtained through natural damping or viscoelastic techniques. It is clear that the technologies represented by flexible spacecraft are many times more complex than in previous generations of rigid spacecraft.
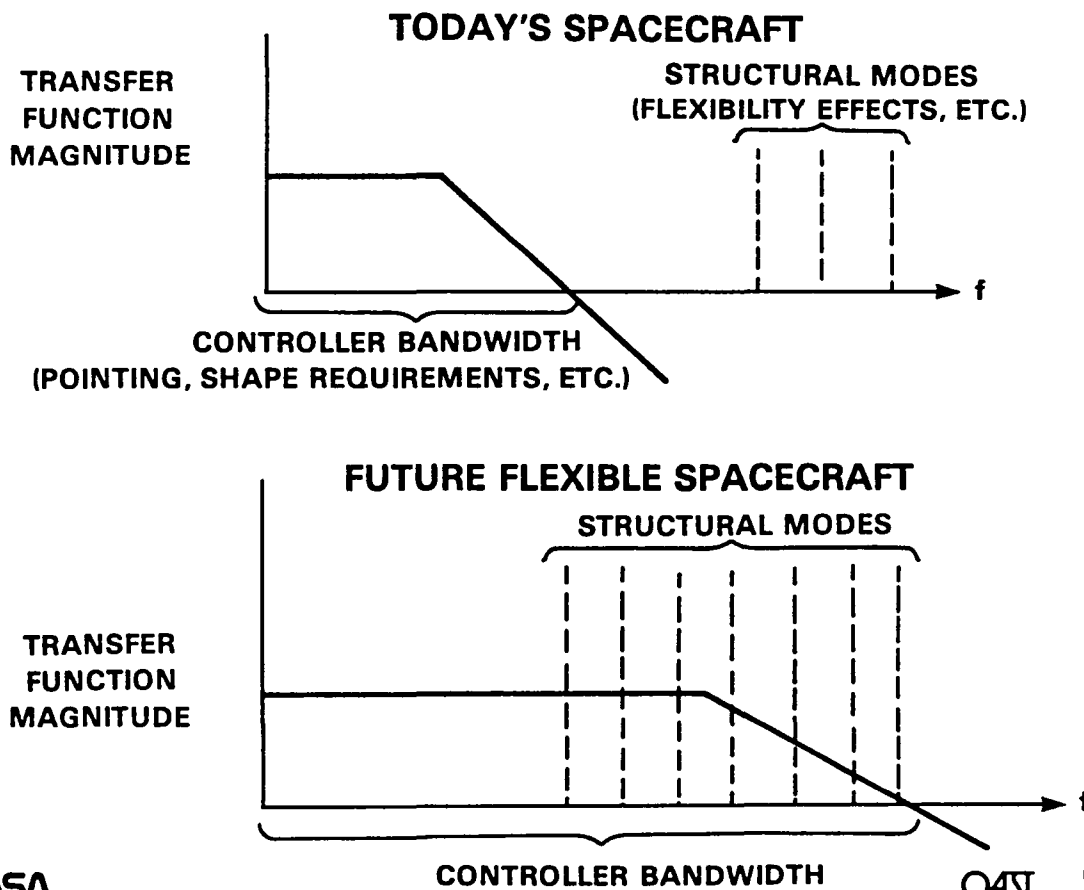
CONTROL OF FLEXIBLE STRUCTURES

DEFINITION

THE ACTIVE SUPPRESSION OF FLEXIBLE BODY
RESPONSES AS DISTINCT FROM PRESENT
PRACTICE OF CONTROL OF RIGID BODY MOTIONS
AND AVOIDANCE OF FLEXIBLE STRUCTURE AND
CONTROL INTERACTION

NASA

This chart illustrates the relative importance of the controller bandwidth used in today's spacecraft versus the structural/controls interaction that will exist in controlling future large flexible spacecraft.

CONTROL OF FLEXIBLE STRUCTURES

TODAY'S SPACECRAFT

TRANSFER
FUNCTION
MAGNITUDE

STRUCTURAL MODES
(FLEXIBILITY EFFECTS, ETC.)

f

CONTROLLER BANDWIDTH
(POINTING, SHAPE REQUIREMENTS, ETC.)

FUTURE FLEXIBLE SPACECRAFT

STRUCTURAL MODES

TRANSFER
FUNCTION
MAGNITUDE

f

CONTROLLER BANDWIDTH

NVSN

OAST

NASA HQ RT84-332(1)
11 8-83

272

The goal of the NASA control of flexible structures technology program is to generate a technology data base that will provide the designer with options and approaches to achieve spacecraft performance such as maintaining geometry and/or suppressing undesired spacecraft dynamics. This technology program will define the appropriate combination of analysis, ground testing, and flight testing required to validate the structural/controls analysis and design tools. This program will provide the designer with the necessary validated tools and approaches so that practical implementation of this technology can be achieved. This plan does not include a definition of all the supporting on-going technologies (i.e., structural concepts, structural damping, joint behavior, etc); however, they will be an important part of the successful development of the necessary tools for the control of flexible structures.

CONTROL OF FLEXIBLE STRUCTURES

PROGRAM GOAL

GENERATE A TECHNOLOGY DATA BASE THAT WILL PROVIDE "OPTION/ APPROACHES" TO ACHIEVE PERFORMANCE GOALS SUCH AS ACCURATE CONFIGURATION OR DESIRED DYNAMIC BEHAVIOR. THESE "OPTIONS/ APPROACHES" WILL INCLUDE:

- STRUCTURAL ANALYSES AND DESIGN TOOLS
    - ACCURATE ANALYTICAL MODELING
    - IMPROVED DAMPING AND NON-LINEARITY REPRESENTATION
    - ANALYTICAL MODEL SIZE REDUCTION

- CONTROLS ANALYSES AND DESIGN TOOLS
    - ADVANCED ALGORITHMS
    - HARDWARE MODELING/EFFECTS
    - IMPLEMENTATION APPROACHES (SENSOR/ACTUATOR LOCATIONS & NUMBERS)

- STRUCTURAL/CONTROL ANALYSES AND DESIGN TOOLS
    - INTERACTIVE/INTEGRATED ANALYSES
    - SYSTEM IDENTIFICATION METHODS
    - CLOSED LOOP SYSTEM MODELING/MODEL SIZE REDUCTION
    - HIERARCHIAL LEVELS OF PASSIVE/ACTIVE CONTROL
    - VALID GROUND TESTS METHODS FOR DESIGN VERIFICATION

NASA

OAST NASA HQ RT84-730 (1) 1-16-84

273

The major technical thrusts that have been defined for this program are shown. This past decade has witnessed a large amount of theoretical work in the area of control of large flexible space structures. This work was motivated by a recognition that large minimum weight space structures will be required for many future missions. The tools necessary to support such designs includes; improved structural analysis, modern control theory, advanced modeling techniques, system identification, and the integration of structures and controls. Practical implementation of these designs has, to date, been impeded by the need for space-qualified hardware in the area of sensors, actuators, and digital processors. In addition, confidence in the integrity of these new design techniques has not been supported by ground and on-orbit testing. The major focus of this plan is directed towards ground and flight test validation.

CONTROL OF FLEXIBLE STRUCTURES

TECHNOLOGY THRUSTS

- ANALYTIC MODELING AND MODEL REDUCTION

- SYSTEM IDENTIFICATION

- INTEGRATED STRUCTURE/CONTROL
  DESIGN METHODOLOGY

- SENSOR AND ACTUATOR DEVELOPMENT

- GROUND TESTING

- ON-ORBIT TESTING

NASA

OAST NASA HQ RT84-341(1)
3-26-84

The size of future large space systems dictates that mult-input, multi-output distributed control systems be given serious attention. Complicating the design and analysis of such a system is the fact that the infinite degree-of-freedom structure is replaced by a finite element model which is used to generate modal data. The resulting equations of motion, which may contain hundreds of modes, become extremely large and time consuming to solve. Model reduction is required to reduce the size of the control design problem while retaining the basic characteristics of the dynamic system. This process is extremely critical since the modes that can be eliminated are not always obvious to the designer. It is not unusual for an instability to be missed entirely by analytical methods but to be present in flight.

The quality of the structural model requires close attention. Many higher frequency modes, that lie within the bandwidth of the actuator, need to be determined with the proper fidelty. Complicating the problem is that many control system design approaches require that the damping properties be known with some precision. Since joints are one of the primary sources of structural damping, improvements in the characterization of the joints will be required.

Separate mathematical models of varying levels of complexity will be required for design purposes. Low order models will be required for quick turnaround to establish, for example, the effect of structural changes or actuator placement on control design. The size of the mathematical model will play a significant role in the number of design iterations that can be accomplished.

CONTROL OF FLEXIBLE STRUCTURES

WBS SUBSET TASKS

ANALYTIC MODELING AND MODEL REDUCTION

A. JOINT DOMINATED/MULTI-CONNECTED STRUCTURE
- LARGE PROBLEMS METHOD EVALUATION

B. LARGE AMPLITUDE, TIME VARYING STRUCTURES
- SIMPLIFIED NONLINEAR METHODS OF CHARACTIZATION
- EVALUATE ARTICULATED LARGE AMPLITUDE STRUCTURAL MOTION
- DEPLOYMENT DYNAMICS

C. OPEN AND CLOSED LOOP MODEL REDUCTION
- EVALUATE REDUCED-ORDER DYNAMIC MODELING TECHNIQUES
- CLOSED-LOOP TRUNCATION METHODS
- OPTIMIZED TRUNCATION

D. CONTROL DRIVEN STRUCTURAL MODELING
- CONTROL-DRIVEN FINITE ELEMENT MODELING

NASA

To achieve the performance levels required for controlling flexible structures, the controller "plant" model needs to be very accurate. This puts great demand on current eigenvalue analyzer techniques since it may be necessary to determine high frequency modes with significant accuracy. It is expected, further, that the physical parameters of the system will change with orbital position and possibly with time (such as an evolutionary space station). Non-linear phenomena and idealized damping characteristics further complicate modeling the "plant". Due to the large size of these structures (which precludes performing ground vibration tests of the complete spacecraft), identification of the dynamic characteristics by observing the response to known disturbances will be necessary to establish the final on-orbit "plant" characteristics. The control system can be a part of the system to be characterized, and it is likely that the control sensors, actuators and processors will be used for the identification process.

CONTROL OF FLEXIBLE STRUCTURES

WBS SUBSET TASKS (CONTINUED)

SYSTEM IDENTIFICATION

A. COMPLEX MODAL METHODS
- CLOSED-LOOP IDENTIFICATION METHODS
- COMPLEX MODAL IDENTIFICATION
- ACCURATE DAMPING IDENTIFICATION

B. PHYSICAL/PDE PARAMETER METHODS
- EVALUATE PDE APPROACHES
- EVALUATE NON-MODAL APPROACHES (MASS, STIFFNESS, DAMPING)
- ACCURATE DAMPING IDENTIFICATION

C. NONLINEAR/TIME VARYING SYSTEMS
- EVALUATE METHODS FOR NONLINEAR/TIME VARYING SYSTEMS

D. INPUT/OUTPUT OPTIMIZATION
- ON-LINE MAXIMUM LIKELIHOOD TECHNIQUES
- ESTIMATOR DESIGN
- HIGH RELIABILITY OFF-LINE
- OPTIMIZED INPUT/OUTPUT LOCATION DESIGNS

NASA

INTEGRATED STRUCTURE/CONTROL DESIGN METHODOLOGY

The development of integrated structure/control design methodology offers the designer the opportunity to achieve performance requirements through the optimum mix of controls and structures. Minimizing the deviation of the structure from some desired shape or a reduction in the dynamic response of the structure can be controlled by varying control law parameters or by varying structural parameters. Optimization studies, which compare control system complexity to structural designs which result in stiffer structures, must be evaluated.

CONTROL OF FLEXIBLE STRUCTURES

WBS SUBSET TASKS (CONTINUED)

INTEGRATED STRUCTURE/CONTROL DESIGN METHODOLOGY

A. MULTIDISCIPLINARY METHODS AND TOOL DEVELOPMENT

- STRUCTURAL DESIGN FOR DYNAMICS
- MULTIDISCIPLINARY OPTIMIZATION
- SIMULTANEOUS CONTROL OF STRUCTURES AND CONTROL
- ADVANCED TECHNOLOGY INTEGRATED DESIGN
- ACTIVE VIBRATION CONTROL

B. STRUCTURE/CONTROL TRADEOFF STUDIES

- FLEXIBLE CONTROLLED STRUCTURES VS. STIFF STRUCTURE
- PARAMETRIC TRADE STUDIES
- SET POINT BETWEEN STRUCTURAL KNOWLEDGE AND CONTROL SYSTEM COMPLEXITY

NASA

OAST NASA HQ RTM 1274(1)
3-27-84

It is generally accepted that the control of flexible structures will require new types of control sensors and actuators. The actuator will have to provide precise input at very low force levels and will need to be compact and light weight. The increased bandwidth and stringent performance requirements will require new types of structural response sensors. Listed are the minimum types of sensors and actuators required to initiate this plan. Additional sensor/actuator developments will be necessary to fully achieve the performance capabilities expected from applying this technology.

CONTROL OF FLEXIBLE STRUCTURES

WBS SUBSET TASKS (CONTINUED)

SENSOR AND ACTUATOR DEVELOPMENT

A. OPTICAL SENSOR CAPABILITY ENHANCEMENT

B. IMBEDDED ACTUATORS

C. "SMART" SENSORS

D. PASSIVE DAMPERS AND STIFFENERS

E. VIBRATION ISOLATORS

NASA

The ground and flight testing philosophy is to gradually increase in test model and research complexity. This will allow uncertainties to be addressed in a structured, organized manner; that is, understanding of the test results as the model characteristics are made more complex. Models that will be tested in the flight validation activities will use flight hardware as a part of their ground testing program.

:

CONTROL OF FLEXIBLE STRUCTURES

TESTING PHILOSOPHY

- MATHEMATICALLY TRACTABLE MODELS

- GRADUAL INCREASE IN TEST MODEL AND RESEARCH COMPLEXITY

- SIMPLE TESTS ON LARGE MODELS VS. COMPLEX TESTS ON SMALL MODELS

- PHENOMENA MODELS USING FLIGHT TYPE HARDWARE

- ADDRESS UNCERTAINITIES INDEPENDENTLY USING COMMON HARDWARE

NASA

OAST   NASA HQ RT84-732 (1)
1-18-84

The approach is one of defining the tests required to validate the technology thrusts presented earlier. The uncertainties associated with each thrust are identified and the necessary test features/characteristics that would be required to address those uncertainties are determined. From these features and characteristics the test models are identified.

CONTROL OF FLEXIBLE STRUCTURES

TEST DEFINITION APPROACH

- **DEFINE UNCERTAINTIES ASSOCIATED WITH TECHNOLOGY THRUSTS**

- **IDENTIFY TEST FEATURES/CHARACTERISTICS TO ADDRESS UNCERTAINTIES**

- **IDENTIFY TEST MODELS**

NASA

OAST

Listed are the major uncertainties that will be addressed during the ground and flight test activities detailed in this plan.

CONTROL OF FLEXIBLE STRUCTURES

UNCERTAINTIES

● **STRUCTURAL MODELING**

- JOINTS/NONLINEAR BEHAVIOR
- MODEL FIDELITY INCLUDING COUPLING/LOCAL EFFECTS
- DAMPING CHARACTERISTICS/FORMULATIONS
- ANALYTICAL MODEL SIZE REDUCTION

● **SENSORS AND ACTUATORS**

- SENSOR ACTUATOR DEADBAND, NOISE
- ACTUATOR SATURATION, HYSLERISIS EFFECTS
- PASSIVE/ACTIVE DEVICE MODELING
- ADVANCED DEVICES WITH INTEGRATED ELECTRONICS

● **CONTROL METHODOLOGIES**

- ACTIVE/PASSIVE CONTROL DEVICE LOCATIONS AND NUMBERS
- ERROR ESTIMATION/EFFECTS/COMPENSATION
- FAILURE EFFECTS
- DESIGN FOR EVOLVING SYSTEMS

NASA

OAST NASA HQ RT84-731 (1)
1-16-84

Listed are the major uncertainties that will be addressed during the ground and flight test activities detailed in this plan.

CONTROL OF FLEXIBLE STRUCTURES

UNCERTANTIES (CONTINUED)

- ## INTEGRATED MODELING/DESIGN
    - ACTIVE/PASSIVE TRADEOFFS
    - MODEL FIDELITY REQUIREMENTS/LIMITS
    - ANALYTICAL APPROACHES
    - SYSTEM IDENTIFICATION ACCURACY/SPEED REQUIREMENTS

- ## TEST METHODS
    - ZERO "G" TESTING
    - SCALE MODEL METHODS, ACCURACY
    - COMPONENT/TEST APPROACHES
    - LARGE MOTION TEST SUSPENSIONS (ACTIVE OR PASSIVE)
    - HYBRID HARDWARE/SOFTWARE SIMULATION
    - ON-ORBIT TESTING

NASA

OAST NASA HQ RT84 1270(1)
3-27-84

The model features that will address the major uncertainties are identified by an "X". Also shown are those model features that would require flight tests to complete the technology validation process.

CONTROL OF FLEXIBLE STRUCTURES

UNCERTAINTIES \ MODEL FEATURES	LARGE-ORDER	LOW FREQ./HIGH AMPL.	LOW DENSITY; DISTR. MASS	MULTIPLE STRUCT COMPONENTS	RIGID BODY; ARTICULATED MOTION	HIGH MODAL DENSITY	MULTI-AXIS COUPLING	JOINT DOMINATED BEHAVIOR	SCALE MODEL	ACTIVE/PASSIVE DAMPING	REPEATED ELEMENTS	DEPLOYABLE
STRUCTURAL MODELING	X		X	X	X	X		X		X	X	X
CONTROL METHODS	X		X	X		X	X		X			
INTEGRATED MODELING/ DESIGN	X		X	X	X	X				X	X	
SENSORS AND ACTUATORS		X					X			X		
TEST METHODS		X	X	X			X	X	X	X		X
FLIGHT TESTING REQUIRED		•	•		•		•	•				•

NASA

OAST   NASA HQ RT84-1280(1)
3-27-84

MODEL FEATURES

Three test models have been identified in this plan. Those features addressed by the test models are identified by an "X". Features that are only partially addressed are indicated by a "?".
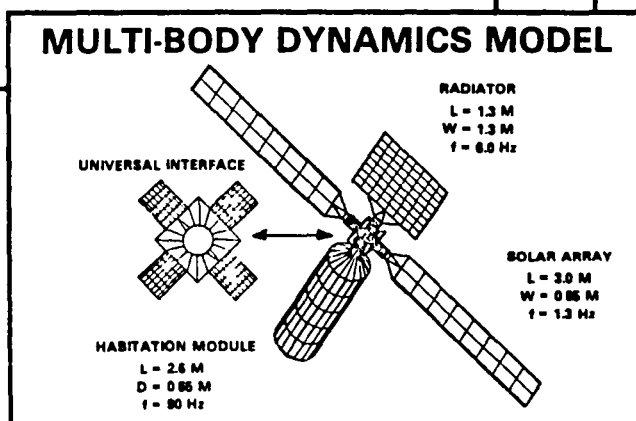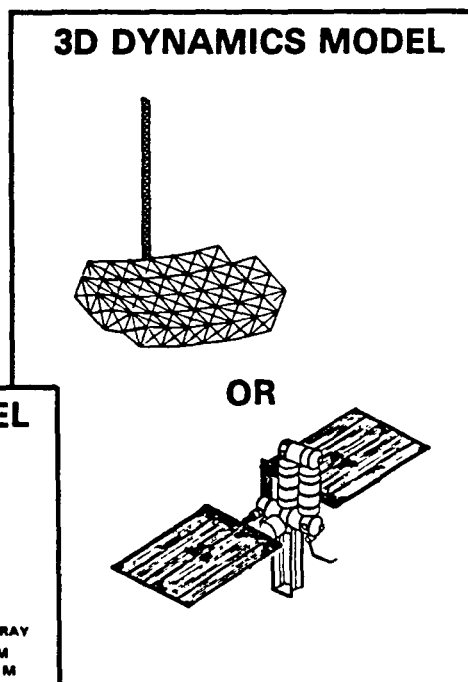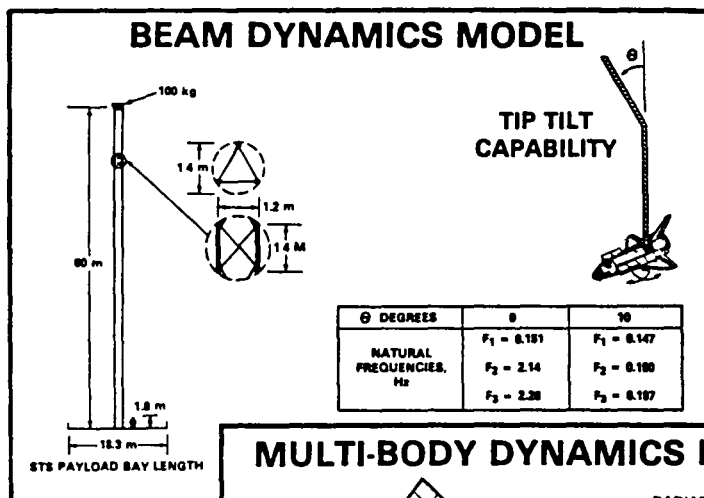
CONTROL OF FLEXIBLE STRUCTURES

MODELS / MODEL FEATURES	LARGE-ORDER	LOW FREQ/HIGH AMPL	LOW DENSITY DISTR. MASS	MULTIPLE STRUCT COMPONENTS	RIGID BODY ARTICULATED MOTION	HIGH MODAL DENSITY	MULTI-AXIS COUPLING	JOINT DOMINATED BEHAVIOR	SCALE MODEL	ACTIVE/PASSIVE DAMPING	REPEATED ELEMENTS	DEPLOYABI·
BEAM DYNAMICS MODEL	X	X	X	?	?	?	?	X	X	X	X	X
MULTI-BODY DYNAMICS MODEL	X	?		X	X	X	X	?	X	?		
3D DYNAMICS MODEL	X	X	X	X	?	X	X	X	X	X	X	X
FLIGHT TESTING REQUIRED		•	•		•		•	•				•

NASA

TEST MODEL DESCRIPTIONS

These are the three major test models included in this plan. The beam dynamics model will focus on structural issues for which it is necessary to test in a space environment. The multi-body dynamics model will focus on the modeling and controllability of multi-body configurations with flexible appendages. The 3-D dynamics model will address the more complex three dimensional problem which is more characteristic of large space structures.

CONTROL OF FLEXIBLE STRUCTURES

TEST MODEL DESCRIPTIONS

BEAM DYNAMICS MODEL

TIP TILT CAPABILITY

Θ DEGREES	0	10
NATURAL FREQUENCIES, Hz	F_1 = 0.151	F_1 = 0.147
	F_2 = 2.14	F_2 = 0.190
	F_3 = 2.28	F_3 = 0.197

100 kg
14 m
1.2 m
1.4 M
60 m
1.8 m
18.3 m
STS PAYLOAD BAY LENGTH

MULTI-BODY DYNAMICS MODEL

UNIVERSAL INTERFACE

RADIATOR
L = 1.3 M
W = 1.3 M
f = 6.0 Hz

SOLAR ARRAY
L = 3.0 M
W = 0.65 M
f = 1.3 Hz

HABITATION MODULE
L = 2.6 M
D = 0.65 M
f = 90 Hz

3D DYNAMICS MODEL

OR

NASA

285

Shown is the Beam Dynamics Model overall schedule. Included are several ground test activities and three flight tests. These activities will be discussed in subsequent pages. A key activitiy shown is the participation of guest investigators which will give the research community an opportunity to evaluate different techniques and approaches.

CONTROL OF FLEXIBLE STRUCTURES

BEAM DYNAMICS MODEL

MAJOR TASKS	FY	84	85	86	87	88	89	90	91
LABORATORY BEAM DESIGN, FABRICATION AND TEST		▨							
SCALED MODEL DESIGN, FABRICATION AND TEST			▨						
EXPERIMENT MODELING, SIMULATION AND SOFTWARE DEVELOPMENT				▨					
EXPERIMENT DESIGN AND FABRICATION				▨					
EXPERIMENT GROUND TEST					▨				
GUEST INVESTIGATORS					▨				
FLIGHT TEST						▽ ▽ ▽			

NASA

286
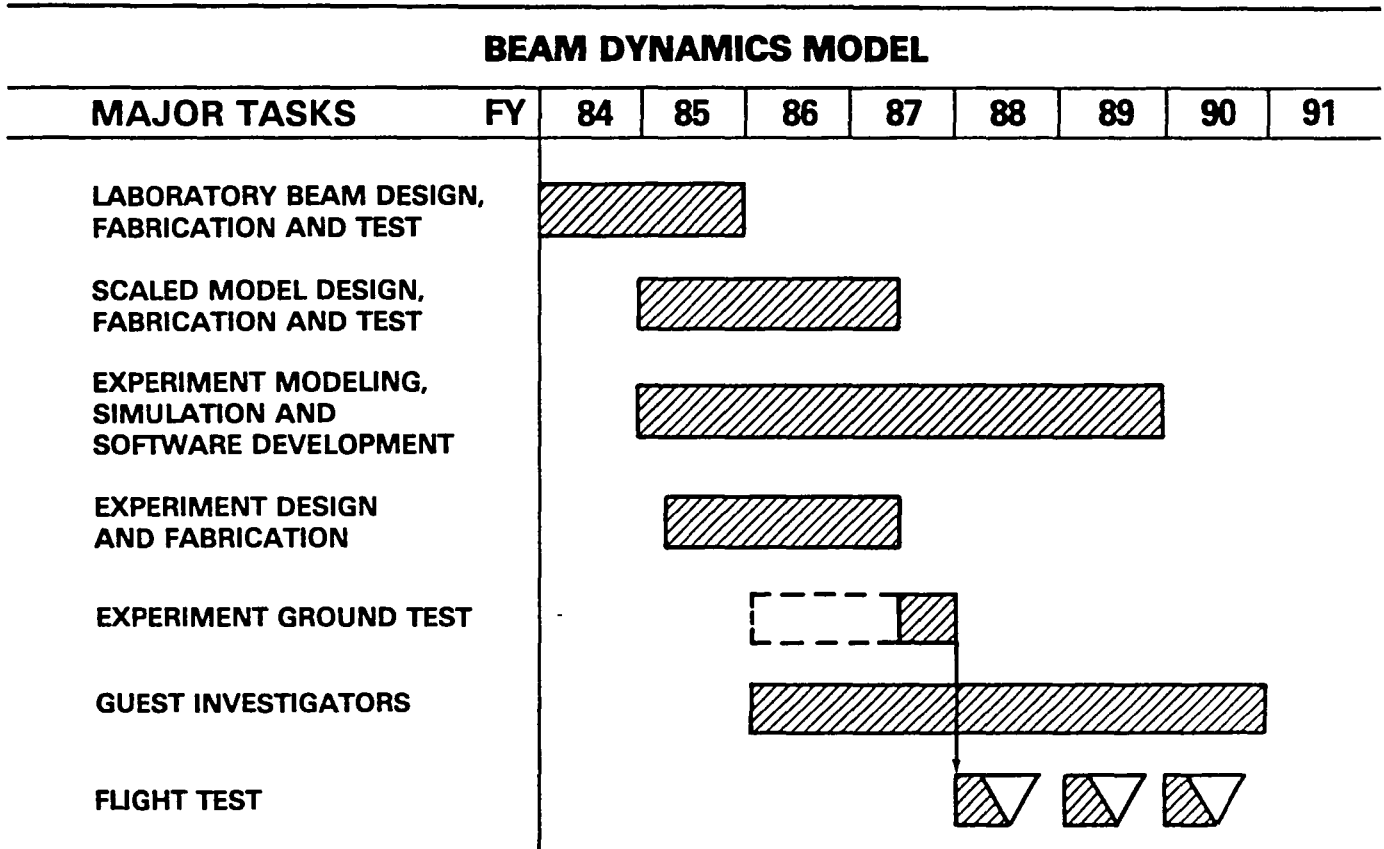
DEPLOYABLE BEAM EXPERIMENT TEST ARTICLES

The figure overviews the progression of test articles to be used in the deployable beam experiment program. The primary test structure is a 60 meter flight article shown in the center of the figure. It is expected to be about 1.2 - 2.0 meters in diameter, of lightweight composite construction, and be sequentially deployable/retractable from a small package while maintaining a cantilevered end condition. To determine its static, dynamic, and thermal performance, it will be tested both on the ground and in orbit (extended from the shuttle as shown in the next figure). The beam will include a capability for changing its physical properties, by tilting one end, in order to change the frequency spacing and cross-axis coupling between modes.

GROUND TESTS

Because of the combination of large size, lightweight construction, and expected low natural frequencies (beginning well below one Hz), the validity of ground test data on the 60m beam is questionable. This situation was deliberately created to simulate the problems of developing future large space structures such as the space station or large antennas. The remainder of the test articles shown are intended to develop accurate analyses for the large beam using smaller articles on which valid ground test data may be obtained. They include a 20m laboratory "prototype" test beam which has similar (but not exact) physical characteristics to the flight article. The purpose of this model is to develop test and analysis methods applicable to the flight beam in advance of its construction. Segments, joints, and structural members identical to those of the flight article will be tested to determine stiffness, hysteresis, deployment characteristics, and thermal behavior for evaluating and calibrating the analytical predictions.

A final research objective is represented by the 1/8 and 1/4 scaled models shown. These will be tested on the ground to develop accurate analytical models once a flight design is available. The analytical models will then be used to predict full-scale ground and flight behavior. The degree to which sub-scale models can be used for developing analyses applicable to large, joint-dominated space structures can thus be determined and, hopefully, increased.

CONTROL OF FLEXIBLE STRUCTURES

GROUND TESTS

SECTIONS/ SEGMENTS
JOINTS
20M LABORATORY PROTOTYPE
60M FLIGHT ARTICLE
1/8 SCALE MODEL
1/4 SCALE MODEL

OBJECTIVES

- DEVELOP GROUND TEST METHODS AND CAPABILITY

- VALIDATE ANALYSES

- EVALUATE SCALING METHODS

- EVALUATE JOINTS/ DAMPING EFFORTS

287
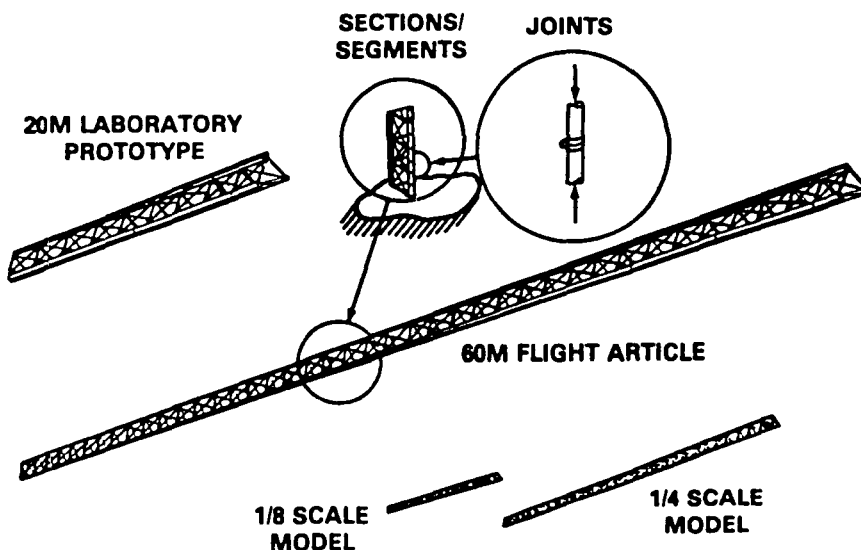
This figure illustrates the flight test sequence planned for the beam dynamics model tests. The objectives of the flight tests are as follows:

Structures

● Develop and ground test the next generation precision deployable truss.
● Evaluate structural modeling techniques through measurement of figure fidelity.
● Evaluate thermal distortion effects.
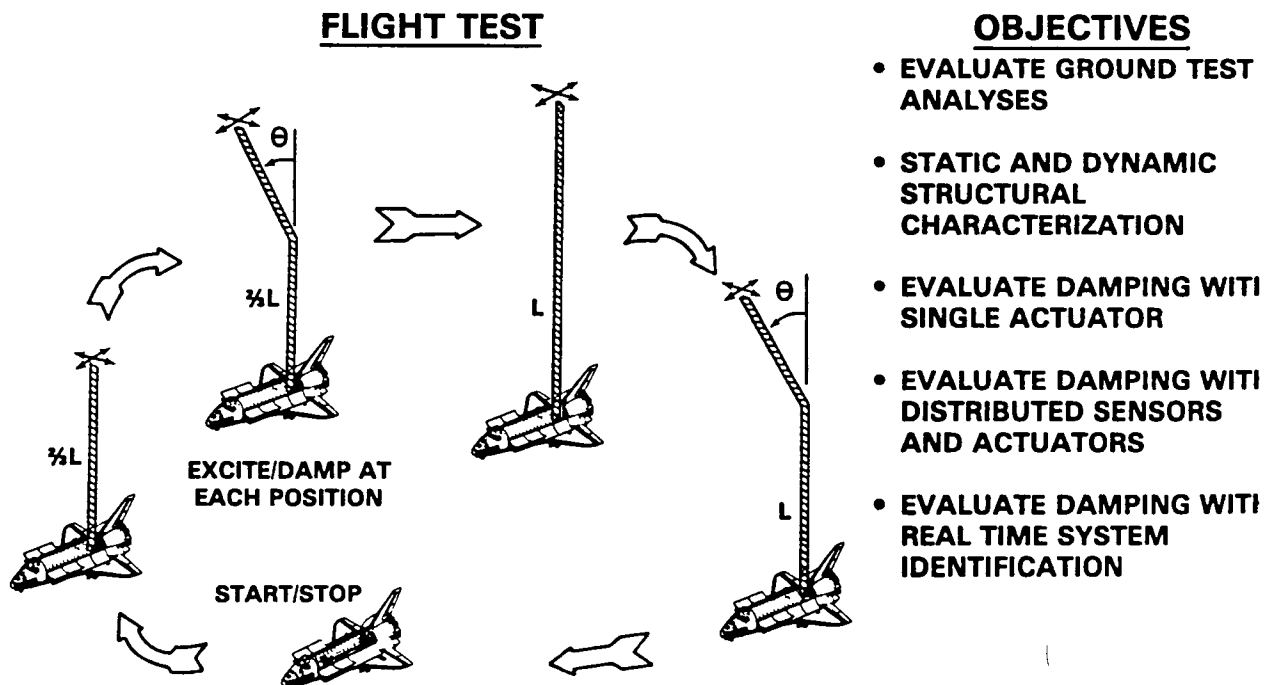● Validate truss deployment.

Dynamics

● Determine the capability of theory and ground testing to predict flight measurements of low-frequency structures.
● Evaluate system identification procedures.
● Evaluate deployment dynamics.
● Evaluate joint damping in zero-g.

Controls

● Provide a dynamically characterized test bed for controls research.
● Evaluate distributed sensor/actuator control techniques.
● Evaluate control techniques with real time system identification.

CONTROL OF FLEXIBLE STRUCTURES

BEAM DYNAMICS MODEL

FLIGHT TEST

EXCITE/DAMP AT EACH POSITION

START/STOP

OBJECTIVES

● EVALUATE GROUND TEST ANALYSES

● STATIC AND DYNAMIC STRUCTURAL CHARACTERIZATION

● EVALUATE DAMPING WITH SINGLE ACTUATOR

● EVALUATE DAMPING WITH DISTRIBUTED SENSORS AND ACTUATORS

● EVALUATE DAMPING WITH REAL TIME SYSTEM IDENTIFICATION

NASA

This is the overall schedule for the multi-body dynamic models. The activities associated with these models are discussed in subsequent pages.

CONTROL OF FLEXIBLE STRUCTURES

MULTI-BODY DYNAMICS MODELS

MAJOR TASKS FY	84	85	86	87	88	89	90	91
GENERIC MODEL DESIGN, FABRICATION AND TEST	▨	▨						
GENERIC MODEL CONTROLS-CONFIGURED FABRICATION AND TEST		▨	▨					
ADVANCED MODEL DESIGN, FABRICATION AND TEST			▨	▨	▨			
EXPERIMENT MODELING, SIMULATION AND SOFTWARE DEVELOPMENT			▨	▨	▨	▨		
EVOLVED MODEL DESIGN, FABRICATION AND TEST					▨	▨	▨	▨

NASA

OAST NASA HQ RTM-1263 1)
3-27-84

289
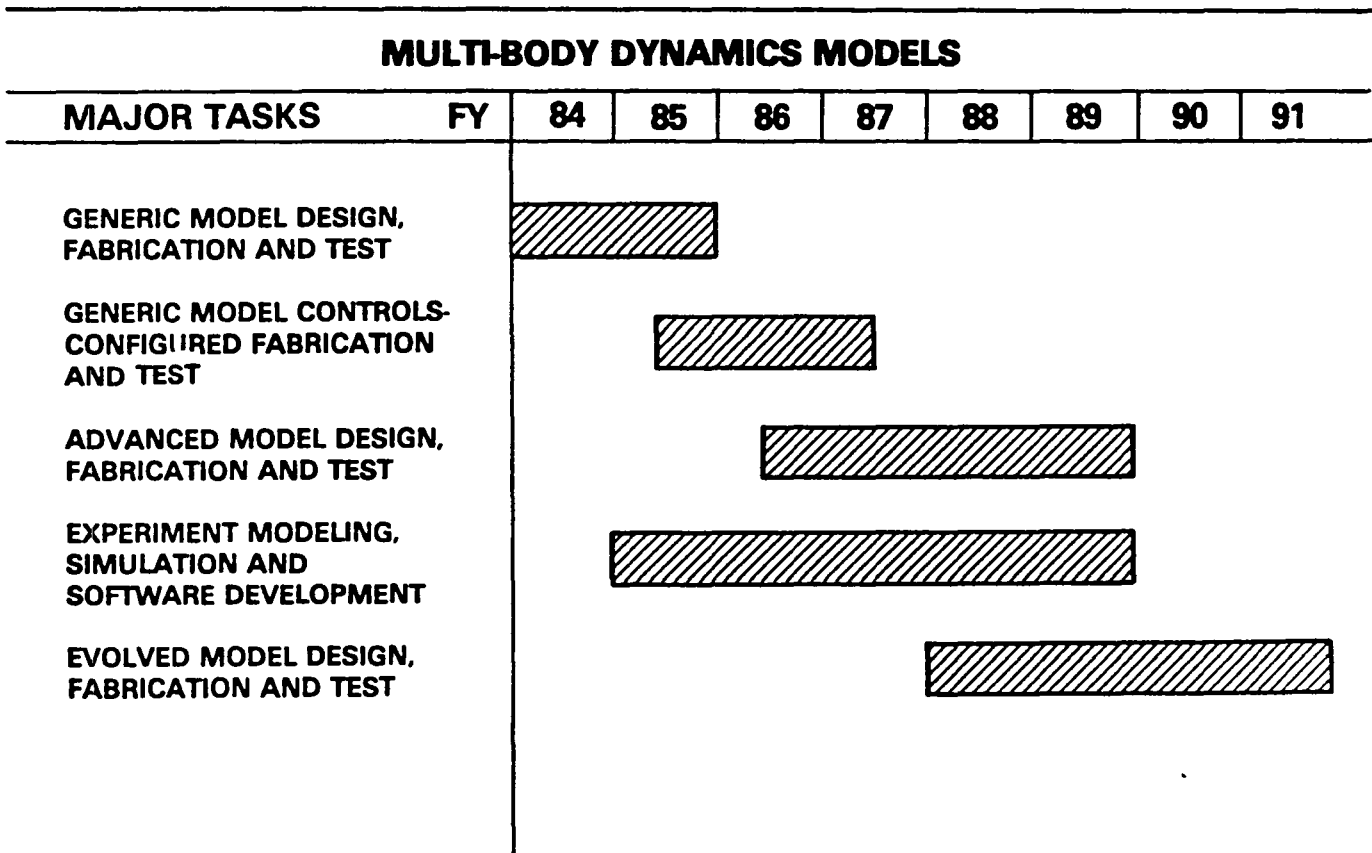
The multi-body dynamic models will address the dynamic characteristics and modeling sensitivities for this class of structural configuration. The generic model will focus on modeling and controlling flexible appendages with rigid-body control techniques. The advanced model will be configured to address evolutionary space station issues (this model can be utilized to evaluate early concerns that may be associated with the initial space station configurations). The evolved model will focus on the evolutionary space station configuration. These models are not intended to be scaled or replica models of the space station, but are to be generic laboratory models designed to develop the technology data base.

CONTROL OF FLEXIBLE STRUCTURES

MULTI-BODY DYNAMIC MODELS

GROUND TEST

GENERIC MODEL **ADVANCED MODEL** **EVOLVED MODEL**

OBJECTIVES

- EVALUATE DYNAMIC CHARACTERISTICS

- DETERMINE MODELING SENSITIVITIES

- EVALUATE VIBRATION SUPPRESSION TECHNIQUES ON SOLAR ARRAY RESPONSE

- EVALUATE GROUND TEST METHODS AND CAPABILITY
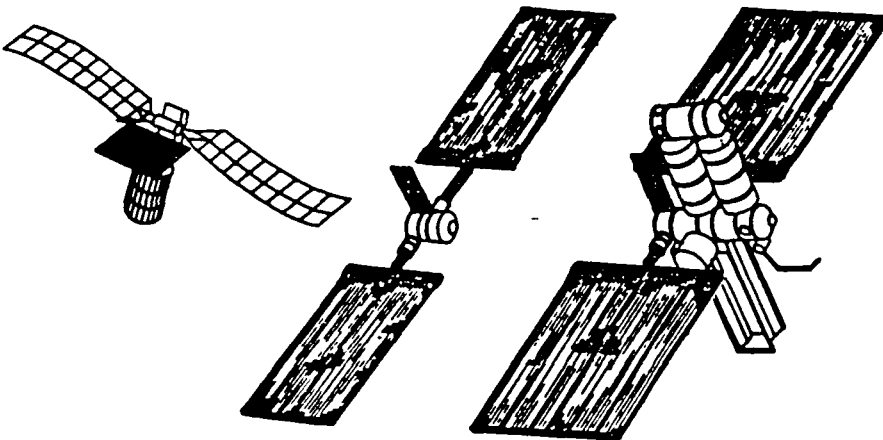
NASA

OAST NASA HQ RT84-1382 (1) 2-12-84

290

This is the overall schedule for 3D dynamics model. The activities are discussed in subsequent pages. A key activity shown is the participation of guest investigators which will allow the research community to be involved in the program.

CONTROL OF FLEXIBLE STRUCTURES

3D DYNAMICS MODEL

MAJOR TASKS FY	84	85	86	87	88	89	90	91	92
GRILLAGE DESIGN, FABRICATION AND TEST									
SCOLE DESIGN, FABRICATION AND TEST									
DEFINITION OF SCALED AND EXPERIMENT MODELS									
SCALED MODEL DESIGN, FABRICATION AND TEST									
EXPERIMENT MODELING, SIMULATION AND SOFTWARE DEVELOPMENT									
EXPERIMENT DESIGN AND FABRICATION									
EXPERIMENT GROUND TEST									
GUEST INVESTIGATORS									
FLIGHT TEST									

VIASA

OAST NASA HQ RT84-1258(1) 3-27-84

291

ACTUATOR PLACEMENT ON A TWO-DIMENSIONAL GRILLAGE

The objective of this research is to develop a technique for determining optimum actuator locations and optimum actuator gains for controlling vibrations of flexible structures. The flexible grillage shown in the figure has 88 nodes which are considered as potential damper locations by an optimization algorithm. The final designs are shown to the right of the grillage model. The upper figure shows the optimum number of force actuators, the optimum locations, and the optimum gains in a bar graph to the right. Similar results are shown for the same performance criterion but with torque actuators.

NASA
1-83-5685
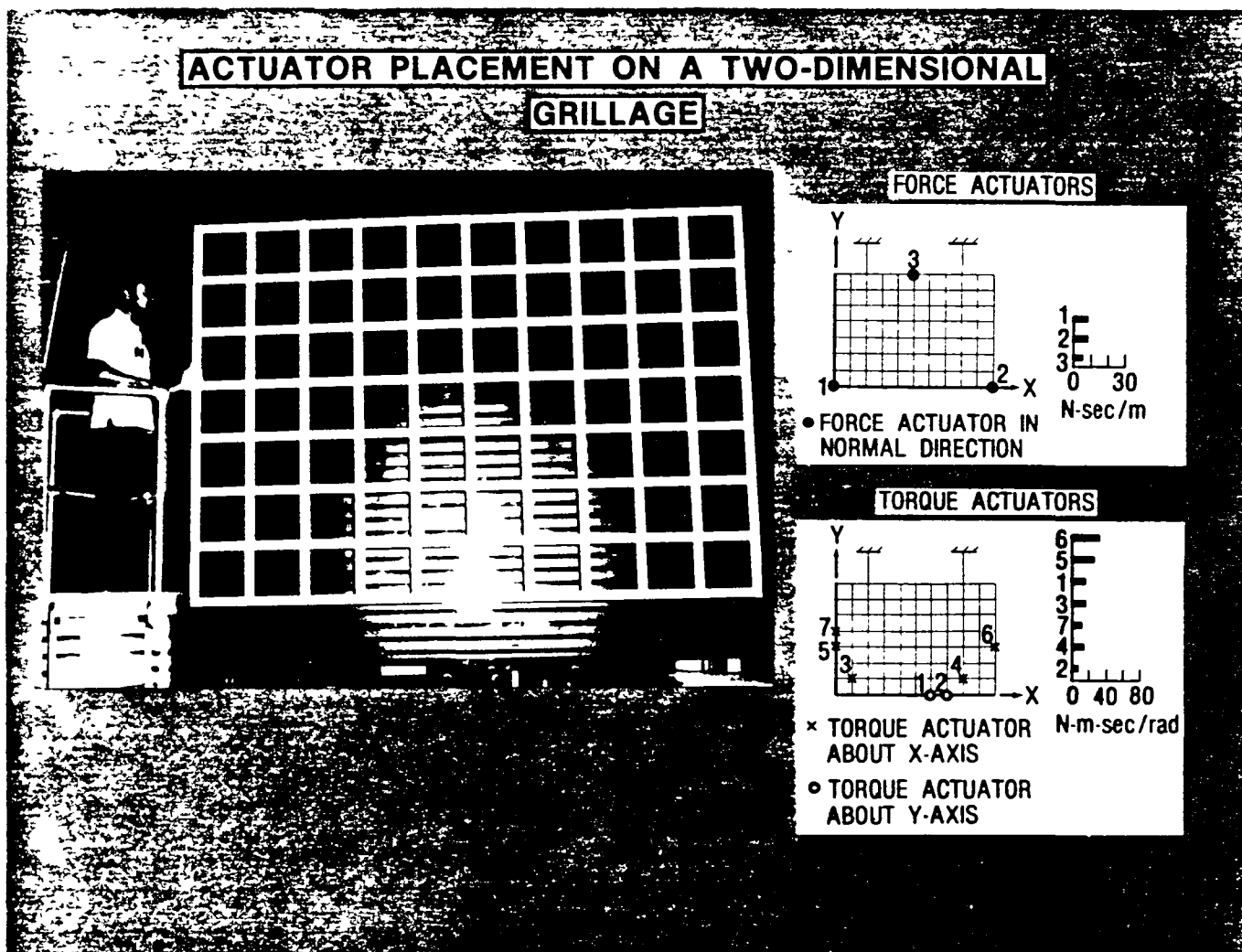
The overall objective of the Spacecraft Control Laboratory Experiment (SCOLE), is to compare different approaches to control, state estimation, and system identification. The control objective is to rapidly slew or change the line-of-sight of an antenna attached to the space shuttle and to damp the induced structural dynamics to the degree required for precise pointing of the antenna. The measure of system performance will be the time required to slew, settle and maintain line-of-sight within a specified angle.

The program has two principal parts. The first part of the program uses a mathematical model of the shuttle/antenna configuration to address the following problem: What control policy minimizes the time to slew to a target and to stabilize so that the line-of-sight error is held within a specified angle. The maximum moment and force generating capability will be limited but can be lumped or distributed about the configuration as required. Random broadband disturbances will be applied to the configuration. A complete set of guidelines and pertinent information will be supplied to interested parties. The second part of the program is to validate in the laboratory the system performance of the designs which have been developed earlier. The experimental model will consist of a dynamic model of the space shuttle with an antenna reflector attached by means of a flexible beam. The model will be extensively instrumented and will have force and moment generating devices for both control and disturbance generation. A simple flexible tether which allows complete angular freedom in yaw, and limited freedom in pitch and roll will be used for suspending the model.

CONTROL OF FLEXIBLE STRUCTURES

SPACECRAFT CONTROL LABORATORY EXPERIMENT (SCOLE)

CONTROL OBJECTIVE:
TO SLEW, POINT, AND STABILIZE THE RF LINE-OF-SIGHT OF A FLEXIBLE, SHUTTLE ATTACHED ANTENNA, IN MINIMUM TIME

SYSTEMS IDENTIFICATION:
TO CREATE CONTROL INPUTS, THEN MODEL THE DYNAMIC SYSTEM FROM RESPONSE MEASUREMENTS

PITCH

5 DEGREES OF FREEDOM

YAW

ROLL

TARGET

TETHER

RF LINE-OF-SIGHT

SHUTTLE MODEL

CONTROL MOMENTS AND FORCES

SENSORS. ACCELEROMETERS RATE GYROS ATTITUDE

FLEXIBLE MAST

ANTENNA REFLECTOR

CONTROL MOMENTS, DISTURBANCES

NASA

OAST NASA HQ RT84-1254(1) 3-27-84
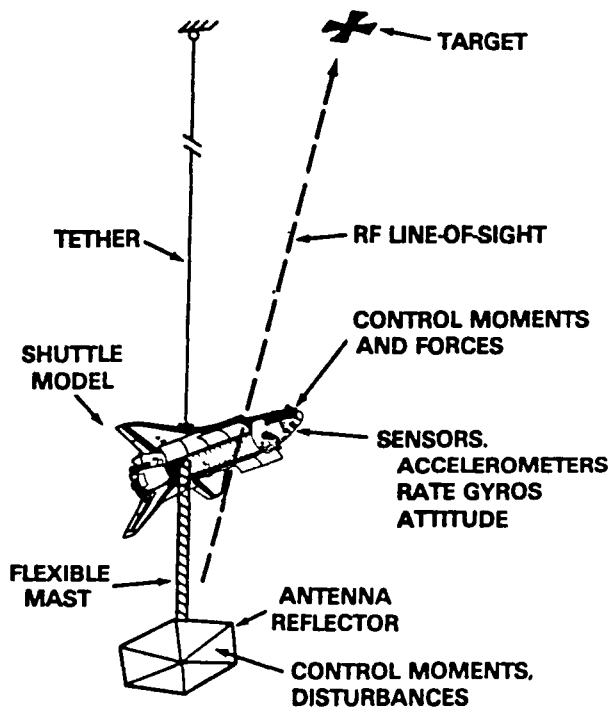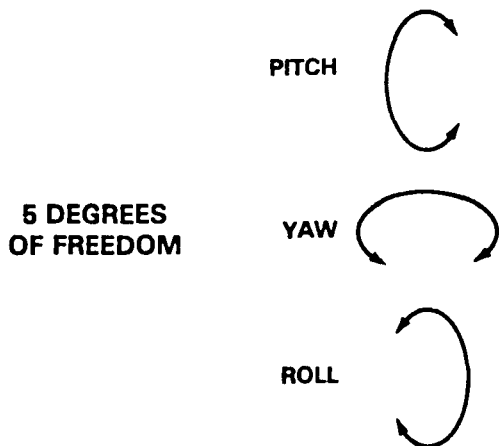
This chart illustrates the potential 3-D dynamics model configurations. As a precursor to a full scale development program, such as an antenna or space station, a more complex model will be needed to validate the necessary technology. At this time it is recommended that the program proceed with those activities identified for the next two years and in FY 86/87 conduct a definition study that would determine which configuration is appropriate and what level of complexity will be required.

CONTROL OF FLEXIBLE STRUCTURES

3D DYNAMICS MODEL

GROUND/FLIGHT TESTS

OR
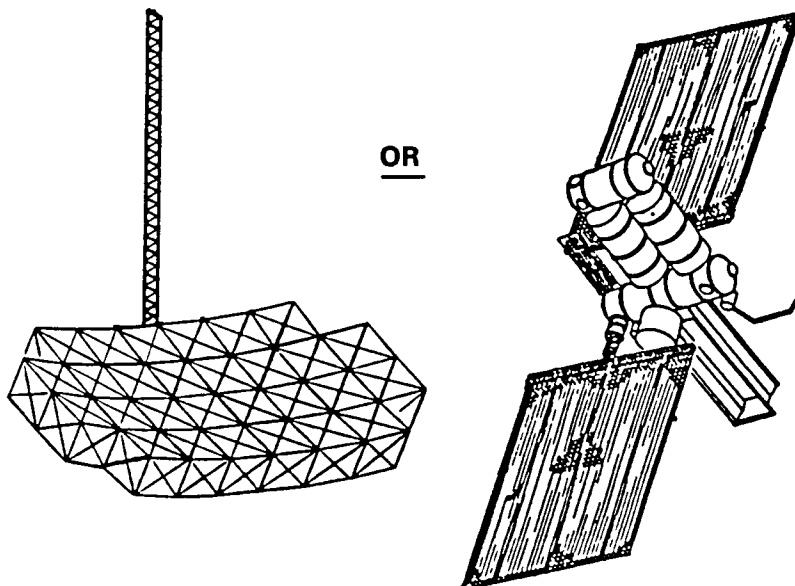
OBJECTIVES

- **EVALUATE SCALING METHODS**

- **EVALUATE GROUND TEST METHODS AND CAPABILITIES**

- **EVALUATE MULTI-AXIS CONTROL (COUPLED) TECHNIQUES**

- **VALIDATE ANALYSES AND CONTROL LAWS**

NASA

OAST   NASA HQ RT84 1257(1)

294

This is the overall schedule for the technology plan. As mentioned previously, it represents an increase of model and research complexity with time.

CONTROL OF FLEXIBLE STRUCTURES

SCHEDULE
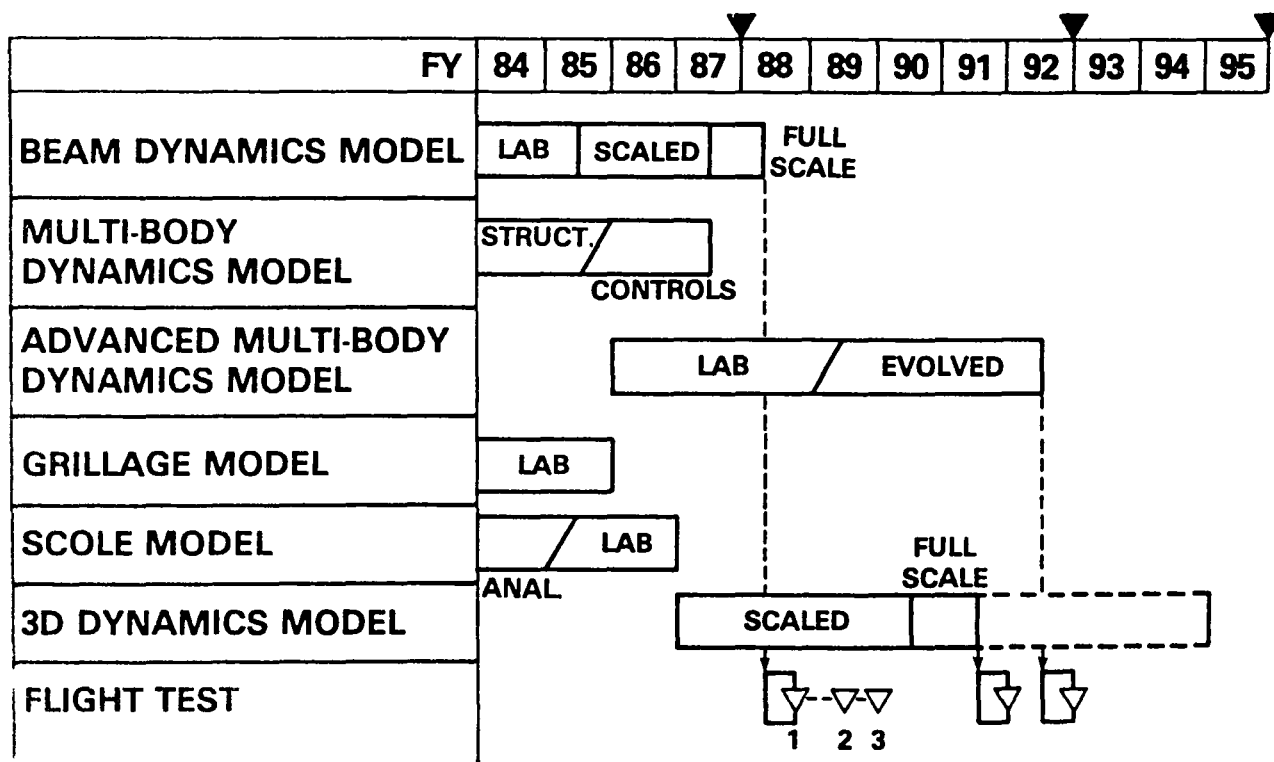
FY	84	85	86	87	88	89	90	91	92	93	94	95

BEAM DYNAMICS MODEL — LAB | SCALED | FULL SCALE

MULTI-BODY DYNAMICS MODEL — STRUCT. / CONTROLS

ADVANCED MULTI-BODY DYNAMICS MODEL — LAB / EVOLVED

GRILLAGE MODEL — LAB

SCOLE MODEL — ANAL / LAB

3D DYNAMICS MODEL — SCALED | FULL SCALE

FLIGHT TEST — 1 2 3

NASA

OAST NASA HQ RT84-126211
3-27-84

295

This chart illustrates the relationships and interaction of the major activities required to achieve the goals of this technology plan. It should be emphasized that the program goals can only be accomplished if all the major thrusts and their activities are addressed in an integrated program.

CONTROL OF FLEXIBLE STRUCTURES

THRUSTS	ACTIVITIES	GOALS

THRUSTS
- ANALYTICAL MODELING AND MODEL REDUCTION
- INTEGRATED STRUCTURAL/ CONTROL DESIGN METHODOLOGY
- SENSORS AND ACTUATORS
- SYSTEM IDENTIFICATION
- GROUND TESTING
- ON-ORBIT TESTING

ACTIVITIES
- DEVELOP STRUCTURAL DYNAMIC & CONTROL ANALYTICAL MODELS & DESIGN TOOLS
- VERIFY ANALYSIS & TEST METHODS ON SCALE MODELS & LARGE COMPONENTS
- DEVELOP INTEGRATED STRUCTURAL/CONTROL ANALYSIS & DESIGN TOOLS
- HARDWARE CONCEPT
- OPTIMIZATION METHODS
- HARDWARE DEFINITION
- SYSTEM I.D. TECHNIQUES
- SYSTEM DESIGN APPROACHES
- TESTING APPROACHES
- GROUND TEST VERIFICATION
- FLIGHT TEST APPROACHES
- FLIGHT EXPERIMENT DEFINITION
- FLIGHT VERIFICATION

GOALS
- DESIGN PERFORMANCE DATA BASE
- VALIDATED ANALYTICAL TOOLS
- INTEGRATED STRUCTURE/ CONTROL DESIGN METHODOLOGIES
- GROUND AND FLIGHT TEST METHODS

NASA

OAST NASA HQ RT84 12671(1)
3-27-84

296

CONTROL OF FLEXIBLE STRUCTURES

SUMMARY

PROGRAM THRUSTS

- ANALYTIC MODELING AND MODEL REDUCTION

- SYSTEM IDENTIFICATION

- CONTROL LAW DESIGN METHODOLOGY

- INTEGRATED STRUCTURE/ CONTROL DESIGN METHODOLOGY

- SENSOR AND ACTUATOR DEVELOPMENT

- GROUND AND IN-SPACE TESTING
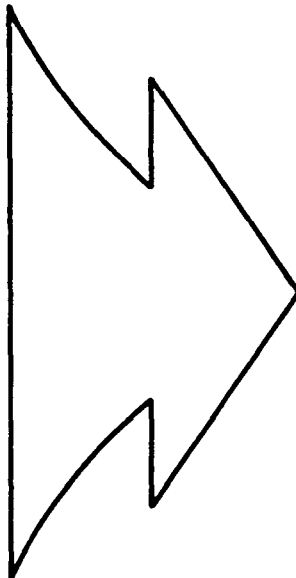
PAYOFFS

- VALIDATED ANALTYICAL TOOLS AND ALGORITHMS

- NEW METHODOLOGY FOR INTEGRATED STRUCTURE/ CONTROL DESIGN

- NEW METHODOLOGY FOR CONTROL LAW DESIGN

- DESIGN/PERFORMANCE DATA AND DATA BASES

- RELIABLE, EFFICIENT CONTROL SENSORS AND ACTUATORS

- GROUND AND IN-SPACE VALIDATION OF FLEXIBLE SPACE SYSTEM TESTING TECHNIQUES

NASA

OAST NASA HQ RT84-344(1)
11-8-83

SPACE STATION CONFIGURATION AND FLIGHT DYNAMICS ID

E. Mettler and **M. H. Milman**
Jet Propulsion Laboratory
California Institute of Technology
Pasadena, CA 91109

ABSTRACT

The Space Station will be assembled in low earth orbit by a combination of deployable and space erectable modules that are progressively integrated during successive flights of the Shuttle. The crew assisted space construction will result in a configuration which is a large scale composite of structural elements having connectivity with a wide range of possible end conditions and imprecisely known dynamic characteristics. The large scale static and dynamic behavior of such a system is not practical to ground test and calibrate -- this must be done in-situ during initial build-up, periodically in various mission modes, and over its lifetime as the configuration evolves. This paper describes the generic applications of Flight Dynamics Identification to the candidate Space Station configurations currently under consideration by NASA. Identification functions are categorized, and the various methods for extracting parameter estimates are correlated with the sensing of specific characteristics of interest to both engineering subsystems and users of the Station's commercial and scientific facilities. On-board implementation architecture and constraints are discussed from the viewpoint of maximizing integration of the Identification process with the flight subsystem's data and signal flow. Finally, the important and rapidly developing application of remote sensing by electro-optic instruments of extended space structures is assessed and sensor equipment capabilities are detailed.

INTRODUCTION

NASA's Space Station initiative will be entering the formal Concept Definition phase in the near future. During the past year-and-a-half Space Station Task force studies have explored configuration concepts and requirements for missions, systems, and payloads. Support of these studies at JPL in the area of guidance/control has emphasized the flight dynamics of generic configurations and control/structures interactions with the station and its payloads.

The large scale dynamical behavior of the station's composite structure can only be predicted, not ground tested, on the basis of models limited by parameter uncertainties and simplifying assumptions. Recognition of this has motivated the general application of Systems Identification technology to enable the on-orbit station's validation during initial assembly and expansion, and performance verification/calibration during flight operations.

The relationship of the Identification (ID) process to the other on-board functions is that of an in-situ data-base generator which serves engineering subsystems and applications payloads. This user group is expected to include scientific, commercial, and technology experiments in addition to the flight subsystem. In this context, the ID processing is a concurrent utility providing maintenance of performance and user health via determination of actual parameter values and refined models of the system. User functions which would be supported by Flight Dynamics ID include Momentum Management, Attitude Determination, Disturbance Characterization, Anomaly Diagnostics and Fault Detection, Payload Stabilization/Pointing and Micro-g isolation, Dynamic Decoupling Controllers for Flex-Appendages, and calibration/modification of prediction models.

This paper is intended to provide a broad perspective for the application of Systems ID methods and technology to the diverse operational needs of the Space Station, with special emphasis on the generic issues involved with large space structures in-orbit construction, configuration evolution, and user accommodation.

SPACE STATION CONFIGURATIONS

The five major classes of Space Station configurations that have been under consideration by NASA are shown conceptually in Figures 1 through 5. They are called the PLANAR Station, the POWER TOWER (or Gravity Gradient Station), the BIG T, the DELTA, and the SPINNER (actually a Dual Spin Station).

Some of the key differentiators among the configurations are as follows: The PLANAR concept has both inertial and earth-fixed orientation capability; all others have only one or the other orientation capability. The two basic solar array concepts are deployable articulated arrays, and fixed space erectable panels that are installed on large area support structures. Deployable arrays do not require orbital assembly, are efficient in that cell area is a minimum due to sun pointing articulation, and have inherently low natural frequencies. Fixed panels have higher natural frequencies and must compensate for a non-optimum sun aspect by oversized cell areas.

The choice of a solar array concept will affect controllability constraints. Configurations with fixed appendages (arrays and radiators) must maintain the station geometric axes oriented close to the required attitude with respect to the sun and shadow zones, or else the power and thermal control systems will suffer significant losses/degradation. Maintaining geometric axes aligned under changing configuration and mass property conditions over the mission life may be a severe problem for most configurations which have fixed arrays and radiators. However, concepts which have articulated appendages can permit the control system to operate under the most favorable conditions by controlling the principal axes (instead of the geometric axes) with no penalties, since the arrays and radiators can be oriented separately as required.

Two basic support schemes for the pressurized modules are used in the concepts. In one scheme, the modules are supported only by their direct

docking connections to each other. In the other scheme large truss structures are used to support each module separately from the linkage between modules. These two methods will have somewhat different module replacement impacts from the standpoint of support to be provided by the Shuttle during such an exchange or expansion of modules.

More recently, NASA has narrowed its Space Station concepts to three reference configurations, each with five pressurized modules and framework structures from 300 - 400 feet long. The solar array electrical power generation capacity illustrated in all three concepts is from 75 - 120 Kw, and compares to the Skylab maximum capability of 23 Kw. Brief descriptions of the three reference configurations are given in the following paragraphs.

POWER TOWER Station - The Power Tower concept gets its name from its over 300 ft. tall mast on which are mounted four pairs of articulated solar arrays across a 200 ft. span. At the opposite end is a cluster of five pressurized modules each from about 22 - 35 feet long. This configuration would orbit with the module end always pointed at the Earth to allow Earth observation payloads to have a clear field-of-view. Celestial viewing instruments would be mounted at the top of the tower, where they would have an unobstructed view of deep space. The Power Tower could be enlarged asymmetrically as a result of its control mode that would try to balance torques due to aerodynamics against the station's gravity gradient torque.

POWER TOWER
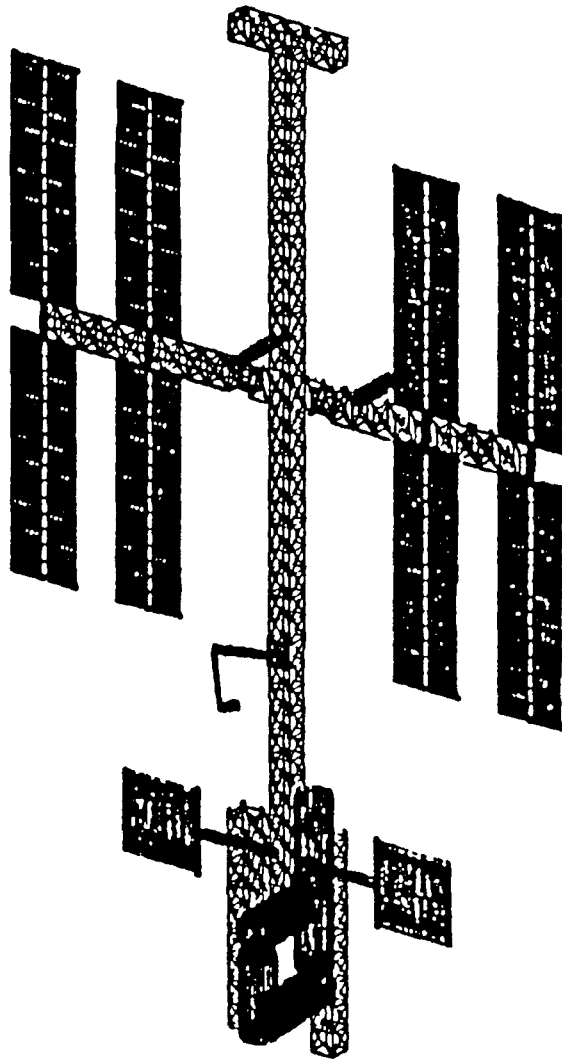
Figure 1

PLANAR

Figure 2

305
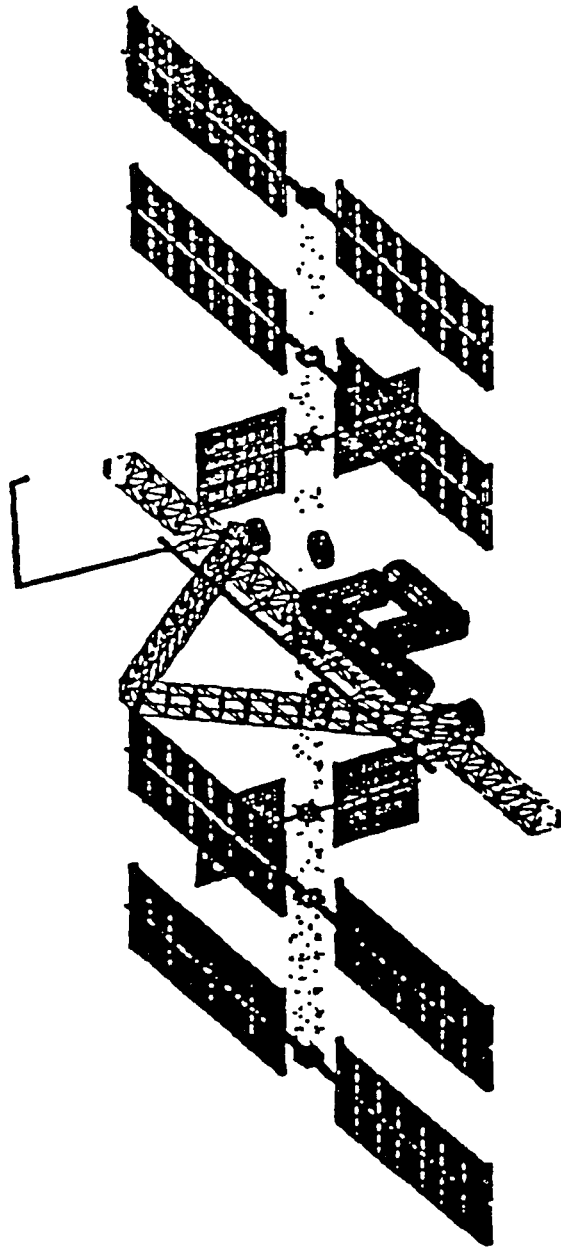
BIG "T" CONFIGURATION

SPINNER CONFIGURATION

←DESPUN CORE
MODULES

PERPENDICULAR TO
THE ECLIPTIC
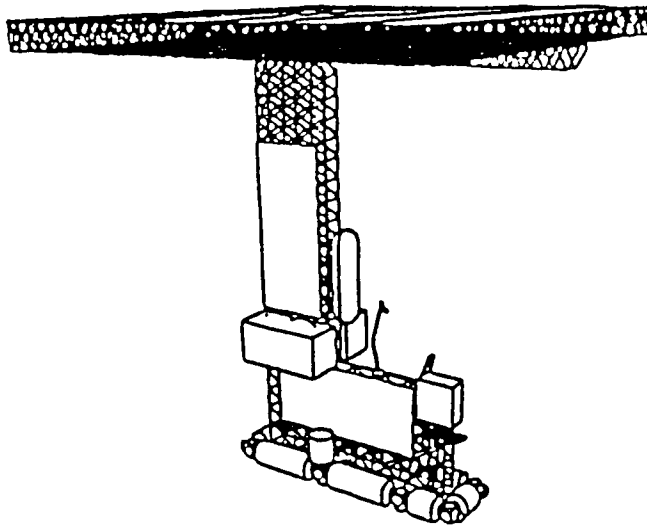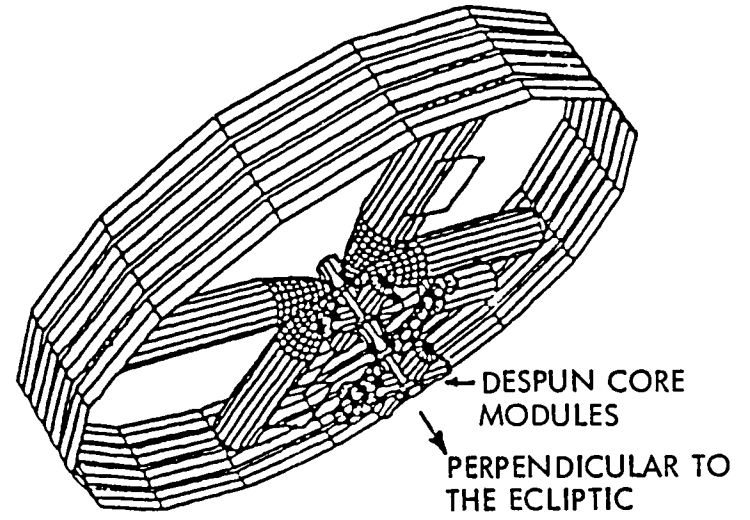
Figure 3

Figure 4

DELTA TRUSS
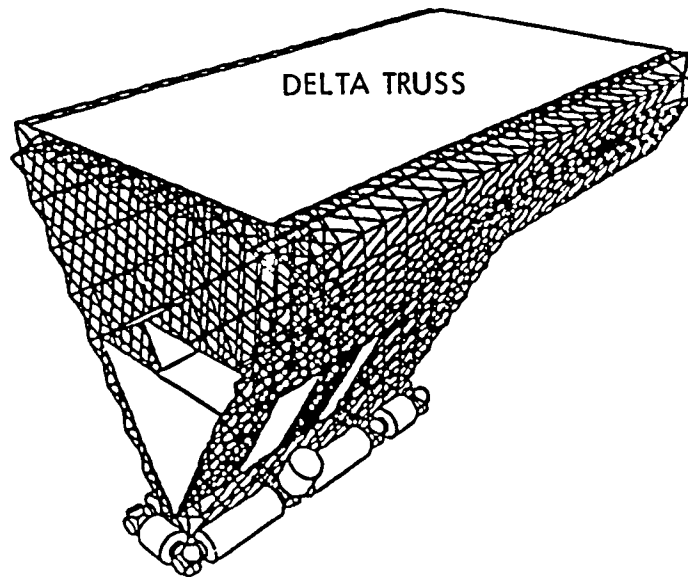
Figure 5

PLANAR Station – The Planar station configuration would be flown more horizontally in relation to the Earth. The entire station could be pointed either towards the Earth or deep space depending on mission needs. The five pressurized modules would be mounted in the center of a 300 ft. long strong-back truss structure. Two pairs of large solar arrays would be mounted on each end of the structure. A large 'A' frame extending some 80 ft. above the modules would support scientific and applications payloads. The control concept is to keep aerodynamic drag and gravity-gradient torques as close to zero as practical, and would require the station to fly with its arrays edge-on to the velocity vector and to expand in a symmetrical pattern.

DELTA Station – The Delta station derives its name from the triangular shape of its structure. The top of this station would be a 175 by 125 ft. area of fixed solar cells. Extending down from this roof would be a rigid V-shaped truss structure that supports a cluster of five modules at the bottom. The advantage of this concept is that it provides large areas for mounting external payloads. The large solar array roof would always be pointed at the sun. A possible control mode would combine CMG's (Control Moment Gyros) with a giant magnetic torquing system. Wiring to form torquing coils would be placed around the outer periphery of the Delta structure, and when energized, would interact with the Earth's magnetic field.

Controllability and dynamics are major drivers to concept evaluation and must be considered for each stage of initial build-up and evolution over the system life, including with and without the shuttle attached and for changing payloads and mission tasks. Figures 6 and 7 illustrate the large incremental changes that will be involved in the build-up of the Power Tower Station. This is generic to all the concepts and is truly construction in space. As to basic rigid body controllability, all three reference configurations are controllable in all mission modes using some form and combination of CMG's, magnetic torquers, and RCS (reaction control system).

POWER TOWER AT BEGINNING OF SECOND FLIGHT
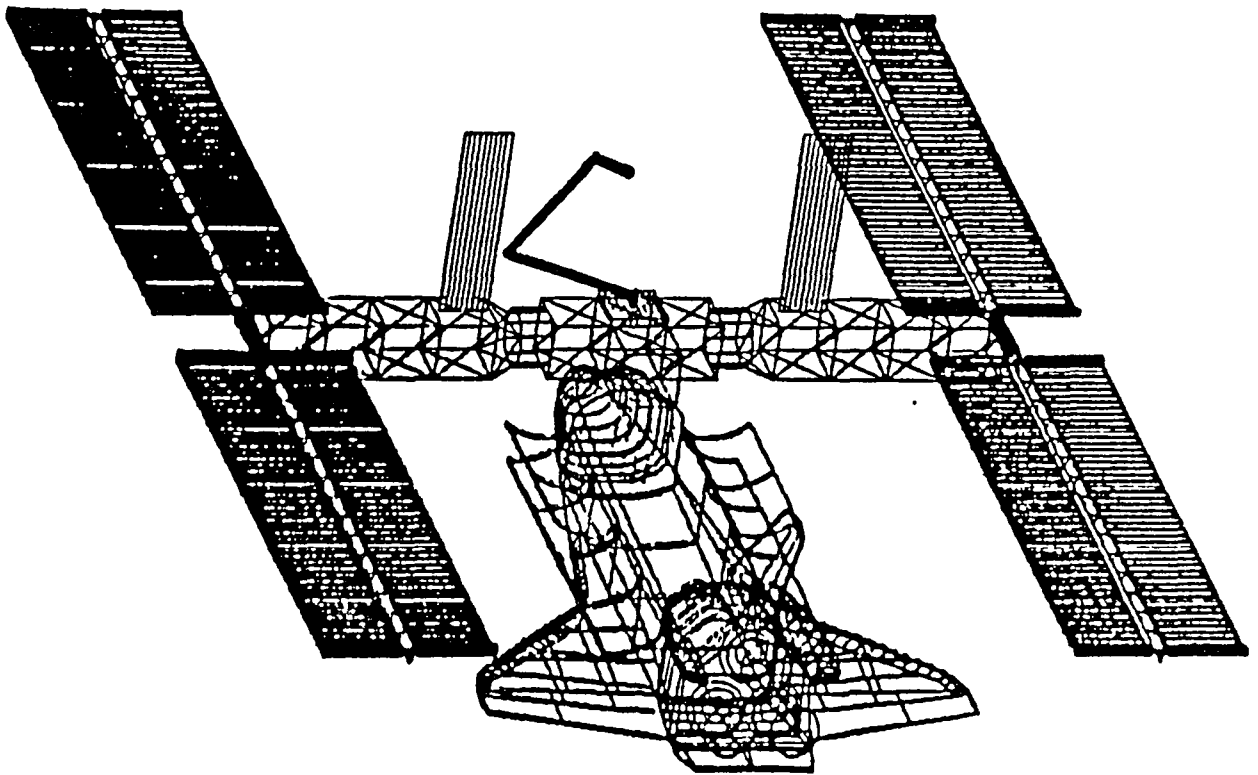
Figure 6

POWER TOWER AFTER SECOND FLIGHT
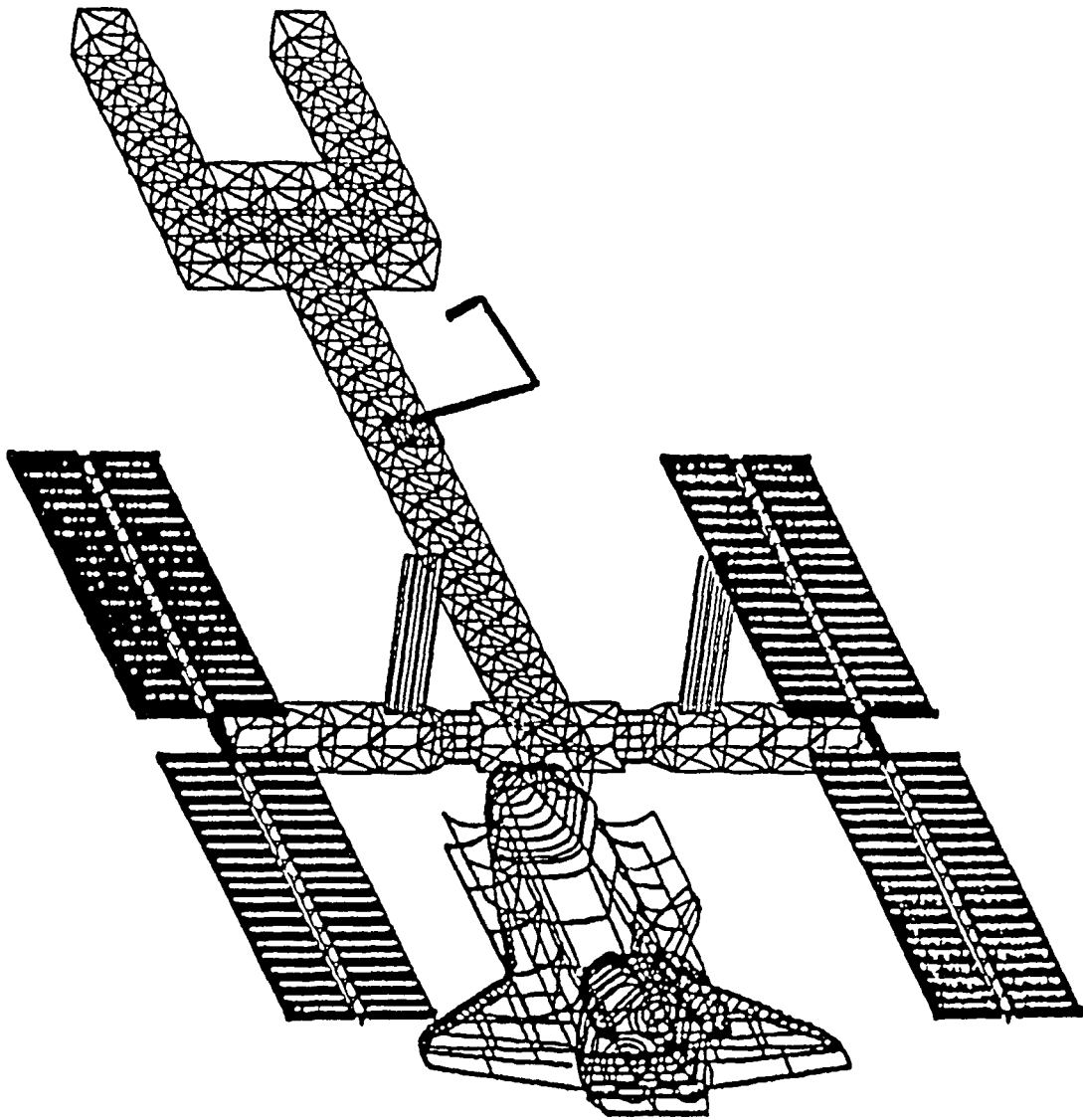
Figure 7

The CMG controllers would operate with an overall closed-loop bandwidth of 3-6 millihertz (0.003-0.006 Hz), and the lowest flex-body natural frequencies are at least a decade higher as shown in Figure 8. Thus it appears there is adequate frequency separation between the core station attitude controller and the structural modes dominated by the large solar arrays. The real issue is that the payloads requiring precision stabilization do not have that advantage - their controllers and structures will be totally enveloped by the vibration spectra of the station flex-body modes which will extend well into the several hertz range. As this paper will suggest, the payload accommodation requirements can be satisfied using Flight Dynamics ID in conjunction with techniques of active disturbance control/suppression.
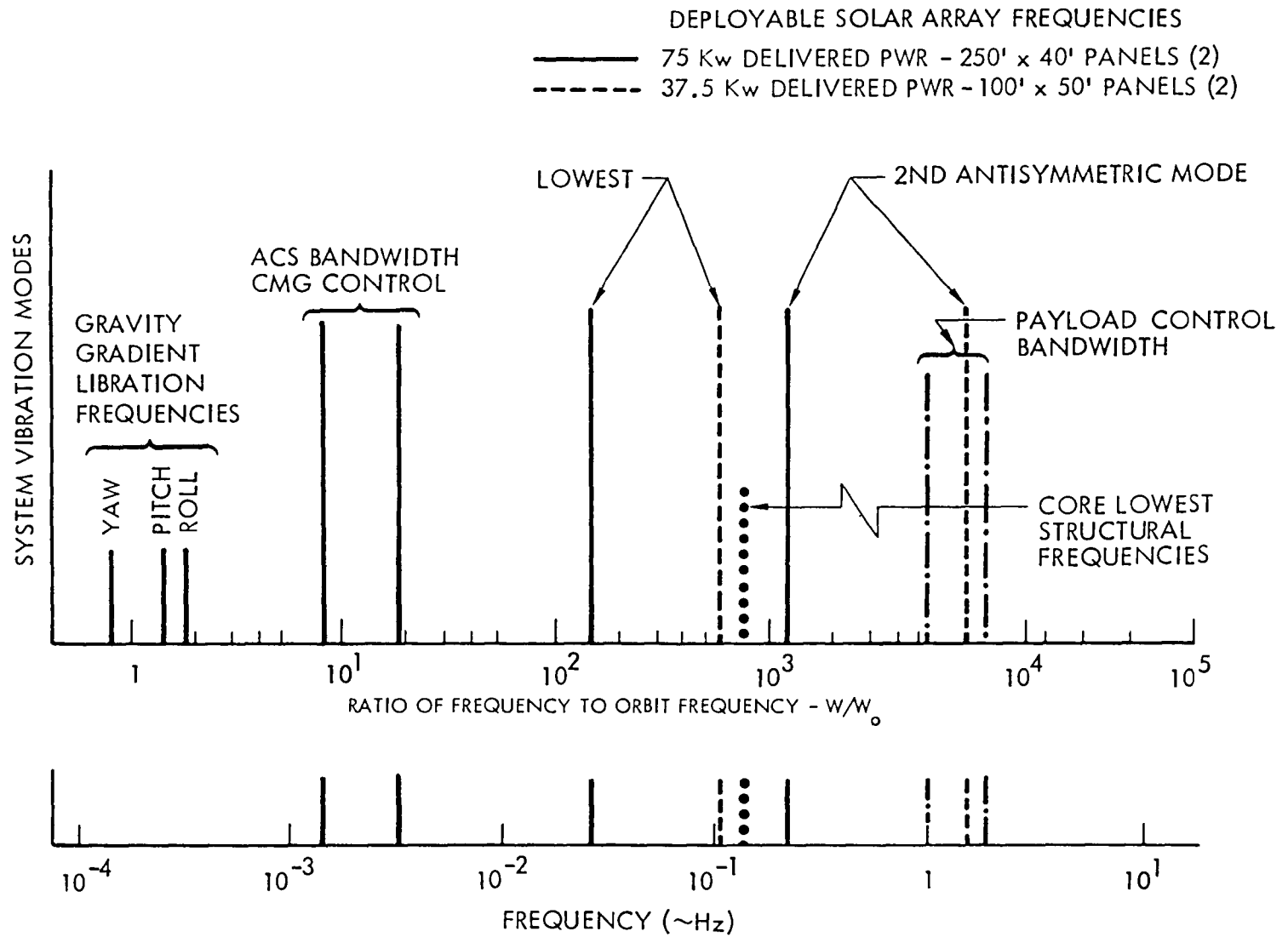
Figure 8

FLIGHT DYNAMICS ID FUNCTIONS

The Space Station Flight Dynamics Identification capability will be embodied in on-board software that will monitor performance, determine actual mass properties, characterize and identify disturbances and flexible body dynamics. The ID software is likely to incorporate fast algorithms for large scale modal parameter ID, allow optimal input selection, employ parallel processing techniques, and contain strategies for sensor options and collection of spatially distributed data. It will enable measurement and evaluation of critical structural and control parameters in open-loop and closed-loop modes, and establish a database for reduction of uncertainties in control/structure dynamic interaction and compatability. The physical system to be identified will include the Space Station solar panels and flex appendages, multi-payload disturbance interactions, and core structure disturbances from machinery, fluid slosh, crew IVA/EVA, venting, propulsion, and remote manipulator activity. The overall functional form of the ID process is illustrated below (Figure 9).

ANALYTICAL MODEL PARAMETER DETERMINATION PROCESS

[ON-LINE] INPUT/OUTPUT SIGNALS OF THE SYSTEM DURING
OPERATION USED TO IDENTIFY A MODEL IN REAL-TIME

[OFF-LINE] OPERATING SIGNALS RECORDED FOR LATER ANALYSIS
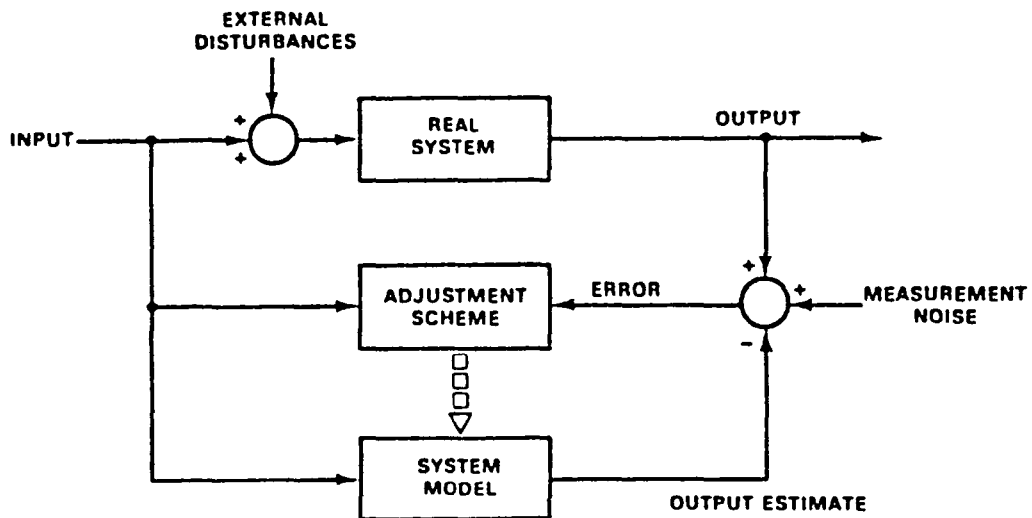
Figure 9

Major Flight Dynamic ID functions and specific task examples for the space station are categorized below along with a brief discussion of the associated justifications:

(A) Verification/Calibration of predicted global static and dynamic behavior of the system in-situ.

Detailed physical models of integral elements and small scale interconnected elements will be generated in the design and ground test/validation phases. However, the integrated in-situ configuration will be a large scale composite of elements using deployable and/or space erectable technologies having connectivity with a wide range of possible end-conditions and imprecisely known characteristics, e.g., damping, hysteresis, deadband, non-linear stiffness. The large scale static and dynamic behavior of such systems is not practical to ground test and must be calibrated in all operational modes and as part of assembly staging/checkout in orbit. Final data processing is assumed to be by ground support, but significant sensor signal processing is expected to be done onboard as part of data acquisition and telemetry.

M and ID (Measure and Identify) structural geometry and mass properties of the integrated configuration during assembly and build-up phases, servicing of free-flyers and deployment/berthing of OMV, OTV, and resupply mass redistribution, including Shuttle berthing.

M and ID rigid body system dynamics in all mission phases including rotational states (position, rate, acceleration) translational states (position, rate, acceleration) relative alignment between core modules, and between attached bodies and core, quasi-steady state forces and torques (solar, aero gravity gradient), and center of mass, center of pressure, barycenter of gravity gradient.

(B) Precise definition/location of local structural resonances and associated damping, transmissibility, frequency (s) and stability over the range of environmental conditions, e.g., thermal, aero, gravity gradient.

The Space Station will be a large flexible structure with low natural frequencies that are closely spaced, joint dominated, non-linear, and which will be within the bandwidth of articulated appendages and payload controllers (Figure 10). Control/Structures interaction design methodologies can include basic frequency separation, gain shaping (low, high, passband, and notch filters), passive damping and active mode suppression. All methods are dependent on predetermined physical models and the derived controller parameters. Re-programmability of control filters and active dampers should be assumed. Hence, the need for local dynamics ID on-orbit to provide the data for calibration/update of compensation filters and active dampers. Sensor signal processing and essential data processing are performed onboard.

M and ID dynamic coupling between attached bodies and the core structure in all mission phases. These appendages include the solar panels, radiators, antennas, payloads, berthing/servicing hangers and trusses, and especially the berthed vehicles – Shuttle, OMV, OTV, and free-flyers (FF).

M and ID interactions of system structural modes with the ACS in all operational phases, i.e., initial deployment, assembly, build-up, normal cruise, including IVA and EVA, re-orientations (LV and inertial), reboost, resupply by Shuttle (logistics and payloads), and servicing FF, OMV, OTV, activities.
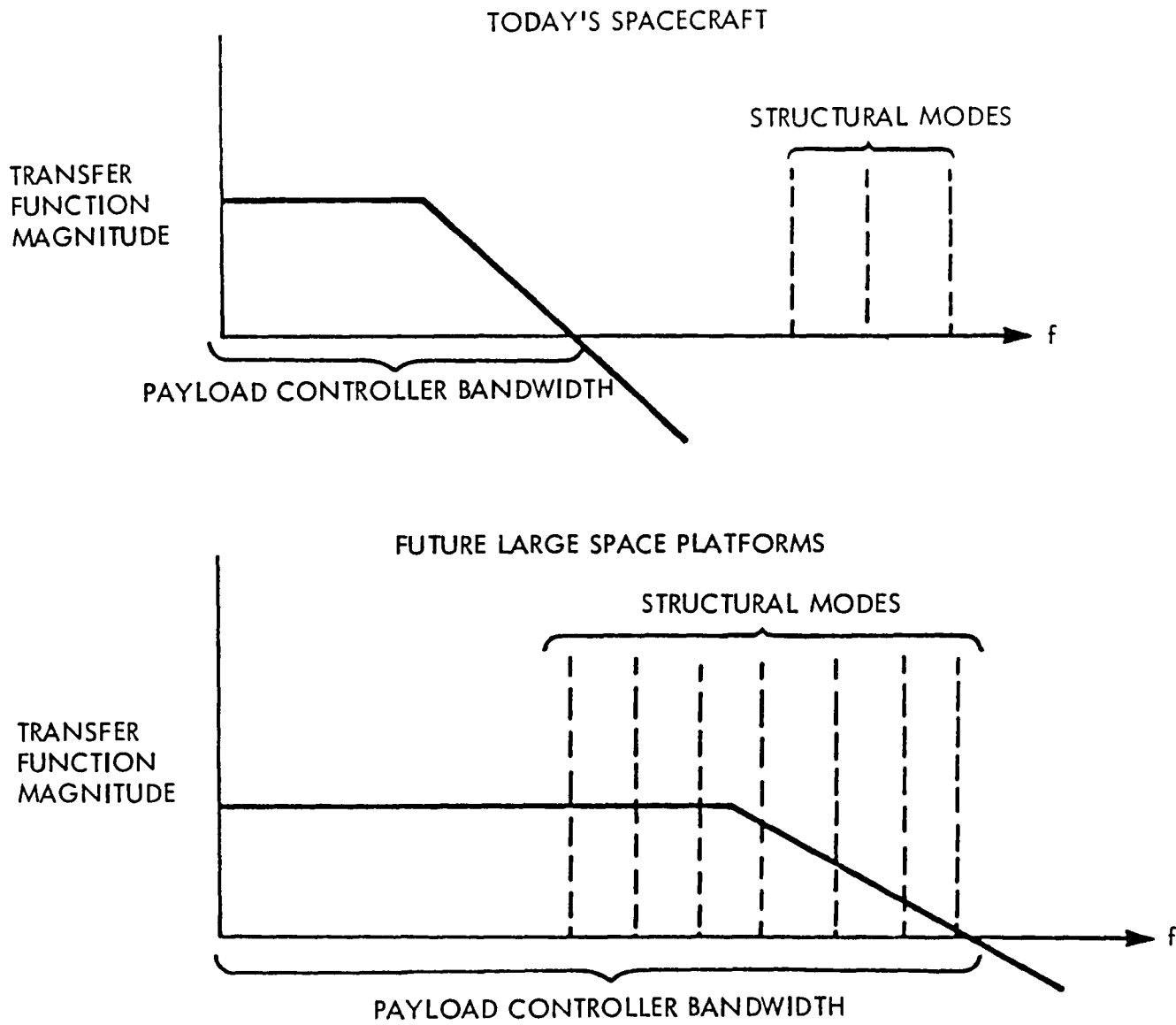
Figure 10

(C) Real/near-real time tracking of time-varying dynamic parameters required for self-tuning controllers.

It can be assumed that some performance critical controllers for local disturbance suppression, global stabilization, payload articulation, etc., will need parameter identifers and state observers as part of the real-time closed loop control function, Figure 11. In this context, it is more realistic to consider the problem as one of tracking perturbations about an expected value rather than the determination of absolute values in real time. It can also be viewed as parameter-error tracking vs determination. This approach can apply to mass properties changes, disturbance frequency drift, axis cross coupling variations, jump-resonances, mode-coupling changes, etc. Signal and data processing are done on-board.

M and ID all external dynamic disturbance sources, including assembly activities and RMS operation, space erectable construction tool use, EVA, berthing/soft docking, flex-body behavior of attached structures, payload articulation/translation, solar panels, radiators and antennae articulation, and slosh oscillations of fuels, cryogens, life support liquids.

M and ID all internal dynamic disturbance sources, including machinery vibration, IVA, venting, propulsion and ACS effectors, fluid transfer and mass redistributions, and experiment activities.

POTENTIAL SPACE STATION USERS

60% OF USER NEEDS ILLUSTRATED BELOW IN TERMS OF
STATION STABILITY AND LINEAR ACCELERATION

STATION LINEAR "g" – LEVEL*

DOCKING

MAN-PUSH OFF

$\geqslant 10^{-2}$ g

10^{-3} g

10^{-4} g

10^{-5} g

TECHNOLOGY DEVELOPMENT
CFS, FMT, CAP, CG, MPTL, COMF, SPC

COMMERCIAL PROCESSING
MPF, CML

LIFE SCIENCES
CELSS

MAT'L TECH ·
CGSP, CP, FCP

PHYSICS EXP ·
CRY, GRE, FLD

PRESSURIZED MODULE PAYLOADS REQUIRING
FREQUENT ASTRONAUT TENDING

STATION ATTITUDE STABILITY (JITTER)*

DOCKING

MAN-PUSH OFF

DEGREE

ARCMIN

ARCSEC

$\leqslant$ 1/10
ARCSEC

LARGE STRUCTURES TECH DEV
AAC, ACDE, LSTE, LACO, ZAR

GEOSCIENCES ·
AVHER, LASMRR

HIGH ENERGY OBSERVATIONS ·
LAMAR, BTM, HRS

LOW ENERGY OBSERVATIONS
SIRIF, STARLAB, FUSE

PLANET OBS
PST, FTS

SOLAR OBS
ASO SOT P/OF

EXTERNALLY ATTACHED PAYLOADS REQUIRING
PERIODIC ASTRONAUT SERVICING

*TYPICAL EFFECT ON RIGID CORE MODULES WITH LOW BANDWIDTH
CMG CONTROLLER (0.001 Hz) AND SOLAR ARRAY FUNDAMENTAL BENDING MODE OF 0.04 Hz

Figure 11

317

FLIGHT DYNAMICS ID METHODOLOGY

The User-friendly Space Station operates in a relatively 'dirty' dynamic environment, and yet demands micro-g conditions for scientific and commercial payloads and sub-arcsecond pointing stability for astrophysics experiments. Regardless of which particular system design is finally chosen for the station, achieving these objectives will require identifying, by various sensing and processing methods, a number of parameters that contribute to the dynamics of the station. These parameters characterize the gross system mass properties, flex-body interactions, disturbance environment, and control system response and stability. Table 1 provides a correlation of application categories with parameters, sensing, and ID processing methods.

A simplified overview of the end-to-end Flight Dynamics ID process is shown by Figure 12. The diagram maps the general flow of information, the major blocks of system interaction and some of the elements within those blocks, from the input signals that disturb and deliberately excite the system to the various users of highly processed ID data.

One of the major control system design challenges the Space Station presents is the estimation of these parameters as they undergo dramatic variations during configuration change in build-up and later in evolution during the multi-decade life of the system. Closed-loop estimation and ID can provide independent verification of the predicted behavior of the Station and its elements, and also refine the ground modeling approximations to enable anomaly/fault detection monitoring and diagnostics which are vital to the safe operations of the system.

The most fundamental mass properties to estimate are those associated with the major system control functions such as attitude control, momentum management, and reboost maneuvers. The parameters of interest here are the entire system mass, the mass center, and inertia tensor. Obviously, each of these parameters changes significantly with any major configuration

SPACE STATION FLIGHT DYNAMICS ID METHODOLOGY

APPLICATION CATEGORY	MODEL PARAMETERS	SENSORS	ID METHOD*
RIGID BODY	CENTER OF MASS, CENTER OF PRESSURE, BARYCENTER, INERTIA TENSOR	GYROS, ACCELERO-METERS, STAR TRACKERS, NAVIGATION	KALMAN FILTER, LEAST SQUARES, MAX. LIKELIHOOD
QUASI-STATIC DISTUBANCES	SOLAR PRESSURE, AERO-DRAG, GRAVITY GRADIENT, MAGNETIC FIELDS, THERMAL DISTORTION	ATTITUDE CONTROL AND DETERMINATION, NAVIGATION, E-O INSTRUMENTS, MAGNETOMETERS	KALMAN FILTERS, LEAST SQUARES, MAX. LIKELIHOOD
DYNAMIC DISTURBANCES	MASS TRANSFER, CREW MOTION, FLUID SLOSH, MACHINERY VIB, ARTICULATIONS, VENTING	GYROS, ACCELERO-METERS, GIMBAL ANGLES, VIBRATION PICK-UPS	FAST FOURIER TRANSFORM, SIGNATURE CORRELATION, MAX. ENTROPY
FLEXIBLE BODY INTERACTIONS WITH CONTROL SUBSYSTEMS	FREQUENCIES, DAMPING, MODE SHAPES, COUPLING FACTORS	GYROS ACCELERO-METERS, REMOTE E-O SENSORS, ACS MOMENTUM EXCHANGES	MAX. ENTROPY, MAX. LIKELIHOOD, EIGENVALUE/ EIGENVECTOR
CONNECTED BODY RELATIVE ALIGNMENT	ALIGNMENT TRANSFORMATIONS	REMOTE E-O SENSORS	LEAST SQUARES, PASSIVE MODE ONLY
CALIBRATION OF SENSORS AND EFFECTORS	GYRO DRIFT, ACCEL-EROMETER BIAS, CMG RESPONSE, THRUST PROFILE, MAGNETIC TORQUER FIELD	STAR TRACKERS, NAVIGATION, MAGNETOMETERS	KALMAN FILTERS, LEAST SQUARES.

*UNLESS INDICATED, ALL METHODS MAY EMPLOY BOTH PASSIVE AND ACTIVE MODES OF DELIBERATE DYNAMIC EXCITATION, INCLUDING VEHICLE ORIENTATION CHANGES.

Table 1

alteration such as shuttle berthing, assembly, deployments, etc. It is equally obvious that these parameters will require updates to adjust control gains, filter constants, and momentum exchange strategy. It is however, important to note that nontrivial parameter variations can occur during relatively 'quiet' operations. For example, sun pointing of the large solar arrays can produce variations of inertia per quarter orbit on the order of 15%, and aerodynamic drag torques will also fluctuate over minimum to maximum values as the arrays rotate with respect to the velocity vector. Therefore, updating of the rigid-body properties is not a static activity, and is more appropriately viewed as determining a time-varying profile which may require a multi-orbit process to identify and refine each time it is performed.

It is most desirable to be able to perform an ID procedure without any impact on normal Space Station operations. For instance, the kinematic relation given by

$$A_{ac} = A_{cm} + \dot{W} \times p + W \times (W \times p) + \text{accelerometer error}$$

can be used to estimate the center of mass in a completely passive manner. Here, A_{ac} is accelerometer data, A_{cm} is the true center of mass acceleration, W is the instantaneous Station angular velocity vector, and p is the vector from the center-of-mass to the accelerometer. A recursive Gauss-Markov estimator can be constructed for determination of p. The factors contributing to how well this vector can be estimated include observability (non-zero angular rates along the body axes), the accuracy of the measurement and inference of W and $\dot{W}$ respectively, and the validity of assumptions regarding the unknown and unmeasured A_{cm} (very small accelerations since net forces on the system are quite small).

The above estimation scheme contrasts with that required for inertia or mass parameters, in that these require a change in the system angular and linear momentum in order to obtain any information; hence a known torque or force input must be created. Treating the Station as a rigid

SPACE STATION FLIGHT DYNAMICS IDENTIFICATION
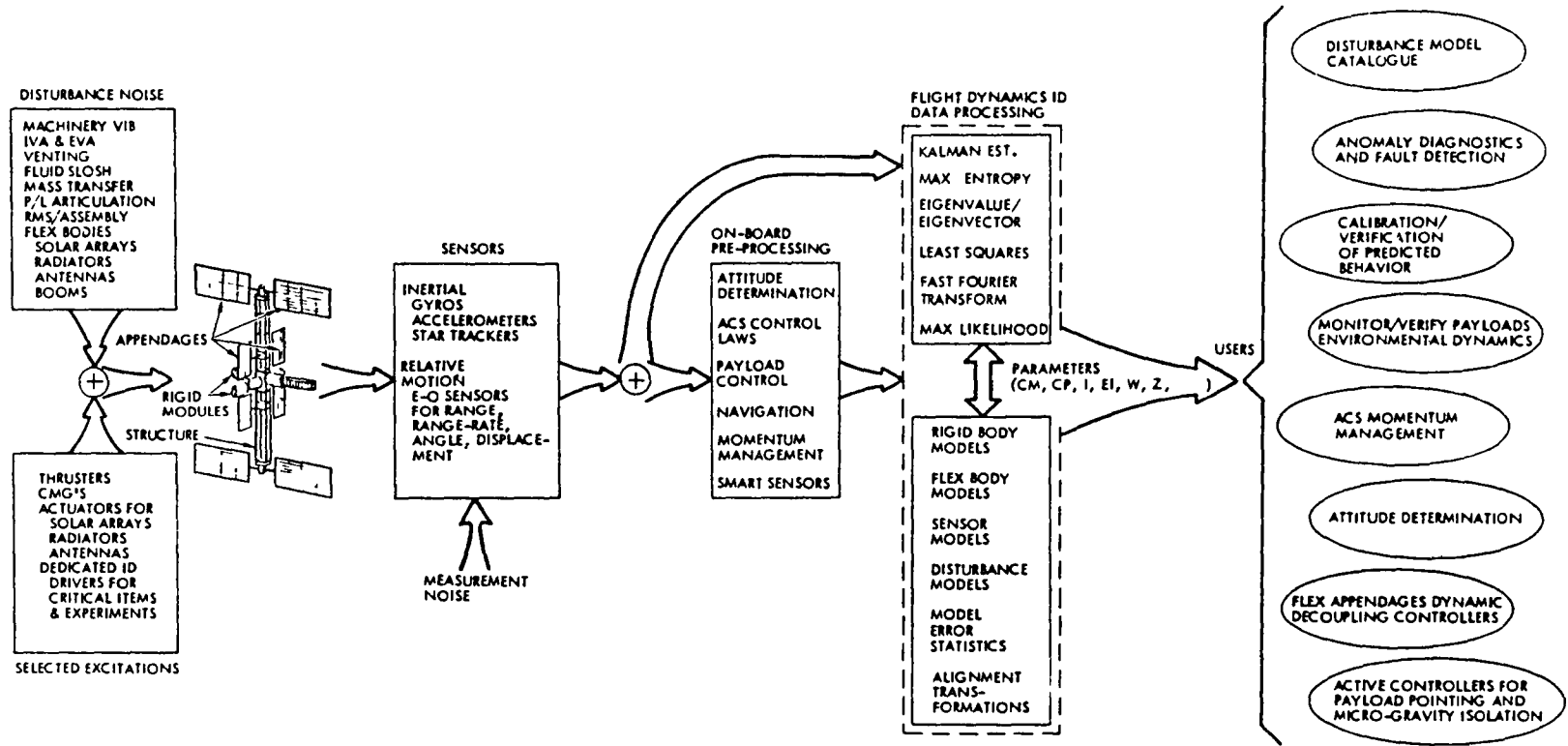
Figure 12

body for the moment, i.e., lumping flexibility effects, crew motion, fuel slosh, etc., together as small disturbances, the pertinent equations of motion involving the inertia are simply

$$I\dot{W} + W \times IW = T_c + T_d \qquad ,$$

where T_c and T_d represent control and disturbance torques, respectively. Given a nominal estimate I_o of I, it is not difficult to develop schemes to estimate the difference $\Delta I = I - I_o$, assuming the availability of angular rate data (measured or inferred). But in order for ΔI to be observable it is necessary that known torques be applied in three independent directions. To give an idea of how this factor and some others enter into the estimation problem, assume that $|\Delta I| \ll |I_o|$, then the dynamics have the approximate form

$$I_o\dot{W} + W \times I_oW + W \times \Delta IW + \Delta I I_o^{-1} \, W \times I_oW =$$

$$T_c + \Delta I I_o^{-1} \, T_c + T_d + \Delta I I_o^{-1} \, T_d$$

where the symmetric matrix ΔI is characterized by the six parameters, $i_1 \dots i_6$, that are assumed to be constant or slowly varying. Appending these to the dynamical state vector W, leads to a system of the form (ignoring second order terms)

$$\dot{x} = Ax + u + \tilde{T}_d$$

where $x = [\tilde{W}_1 \tilde{W}_2 \ \tilde{W}_3 \ i_1 \dots i_6]'$ $[\tilde{W}_1 \ \tilde{W}_2 \ \tilde{W}_3]' = I_oW$, $u = [T_c' \mid 0]'$ and

$$\tilde{T}_d = [T_d + \Delta I I_o^{-1} T_d \mid 0]'$$

with ' (prime) = transpose,

$$A = \begin{bmatrix} 0 & 0 & 0 & T_1 & T_2 & T_3 & 0 & 0 & 0 \\ 0 & 0 & 0 & 0 & T_1 & 0 & T_2 & T_3 & 0 \\ 0 & 0 & 0 & 0 & 0 & T_1 & 0 & T_2 & T_3 \\ 0 & 0 & 0 & 0 & 0 & 0 & 0 & 0 & 0 \\ 0 & 0 & 0 & 0 & 0 & 0 & 0 & 0 & 0 \\ 0 & 0 & 0 & 0 & 0 & 0 & 0 & 0 & 0 \end{bmatrix}$$

and $[T_1 \quad T_2 \quad T_3]' = I_0^{-1} T_c$. Gyro data yields the observations

$$z(t_i) = H \, x(t_i) + n_i$$

with $H = [I_0^{-1} \mid 0]$. With all these assumptions it is not difficult to show that the state (hence, $i_1...i_6$) can be made observable by allowing T_1, T_2, and T_3 to be time varying.

Constructing an observer for the system above is certainly one way of obtaining an updated inertia estimate and the analysis indicates that the first-order problem can at least be made observable. However, in order for such an observer to be viable it is necessary to return to the previous assumptions and systematically assess their impact on the estimation process. Although it is not our intent to perform such analysis here, two of the more important factors to consider are the magnitude and frequency content of the unmodeled disturbances with respect to the known control torques, and the assumption that the inertia is constant (which it is not). These are the two major contributing factors in making the speed of the estimator versus signal-to-noise ratio tradeoff. Because of the operational realities that the system identification processes must contend with, the implementation issues involved in the extraction of signals embedded in noise and clutter will figure significantly in most applications.

323

Another generic area where system identification can offer a significant Space Station service is in the cataloging and characterization of disturbance forces and torques. Already we have seen that disturbance characteristics can enter nontrivially into the estimation procedures for mass properties. More importantly they can impact other processes as well. For example, momentum management strategies are based on knowledge of quasi-static disturbances (gravity gradient torques and aerodynamic drag most notably), while the more transient disturbances such as those due to crew motion, mass transfers, articulations, etc., can impact payload control systems and experiment packages. In addition to providing inputs to specific users, there is also a global need for creating and maintaining a 'dynamic log' to record and learn the dynamic behavior of the Space Station over the course of the mission. Such a system would probably consist of a data compression and integration service utilizing all the inertial measurements available on the station. This data could also be useful for diagnostics or fault protection by detecting events or behavior not conforming to established statistical trends.

From the brief discussion above of Space Station disturbances, and users that may have interest or concern for its characterization and content, a variety of filtering, identification and signal processing methodologies emerge as potentially applicable. For example, the dominant quasi-static disturbance torques due to gravity gradient and aerodynamic drag appear as input disturbances to the Space Station ACS. Exploiting the fact that these disturbances are configuration and orientation dependent, ACS data collected over several orbits could be partitioned into segments of similar space station orientation and configuration. Within each of these segments the torques can be presumed constant, and a simple observer of the previously outlined type could be defined for their estimation. Assembling the estimated torques obtained from the data segment would yield an orbital torque profile. The correlation between these disturbances and the Station orientation and configuration can again be exploited by utilizing a priori disturbance frequency information in spectral estimator designs. Another alternative for determining the input disturbance torques

uses the fact that the disturbance manifests itself as a bias to the (computed from data) innovations process of a Kalman filter tracking the station rotational dynamics using gyro data as measurement. This is suggestive of a Maximum-Likelihood formulation of the problem. As before, a number of pertinent issues naturally accompany any of these proposed methods.

To obtain measurements and identify the general background noise resulting from the many ongoing simultaneous activities on the Station, spectral estimators operating on the available inertial sensor signals could be used. This would be a basic data processing service, perhaps as simple as an FFT, to obtain the power spectral density of the onboard disturbances at the various locations of inertial sensors. In addition to the time-calculation of this data, spatial correlation should also be possible since most disturbance signals will be received by all of the sensors. It may then be possible to do some simple spatial extrapolation to Space Station areas not directly serviced by an inertial sensor.

This general signal processing function can be sharpened and upgraded as the need arises. High resolution spectral estimators such as the maximum entropy method or eigenvalue/eigenvector analysis would be especially useful in determining disturbance spectra characteristics in frequency ranges that impact payload control devices. These methods can also be used to help characterize dynamic properties of controlled flexible appendages, where precise frequency knowledge is necessary for stabilization and dynamic control. Relatively small inaccuracies in frequency information have been demonstrated in the laboratory [6] to produce control instabilities in flexible structures even in the case of collocated actuation and sensing. For Space Station this problem becomes more acute since the luxury of collocation of sensors and actuators is unlikely.

The spectral methods alluded to above are all based on different model assumptions. Consequently some methods are better suited for some purposes than others. Hybrid approaches and generalizations of these

methods can also be developed [4], [13].

The maximum entropy method [1] is a high resolution spectral estimator that has enjoyed considerable success in several areas including geophysics and radar applications. The method assumes an autoregression model of the signal driven by white noise,

$$x(k) = \sum_{\ell = 1}^{m} a_{\ell} \, x(k-\ell) + \varepsilon_{k} \quad ,$$

where the coefficients $\{a_{\ell}\}$ are to be determined. Given the intensity of the ε_{k} process and estimate of the autocorrelation function $r(t) = E(x(k+t)x^{*}(k))$, the autoregression coefficients are solved for and an estimate of the power spectral density of the $x(k)$ process is obtained. A nice feature of this method is that coefficients corresponding to larger order autoregressive models can be generated recursively. Also the method has been shown to be consistent even in instances where the process is not autoregressive [3].

The eigenvalue/eigenvector method [12] assumes a model consisting of a finite sum of sinusoids of varying frequencies, phases and amplitudes in noise. The method determines the frequencies of these sinusoids based again on the autocorrelation function of the process and the noise covariance.

Both of these methods are well suited to resolve closely spaced spectral peaks. Thus they may have particular application to estimating modal frequencies of flexible structures that possess many packed modes. The maximum entropy method was used in [13] to obtain frequency estimates of the Space Shuttle's flexible remote manipulator system from flight data. The disadvantage of these methods is that they are sensitive to incorrect noise statistic assumptions. The high resolution maximum likelihood method

[9] is more conservative than the other two and gives better sidelobe performance, but at the price of less resolution [1]. Although each method relies on a different model, all of the resulting algorithms are based on assumptions concerning the autocorrelation function r(m) of the process. In practice this function can be approximated by the sampled lagged product operating on the data x(s)

$$\hat{r}(m) = \sum_{s=1}^{n-|m|} x(m+s) \; x^*(s),$$

or ensemble methods that are commonly used in the direct methods of spectral estimation such as FFT. For most of the Space Station applications it can probably be assumed that enough data will be available so that $\hat{r}(m)$ represents a reasonable estimate of r(m). If this is not the case then extrapolation methods can be employed [7], or in some instances these calculations can be be circumvented altogether [5], [11].

For many phenomena of interest on the Space Station a priori dynamical models will be developed, and only a tuning of certain parameters may be required. This situation would probably be encountered in the estimation of flexible appendage dynamics, for example. Here an alternative or complement to the 'black box' approaches of the previously discussed spectral estimators would be the (state space) maximum likelihood method [2], [10]. This maximum likelihood formulation could be employed to improve nominal frequency and damping estimates as well as to update disturbance models. This method could also be used to directly estimate the system mass and stiffness matrices. There are, in addition, several other scenarios in which the maximum likelihood model formulation

$$\dot{x}(t) = F(\theta)x + G(\theta) \; \omega$$
$$z(t_i) = H(\theta) \; x(t_i) + J(\theta)\eta(t_i)$$

is useful. Here θ represents the unknown (vector) parameter to be identified, and ω and η represent the process and observation noise,

respectively. A general scenario arises when this model is interpreted as a linearization about an equilibrium position. It then provides stability information via determination of the parameter θ. Specific applications could involve updating docking or retrieval dynamical models. The need for the latter was graphically illustrated in a recent Shuttle flight where some difficulty was encountered stabilizing the Solar Max satellite.

IMPLEMENTATION ARCHITECTURE AND CONSTRAINTS

Implementation of the Flight Dynamics ID system aboard the Space Station carries with it the need to be as practical and synergistic as possible. In the complex environment of station operations the ID architecture and functioning should accommodate implementation constraints that tend to more closely integrate the ID system into the core station software and hardware elements. For Flight Dynamics ID these constraints are summarized below:

(a) Maximize the use of core station subsystems as real-time data bases. The functions such as Attitude Determination, Flight Control, Navigation, and Momentum Management act as pre-processors to provide smoothed and interpreted data already separated into the distinct bandwidth regimes associated with each function.

(b) Utilize the Attitude Determination/Control and Navigation sensors such as gyros, accelerometers, and star trackers, in addition to relative motion electro-optical sensors that may be part of an on-board alignment transfer and monitoring system.

(c) Employ flight system actuators and effectors such as CMG's, thrusters, RMS, gimbal torque motors, articulation angle and rate encoders, etc., as ID excitation generators. Special purpose or dedicated excitation drivers should be imposed only for critical

items or as part of experiments.

(d)   Allocate ID computational resources on the basis of time dependency. Real-time tasks must have on-board signal and data processing. Those tasks of a non-real-time nature or need should have their signal processing done on-board to serve as a data compression relief for the ground link which will also carry the data processing return from the ID ground support facility.

(e)   Payloads and technology experiments also need to be considered under the constraint guidelines: Payloads will need to provide engineering data to the Station core ID system and should emphasize the use of remote electro-optical sensors that are a part of the flight system. There will most likely be experiment-unique ID processing that will have both real and non-real-time demands on computational resources. This will necessitate careful interfacing with the station Data Management subsystem for ground support and on-board processing needs.

The table below (Table 2) provides the general scale for consideration of sensing requirements in the ID process.

RANGE AND SENSITIVITIES OF PARAMETER M and ID FOR THE SPACE STATION

Parameter or State	System Scale (Max)	Measurement Sensitivity	Measurement Resolution
Size/Distance	500 ft.	10^{-4}	0.01-.05 ft.
Mass (w/Shuttle)	5×10^5 lbs.	10^{-5}	5. lbs
Inertia	10^7 $s\ell-ft^2$	10^{-6}	10. $s\ell-ft^2$
Alignments	2 deg.	10^{-3}	0.002 deg.
Rotation Rate	1. deg/s	10^{-3}	0.001 deg/s
Rotation Accel.	0.1 deg/s^2	10^{-3}	0.0001 deg/s^2
Translation Rate	1. ft/s	10^{-3}	0.001 ft/s
Translation Accel.	10^{-2} g	10^{-4}	10^{-6} g
Frequency	DC -1.0 Hz		0.01 Hz
	1.0 - 20. Hz		0.10 Hz

Table 2

An important integrative factor in the design and implementation of flight dynamics ID will be the automation of M and ID methods/activities to minimize ground and crew workload. This should take the form of supervisory control by crew/ground, i.e., initiate and monitor, terminate or override, and includes pre-programmed diagnostics for anomaly investigations with emphasis on rapid detection of local faults for caution/alarm. This capability will require full access to the sensing data network for integration of ACS, structures and payload information.

To illustrate the on-board implementation of Flight Dynamics ID functions an example architecture using the subsystems of attitude control, precision pointing control, navigation and manipulator control in a space station environment is constructed (see Figure 13). In this architecture the functions of the subsystems are partitioned into levels reflecting considerations of control and data transmission bandwidth. At the highest level (Level 0) this architecture applies a hybrid architectural concept: The SEC (Station Executive Controller) communicates with the four subsystems through subordinate executive controllers designed in part to support the command and data handling required at the station command and control level. Low bandwidth data transmission in support of control functions is a characteristic of this level of the architecture. Such transmission rates are consistent with the fault tolerance required for reliable, autonomous operations of the station system. At lower levels of the architecture, higher bandwidth data rates required for real-time control can be provided through computing and transmission networks more tightly coupled than the hybrid computing architecture at the station command and control level. The following paragraphs discuss implementation concepts for the functions in this example system, beginning at Level 4.

'Smart Devices.' At the lowest level of the architecture (Level 4) reside 'smart' devices. These devices consist of actuators and sensors, integrated with microprocessors, which decode digital data commands and which encode analog outputs. Depending on the device, the digital output data, processed by these devices, can be tailored into a variety of outputs

SYSTEM ID IN THE SPACE STATION COMMAND AND CONTROL ARCHITECTURE
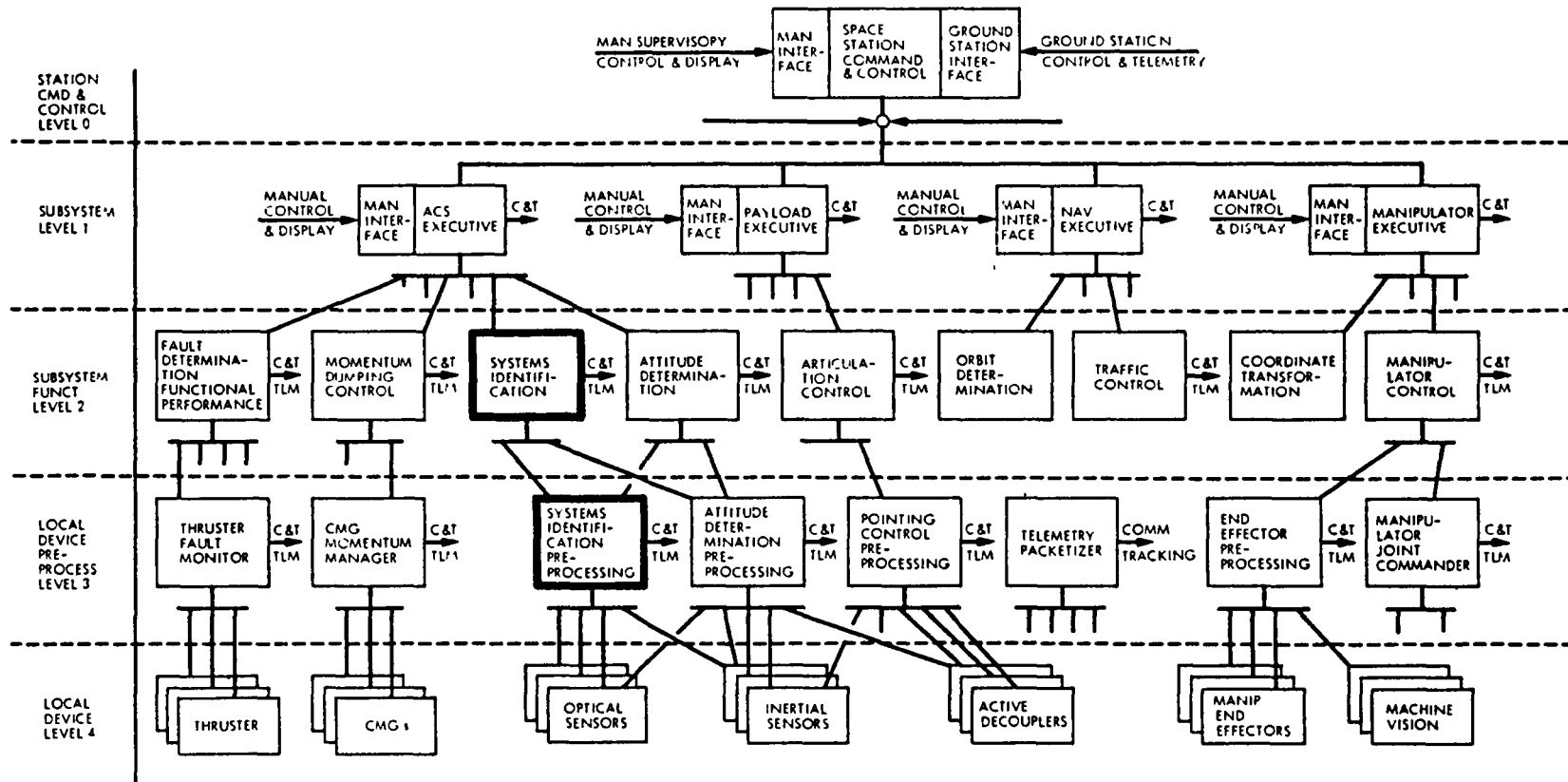
Figure 13

for specific use at the next higher level of control. For example, time sequences of encoded star position data may be processed into two axes of rate and position input for a station attitude control law. Alternately, an average of the position values can be input directly into an ID process which derives data types for subsequent input into an orbit determination computation. More extensive processing may be necessary at this level if, for example, an optical sensor outputs images at a video rate which must undergo Fourier transformation before the resultant frequency spectrum is input to a systems identification algorithm. This sensor can be mounted at the end of a manipulator and may also be used as part of an automated monitoring task of space station structural dynamics. Thus the output would require a different type of processing, consistent with a potential tracking and feature extraction function. Commands input into these devices can be in the form of data decoded by the integrated electronics into calibration parameters or a configuration set-up.

Subsystem Local Device Pre-Processing (Level 3). To satisfy the need for additional data processing of input signals and output commands, dedicated subfunctions can be implemented which connect a set of smart devices at the preprocessing level (Level 3) in the subsystem hierarchy. Such subfunctions, for example, accept the conditioned signals from several sensing devices and develop from these inputs parameter error statistics. Alternatively, other subfunctions may collect sensor data from several sources and edit such inputs for use in an attitude determination process. Also, as an intermediate level in the architecture, these subfunctions perform input and output validation and interpretation consistent with a hierarchical approach to fault protection beginning at the local device level. Lastly, selected sensor and actuator engineering data can be prepared at this level of the architecture for transmission to the communications and tracking subsystem on the Space Station. As a result, data generated by the devices at the lowest level can be collected and further processed or packetized depending on the choice made by the ground

333

crew for the output of this data. Interference with other subsystem functions making use of the data from these devices is then avoided.

Subsystem Functions (Level 2). Data prepared at the local device preprocessing level of the architecture is transmitted to the next higher level (Level 2), where subsystem functions are performed. At this level complex computations associated with subsystem specific tasks such as Flight Dynamics ID, attitude determination, momentum management and payload pointing control can be easily performed given that the burden of input processing and output command generation has been done at the lower levels of the architecture. Consequently, the computational throughput requirements of the functions at Level 2 can be met by machines tailored for specific processing tasks. For example, a 32-bit microprocessor may be chosen to implement the precision processing needed for an estimation and model update function. This microprocessor need not also have the capability of processing high-rate raw sensor data used in the computation. The required input has been preprocessed by separate microprocessors, designed to accept the sensor data, and this input has been transmitted at a lower rate for the estimation computations. This illustrates one more benefit of the hierarchial subsystem architecture: the capability for the use of specialized software and hardware is designed into the system. As a result, new technology in (for example) spectral estimation can be introduced at a specific level of the subsystem, perhaps slaved to an existing subfunction processor for an initial check-out. The design can be validated at this level in an operational environment and eventually replace a process at this level, transparent to the functional performance of the system.

Subsystem Executives (Level 1). At the next level (Level 1) of the architecture, subsystem functions are controlled by local executives for each of the representative station subsystems: attitude control, precision pointing control, navigation and manipulator control. An executive here utilizes the results of several subsystem functions performed at the lower levels of the architecture. These results can be checked for

334

reasonableness by the executive utilizing the System ID data-base before further action is taken. The executive can then issue high level commands to subsystem level functions initiating major control activities. Specific station system-level functions are also supported at this level. For example, an attitude control executive can carry-out space station attitude changes prior to terminal rendezvous and docking with the Shuttle. A navigation executive can implement a correction in orbit inclination. A payload pointing executive can slew a telescope to perform an observation ordered by a mission specialist or ground-based scientist. A manipulator executive can respond to a crew command to move a manipulator arm to engage a piece of equipment outside of a pressurized station module. These types of global system functions can be directed either through an autonomous SEC or by the flight crew. At this level of the architecture the manned and autonomously controlled actions 'look' alike, in that the subsystem executives form a structured interface for the initiation of subsystem functions. As such, both the crew inputs and autonomously directed control actions will require reasonableness validation performed by subsystem executives. Appropriate warnings, which also become part of the crew displays, are issued by the subsystem executives in the presence of unacceptable or improperly directed actions, or in the case of anomalies/faults detected via ID processing.

Station Command and Control (Level 0). Further protection and validation of activities at this level of the architecture is achieved through the supervisory executive control of the SEC. This executive control resides at the highest level (Level 0) of the example architecture where the communication takes place between this executive and the station subsystems. Those actions to be taken by the subsystems with station-wide impact receive high level 'go/no go' sanctions from this executive. The SEC can issue cautions and warnings based on System ID anomaly reports and may override inputs deemed unacceptable or improper in terms of overall station system safety. Since the crew retains the final capability of direct intervention, and changeout or deactivation of devices and components, such SEC control does not represent a significant departure

335

from the spirit of past caveats on manned space system operations.

ELECTRO-OPTIC SENSORS FOR FLIGHT DYNAMICS IDENTIFICATION

The concepts currently being considered for a Space Station call for large, complex structures comprised of subassemblies of quite different structural properties. As the station is assembled and is visited by the Shuttle, carries on operations such as fuel transfer, and undergoes subsequent growth, its configuration will change radically. Consequently, system identification will have to be carried out at intervals and appropriate system identification sensors must be provided.

The chief problem in sensing the relative position and attitude of the rigid modules is the question of sensor and retro-reflector target placement, and the obscuration of modules by other modules or structural elements located between them and the sensor. To minimize the number of sensors required, it will probably be necessary to arrange the target cluster to fold out from the side of the module to get it into the line of sight. The deployment and locking mechanism will have to be carefully designed to insure sufficient rigidity for the target cluster to follow the motion of the module accurately. In order for the sensor to accommodate modules at different ranges it may be necessary to provide more than one size of target cluster and more than one size of target on a module. If necessary these can be coded by their wavelength response and interrogated by different wavelength lasers to avoid confusion in identifying targets in the focal plane.

For the sensing of non-rigid structural members a sufficient number of targets must be distributed over the structure to determine the important bending and torsional modes. The number and distribution of targets will be very dependent upon the type of structural elements. These can have the form of space frames (planar arrays of three-dimensional trusses) and linear elements in the form of long booms.

The problem of sensing appendages divides into two classes depending on whether the elements are articulated or not with respect to the main structure. There are configurations proposed using articulated solar panels and radiators, and there are some designs which fly sun pointing with fixed solar panels and radiators. These sun pointing configurations support the solar panels with three-dimensional trusses which are quite rigid, and with the close proximity of panel and truss should enable both to be sensed by the same sensor. When appendages are articulated the sensor problem becomes more complex because of two interrelated problems. (1) There may be no place to put the sensor that gives a good view of the element and (2) the element presents a changing aspect to the sensor as it is articulated. The approaches to these problems fall into two categories: (a) use multiple sensors and switch to the one with the best view of the element and (b) mount the sensor on the articulated element. The first approach most likely requires a greater number or more complex sensors than the second. There is a trade-off in this regard between a larger number of simpler sensors, and a smaller number in a more complex arrangement. Whatever the hardware tradeoff the software is more complex because of the changing aspect of the target with respect to the sensor.

On the other hand if the sensor is mounted on the articulated element, both the hardware and software are simpler because the element presents an unchanging aspect to the sensor. If the articulation joint is well determined in its degrees of freedom and very rigid otherwise, encoders on the joint will allow the transformation of measurements from the sensor frame of reference to that of the station. If this joint is not well determined the sensors which monitor the main structure must also monitor the location of the sensors on the articulated elements. Although the choice is dependent on the overall Space Station configuration, the mounting of the sensor on the articulated portion would seem to be advantageous.

A distinction is made in the identification of space station non-rigid elements on the basis of their lowest natural frequencies. The presumption

337

is that these frequencies correlate with size and that the lower frequencies imply larger structures. The implication for sensing is that the smaller elements will require fewer targets and higher framing rates for adequate monitoring of their behavior, while the larger elements will require more targets, but lower framing rates.

Table 3 provides a listing of electro-optic sensors currently under development and their characteristics. These sensors all sense more than one point and all require targets attached to the surface or body of interest. All sensors can be configured to measure displacement approximately perpendicular to a surface but may require different sensor locations.

ELECTRO OPTIC SENSORS FOR SPACE STATION FLIGHT DYNAMICS IDENTIFICATION

SENSOR/ DEVELOPER	SENSED VARIABLES	TIME SEQUENCE	PRINCIPLE OF OPERATION	ACCURACY	STATE OF DEVELOPMENT	COMMENTS	
1 Structural Alignment Sensor LMSC	Range sequential measurement	Multi-point sequential measurement	Ranging with modulated laser Beam steering with a movable mirror	±0 025mm	Breadboard	Reading rate is determined both by scanning rate and dwell time per point Quoted accuracy requires 1 sec dwell time Could be modified for angular measurement with development beyond that indicated Not suitable for dynamic control	
2 Shapes JPL	Range and 2 angles	Multi-point quasi-simultaneous	Ranging with pulsed laser using a fiber optics delay and a streak tube vernier Angles by imaging	±0 2mm ±2 arc sec	Breadboard	Provides 3-dimensional location of many (est 50) targets at high enough rates for dynamic as well as static control Will require the development of a space qualified streak tube	
3 Vibration Sensor LMSC	Range and the component of vibration velocity in the range direction (Doppler)	Multi-point sequential for range and multi-point simultaneous for vibration	Ranging with modulated laser and Bragg-cell beam steering Vibration measured by frequency shift in returned beam	±0 025mm for range 0 08μm amplitude resolution for vibration	Laboratory demonstration of vibration sensing with 10 targets	Covers many targets (S/N calculations indicate 50) without moving parts Good bandwidth for vibration Data rate for static measurement is determined by dwell time per target of 0 1 to 1 sec The 1 sec dwell time is required for the quoted accuracy Must be augmented with other sensors for in-surface displacements	
4 Surface-Accuracy Measurement System TRW	2 angles	Multi-point simultaneous or quasi-simultaneous	Angles by imaging	±5 arc sec typical Depends on configuration	Brassboard demonstrated on hoop and column antenna prototype	Requires active targets and wiring harness on surface or individual illuminators for each target Each sensor covers 3-4 targets	These systems require multiple sensors to cover a surface These must be attached to a thermally stable structure or have attitude transfer between sensors Sources or reflect must be visible when line of sight is nearly tangential to the surface Sensor gives angle only Range must be determined independently
5 Retroreflector Field Tracker Ball	2 angles	Multi-point simultaneous or quasi-simultaneous	Angles by imaging	±5 arc sec typical Depends on configuration	Flight model Developed for SEPS	Uses CID detector Covers many points per sensor	
6 Multiple-point Sensor Barnes	2 angles	Multi-point simultaneous or quasi-simultaneous	Angles by imaging	±5 arc sec typical Depends on configuration	Brassboard demonstrated in SEPS configuration	Uses CCD detector Covers many points per sensor	
7 Lasercone Honeywell	Displacement normal to LOS (Single Axis)	Multi-point quasi-simultaneous (very rapid scan)	Laser beam scans linear detector arrays aligned to the surface normals	±1mm	Based on existing land leveling systems Little development work has been done for space	Requires many linear sensor arrays projecting normal to the sensed surface Requires a second sensor to give displacements in the plane of the surface	

Table 3

FINAL COMMENTS

The integration of System Identification methods and technology into the Space Station signal and data processing architecture is seen as a key ingredient in achieving primary operational capabilities. On-orbit Flight Dynamics ID information can enable the Station core subsystems, experiments and payloads, and deployment, assembly and resupply operations to function with minimal ground dependency and intervention. In this context, the ID functions can play a vital role in the overall autonomous operations of the Station and contribute to major cost savings by its impact on ground and crew workloads, safety, and machine efficiency.

The theoretical and experimental basis for ID technology has been well established for some time, and has found wide application in diverse fields such as geophysics, aerodynamics, sonar detection, radar, etc. ID techniques continue to mature and are more easily implemented as the computational hardware and software resources available become more powerful. It has been the goal of this paper to focus attention on the future needs of the Space Station and the importance of applying ID methods and designs in the coming phase of System Definition and concurrent advanced development.

ACKNOWLEDGEMENTS

REFERENCES

1. A. B. Baggeroer, Confidence Intervals for Regression (MEM) Spectral Estimates, IEEE Trans. Inf. Theory IT-22 (1976), pp. 534-545.

2. A. V. Balakrishran, Stochastic Differential Systems 1, Filtering and Control-A Function Space Approach, Lecture Notes in Economic and Mathematical Systems, Springer-Verlag, New York 1973.

3. K. Berk, Consistent Autoregressive Spectral Estimates, Annals of Statistics, 2 (1974), pp. 489-502.

4. C. L. Byrne and R. M. Fitzgerald, Spectral Estimators that Extend the Maximum Entropy and Maximum Likelihood Methods, SIAM J. Appl. Math, 44 (1984), pp. 425-442.

5. J. P. Burg, Maximum Entropy Spectral Analysis, Ph.D. Dissertation, Stanford Univ., Palo Alto, Calif., 1975.

6. D. B. Eldred and D. B. Schaechter, Hardware Verification of Distributed/Adaptive Control, Proc. Workshop on Applications of Distributed System Theory to the Control of Large Space Structures, Pasadena, Ca., 1983, JPL Publication 83-46.

7. A. K. Jain and S. Ranganath, Extrapolation Algorithms for Discrete Signals with Applications in Spectral Estimation, IEEE Trans. ASSP-29, (1981), pp. 830-845.

8. A. H. Jazwinski, Stochastic Processes and Filtering Theory, Academic Press, New York 1970.

9. R. T. Lacoss, Data Adaptive Spectral Analysis Methods, Geophysics, 36 (1971), pp. 661-675.

10. R. E. Main and K. W. Iliff, Formulation and Implementation of a Practical Algorithm for Parameter Estimation with Process and Measurement Noise, SIAM J. Appl. Math, 41 (1981), pp. 558-578.

11. L. Marple, A New Autoregressive Spectrum Analysis Algorithm, IEFE Trans. ASSP-28 (1980), 441-454.

12. V. P. Pisarenko, The Retrieval of Harmonics From a Covariance Function, Geophysics J. Royal Astron. Soc., 33 (1973), pp. 347-366.

13. G. D. Shepard, L. A. Lepanto, R. W. Metzinger, E. Fogel, Application of Identification Techniques to Remote Manipulator System Flight Data, AAS Rocky Mountain Guidance and Control Conference, Keystone, Colorado, Feb. 1983.

14. E. F. Tubbs, Design for Space Station System ID Sensor, JPL Memorandum 347-84-704, 25 April 1984.

15. Autonomous Systems: Architecture and Implementation, JPL Document D-1656, 15 August 1984.

LARGE SPACE STRUCTURE FLIGHT EXPERIMENT

D. C. Schwab
Lockheed Missiles and Space Company
Sunnyvale, CA 94089

S. J. Wang and **C. C. Ih**
Jet Propulsion Laboratory
California Institute of Technology
Pasadena, CA 91109

ABSTRACT

The primary purpose of this work is to provide a first order feasibility analysis of a large space structure flight experiment. The feasibility issues are addressed from the control technologist's point of view. In this paper, control and system identification techniques and algorithms are evaluated with a selected experiment antenna structure through analysis and computer simulation. The required sensor and actuator hardware is assessed and its requirements examined with respect to the current state-of-the-art. The results of this study show that a shuttle attached flight experiment is feasible with moderate advancement of current control technology. The control and identification algorithms are well understood and can be adapted to the flight computers with additional dedicated processors. Although it is necessary to select a focused flight configuration to produce quantitative results, it is believed that, in general, performance requirements and capabilities, timelines, hardware, and algorithms are sufficiently generic in nature and can be applied to other configurations.

I. INTRODUCTION

Future large space structures such as large space deployable antennas and manned space stations present significant control problems due to their large size, structural flexibility, and changing flight configurations. Uncertainties of flight dynamics and disturbances will be orders of magnitude larger than those associated with spacecraft that are in orbit today. To deal with these uncertainties and structural flexibility, advanced control techniques such as inflight system identification, distributed control, adaptive control, etc., will be required. All of these advanced techniques are being developed but none of them have been applied to flight missions. Extensive ground and flight experiments and tests will be necessary to assure good performance and mission safety.

Several experiment articles and configurations have been identified in recent years. Fig. 1 shows four potential antenna flight experiment configurations including three free flyers and one hub-attached shuttle mounted configuration. Fig. 2 shows a feed-attached configuration. The system is a shuttle captive, gimballed, offset feed, shuttle-mounted system, consisting of a 55 mD wrap-rib reflector, an 85m vertical mast, and the STS (Space Transportation System) operational base. Since a detailed 6624-node structural model for the reflector was available through Jet Propulsion Laboratory, and substantial analysis of this feed-attached system for the zero-DOF (degree-of-freedom) gimbal base had already been completed at Jet Propulsion Laboratory [1], the configuration of Fig. 2 was selected for this analysis.

Although the quantitative information was generated with the selected configuration, the results and conclusions are largely generic and insensitive to the particular configuration since:

a)   All reflectors considered are in the 50 to 100m class. The lowest modal frequency can be expected to vary much less than an order of magnitude among the reflectors.

b)   The required reflector surface accuracy depends upon RF (radio frequency) wave length. Hence, surface quality requirement is not governed by the particular hardware selected for the configuration.

c)   All configurations employ one or two masts of approximately 100m. The low system frequencies are dominated by the mast.

d)   The inertia characteristics of the various systems should not vary by more than a factor of four. Hence, actuator sizing requirements will have the same approximate values for all configurations.

The results of this study show that the control hardware and algorithms required for the experiment are reasonable and the experiments are technically feasible.

In Section II the designs for several major experiments are described; the system architecture, sensor, actuator, and processing capability requirements are discussed in Section III; in Section IV, a higher dimensional controlled attachment configuration is analyzed; and the conclusions are summarized in Section V.

| HOOP COLUMN FREE FLYER | TRUSS FREE FLYER |
| CUP-UP SHUTTLE MOUNTED WRAP RIB | WRAP RIB FREE FLYER |
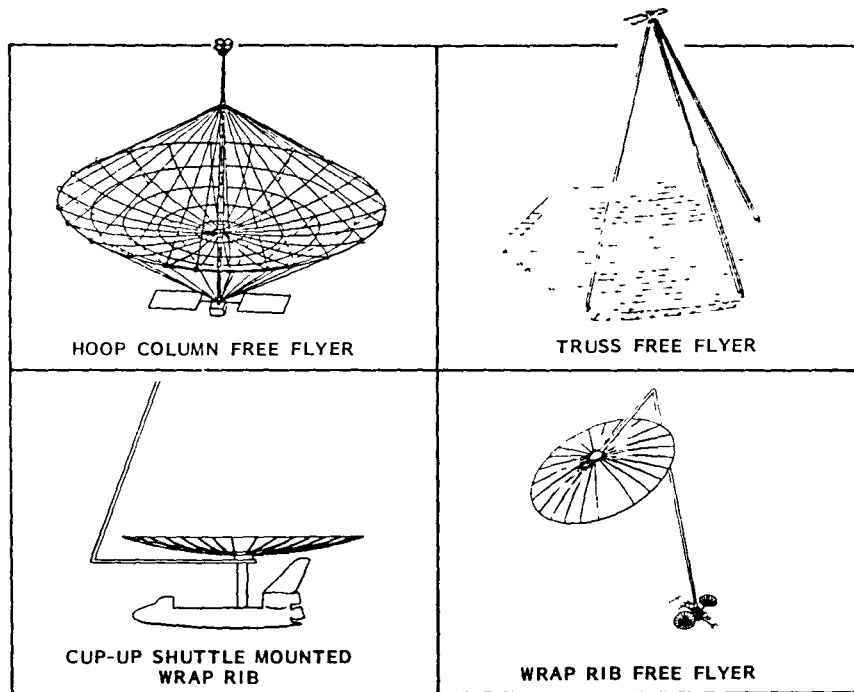
Fig. 1 Potential large space antenna flight experiment configurations.
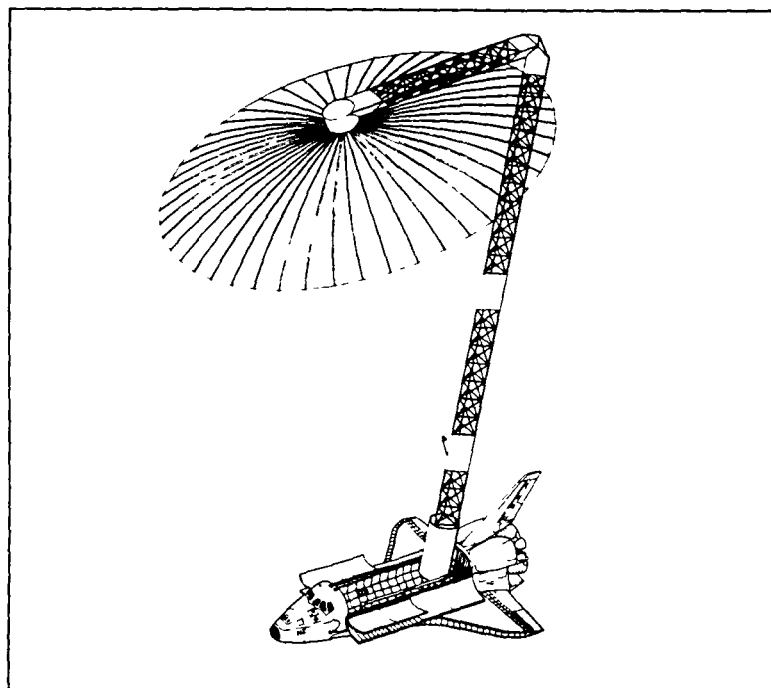
Fig. 2. Feed-attached flight experiment configuration.

II. EXPERIMENTS DESIGN

The experiments recommended for the flight are discussed in this section. The primary experiments are divided into three major areas: identification, control, and maneuver.

A. Geometry Identification

The purpose of the geometry identification experiment is to estimate the shape, orientation, and surface quality of the experimental antenna. This experiment is further divided into three parts, the boom geometry ID (identification), the reflector hub ID, and the reflector surface ID.

This experiment employs 48 retroreflectors symmetrically distributed along 8 of the ribs of the reflector surface, 4 placed on the lower* surface of the hub, and 3 on each of the long and short booms. The positional information of the retroreflectors are picked up by a laser measurement device. A Kalman filter is employed to estimate the reflector surface and the boom orientation. Fig. 3 shows the coordinates of the retroreflectors on the antenna dish in a local body frame. It is assumed that the laser device measures the positions of retroreflector targets simultaneously and provides range, azimuth, and elevation data for each target. With the projected JPL SHAPES sensor, the entire target set can be sampled in approximately 0.1 second. This experiment is assumed to be static for which residual antenna and boom dynamics are neglected within the estimation process. Structural ringing is considered, however, in the performance evaluation and timeline definition.
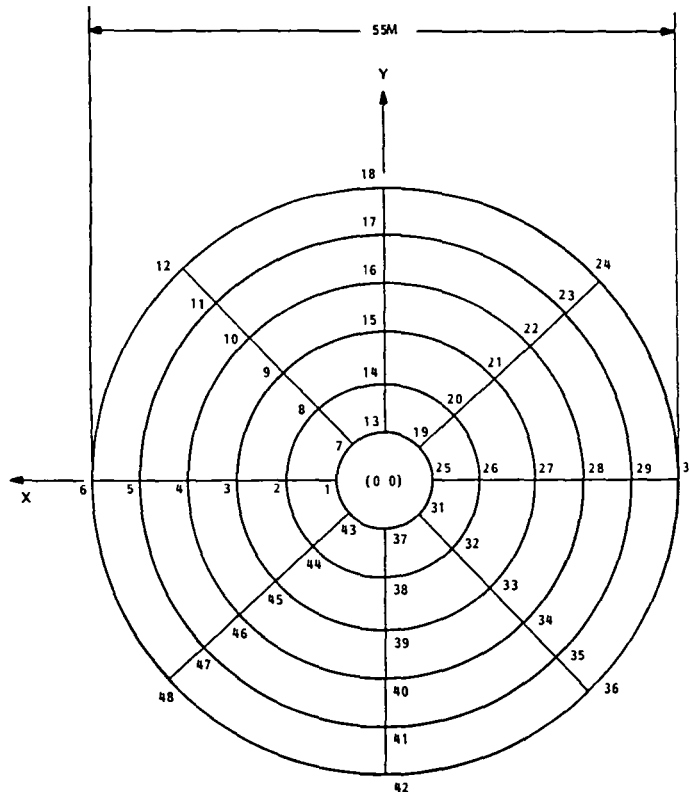
Fig. 3 Retroreflector targets layout on antenna reflector

---

* lower here refers to the feed or the shuttle side.

Fig. 4 shows a functional block diagram of the experiment. The estimation process assumes that the antenna surface can be described as a paraboloid of revolution, the hub as a planar surface, and the booms as straight lines. The reflector surface shape ID experiment uses a nine-state extended Kalman filter; the hub ID uses a three-state Kalman filter; and the boom ID uses a six-state Kalman filter. The estimated parameters define a spatial model of the reflector surface, hub, and boom, and an estimate of the quality of the surface.
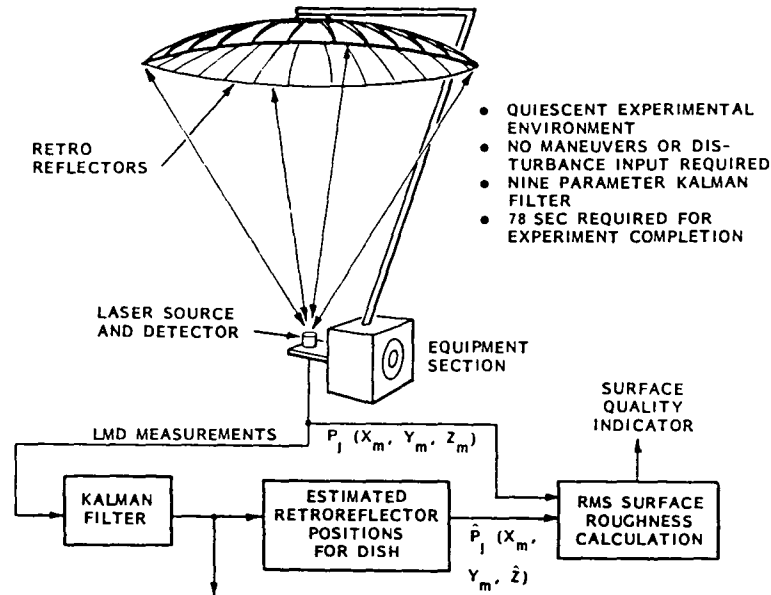
Fig. 4. Functional diagram of geometry identification experiment.

The ID experiment has two performance requirements, i.e., surface quality requirement, and tilt and defocus requirement; each one leads to a requirement on RMS distance between the fit of a true parabola and an estimated parabola.

The system performance index is a preflight assessment carried out using a detailed simulation truth model. The goal of this assessment is to specify the accuracy to which the fundamental parabola of the deployed reflector, the fundamental plane of the hub, and the fundamental lines of the booms can be identified.

Fig. 5 shows a fundamental parabola which is the parabola that fits the actual deployed reflector surface best. Similar constructions can be made for the hub and booms. Define $\in_j$ to be the difference between the Z coordinates of the estimated target locations, $\hat{P}_{1j}$, and the target locations represented by the truth model, P_j, i.e.,

$$\in_j = Z_j - \hat{Z}_{1j} \tag{1}$$

The RMS (root-mean-square) value of $\in_j$ should be on the order of 10% of 1σ surface roughness specification. Note that $\in_j$ is a preflight assessment. The RMS value of the differences between the flight data target measurements, P_{mj}, and the estimated target measurements, $\hat{P}_{2j}$, provide a measure of the degree to which the actual surface is nonparabolic. Define

349

$$\delta_j = Z_{mj} - \hat{Z}_{2j} \qquad (2)$$

where, δ_j is the surface roughness at the jth target location, determined upon processing of the flight data. The experiment performance index is used to determine the nonparabolic nature of the dish. Accurate shape determination can only be achieved when $\delta_j \gg \epsilon_j$.
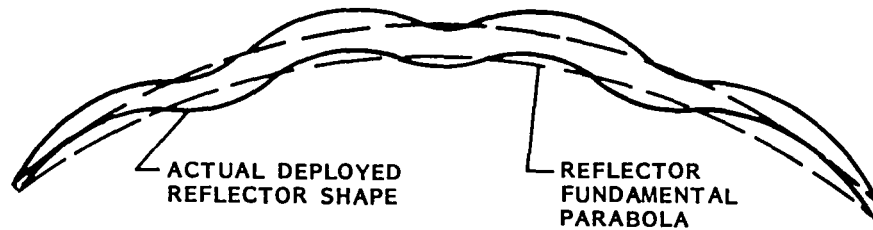
Fig. 5. Reflector fundamental parabola and the actual deployed reflector shape.

B.   Mass Properties Identification

The mass properties identification experiment is designed to test the capability of providing estimates of the mass, center of mass, and moment of inertia of the flight experiment test article. All of the quantities of interest appear in the two-body equations of motion describing the coupled Space Shuttle and the experiment dynamics and kinematics. An extended Kalman filter has been formulated with both the dynamic states (angles and rates) and the mass property parameters of interest appearing in the state vector. By commanding large relative angular motion between the bodies, all of the mass properties are rendered observable.

Experiment performance evaluation is conducted by simulation of a simplified planar two-body case. The gimbal angles used are then generalized to the three dimensional case to establish an experiment timeline. These results have also been used for developing the detailed mathematical models and filter algorithms, the associated software and data processing requirements, and the experiment hardware requirements. Fig. 6 shows a block diagram of how a detailed mathematical model is used with an implementation of the filter algorithms to determine performance.

The area inside the box above the dotted area in Fig. 6 represents the truth model, with control torques and environmental torques different from those supplied to the filter implementation. The "true" mass properties are available only to the truth model, and truth model dynamic and kinematic integrations are more precise than those required for an on-board algorithm. The filter implementation processes commanded torques to estimate the mass property parameters of interest. The commanded torques can include deterministic errors and the measured difference between "true" and estimated angles and rates.
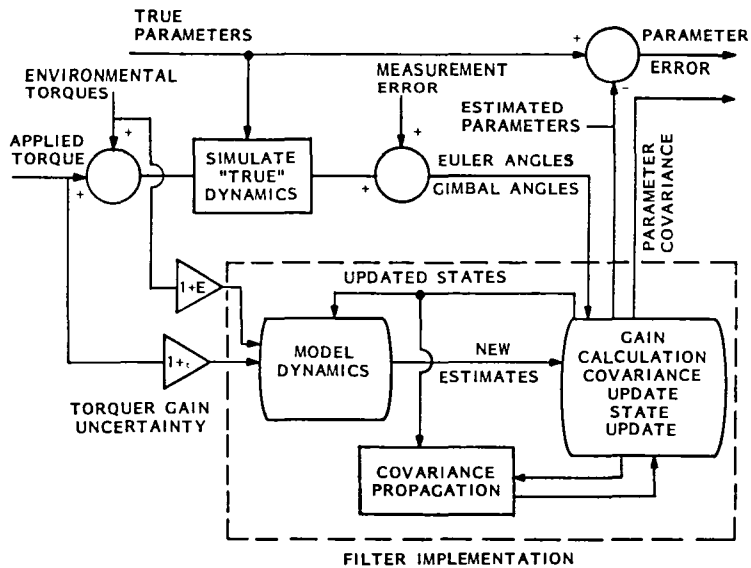
Fig. 6. Performance evaluation block diagram for mass properties identification.

Two related measures of performance are indicated in Fig. 6. The filter state covariances provide one estimate of the parameter uncertainty, while the difference between estimates and "true" mass property parameters provides another. This second performance measure is more accurate in the sense that deterministic errors are not well represented by a covariance. Because of uncertainties in the way the effects of various deterministic error sources combine, a large number of samples of this second "estimate error" performance measure are required to provide a measure of filter performance with high confidence.

C. System Mode Identification

This experiment is to identify the natural frequencies, damping ratios, and mode shapes of the deployed experimental antenna system.

The approach for this experiment requires ground computer support. A mathematical model of the shuttle and the antenna system will be required for the ground computer. The motion and vibration of the shuttle and the antenna system, and the control or actuation inputs are measured and recorded for ground processing. Since the number of parameters to be estimated is large, any of the well-known identification approaches including maximum likelihood, extended Kalman filter, etc., will likely be ill-conditioned, and require substantial amounts of off-line data processing. Therefore, techniques to improve the conditioning of the identification problem are applied first, followed by a relatively few iterations of the identification algorithm.

The identification starts with deploying the antenna and performing a series of tests. These tests consist of both wide-band and narrow-band excitations of the system. The data obtained are recorded, transmitted to the ground, and processed using the algorithms to be discussed in this section.

351

In the first phase of this experiment, the two-body structure is excited by applying torques at the shuttle, the bus, and the hub to provide a broad-band response of the frequency spectrum. The disturbance is applied for one second, followed by measurements taken for 100 seconds.

Fast Fourier transform methods are then applied via ground computer to compute prominent frequencies. Then begins the narrow band excitation. In this phase, each frequency determined from the first phase is excited by applying torques in increasing frequency, beginning at a frequency slightly less than the frequency of interest and extending to a frequency slightly higher.

The time required for this second phase depends upon the number and value of the frequencies to be estimated. The major frequencies are expected to exist between .1 Hz and 2 Hz, with higher densities at the lower frequencies. For a conservative estimate, 50 frequencies all at .1 Hz are used resulting in a 24-hour experiment.

The process of extracting a large number of parameter estimates forms a high-order nonlinear minimization problem. As stated in the preceding paragraph, this minimization procedure can be numerically ill-conditioned, and its convergence can be quite sensitive to initial parameter estimates. As such, it is prudent to use any method available to improve upon initial parameter estimates, especially if this improvement can be obtained at virtually no extra expense. To this end, the following algorithms are used:

1) Fast Fourier transforms (FFT) to obtain improved modal frequency information.

2) Eigenvalue-eigenvector perturbation (EEP) techniques to obtain first order corrections to mode frequency and mode shape data.

3) Narrow-band excitation of the antenna system near the predicted modal frequencies, to maximize the information content of the sensed signal, and to improve upon the a priori damping ratio estimates.

After improved initial parameter estimates are obtained, the least square estimation (LSE) procedure is invoked. This procedure makes use of all the sensor data and a mathematical model of the structure to iteratively improve the modal parameter estimates. The LSE procedure begins with initial estimates of system parameter values. This set of parameters consists of natural frequencies, damping ratios, mode shapes, masses, inertias, stiffnesses, etc. LSE is the process by which a performance measure, J, is minimized with respect to the parameters while maintaining the dynamic constraint of the system. Analytically this process may be written as

$$\underset{a}{\text{Min}} \; J = \int_{o}^{T} [(z - Hx)^T R^{-1} (z - Hx) + w^T Q^{-1} w] \, dt \qquad (3a)$$

$$\text{subject to} \quad \dot{x} = F(a) \, x + G(a) \, u + \Gamma(a) \, w \qquad (3b)$$

$$z = H(a) \, x + v$$

352

where w and v are process and measurement noises with power spectral densities Q and R, respectively.

A block diagram of the entire procedure used to obtain parameter values is shown in Fig. 7.
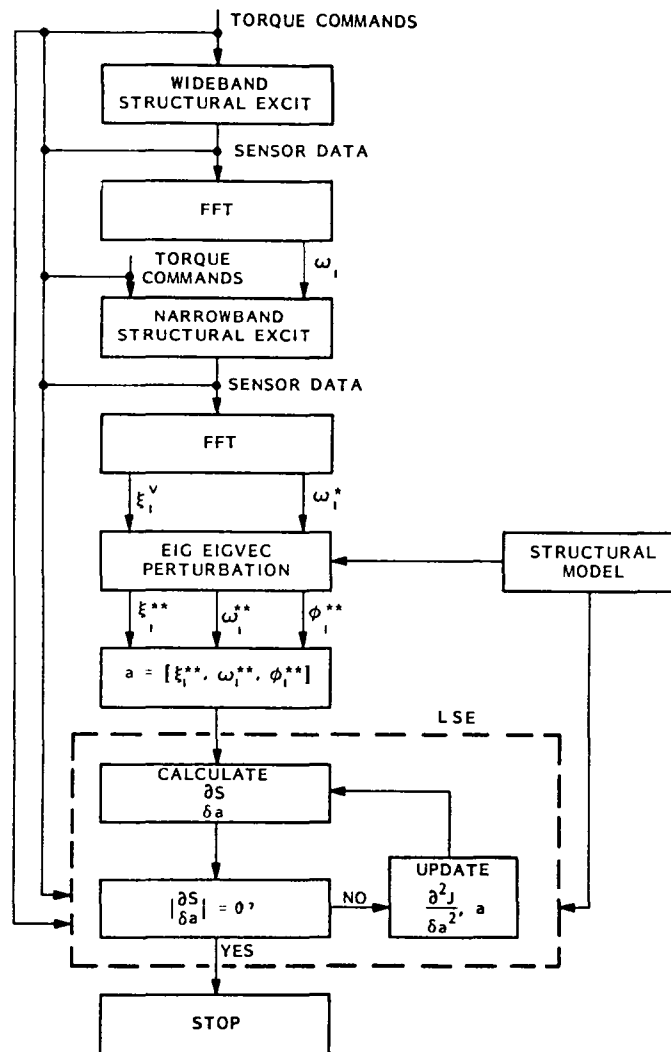
Fig. 7 Modal identification flow chart

A typical LSE case is summarized below. The unknown parameter vector consists of three modal frequencies, two damping ratios, two mode shapes associated with actuation, and two mode shapes associated with sensing. Fig. 8 provides a graphic description of the experiment and the parameters to be identified. The highlighted quantities in the table are the parameters that are identified. Modal frequencies and damping ratios are easily understood. The mode shape parameters are highlighted again on the schematic for better physical interpretation of these parameters. The iterative values of the parameters are shown in Table 1.

This identification procedure begins with a 1 sec step applied to all the actuators. During this one second and for an additional nine seconds, all of the sensors are sampled at a 10 Hz rate. The total of 100 samples of data from each of 18 sensors is processed off-line to yield the results tabulated in Table 1. The "START" column contains the starting

MODE NO	FREQ (RAD/SEC)	DAMPING RATIO	MODE SHAPE	DESCRIPTION
1	0 0	0 0		
2	0 0	0 0		
3	0 0	0 0		
4	0 0	0 0		
5	0 0	0 0		
6	0 0	0 0		
7	0 592	0 01	0 0826	c_s^x
8	0 942	0 01		
9	1 236	0 01		
10	1 247	0 01		
11	1 328	0 01		
12	1 421	0 01		
13	1 773	0 01	0 0642, 0 0344	T_2^Y, ρ_4^x
14	1 944	0 01		
15	6 053	0 01		
16	9 763	0 01	-243 4728	T_s^x
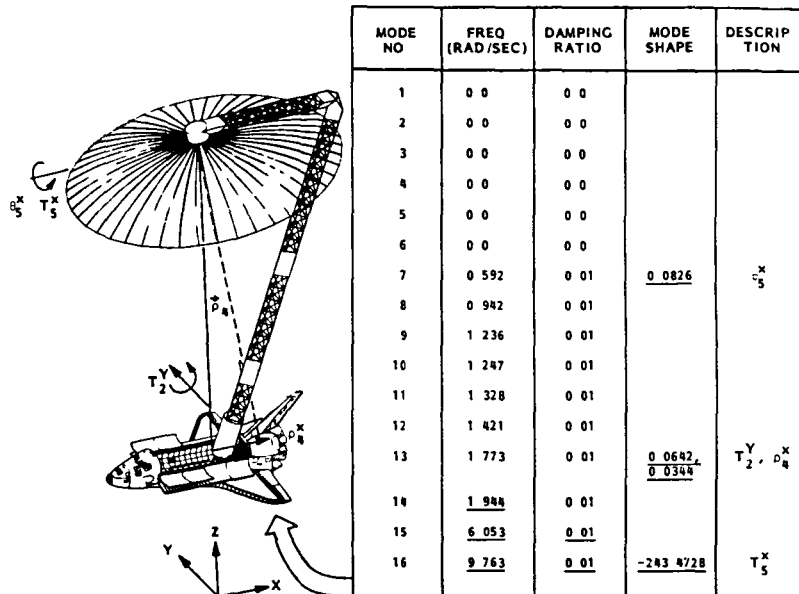
Fig. 8 Modal identification

Table 1. Typical system ID performance

PARAMETERS	START	ITERATION NO 1	ITERATION NO 2	ITERATION NO 3	ITERATION NO 4	ITERATION NO 5	ITERATION NO 6	TRUE
MODAL FREQUENCIES	2 0	1 9416	1 9200	1 9164	1 9205	1 9186	1 9160	1 940
	6 0	6 0	6 0	6 0	6 0001	6 0001	6 0002	6 0530
	10 0	9 9981	9 9971	9 9940	9 9741	9 9655	9 9362	9 7620
DAMPING RATIOS	0 0	0 0	0 0	-0 0001	-0 0001	-0 0001	-0 0001	-0 0050
	0 0	-0 0022	-0 0031	-0 0038	-0 0071	-0 0083	-0 0101	-0 0050
MODE SHAPES	0 0600	0 0692	0 0789	0 0764	0 0793	0 0787	0 0776	0 0826
	0 0600	0 0685	0 0576	0 0551	0 0405	0 0359	0 0285	0 0642
	-240 0	-240 0001	-240 0001	-240 0003	-240 0013	-240 0017	-240 0062	-243 4728

estimates of the parameter value. Each successive column is obtained by passing through the same set of sensor data while iteratively updating the dynamic model. After several iterations, there is little change in the parameter value. In the last column, the true parameter values are given.

It should be pointed out that for this simulation, all the mode shape values in the model have been perturbed by 5%, but that only a few selected mode shape parameters are allowed to be varied. The estimation procedure does its best to account for these unmodeled parameter errors by adjusting the relatively few parameters that have been freed. This explanation accounts for the convergence of the parameter vector to a value that is biased from the true value.

D.   Control Experiment

The objective of the control experiment is to conduct on-orbit demonstration of distributed control for large space structures. This experiment will also study the control capability of currently available actuators for damping augmentation control, hub/feed orientation control, and line-of-sight pointing control of the 55mD antenna structure with the following control configurations:

1)   Control effort provided only by torques at the bus;
2)   Control effort provided by torques at the bus and the hub;
3)   Control effort provided by torques at the bus and the hub; and by force actuators at the hub.

The control experiments are performed with the gimbals unlocked. Nine different controllers are designed and evaluated on the ground and to be verified during this experiment. A sufficient period of time should be included for recalibration of the equipment, transferring data onto tape,. and loading control software for the next testing. A typical control experiment timeline is shown in Fig. 9.
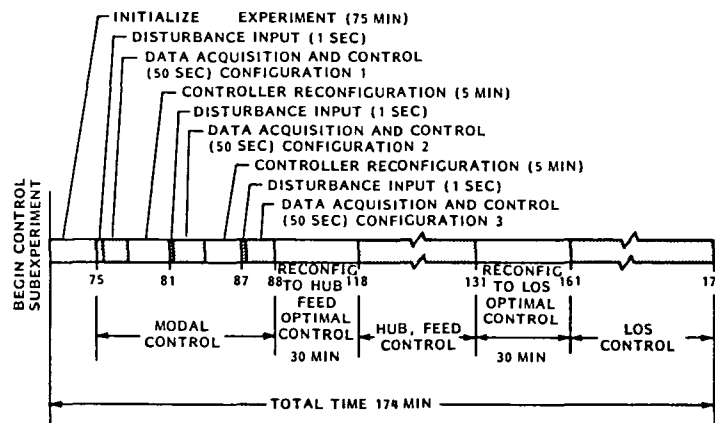
Fig. 9 Control experiment timeline

LQG (Linear Quadratic Gaussian) control laws have been used for the various control experiment designs. Fig. 10 shows the basic LQG control process. The control system consists of a steady-state Kalman filter, which is used to construct the system states, and an optimal state feedback controller which utilizes the estimated system states to provide an optimal feedback path to the system.

Consider a stochastic system of the form

$$x(k+1) = \Phi \, x(k) + w(k) \quad , \quad Q_d = E[w^T w]$$

$$y(k) = Hx(k) + v(k) \quad , \quad R_d = E\,[v^T v] \tag{4}$$

355
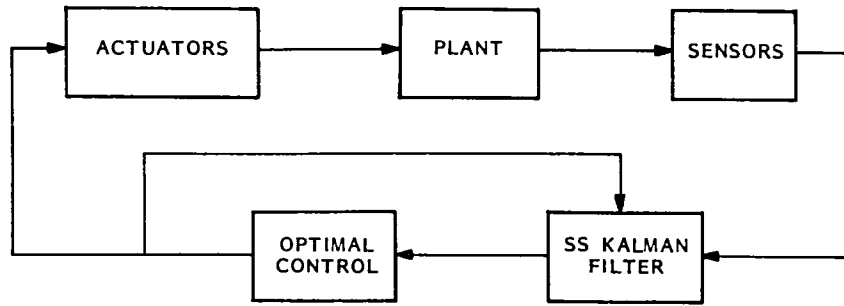
Fig. 10 LQG control system block diagram

Where the system state $x(\cdot)$ and the output measurement $y(\cdot)$ are of appropriate dimensions and where $w(\cdot)$ and $v(\cdot)$ are random sequences of zero mean and covariances Q_d and R_d, respectively. The filter equation is,

$$\hat{x}(k+1) = \Phi \hat{x}(k) + K [y(k) - H \hat{x}(k)] \tag{5}$$

where the constant (steady-state) filter gain matrix K is

$$K = P_e H^T R_d^{-1} \tag{6}$$

and P_e is found from the steady-state solution to the following equations

$$P(k+1) = M(k+1) - M(k+1) H^T [R_d + H M(k+1) H^T]^{-1} H M(k+1) \tag{7a}$$

$$M(k+1) = \Phi P(k) \Phi^T + Q_d \tag{7b}$$

the steady-state is achieved when

$$P(k+1) = P(k) = P_e$$

and

$$M(k+1) = M(k)$$

Note that $P(k)$ is the covariance matrix of the estimation error after measurements.

For the control law, consider the dynamical system, ignoring the disturbances and noises for the time being since they do not affect the control law design,

$$x(k+1) = \Phi x(k) + \Gamma u(k)$$
$$\tag{8}$$
$$y(k) = H x(k)$$

356

the control input u(k) is selected such that the following quadratic performance index is minimized,

$$J = \sum \begin{bmatrix} x^T(k) & u^T(k) \end{bmatrix} \begin{bmatrix} A_d & S_d^T \\ S_d & B_d \end{bmatrix} \begin{bmatrix} x(k) \\ u(k) \end{bmatrix} \tag{9}$$

The control law is of the form

$$u(k) = C \hat{x}(k) \tag{10}$$

In order to formulate it as a standard optimal control problem, a system equivalent to eq. (9) but without cross terms (i.e., $S_d = 0$) is obtained as follows:

Let $\bar{x}(k) = x(k)$ and $\bar{u}(k) = B_d^{-1} S_d^T x(k) + u(k)$, then

$$\bar{x}(k+1) = \bar{\Phi}\, \bar{x}(k) + \bar{\Gamma}\, \bar{u}(k) \tag{11}$$

$$\bar{y}(k) = \bar{H}\, \bar{x}(k) \tag{12}$$

$$J = \sum \begin{bmatrix} \bar{x}^T(k) & \bar{u}^T(k) \end{bmatrix} \begin{bmatrix} \bar{A}_d & 0 \\ 0 & \bar{B}_d \end{bmatrix} \begin{bmatrix} \bar{x}(k) \\ \bar{u}(k) \end{bmatrix} \tag{13}$$

$$\bar{u}(k) = \bar{C}\bar{x}(k) \tag{14}$$

where

$$\bar{A}_d = A_d - S_d B_d^{-1} S_d^T \tag{15a}$$

$$\bar{B}_d = B_d \tag{15b}$$

$$\bar{\Phi} = \Phi - \Gamma B_d^{-1} S_d^T \tag{15c}$$

$$\bar{\Gamma} = \Gamma \tag{15d}$$

$$\bar{C} = C + B_d^{-1} S_d^T \tag{15e}$$

from eq. (15e), steady-state control gain matrix C is

$$C = \bar{C} - B_d^{-1} S_d^T \tag{16}$$

where

$$\bar{C} = -\bar{B}_d^{-1} \bar{\Gamma}^T \bar{\Phi}^{-T} (\bar{P} - \bar{A}_d) \tag{17}$$

and P is obtained as follows: setting up the Hamiltonian matrix

$$
\mathcal{H} =
\begin{bmatrix}
\bar{\Phi} + \bar{\Gamma}\bar{B}_d^{-1}\bar{\Gamma}^T\bar{\Phi}^T A_d & -\bar{\Gamma}\bar{B}_d^{-1}\bar{\Gamma}^T\bar{\Phi}^{-T} \\
\\
-\bar{\Phi}^{-T}\bar{A}_d & \bar{\Phi}^{-T}
\end{bmatrix}
\tag{18}
$$

if M is defined as

$$
M \triangleq [\, M_1 \;\; M_2 \,] \triangleq
\begin{bmatrix}
M_{11} & \vdots & M_{12} \\
& \vdots & \\
M_{21} & \vdots & M_{22}
\end{bmatrix}
\tag{19}
$$

where M_1, M_2 consist of the eigenvectors of $\mathcal{H}$ associated with the stable eigenvalues Z_i and the unstable eigenvalues $\dfrac{1}{Zi}$ of $\mathcal{H}$, respectively,

then

$$
P = M_{21}\, M_{11}^{-1}
\tag{20}
$$

The steady-state filter and control gains are computed prior to the flight time and stored in the flight computer. For a system of 22 states, 15 inputs, and 9 outputs at a sample rate of 64 Hz, 98560 multiplications and 96576 additions will have to be performed per second.

To predict performance, a five-body dynamical system model is formulated which consists of the shuttle, the bus, the long boom, the short boom, and the 55 mD dish. Fig. 11 shows the bodies and their body coordinate system. The reference coordinate frame is defined as the body 1 frame.

A full-order finite-element model is obtained first and controllability and observability are checked. A number of states, control inputs, and ouputs are then deleted from the full-order model using model reduction techniques to yield a reduced-order model. The reduced model has the form,

$$
x = Fx + Gu + w
$$
$$
y = Hx + v
\tag{21}
$$

where

$$
u = \begin{bmatrix} F_{5x} & F_{5y} & F_{5z} & T_{2x} & T_{2y} & T_{2z} & T_{5x} & T_{5y} & T_{5z} \end{bmatrix}^T
\tag{22}
$$

$$
y = \begin{bmatrix} \dot{\Theta}_{2x} & \dot{\Theta}_{2y} & \dot{\Theta}_{2z} & \dot{\Theta}_{5x} & \dot{\Theta}_{5y} & \dot{\Theta}_{5z} & \Theta_{2x} & \Theta_{2y} & \Theta_{2z} & \Theta_{5x} & \Theta_{5y} & \Theta_{5z} & \rho_{3x} & \rho_{3y} & \rho_{3z} \end{bmatrix}^T
\tag{23}
$$

$$
x = \begin{bmatrix} \dot{q}_1 & q_1 & \dot{q}_2 & q_2 & \cdots & \dot{q}_{11} & q_{11} \end{bmatrix}^T
\tag{24}
$$

where

F_{ij} and T_{ij} are the j-component of external force and external torque applied to body i.

$\dot{\Theta}_{ij}$ and Θ_{ij} are the angular rate and amplitude of body i about its j-axis.

$\dot{q}_i$ and q_i, i = 1,2,3 are modal rate and amplitude of bus roll, pitch and yaw modes, respectively.

$\dot{q}_i$ and q_i, i=4,...,11 are modal rate and amplitude of modes 4 through 11.

ρ_{3j} is the translational displacement of the upper end of body 3 (the elbow) along its j-axis.
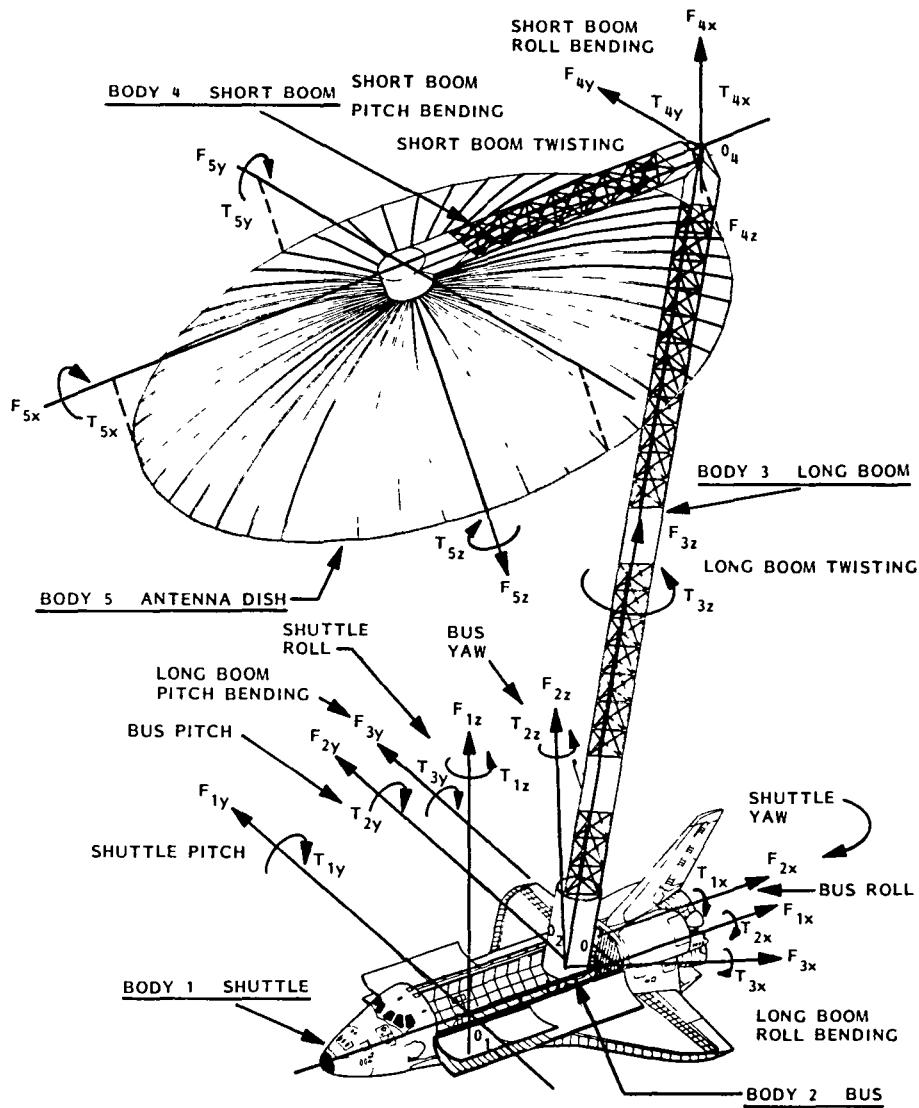
Fig. 11 A five-body system for the flight experiment

359

The discrete-time version of the reduced-order model is of the form

$$x(k+1) = \Phi\, x(k) + \Gamma\, u(k) + w(k)$$

$$y(k) = H\, x(k) + v(k)$$

(25)

where

$$\begin{bmatrix} \Phi & \Gamma \\ & \\ 0 & I \end{bmatrix} = \text{EXP}\left\{ \begin{bmatrix} F & G \\ & \\ 0 & 0 \end{bmatrix} \Delta T \right\}, \qquad \Delta T = 1/64 \text{ second} \qquad (26)$$

The filter gain matrix K is selected by balancing the fast convergence time associated with a high gain against the small initial transient errors associated with a low gain. Table 2 shows the open-loop model poles and the poles of the steady-state filter.

Table 2. Model and filter poles

MODE NO.	OPEN-LOOP MODEL POLES				FILTER POLES			
	REAL PART	IMAG PART	MODAL FREQ (Hz)	DAMPING	REAL PART	IMAG PART	MODAL FREQ (Hz)	DAMPING RATIO
1	0	0	0	0.01	-0.08	0	0.012	1.0
2	0	0	0	0.01	-0.08	0	0.013	1.0
3	0	0	0	0.01	-0.08	0	0.013	1.0
4	-0.0059	0.59	0.09	0.01	-0.2	0.59	0.1	0.33
5	-0.0094	0.94	0.15	0.01	-0.2	0.94	0.15	0.21
6	-0.0124	1.24	0.20	0.01	-0.2	1.24	0.20	0.16
7	-0.0125	1.25	0.20	0.01	-0.2	1.25	0.20	0.16
8	-0.0133	1.33	0.21	0.01	-0.2	1.33	0.21	0.15
9	-0.0142	1.42	0.23	0.01	-0.2	1.42	0.23	0.14
10	-0.0177	1.77	0.28	0.01	-0.2	1.77	0.28	0.11
11	-0.0194	1.94	0.31	0.01	-0.2	1.94	0.31	0.10

D.1 Damping Augmentation Control

The objective of this experiment is to design a controller to actively suppress vibration of the flight system and to predict performance of the controller through evaluation with the full-order model. Following the control gain C_{12} design, the closed-loop poles are yielded as shown in Table 3 for the case of controller configuration 2. Nearly 100% damping for the rigid modes and above 50% for the flexible modes are observed in Table 3.

360

Table 3. Closed-loop poles for system with damping-augmentation controller configuration 2

REAL PART (RAD/SEC)	IMAGINARY PART	MODAL FREQUENCY (Hz)	DAMPING RATIO
-0.5	0	0.08	1.0
-0.5	0.001	0.08	0.99
-0.5	0.003	0.08	0.99
-1.2	0.59	0.21	0.90
-1.2	0.93	0.24	0.79
-1.2	1.17	0.27	0.71
-1.2	1.22	0.27	0.70
-1.2	1.28	0.29	0.68
-1.2	1.39	0.29	0.65
-1.2	1.75	0.34	0.57
-1.2	1.92	0.36	0.53

The performance of the system is evaluated by using the following equation,

$$
\begin{bmatrix} x(k+1) \\ \hat{x}(k+1) \end{bmatrix} = \begin{bmatrix} \Phi_F & \Gamma_F C_{12} \\ KH_F & \Phi - KH + \Gamma C_{12} \end{bmatrix} \begin{bmatrix} x(k) \\ \hat{x}(k) \end{bmatrix}, \begin{bmatrix} x(0) \\ \hat{x}(0) \end{bmatrix} = \begin{bmatrix} x_0 \\ 0 \end{bmatrix} \tag{27}
$$

where the subscript F refers to the full-order system. The full system state x (·) has a dimension of 30 and the estimator state $\hat{x}$ (·) has a dimension of 22. Since for controller configuration 2 there are 6 torque actuator components, C_{12} has a dimension of 6 x 22. The estimator gain K has a dimension of 22 x 15 reflecting the 15 outputs. The initial conditions used for simulations are: (1) zero for both the modal amplitude and rate of rigid body modes, (2) zero for modal amplitude, 0.0023 for modal rate of flexible modes. Fig. 12 shows the closed-loop responses for the actual system state and the corresponding estimated state for mode 5. The closeness of these results indicates good filter performance. Fig. 13 shows the bus and hub angular displacements and the elbow translational displacements. These simulated time histories show high closed-loop damping. For instance, the settling time (time required for the transient to damp to 5% of its peak value) is less than 30 seconds for the closed-loop system while the open-loop settling time is approximately 10 minutes.

The maximum angular rate of the bus and hub observed are 0.12 deg/sec and 0.007 deg/sec, respectively; the maximum displacements are less than 0.1 deg for both the bus and the hub, and 0.3 feet for the elbow. Table 4 shows the maximum force and

361

torque amplitudes required and the settling time for this experiment. For controller configuration 1, the maximum torque is 34 ft-lbs and a settling time of 50 seconds. For controller 2, by adding actuator T_5 at the hub, the required maximum torque has dropped to 16 ft-lbs, whereas by the addition of force actuators F_5 at the hub, the required peak torque level has dropped to 2.6 ft-lbs. The required peak force amplitude is 0.6 lb.

TIME (SEC)
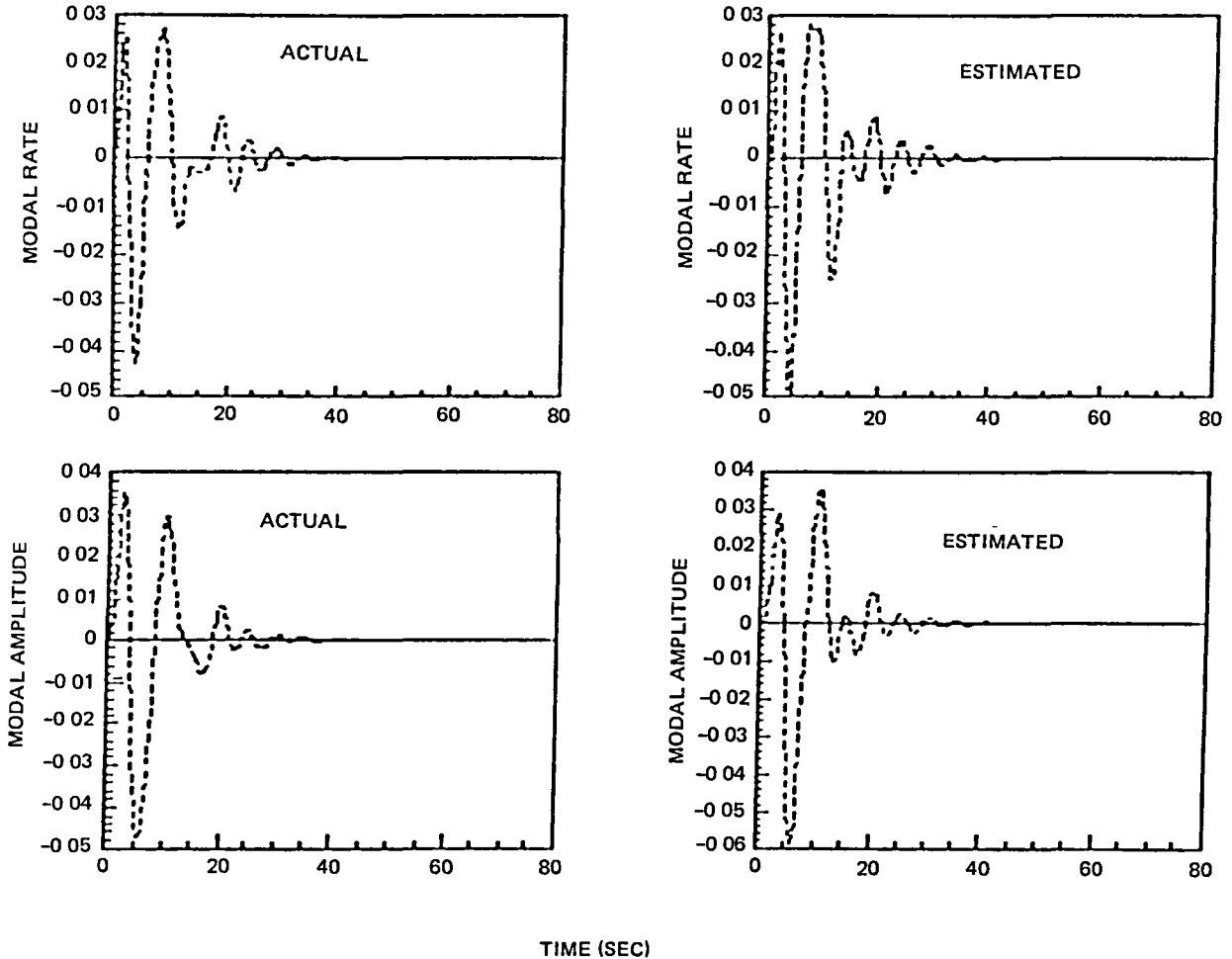
Fig. 12 Closed-loop state responses for mode 5

D.2   Hub and Feed Orientation Control

The purpose of this experiment is to evaluate performance of a controller that is designed to maintain the orientation of the hub with respect to the feed. The emphasis here is to control those modes which strongly affect the hub and feed orientation. Let ρ_{HF} and Θ_{HF} be the linear and angular displacement vectors of the hub relative to the feed, the output model is,

$$\begin{bmatrix} \rho_{HF} \\ \Theta_{HF} \end{bmatrix} = H_{HF} x \qquad (28)$$

362

where the measurement matrix H_{HF} is of dimension 6 x 22 and has zero odd columns. The control gain matrix C_{22} is designed to minimize
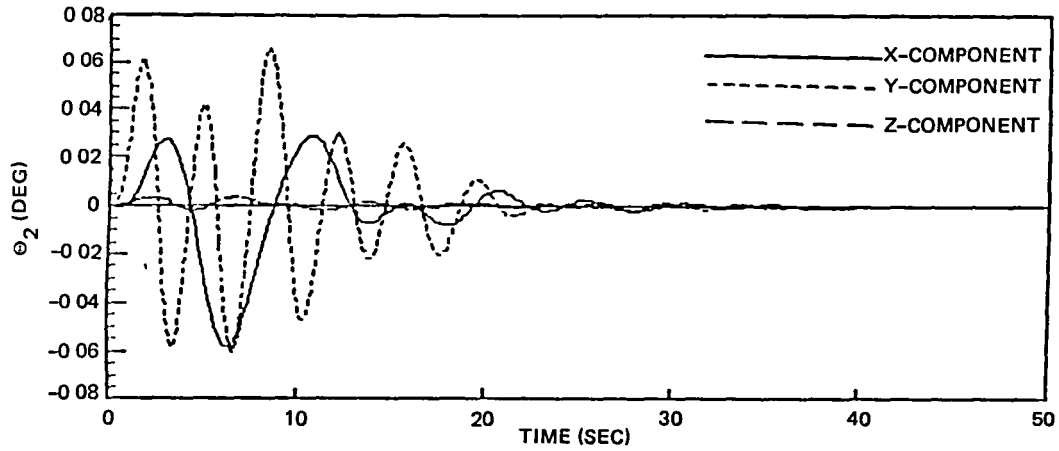
(a) Bus angular displacements
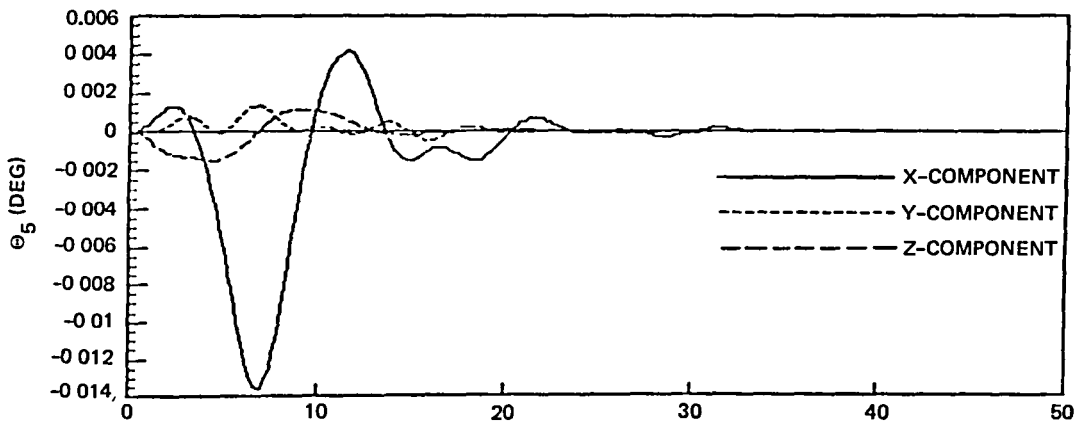
(b) Hub angular displacements
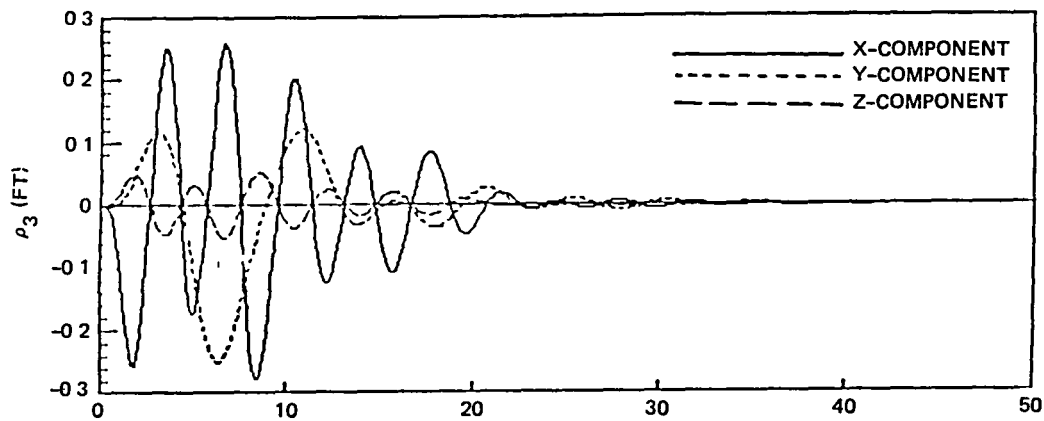
(c) Elbow translational displacements

Fig. 13 System response for damping augmentation experiment

Table 4. Required peak force and torque amplitudes
and the system settling time for damping augmentation control

	CONTROLLER CONFIGURATION 1	CONTROLLER CONFIGURATION 2	CONTROLLER CONFIGURATION 3
MAXIMUM FORCE/TORQUE AMPLITUDES (LB/FT-LB)	$T_2 = 34.0$	$T_2 = 16.0$ $T_5 = 12.0$	$F_5 = 0.6$ $T_2 = 0.4$ $T_5 = 2.6$
RESULTING FORCE/TORQUE SETTLING TIME (SEC)	50.0	30.0	30.0

$$J = \lim_{t \to \infty} E \left\{ \begin{bmatrix} P_{HF} \\ \Theta_{HF} \end{bmatrix}^T \begin{bmatrix} P_{HF} \\ \Theta_{HF} \end{bmatrix} + \alpha \, u^T(k)u(k) \right\} \tag{29}$$

or

$$J = \lim_{t \to \infty} E \left\{ x^T(k) \, H_{HF}^T \, H_{HF} \, x(k) + \alpha u^T(k)u(k) \right.$$

$$\left. + \alpha_{RB} \, x_{RB}^T(k) x_{RB}(k) \right\} \tag{30}$$

where α is chosen to be 10^{-10} and $\alpha_{RB} = 10^{-4}$. Since the rigid body modes (x_{RB}) have no effects on the relative motion of the hub and feed, their weight α_{RB} is chosen to be small. The resulting closed-loop poles for controller configuration 2 are shown in Table 5.

Fig. 14 shows the simulated time histories for the hub-to-feed translation and rotation with controller configuration 2 in place. These plots show that the transients are damped out in approximately 40 seconds. In Table 6, the resulting maximum control torques and forces for the three controller configurations are tabulated along with the corresponding settling time. Again, as in the case of vibration damping control, by adding actuators at the hub the actuation requirement at the feed was drastically reduced due to the fact that the controllability at the hub is greater than that at the feed. The torque levels for the hub actuators can also be significantly reduced by employing a force actuator at the hub (controller configuration 3).

Table 5 Closed-loop poles for system with hub and feed controller configuration 2

REAL PART (RAD/SEC)	IMAGINARY PART	MODAL FREQUENCY (Hz)	DAMPING RATIO
-0.02	1.33	0.21	0.02
-0.04	0	0.006	1.0
-0.07	0.07	0.02	0.67
-0.23	0.30	0.06	0.61
-0.25	0.71	0.12	0.33
-0.54	0.76	0.15	0.58
-0.67	0	0.11	1.0
-1.25	0.95	0.25	0.79
-3.32	3.04	0.72	0.74
-4.92	0	0.78	1.0
-9.91	0	1.58	1.0
-14.0	0	2.23	1.0
-103.12	0	16.41	1.0
-111.12	0	17.69	1.0
-276.49	0	44.0	1.0
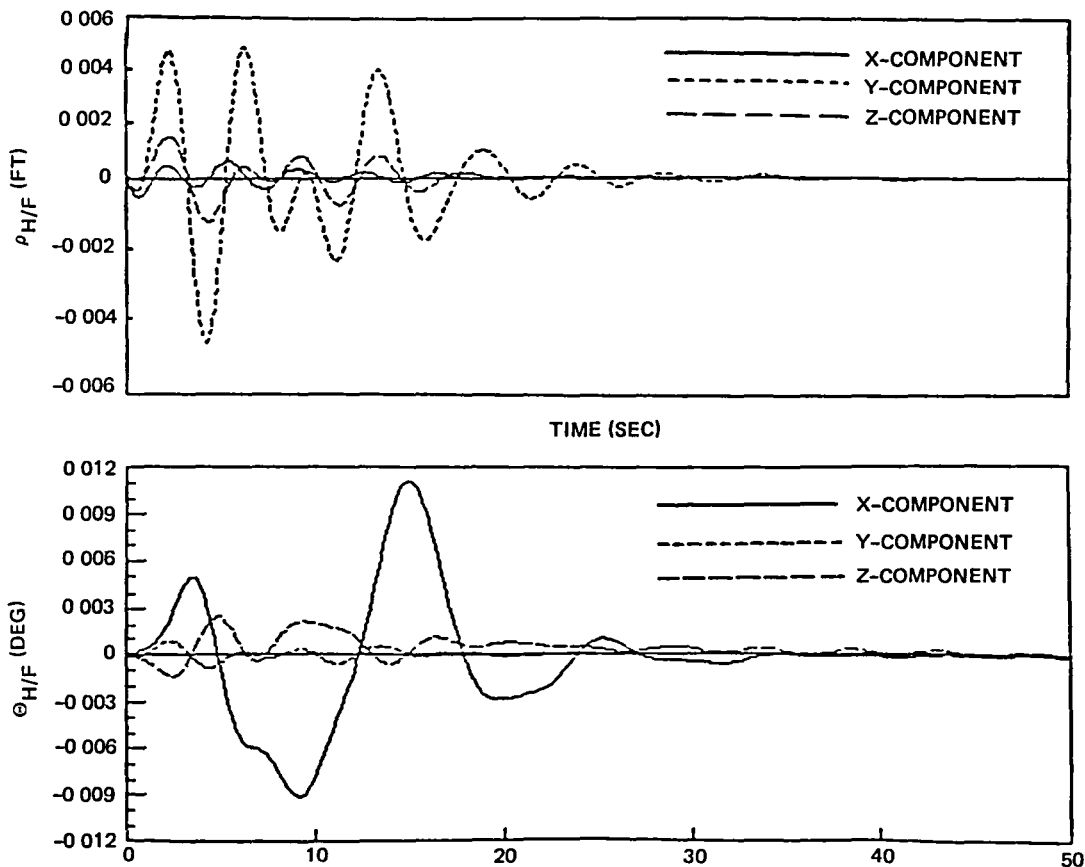
Fig. 14 Hub-to-feed linear and angular displacements with hub and feed controller configuration 2

365

Table 6. Maximum torque and force amplitudes and settling times for three hub and feed controller configurations.

	CONTROLLER CONFIGURATION 1	CONTROLLER CONFIGURATION 2	CONTROLLER CONFIGURATION 3
MAXIMUM FORCE/TORQUE AMPLITUDES (LB/FT-LB)	$T_2 = 30.0$	$T_2 = 0.4$ $T_5 = 11.0$	$F_5 = 0.15$ $T_2 = 0.45$ $T_5 = 1.15$
RESULTING FORCE/TORQUE SETTLING TIME (SEC)	50.0	40.0	35.0

D.3 Line-of-Sight (LOS) Pointing Control

The LOS errors are defined as the lateral components of the projections of the hub unit normal vector onto a reference, in this case, body 1 frame at time zero. The hub attitude angles Θ_{5x}, Θ_{5y}, Θ_{5z} with respect to the reference frame can be modeled as follows,

$$\begin{bmatrix} \Theta_{5x} \\ \Theta_{5y} \\ \Theta_{5z} \end{bmatrix} = H_{LOS} x \tag{31}$$

the LOS pointing errors are then

$$\begin{bmatrix} LOS_x \\ LOS_y \\ LOS_z \end{bmatrix} = \begin{bmatrix} \Theta_{5z} \end{bmatrix}^3 \begin{bmatrix} \Theta_{5y} \end{bmatrix}^2 \begin{bmatrix} \Theta_{5z} \end{bmatrix}^1 \begin{bmatrix} 0 \\ 0 \\ 1 \end{bmatrix}$$

$$= \begin{bmatrix} \sin\Theta_{5x} \sin\Theta_{5z} - \cos\Theta_{5x} \sin\Theta_{5y} \cos\Theta_{5z} \\ \sin\Theta_{5x} \cos\Theta_{5z} + \cos\Theta_{5x} \sin\Theta_{5y} \sin\Theta_{5z} \\ \cos\Theta_{5x} \cos\Theta_{5y} \end{bmatrix} \tag{32}$$

The steady-state control gain matrix C_{32} is selected to minimize the following performance index J:

$$J = \lim_{t \to \infty} E \left\{ x^T(k) H_{LOS}^T H_{LOS} x(k) + \alpha \, u^T(k) u(k) \right\} \tag{33}$$

where $\alpha = 10^{-15}$. Some of the modes are lightly damped, a shift algorithm is used to modify the control design which yields higher damping to the closed-loop system modes. The closed-loop poles corresponding to LOS controller configuration 2 are shown in Table 7. The time histories for LOS pointing errors are shown in Fig. 15. The maximum LOS pointing error is 140 micro-radians and settling time is approximately 35 seconds. The maximum torque level is 14 ft-lbs as shown in Table 8 along with that for other controller configurations.
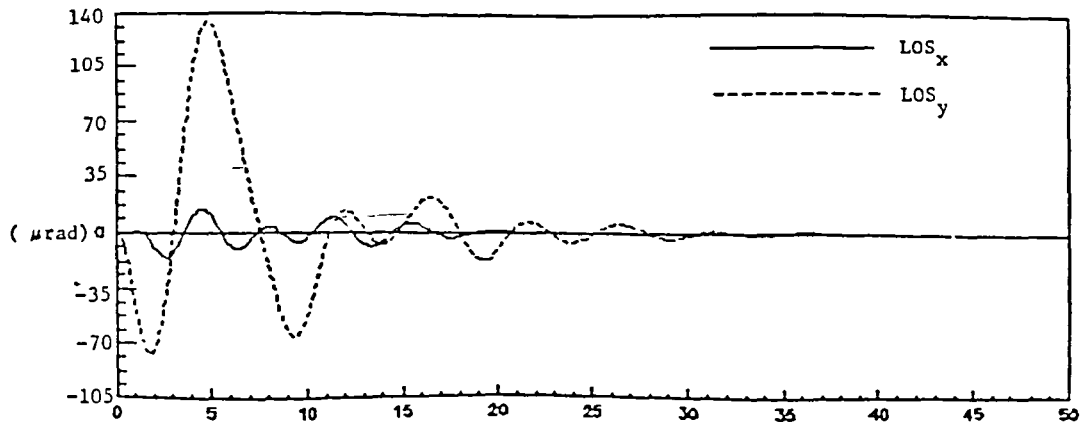
Fig. 15 Line-of-sight pointing errors with LOS controller configuration 2

Table 7. Closed-loop poles for system with LOS pointing
controller configuration 2

REAL PART (RAD/SEC)	IMAGINARY PART	MODAL FREQUENCY (Hz)	DAMPING RATIO
-0.90	1.35	0.26	0.55
-0.91	0	0.14	1.0
-0.96	1.72	0.31	0.49
-0.99	1.13	0.24	0.66
-1.07	1.34	0.27	0.62
-1.08	0.57	0.19	0.88
-1.09	1.00	0.24	0.73
-1.19	1.17	0.26	0.71
-1.19	0	0.19	1.00
-1.99	1.83	0.43	0.73
-6.79	6.24	1.47	0.74
-6.85	6.30	1.48	0.74

367

Table 8. Maximum torque and force amplitudes and settling times
for three LOS pointing controller configurations

	CONTROLLER CONFIGURATION 1	CONTROLLER CONFIGURATION 2	CONTROLLER CONFIGURATION 3
MAXIMUM FORCE/TORQUE AMPLITUDES (LB/FT-LB)	$T_2 = 100.0$	$T_2 = 14.0$ $T_5 = 14.0$	$F_5 = 0.6$ $T_2 = 2.7$ $T_5 = 6.0$
RESULTING FORCE/TORQUE SETTLING TIME (SEC)	40.0	30.0	30.0

D.4 Summary and Conclusions

Nine multi-input multi-output controllers were designed and evaluated with the full-order model. The results show that all the controllers have yielded desirable performance with actuator torques and forces well within the range of state-of-art hardware. The settling time is relatively fast considering the large size of the flight experiment structure. The spillover problems are minimal with nominal parameter values. Control system robustness and design options have been investigated and will be presented in a forthcoming paper.

E. Slew Experiment

The objectives of this experiment are to (1) investigate command techniques for maneuvering the antenna structure while minimizing flexible body vibrations, (2) measure and compare antenna jitter induced by several different command generators, and (3) verify analytical prediction of such antenna jitter.

In this experiment, the performance capabilities and operational constraints of three command generators -- Versine, Guass Filter, and Optimal -- will be compared. However, only the most widely known of the three, the Versine slew, is focused in this work. It is expected that the Versine slew will exercise the command and sensing systems with this experiment to a degree representative of all three.

The Versine slew experiment consists of two basic steps -- applying a slew command to the antenna structure, and measuring the vibration. Antenna rib and LOS vibration are used to measure the slew performance. A functional block diagram of this experiment is shown in Fig. 16. The command consists of two torque pulses separated by a constant velocity coast. This is computed by an on-board computer according to parameters either loaded before the flight, or input during flight. A CMG (Control Moment Gyro) cluster is mounted on the equipment section to supply torque and

momentum consistent with a maximum rate of 1 deg/min and a maximum acceleration of 4 deg/min^2. The 1 deg/min rate is the driver for CMG sizing. The dish retroreflector target measurements along with other measurements are stored and telemetered to the ground for processing.
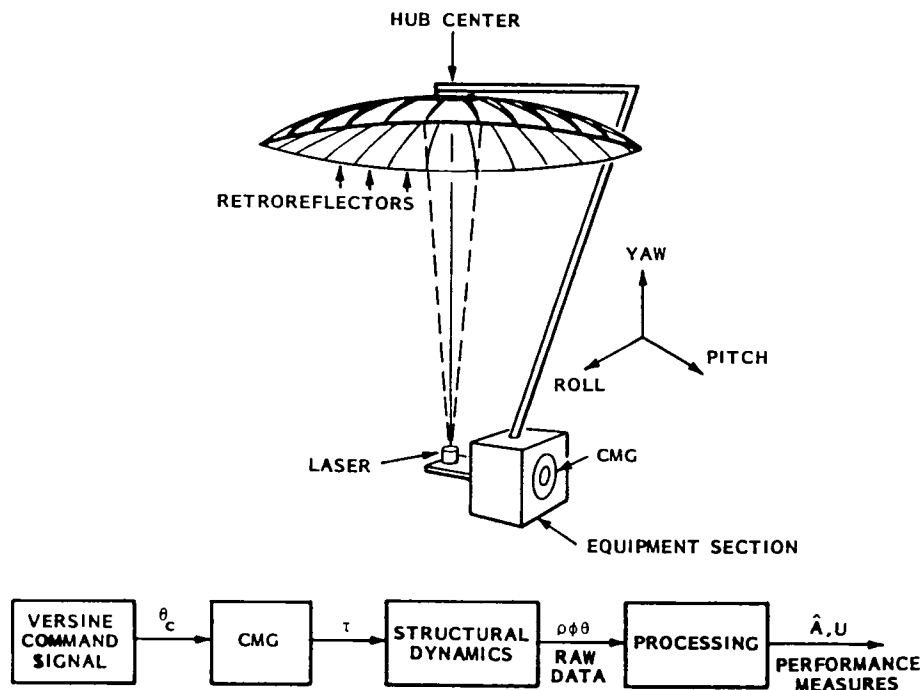
Fig. 16 Functional block diagram of slew experiment

The LOS vibration can be measured by measuring a unit vector of the hub normal, relative to the equipment section to isolate rigid body motion. The coordinates of this vector can be extracted from the hub retroreflector target positions. The LOS unit vector jitter represents primarily the effects of the long boom bending in response to the bus movement. Analysis has shown that the short boom and dish vibrations are negligible compared with long boom motions. Since it is of interest to know the dish deflections, one of the deflections is measured. From analysis, position 42 (see Fig. 3) shows consistently the largest deflection for both pitch and roll motions, and hence, the deflection of this point relative to the hub is measured and forms part of the index.

The Versine command is a sequence of four pulses, each described by

$$\Theta_v = \pm M \, [1 - \cos \omega_p (t - T_i)] \quad , \tag{34}$$

$$T_{i-1} < t < T_i \quad , \qquad i = 1, 2, 3, 4$$

where Θ_v is the jerk command signal, M, the command amplitude (one-half the peak amplitude), ω_p, the angular rate asssociated with the jerk pulse, and T_i, the delay time to the current pulse. It is not the Θ_v profile which the experiment maneuver torque follows, instead, it is the first integral of Θ_v, $\ddot{\Theta}_c$, that it follows. $\ddot{\Theta}_c$ is,

$$\ddot{\Theta}_c = \pm M \, [t - (1/\omega_p) \sin \omega_p (t - T_i)] + \text{constant} \tag{35}$$

369

where the constant is the maximum acceleration attained and is added only during the pulseless portion of the first and third intervals and the active portion of the second and fourth intervals. Θ_c will be sent to the CMG package via a D/A converter to produce a torque about one or more of the axes. Table 9 tabulates the experimental slew parameters.

Table 9. Summary of experimental slew parameters

NO.	τMAX (FT-LB)	JERK ($^\circ$/SEC^3)	RATE ($^\circ$/MIN)	ACCELERATION ($^\circ$/MIN^2)
1	54.6	7.24-05	1.0	3.95
2	48.9	7.32-05	0.98	3.6
3	49.2 (ROLL) 11.4 (YAW)	7.24-05	1.0	3.95
4	44.8 (ROLL) 10.4 (YAW)	7.32-05	0.98	3.6

III. SYSTEM ARCHITECTURE AND HARDWARE REQUIREMENTS

To achieve the experiments as described in Section II, a fully equipped control system is required. Fig. 17 shows the flight experiment hardware configuration. At the bus, a 3-axis torque capability is provided by a complex of four 1300 ft-lb-sec control moment gyros. Gimbal torquers, one along each gimbal, provide capability to desaturate the CMG's. Two star sensors provide bus attitude reference information. Bus angular velocity is measured via a 3-axis gyro package. A laser optical sensor, SHAPES, is also included in the bus hardware. Digital encoders, at the gimbals, provide orientation information between the shuttle and the experiment.

The hub equipment is similar to that of the bus. Four 225 ft-lb-sec CMGs provide torque actuation. Force actuation is made available by a 3-axis reaction control system. Two star sensors and a gyro package are also mounted at the hub to measure hub attitude and angular rate, respectively. Table 10 shows a complete list of required control hardware.

A.   Actuator Requirements and Selection

The requirements of actuators are obtained through analysis and simulation of control, mass properties ID, mode ID, geometry ID, and slew maneuver experiments. Table 11 tabulates the actuation requirement by location and experiment functions and Table 12 shows the combined requirements for actuators.

Candidate hub force actuators, i.e., thrusters, are not off-the-shelf items. The pressure pulses from reaction thrusters have their own characteristic shape, which is unlikely to be the same as that of the desired force. The pulse-width, which may be

370

as low as 15-18 msecs, can be controlled in order to approximate the shape of the desired force; however, considerable analysis will be required to determine how to achieve best results. These thrusters will require development.
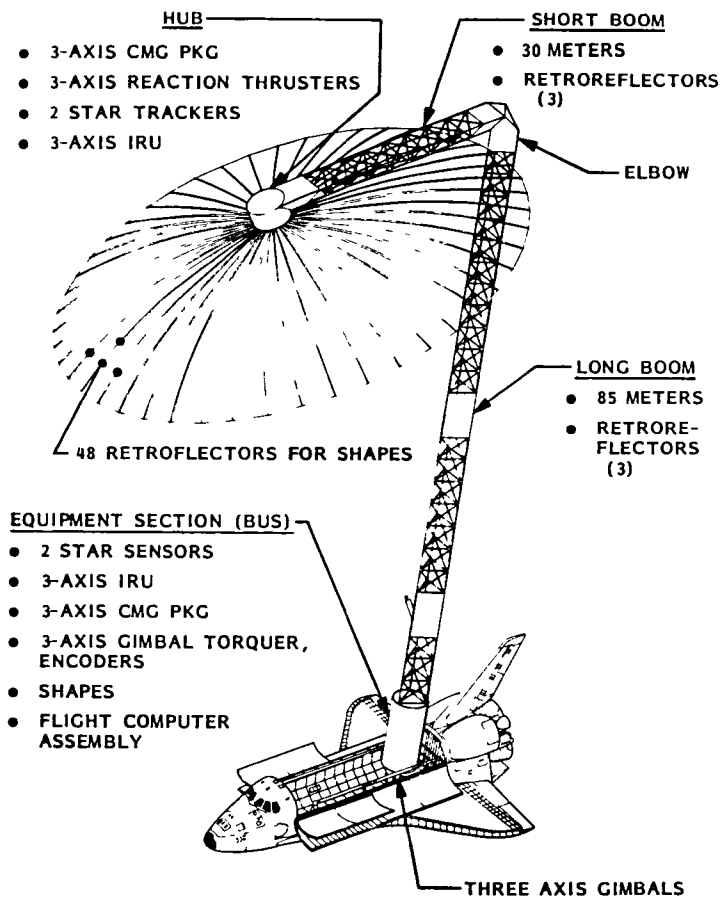
Fig. 17 Flight experiment hardware configuration

Table 10. Flight experiment control hardware

ITEM	VENDOR	LOCATION	NO REQUIRED	UNIT WEIGHT (LB)	UNIT VOLUME (IN³)	AVG UNIT POWER (WATTS)	COMMENTS
CONTROL MOMENT GYRO ASSEMBLY	SPERRY	EQUIPMENT SECTION	3	260	43, 33 70	48	1300 FPS, PEAK POWER ≈ 700 W
STAR SENSOR	BALL	EQUIPMENT SECTION	2	20 3	6 5 8 2 12	23 1	
INERTIAL REF PKG	BENDIX	EQUIPMENT SECTION	1	12	6, 8, 5 1	11/ CHANNEL	
SHAPES	–	EQUIPMENT SECTION	1	33		20	IN DEVELOPMENT AT JPL
EXP COMPUTER ASSEMBLY	ROCKWELL	EQUIPMENT SECTION	1	110	18, 19, 13	100	24 BIT WORD
FLIGHT RECORDER							
CONTROL MOMENT GYRO ASSEMBLY	SPERRY	HUB	3	115	35 23	48	225 FPS PEAK POWER 250 W
STAR SENSOR	BALL	HUB	2	20 3	6 5 8 2 12	23 1	
INERTIAL REF PKG	BENDIX	HUB	1	12	6 8 5 1	11/ CHANNEL	
THRUSTER COMPLEX	–	HUB	6	2 7	7, 5 2	10	
TORQUE MOTOR ASSEMBLY	LMSC	GIMBAL	3	200	24 x 20d	–	280 W PEAK POWER
TORQUE MOTOR ELECT	LMSC	GIMBAL	1	20	5 9 12		
DIGITAL ENCORDER	BEC	GIMBAL	3				

371

Table 11. Actuation requirement by location

LOCATION	EXPERIMENT	TORQUE/FORCE	TIME/MOMENTUM	BANDWIDTH	ACCUR/RESOL
BUS	SLEW	70 FT-LB	820 FT-LB SEC	2 Hz	2 IN LB
BUS	MASS PROP	10 FT-LB	100 SEC		2-10%
BUS	MASS PROP	100 FT-LB	1000 FT-LB SEC		2-10%
BUS	CONTROL	100 FT-LB		4 Hz	
BUS	MODE ID	21 FT-LB		15 Hz	
HUB	CONTROL	0.6 LB		3.5 Hz	
HUB	MODE ID	21 FT-LB		15 Hz	
HUB	CONTROL	14 FT-LB		3 5 Hz	
SHUTTLE	MODE ID	21 FT-LB		15 Hz	

Table 12. Combined actuator requirements

DEVICE	LOCATION	FORCE/TORQUE	MOMENTUM	BANDWIDTH	ACCURACY
FORCE ACTUATOR	HUB	0.6 LB		3.5 Hz	
GIMBAL TORQUER	BUS	21 FT-LB		15 Hz	2-10%
CMG	BUS	100 FT-LB	1000 FT-LB SEC	15 Hz	2-10%
CMG	HUB	21 FT-LB		15 Hz	

The torque motor likewise cannot be specified off-the-shelf. It is comprised of the torque motor assembly (TMA) and torque motor electronics (TME). The TMA requires two torque motors, bearings, a housing, encoders, transflex cables and a temperature control unit. The TME is the more expensive unit, requiring significant new development.

Gimbal torquers are required to provide means for CMG desaturation, and to provide relative torque, rather than inertial torque, for the mass properties experiment. The gimbal torquers also apply torque to the shuttle for the mode ID experiment.

A control moment gyro which meets both torque and momentum requirements at the equipment section is the Sperry M1300. Its relevant specifications are:

Angular Momentum:	1300 ft-lb-secs
Torque:	2200 ft-lbs
Bandwidth:	20 Hz closed-loop

This CMG will also meet the 2% accuracy requirement at most values of applied torque, though it may require some modification to meet that requirement for low

372

values of applied torque. There is also a trade-off between bandwidth and accuracy. The enclosed-loop response is more accurate than the open-loop response, but has a lower bandwidth.

The Sperry M225 CMG meets the requirements for the torque applied at the hub, except for the bandwidth. Relevant specifications are:

Angular Momentum:	225 ft–lb–secs
Torque:	225 ft–lbs
Bandwidth:	12 Hz closed–loop

As with the M1300, three of these CMGs are required in order to apply 3-axis torque. Angular momentum capacity and the torque capability considerably exceed requirements.

B.   Sensor Requirements and Selection

The requirements are summarized in Table 13. These requirements are also arrived through analysis and simulation of the experiments. Table 14 shows the overall requirements for sensors.

Table 13. Sensor requirements by location

LOCATION	PHYS QTY	EXPERIMENT	ACCURACY	MAX VALUE	BANDWIDTH
BUS	ATTITUDE	MODE ID	0.01°		15 Hz
BUS	ATTITUDE	CONTROL		0.8°	3.5 Hz
BUS	ATTITUDE	MASS PROP	21 SEC	90.0°	
HUB	ATTITUDE	MODE ID	0.1°		15 Hz
HUB	ATTITUDE	CONTROL		0.025°	18 Hz
HUB	ATTITUDE	MASS PROP	42 SEC	90.0°	
SHUTTLE	ATTITUDE	MODE ID	0.01°	0.01°	15 Hz
SHUTTLE	ATTITUDE	MASS PROP	21 SEC	90.0°	
BUS	ATTITUDE RATE	MODE ID	0.01°/HR		15 Hz
BUS	ATTITUDE RATE	CONTROL		1.5°	3.5 Hz
HUB	ATTITUDE RATE	MODE ID	0.01°/HR		15 Hz
HUB	ATTITUDE RATE	CONTROL		0.035°	18 Hz
SHUTTLE	ATTITUDE RATE	MODE ID	0.01°/HR		15 Hz
BUS TO ELBOW	VECTOR	CONTROL			
BUS TO HUB	VECTOR	MODE ID	0.39 IN.		10 Hz

The Bendix 64 RIG, versions of which have been used on the Space Telescope and are to be used on Talon Gold, is a candidate to meet the accuracy requirements for IRU. The random drift is 0.001 deg/hr (1σ). For Talon Gold, which has two 7-day missions, 4 gyros per box are used for reliability. The Ball Aerospace NASA Standard Star Tracker is an appropriate choice for star tracker. The stated accuracy is 10 sec (1σ) calibrated. Two units at each location (hub and bus) are desirable for redundancy and improved accuracy.

373

Table 14. Combined sensor requirements

DEVICE	LOCATION	PRECISION	BANDWIDTH	RANGE	DATA SET
IRU	HUB	0.01°/HR	18 Hz		
IRU	BUS	0.01°/HR	15 Hz		
STAR SENSOR	HUB	0.01°	18 Hz		
GIMBAL ENC	TMA	30 SEC	15 Hz	90°	
SHAPES	BUS	±0.0012 IN.	2 Hz	±39.4 IN.	50-150
		±0.1 SEC		±3 MIN	RETRO-FLECTORS

The bus star tracker could encounter field of view blockage by the antenna. Should this problem arise, the estimators could be configured to use the bus to hub coordinate transformation to translate star tracker updated measurements from the hub to the bus with the information from the laser optical measurement (SHAPES).

The required shuttle attitude and attitude rate can be measured with the shuttle hardware or with the gimbal encoders. The gimbal encoders presently considered are 16-bit space-rated absolute encoders made by BEI for the Galileo project. The encoder has an accuracy of approximately 10 arcsec.

The SHAPES sensor is important to the geometry ID and slew experiments. It also measures bus to hub vector for mode ID and bus to elbow vector for the damping experiments. The SHAPES sensor involves a single sensor at the bus and retroreflectors at the ribs, hub, and booms. Depending on the data rate and the number of targets required, two sensors may be required.

C.   Data Processing Requirements

Table 15 summarizes the data processing requirements for each experiment. The throughput and storage requirements are stated in million operations per second (MOPS) and mega bytes (M-bytes), respectively. Throughput requirements are dominated by control experiments which require real-time processing in the amount of 109,000 additions and 110,000 multiplications per second. For the case of three machine operations per addition and four per multiplication, a total of 0.767 MOPS of throughput is required. This estimate is conservative since the sparse nature of the system matrices has not been exploited. Storage requirements are dominated by the slew experiment. Assuming 24-bit per word, 74.7 M-bytes will be required.

D.   Flight Experiment Timeline

The time expenditure requirements for each of the proposed experiments are summarized in Table 16. The overall experiment timeline with margins for contingencies is shown in Fig. 18(a) and that with margins set to zero is shown in Fig. 18(b).

374

Table. 15. Data processing requirements

EXPERIMENT	THROUGHPUT (MOPS)	STORAGE (M-BYTES)
GEOMETRY ID	<0.01	0.03
MODE ID	<0.01	2.4
MASS PROPERTIES ID	<0 01	5.5
CONTROL	0 767	0.15
SLEW	<0.01	74.7

Table 16. Experiment time requirements

EXPERIMENT	SINGLE ITERATION	NO. OF ITERATIONS	TOTAL PROG TIME	CONTINGENCY	TOTAL SUBEXP TIME	CUMULATIVE ON-ORBIT TIME
1. STATIC GEOM	15 SEC	3	45 SEC	30 MIN	31 MIN	24 5
2. MODE ID	24 HR	1	24 HR	18 HR	42 HR	66.5
3. CONTROLS	3.5 HR	1	3.5 HR	7 HR	10.5 HR	77.0
4. SLEW	8 HR	1	8 HR	4 HR	12 HR	89.0
5. MASS PROP ID	73 HR	1	73 HR	24 HR	97 HR	186.0
TOTAL	108.5 HR	–	108.5 HR	53.5 HR	162 HR	186 0
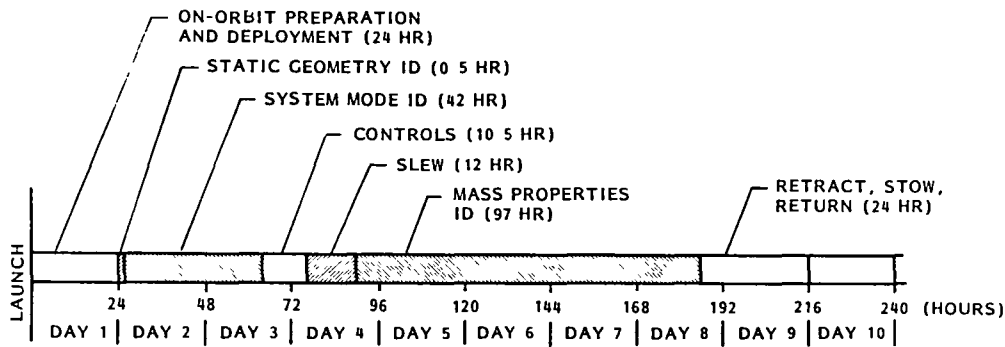
Fig. 18(a) Flight experiment timeline with contingencies included
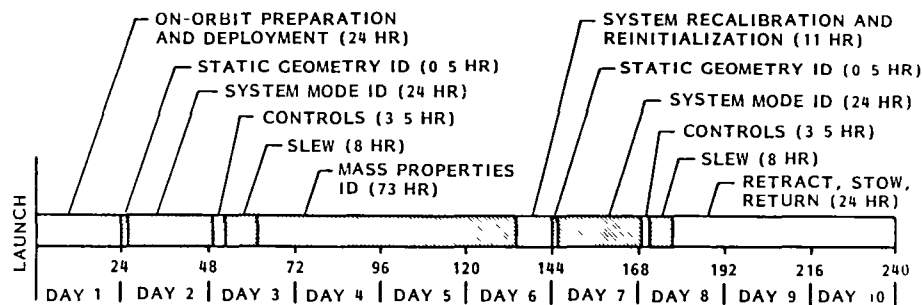
Fig. 18(b) "Nominal performance" flight experiment timeline with contingency times set to zero. Nine day flight plan

375

IV. Higher Dimensional Controlled Attachment Configuration

The method of attachment of the antenna structure to the shuttle ultimately determines the extent to which experiments can be performed and the quality of such experiments. In Ref. 1, the simplest form of attachment-zero DOF attachment was considered. Such attachment has the advantage of simplicity and low cost. For certain types of experiments, this is quite desirable since its dynamical properties are quite close to those of a free flier antenna. Fig. 19 shows the modal frequency spectra of a shuttle-rigidly-attached system and two free flier antennas. As indicated in Fig. 19, most of the modal frequencies of these systems only shifted very slightly. The free flier antennas in the figure are lighter at the feed locations compared with those studied in References 2 and 9. The frequency spectrum of the Land Mobile Satellite System [9, 5] is even closer to the shuttle attached case.
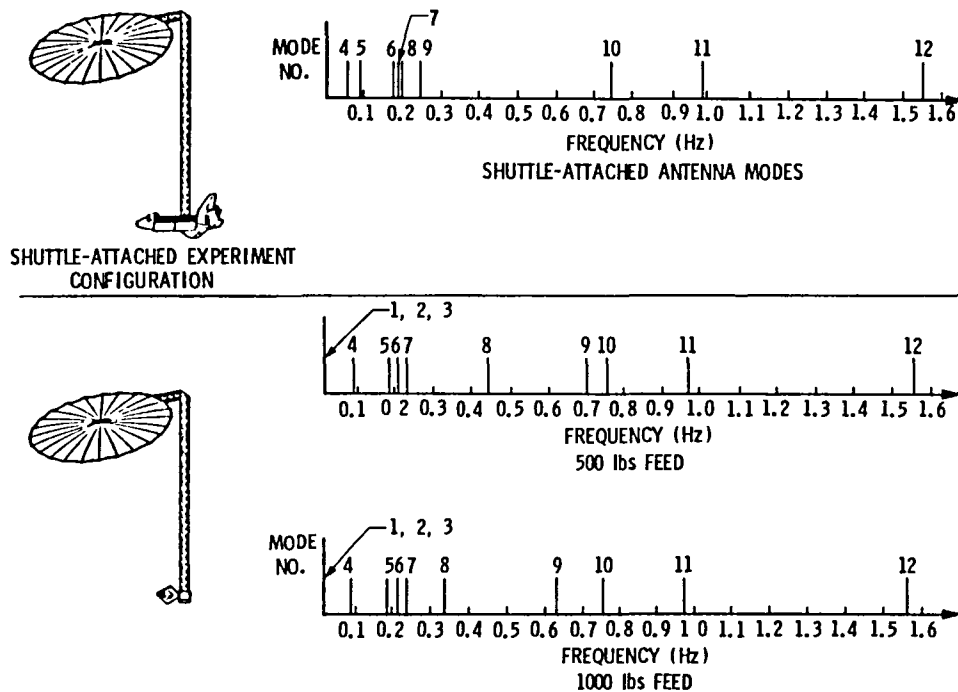
Fig. 19 Modal frequencies of a shuttle-attached system and
two free flier antennas

This configuration also has its drawbacks due to lacking of capability of slew and disturbance isolation. The method, a 3-DOF gimballed attachment, that has been the base for the experiment design of Section III has removed some of the shortcomings of the rigidly attached case at additional cost.

The dynamic disturbances from the shuttle may be decomposed into rotational and translational ones. The former can be decoupled through a 3-DOF gimbal system such as the one employed in Section III. The translational motions or disturbances, however, require a more complex interface system. Since the translational motions of the shuttle relative to the antenna can have the most detrimental effect to the experiment structure, and the capability of conducting certain experiments in a disturbance free environment is desired, we are prompted to look into the concept of a 6-DOF controlled attachment interface system.

A conceptual model of this system is illustrated in Fig. 20. This interface system is mounted in the shuttle payload bay near the c.m. The system has its own sensing and control mechanisms for tracking the antenna boom tip motion without touching the boom structure during free-flier experiment periods. This mode of operation starts by uncaging the boom tip and the tip section motion is tracked by the interface system inside a one-meter sphere. Between the boom tip and the inner axis assembly of the interface system, there is a six-DOF sensing system providing the intelligence for the interface controller to track the boom position. After the system reaches the one-meter sphere tracking boundary, the sensing system will provide positional information to derive antenna station keeping data needed to reposition the antenna and hence the interface to their starting position. Once repositioned, the free drift mode of operation can be initiated. In this mode of operation the antenna and the shuttle are separate inertial entities in which the antenna is a free structure flying in tight formation with the shuttle, with one centimeter separation from the inner structure of the six-DOF tracker controller.

In order to obtain long free drift periods, one has to place the antenna c.m. co-orbital with the shuttle c.m. For this purpose, it is necessary for the shuttle to fly in the nosedown nadir attitude.

A realizable flight experiment architecture is illustrated in Fig. 21. This configuration is reduced to the rigidly attached or the 3-DOF gimballed configurations if one freezes all or the three translational axes, respectively.

The c.m. compatibility in maintaining co-orbital flight is not the only factor that determines the free drift period, the aerodynamic effect is also important. For a hub-attached antenna, using the predicted atmospheric densities for 1986 and 1990, the antenna aerodynamic drag forces are computed as plotted in Fig. 22, at 300 km and 400 km altitude. The corresponding shuttle and antenna separation distances and rates for a 5 minute drift period are plotted in Fig. 23. From these estimates, for a 400 km or higher orbit, a 5 minute free drift period is achievable. For many experiments, 5 minutes is sufficient.
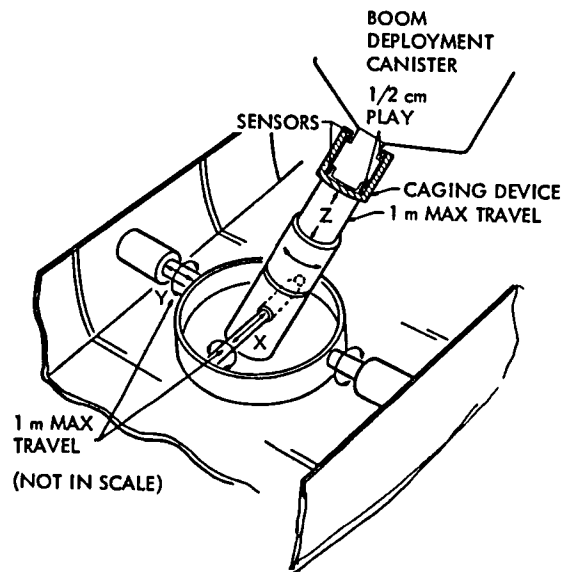
(a) Concept illustration

Fig. 20 Six-DOF controlled attachment interface system

377
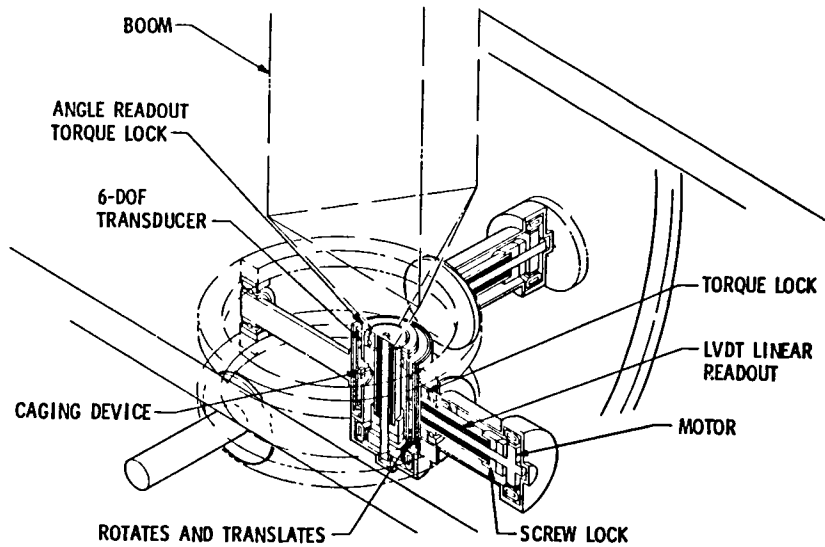
(b) System assembly -- conceptual design

Fig. 20 Six-DOF controlled attachment interface system
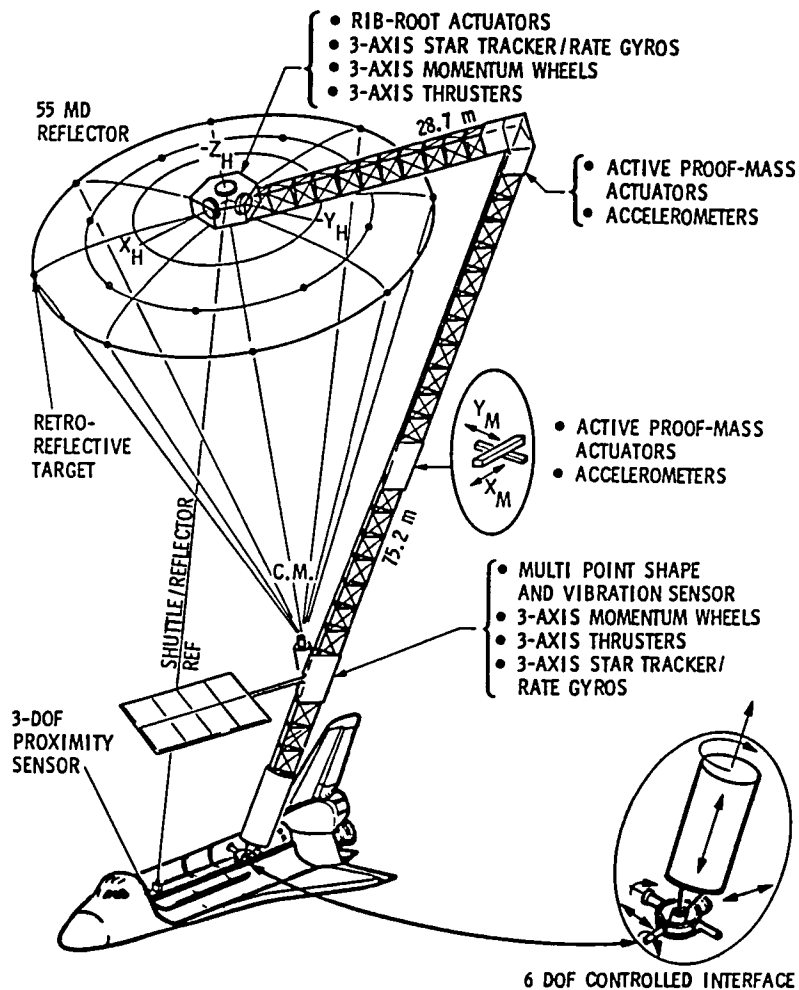
Fig. 21 Flight experiment architecture with 6-DOF controlled
attachment interface
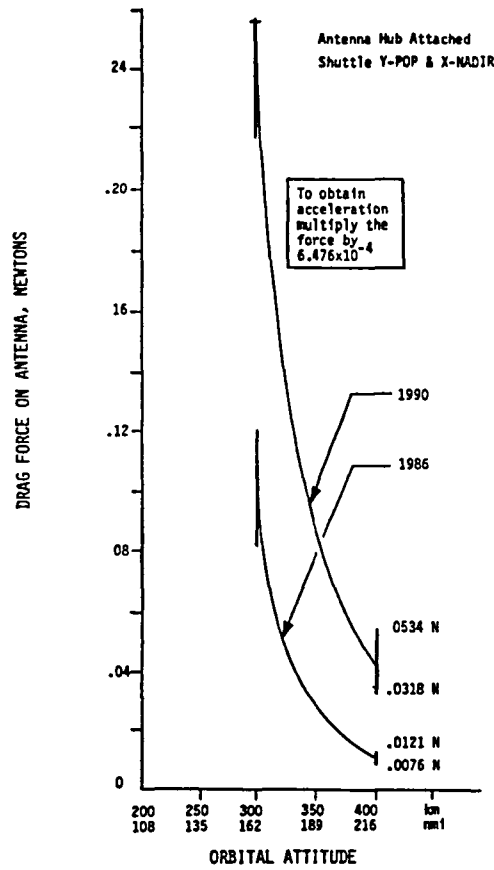
Fig. 22 Predicted antenna aerodynamic drag force
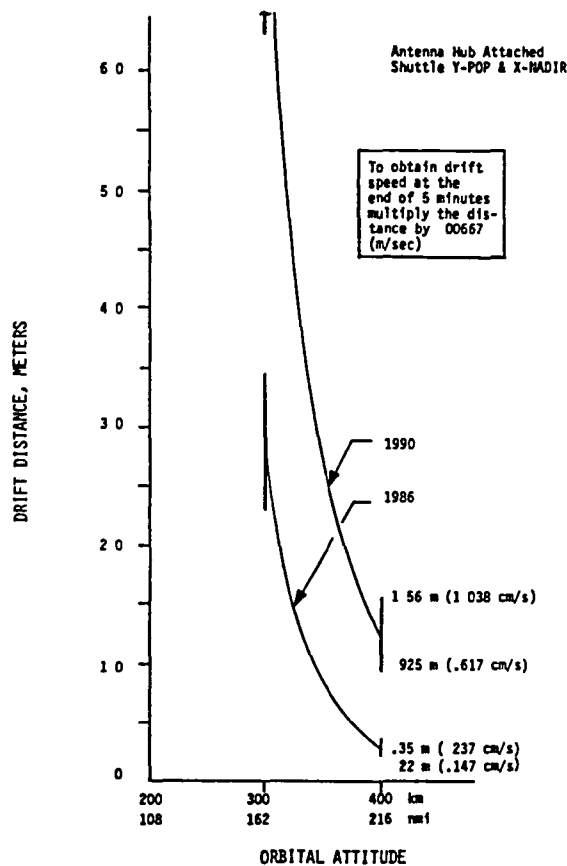
Fig. 23 Predicted 5-minute shuttle-antenna separation distance due to aerodynamic effect

379

V. CONCLUSIONS

Based on the results of this study, it is concluded that a shuttle attached antenna flight experiment is feasible. The control and identification algorithms are reasonably well understood and can be adapted to current flight computers. The required control and identification hardware are available with the exception of the SHAPES sensor. The latter is still under development at JPL. The following is a list of specific conclusions:

1. Flexible body dynamics will no longer be a second order effect, instead, they will be the major parameters in future spacecraft designs.

2. The point of attachment of a three degree-of-freedom gimbal can be optimized as a function of expected disturbances. Vernier thruster firings during active experimental periods will not disrupt performance for 1 GHz RF (radio frequency) level.

3. A flight experiment to verify performance of a 10 GHz system is likely to require a six degree-of-freedom gimbal or a free flier antenna. Most of the experiments conceived to date can be accomplished during the free-drift period with a six degree-of-freedom decoupling system.

4. The proposed geometry identification is feasible and within the bounds of current state-of-the-art technology assuming SHAPES sensor performance at current design specification levels. Under quiescent conditions, it should provide surface roughness information adequate for 10 GHz reflector quality verification. Performance for 1 GHz reflector will have one order of magnitude margin.

5. Results of mass property identification experiments indicate that some of the parameters are only weakly observable. Estimator performance obtained to date has not met the baseline requirements. The probability of estimating all significant parameters is low and maneuvers are very time consuming. More studies in the optimization of the identification strategy will be required.

6. The system mode identification experiment is feasible. The system can be configured to operate within the time constraints of a shuttle captive mission and is expected to provide parameter data to the required 1% accuracy. This experiment should meet all key objectives.

7. The control experiment is feasible. Hardware requirements are within bounds of current technology. The required control torques and forces are well within the dynamic ranges of the state-of-the-art actuators. The settling time is relatively fast considering the large size of the flight experiment structure.

8. The slew experiment is feasible and within the limits of current actuator state-of-the-arts.

9. The complete experiment can be accomplished during a nine-day shuttle mission.

10. A substantial ground test and development program is required and must precede the flight experiment.

ACKNOWLEDGEMENT

REFERENCES

1. Wang, S. J., Y. H. Lin, and C.H.C. Ih, "Dynamics and Control of a Shuttle Attached Antenna Flight Experiment", presented at the 1983 AIAA Guid. and Cont. Conference, August 15-17, 1983, Gatlinburg, TN. To appear in Journal of Guidance, Control, and Dynamics, Nov.-Dec., 1984.

2. Wang, S. J., and J. M. Cameron, "Dynamics and Control of a Large Space Antenna", presented at 1982 AIAA Guidance and Control Conference, San Diego, August 9-11, 1982. Conf. Proc. pp. 394-402 J. of Guidance, Control, and Dynamics, Vol. 7, No. 1, Jan-Feb 1984, pp. 69-76

3. Rodriguez, G, J. Cameron, and M. Milman, "Shape Determination for Large Space Antennas", presented at the 4th VPI and SU/AIAA Symposium on Dynamics and Control of Large Structures, June 6-8, 1983, Blacksburg, VA.

4. NASA Ad Hoc Study Team on Integrated Controls/Structures Flight Experiment. Requirements and Objectives Panel; Keto Soosar, Chairman.

5. Naderi, F., "Land Mobile Satellite Service", JPL Publication 82-19 Part II, February 1982.

6. Van Vactor, D., "Gaussian Filtering as Applied to the Reduction of Vehicle Vibration", LMSC EM 7026, July 1977.

7. Breakwell, J. A., "Optimal Feedback Slewing of Flexible Spacecraft", AIAA Journal of Guidance and Control, Vol. 4, No. 9, September-October, 1981.

8. JPL/LMSC Report on Shuttle Attached Antenna Flight Experiment Definition Study.

9. Cameron, J. M., M. Hamidi, Y. H. Lin, and S. J. Wang, "Distributed Control of Large Space Antennas," presented at Workshop on Applications of Distributed System Theory to the Control of Large Space Structures, July 14-16, 1982, proc. pp. 225-247.

TIME-OPTIMAL BANG-BANG SLEW OF RIGIDIZED SCOLE CONFIGURATION

J. G. Lin*
Northeastern University, Boston, MA 02115
and
Control Research Corporation, Lexington, MA 02173

L. W. Taylor, Jr.**
NASA Langley Research Center
Hampton, VA 23665

ABSTRACT

This paper addresses (i) an application of the well-known time-optimal bang-bang control theory to the design of minimal-time limited-torque single-axis slew maneuvers for the rigidized configuration of NASA Langley Research Center's **Spacecraft Control Laboratory Experiment** (SCOLE) and (ii) the associated generic side effects due to spillover of slew motions and applied torques. Numerical experiments that helped pinpoint the specific causes of performance degradation are discussed. Analytical as well as scientifically interesting numerical research results are given.

I. INTRODUCTION

New space systems including various configurations of space antennas and platforms, which are to be deployed or erected in space by the Space Shuttle in the near future, have large-scale, lightweight, extremely flexible but lightly damped support structures. Computer-aided or computerized active control of their structural vibrations is generally considered necessary for such large space structures (LSSs) to meet stringent stability and pointing requirements. Standard applications of modern control and estimation theory with various state-of-the-art multivariable design techniques, however, have encountered several technological challenges of generic nature. For example, many numerical examples and laboratory experiments already demonstrated that control and observation spillover can even introduce closed-loop instability, in addition to severely degrading the optimally designed (reduced-order) modern control systems.

Various approaches to designing vibration control systems for LSSs have been proposed, and separate laboratory experiments conducted to demonstrate specifically some of the proposed approaches. Under the cognizance of the Spacecraft Control Branch at the NASA Langley Research Center, a new NASA program was initiated last year to promote direct comparison of different design techniques against a common laboratory experiment that is to be specifically resembling a large space antenna attached to the **Space Shuttle** by a flexible mast.

The primary control objective of the Spacecraft Control Laboratory Experiment (SCOLE) includes the task of directing the RF line of sight (LOS) of the antenna-like configuration (see Figs. 1, 2) towards a fixed target, under the conditions of minimum time and limited control efforts [1]. An intuitively appealing common-sense approach to reorienting a flexible space structure is to **slew it like a rigid body in a minimum time first, and to damp out the excited vibrations afterwards.** Such a two-stage approach will undoubtedly be very desirable and practical, if the excited vibrations can be suppressed to satisfaction in a reasonable time. First, the design of attitude control for such a structure then will not have to be complicated by including the presence and interactions of structural modes. Secondly, the current Space Shuttle is under the single-axis rigid-body time-minimal bang-bang control of the Digital Auto-Pilot (DAP) when it is in the orbit.

In this paper, we shall focus on the first part of the two-stage approach, namely, the design of time-minimal single-axis open-loop slew maneuvers under the assumption that the whole SCOLE is a rigid body. We

---

* Adjunct Professor and Visiting Senior Research Associate, Department of Electrical and Computer Engineering.
** Branch Head.

CONTROL OBJECTIVE
    TO SLEW, POINT, AND STABILIZE THE RF
    LINE-OF-SIGHT OF A FLEXIBLE, SHUTTLE
    ATTACHED ANTENNA, IN MINIMUM TIME.

SYSTEMS IDENTIFICATION.
    TO CREATE CONTROL INPUTS, THEN MODEL
    THE DYNAMIC SYSTEM FROM RESPONSE
    MEASUREMENTS

TARGET

*SPACECRAFT CONTROL LABORATORY
 OF THE FLIGHT DYNAMICS AND
 CONTROL DIVISION
 BUILDING 1232

TETHER

RF LINE-OF-SIGHT

CONTROL MOMENTS AND FORCES

SHUTTLE MODEL

SENSORS:
    ACCELEROMETERS
    RATE GYROS
    ATTITUDE

FLEXIBLE MAST

PITCH

5 DEGREES
OF FREEDOM

YAW

ANTENNA REFLECTOR

ROLL

CONTROL MOMENTS, DISTURBANCES

Fig. 1. Spacecraft Control Laboratory Experiment (SCOLE).

Fig. 2. The Shuttle/Antenna Configuration in SCOLE.

384

applied the standard theory of time–optimal control to each of the Shuttle body axes separately, but made an extension to encompass various bang–pause–bang control.

The single–axis slew maneuvers designed were then evaluated against simulations of SCOLE's 3–axis rigid dynamics. Through such numerical results, the reader will see that even in the context of rigid–body dynamics, spillover can cause significant dynamic interactions and thereby induce sizable undesirable motions. A theoretical analysis of SCOLE's 3–axis rigid–body dynamic equations followed by the interesting results of three numerical experiments will be presented to provide the reader with insights on the causes of the dynamic interactions and the remedies suggested in this paper.

II. ROTATIONAL DYNAMICS OF RIGIDIZED SCOLE

The equation of rotational motion of the rigidized SCOLE configuration,* referrred to as **RSCOLE** throughout this paper, is given by the following nonlinear matrix–vector differential equation:

$$I\,\dot{\omega} + [\omega X]\,I\,\omega = \tau \tag{1}$$

where

$$I = \begin{bmatrix} I_{xx} & -I_{xy} & -I_{xz} \\ -I_{xy} & I_{yy} & -I_{yz} \\ -I_{xz} & -I_{yz} & I_{zz} \end{bmatrix}$$

$I_{xx}=1{,}132{,}508; \quad I_{yy}=7{,}007{,}447; \quad I_{zz}=7{,}113{,}962; \quad I_{xy} = -7{,}555; \quad I_{xz}=115{,}202; \quad I_{yz}=52{,}293$

$$\omega = \begin{bmatrix} \omega_x \\ \omega_y \\ \omega_z \end{bmatrix} \qquad [\omega X] = \begin{bmatrix} 0 & -\omega_z & \omega_y \\ \omega_z & 0 & -\omega_x \\ -\omega_y & \omega_x & 0 \end{bmatrix} \qquad \tau = \begin{bmatrix} \tau_x \\ \tau_y \\ \tau_z \end{bmatrix}$$

The RSCOLE's inertial (earth) angular velocity ω is expressed in the Shuttle's "roll–pitch–yaw" body axes which are respectively denoted by x, y, z. So are the applied torque τ. The following two kinds of torque are available for controlling RSCOLE.

(a). **Control moments** can be applied to both the Shuttle and reflector bodies of 100,000 each axis. The moment commanded for each axis is limited to 100,000. In other words, the applied torque can be expressed as a weighted sum of three independent vectors of limited magnitude as the following:

$$\tau = \begin{bmatrix} 1 \\ 0 \\ 0 \end{bmatrix} M_{xlm}\,u_x + \begin{bmatrix} 0 \\ 1 \\ 0 \end{bmatrix} M_{ylm}\,u_y + \begin{bmatrix} 0 \\ 0 \\ 1 \end{bmatrix} M_{zlm}\,u_z \tag{2a}$$

where $M_{xlm} = M_{ylm} = M_{zlm} = 100{,}000$; u_x, u_y, and u_z denote three independent scalar control variables, each having absolute value limited to 1.

(b). **Control forces** can also be applied at the center of the reflector in the x and y directions only. The force commanded in the particular directions is limited to 8,000. In other words, the resulting torque can be

---

* Presented in this paper are preliminary research results which were originally based on a "hypothetical" rigidized configuration that does not represent all aspects of the latest version [1] of SCOLE, which was presented earlier during this Workshop. We thought these "older" numerical results and technical problems were scientifically interesting and still worth sharing with coworkers elsewhere. In order to avoid any confusion or misinterpretation that may arise, all the numbers are therefore presented as dimensionless quantities. New results corresponding to the specific latest version will be made available or presented elsewhere as soon as they are written up.

expressed as a weighted sum of two indenpendent vectors as follows:

$$\tau = \begin{bmatrix} 0 \\ -130 \\ 32.5 \end{bmatrix} F_{xlm} \; v_x + \begin{bmatrix} 130 \\ 0 \\ 18.75 \end{bmatrix} F_{ylm} \; v_y \tag{2b}$$

where $F_{xlm} = F_{ylm} = F_{zlm} = 8{,}000$; v_x and v_y are two magnitude–limited independent control variables, $|v_x| \leq 1$, $|v_y| \leq 1$.

Notice that in the second kind, when a force is applied on the reflector, say, in the x–direction, it also spills over the z–axis with fairly large torque. Of course, such a direct spillover clearly is not desirable for truly single–axis slew maneuvers. One will see later in this paper that, even the pure moments of the first kind already can induce significant undesired motions about the other axes due to some indirect spillover. The induced motions will then become more severe if direct torque spillover is permitted. Here, we shall concentrate on the **torque of the first kind**, though interesting results were also obtained for the second kind.

III. TIME–OPTIMAL SINGLE–AXIS SLEW MANEUVERS

Single–axis slew maneuvers usually assume that torques can be applied to any individual axis separately, that the nonlinear portion $[\omega X]I\omega$ in the dynamics is negligible, and that the inertia matrix I is diagonal, having only principal moments of inertia. Consequently, when a torque is applied to only a single axis, a separate equation of motion results:

when	$\tau_y = \tau_z = 0,$	$I_{xx} \, \dot{\omega}_x = \tau_x$;	(3a)
when	$\tau_x = \tau_z = 0,$	$I_{yy} \, \dot{\omega}_y = \tau_y$;	(3b)
when	$\tau_x = \tau_y = 0,$	$I_{zz} \, \dot{\omega}_z = \tau_z$.	(3c)

It is not difficult to see that under these simplifying assumptions, perfect independent single–axis slew maneuvers are possible for all the three axes. In the reality of the SCOLE article, however, such ideal conditions do not exist. Since all the built–in navigation and control systems for the Space Shuttle are instrumented with respect to the Shuttle's body axes, we cannot enjoy the convenience of selecting the principal axes of the whole RSCOLE. The technically convenient, but unrealistic, third assumption is not really needed, anyway, though the other two are.

There are two common approaches to making the nonlinear terms sufficiently small. The first is to reduce, if not eliminate, all products of inertia (say, by using RSCOLE's principal axes) and also to make RSCOLE symmetric (say, by redesigning its configuration) so that all the moments of inertia are identical. It is impractical to take such an approach, though. The second approach is **to limit the angular velocity** ω_x, ω_y, and ω_z. The Digital Auto–Pilot (DAP) in the Space Shuttle has been designed for operation under such a limited condition and also for maintaining such a condition. Following the approach taken for the DAP, we **impose a slew rate limit on the design** of various single–axis slew maneuvers.

Using the second assumption, we can reduce the equation of motion (1) to the following simpler form:

$$I \, \dot{\omega} = \tau \tag{4}$$

Expanding and rewriting it in the component form, we have

$$d \, \dot{\omega}_x = (49.8507 \times 10^{12} - I_{yz}{}^2) \, \tau_x + (I_{xz} \, I_{yz} + 7.1140 \times 10^6 \, I_{xy}) \, \tau_y + (I_{xy} \, I_{yz} + 7.0074 \times 10^6 \, I_{xz}) \, \tau_z \tag{5a}$$

$$d \, \dot{\omega}_y = (I_{xz} \, I_{yz} + 7.1140 \times 10^6 \, I_{xy}) \, \tau_x + (8.0566 \times 10^{12} - I_{xz}{}^2) \, \tau_y + (1.1325 \times 10^6 \, I_{yz} + I_{xy} \, I_{xz}) \, \tau_z \tag{5b}$$

$$d \ \dot{\omega}_z = (I_{xy} I_{yz} + 7.0074 \times 10^6 I_{xz}) \ \tau_x + (1.1325 \times 10^6 I_{yz} + I_{xy} I_{xz}) \ \tau_y + (7.9360 \times 10^{12} - I_{xy}^2) \ \tau_z \quad (5c)$$

$$\text{where} \quad d = 56.4563 \times 10^{18} - 7.1140 \times 10^6 I_{xy}^2 - 7.0074 \times 10^6 I_{xz}^2 - 1.1325 \times 10^6 I_{yz}^2 - 2 I_{xy} I_{xz} I_{yz} \quad (5d)$$

Notice that all the products of inertia were kept as parameters. The parametrization is very useful in developing various single-axis slew maneuvers for both the "actual" and the "idealized" simulation cases, respectively, and in conducting in-depth analysis of the numerical results obtained.

Applying the first assumption, we then get the following "decoupled" set of equations:

$$\text{when} \quad \tau_y = \tau_z = 0, \qquad d \ \dot{\omega}_x = (49.8507 \times 10^{12} - I_{yz}^2) \ \tau_x \ ; \qquad (6a)$$

$$\text{when} \quad \tau_x = \tau_z = 0, \qquad d \ \dot{\omega}_y = (8.0566 \times 10^{12} - I_{xz}^2) \ \tau_y \ ; \qquad (6b)$$

$$\text{when} \quad \tau_x = \tau_y = 0, \qquad d \ \dot{\omega}_z = (7.9360 \times 10^{12} - I_{xy}^2) \ \tau_z \ . \qquad (6c)$$

Therefore, under the weaker and more practical set of assumptions, we have arrived at a set of independent equations, similar to the ideal (3a)-(3c), required for developing individual single-axis slew maneuvers for each axis **without having to assume the absence of the products of inertia.**

Now that each axis has a separate equation of motion, of the same generic form, we shall focus our discussions on the x-axis, i.e. roll axis, throughout the remainder of this section. All the following discussions and formulas are directly applicable to the other two axes.

Since the torque τ_x is bounded in magnitude, we rewite it explicitly as

$$\tau_x = \tau_{xlm} \ u_x \qquad (7)$$

with τ_{xlm} denoting the magnitude limit, and u_x the magnitude-limited scalar variable, as in (2a). Substituting (7) in (6a) yields a standard equation commonly seen in the theory of time-optimal bang-bang control:

$$\dot{\omega}_x = b_x \ u_x \qquad (8)$$

$$\text{where} \quad b_x = (46.8507 \times 10^{12} - I_{yz}^2) \ \tau_{xlm} \ / d \ , \qquad |u_x| \leq 1.$$

Now, let δ_x denote the angular displacement about x-axis at time t; δ_{xi} and δ_{xf}, its initial and final values, respectively, and δ_{xd} the desired slew angle about x-axis. Then, the slew error at time t is given by

$$e_x = \delta_x - \delta_{xi} - \delta_{xd} \ . \qquad (9)$$

Since the main objective of the slew maneuver is to achieve the desired slew angle, i.e., zero final slew error, at the final time, it follows from (9) that

$$\delta_{xf} = \delta_{xi} + \delta_{xd} \ . \qquad (10)$$

Thus, we have the following explicit expression for the initial slew error

$$e_{xi} = - \delta_{xd} \ . \qquad (11)$$

Differentiating both sides of (9) twice yields

$$\dot{e}_x = \omega_x \qquad (12a)$$

$$d \ \dot{e}_x \ /dt = \dot{\omega}_x = b_x \ u_x \qquad (12b)$$

Putting (12) into a standard state-space form, we have

$$\frac{d}{dt} \begin{bmatrix} e_x \\ \dot{e}_x \end{bmatrix} = \begin{bmatrix} 0 & 1 \\ 0 & 0 \end{bmatrix} \begin{bmatrix} e_x \\ \dot{e}_x \end{bmatrix} + \begin{bmatrix} 0 \\ b_x \end{bmatrix} u_x$$

where $(e_x , \dot{e}_x)$ is the state vector. Now, we can state a corresponding time-optimal slew problem as the following standard time-optimal control problem: transfer the nonzero initial state $(e_x , \dot{e}_x) = (-\delta_{xd} , \omega_{xi})$ to

387

the origin of the state space ,i.e., $(e_x , \dot{e}_x) = (0 , 0)$, in the minimum time using control u_x subject to the constraint $|u_x| \leq 1$ at all time. As is well known, the standard result is a <u>bang-bang control</u>.

Our problem, however, is slightly more complicated than the above, since we need (i) to take into account the imposed limit ω_{xlm} on the slew rate ω_x, and (ii) to express the resulting control u_x explicitly as a function of time t. Such a time-optimal slew strategy is in general a "bang-pause-bang" (**BPB**) control having two switches, with the standard bang-bang (**BB**) control of only one switch as a degenerate case. The general form can be expressed as follows:

$$
\begin{aligned}
u_x &= u_0 & 0 &\leq t \leq t_1 \\
&= 0 & t_1 &< t < t_2 \\
&= -u_0 & t_2 &\leq t \leq t_3 \\
&= 0 & t &> t_3 .
\end{aligned}
$$

The switching times t_1 , t_2 , and t_3 of a typical BPB slew maneuver with positive initial switch direction, $u_0 = +1$, are determined as follows.

Define $\text{test} = \delta_{xd} + \omega_{xi}^2 /(2b_x)$ (13)

If $\text{test} \geq \omega_{xlm}^2 /b_x$ while $\omega_{xi} \leq \omega_{xlm}$,

then $t_1 = (\omega_{xlm} - \omega_{xi}) /b$ (14a)

$t_2 = \text{test} /\omega_{xlm} - \omega_{xi} /b_x$ (14b)

$t_3 = \omega_{xlm} /b_x + t_2$;   (14c)

but, if $\text{test} \leq \omega_{xlm}^2 /b_x$ while   either   (i) $\delta_{xd} \geq 0$ and $\omega_{xi} \leq \sqrt{2b_x \delta_{xd}}$,

or   (ii) $\delta_{xd} \leq 0$ and $\omega_{xi} \leq -\sqrt{-2b_x \delta_{xd}}$,

then $t_1 = (-\omega_{xi} + \sqrt{b_x \text{ test}}) /b_x$ (15a)

$t_2 = t_1$ (15b)

$t_3 = \omega_{xi} /b_x + 2t_1$ (15c)

Observe that these formulas were expressed in terms of the x-axis parameters. Formulas corresponding to the other two axes can be easily obtained by substituting x by y and z, respectively. Recall that we have retained the factor b_x (and b_y, b_z) as a function of the I_{xy}, I_{xz}, and I_{yz}. Thus, by selecting their values accordingly, we also can easily obtain correct time-optimal single-axis slew maneuvers for applying to any **three-axis** simulation of RSCOLE dynamics.

IV. RESULTS OF NUMERICAL SIMULATION

This section presents numerical simulation results of applying the above time-optimal single-axis slew strategy to RSCOLE for a 20°-slew respectively in the x, y, and z axes. Results for other slew angles, not reported here, are quite similar in dynamic nature, although some have somewhat better LOS performance.

Two different cases, the "actual" and the "idealized", were simulated for sake of comparison and evaluation. The **actual case** used RSCOLE's given values in the simulation of the complete 3-axis nonlinear dynamics (1). The **idealized case** is the same as the actual except that all three products of inertia were set to zero. In each case, the RSCOLE was subject to three independent time-optimal single-axis slew maneuvers respec-

tively about x-, y-, and z-axis. The entire time function for the BPB control of each maneuver, was generated in advance by a general subroutine. Such slew control functions were <u>appropriately adjusted</u> for the actual and the idealized case, respectively, according to the specific values given to the parameters I_{xy}, I_{xz}, I_{yz}.

The slew rate for each axis was preliminarily limited to 4; i.e., $\omega_{xlm} = \omega_{ylm} = \omega_{zlm} = 4.*$

The applied torque terminates at t_3, but the numerical results and the corresponding plots were extended beyond t_3 so as to show RSCOLE's subsequent motions, if any, after the end of the specific slew maneuver.

All the dynamic simulations started with zero initial conditions: namely, $\omega_x = \omega_y = \omega_z = 0$ and $\delta_x = \delta_y = \delta_z = 0$ at $t = 0$.

It is not difficult to see that, under zero initial conditions, the idealized case should behave **like three in-dependent single-axis dynamic systems**, though it still is a 3-axis dynamic system nonlinearly copupled through differences in RSCOLE's moments of inertia, as in the most commonly considered situation. Thus, we use the idealized case to check as well as to demonstrate the design of the corresponding single-axis slew maneuvers. Moreover, we also use such idealized results as the characteristic references for the evaluation and analysis of the actual results. The results are now summarized as follows.

Roll-Axis Slew

Idealized Case. Fig. 3 shows the time history of the roll-axis (x-axis) slew angle and slew rate in the idealized case when a time-optimal single-axis slew maneuver was only applied to the x-axis. The numerical results are all exactly as what we would expect them to be for a completely decoupled system: the roll angle achieved the desired value at the final time t_3 =30.100, and then maintained it afterwards; the roll slew rate rose, fell, and diminished exactly as designed. No motion at all was induced in any of the other two axes. The 3-axis dynamics really behaved like three separate independent 1-axis dynamics.

Actual Case. Figs. 4(a)-(c) show the results in the actual case. As shown in Fig. 4(a), the roll-axis motion behaves virtually as designed: it practically attained the desired slew angle at the final time t_3 =30.075, only 0.05% smaller than the desired.

In contrast to the idealized case, there were, however, some observable motions induced in other two axes. As shown in Fig. 4(b), the induced pitch-axis motion was oscillatory but rather minor before the final time; it started to rise steadily afterwards with a virtually constant rate of 0.015.

Fig. 4(c) shows that the induced yaw-axis motion is slightly more observable. It had a virtually steady growth after t=10 (much before the torque was to switch from the positive extreme to the negative extreme) with a virtually constant rate of 0.03. This rate is twice as large as that of the pitch-axis motion.

Pitch-Axis Slew

Idealized Case. Fig. 5 represents the results of y-axis (pitch) slew maneuver in the idealized case. The results again confirmed what would be expected and desired from the design. The desired 20° slew was attained at the final time t_3 =74.873, and was maintained afterwards. No motions in other two axes were induced.

Actual Case. Figs. 6(a)-(c) correspond to the actual case. Unlike the preceeding roll-axis slew, such results would greatly surprise those who had adhered to their simplistic intuition derived from the common results of the standard BB control theory. Fig. 6(a) shows that the final pitch slew angle was only 6.74°, far far away from the desired 20°. It also shows that the angle peaked to 8.38° at about t=39, then dropped back to near zero before slowly rising up again. It would be more surprising to see that the pitch slew rate started to **decline sharply** at about t=29. It was supposed to keep on increasing with a constant slope until t_1=37.44, the time when the torque switched from the positive extreme to the negative extreme. Moreover, the pitch

---

* The high limit was intended only to avoid the "pause" period so that an easy check can be made with our common intuition of bang-bang control. The pause periods were not avoided when the forces on the reflector were applied, which generated much larger torques.
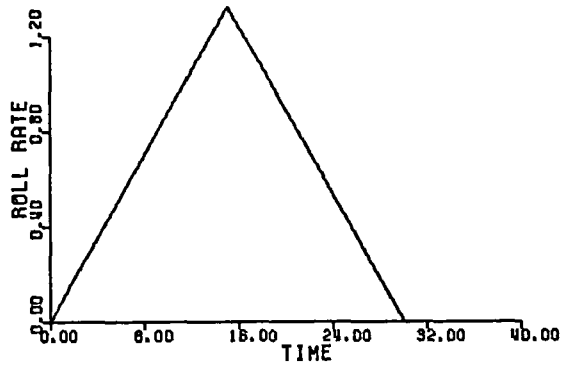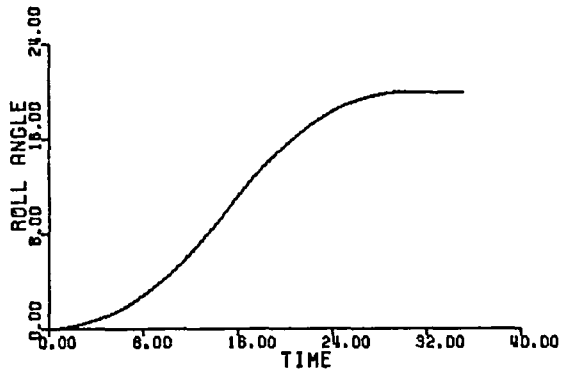
Fig. 3. Roll angle and rate during Roll–Axis BB Slew (Idealized Case).
$t_1 = 15.05 = t_2$, $t_3 = 30.1$.
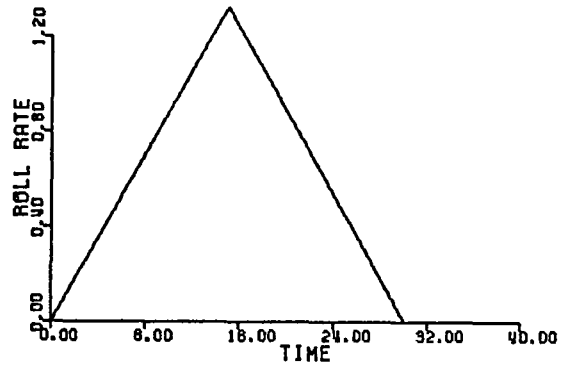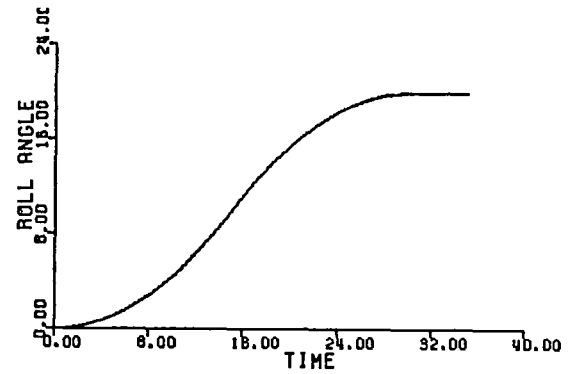
Fig. 4(a). Roll angle and rate during Roll–Axis BB Slew.
$t_1 = 15.038 = t_2$, $t_3 = 30.075$.
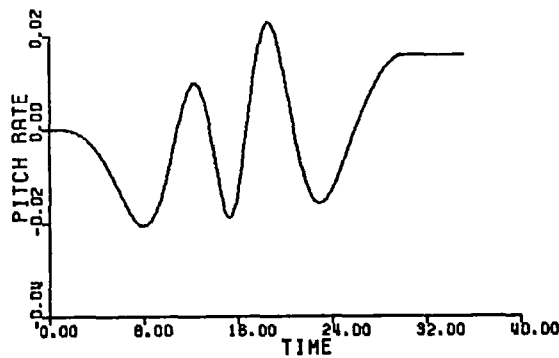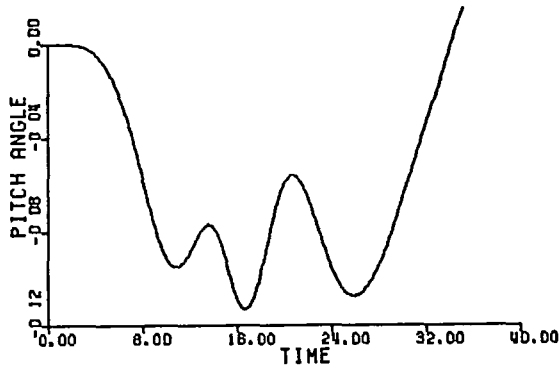
Fig. 4(b). Induced pitch angle and rate during Roll–Axis BB Slew.
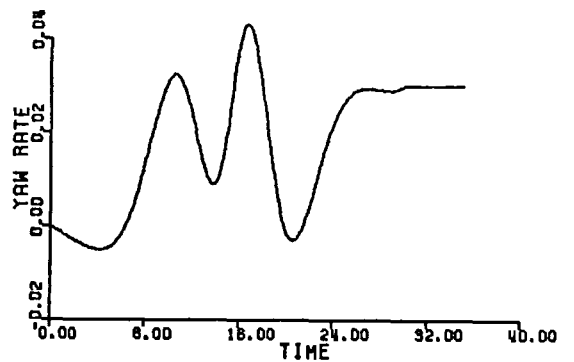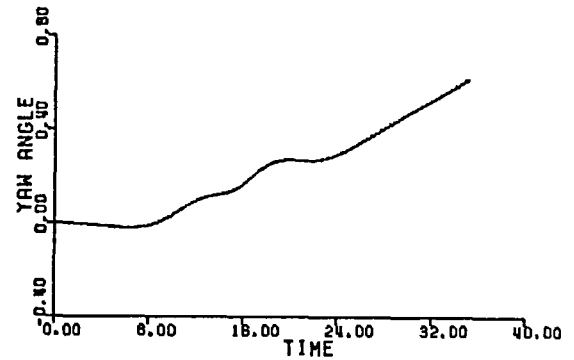
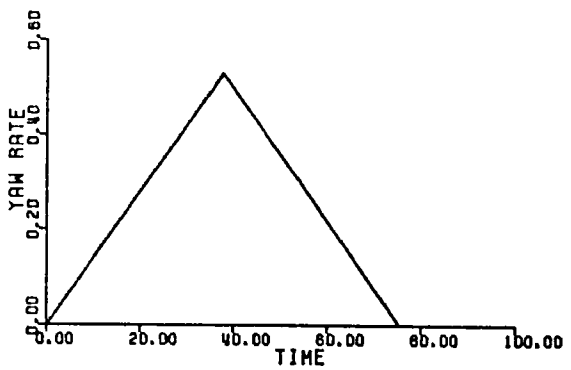Fig. 4(c). Induced yaw angle and rate during Roll–Axis BB Slew.

390
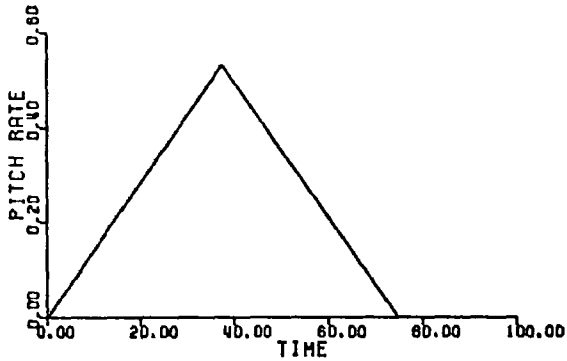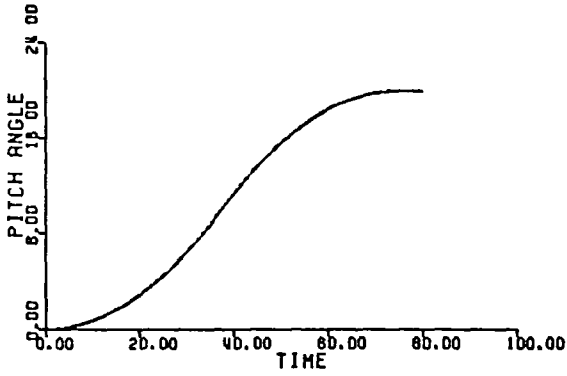
Fig. 5. Pitch angle and rate during Pitch-Axis BB Slew (Idealized Case). $t_1 = 37.436 = t_2$, $t_3 = 74.873$.
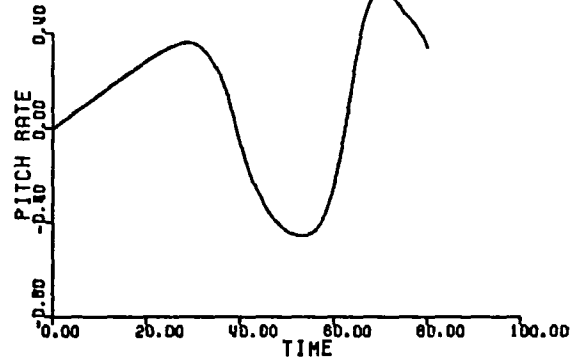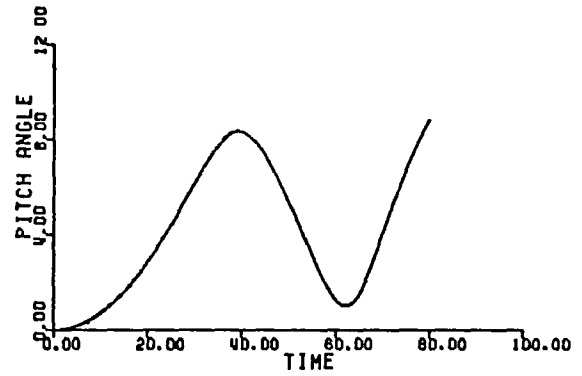
Fig. 6(a). Pitch angle and rate during Pitch-Axis BB Slew. $t_1 = 37.435 = t_2$, $t_3 = 74.871$.
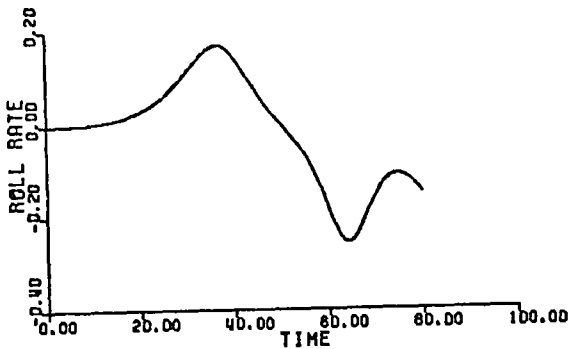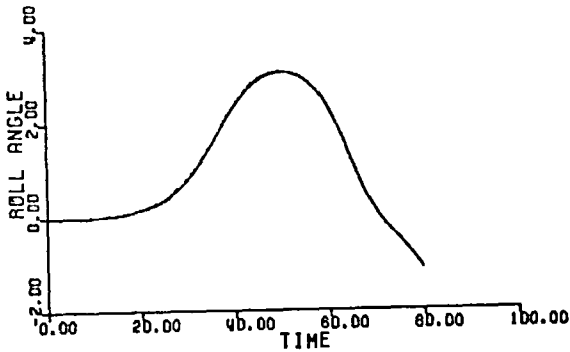
Fig. 6(b). Induced roll angle and rate during Pitch-Axis BB Slew.
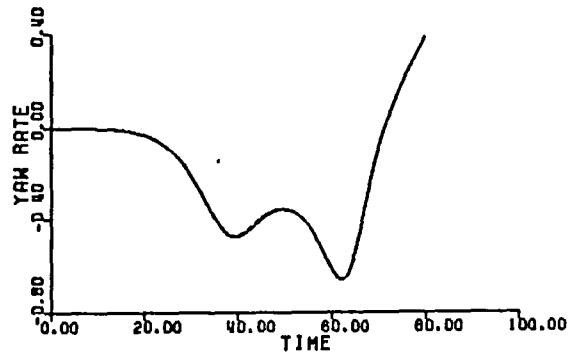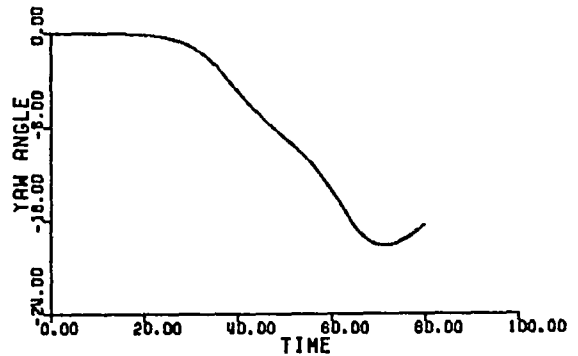
Fig. 6(c). Induced yaw angle and rate during Pitch-Axis BB Slew.

391

slew rate even plunged to a relatively large <u>negative</u>** value (−0.457)! The BB slew rate should always be positive , as in the idealized case.

Fig. 6(b) characterizes the induced rotation about the roll axis. Both the roll angle and rate started to pick up at about the same time when the pitch angle and rate started to decline. The pitch angle increased to peak value of $3.074°$ at about t=50, long after the torques had switched from positive extreme to negative extreme!.

Fig. 6 (c) characterizes the motion induced about the yaw axis. Similarly to the induced roll−axis motion, the induced yaw−axis angle and rate also started to increase at about the same time as the pitch angle and rate started to decline. Quantitatively, the induced yaw motion is much more distinctive and undesirable, however: the yaw angle consistantly decreased from zero to the valley value of $-18.112°$ at t=71.1 (quite before the torque was to be terminated). Ironically, it was the induced yaw slew angle, not the desired pitch slew angle, which increased to a magnitude close to $20°$!

An analysis of the failure in pitch−axis slew maneuvers, some interesting insights, and some useful findings are postponed to next two sections.

Yaw−Axis Slew

Idealized Case. Fig. 7 shows the results of yaw−axis slew maneuver in the idealized case. As before, the results confirmed what would be desired and expected from the design. The desired $20°$ slew was attained at the final time t_3 =75.44. No motions were induced in other axes.

Actual Case. Figs. 8(a)−(c) show the results of yaw−axis slew maneuver in the actual case. Fig. 8(a) shows that the yaw−axis slew performance lies between those of the roll−axis and pitch−axis slew maneuvers. The desired $20°$ slew was not achieved, but the yaw slew angle did consistantly increase towards $20°$ and reached a peak value of $17.482°$ at t=72 before dropping back to $17.372°$ at the final time t_3 =75.376. The yaw slew rate at final time t_3 was **not positive** (−0.067).

There was some induced motion in the roll axis, though Fig. 8(b) shows that it is not very significant. The induced motion in the pitch axis is not ignorable, however. As shown in Fig. 8(c), the pitch angle consistantly increased in the negative direction and reached its valley value of $-7.388°$ at t=58. The induced yaw slew rate at the final time is relatively large: 0.104.

V. ANALYSIS AND DISCUSSIONS

Some reasonable degradation of the slew performance should be expected when evaluating against the actual case, since the design of the time−optimal BB single−axis slew maneuvers was based on practical simplifying assumptions. The roll−axis slew performance should therefore be considered very satisfactory; the yaw−axis slew performance could be considered marginally acceptable, depending on the precision standard used; however, the pitch−axis slew performance could not be considered acceptable in any standard. We were very puzzled. Some indepth theoretical analysis of the SCOLE's dynamics, particularly that of the pitch−axis slew maneuver, later shed some light on the potential causes of the performance degradation. In what follows, we shall briefly describe the analysis and our findings. The focus will be on the pitch−axis slew for an obvious reason, though the same arguments and analysis are also applicable to roll− and yaw−axis slew maneuvers when the appropriate symbolic and quantitative substitution are made.

Since the pitch−axis slew performance was perfect for the idealized case, the degradation in the actual case must be resulted from the coupling with the other axes through the nonlinear Coriolis product $[\omega X] I \omega$ and the nondiagonal inertia matrix I in Eq. (1). And it must be the **presence of nonzero products of inertia**, but not the nonzero differences in moments of inertia, that causes the consequent performance degradation. For, the idealized case did not neglect the Coriolis product at all, and RSCOLE's moments of inertia were all properly taken into account in the usual way; only the products of inertia were set equal to zero. Nonzero products

---

** It is large compared to the peak value of +0.528 in the idealized case; see Fig. 5.
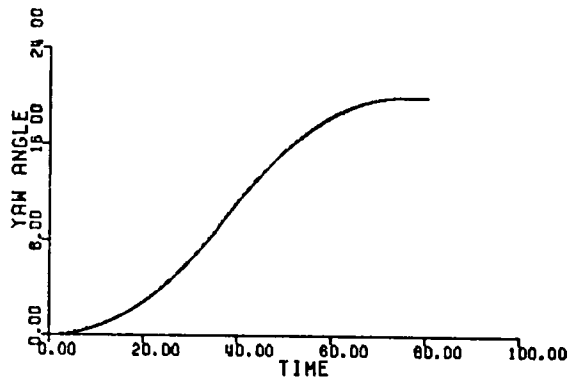
Fig. 7. Yaw angle and rate during Yaw–Axis BB Slew (Idealized Case).
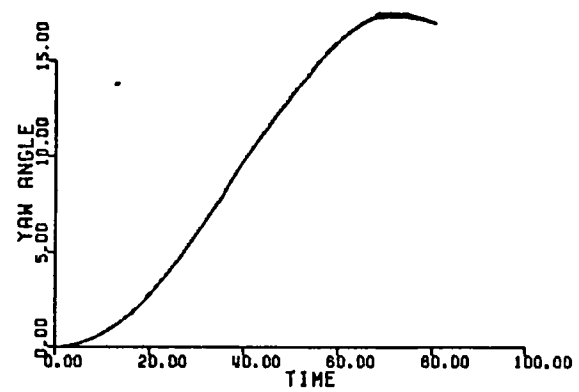$t_1 = 37.72 = t_2$, $t_3 = 75.44$.
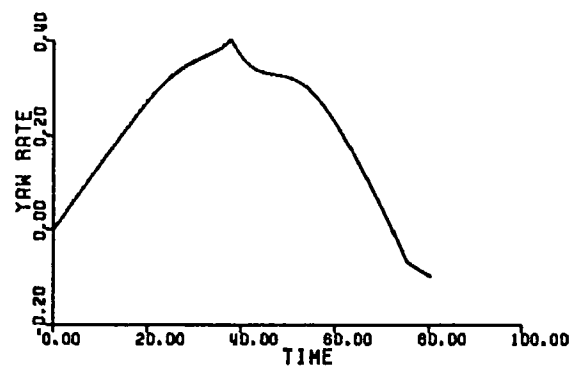
Fig. 8(a). Yaw angle and rate during Yaw–Axis BB Slew.
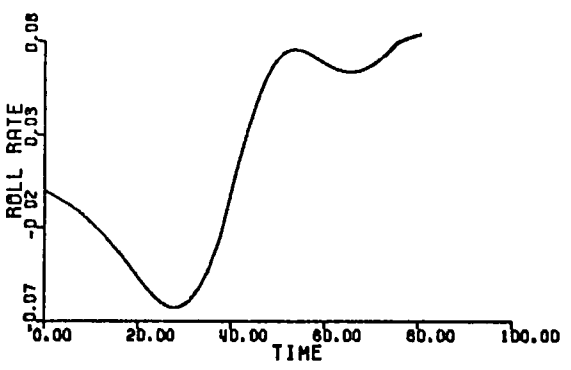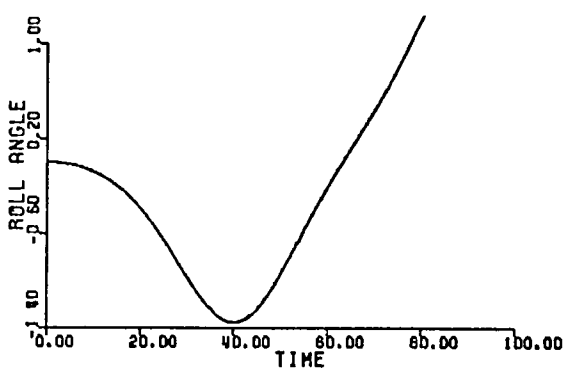$t_1 = 37.688 = t_2$, $t_3 = 75.376$.

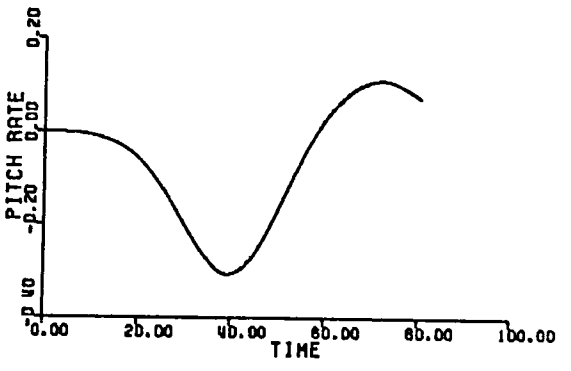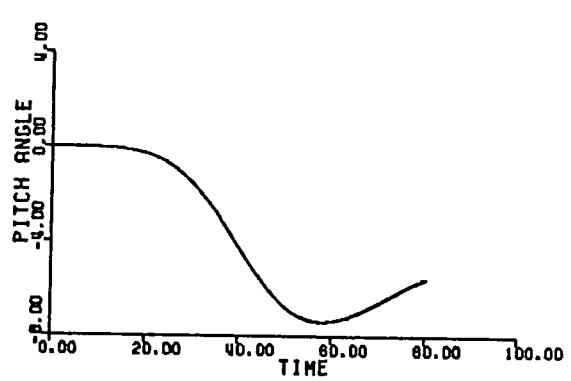Fig. 8(b). Induced roll angle and rate during Yaw–Axis BB Slew.

Fig. 8(c). Induced pitch angle and rate during Yaw–Axis BB Slew.

393

cause the spill of pitch–axis momenta and slew torque, and hence the performance degradation.

To see this and more, expand the 3–axis dynamic equation (1) with $\tau_x = \tau_z = 0$ for both the idealized and the actual cases. First, in the idealized case, we have as usual the following simple system of equations:

$$d_0 \, \dot{\omega}_x = -5.3098 \times 10^{18} \, \omega_y \, \omega_z \tag{16a}$$

$$d_0 \, \dot{\omega}_y = 48.1903 \times 10^{18} \, \omega_x \, \omega_z + 8.0566 \times 10^{12} \, \tau_y \tag{16b}$$

$$d_0 \, \dot{\omega}_z = -46.6234 \times 10^{18} \, \omega_x \, \omega_y \tag{16c}$$

where $\quad d_0 = 56.4563 \times 10^{18}$ (16d)

Now, in the actual case, we get* the following rather complicated system:

$$d_1 \, \dot{\omega}_x = -0.5983 \times 10^{15} \, \omega_x^2 + 2.6128 \times 10^{18} \, \omega_y^2 - 2.6122 \times 10^{18} \, \omega_z^2 + 1.0047 \times 10^{18} \, \omega_x \, \omega_y$$

$$+0.1334 \times 10^{18} \, \omega_x \, \omega_z - 5.4022 \times 10^{18} \, \omega_y \, \omega_z - 4.7722 \times 10^{10} \, \tau_y \tag{17a}$$

$$d_1 \, \dot{\omega}_y = -927.0506 \times 10^{15} \, \omega_x^2 - 2.0547 \times 10^{15} \, \omega_y^2 + 929.1052 \times 10^{15} \, \omega_z^2 - 0.7689 \times 10^{18} \, \omega_x \, \omega_y$$

$$+48.1136 \times 10^{18} \, \omega_x \, \omega_z - 0.0624 \times 10^{18} \, \omega_y \, \omega_z + 8.0433 \times 10^{12} \, \tau_y \tag{17b}$$

$$d_1 \, \dot{\omega}_z = -66.6782 \times 10^{15} \, \omega_x^2 + 102.15 \times 10^{15} \, \omega_y^2 - 35.4718 \times 10^{15} \, \omega_z^2 - 46.5332 \times 10^{18} \, \omega_x \, \omega_y$$

$$-0.7701 \times 10^{18} \, \omega_x \, \omega_z - 1.0006 \times 10^{18} \, \omega_y \, \omega_z + 5.8352 \times 10^{10} \, \tau_y \tag{17c}$$

where $\quad d_1 = 56.3599 \times 10^{18}$ (17d)

Momentum Spillover. Observe that each of the three component equations (17a)–(17c) contains not only the three usual cross–product terms $\omega_x\omega_y$, $\omega_x\omega_z$, and $\omega_y\omega_z$ as in (16a)–(16c), but also three other unusual square terms ω_x^2, ω_y^2, and ω_z^2, all attributable to nonzero products of inertia. And notice, in particular, that the ω_y^2 terms in the two component equations, (17a) and (17c), have extremely large coefficients. Physically, this means that angular momenta (or equivalently, rotational motions) about the pitch axis will <u>spill over to the other two axes</u> and then be <u>picked up there with extreme sensitivity</u>. As a result, even there were no torque applied to the two other axes, significant motions still can be generated indirectly by the torque applied only to the pitch axis. Any terms in (17a) and (17c) containing ω_y can be considered as pickup of pitch–axis momentum spillover.

Also notice that in the second equation, which is responsible for the pitch–axis slew maneuver, both the ω_x^2 and ω_z^2 terms have extremely large coefficients as well. This means that any momenta present in the other axes will be <u>picked up with extreme sensitivity</u>: as a result, the pitch–axis rotation can be severely affected even by small rotations about any of the other two axes.

After having such insights, it is not difficult to visualize that some snowballing effect, similar to a **positive feedback** or a **vicious circle**, can be produced by momentum spillover and pickup through such large square terms. And such an effect can be the reason for the rapid decrease in the pitch–axis motions and the simultaneous rapid increase in the induced roll– and yaw–axis motions.

Indirect Torque Spillover. Equations (17a) and (17c) also indicate that the torque τ_y intended only for the pitch–axis slew also spill over to other axes, each with a fairly large non–negligible influence coefficient. In contrast, (16a) and (16b) indicate that no such spillover exist at all in the idealized case. It is the presence of nonzero products of inertia that creates such indirect spillover of pitch–axis torque. As a result, severe motion will also be induced in the other two axes whenever torque τ_y is applied. Such induced motions and momenta could be fed back to adversely affect the pitch–axis slew maneuvers through the pickup of ω_x^2 and ω_z^2 in the pitch–axis component.

---

* Thanks to the great help of MIT's symbolic manipulation system MACSYMA.

394

In pitch-axis slew maneuver, the combined effect of such momentum and torque spillover is the deviation of the actual pitch-axis angular acceleration from the applied. We thus defined the pitch axis **slew acceleration deviation (SAD)** as an index for pitch-axis slew performance degradation, and calculated it as the percentage of the applied pitch-axis slew acceleration:

$$SAD_y = 100 \; (\alpha_{ya} - \dot{\omega}_y)/\alpha_{ya} \qquad (18a)$$

where α_{ya} denotes the applied y-axis slew acceleration : $\quad \alpha_{ya} = \dfrac{8.0566 \times 10^{12} - I_{xz}^{2}}{d} \; \tau_y \qquad (18b)$

When torque τ_y is zero, SAD is defined to be zero to avoid division by zero. Substituting (17b) along with the nonzero products of inertia in (18), we can easily see that SAD_y represents the combined effect of picking up its own momenta and, in particular, those spilled over from the other two axes through the square or cross-product terms. Specifically,

$$SAD_y = 100 \quad [-927.0506 \times 10^{15} \; \omega_x^{2} - 2.0547 \times 10^{15} \; \omega_y^{2} + 929.1052 \times 10^{15} \; \omega_z^{2}$$

$$-0.7689 \times 10^{18} \; \omega_x \, \omega_y + 48.1136 \times 10^{18} \; \omega_x \, \omega_z - 0.0624 \times 10^{18} \; \omega_y \, \omega_z \;] \; / \; (8.0433 \times 10^{12} \; \tau_y)$$

Trivially and naturally, SAD_y is identically zero for the idealized case. It is interesting to note that, in the actual case, if there are no motions induced through momentum or torque spillover at all, the deviation will also be negligibly small. For example, even at both the top limit of the applied torque and the imposed slew rate limit, i.e., $\tau_y = \tau_{ylm} = 100,000$, and $\omega_y = \omega_{ylm} = 4$, we only have

$$SAD_y = 100 \; \frac{2.0547 \times 10^{15} \; \omega_y^{2}}{8.0433 \times 10^{12} \; \tau_y} = 4.09 \; \% \; !$$

VI. **Further Numerical Results**

Numerical studies on the degradation of the single-axis slew performance were then conducted, with the special attention focused on the actual case of pitch-axis slew. The SAD was computed and plotted for each single-axis slew maneuver mentioned above. Fig. 9(a) shows that the SAD for the roll-axis slew maneuver lies between +0.47% and −0.4%, which is practically negligible. This certainly explains why the roll slew angle and rate were virtually perfect even in the actual case.

Fig. 9(b) shows that the SAD for pitch-axis maneuver started to grow very rapidly after t=22, and reached the peak of +1,003% at t=63, though it plunged from +443% to −445% earlier around the switching time t_1. This also can explain why pitch slew angle and rate never could come close to what were desired.

Fig. 9(c) shows that the SAD for the yaw-axis slew maneuver is still uncomfortably large, though it is not as wild as that for the pitch-axis maneuver, and has a peak value of +88.73%. Such is still a fairly large deviation. This appropriately explains why the yaw slew and rate could not actually attain the desired value, though not extremely far away from it.

In order to pinpoint the specific causes of the performance degradation in the pitch-axis slew maneuver, and specifically, the extremely large slew acceleration deviation, three numerical experiments were conducted: (a) no indirect pitch-axis torque spillover at all; (b) no momentum spillover ω_y^2 to roll or yaw axes; (c) neither the indirect torque spillover nor the momentum spillover ω_y^2.

Fig. 10(a) shows that eliminating the indirect spillover from the applied pitch-axis torque to the other two body axes made no visible improvement. This SAD, as shown by Fig. 10(a), is virtually identical to and equally as bad as before, compared to Fig. 9(b).

Eliminating the pickup of ω_y^2 by the two axes, however, did delay and reduce SAD's growth significantly as shown by Fig. 10(b). There were virtually no visible SAD before the first switching time t_1 =37.43, and the deviation swung only between −150% and +209% now; the peak and valley values are 5 times smaller than
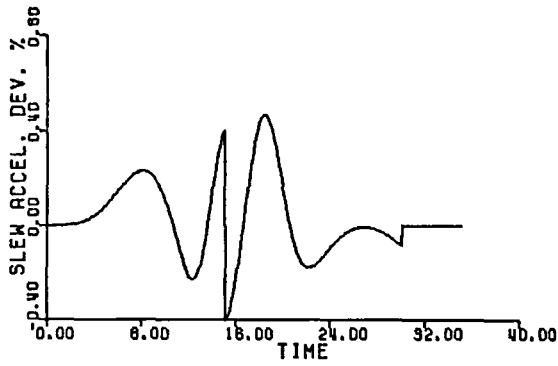
Fig. 9(a). Roll–axis Slew Acceleration Deviation during Roll–Axis BB Slew. $t_1 = 15.038 = t_2$, $t_3 = 30.075$.
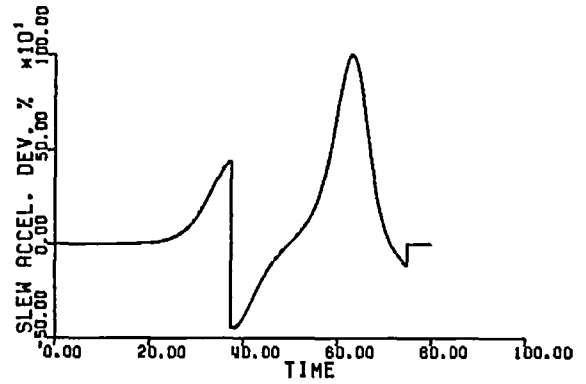

Fig. 9(b). Pitch–axis Slew Acceleration Deviation during Pitch–Axis BB Slew. $t_1 = 37.435 = t_2$, $t_3 = 74.871$.
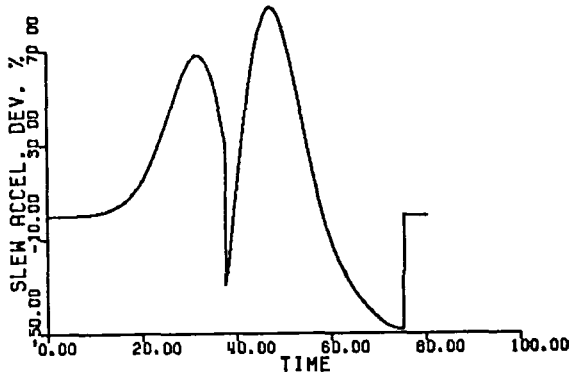

Fig. 9(c). Yaw–axis Slew Acceleration Deviation during Yaw–Axis BB Slew. $t_1 = 37.688 = t_2$, $t_3 = 75.376$.
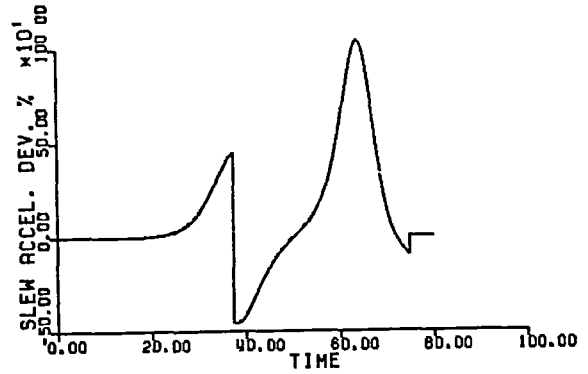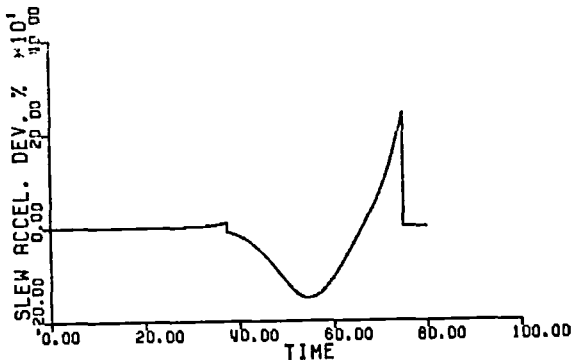

Fig. 10(a). Pitch–axis Slew Acceleration Deviation during Pitch–Axis BB Slew (Experiment a). $t_1 = 37.435 = t_2$, $t_3 = 74.871$.

Fig. 10(b). Pitch–axis Slew Acceleration Deviation during Pitch–Axis BB Slew (Experiment b).
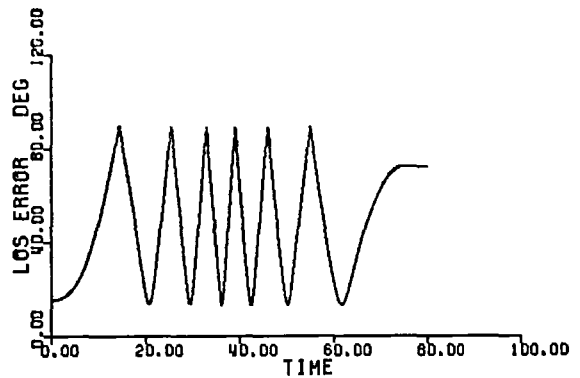
Fig. 10(c). Pitch–axis Slew Acceleration Deviation during Pitch–Axis BB Slew (Experiment c).
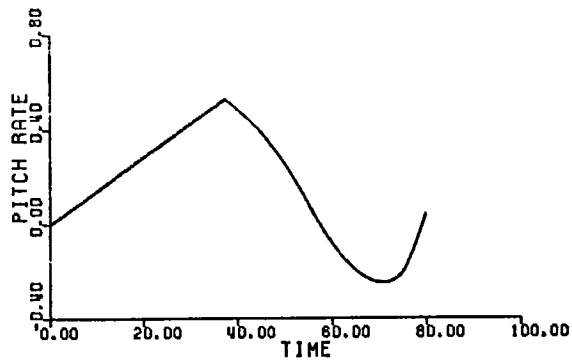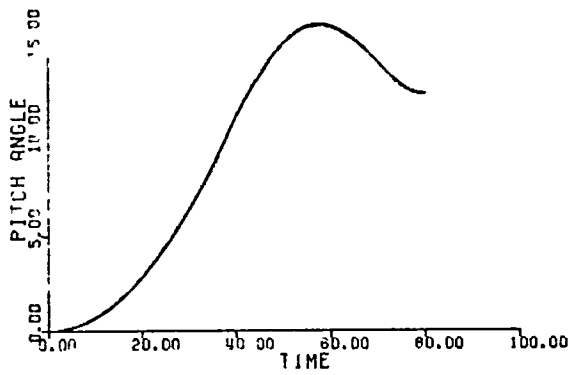
Fig. 11(a). Pitch angle and rate during Pitch-Axis BB Slew (Experiment b).
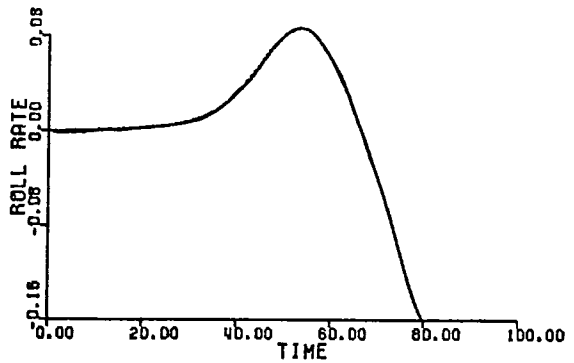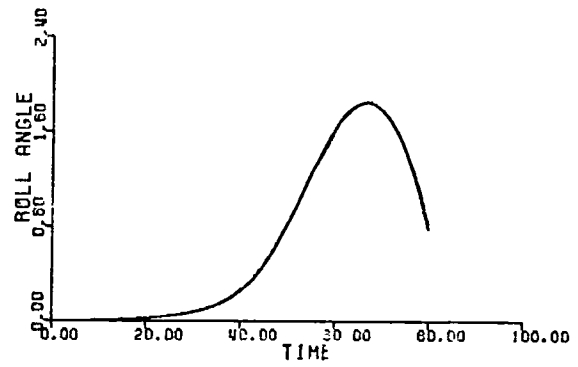
Fig. 11(b). Induced roll angle and rate during Pitch-Axis BB Slew (Experiment b).
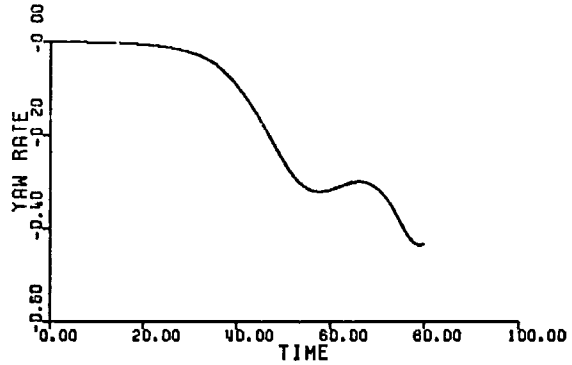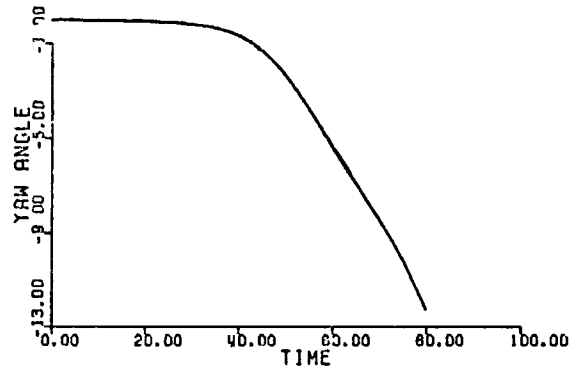
Fig. 11(c). Induced yaw angle and rate during Pitch-Axis BB Slew (Experiment b).
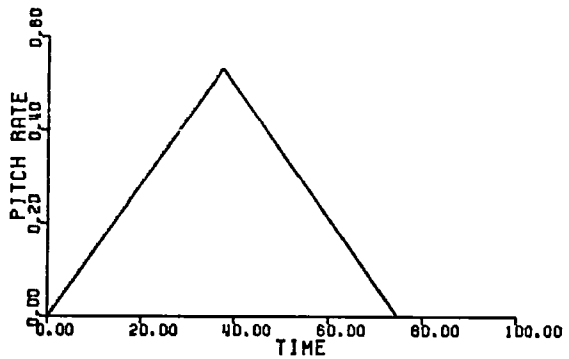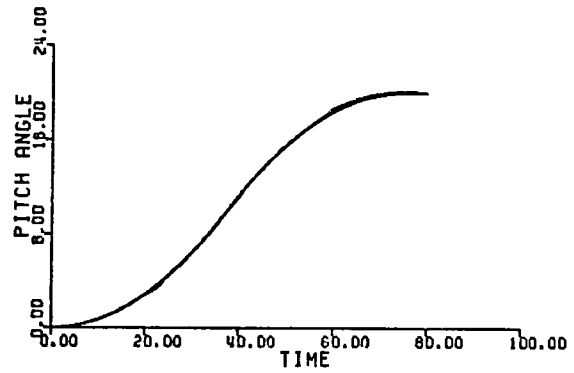
Fig. 12. Pitch angle and rate during Pitch-Axis BB Slew (Experiment c).

before.

The most exciting and dramatic was the experiment with both the torque spillover and the ω_y^2 pickup in the other two axes assumed to have been eliminated. Although all the products of inertia remained nonzero and large as before, the slew performance was virtually identical to the idealized case.* As shown in Fig. 10(c), the maximum and minimum of the SAD were **only +0.07% and −0.07%**, respectively!

As expected from the SAD shown by Fig. 10(a), all the angular motions in Experiment (a) are virtually identical to those shown by Fig. 4(a)–(c). Fig. 11(a) shows that the pitch slew angle in Experiment (b) is now able to continue to increase from 8° to 16° before dropping to 13° at the final time. Fig. 11(b)–(c) show that the induced roll and yaw motion were significantly moderated, as well.

As can be predicated from observing the nearly zero SAD history in Fig. 10(c), all the angular motions in Experiment (c) are practically perfect. The pitch–axis slew motion (Fig. 12) is practically the same as that of the idealized case (Fig. 3). And there were no induced motion in either roll or yaw axes to speak of.

VII. CONCLUSION

Bang–bang control functions (of time) were designed for time–optimal slew maneuvers of RSCOLE about Shuttle's roll–pitch–yaw axes, respectively, under the conditions of limited control torques and minimum time. Such single–axis maneuvers were carefully developed under weaker and more practical assumptions for simplifying RSCOLE's dynamics than an application of the standard bang–bang control theory normally would. The control functions are adjustable with respect to products of inertia, moments of inertia, slew angles desired, slew rate limits, torque magnitude limits, etc., for correct applications to any specific simulation of RSCOLE's dynamics.

Such single–axis slew maneuvers were first applied to an idealized case of RSCOLE, where all products of inertia were assumed to be zero. All performed perfectly as if the idealized 3–axis dynamics were nothing but three completely separate 1–axis dynamics. These single–axis slew maneuvers were then applied to the actual case of RSCOLE, with the parameters for products of inertia in the slew control functions also adapting the RSCOLE's actual large values. The results were mixed: virtually perfect performance in the roll–axis slew, marginally acceptable in the yaw–axis slew, but totally unacceptable in the pitch–axis slew.

Through in–depth analytical studies and the numerical experiments that followed, we found out that the degradation and breakdown of some of the slew performance were resulted from excessive induced motions in the two axes other than the specific slew axis, and that such undesirable induced motions were casused by spillover of either slew momenta or applied torque. These studies and experiments also revealed that both momentum and torque spillover are general properties of RSCOLE's dynamics; any other kind of single–axis control (such as energy–optimal, or heuristic, etc.) will also induce undesired motions and suffer from momentum/torque spillover, so long as independent single–axis control is assumed but not validated.

We found that SAD is a useful true index of slew performance degradation. It represents the combined effect of torque spillover, momentum spillover, and picking up of induced motions by the slew axis. The larger the SAD, the worse the single–axis slew performance. Conversely, independent single–axis slew maneuvers (time–optimal, energy–optimal, or any other kind) are possible if the SADs in the single axes of slew are consistently negligible.

Making all products of inertia zero and all moments of inertia identical is ideal for eliminating SAD. The following are some less ideal but more practical approaches to reduction of SADs.

(a) Lower the magnitude limits of the torques and forces available for slew maneuvers. This essentially to reduce torque spillover directly and momentum spillover indirectly. Obvious consequences are an increase in the

---

* Recall that all the products of inertia were assumed to be zero in the idealized case.

reduce torque spillover directly and momentum spillover indirectly. Obvious consequences are an increase in the minimum time required and a decrease in the average of control energy applied.

(b)   Impose lower (tighter) slew rate limits on the design of single-axis slew maneuvers. The resulting slew maneuvers will likely take the general form of bang-pause-bang control. This is essentially to moderate the average of the control energy applied to RSCOLE, and to elongate the minimum time required.

(c)   Divide the desired slew angles into sufficiently small parts and design the single-axis slew maneuvers to perform for the small parts step by step. The final state of one step must be taken as the initial state of the next step. Consequently, this approach will substantially increase the time required for accomplishing the desired slew angles.

(d)   Use a spillover-reduction synthesizer to reduce the indirect torque spillover and an appropriate nonlinear state feedback to compensate for momentum spillover. Results from the numerical experiments have convincingly demonstrated that eliminating torque spillover to roll and yaw axes, while eliminating even only the momentum spillover ω_y^2 to the other two axes, can reduce the extremely large pitch-axis SAD to virtually zero. This approach will likely increase the complexity of the slew control system but, in contrast with the other approaches above, need not elongate the minimum time required.

A proper combination of these approaches can effectively reduce or restrain SADs to reasonably levels and, hence, render single-axis slew maneuvers feasible. Nevertheless, the fourth approach can be more assuring than any other because it is more active and direct in solving the deviation problem.

ACKNOWLEDGEMENTS

REFERENCES

[1]   L.W. Taylor, Jr., and A.V. Balakrishnan, "A Mathematical Problem and a Spacecraft Control Laboratory Experiment (SCOLE) Used to Evaluate Control Laws for Flexible Spacecraft... NASA/IEEE Design Challenge," presented at Workshop on Identification and Control of Flexible Space Structures, June 4-6, 1984, San Diego, Calif.

EXPERIMENTS IN STRUCTURAL DYNAMICS AND CONTROL USING A GRID

R. C. Montgomery
NASA Langley Research Center
Hampton, VA 23665

Introduction

Future spacecraft are being conceived that are highly flexible and of extreme size. The two features of flexibility and size pose new problems in control system design. Since large scale structures are not testable in ground based facilities, the decision on component placement must be made prior to full-scale tests on the spacecraft. Also, when the control system is placed into operation, it must be done with modelling knowledge less than that required to obtain the best performance. Components must be physically distributed to satisfy maneuver load requirements and for performance monitoring of large scale structures. Also, the current electronics technology supports "smart" control system components wherein the functional description of the component can be programmed by the control system designers. This is a new capability, not previously available, that can influence control system architecture and logic processing ability. Hence, the two questions put forth on the first slide arise and it is the goal of the research program at Langley to provide at least partial answers to the questions.

RESEARCH QUESTIONS

* How should physically distributed components play together on a highly flexible structure?

* How should "smart" components be used? Their logic distributed?

Within the context of a control system that employs physically distributed "smart" sensors and actuators, control law research is also directed at solving problems of inadequate modelling knowledge prior to operation required to achieve peak performance. Another crucial problem addressed is accommodating failures in systems with smart components that are physically distributed on highly flexible structures. Parameter adaptive control is a method of promise that provides on-orbit tuning of the control system to improve performance by upgrading the mathematical model of the spacecraft during operation. Specific questions to be answered are: what limits does on-line parameter identification with realistic sensors and actuators place on the ultimate achievable performance of a system in the highly flexible environment? Also, how well must the mathematical model used in on-board analytic redundancy be known and what are the reasonable expectations for advanced redundancy management schemes in the highly flexible and distributed component environment?

RESEARCH GOALS

Quantify limitations of:

* parameter adaptive control

* analytic redundancy of both sensors and actuators to improve system level reliability

To answer the questions put forth in the last two slides a theoretical/ experimental research activity is in progress. The experimental phase employs a two-dimensional grid structure. The grid is a 7 ft x 10 ft planar structure, made by overlaying aluminum bars of rectangular cross section, suspended by 2 footcables at two locations on the top horizontal bar. The bars are located on 1 foot centers resulting in 8 horizontal and 11 vertical bars.

GRID APPARATUS
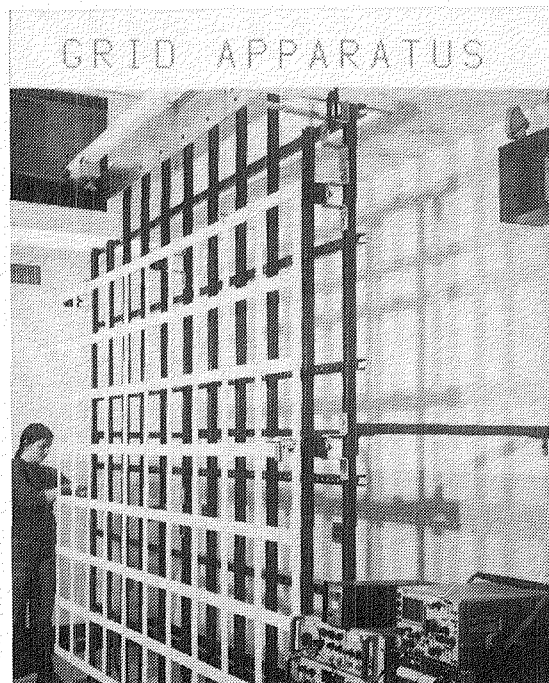
To date, experiments have been conducted to define the dynamics of the grid. An air jet was used to excite the grid at several frequencies impinging on it at point 1, normal to the plane of the grid. For each frequency, the excitation was applied until a 1 inch amplitude was obtained. Then, the excitation was removed and records were made of the output of 9 noncontacting position sensors located at points 1 through 9.

SCHEMATIC OF GRID
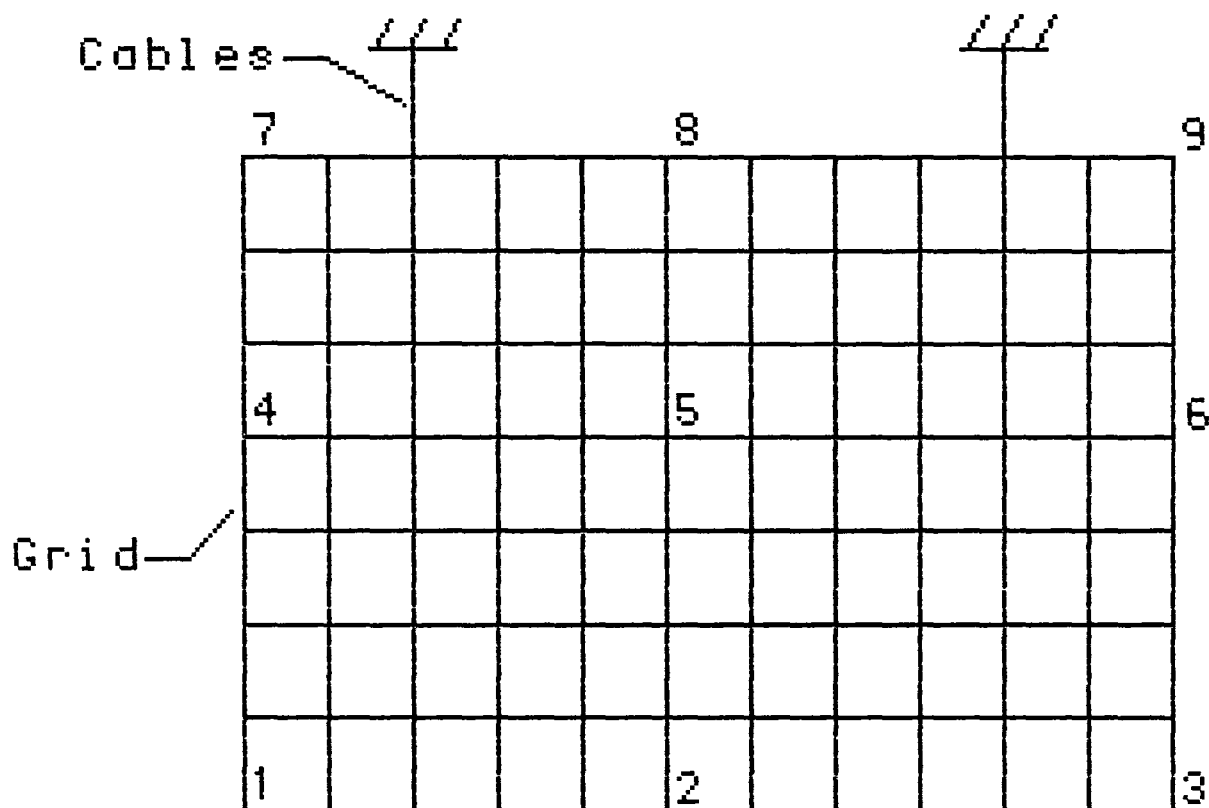
Numbers indicate position sensors

The setup for recording and processing experiment data is shown on this slide. The free-decay response for 5 seconds was recorded in real time using the Control Data Corporation Cyber 175 system. A total of eight runs at different air jet excitation frequencies were made. The data for these runs is currently available on the Langley central computer system for interested researchers to use. The slide indicates the setup currently available to conduct control experiments on the grid. The Electronic Associates Incorporated Pacer/680 hybrid computer is used to generate current commands to torque wheel actuators to be described later in the presentation. Deflection sensors, rate gyros, and accelerometers are used to sense the motion of the grid. These sensors provide inputs to the CDC Cyber 175 system for advanced control law processing and to the EAI system for analog compensation, and optionally, processing control laws that have small computational requirements without tying up the CDC real-time system.

SIGNAL DISTRIBUTION

405
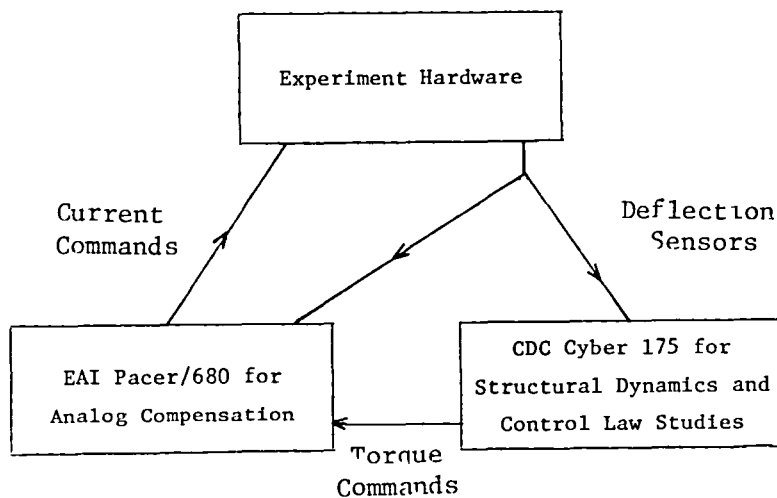
A finite element analysis was made of the grid which resulted in the frequencies shown on the "analysis" row of the slide. For each data tape recorded as described previously, an FFT analysis has been made which produced significant output at the frequencies indicated in the associated "tape" rows of the slide.

GRID FREQUENCIES
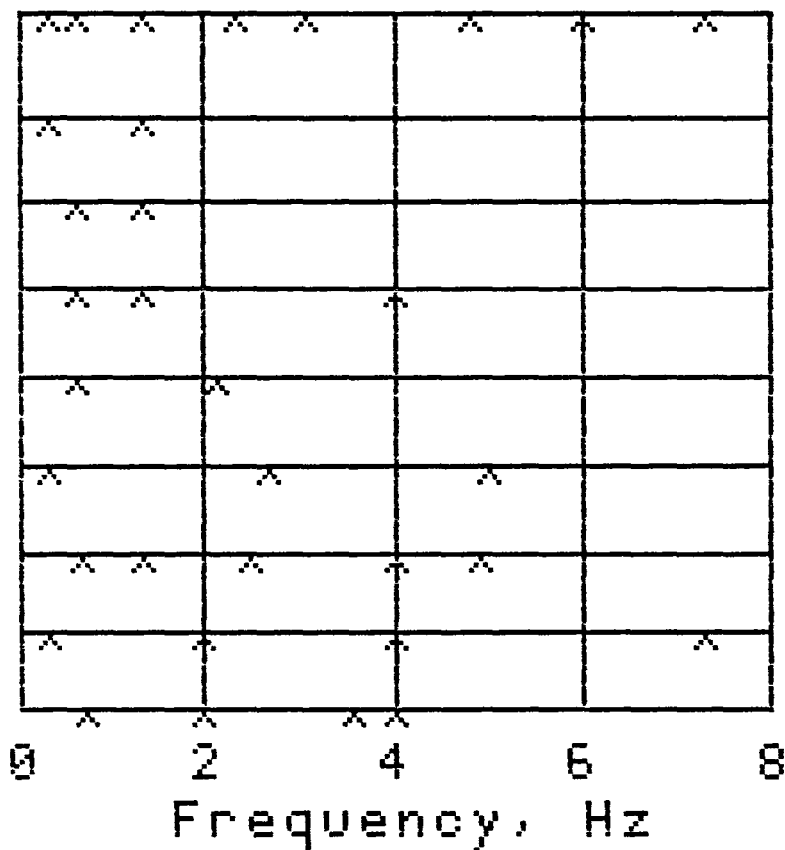
In order to address the issues of distributed "smart" components, "smart" actuators have been designed and will be operated in the configuration shown in the slide. The actuators are designed to produce torque output by reacting against the inertia of a wheel. The torque is produced by motors mounted to the grid. Current is provided by current amplifiers which receive inputs either from the microprocessor shown or from the central processor. Each "smart" actuator has a dedicated microprocessor to effect local closed-loop control. The optical sensor provides the required feedback signal in the form of a square-wave whose frequency is proportional to the angular speed of the wheel. Currently, processor communication is hierarchical with the processors communicating with only the central processor. Plans call for the processors to communicate with each other in a control network as well as with the central processor. This would leave the central processor with the functions of overall system planning, scheduling, and monitoring. The central processor is a Charles River Data Systems processor with a UNOS operating system. Sensors to be used include rate gyros and accelerometers that are grid mounted and interfaced to the central system through analog-to-digital converters. These sensors will be used for performance monitoring and for feedback control. Position sensors are also included in the configuration, interfacing to the central processor, but will be used only for performance evaluation.


"SMART" ACTUATOR
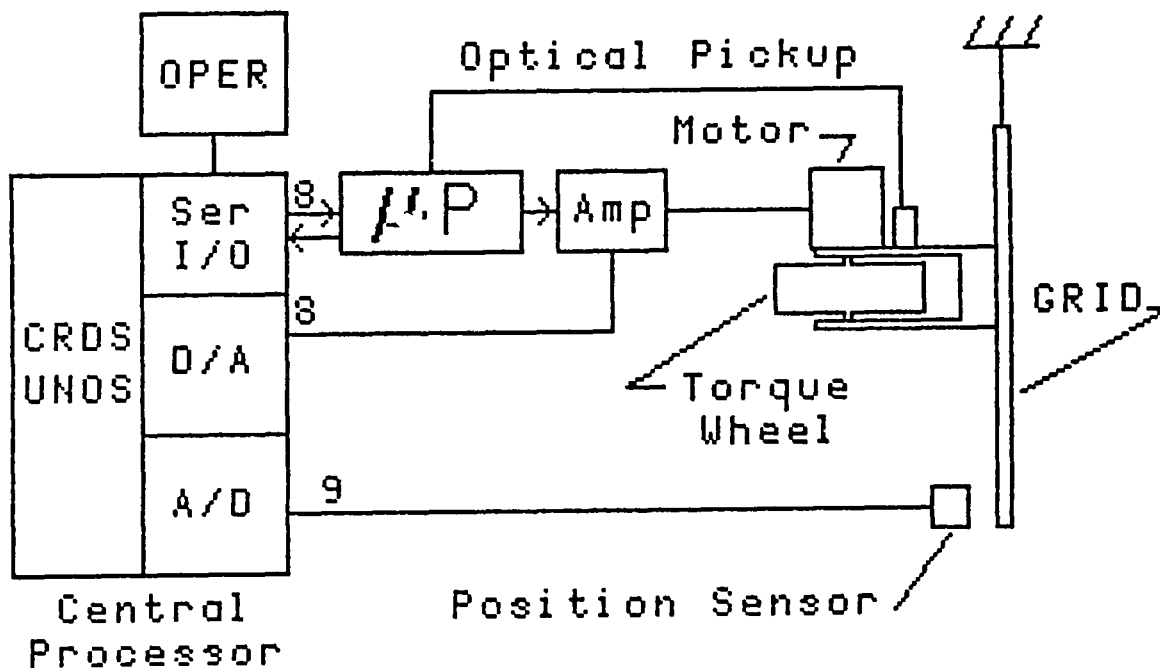
This photograph shows the wheel assembly. Note the pattern on the wheels that is used by the optical sensor to generate the square-wave input to the local wheel processor. The entire assembly weighs 2 lbs and produces 20 oz-in. of torque..
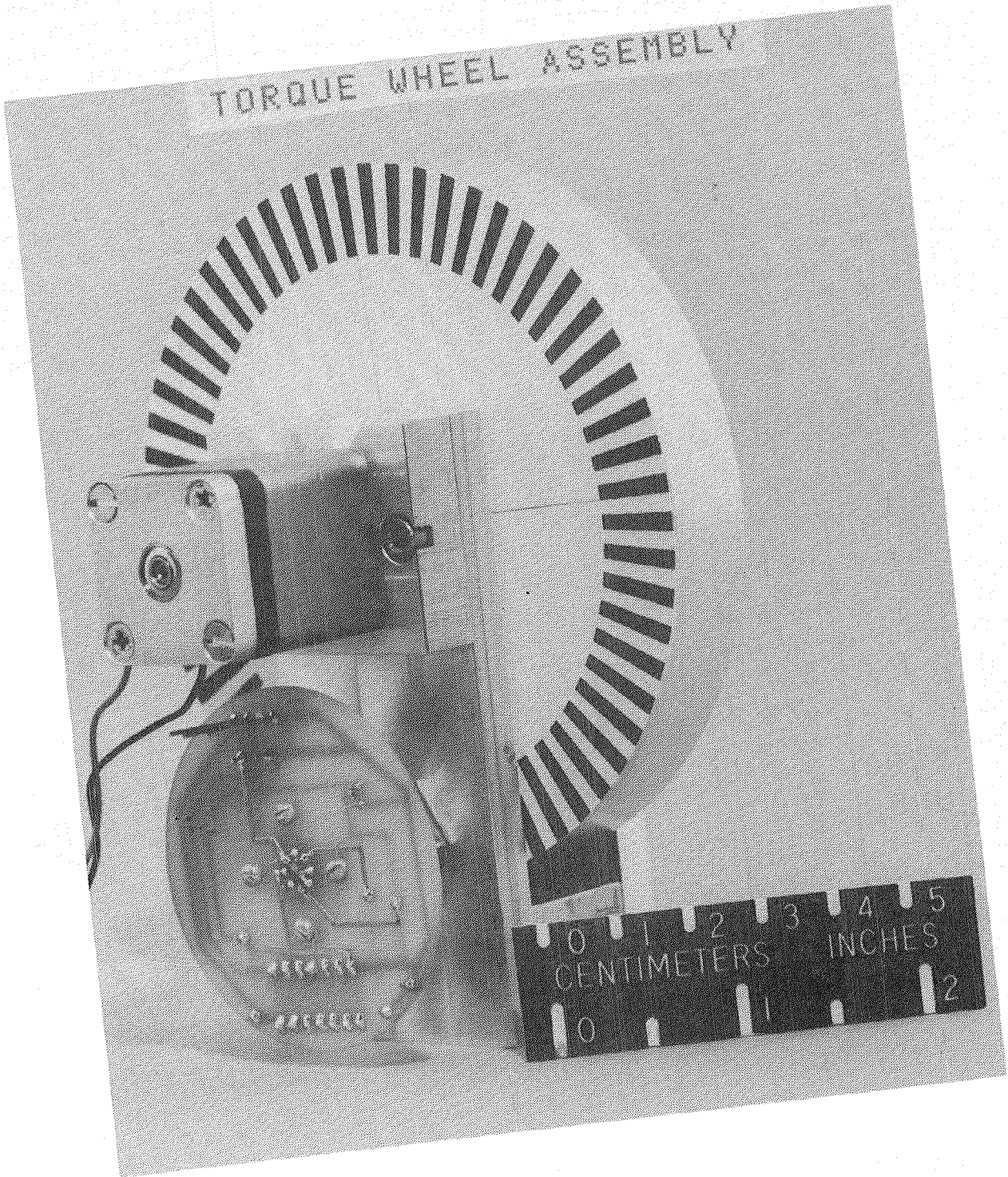
This photograph shows a side view of the wheel assembly. The optical sensor is contained in the threaded casing (lower left portion of the figure).

ASSEMBLY SIDE VIEW
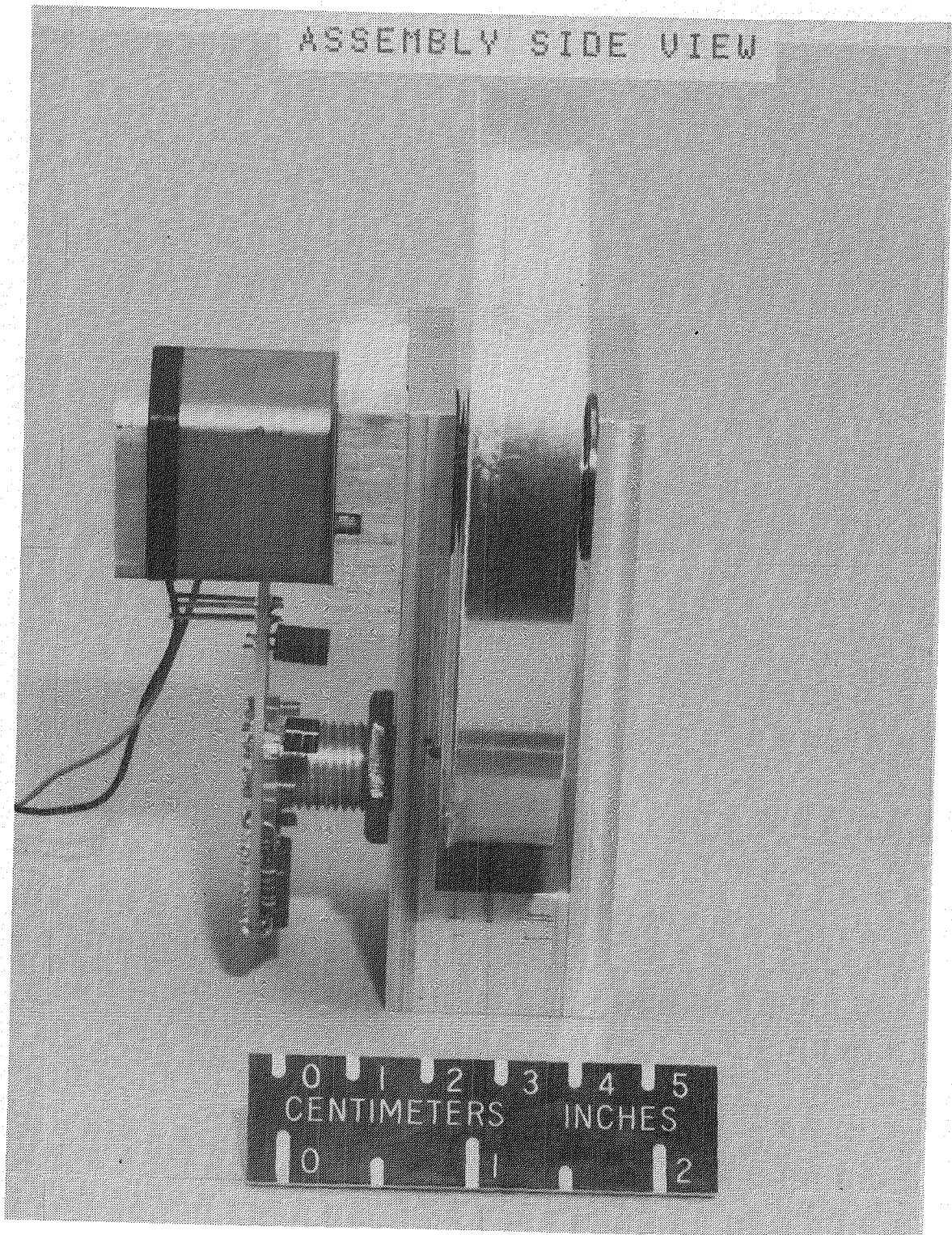
This is a photograph of the local processor and its associated digital-to-analog converter. The processor is an Intel 8051 processor which communicates with the central processor at asynchronous rates of 19,200 BAUD. Synchronous I/O rates of 1 megabit/sec are supported by the processors but are not currently used in the configuration.
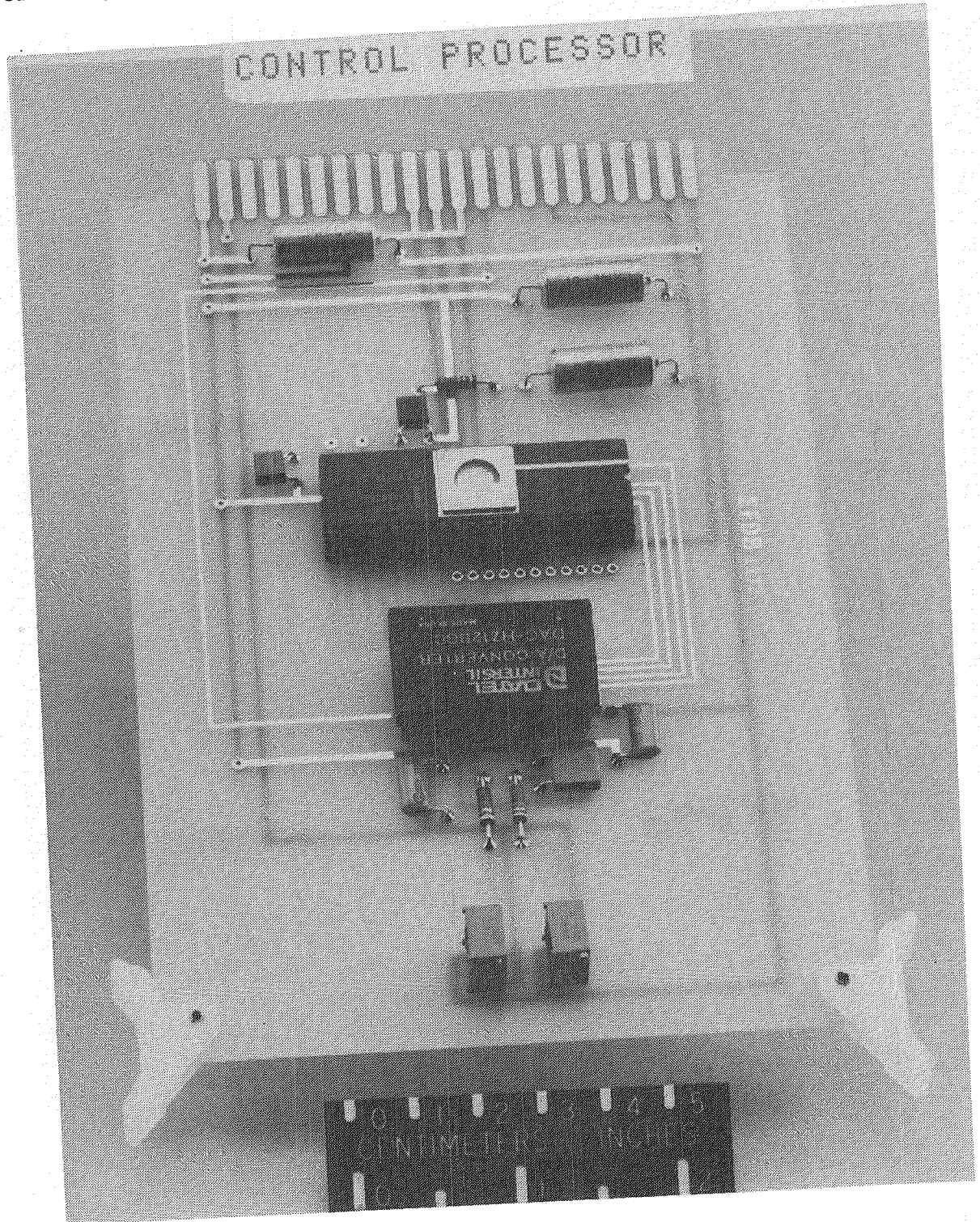
This is a photograph of the power amplifier. Current levels of up to 5 amps are possible with this unit in the operational amplifier current feedback configuration used here.
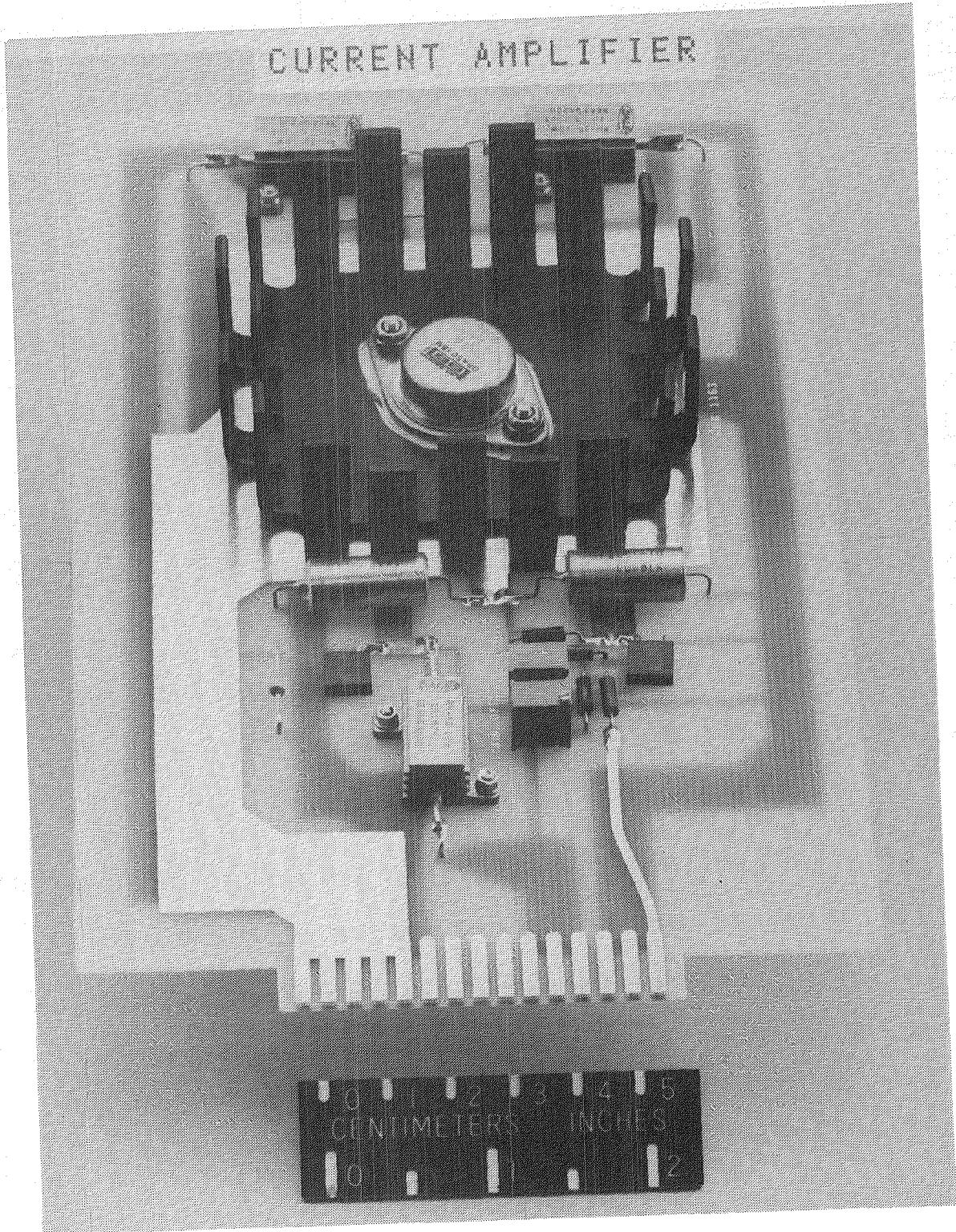
This presentation has been a report on the status of the grid experiment at the Langley Research Center. Also, a summary of experiments made to date has been presented. Currently, the central computer (CRDS) is operational in the system. Software to drive the actuators in the network mode is scheduled for the summer of 1984. Experiments completed to date involve free-decay tests with data reduction by the Least Square Lattice filter method and by the Equivalent Realization Algorithm both of which are included in the proceedings of the 1984 American Control Conference.

EXPERIMENT STATUS

CURRENT GRID HARDWARE:

CRDS system hardware operational

software scheduled summer '84

"Smart" torque wheels available

EXPERIMENTS:

Data tapes on free-decay mode

Impulse response at all 88 nodes

System ID by lattice filter
and by ERA

THE EXPERIMENTAL COMPUTER CONTROL OF A TWO-DIMENSIONAL HYPERBOLIC SYSTEM

Y. Yam
University of California
Los Angeles, CA 90024

J. H. Lang and D. H. Staelin
Massachusetts Institute of Technology
Cambridge, MA 02139

T. L. Johnson
Bolt Beranek and Newman Incorporated
Cambridge, MA 02238

Abstract

The experimental computer control of a two-dimensional hyperbolic system is described. The system consists of a 5-foot gold-coated rubber membrane mounted on a circular cylindrical drum. Seven electrodes reside on a command surface located behind the membrane inside the drum. These electrodes served as capacitive sensors and electrostatic force actuators of transverse membrane deflection. The membrane was modelled as flat, isotropic and uniformly tensioned. Transverse membrane deflections were expanded in normal modes. Controllers regulating membrane deflection are designed using aggregation and design procedures based upon sensor and actuator influence functions. The resulting control laws were implemented on a minicomputer in two sets of experiments. The first set studies modal pole placement and direct regulation of simulated modal noise. The second set investigates the indirect regulation of simulated noise in a residual mode via spillover at different synthesized spillover levels. The experimental study confirms the theoretically predicted behavior of the system, usefulness of the aggregation and design procedures, and the expectation that spillover can be made a beneficial source of damping in residual systems.

I. Introduction

Large, flexible antennas that utilize electrostatic forces for figure control are referred to as Electrostatically Figured Membrane Reflectors (EFMR) [1-3]. The advantages of EFMR lie in their simplicity, inexpensive and low-mass construction, and low surface-tolerance-to-aperture-diameter ratio potentially achievable through the spatially gentle influence functions of their actuators. In their most favorable geometries, EFMR can exhibit Rayleigh-Taylor instabilities. These instabilities can be controlled, however, with only a modest number of control electrodes, yielding a precise, deep-dish reflector. The electrostatic actuators therefore serve both to stabilize the reflector when necessary, and to provide fine-scale figure control.

Controller design for large EFMR space structures is not straight forward. On one hand, a control law of low order and complexity is desired due to limited computing resources. On the other hand, spillover coupling between the control system and degrees of freedom neglected in obtaining the design model for the EFMR may lead to an unacceptable reduction in the stability margin of EFMR deflections. A controller design technique that

413

aggregates a large EFMR model based upon the influence of the sensors and actuators was presented in [4] and [5]. Under certain conditions, this technique produces reduced-order controllers with collocated sensors and actuators which are stabilizing for the overall system. The present work adopts this technique to produce closed-loop controls for a two-dimensional hyperbolic model of an EFMR. The controllers are implemented on a Data General Nova-4 computer.

Experimental control studies involving systems governed by hyperbolic partial differential equations have been reported in [6]-[8]. In [8], Lang and Staelin utilized linear-quadratic-Gaussian controllers applied through nine sensor and actuator pairs to successfully stabilize three open-loop unstable deflection modes of a noisy flexible membrane. The present experimental system has a sensor noise-to-signal ratio of 0.01 to 0.02, and can be open-loop unstable. However, here, it is assumed to be noise free, and is operated in the more manageable open-loop-stable regime in spite of the fact that the controller design technique can readily accomodate unstable systems. The main objective of this work is to verify the anticipated effects of the controller on the system, including the introduction of damping into the spillover modes through nonzero spillover. The experiments also serve to explore the concept of EFMR, and to reveal some of the practical issues concerning computer-based feedback control of distributed systems.

II. System Description

The experimental distributed system is pictured in Figure 1. It consists of a flexible conducting membrane mounted initially without tension on a circular hoop which then slips over a cylindrical drum, thereby stretching the membrane over it. The axial hoop position can be set at eight different locations around its perimeter so as to adjust the membrane tension and profile. The membrane consists of two pieces of 0.9 m by 1.8 m gold-coated gum rubber membranes, glued together to achieve the required dimensions. The seam between the membrane halves is 0.6 cm wide and is not observed to cause any anisotropic membrane dynamics. A command surface, constructed with seven electrodes on cardboard ribs with a figure approximating that of the suspended membrane, is placed inside the cylindrical drum. This command surface structure rests on top of an adjustable tripod stand so that a uniform membrane-command surface separation is obtained. The membrane is oriented so that gravitation forces point normal to the membrane in the direction of the command surface.

The layout and dimensions of the command surface electrodes in polar coordinate are shown with dotted lines in Figure 2. The electrodes serve both as actuators and sensors for the system. As sensors, the electrodes capacitively sense the membrane deflections via a bridge circuit. As actuators, the electrodes are driven by high voltage amplifiers, independently addressable by the computer. The membrane is grounded, producing a transverse electrostatic force between the membrane and command surface which serves as the distributed control. Sensing and actuation can operate simultaneously on any electrodes.

A Data General Nova-4 computer served to support all experiments. At the start of each sampling period the seven capacitance measurements of membrane deflection, spatially averaged over the electrode areas, are recorded serially by the computer. These measurements drive the digital computations

of digital control voltage commands. The commands are then promptly issued serially to registers where they are converted to analog signals that drive the electrode amplifiers. Computation delays was ignored. The sampling period was 4.84 msec.

III. System Dynamics

The equilibrium membrane position arises under the combined influences of gravity and a set of bais voltages on the electrodes. Actual bias voltages, denoted by $V_b(i)$, i=A,....,G, where the index corresponds to the labelling of Figure 2, are applied to the command surface electrodes for several reasons. First, control voltages during experiments are superimposed on these biases, allowing the implementation of negative control voltages. Second, the biases can adjust if necessary for any slight nonuniformity in the equilibrium separation between the membrane and different electrodes. The static bias voltages are $V_b(A)=1.5$ Kv, $V_b(i)=4$ Kv, i=B,....,G.

The membrane dynamics are determined by modelling the membrane as flat, isotropic, and uniformly tensioned. The transverse membrane deflection about its equilibrium, $h(r, \theta, t)$, defined as positive towards the command surface, obeys

$$\rho \frac{\partial^2}{\partial t^2} h(r, \theta, t) = T\frac{1}{r}\frac{\partial}{\partial r} r \frac{\partial}{\partial r} h(r, \theta, t) + T\frac{1}{r^2}\frac{\partial^2}{\partial \theta^2} h(r, \theta, t) - \bar{\beta}\frac{\partial}{\partial t} h(r, \theta, t) + v(r, \theta, t) \tag{1}$$

$$h(R, \theta, t) = \emptyset$$

where $\bar{\beta}$ denotes the coefficient of viscous damping, T denotes the uniform radial and azimuthal tension, and R denotes the radius of the membrane which is 0.762 m. The differential transverse electrostatic surface force density, $v(r, \theta, t)$, is given by

$$v(r, \theta, t) = \frac{\varepsilon_o}{2} \left[\left(\frac{V_B(r, \theta) + u(r, \theta, t)}{H - h(r, \theta, t)} \right)^2 - \left(\frac{V_B(r, \theta)}{H} \right)^2 \right] \tag{2}$$

Here, $u(r, \theta, t)$ denotes the distributed control voltage and $V_B(r, \theta)$ denotes the distributed bias voltage,

$$V_B(r, \theta) = \sum_{i=A}^{G} V_b(i) A_1(r, \theta) \tag{3}$$

where $A_i(r, \theta)$ denotes the influence function of the ith electrode. Equation (2) is linearized with $h(r, \theta, t) \ll H$ and $u(r, \theta, t) \ll V_B(r, \theta)$, and the result is substituted into (1) to yield

$$\rho\frac{\partial^2}{\partial t^2} h(r, \theta, t) = T\frac{1}{r}\frac{\partial}{\partial r} r \frac{\partial}{\partial r} h(r, \theta, t) + T\frac{1}{r^2}\frac{\partial^2}{\partial \theta^2} h(r, \theta, t) - \bar{\beta}\frac{\partial}{\partial t} h(r, \theta, t) + V(r, \theta, t) + U(r, \theta, t) \tag{4}$$

$$h(R, \theta, t) = \emptyset$$

with

415

$$V(r, \theta, t) = \frac{\varepsilon_o \, V_B^2(r, \theta) \, h(r, \theta, t)}{H^3} \tag{5}$$

$$U(r, \theta, t) = \frac{\varepsilon_o \, V_B(r, \theta) \, u(r, \theta, t)}{H^2} \tag{6}$$

Modal decomposition [9] is readily carried out for (4) and yields

$$h(r, \theta, t) = \sum_{m=0}^{\infty} \sum_{n=1}^{\infty} \sum_{q=0}^{1} h_{mnq}(t) \, \psi_{mnq}(r, \theta) \tag{7}$$

where

$$h_{mnq}(t) = \int_0^R \int_0^{2\pi} h(r, \theta, t) \, \psi_{mnq}(r, \theta) \, r \, dr \, d\theta \tag{8}$$

$$\psi_{mnq}(r, \theta) = \lambda_{mnq} \, J_m(\alpha_{mn} r/R) \, \cos(q\pi/2 - m\theta) \tag{9}$$

with $\lambda_{0n} = \pi[R \, J_1(\alpha_{0n})]^{-1}$, and $\lambda_{mn} = \pi/2[R \, J_{m+1}(\alpha_{mn})]^{-1}$ for $m \neq 0$. Here, J_m is the mth order Bessel function of the first kind and α_{mn} is the nth zero of J_m. The eigenfunctions $\psi_{mnq}(r, \theta)$ are orthonormalized. For $m \neq 0$, modes $(m,n,0)$ and $(m,n,1)$ have the same natural frequency, constituting degeneracy. The index q is always zero for $m=0$ case since $\psi_{0n1}(r, \theta) = 0$.

The velocity $\partial/\partial t \, h(r, \theta, t)$ and $U(r, \theta, t)$ are expressed with modal amplitudes $\dot{h}_{mnq}(t)$ and $U_{mnq}(t)$, respectively. Substituting these expressions into (4) yields the following infinite set of finite dimensional modal dynamics

$$\frac{d}{dt} \begin{bmatrix} h_{mnq}(t) \\ \dot{h}_{mnq}(t) \end{bmatrix} = \begin{bmatrix} 0 & 1 \\ -\frac{T}{\rho}\frac{\alpha_{mn}^2}{R^2} + \frac{\varepsilon_o v_o^2}{\rho H^3} & -\frac{\beta}{\rho} \end{bmatrix} \begin{bmatrix} h_{mnq}(t) \\ \dot{h}_{mnq}(t) \end{bmatrix} + \begin{bmatrix} 0 \\ \frac{1}{\rho} \end{bmatrix} U_{mnq}(t) \tag{10}$$

where $V_B(r, \theta)$ is approximated by a uniform bias v_o. For mode $(0,1,0)$ where electrode A was most effective in providing the bias, v_o could be reasonably chosen as 2 Kv. Experimental measurements indicate that $T > 7$ N/m for this mode. Then, with $\alpha_{01} = 2.404$, it followed that $\varepsilon_o v_o^2/(\rho H^3) = 44$ sec^{-2}, a number considerably smaller than $T/\rho(\alpha_{01}/R)^2$ which is greater than 290 sec^{-2}. The same conclusion is reached with greater strength for all other modes. Consequently, the term $V(r,\theta,t)$ was dropped from (4). This means that the electrostatic bias does not affect appreciably the open loop membrane dynamics, in comparison to the bias of gravity, which is estimated to be equivalent to an electrostatic bias of 11 Kv. To support this result, no shifts in modal frequencies were observed experimentally as the bias voltages varied from 0 Kv to 5 Kv. Consequently, the modal dynamics (10) for mode (m,n,q) become

416

$$\frac{d}{dt}\begin{bmatrix} h_{mnq}(t) \\ \dot{h}_{mnq}(t) \end{bmatrix} = \begin{bmatrix} 0 & 1 \\ -\frac{T}{\rho}\frac{\alpha^2_{mn}}{R^2} & -\beta \end{bmatrix}\begin{bmatrix} h_{mnq}(t) \\ \dot{h}_{mnq}(t) \end{bmatrix} + \begin{bmatrix} 0 \\ \frac{1}{\rho} \end{bmatrix} U_{mnq}(t) \tag{11}$$

with $\beta = \bar{\beta}/\rho$. The open loop natural frequency, $\rho^{\pm}_{mnq}$, are given by

$$\rho^{\pm}_{mnq} = -\beta/2 \pm \sqrt{(\beta/2)^2 - T/\rho(\alpha_{mn}/R)^2} \tag{12}$$

The system is open loop stable.

IV. The Actuators

As shown in Figure 3, the actuators comprise a D/A converter, multiplexer, seven sets of sample and hold circuits, and amplifiers connected to each electrode. To issue a control command, the computer issues the address and the corresponding digital actuator command to the multiplexer and D/A converter, respectively. The actuator command ranges from 0 to 4095, and yields a proportional analog signal between 0 and 5 v at the D/A converter output. This analog signal is then directed, via the multiplexer, to the proper sample and hold circuit and then to the amplifier of the addressed electrode. The amplifiers have gains of 1500. The gain of each actuator is 1 Kv to 546 units of digital actuator command, designated here as an "actuator command unit" (acu). The rise time for each amplifiers is 3 ms whereas the characteristic time of membrane deflections is well above 100 ms. The actuator dynamics are ignored. Additionally, the actuator voltages, which are temporally constant over the 4.84 msec sampling period, are approximated as continuous function of time.

Denote the seven independent digital actuator commands by $u_A(t)$ through $u_G(t)$, expressed in acu, where the subscript corresponds to the labelling of Figure 2. The distributed actuator voltage at time t are expressed, in units of Kv, as

$$u(r, \theta, t) = \frac{1}{546}\sum_{i=A}^{G} u_i(t) A_i(r, \theta) \tag{13}$$

Substitution of (3) and (13) into the equilivant of (8) for $U(r, \theta, t)$ of (6) yields

$$U_{mnq}(t) = \frac{1}{546}\frac{\varepsilon_o}{H^2}\sum_{i=A}^{G} \bar{b}_{mnq\ i}\ V_b(i)\ u_i(t) \tag{14}$$

where for $i = A, \ldots, G$,

$$\bar{b}_{mnq\ i} = \int_0^R \int_0^{2\pi} A_i(r, \theta)\ \psi_{mnq}(r, \theta)\ rdrd\theta \tag{15}$$

$A_i(r, \theta)$ is taken as unity when the argument falls within the ith electrode, and is zero otherwise. For simplicity, the actual integration assumes the electrodes to have the layout and dimensions shown by the solid lines in

Figure 2. This simplification does not generate any significant error.

V. The sensor

As shown in Figure 3, the sensors comprise seven bridge circuits, a multiplexer, a signal processor, and an A/D converter. The bridges share a common reference leg to simplify the circuitry and are driven by a 250-KHz sinusoidal input. Their outputs are individually addressable through the multiplexer. The addressed output is rectified, integrated, and converted to digital form. Each electrode measurement is updated every 28 μs. Measurement noise is reduced by averaging five consecutive measurements from the same sensor. To ensure that all transients decay when switching to a new sensor, 140 μs of data are ignored before recording the five measurements.

The output V_i from the ith sensor bridge circuit is given by

$$V_i = V_o \left(\frac{1}{1 - \omega_o^2 L_i (C_i + Cm_i)} - \frac{1}{1 - \omega_o^2 L_r C_r} \right) \sin \omega_o t \qquad (16)$$

where Cm_i, C_i, L_i, C_r, L_r, ω_o, and V_o are as shown in Figure 3. Cm_i denotes the active capacitance contributed by the membrane,

$$Cm_i = \int_0^R \int_0^{2\pi} \frac{\varepsilon_o A_i(r, \theta)}{H - h(r, \theta, t)} r \, dr \, d\theta \qquad (17)$$

Here, The same influence function $A_i(r, \theta)$ is used because the ith sensor and actuator share the same electrode. Rectification of V_i, integration, and A/D conversion yield a digital signal $\bar{y}_i$ proportional to the amplitude of V_i,

$$\bar{y}_i = G_p V_o \left(\frac{1}{1 - \omega_o^2 L_i (C_i + Cm_i)} - \frac{1}{1 - \omega_o^2 L_r C_r} \right) \qquad (18)$$

The units of $\bar{y}_i$ are termed sensor measurement unit (smu). The signal processing gain, G_p, has units of smu/volt. Equation (17) is substituted into (18), and the result is linearized for $h(r, \theta, t) \ll H$ and $2\omega_o^2 L_1 Cm_i \ll (1 - \omega_o^2 L_i C_i)$ to yield

$$\bar{y}_i = \bar{y}^0_i + \frac{\varepsilon_o G_p V_o \omega_o^2 L_i}{H^2 (1 - \omega_o^2 L_i C_i)^2} \int_0^R \int_0^{2\pi} A_i(r, \theta) h(r, \theta, t) r \, dr \, d\theta \qquad (19)$$

where $\bar{y}^0_i$ is the sensor measurement at $h(r, \theta, t) = 0$, and is determined experimentally. The ith sensor measurement is now defined as the differential measurement $y_i = \bar{y}_i - \bar{y}^0_i$. Substitution of (7) into (19) then yields

$$y_i = G_i \bar{\gamma}_s \sum_{m=0}^{\infty} \sum_{n=1}^{\infty} \sum_{q=0}^{1} \bar{b}_{mnq\,i} h_{mnq}(t) \qquad (20)$$

where $G_i = \varepsilon_o \omega_o^2 L_i H / (1 - \omega_o^2 L_i C_i)^2$, $\bar{\gamma}_s = G_p V_o / H^3$, and $\bar{b}_{mnq\,i}$ is as defined in

418

(15). G_i is dimensionless and is the ith sensor gain. $\overline{\gamma}_s$ has units of smu/m^3.

VI. Model Verification and Parameter Identification

Measurements of single-mode step response are the primary means for model verification and parameter indentification. Using the flexibility afforded by seven independent actuators, step responses of seven lower order modes are excited singly. In order of increasing frequency, these seven modes are: (0,1,0), (1,1,0), (1,1,1), (2,1,0), (2,1,1), (0,2,0), and (3,1,0). For convenience, they are referred to as modes 1 through 7. respectively. Similarly, the corresponding $\overline{b}_{mnq\ i}$ are denoted by $\overline{b}_{k1}$, k=1,..,7. From (11), (14), and (20), the system model containing these seven modes is given by

$$\frac{d}{dt}\begin{bmatrix} h_1 \\ \vdots \\ h_7 \\ \dot{h}_1 \\ \vdots \\ \dot{h}_7 \end{bmatrix} = \begin{bmatrix} 0 & & 1 & \\ & \ddots & & \ddots \\ & 0 & & 1 \\ -\omega_1^2 & & -\beta & \\ & \ddots & & \ddots \\ & -\omega_7^2 & & -\beta \end{bmatrix} \begin{bmatrix} h_1 \\ \vdots \\ h_7 \\ \dot{h}_1 \\ \vdots \\ \dot{h}_7 \end{bmatrix} + \frac{0.3048}{546\ H^2}\varepsilon_o\ B \begin{bmatrix} 0 \\ \vdots \\ 0 \\ V_b(A)\ u_A \\ \vdots \\ V_b(G)\ u_G \end{bmatrix}$$

$$y^{(e)} = \begin{bmatrix} y_A \\ \vdots \\ \vdots \\ y_G \end{bmatrix} = \gamma_S \begin{bmatrix} G_A & & \\ & \ddots & \\ & & G_G \end{bmatrix} B^T \begin{bmatrix} h_1 \\ \vdots \\ \vdots \\ h_7 \end{bmatrix}$$

(21)

where $\gamma_S = 0.3048\ \overline{\gamma}_S$, $\omega_i^2 = T/\rho\ (\alpha_{mn}/R)^2$ denotes the squared modal frequency for mode i, and B denotes the 7x7 matrix with entries $b_{ij} = \overline{b}_{ij}/0.3048$ where i=1,....,7, and j=A,....,G. The entries of B are given in the table below.

J i	A	B	C	D	E	F	G
1	1.1333	0.2697	0.2697	0.2697	0.2697	0.2697	0.2697
2	0.0000	0.4237	0.0000	-0.4237	-0.4237	0.0000	0.4237
3	0.0000	0.2446	0.4892	0.2446	-0.2446	-0.4892	-0.2446
4	0.0000	0.2465	-0.4930	0.2465	0.2465	-0.4930	0.2465
5	0.0000	0.4270	0.0000	-0.4270	0.4270	0.0000	-0.4270
6	1.0270	-0.3189	-0.3189	-0.3189	-0.3189	-0.3189	-0.3189
7	0.0000	0.4267	-0.4267	0.4267	-0.4267	0.4267	-0.4267

The relative magnitudes of G_A, ..., G_G are determined experimentally. A uniform voltage step on the electrodes displaces the membrane with axial symmetry. The incremental steady state sensor measurements for electrode B,....,G therefore enable determination of the relative magnitudes of their gains. The displacement over electrode A is not necessarily the same. However, G_A is determined tentatively in just the same way. Rpeated recalculation of the relative gains found them to be temporally stable and insensitive to slight changes in step amplitudes.

The gains are normalized by assigning G_G to have a value of 1. The ratio

between the actual and assigned value of G_G was absorbed into the unknown parameter γ_s . Utilizing not the original input $u^{(e)}=[u_A \ldots u_G]^T$ and measurement $y^{(e)}=[y_A \ldots y_G]^T$, but instead the new input

$$
u^{(m)} = \begin{bmatrix} u_1 \\ \cdot \\ \cdot \\ \cdot \\ u_7 \end{bmatrix} = B \begin{bmatrix} \frac{V_b(A)}{V_b(G)} & & & \\ & 1 & & \\ & & \cdot & \\ & & & 1 \end{bmatrix} u^{(e)} \tag{22}
$$

and measurement

$$
y^{(m)} = \begin{bmatrix} y_1 \\ \cdot \\ \cdot \\ \cdot \\ y_7 \end{bmatrix} = (B^T)^{-1} \begin{bmatrix} G_A & & \\ & \cdot & \\ & & \cdot \\ & & & G_G \end{bmatrix} y^{(e)} \tag{23}
$$

the system model becomes

$$
\frac{d}{dt} \begin{bmatrix} h_1 \\ \cdot \\ \cdot \\ h_7 \\ \dot{h}_1 \\ \cdot \\ \cdot \\ \dot{h}_7 \end{bmatrix} = \begin{bmatrix} \emptyset & & & 1 & & \\ & \cdot & & & \cdot & \\ & & \emptyset & & & 1 \\ -\omega_1^2 & & & -\beta & & \\ & \cdot & & & \cdot & \\ & & -\omega_7^2 & & & -\beta \end{bmatrix} \begin{bmatrix} h_1 \\ \cdot \\ \cdot \\ h_7 \\ \dot{h}_1 \\ \cdot \\ \cdot \\ \dot{h}_7 \end{bmatrix} + \gamma_A \begin{bmatrix} \emptyset \\ \cdot \\ \cdot \\ \emptyset \\ u_1 \\ \cdot \\ \cdot \\ u_7 \end{bmatrix} \tag{24}
$$

$$
y^{(m)} = \gamma_s \begin{bmatrix} h_1 \\ \cdot \\ \cdot \\ \cdot \\ h_7 \end{bmatrix}
$$

where $\gamma_A = 0.3048 \ \varepsilon_o V_b(G)/(546H^2 \rho)$, and $V_b(B)=\ldots=V_b(G)$. γ_A has unit m/acu/sec^2. The model (24), or equivalently (21), is then verified experimentally by letting

$$
u^{(m)} = [\ \overbrace{\emptyset \ldots \emptyset \ 1 \ \emptyset \ldots \emptyset}^{i} \ ]^T \ v(t)
$$

with $v(t)$ a nonzero input voltage, and observing that only the ith measurement of $y^{(m)}$ is nonzero, indicating the excitation of only the ith mode. $u^{(m)}$ and $y^{(m)}$ are termed the modal control input and sensor measurement, respectively. They constrast with $u^{(e)}$ and $y^{(e)}$, which are identified directly with the electrodes. The symbols used in the figures to denote $y_A, \ldots, y_G$, $y_1, \ldots, y_7$, and $u_A, \ldots, u_G$ are as given in the table below.

$y^{(e)}$	y_A	y_B	y_C	y_D	y_E	y_F	y_G
$y^{(m)}$	y_1	y_2	y_3	y_4	y_5	y_6	y_7
$u^{(e)}$	u_A	u_B	u_C	u_D	u_E	u_F	u_G
Symbol	⬓	◉	◀	+	✕	◈	✛

Figure 4 shows the step input $u^{(e)}$ and the step responses of $y^{(e)}$ and $y^{(m)}$ for mode 2. The excitation of mode 2 was clearly demonstrated by $y^{(e)}$: one side of the membrane, characterized by y_B and y_G, have the same response, but opposite to the other side, characterized by y_D and y_E. The nodal line includes y_C, y_F, and y_A. The deflection amplitudes for both sides are approximately the same, a fact obscured in the figure due to the different sensor gains. In addition, $y^{(m)}$ indicates that mode 2 is almost exclusively excited, and that y_1, y_3,....., y_7 are more or less inactive. Similar observations of mode 3, 4, 5, and 7 indicated that (24), hence (21), yields reasonable descriptions for them.

The same is not true for mode 1 and mode 6 which are not excited according to (24). To test whether the ad hoc determination of G_A was responsible, modal experiments utilizing various values for G_A and different electrostatic bias voltages $V_b(i)$ are executed. All fail to excite and sense mode 1 and 6 exclusively. A more elaborate model is required to characterize these two modes accurately.

Table 1 tabulates for the seven modes the characteristic patterns of nodal lines, the measured frequencies, $\omega_i/2\pi$, the product $\gamma_A\gamma_S$, the experimental membrane tension T_e, $T_e = \omega_i^2 (R/\alpha_{mn})^2$, and the theoretical frequencies at T=4.57 N/m. Approximated values were shown for mode 1 and mode 6. β was determined to be 7.4 ± 1 sec^{-1}. The parameters were observed to drift slowly as the membrane aged and were updated before each set of experiments to ensure an accurate model.

VII. Control System Design

An aggregation and control system design technique based upon sensor and actuator influence functions is presented in [4] and [5]. The technique designs a controller which can stabilize an aggregated design model, while simultaneously satisfying control system constraints that guarantee the non-destabilization of the residual plant. Consider the following second-order matrix system with collocated sensor and actuator and displacement measurement,

$$\eta = -\Omega^2 \eta - \beta\dot{\eta} + D_e \eta + B u$$
$$y = \Pi_{CB} B^T \eta$$

(25)

where η is an n_η-vector of modal amplitudes, u is a n_u-vector of control input, y is an n_y-vector of modal deflections, $n_y = n_u$, Π_{CB} is a invertible $n_u \times n_u$ matrix, β is the uniform modal damping coefficient, and $\Omega^2 =$diag$[\omega_1^2 .... \omega_n^2]$, $\omega_i^2 \geq 0$, i=1,...,n_η, are the squared modal frequencies. D_e represents any destabilization forces in the system, and, for convenience, is assumed to take the form $D_e = d I$. The aggregation technique

421

partitions B and constructs the transformation matrix U according to

$$B = \begin{bmatrix} B_a \\ B_r \end{bmatrix} \quad \text{and} \quad U = \begin{bmatrix} B_a{}^T & B_a{}^T S^T \\ -S & I \end{bmatrix}$$

where B_a is a $n_a \times n_a$ matrix, B_r is a $n_r \times n_a$ matrix, with $n_a = n_u$ and $n_r = n_\eta - n_a$, and $S = B_r B_a{}^{-1}$ is the spillover matrix. Defining $\underline{n} = [\underline{n}_a \ \underline{n}_r]^T = U\eta$, (25) is transformed into

$$\begin{bmatrix} \ddot{n}_a \\ \ddot{n}_r \end{bmatrix} = - \begin{bmatrix} \underline{\Omega}^2_{aa} & \underline{\Omega}^2_{ar} \\ \underline{\Omega}^2_{ra} & \underline{\Omega}^2_{rr} \end{bmatrix} \begin{bmatrix} \underline{n}_a \\ \underline{n}_r \end{bmatrix} - \beta \begin{bmatrix} \dot{n}_a \\ \dot{n}_r \end{bmatrix} + d \begin{bmatrix} \underline{n}_a \\ \underline{n}_r \end{bmatrix} + \begin{bmatrix} B^T B \\ \emptyset \end{bmatrix} u$$

$$y = [\ \Pi_{CB} \ \emptyset \ ] \begin{bmatrix} \underline{n}_a \\ \underline{n}_r \end{bmatrix}$$

(26)

where $\underline{n}_a$ is a $n_a \times 1$ vector, $\underline{n}_r$ is a $n_r \times 1$ vector, and $\underline{\Omega}^2 = U\Omega^2 U^{-1}$ is partitioned appropriately. The aggregated design model is

$$\ddot{\underline{n}}_a = - \underline{\Omega}^2_{aa} \underline{n}_a - \beta \dot{n}_a + d \underline{n}_a + B^T B \, u$$

$$y = \Pi_{CB} \underline{n}_a$$

(27)

Let $\omega^2 a_i$ and $\underline{R}_a$ respectively denote the eigenvalues and right eigenvector matrix of $\underline{\Omega}^2_{aa}$ scaled so that $\underline{\Omega}^2_{aa}\underline{R}_a = \underline{R}_a \underline{\Omega}^2_{a}$ and $\underline{R}_a{}^T (B^T B)^{-1} \underline{R}_a = I$, with $\underline{\Omega}^2_a = \text{diag}[\ \omega^2 a_i, \ldots, \omega^2 a_{n_\eta} \ ]$. A controller of the form

$$\dot{z} = F z + G y$$

$$u = H z + K y$$

(28)

can then be constructed with dimension $n_z = n_a = n_u$ and parameters

$$F = - \begin{bmatrix} f_1 & & \\ & \ddots & \\ & & f_{n_z} \end{bmatrix}, f_i > 0 \text{ and real}, \quad G = \begin{bmatrix} g_1 & & \\ & \ddots & \\ & & g_{n_z} \end{bmatrix} \underline{R}_a{}^{-1} \Pi_{CB}$$

$$H = (\underline{R}_a{}^T)^{-1} \begin{bmatrix} g_1 & & \\ & \ddots & \\ & & g_{n_z} \end{bmatrix} \quad , \quad K = -(\underline{R}_a{}^T)^{-1} \begin{bmatrix} k_1 & & \\ & \ddots & \\ & & k_{n_z} \end{bmatrix} \underline{R}_a{}^{-1} \Pi_{CB}{}^{-1}$$

(29)

where, for $i = 1, \ldots, n_z$, $f_i = \tilde{f}_i \ \Delta_i^{1/2}$, $g_i = \tilde{g}_i \ \Delta_i^{3/4}$, $\Delta_i = |d - \omega^2 a_i - k_i|$, and k_i is chosen so that $(d - \omega^2 a_i - k_i) < 0$. The form of (28) and (29) stabilize the reduced order designed model (27), and at the same time guarantee the non-destabilizing of the residual plant. According to [4] and [5], they constitute a stabilizing controller for the overall plant.

VIII. Single-mode Experiments

The first experiments involve only mode 2. The modal inputs for all

other modes were zero. The truncated model is

$$\frac{d}{dt}\begin{bmatrix} h_2 \\ \dot{h}_2 \end{bmatrix} = \begin{bmatrix} \varnothing & 1 \\ -\omega_2^2 & -\beta \end{bmatrix}\begin{bmatrix} h_2 \\ \dot{h}_2 \end{bmatrix} + \begin{bmatrix} \varnothing \\ \gamma_A \end{bmatrix} u$$

$$y_2 = \gamma_S h_2$$

(30)

The individual values of γ_A and γ_S are irrelevant to the experimental outcome and can be assigned any values so long as their product agrees with that experimentally determined. This paper sets $\gamma_A = \gamma_S = (\gamma_A \gamma_S)^{1/2}$. The aggregation technique described in the previous section yield mode 2 as the sole aggregated state. The parameters are $d=\varnothing$, $B=\gamma_A$, $\Pi_{CB} = \gamma_S / \gamma_A$, $\underline{\omega}^2 = \omega_2^2$, and $\underline{R}_a = \gamma_A$. The subscript i of $\underline{\omega}a_i$ is dropped since $n_z = 1$. There is no residual state. The controller parameters, (29), are $F=-f$, $G=g/\gamma_S$, $H=g/\gamma_A$, and $K=-k/\gamma_A\gamma_S$, where $f=\tilde{f}\Delta^{1/2}$, $g=\tilde{g}\Delta^{3/4}$, and $\Delta = |-\omega_2^2 -k|$. With the controller formed as

$$\dot{z} = -f z + (g/\gamma_S)y_2 + \tilde{u}_z$$

$$u_2 = (g/\gamma_A)z - (k/\gamma_A\gamma_S)y_2 + \tilde{u}_2$$

(31)

the composite system becomes

$$\frac{d}{dt}\begin{bmatrix} z \\ h_2 \\ \dot{h}_2 \end{bmatrix} = \begin{bmatrix} -f & g & \varnothing \\ \varnothing & \varnothing & 1 \\ g & -\omega_2^2-k & -\beta \end{bmatrix}\begin{bmatrix} z \\ h_2 \\ \dot{h}_2 \end{bmatrix} + \begin{bmatrix} \tilde{u}_z \\ \varnothing \\ \gamma_A\tilde{u}_2 \end{bmatrix}$$

(32)

where probes $\tilde{u}_z$ and $\tilde{u}_2$ have been added. Denote the eigenvalues and eigenvectors of the complex conjugate mode pair in (32) by ρ and ρ^*, and $\mathcal{R}$ and $\mathcal{R}^*$, respectively, where $\rho = -\delta + i\omega$, $i = \sqrt{-1}$, and

$$\mathcal{R} = i1/2 [g/(\rho+f) \quad 1 \quad \rho]^T$$

(33)

A modal step response for (30) is induced by setting

$$\begin{bmatrix} \tilde{u}_z \\ \varnothing \\ \gamma_A\tilde{u}_2 \end{bmatrix} = (\mathcal{R} + \mathcal{R}^*)$$

or

$$\tilde{u}_z = -\{g \gamma_A/[(f-\delta)^2 + \omega^2]\}v(t)$$

$$\tilde{u}_2 = v(t)$$

(34)

where $v(t)$ is a step input issued at $t=\varnothing$. The first part of this set of experiments therefore involves calculating ρ and $\mathcal{R}$ from (32), issuing the modal step (34) through $\tilde{u}_z$ and $\tilde{u}_2$, and analyszing the step response to obtain

experimental values for   for different values of controller gains. The open loop modal parameters $\omega_2/2\pi$, β , and $\gamma_A\gamma_s$ are determined to be 3.87±0.4 sec^{-1},   13.86±1.5 sec^{-1},   and $(5.1\pm0.3)x10^5$ smu/m^2/acu/sec^2, respectively.

Figure 5 shows the comparison between the experimental and theoretical root locus for ρ. Theory predicts an increase in damping with minimal change in frequency as $\tilde{g}$ is increased, and an increase in frequency with a slight increase in damping as k is increased. The experimental results confirm these theoretical prediction to within an uncertainty of 15%. Modes 1, 3, 4, 5, 6, and 7 were virtually non-excited.

The second part of the single-mode experiments studied noise regulation. $\tilde{u}_z$ is set to zero and $\tilde{u}_2$ is used to issue random commands to the actuators, simulating the existence of noise disturbances. For the jth sampling period, j $\tau\leqslant t<(j+1)\tau$, $\tilde{u}_2=W_j$, where W_j is a set of normally distributed random variables with zero mean and standard deviation N. Natural frequencies of the participating closed loop system (32) are less than 10 Hz during the experiments. The implemented noise was therefore modelled as white, although its high frequency components were filtered out above the actuator bandwidth of approximately 60 Hz.

The steady state covariance matrix of $[z\ h_2\ \dot{h}_2]^T$, denoted by P, obeys the following Lyapunov equation

$$A\ P\ +\ P\ A^T\ =\ -\tau\gamma_A^2\ N^2 \begin{bmatrix} 0 & 0 & 0 \\ 0 & 0 & 0 \\ 0 & 0 & 1 \end{bmatrix} \tag{35}$$

where

$$A\ =\ \begin{bmatrix} -f & g & 0 \\ 0 & 0 & 1 \\ g & -\omega_2^2-k & -\beta \end{bmatrix}$$

Equation (35) is solved analytically. σ_2, the square root of the variance of modal observation $y_2=\gamma_s h_2$, is given as

$$\sigma_2\ =\ \gamma_s[\ \mathscr{E}(h_2^2)]^{1/2}\ =\ \gamma_A\gamma_s N \left[\frac{\tau}{2\beta}\ \frac{[f\ -\ \frac{1}{(f+\beta)}(\frac{g}{f}\ -\omega_2^2\ -\ k)]}{(\omega_2^2\ +\ k\ -\ \frac{g^2}{f})[f\ +\frac{1}{(f+\beta)}(\frac{g^2}{\beta}\ +\omega_2^2\ +\ k)]}\right]^{\frac{1}{2}}$$

σ_2 is well defined only for ($\omega_2^2+k-g^2/f)>0$, which is the condition imposed on the controller to yield a stable A. The experimental counterpart of σ_2, σ_2^E, is taken as the standard deviation of y_2 over a time interval of 1.0648 sec, recorded after the noise-driven closed loop system runs for 4.84 sec, a time sufficiently long to reach steady state. Changes in this delay result in less than a 15% variation for σ_2^E, which is taken as the experimental error. Repeated determination using the same waiting time shows only minor changes in σ_2^E. For these experiments, $\omega_2^2/2\pi=3.76\pm0.4$ sec^{-1}, β =9.2±1.2 sec^{-1}, and $\gamma_A\gamma_s=(5.3\pm0.5)x10^5$ smu/m^2/acu/sec^2. N is 0.366 acu m.

Figure 6 compares σ_2 and σ_2^E for f=0.9, and k=0, 530, and 1060, where $\tilde{g}$ increases from 0.0 to 0.6 or 0.8. Typical experimental and theoretical errors

are shown. The error in σ_2 originates from the errors in identifying $\omega_2^2/2\pi$, β, and $\gamma_A\gamma_S$. σ_2 and σ_5^E agreed to within the uncertainties. Again, other modes are observed to be virtually non-excited.

The single-mode experiments demonstrate the ability to change the membrane dynamics through feedback control and verify the anticipated effect of the controller on the aggregated system. Further, they demonstrate the flexibility of control afforded by those control systems design within the constraints of [4-5] which are used to guarantee the stability of the residual system.

IX. Two-Mode Experiments

This set of experiments investigates the noise regulation of a closed-loop controlled system as a function of spillover. Keeping only mode 2 and mode 5, the system in second order form is

$$
\begin{bmatrix} \ddot{h}_2 \\ \ddot{h}_5 \end{bmatrix} = - \begin{bmatrix} \omega_2^2 & \emptyset \\ \emptyset & \omega_5^2 \end{bmatrix} \begin{bmatrix} h_2 \\ h_5 \end{bmatrix} - \beta \begin{bmatrix} \dot{h}_2 \\ \dot{h}_5 \end{bmatrix} + \gamma_A \begin{bmatrix} u_2 \\ u_5 \end{bmatrix}
$$

$$
\begin{bmatrix} y_2 \\ y_5 \end{bmatrix} = \gamma_S \begin{bmatrix} h_2 \\ h_5 \end{bmatrix}
$$

(36)

Spillover is introduced by synthesizing the input and observation of mode 5 as

$$
u_5 = s\, u_2 + \tilde{u}_5
$$

and (37)

$$
y = y_2 + s\, y_5 = \gamma_S [1 \ s] \begin{bmatrix} h_2 \\ h_5 \end{bmatrix}
$$

With (37), (36) becomes

$$
\begin{bmatrix} \ddot{h}_2 \\ \ddot{h}_5 \end{bmatrix} = - \begin{bmatrix} \omega_2^2 & \emptyset \\ \emptyset & \omega_5^2 \end{bmatrix} \begin{bmatrix} h_2 \\ h_5 \end{bmatrix} - \beta \begin{bmatrix} \dot{h}_2 \\ \dot{h}_5 \end{bmatrix} + \gamma_A \begin{bmatrix} 1 \\ s \end{bmatrix} u_2 + \begin{bmatrix} \emptyset \\ \tilde{u}_5 \end{bmatrix}
$$

$$
y = \gamma_S [1 \ s] \begin{bmatrix} h_2 \\ h_5 \end{bmatrix}
$$

(38)

Setting $\tilde{u}_5 = \emptyset$, (38) is in the form describing a system with one collocated sensor-actuator pair, and with mode 5 acting as the spillover mode to mode 2. The parameter s is the spillover coefficient. Figure 7 shows for $s = \emptyset.\emptyset$, $\emptyset.2$ and $\emptyset.5$ the step responses when probing the synthesized system with a step input of u_2. An increased excitation of mode 5 relative to mode 2 is observed as s is increased. Other modes are virtually non-excited. This demonstrates that synthesized spillover from mode 2 to mode 5 is achieved as predicted by (38).

With $d = \emptyset$, $B = \gamma_A [1 \ S]^T$, and $\Pi_{CB} = \gamma_S/\gamma_A$, the aggregation and control

425

system design technique yield $\underline{\omega}_a^2 = (\omega_2^2 + s^2 \omega_5^2)/(1+s^2)$, $\underline{R}_a = (1+s^2)^{1/2}$, and a controller of the form,

$$\dot{z} = -f z + \{g/[\gamma_S(1+s^2)^{1/2}]\}y$$

$$u_2 = \{g/[\gamma_A(1+s^2)^{1/2}]\}z - \{k/[\gamma_A\gamma_S(1+s^2)]\}y \tag{39}$$

where $f=\tilde{f}\Delta^{1/2}$, $g=\tilde{g}\Delta^{3/4}$, and $\Delta = |-\underline{\omega}_a^2 - k|$.

The controller (39) is implemented for (38) with $\tilde{u}_5$ actually used to simulate a modal noise drive of mode 5, that is, $\tilde{u}_5 = W_j$ for $j\tau \leqslant t < (j+1)\tau$. Again, treating the noise as white, the root mean variances of y_2 and y_5, designated by σ_2 and σ_5, are calculated from the corresponding Lyapunov equation. Similarly, the counterparts of σ_2 and σ_5, σ_2^E and σ_5^E, are taken as the standard deviations of y_2 and y_5 over a time interval of 1.0648 sec, recorded after a waiting period of 7.26 sec. The parameters $\omega_2/2\pi$, $\omega_5/2\pi$, β, and $_5\gamma_S\gamma_A$ are 3.77±0.2 sec^{-1}, 4.66±0.1 sec^{-1}, 9.6±1 sec^{-1}, and $(6.0\pm0.4)\times10^5$ smu/m^2/acu/sec^2, respectively. N is 0.55 acu m.

Figures 8 and 9 compare σ_5 with σ_5^E, and σ_2 with σ_2^E, respectively, for $\tilde{f}=0.9$, $k=1200$, and different values of $\tilde{g}$ and s. They reveal the gradual regulation of modal noise in mode 5 and enhancement of modal noise in mode 2 as s takes on larger values and induces more coupling between the two modes. Typical experimental and theoretical uncertainties are estimated as described before in Section VIII. The reasons for the apparently larger discrepancy between σ_2 and σ_2^E include unmodelled noise sources in the system and additional spillover coupling between modes 2 and 5 due to inadequate modelling. These effects are dominated by the larger σ_5 in Figure 8.

The present set of experiments are important for several reasons. First, these experiments confirm the anticipated effect of the controller in actually damping and stabilizing the residual system through nonzero spillover. Thus, spillover need not always be minimized. Second, these experiments confirm the usefulness of the aggregation and controller designed techniques developed in [4-5]. In particular, the guaranteed non-destabilization of the residual system through adherence to controller design constraints is apparent in these experiments.

X. Conclusion

The experimental computer control of a two-dimensional hyperbolic system are reported. The system consists of a five-foot diameter gold-coated rubber membrane stretched over a circular cylindrical drum with seven electrodes acting both as capacitive sensors and electrostatic force actuators. The electrodes reside on a command surface located behind the membrane inside the drum. The experiment simulates a electrostatically figured membrane reflector (EFMR). The membrane is modelled as flat, isotropic, and uniformly tensioned. Closed-loop controllers, obtained according to the aggregation and control system design technique based upon sensor and actuator influence functions [4-5], are implemented via a Data General NOVA-4 computer. These techniques are designed to guarantee the stability of both the aggregated and residual systems during closed-loop control by controllers based only on the aggregated system.

Two set of experiments are described. The first involves only one mode

and studies the modal pole placement and noise regulation at different controller gains. It demonstrates the ability to change the membrane dynamics through feedback control and verifies the anticipated effect of the controller on the aggregated system. The flexibility of control afforded by controllers designed to guarantee stability of the residual system through control system constraints [4-5] is also demonstrated. The second set of experiments involves two modes. The input and observation of one mode are synthesized so that it acts as a spillover mode to the other. The regulation of noise in the spillover mode as a function of synthesized spillover is investigated. This set of experiments confirms the expectation that spillover can be made a beneficial source of damping in residual systems and so spillover need not always be minimized. It also demonstrates the usefulness of the aggregation and control system design techniques developed in [4-5]. Overall speaking, both set of experiments confirm the theoretical predictions to within reasonable experimental uncertainty. Finally, these experiments add credibility to the EFMR concept and help demonstrate the computer-based control technology required by the concept.

Acknowledgement

References

1. Lang, J.H., Gersh, J.R. and Staelin, D.H., "Electrostatically Controlled Wire-Mesh Antenna," Electronic Letters, Vol. 14, No. 20, pp. 655-656, September 1978.
2. Mihora, D.J. and Redmond, P.J., "Electrostatically Formed Antennas," Internal Memorandum 2222, General Research Corporation, Santa Barbara, CA, March 1979.
3. Lang, J.H. and Staelin, D.H., "Electrostatically Figured Reflecting Membrane Antennas for Satellites," IEEE Transactions on Automatic Control, Vol. 27, No. 3, June 1982, pp. 666-670.
4. Yam, Y., Lang, J.H., Johnson, T.L., Shih, S., and Staelin, D.H., "Large Space Structure Model Reduction and Control System Design Based Upon Actuator and Sensor Influence Functions," Proceedings of the Workshop on Applications of Distributed   System Theory to the Control of Large Space Structures, Pasadena, CA, July 14-16, 1982.
5. Yam, Y., "large Space Structure Model Reduction and Control System Design based upon Sensor and Actuator Influence Functions," Sc.D. dissertation, Department of Aeronautics and Astronautics, Massachusetts Institute of Technology, Cambridge, Massachusetts 02139, 1983.
6. Melcher, J.R. and Warren, E.P., "Continuum Feedback Control of a

Rayleigh-Taylor Type Instability," The Physics of Fluids, Vol. 9, No. 11, pp. 2085-2094, November 1966.

7. Breakwell, J.A. and Chambers, G.J., "The Toysat Structural Control Experiment," Proceedings of the Workshop on Applications of Distributed System Theory to the Control of Large Space Structures, Pasadena, CA, July 14-16, 1982.

8. Lang, J.H. and Staelin, D.H., "The Computer-Controlled Stabilization of a Noisy Two-Dimensional Hyperbolic System," IEEE Transactions on Automatic Control, Vol. 27, No. 5, October 1982, PP. 1033-1043.

9. Butkov, E., Mathematical Physics, Addison-Wesley Publishing Company, Inc., 1968.

Figure 1:
Construction details of the experimental system.
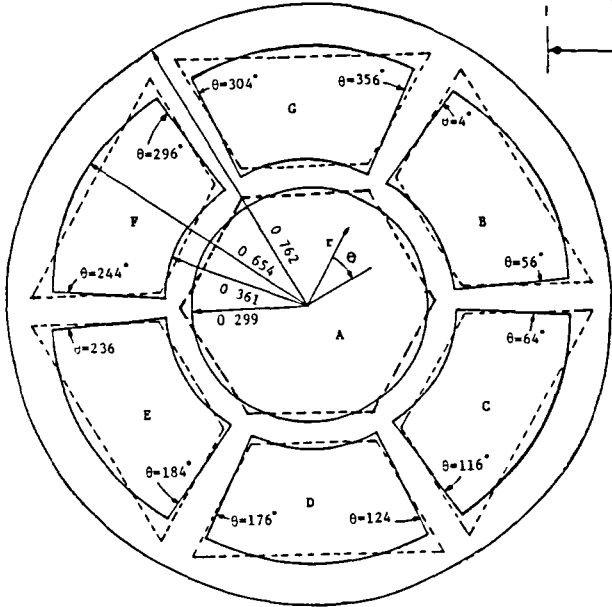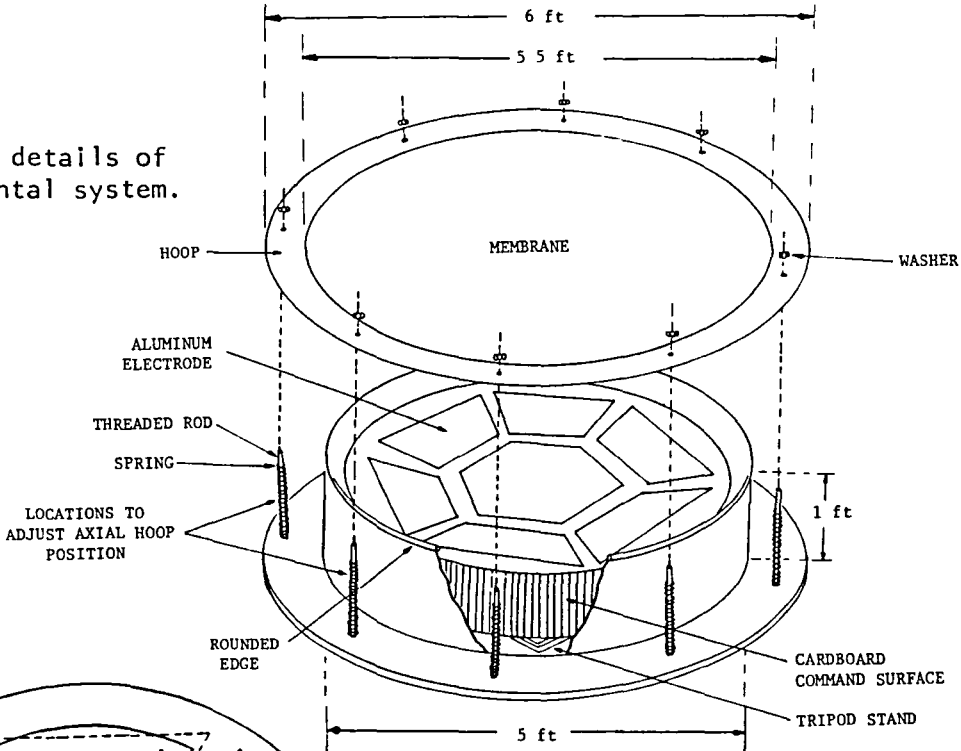
Figure 2:
Exact and approximate electrode layout and dimensions in polar coordinate. Radial dimensions are in meters.

NUMBER OF DATA POINTS = 235
ONE SYMBOL IS PLOTTED FOR EVERY 20 DATA POINTS
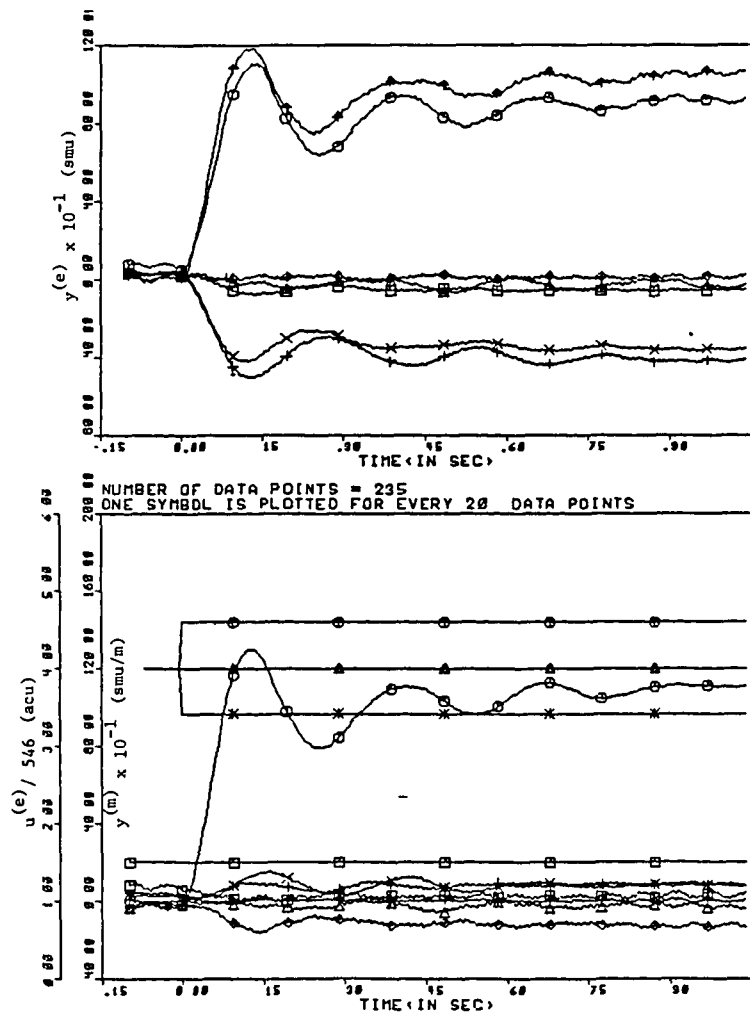
Figure 4: Modal step response of mode 2.

V_o=amplitude
ω_o=250 KHz SINE
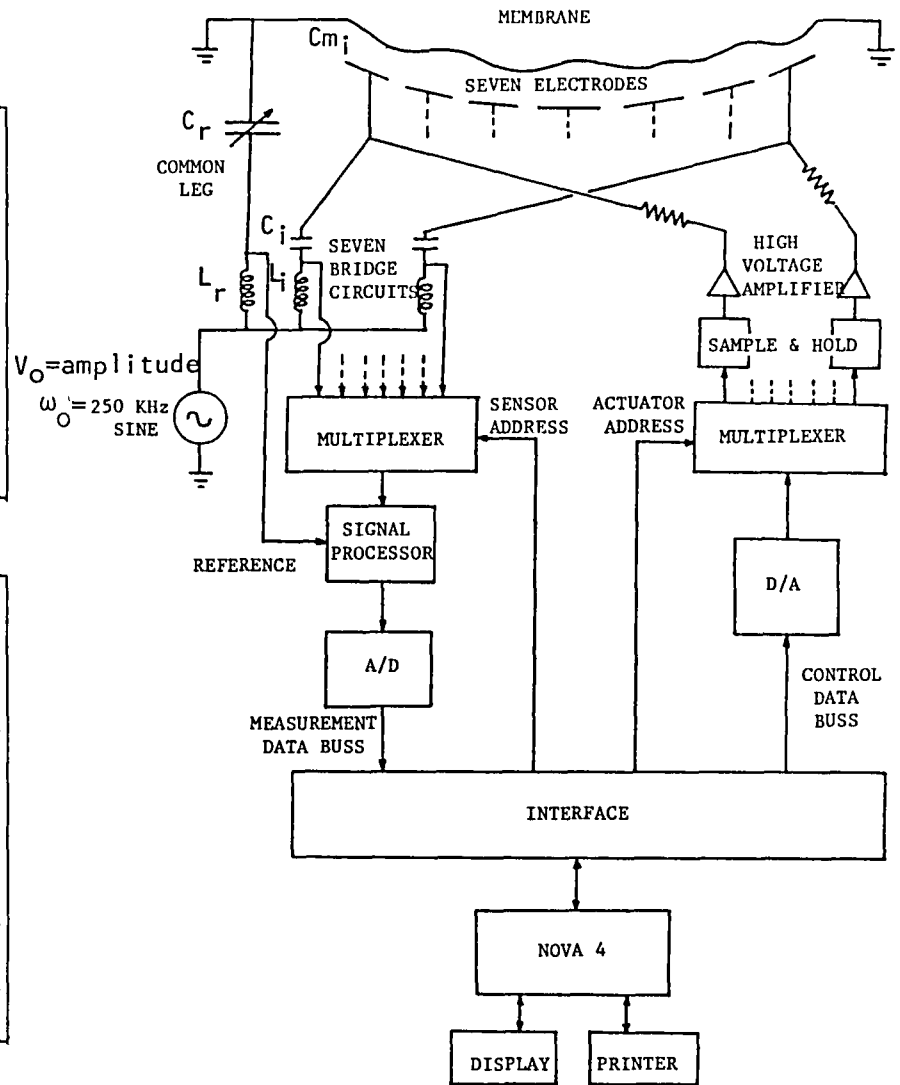
Figure 3: A functional diagram of the membrane reflector control experiment.

Figure 5: Comparison between experimental and theoretical pole locations.
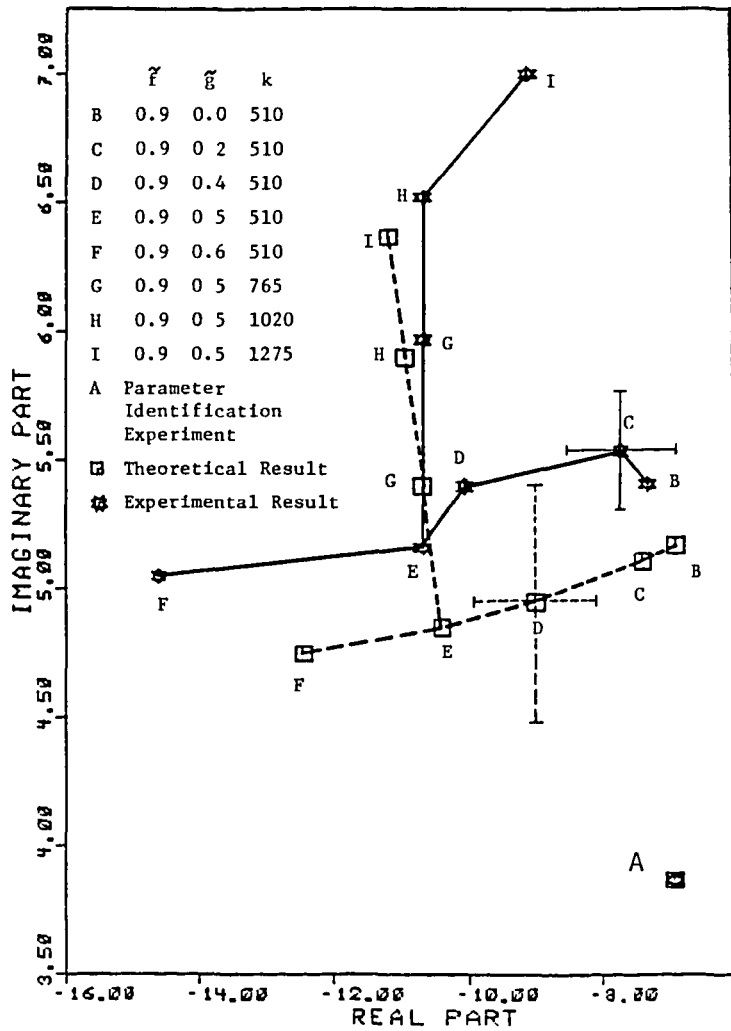
mode number	$\frac{\omega_1}{2\pi}$ (sec^{-1})	$\gamma_A \gamma_S \times 10^5$ (smu/m^2/acu/sec^2)	Experimental Te (N/m)	Theoretical $\frac{\omega_1}{2\pi}$ with T=4 57 N/m (sec^{-1})
1	3 02 ± 0 6		8 67 ± 0.4	2 19
2	3 84 ± 0 4	2 72 ± 0 26	5 52 ± 1 2	3 49
3.	3 72 ± 0 4	2.50 ± 0 24	5 18 ± 1 2	3 49
4	4 61 ± 0 4	3 60 ± 0 5	4.43 ± 0 8	4 68
5.	4 60 ± 0 4	3 60 ± 0 5	4 41 ± 0 8	4 68
6	4 39 ± 0 2		3 84 ± 0 4	5 03
7	5 17 ± 0 15	3 ± 0 4	3 61 ± 0 3	5 81

Table 1: Results from model verification and parameters identification experiments.
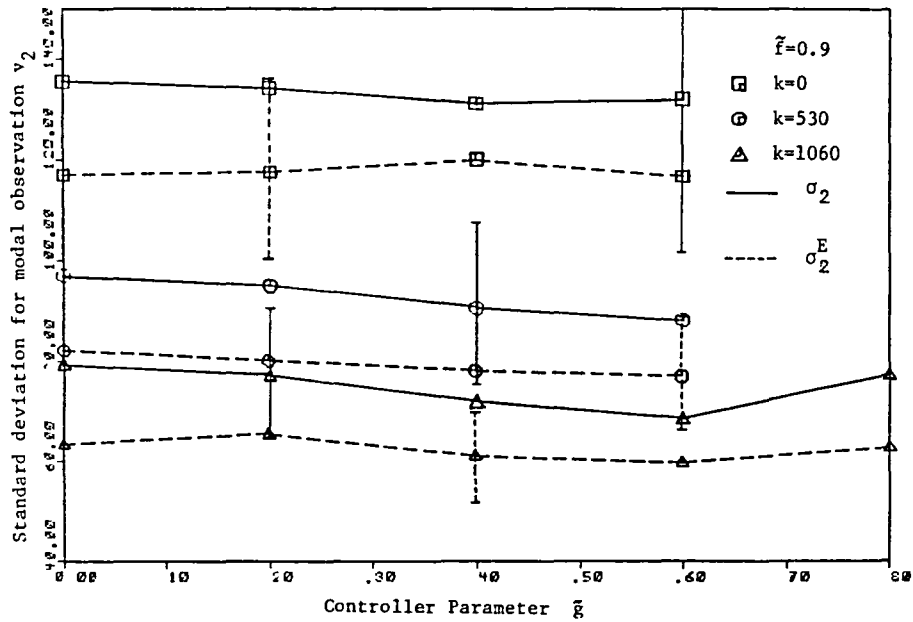
Figure 6: Comparison between theoretical and experimental standard deviation for modal observation y_2.
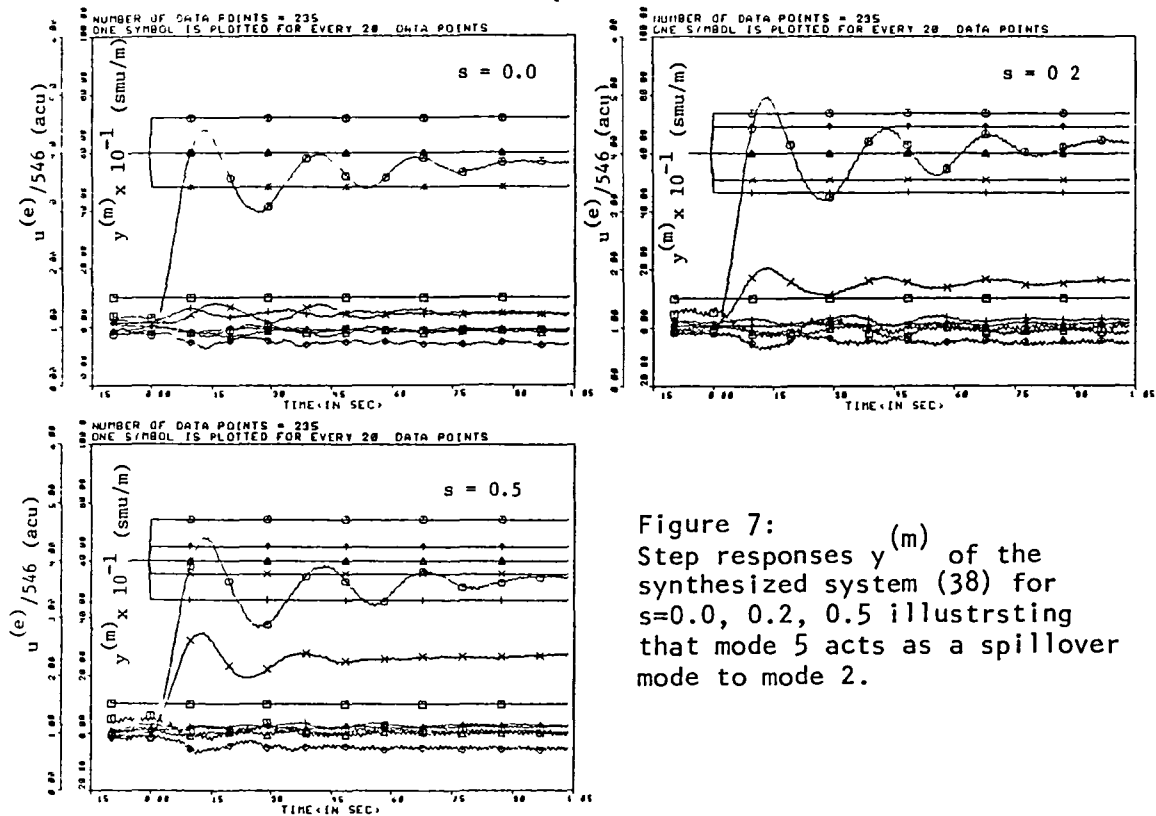
Figure 7:
Step responses $y^{(m)}$ of the synthesized system (38) for s=0.0, 0.2, 0.5 illustrsting that mode 5 acts as a spillover mode to mode 2.
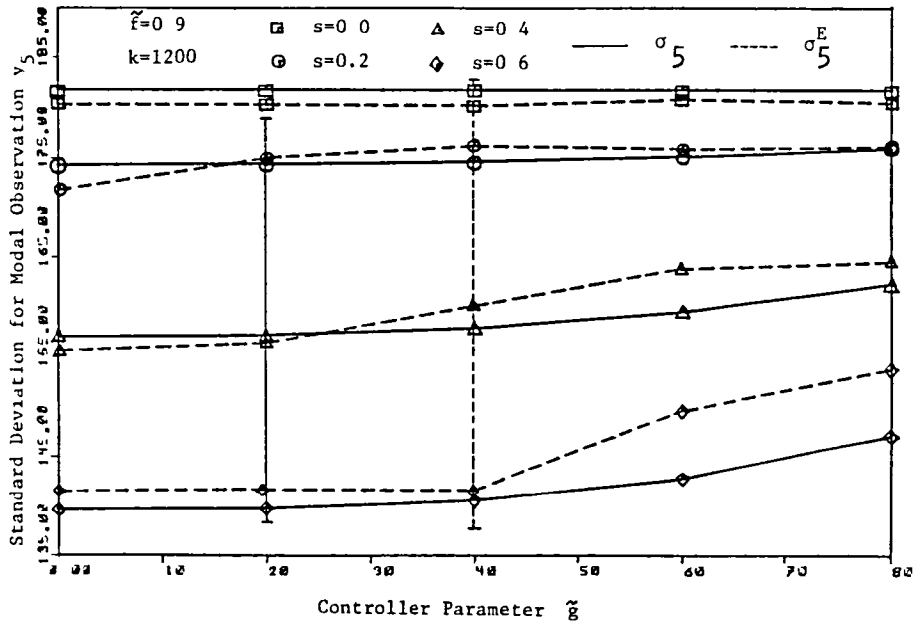
Figure 8: Comparison between experimental and theoretical standard deviation for modal observation y_5 at different synthesized spillover levels.
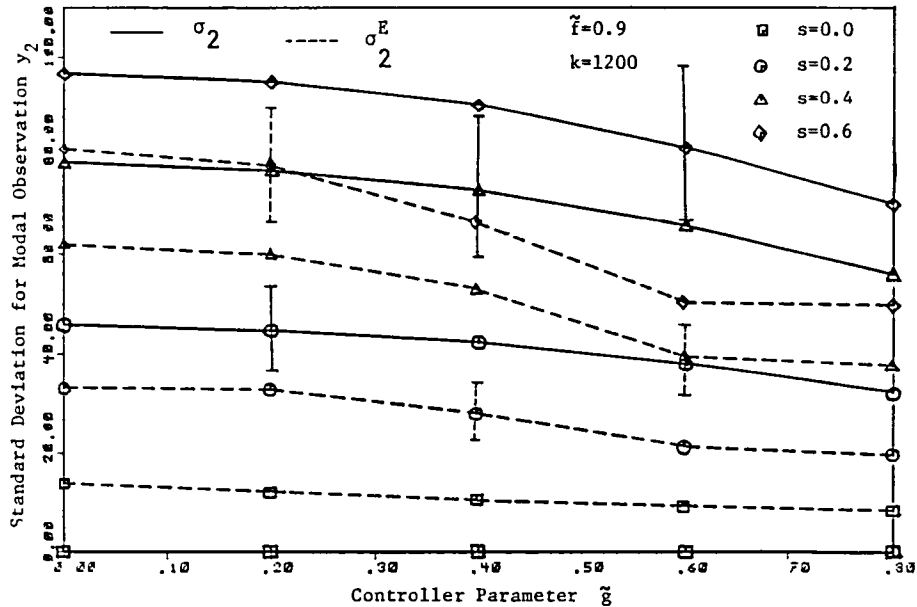
Figure 9: Comparison between experimental and theoretical standard deviation for modal observation y_2 at different synthesized spillover levels.

432

RATIONALE FOR AN EXPERIMENTAL TEST FOR FLEXIBLE SPACE STRUCTURE ATTITUDE CONTROL

Th. Lange, G. Heimbold, B. Schaefer, and **H. Holzach**
Deutsche Forschungs- und Versuchsanstalt
fuer Luft- und Raumfahrt, e V. (DFVLR)
Oberpfaffenhofen, 8031 Wessling, FRG

ABSTRACT

On the basis of study results critical control problems have been identified to be investigated in more detail in a laboratory experiment [1]. The test-setup requirements are defined according to a concept permitting ideal conditions and the implementation of realistic performance constraints as well. The test element is a wire suspended plate being controlled by an array processor via high performance sensors and actuators. First results of component tests indicate the feasibility of this concept.

1. INTRODUCTION

Large flexible spacecraft require advanced attitude control systems as the associated broad-band vibration spectrum interferes with the required control bandwidth, which may cause severe stability problems. Moreover, these may not be detected during design, as on principle, only an approximative plant description can be used for that purpose. A laboratory experimental test is an appropriate procedure to study the critical design problems more realistically and to enhance confidence in the controller design methods.

2. BASELINE OF CONTROLLER DESIGN

The objective of an attitude control system for large flexible spacecraft is in most applications the line-of-sight control of an antenna or an instrument. The associated high pointing accuracy requirements demand the inclusion of active structural vibration damping into the overall control

---

[1] This work has been done under ESA contract 5310

concept. These vibrations are characterized by a large number of space dependent mode shapes to be effectively controlled using various sensors and actuators distributed over the structure.

This complex control task is favorably solved by a well known dual- design approach consisting of a narrow band high-authority controller (HAC), primarily dedicated to attitude control, combined with a wide-band low-authority controller (LAC), increasing the structural damping [1]. Designing the LAC as a support for the basic HAC configuration, the required control accuracy can be achieved in addition to a high degree of robustness and stability of the overall system.

Based on this concept, extensive numerical studies have been performed [2] providing velocity feedback for LAC and a standard Riccati desin with observer for HAC. Simple generic models have been investigated, e.g. a flexible beam, the flexible plate model developed at the Purdue university [3] and a more complex model consisting of three coupled plates with different material and geometric parameters, referred to as the distributed flexibility model. The goal of these studies has been to find out critical design problems and to define a strategy suitable for further investigations by means of a laboratory experiment.

3. CRITICAL DESIGN PROBLEMS

The key problem of flexible structure control is the requirement of controlling an infinite order dynamic system by a finite order control system. The solution of this problem by using a reduced order model for design purposes may lead to a reduction of the structural damping with respect to the residual modes, in general referred to as spillover The probability of this phenomenon to occur depends primarily on the dynamics of the structure to be controlled. Critical in this respect are densely packed modes, which is typical for large space structures of more than one dimension. In this respect the flexible beam has been found not to represent a relevant example. With the other two models, the appearance of densely packed modes depends largely on the geometric dimensions involved.

A first decisive step in the overall control system design is the positioning of sensors and actuators which essentially determines the controller performance to be achieved. The actual sensor/actuator configuration provides not only a balanced sensitivity with respect to the controlled modes but moreover is often used to derive criteria which of the residual modes should be retained in the approximative plant representation of reduced order. In general two different methods are possible to determine appropriate sensor/actuator locations on flexible structures. In a first approach the positioning task leads to an investigation of some direct measures of performance. With a given controller structure it can be considered to be part

of the controller design procedure (integrated design). A second approach uses indirect performance measures provided by an analysis of observability and controllability.

Many of the positioning concepts using direct methods which are available from literature are closely related to the problem of state estimation and reconstruction. By investigation of an overall controller performance index the sensor/actuator positioning task can be formulated as a parameter optimization problem. Since the choice of the parameters must be such that no constraints on the possible locations are violated it can advantageously be solved by a constraint numerical optimization using nonlinear programming technique. In [4] this method has successfully been applied to an analytical beam model using the energy extracted from the system by the controller as an overall quadratic performance index. However, with more complex structures, which in general are approximated by finite element models, the numerical effort is considerably increased and hardly tolerable for practical design purposes Here a second method using indirect performance measures is superior.

Indirect measures of performance are concerned with assigning physically meaningful scalar measures of the quality of observability and controllability and permit an assessment of the performance of the high-order system when control is based upon a low order model [5]. Moreover they can advantageously be used in a dominance analysis of the system to identify the relevant modes and states which are determined by the actual sensor/actuator configuration. Using these scalar measures, an iterative procedure permits the definition of appropriate locations of sensors and actuators which retain the modes to be controlled in the reduced order model with sufficient sensitivity. Final goal of this procedure is to find a trade-off solution of the numbers of sensors and actuators to be mounted, to determine their arrangement according to the gridpoints available from the finite element analysis and to associate them to HAC and LAC, which in general require a different kind of information.

Directly related to the positioning problem is the feedback structure of the damping control (LAC). The integrated design studies [4] yield optimal results only with respect to the design model performance ,e.g. minimum gain, with dislocated sensors and actuators. Similarly, with predetermined positions, global feedback, i.e. permitting dislocated feedback branches, requires lower gains than a local (colocated) feedback structure. However, the residual modes may be poorly damped and sometimes even spillover occurs. But this can be overcome by a prescribed absolute damping constraint corresponding to one exponential decay time constant for all oscillation components. For a sufficiently large design model, the damping augmentation required from the controller approaches zero with increasing modal frequency. According to the numerical results available, this condition is expected to reduce the probability of spillover at the same time.

The key control problem, however, is the adequate selection of bandwidth, e.g. the roll-off frequency. Attitude control requires a small bandwidth just

including two or three low-frequency modes. With densely packed modes, it is not easy to find an appropriate location of the roll-off frequency, which should not be close to any vibration frequency. This may cause stability problems hardly to be compensated for by the superimposed low-authority control.

The problems identified so far are associated to an idealized system neglecting all hardware restrictions, e.g. assuming infinitely broadband sensors and actuators and an infinitely fast computation speed. Hardware bandwidth limitations are affecting primarily the high-frequency LAC performance, requiring a roll-off frequency to be considered in the design model including the phase shift due to computer sampling time. Note, that these parameters cannot simply be neglected, once they are associated to sufficiently high structural vibration frequencies hardly to be detected by open loop measurements. Preliminary hardware experiments indicate, that an instability generated by these constraints may even reveal structural vibration frequencies of more than 100 Hz not to be identified by an ordinary modal survey test. Adding the impact of amplifier saturation ,sensor noise and inherent nonlinearities, a reduced performance as compared to the ideal design will have to be taken into account.

4. DEFINITION OF TEST SETUP

According to the problems outlined so far, a two-staged test procedure is envisaged, referred to as ideal and realistic approach. The test requirements are basically defined by the ideal approach, serving for a better understanding of the physical implications involved. The realistic approach, which will be verified by implementing software constraints in the real-time processor in addition to external filtering and noise stimulation is intended to demonstrate the application constraints and to support assessments concerning the realization effort to be expected for future large space structures.

4.1 Structural Element

The laboratory test to be performed under ideal conditions requires a simple setup to minimize environmental impact, which can hardly be modelled and may produce non-relevant results with respect to the testing goals. The requirements, however, defined above, demand a trade-off solution. The selected test element is a rectangular homogeneous thin plate suspended vertically by two light, parallel cables (Fig.1). This permits almost free structural vibrations comparable to what should be expected under spatial conditions. The density of the modal frequency spectrum can be influenced by respective

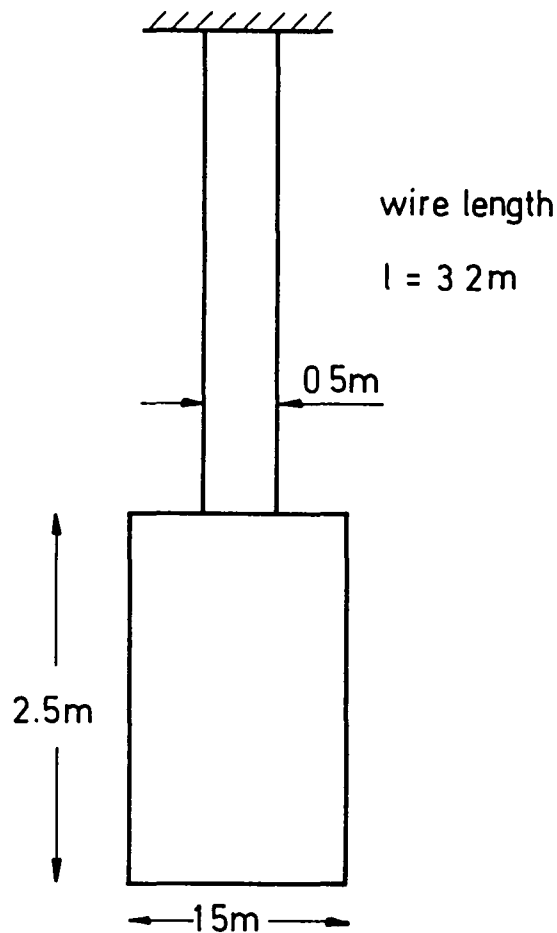dimensioning of the lengths of the edges a and b resp. and by the plate thickness.

Figure 1. Vertically suspended plate.

Gravity has a severe influence on the dynamics being equivalent to an additional stiffness parameter increasing the modal frequencies. This applies also for the quasi-rigid body eigenfrequencies comprising two bending frequencies and one torsional frequency. The torsional mode is utilized as main attitude control degree of freedom. The rigid body modes, which would have zero eigenfrequencies with zero g, should exhibit a frequency well below the structural frequencies to obtain relevant simulation parameters. This turns out to be difficult for all rigid body modes, but for the torsional motion, this will be satisfied

The first 15 eigenfrequencies are shown in table 1, where the results of an approximative analytical approach for structural design purposes based on classical thin plate theory, is compared to FEM results. The first three modes are rigid body modes, the first one being associated to the torsional mode. The elastic deformation modes are densely packed, especially the modes number 4 and 5, number 6 through 9 and number 14 and 15.

Mode number	Frequency	
	Analytical model	FEM
1	0.16	0.15
2	0.23	0.23
3	0.92	0.75
4	1.46	1.46
5	1.98	1.96
6	3.27	3.18
7	3.57	3.56
8	4.07	4.18
9	4.62	4.58
10	5.73	5.64
11	6.66	6.84
12	7.61	7.63
13	9.06	9.12
14	9.74	10.04
15	9.95	10.19

Table 1. Results of modal analysis

4.2 Sensors and actuators

For space application of flexible structure control, inertially referenced devices are required for measurement and feedback actuation. These are mainly accelerometers and/or gyros for measurement, proof mass actuators and control moment gyros for force or torque feedback resp. For the defined testing goals, e.g the ideal approach, regarding the effect of gravity and the accuracy requirements, none of these instruments is considered to be adequate. Moreover, their weight being attached to the structure is prohibitive, considering the change of positions required for different tests and the impact on the dynamics, of the test element, which would have to be re-evaluated for each configuration. Therefore non-contacting devices with light masses to be attached to the test element and providing ground references have been preferred.

According to the experiences from previous LFS experiments [6] the main realization problem is considered to be the ideal actuator performance, especial-

438

ly the independance of the actuator force from the relative motion of the flexible test element. For this purpose, a special electromagnetic system has been developed with permanent magnet bars being free to move back and forth in the center of ground fixed actuator coils. These coils have a special winding profile yielding a nearly constant magnetic driving field within the displacement range. Then the basic force component, being proportional to the product of coil magnetic field and permanent magnet field at the front end of the bar is also about constant. However, the magnet has a considerable stray field, as no closed iron field path is provided. The total magnetic force being reduced by the stray field losses, can be optimized at best to be about linearly dependent from displacement in the operation area. Hence two adjacent coil and magnet systems are necessary to provide for a definite compensation in order to meet the design requirements (see Fig.2).
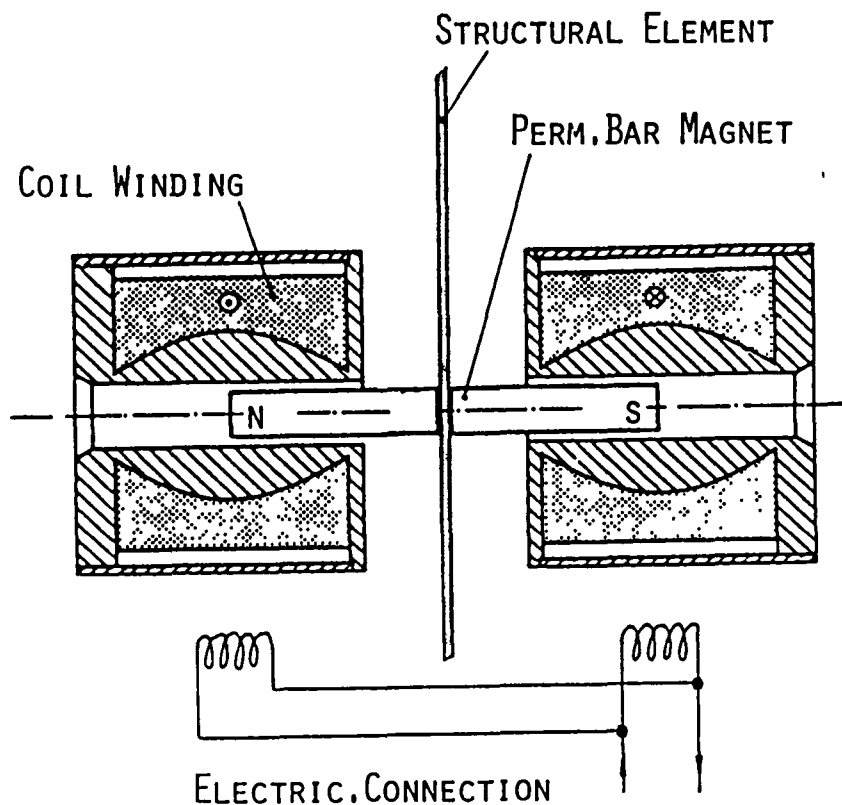
Figure 2. Electrodynamic force actuating system.

Fig.3 shows the theoretical curves of force vs. displacement Δx. The basic force component in the coil center ($\Delta x=0$) is taken as a reference for the percentage force deviation ΔF.
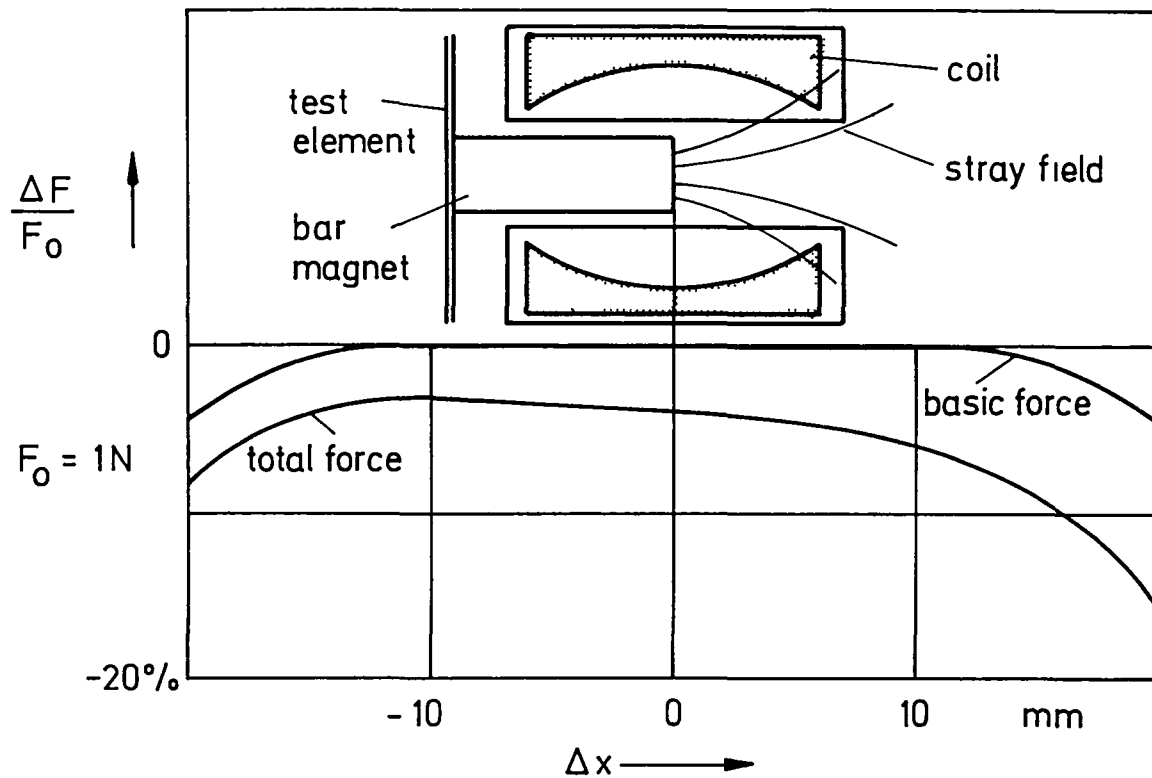
Figure 3. Magnetic force vs. displacement. Numerical results,single coil.

The coils are driven by current amplifiers with a bandwidth of about 150 Hz. Thus there is virtually no damping effect due to the relative motion of the magnets, since eddy currents are prevented by the high output impedance of the driver amplifier.

There are no non-linear coupling problems associated to the sensing systems, since they are based on the optical principle. Two kinds of sensors are used. The reference point for attitude control being located in the center of the plate, is monitored by a two-axis autocollimator system. The vibration sensing system is realized by electro-optical displacement transducers utilizing the diffuse reflection of a light beam for measurement. Thus the motion of any point of the target can be determined. Colocated measurement, which is desired here, is performed by using the top end of the magnet as a reflection target. The resolution is in the order of 0.1 percent full scale referred to

a deflection range of ±10 mm. Fig. 4 shows the measurement principle for colocation.
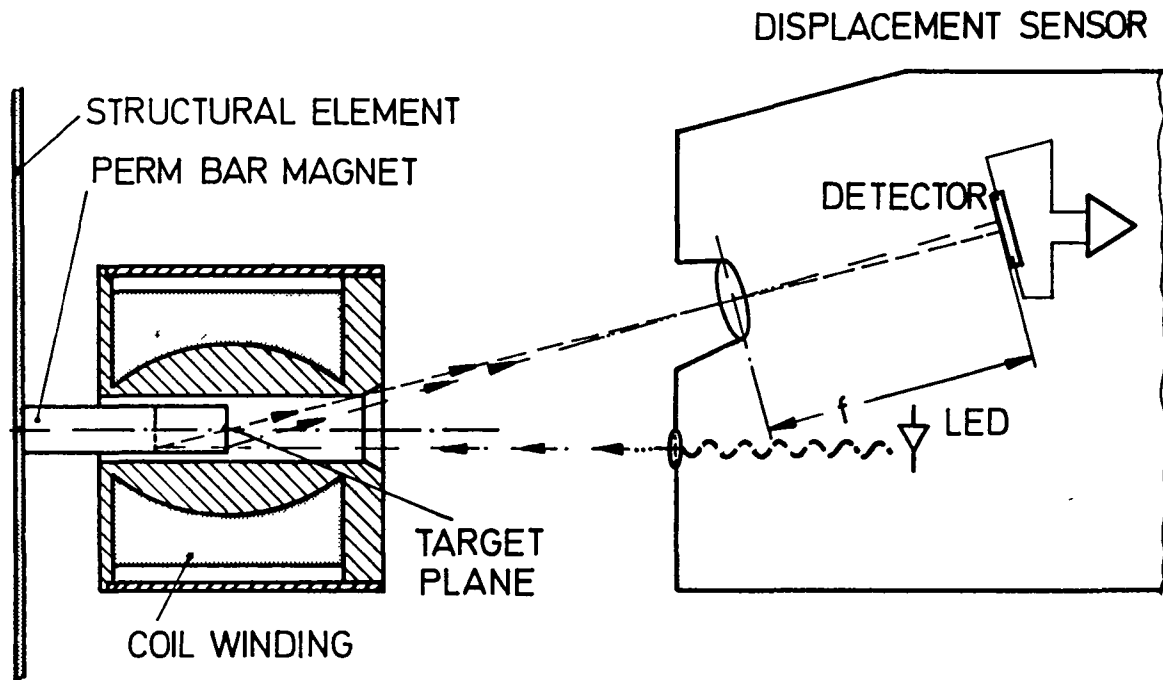
Figure 4. Principle of displacement measurement.

4.3 Real Time Processor

The data processing system finally consists of an array processor FPS 100 with a fast A/D and D/A converter system DSK 36000, hosted by a PDP 11/60. The software permits real time data processing and computation of the control law without the host computer being used in the loop. This mode permits very low sampling times in the order of ms.

Part of computation time is required for input-output and data formatting , another one for the computation of the control laws. In addition, as the controller needs displacement and velocity information, the measurements from the displacement transducers have to be differentiated numerically. This is possible due to the low noise level of the optical instruments in the frequency range of interest, i.e. up to 100 Hz. Shaping filters are provided to cut off the high frequency sensor noise.

5. TEST PLANNING

It is neither possible nor meaningfull to consider the permutation of all relevant controller parameter variations for test. Therefore, a defined strategy will be persued. Starting with various sensor and actuator positions, at first a few alternatives for the LAC design will be extracted to be further used supporting the HAC attitude control performance.

In addition to the number of sensors and actuators selected, also the arrangement is of interest. Both symmetrical and non- symmetric configurations will be tested. Due to technical constraints, symmetric arrangements with respect to the mode shapes and the attitude control reference point will often be preferred. Permitting an unsymmetric assembly however, a better comprehension of the design model modes is possible, as there is less inherent redundancy.

The second test parameter is provided by the different feedback configurations, e.g global and local feedback. Usually local feedback is recommended, as in theory, this provides a safeguard with respect to spillover. However, in addition to the considerations outlined previously, global feedback may serve for the investigation of the spillover effect itself, as an operation close to instability is expected to provide more information about the validity of the dynamic models beeing used.

The most promising solutions obtained during this first phase will be used to test the interaction of HAC and LAC control schemes in terms of required bandwidth, overall pointing accuracy and disturbance rejection. Alternatively, an overall broad-band controller shall be used to compare performance and design effort and the figures of merit of the different approaches.

6. FIRST TEST RESULTS

Some test setup components have been already tested showing encouraging results.

A flexible plate has been suspended according to Fig.1 in a preliminary setup The suspension, which had been suspected to possibly produce static instability, e.g. lateral buckling under the influence of gravity, turns out to be feasible. No deformations affecting the sensor and actuator implementation have been observed.

Another concern has been air damping to possibly increase the structural damping considerably. This has not been observed either. Probably rather a spring effect is associated to the air cushions at the plate surface than a dissipation effect.

Dynamically, densely packed modes are present, but slightly different frequencies and respective mode shapes as compared to the structural analysis have been identified. This is probably due to a material anisotropy, which cannot be completely avoided. The final test element however will have to be carefully cut and screwed for the setup, in order to minimize these effects.

Optical sensor systems of the selected type have been already used for active structural vibration damping tests in an analog feedback loop including differentiation networks [7]. Output filtering with 600 Hz roll-off frequency has been sufficient to eliminate the effect of noise overloading the feedback amplifiers.

The actuator coils manufactured according to a predetermined winding geometry need some calibration, e.g. additional compensation windings to achieve a required accuracy of less than 1 percent deviation from the commanded force level within a ±10 mm deflection range of the flexible test element. Fig.5 shows the performance of an actuator system, which also has already been proved [7].
The array processor has so far not been tested in a closed loop operation. Open loop test runs however with an assumed 15th order controller including the numerical differentiation and 5 input/ output channels representing a maximum controller configuration result in input-output cycle times of less than 5 ms.

7. SUMMARY

The problems of LFS control are characterized by the infinite bandwidth of structural vibrations, which cannot be accounted for in the dynamic design model. This may lead to instability even, if ideal control hardware is assumed, which can be concluded from preceding numerical investigations. Additional performance limitations are expected to occur due to hardware constraints.

A laboratory experiment is proposed to investigate the key problems in more detail. The test setup requirements being defined by the idealized control system are extremely high demanding a high speed processor and special hardware component developments. First tests on component level indicate the feasibility of the system presently being developed.
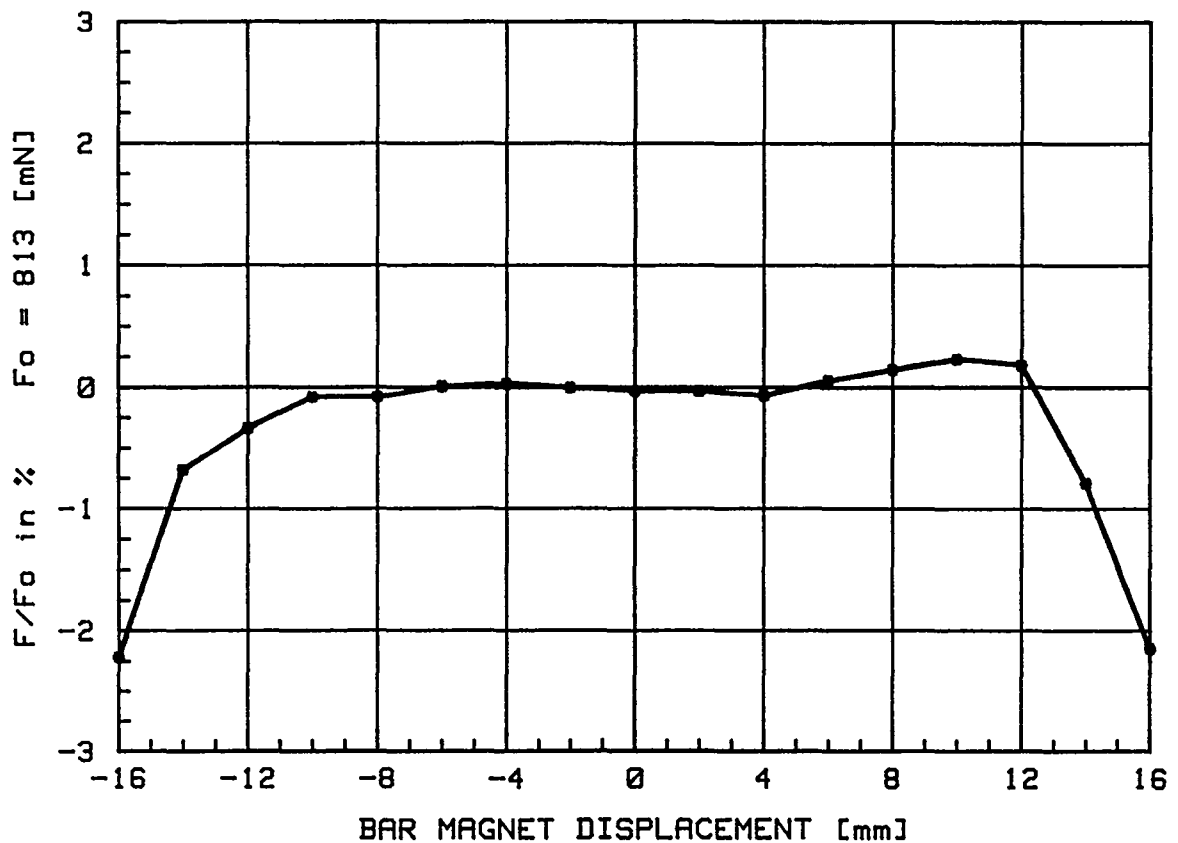
Figure 5. Magnetic force vs. displacement. Measurement results of dual coil system.

8. REFERENCES

1. Gupta, N.K., Lyons, M.G., Aubrun, J.N., Margulies, G.:
   Modeling, Control and System Identification Methods for Flexible Structures.
   AGARDograph No. 260, Spacecraft Pointing and Position Control, Nov. 1981, pp. 12/1-12/41.

2 DFVLR / DORNIER SYSTEM:
   Study on Investigation of the Attitude Control of Large Flexible Spacecraft.
   ESTEC Contract No. 5310/82/NL/BI Phase I Final Report, 1984

3. Hablani,H.B.:

Generic Model of a Large Flexible Space Structure for Control Concept
Evaluation
AIAA 19th Aerospace Sciences Meeting ,St Louis, Missouri, Jan 1981

4   Schulz, G., Heimbold, G.:
Dislocated Actuator/Sensor Positioning and Feedback Design for Flexible
Structures.
Journal of Guidance, Control and Dynamics, Vol. 6, No. 5, 1983,
pp. 361-367.

5. Skelton, R.E.:
Observability Measures and Performance Sensitivity in the Model
Reduction Problem.
International Journal of Control, Vol. 29, No. 4, 1979, pp. 541-556.

6. Schaechter, D.B.:
Hardware Demonstration of Flexible Beam Control
AIAA Journal of Guidance and Control, Vol. 5, No. 1, 1983, pp. 48-53.

7. Schaefer, B., Holzach, H.:
Experimental Research on Flexible Beam Modal Control
AIAA Dynamics Specialists Conference, Palm Springs, Ca., May 17-18,
1984.

NUMERICAL AND EXPERIMENTAL EVALUATION FOR SINGLE-AXIS CONTROL OF AN LSS LABORATORY MODEL

Y. Ohkami, O. Okamoto, S. Yoshimura, T. Kida, and I. Yamaguchi
National Aerospace Laboratory
Chofu Jindaiji 1880, Tokyo, Japan

Abstract

One of the major problems of LSS attitude control design stems from the modeling uncertainties due to modal truncation errors and modal parameter estimation errors. In this paper, this modeling problem is investigated by evaluating poles and zeros of the frequency response functions, described in terms of constrained or unconstrained modes. The frequency domain approach is utilized to evaluate the results of modal analyses and direct output feedback controller experiments using a simple flexible spacecraft model consisting of a rigid primary body and flexible alminum beam(s) with a control moment gyro as an actuator. The modal data are compared under the conditions that the model is constrained as the canti-lever and it is rotationally free on a single-axis air bearing table. In addition, the open-loop responses are experimentally examined under the impulsive disturbance to the appendage. The results of the control experiments show that the first vibration mode of the appendage and the interacted rotational motion of the primary body are damped in a short time as predicted by the numerical analysis, to produce damping ratio of 10-20%.

1. Introduction

The main purpose of this paper is to evaluate numerically and experimentally the poles and system zeros determined by the algorithms in Ref. 1 for an LSS control system. In order to do so, we consider a simple LSS model consisting of an alminum beam attached to a primary body which has been studied in Ref. 2. A prototype control moment gyro (CMG) is used as an actuator and direct rate/position feedback schemes are investigated. The beam(s), the table as a rigid primary body and the CMG are supported by the single axis air bearing table (Ref. 4) allowing the model to rotate freely about the local vertical axis. The ground experiments related to the LSS control have already been summarized briefly in Ref. 5, and some of the experiments reported in more detail in Refs. 6-9 but few studies have been reported on the experiment of the control of the flexible structures using CMG as an actuator (Ref. 9).

For the simple model stated above, the transfer function of the system is derived analytically taking the first and the second vibration modes of the appendage into account. The poles and zeros are briefly examined numerically. Then, the open-loop responses are studied experimentally under the impulsive disturbance to the flexible beam. The impulse response is stored in the

computer system and analyzed in time domain to produce damping ratios by a curve fitting method. The power spectra of the time histories are also computed in real-time.

The experimental results are well compared with the analytical results, and they are summarized as follows. The poles and zeros found in the experiments are in good accordance with those of the analytical model. However, the damping characteristics has a substantial discrepancy between the experimental and analytical results. This may be attributable to the mode shapes and CMG parameter uncertainties, such as damping coefficent for gimballing rate and also to the estimation error of damping ratio. It is also concluded that in this configuration, the CMG damps out the first vibration mode with a damping ratio of 10~20% depending upon the position/rate feedback gain. The second mode is not damped by controlling the table because of a small amount of coupling.

The other important conclusion drawn by this pole-zero evaluation approach is that there should exist a maximum attainable damping ratio determined by the modal parameters only, if the CMG is passively used, or equivalently, the direct colocate rate feedback is employed in a similar configuration.

2. Modeling and Pole/Zero Determination[1]

For a class of LSS, the linearized dynamical equations for small elastic deformation are given by

$$M^{*}\ddot{q} + h^{T}\ddot{w} = u_{o} + B_{ve}\,u_{e} \tag{1}$$

$$M\ddot{w} + D\dot{w} + Kw + h\,\ddot{q} = B_{ee}u_{e} \tag{2}$$

where $q^{T} = [r^{T},\ \theta^{T}] \in R^{6}$ consists of the mass center translational displacement r R^{3} and the rotational angle $\theta \in R^{3}$ of the total vehicle, and the variable $w^{T} = [w_{1}^{T},\ \dots\ w_{Na}^{T}]$ represents the small deformation w_{1} of the ith appendage. The total mass matrix $M^{*} = $ block-diag $[m^{*};\ I^{*}]$ combines the total vehicle mass m^{*} and its inertia matrix I^{*} referred to the mass center in the undeformed state. The matrices M, K and D are also block diagonal. The diagonal block entries of the matrices M and K are the mass matrices M_{1} and the stiffness matrices K_{1} ($i = 1,\ \dots,\ Na$) of the ith appendage and both are intrinsically symmetric and positive definite, $M_{1} = M_{1}^{T} > 0$, $K_{1} = K_{1}^{T} > 0$. Additionally, the damping coefficient matrices D_{1} ($i = 1,\ \dots,\ Na$) are assumed positive definite and symmetric $D_{1} = D_{1}^{T} > 0$. The matrix h denotes the dynamical coupling between the elastic vibration of the appendages and the vehicle translational and rotational motions. Consider the case when actuators and sensors are distributed both on the central rigid body and the elastic appendages. Then, the inputs to the system can be defined by u_{o} and u_{e} in Eqs. (1) and (2), where u_{o} is the control force and torque due to the actuators located on the reference body and u_{e} at the k actuator points located on the appendages and B_{ve} and B_{ee} are the influence matrices.

Similarly, the output of the system is assumed to measure the translational and angular displacement y_o of the total vehicle and the elastic deformation y_e at m sensor points located on the appendages.

$$y_o = q \tag{3a}$$

$$y_e = C_{eo}q + C_{ee}w \tag{3b}$$

where C_{eo} and C_{ee} are the observation matrices.

It is noted that the total vehicle motion of Eq. (1) is excited by the sum of u_o and u_e, while the appendage vibration is excited only by u_e. On the other hand, the measurements of appendage sensors of Eqs. (3a) are affected by the sum of q and w, while that of primary body sensors are only by q.

The multi-input multi-output (MIMO) system with the inputs u_o, u_e and the outputs y_o, y_e may be decomposed into the submatrices, G_{oo}, G_{oe}, G_{eo} and G_{ee} as

$$\begin{bmatrix} y_o \\ y_e \end{bmatrix} = \begin{bmatrix} G_{oo}(s) & G_{oe}(s) \\ G_{eo}(s) & G_{ee}(s) \end{bmatrix} \begin{bmatrix} u_o \\ u_e \end{bmatrix} \tag{4}$$

For investigation of input-output relations, Eq. (4) is rewritten by linear combinations of the following four types of input-output relations.

$$y_o = G_{oo}(s) u_o \tag{5a}$$

$$y_o = G_{oj}(s) u_j \tag{5b}$$

$$y_i = G_{io}(s) u_o \tag{5c}$$

$$y_i = G_{ij}(s) u_j \tag{5d}$$

Eqs. (5) are interpreted as the frequency-domain response from resultant force/torque inputs at a certain point j either on the rigid body or the appendage of the vehicle, to translation/rotation measurements at another point i. It is noted that all of Eqs. (5) denote 6 inputs 6 outputs multivariable systems with 6x6 square matrix transfer functions. The primitive model of Eqs. (1) can be efficiently represented in the modal space, i.e., constrained modes or unconstrained modes. Although constrained/unconstrained mode issue is of practical importance[11], [12], both formulations are treated here without any preference.

Constrained modes are calculated for each appendage by fixing the reference rigid body by q = 0 in Eqs. (1) and (2). Using the obtained mode shape Φ_i^c of the ith appendage and transforming w_i into η_i by $w_i = \Phi_i^c \eta_i$, Eqs. (1)-(3) become

$$M^* \ddot{q} + P^T \ddot{\eta} = u_o + B_{ve} u_e \tag{6a}$$

$$\ddot{\eta} + D^c \dot{\eta} + \omega^2 \eta + P \ddot{q} = \Phi^{cT} B_{ee} u_e \tag{6b}$$

$$y_o = q \tag{6c}$$

$$y_e = C_{eo} q + C_{ee} \Phi^c \eta \tag{6d}$$

where Φ^c, D^c and ω^2 are block diagonal matrices whose diagonal entries are Φ^c_1, D^c_1, ω^2_1, respectively. The modal coordinates denoted by $\eta^T = [\; \eta^T_1, \; \dots \; \eta^T_{Na}]$ collect the constrained modes of all appendages. The retained mode number is assumed N where $N = N_1 + \dots + N_{Na}$. The coupling coefficient matrix $P^T = h^T \Phi^c$ includes linear modal momentum coefficients and angular modal momentum coefficients.

Alternatively, Eqs. (1)-(3) are also represented by unconstrained modes as

$$\ddot{\eta}_o = \Phi^{uT}_1 u_o + \Phi^{uT}_1 B_{ve} u_e \tag{7a}$$

$$\ddot{\eta}_e + D^u \dot{\eta}_e + \sigma^2 \eta_e = \Phi^{uT}_2 u_o + (\Phi^{uT}_2 B_{ve} + \Phi^{uT}_3 B_{ee}) u_e \tag{7b}$$

$$y_o = \Phi^u_1 \eta_o + \Phi^u_2 \eta_e \tag{7c}$$

$$y_e = C_{eo} \Phi^u_1 \eta_o + (C_{eo} \Phi^u_2 + C_{ee} \Phi^u_3) \eta_e \tag{7d}$$

In Eqs. (7), unconstrained modal coordinates η and corresponding eigenvector Φ^u are defined by

$$\eta = \begin{bmatrix} \eta_o \\ \eta_e \end{bmatrix} \tag{8}$$

$$\Phi^u = \begin{bmatrix} \Phi^u_1 & \Phi^u_2 \\ 0 & \Phi^u_3 \end{bmatrix} \tag{9}$$

where η_o and η_e are rigid body modes and elastic vibration modes, respectively, and Φ^u_1, Φ^u_2 and Φ^u_3 are the corresponding mode shapes. These unconstrained modal parameters are obtained either by direct modal analysis of Eqs. (1) under the free-free boundary condition or by the transformation from Eqs. (6) of the constrained modal space representation.

The pole/zero determination algorithms have been developed for the constrained and unconstrained modes as briefly outlined as follows: The poles and zeros of Eqs. (5) are the eigenvalues of a matrix A defined by

$$A = \begin{bmatrix} 0 & U_N \\ -R\sigma^2 & -RD \end{bmatrix} \tag{10}$$

where U_N is the N-dimensional unit matrix, σ^2 the modal frequencies, D the modal damping and R is the matrix expressed in terms of the modal functions and B_v and B_e. For the both approaches of the constrained and unconstrained modal analyses employed, the construction methods of the matrices R, σ^2 and D (hence A) have been developed and programmed in computer code. Fig. 1 illustrates the four different procedures (Path I, IIa, IIb and III) developed here to produce the poles and zeros of the system explained as follows.

Path I is the algorithm for the constrained modes which are given by the FEM analysis or the vibration test for each appandage.

Path IIa and Path IIb are both based on the algorithm for the unconstrained modes. Path IIa utilizes the constrained modal data as in Path I, but the system equation with the constrained modes is converted into another set of unconstrained modal equation, which is used the pole/zero determination algorithm as in Path IIb. On the other hand, Path IIb utilizes the unconstrained modal data given by FEM analysis, usually followed by a transformation from the inertial to body frame.

Path III produces immediately the poles and zeros of the total system if the model is supported in a translationally and/or rotationally free condition. The FFT analysis utilizes appropriate force/torque inputs, such as inpulse by an impact hammer or random excitation, to produce transfer functions in a non-parametric manner. However, the results usually contain errors due to the gravity, airdrag and other experimental limitations.

3. Experiments and Results

In this section, the modeling approaches and the algorithms developed so far are applied to a simple model that permits all the four approaches in Fig. 1. In addition, control experiments are performed utilizing the direct output feedback schemes.

3.1 Flexible Spacecraft Model

The simple flexible spacecraft model under consideration is shown schematically in Fig. 2. The model consists of the rigid primary body and the flexible appendage attached to the primary body. The former is a single-axis air bearing table of 700 mm in diameter with a single-degree-of-freedom CMG on board and the latter is a 3 mm thick alminum beam of 1500 mm in length and 100 mm in height.

The modal analysis of the beam has been carried out employing both unconstrained modes and constrained modes, followed by the numerical determination of poles and zeros. The major results are shown in Table 1 (Ref. 2). Fig. 3 illustrates the measured shapes of the 1-st and 2-nd modes together with the numerical results. For this simple model, the both coincide well. The system poles, identical to the system eigenvalues, are compared with each other for the various methods of determination (Path I, IIa, IIb and
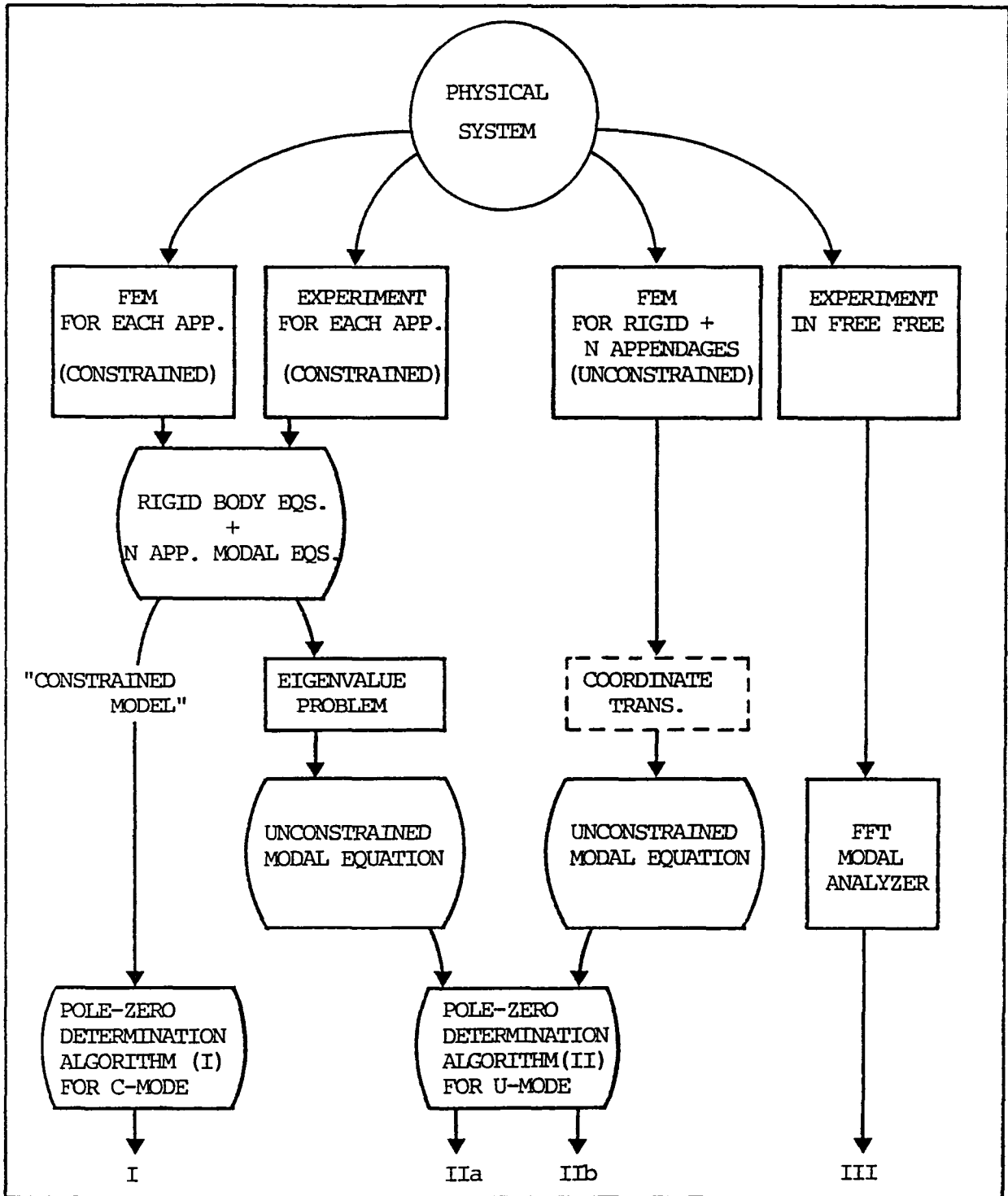
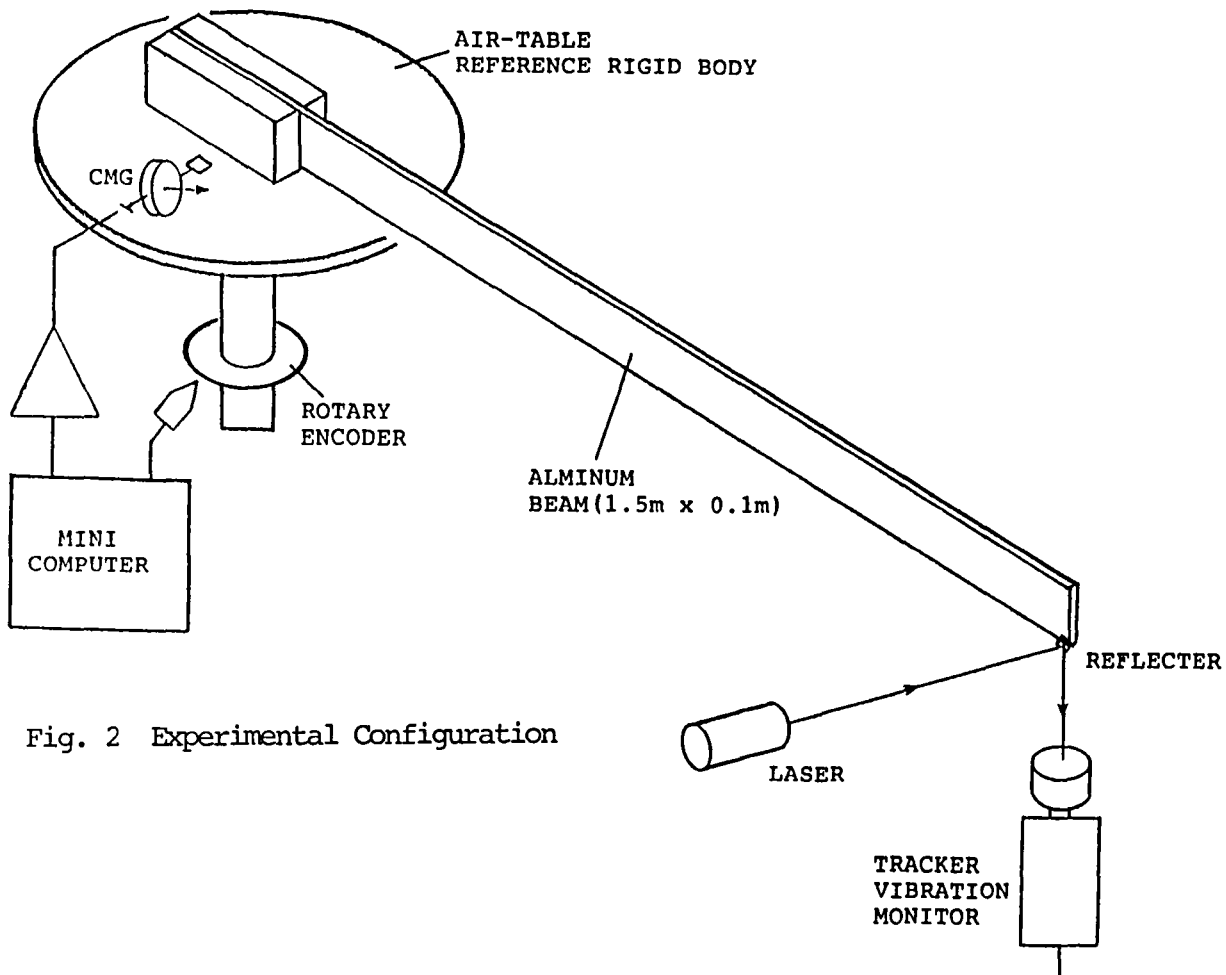Fig. 1 Approaches for Modeling and Pole/Zero Determination

Fig. 2 Experimental Configuration

Table 1 Modal Data and Moment of Inertia

	1st mode	2nd mode
ω_i	1.07 Hz	6.84 Hz
P_i	1.01	-0.177
ϕ_i	-0.748	0.212

Moment of Inertia

$I = 2.66$ kg$\cdot$m^2 (Total)

$= 1.065$ kg$\cdot$m^2 (Appendage only)

Table 2 Parameters of CMG

Mass	3.8	kg
H	7.90×10^{-1}	N$\cdot$m$\cdot$s
$\theta_{g\ max}$	±60.9	deg
C_g	2.22×10^{-2}	N$\cdot$m$\cdot$s
I_g	3.16×10^{-4}	kg$\cdot$m^2
K_T	1.33×10^{-3}	N$\cdot$m$\cdot$V^{-1}

453
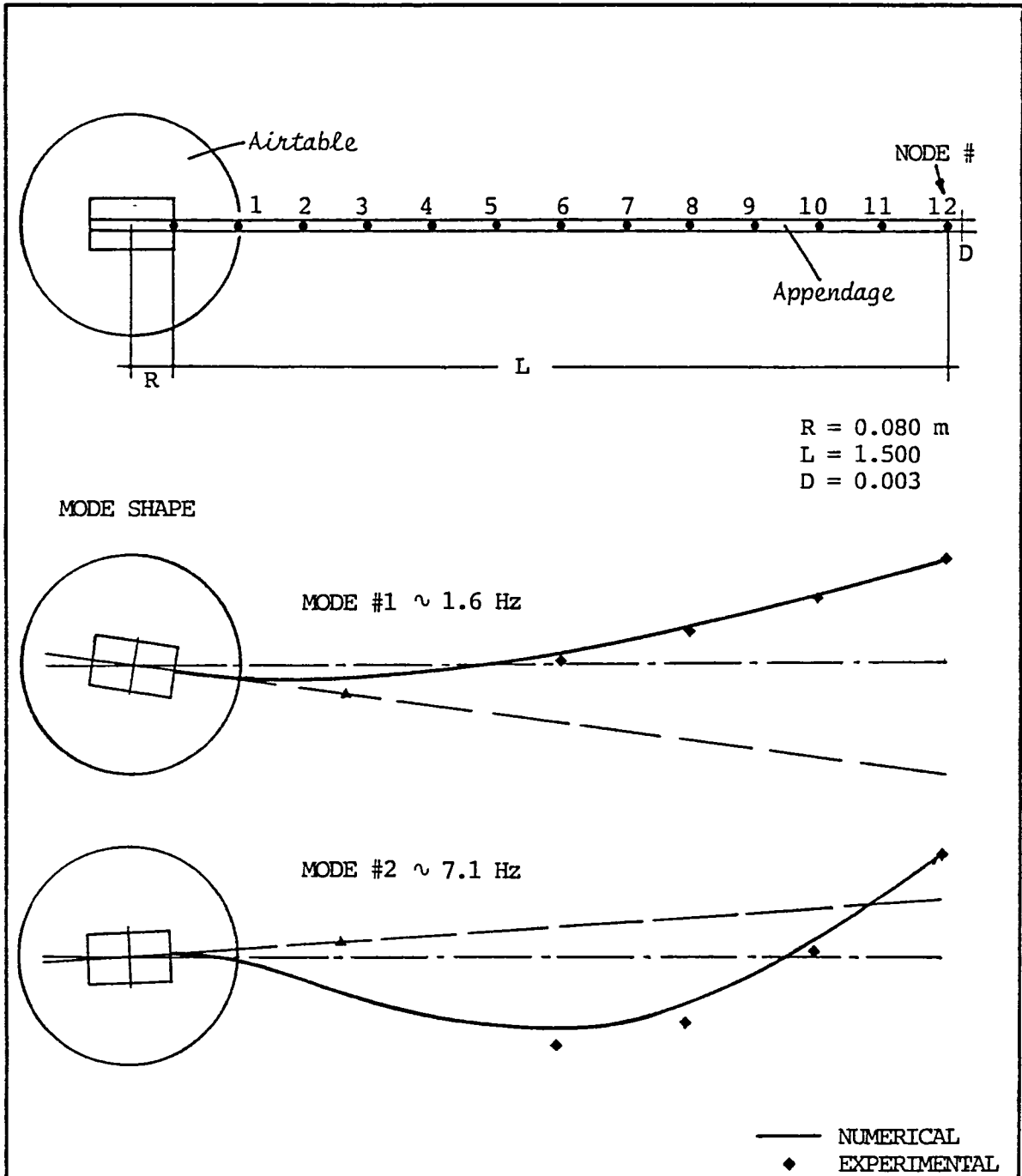
Fig. 3 Appendage Dimension and Unconstrained Vibration Modes
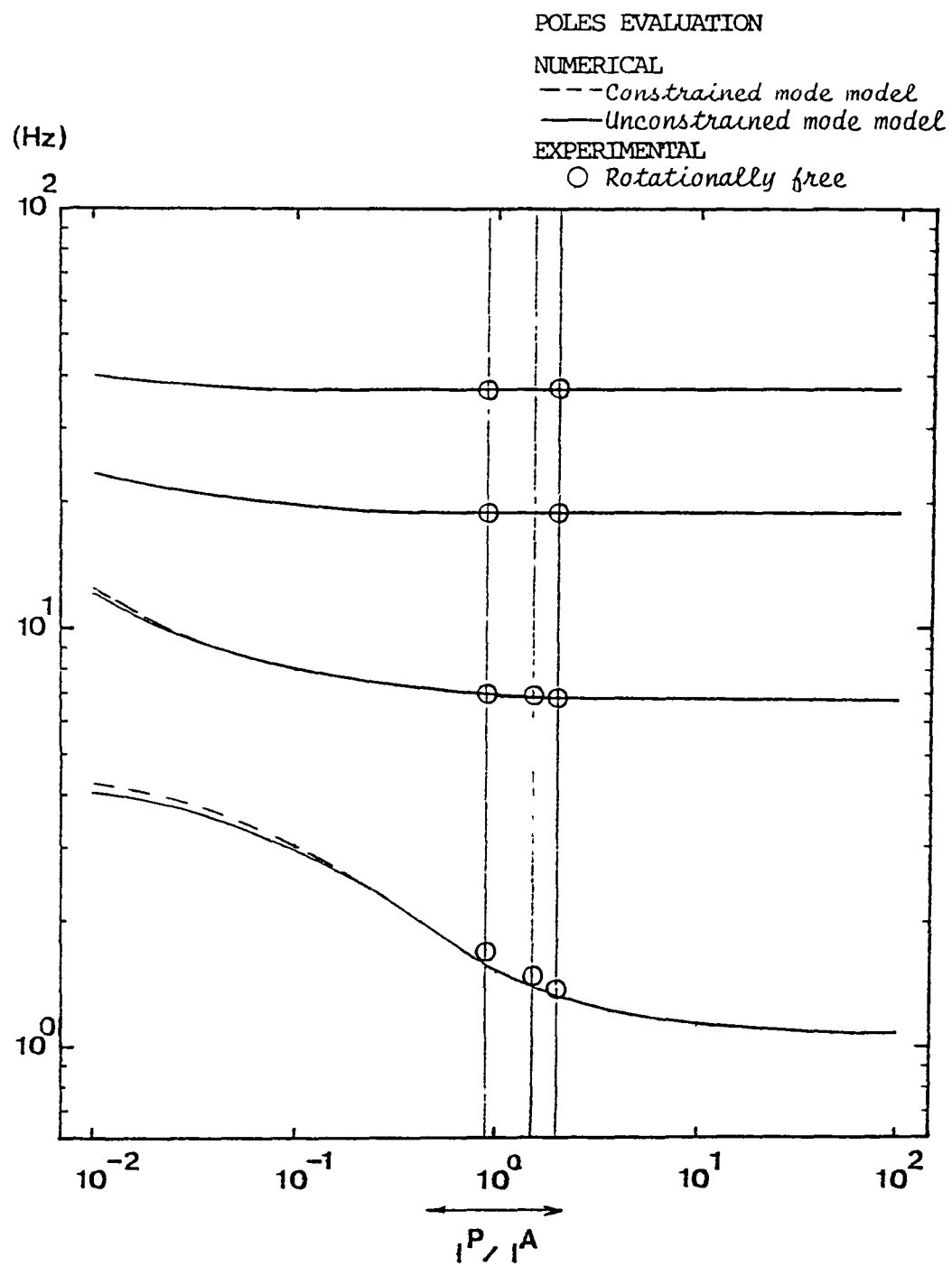
Fig. 4 Comparison of the Poles Determination by the 4 Modes

III). The results are shown in Fig. 4, where the abscissa is moment-of-inertia ratio of the primary body to the appendage. It has been shown that for this simple model there is no appreciable difference between the three numerical methods in Fig. 1 even if the moment-of-inertia ratio approaches to 0.001.[2] The modal frequencies obtained experimentally are not different from the numerical results.

3.2 Experiment Configuration

The rotational angle of the air bearing table, θ, is read out by a magnetic scale detector with resolution of 0.005 deg. and range of $-180 - +180$ deg. The tip deflection of the beam is detected by an optical measuring system consisting of a laser oscillator, a laser beam reflector at the tip, and the two-dimensional light-point tracker (image disector). The gimbal angle of CMG, θ_g, is also monitored through a linear-synchronous-type pickoff device incorporated in the CMG. Power spectra of the rotational angle outputs and tip deflection are computed by the real time FFT analyzer.

CMG is one of the momentum-exchange devices, and is well-known as one of the effective actuators for the control of the flexible (especially large) space structures. The dimensions and the parameters of the CMG fabricated for research purposes are shown in Table 2 (Ref. 3).

3.3 Transfer Function of the System

Assuming that the appandage has two vibration modes, η_1 and η_2 with zero modal damping and the gimbal angle θ_g of the CMG is controlled by the direct feedback of the table angle with gain K_p and its rate with gain K_r, the system equation of 1-DOF motion is expressed by the following simpler form of Eqs. (6) (Refs. 1 and 3)

$$I\ddot{\theta} + p_1\ddot{\eta}_1 + p_2\ddot{\eta}_2 + H_c\dot{\theta}_g = T_e \tag{11}$$

$$\ddot{\eta}_1 + \omega_1^2\eta_1 + p_1\ddot{\theta} = \phi_1 T_e^a \tag{12}$$

$$\ddot{\eta}_2 + \omega_2^2\eta_2 + p_2\ddot{\theta} = \phi_2 T_e^a \tag{13}$$

$$I_g\ddot{\theta}_g + c_g\dot{\theta}_g - H_c\dot{\theta} = K_T(K_r\dot{\theta}) - K_T K_p(\theta_c - \theta) \tag{14}$$

where H_c ($= H \cos\theta_g$) is the nominal spin axis conponent of the CMG angular momentum, K_T is the amplifier gain, and T_e is the force to the appendage. The other parameters are given in Tables 1 and 2.

Taking Laplace transformation of Eqs. (11) - (14) under the assumption that H_c is constant yields the system block diagram of Fig. 5 and matrix form

$$H(s) X(s) = T(s) \tag{15}$$

where $H(s)$ is the system matrix transfer function defined by

$$
H(s) = \begin{bmatrix} Is^2 & P_1 s^2 & P_2 s^2 & H_c s \\ p_1 s^2 & s^2 + \omega_1^2 & 0 & 0 \\ p_2 s^2 & 0 & s^2 + \omega_2^2 & 0 \\ -(H_c + K_r K_T)s & 0 & & I_g s^2 + C_g s \end{bmatrix} , \tag{16}
$$

$$
X(s) = \begin{bmatrix} \theta(s) \\ \eta_1(s) \\ \eta_2(s) \\ \theta_g(s) \end{bmatrix} \text{ and } T(s) = \begin{bmatrix} T_e(s) \\ \Phi_1 T_e^a(s) \\ \Phi_2 T_e^a(s) \\ 0 \end{bmatrix} \tag{17}
$$

The frequency response of this system will be examined by root-locus plots as compared by the experimental results in the next section.
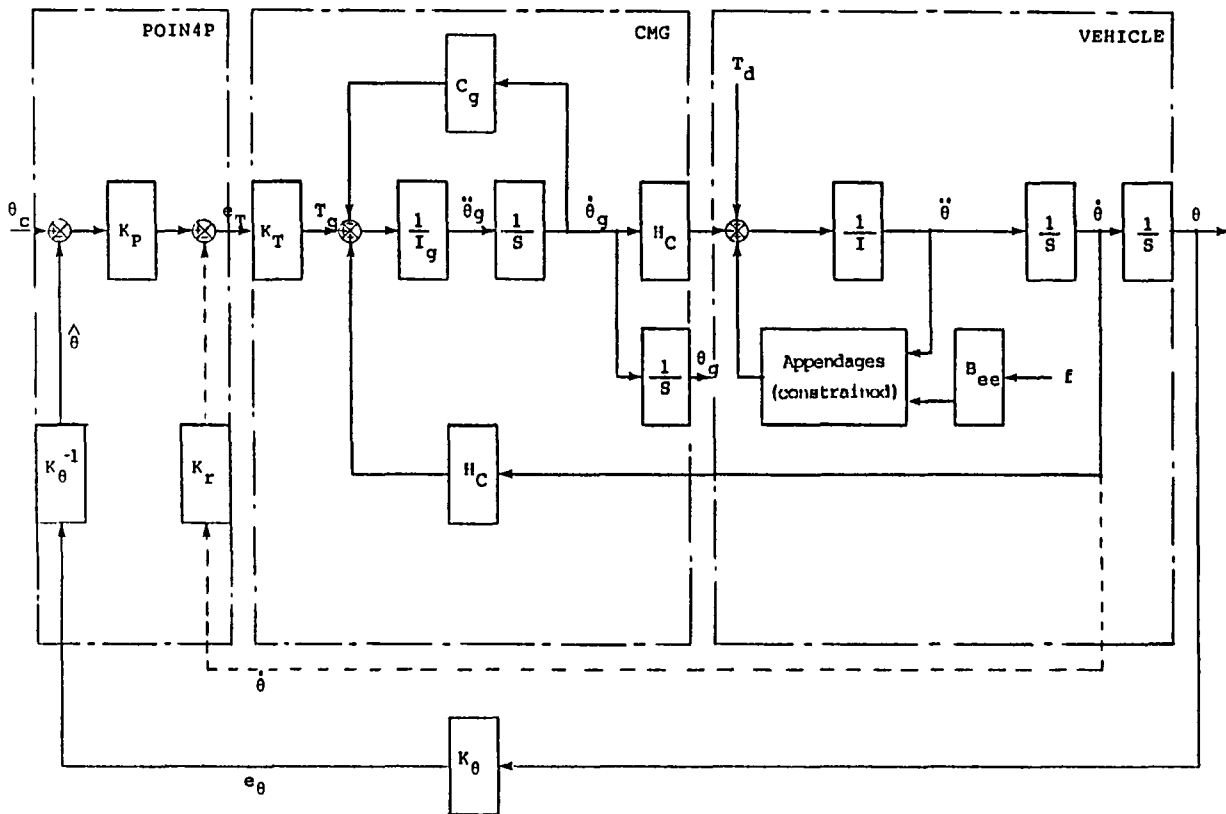
Fig. 5 System Block Diagram

3.4 Control Experiments - results and evaluation -

Two kinds of the control experiments have been carried out: The one is the direct colocate velocity feedback scheme[13] without angular position feedback, and the other is the direct colocate position feedback of passively damped system. In either case, the input signal (measurement) is the table angle and its rate is computed in real-time by a curve-fitting algorithm of successive least square methods.

The angle and/or its rate are fed back to the CMG torquer. The CMG gimbal angle and the appendage tip deflection are also monitored but are not used as controller input. To investigate the controller performance, the damping ratios of the 1-st vibration mode are calculated from the time histories of the table angle together with the power spectra in the relevant frequency region.

Examples of the impulse responses and their power spectra are illustrated in Fig. 6 for the position feedback case of K_p=-200 and K_p=-2000. The impulse is applied to a specified point of the appendage that minimizes the 2nd mode vibration. It is observed that the damping for K_p=-2000 is smaller than that for K_p=-200 at about 1 Hz and that the second mode at about 7 Hz is not damped. Fig. 6(c) shows the magnitude of the transfer function from the angle reference, $_c$, to the table angle, , for two different gains. It can be seen that for the lower position gain (K_p=-200) the magnitude begins to decrease at about 0.1 Hz but it is less than -30 dB at the first modal frequency of about 1.5 Hz. For the higher position gain (K_p=-2000), the magnitude maintains 0 dB up to about 1 Hz meaning that the controller bandwidth for the rigid body mode is extended. The magnitude at the 1st mode frequency is above -10dB, which results in a smaller damping of the 1st vibration mode, as shown in Fig. 6(b). The sharp dip of Fig. 6(c) clearly shows the zero of system, which is independent of the position feed bacak gain.

Figs. 7 show the measured and numerical results for the damping ratios as a function of rate feedback gain K_r or angle feedback gain k_p, and Figs. 8 are the root-locus with zooming in the vicinity of the 1-st vibration mode. In case of the rate feedback scheme with K_p = 0, the passive damping is already provided by the CMG, so that the rate feedback gain K_r can be made negative as well as positive. The maximum damping is obtained in the negative region of K_r, that amounts to 14% as seen from Fig. 7(A). This is also interpreted in the root-locus of Fig. 8(A), in which the passive CMG damping is obviously in excess of the optimum value resulting in a smaller 1-st mode damping than the maximum value. Therefore, for a negative value of the rate feedback gain, which would make the system unstable without CMG, the maximum damping ratio is attained as seen from Fig. 7(A) and Fig. 8(A). Fairly good correlation is observed between the numerical and the experimental results. It is noted that for the single axis case the CMG damping may be considered a colocate rate feedback and equivalent to the rate direct feedback of any kind represented by K_r. In other words, even if the CMG momentum, H_c, changes, the system pole in Fig. 8(A) still on the same circle of the pole trace, and this change can be compensated simply by varing the rate gain K_r. It also should be noted that the maximum attainable damping is expressed only in terms of the modal parameters. The formal discussion on this fact, however, is omitted here.
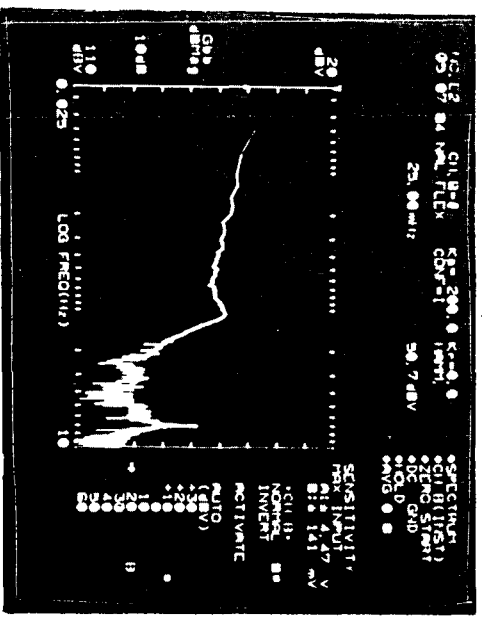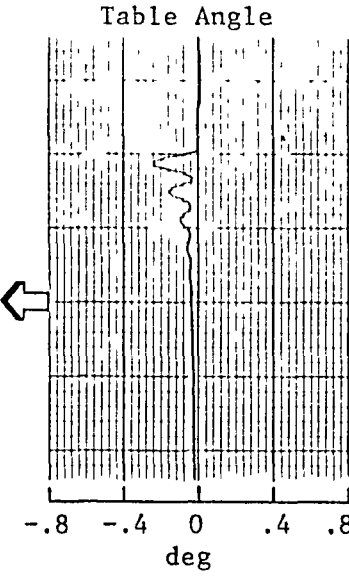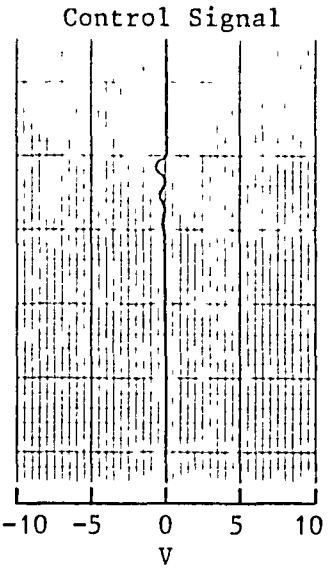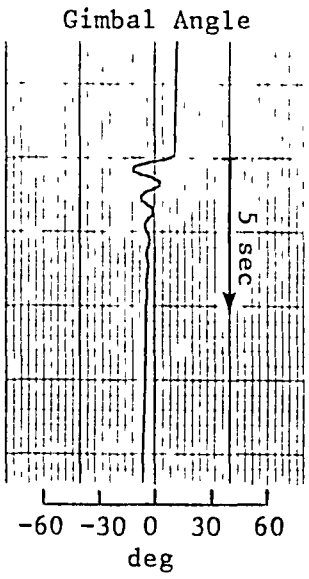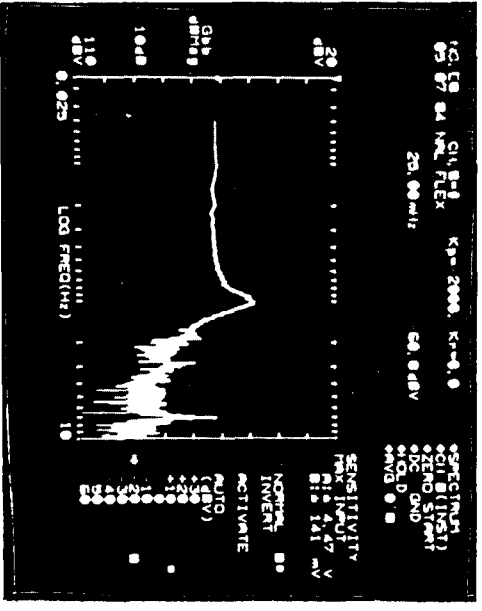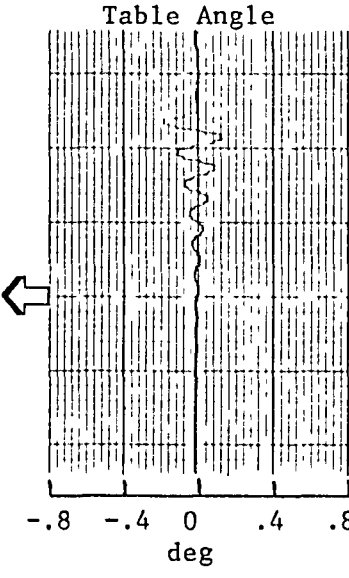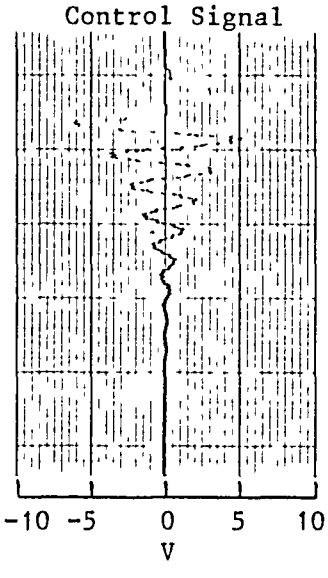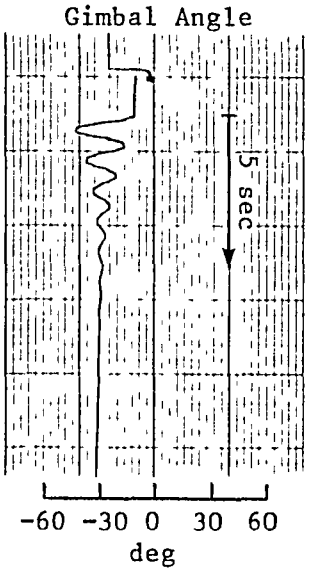
Fig. 6   Impulse Responses and Power Spectra for Direct Position Feedback Control

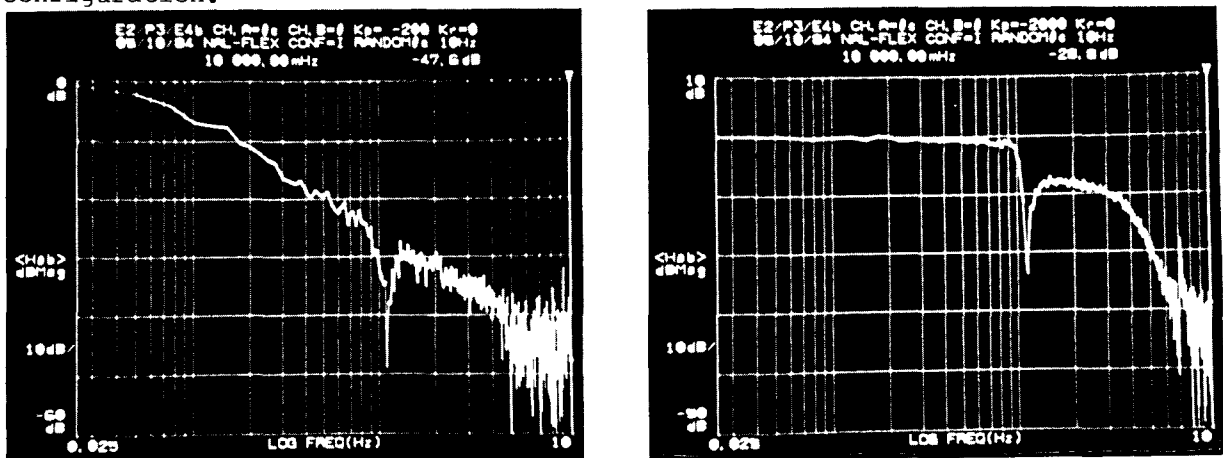(A) $K_p = -200$, $\zeta = 10.09$ %

(B) $K_p = -2000$, $\zeta = 7.60$ %

In case of the position feedback only with the CMG passive damping (K_r=0), the 1-st mode damping increases slightly for 0<K_p<700 and then decreases rapidly for larger values of K_p, as seen from Fig. 7(B). This is also interpreted in the root-locus of Fig. 8(B), where the locus starts at the system pole including the CMG dynamics and approaches to the system zero on the imaginary axis. In Fig. 7(B), the numerical values are plotted together, but there is a substantial difference between the two, although both have a similar tendency. This difference may be attributed to the estimation errors of damping, modal parameters, and measuring systems accuracy.

4. Conclusion

A preliminary analysis is carried out numerically and experimentally on poles and zero evaluation for the system consisting of a rigid primary body with a single-degree-of-freedom control moment gyro on board and a flexible aluminum beam.

The experimental results are well compared with the analytical results, and they are summarized as follows. The poles and zeros found in the experiments are in good accordance with those of the analytical model. However, the damping characteristics has a substantial discrepancy between the experimental and analytical results. This may be attributable to the mode shapes and CMG parameter uncertainties, such as damping coefficent for gimballing rate and also to the estimation error of damping ratio. It is also concluded that in this configuration, the CMG damps out the first vibration mode with a damping ratio of 10-20% depending upon the position/rate feedback gain. The second mode is not damped by controlling the table because of a small amount of coupling.
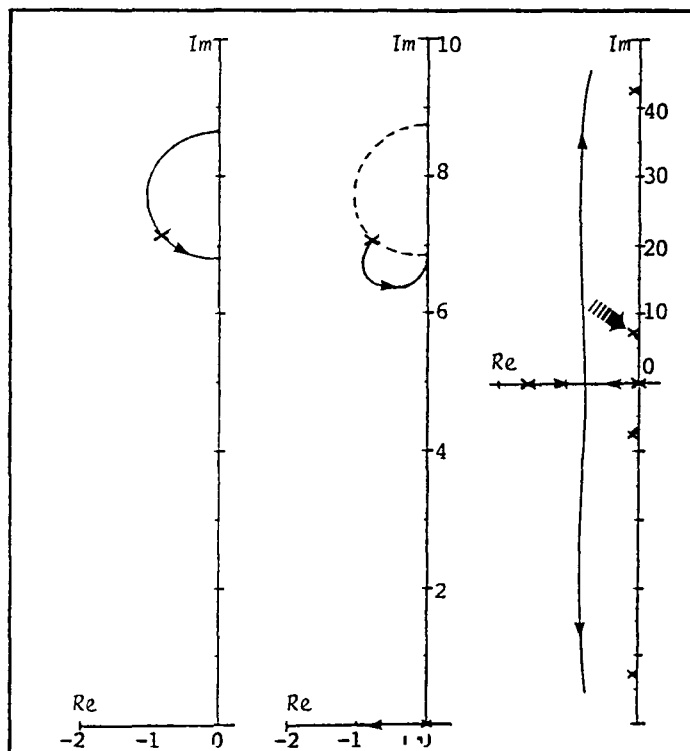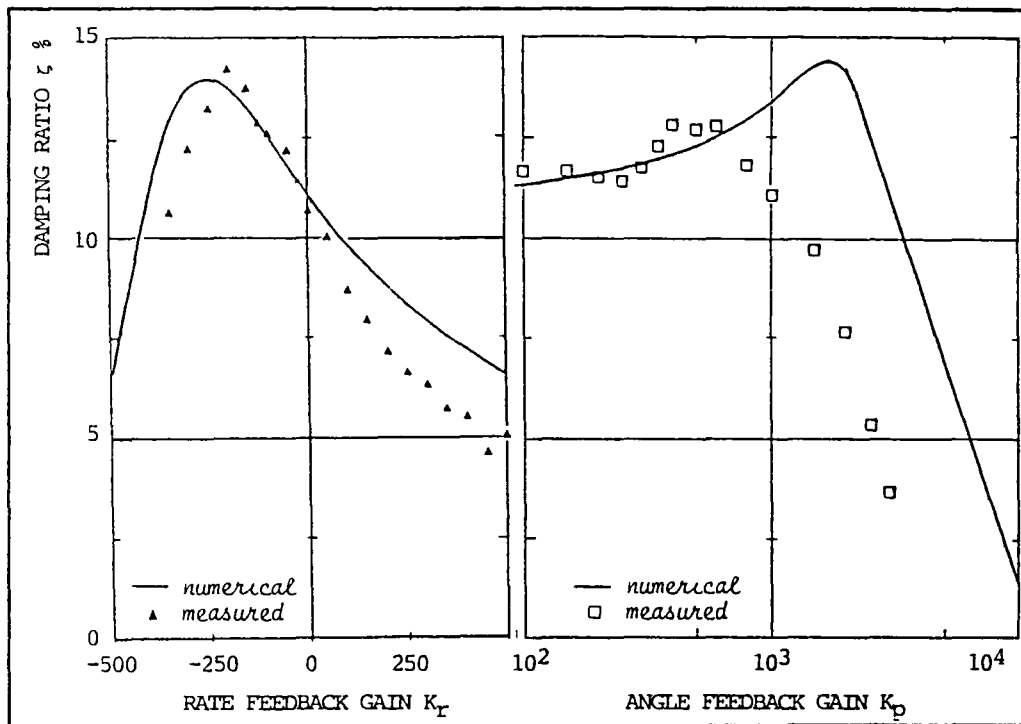
The other important conclusion drawn by this pole-zero evaluation approach is that there should exist a maximum attainable damping ratio determined by the modal parameters only, if the CMG is passively used, or equivalently, the direct colocate rate feedback is employed in a similar configuration.

(1) K_p=-200   (2) K_p=-2000

Fig. 6(c)   Transfer Function ($\theta_c \rightarrow \theta$, θ_c; Random Excitation)

Fig. 7 Results of Damping Ratio Measurements Compared with Numerical Results for Direct Rate and Position Feedback.

(A) Rate Feedback   (B) In the Vicinity of 1st Mode   (C) Overall

Position Feedback

Fig. 8 Root Locus of the 1st Appendage Mode for Rate and Position Feedback.

461

References

1. Y. Ohkami, T. Kida and S. Sanbongi, "A Method of Frequency Domain Representation of Flexible Spacecraft Control Systems", 4th VPI & SU/AIAA symposium on Dynamics and Control of Large Structures, 1983.

2. T. Kai and Y. Ohkami "Truncation Error Estimation of a Spacecraft Model with a Flexible Appendage" 14th International Symposium on Space Technology and Science, Tokyo, May 27 – June 1, 1984.

3. S. Yoshimura, H. Kamimura, and T. Yamanaka, "An Experimental Investigation of a Single-Degree-of-Freedom Control Moment Gyro on a Pendulum", NAL TR-641, November 1980, in Japanese.

4. C. Murakami, O. Okamoto, A. Nakajima, and T. Kida, "A Single-Axis Air Bearing Table for Research of Spacecraft Attitude Control", NAL TM-257, May 1974, in Japanese.

5. R.R. Strunce, Jr. and J. D. Turner, "Enabling Technologies for Large Precision Space Systems", NASA CP-2269, Large Space Antenna Systems Technology - 1982 Part 2, NASA Langley Research Center, November 30 - December 3, 1982, pp.601-624.

6. D.B. Schaechter, "Hardware Demonstration of Flexible Beam Control", J. of Guidance, Control and Dynamics, Vol.5, No.1, pp.48-53, Jan.-Feb. 1982.

7. F.E. Thau, R.C. Montgomery, and G.C. Horner, "On-Line Structural Parameter Identification", AIAA Guidance and Control Conference, No.81-1846, pp.530-539, August 1981.

8. J.A. Breakwell, "Optimal Feedback Slewing of Flexible Spacecraft", J. of Guidance and Control, Vol.4, No.5, pp.472-479, Sept.-Oct. 1981.

9. J.N. Aubrun and J.A. Breakwell, "Computer Analysis and Ground Testing of Large Space Systems Control Strategies", NASA CP-2269, Large Space Antenna Systems Technology - 1982 Part 2, NASA Langley Research Center, November 30 - December 3, 1982, pp.665-685.

10. D. Poelaert, "Spacecraft dynamic analysis using cantilevor modes of the appendages - application to the Space Telescope" ESA STR-206, October 1981.

11. P.C. Hughes and R.E. Skelton, "Controllability and Observability for Flexible Spacecraft", Journal of Guidance and Control, vol.3, No.5, 1980, pp.452-459.

12. H.B. Hablani, "Constrained and Unconstrained Modes: Some Modeling Aspects of Flexible Spacecraft", Journal of Guidance and Control, Vol.5, No.2, 1982, pp.164-173.

13. M.J. Balas, "Direct Velocity Feedback Control of Large Space Structures," J.G. & C. Vol.2, No.3, pp.252-253, 1979.

ON THE MEASUREMENT OF MATERIAL DAMPING IN A SIMULATED SPACE ENVIRONMENT

D. L. Edberg
Stanford University
Stanford, CA 94305

ABSTRACT

A new, experimental method of measuring the material damping of test models is presented. The method involves measuring the decay of free vibrations as the model is lofted into free-fall in a vacuum. Vibration signals are transmitted through the vacuum by a miniature telemetry system. The resulting data are recorded and later analyzed using a fast Fourier transform technique to determine the percent critical damping. The experimental apparatus offers a unique means to reset the experiment without breaking the vacuum, which reduces the time between runs.

1. INTRODUCTION

It seems quite certain that sooner or later large space structures will be orbiting the earth. Because all of them will have some sort of geometry or pointing requirements, there is a need for knowledge of their response to various excitations. In particular, the time needed to reduce vibrations to a certain level can be very important. Thus, information on the dynamic properties of the large space structure is necessary.

The mass and stiffness properties of a given structure are relatively easy to measure or compute analytically. However, information on the damping properties in general cannot be determined without experimental testing. Since the dissipation only occurs with vibration, a dynamic test is required.

The conditions of this test are quite important. In particular, the conditions of the test can interfere and even dominate the results. For example, support conditions, aerodynamic dissipation, and instrumentation wiring all influence the measurements being taken. The ideal situation, then, would be to eliminate all of these effects.

A method which eliminates the first two of these influences is documented in the literature [1]-[3]. Briefly, the vibration test is performed in a vacuum chamber. A small model was instrumented with strain gages and launched in a free-free vibration mode. The resulting vibration data were obtained with small instrumentation wires trailing the specimen. The method may only be used with so-called "one-dimensional" structures, or structures vibrating in one dimension, because of possible interference of the trailing wires. We now propose a new method which eliminates any damping caused by instrumentation wiring, and allows the testing of any one-, two-, or three-dimensional models.

2. USE OF A TELEMETRY SYSTEM FOR VIBRATION MEASUREMENT

An obvious means of eliminating the interference of the wiring is to eliminate the wiring itself. Of course, some other means of data transmission must be employed instead. Both optical and radio transmission schemes were studied, but the author's familiarity with radio-controlled models led to the choosing of the latter.

Of course, there are some drawbacks to the idea. A telemetry system adds mass to the system under test, but the additional mass adds no damping, if carefully designed. The only effect of the mass is to change the modeshape, which can easily be included in the analysis. Practically, the mass of the telemetry system should be kept as small as possible to reduce that change.

After considerable searching, a miniature transmitter was found that was suitable for the telemetry system (Figure 1). Its small size and mass (8 x 8 x 3 mm, 0.5 g) were found to be ideal, as its zero to 20,000 Hz bandwidth and FM transmission. The transmitter was originally designed for biological implantation, which gives it rugged solid-state construction.

In order to accommodate various signal levels (the miniature transmitter can accept a ±10 mV maximum input signal), an instrumentation amplifier was added to the circuit. The particular unit used here can run on the same power source as the transmitter, with very small current drain. The amplifier gain is controlled by a single resistor.

2. A strain gage forms the active leg of a Wheatstone bridge, whose output can be trimmed to zero by a trimpot. The output of the bridge is fed to the instrumentation amplifier mentioned previously. The capacitors are filters for the power supply, and a resistor is placed in series with the bridge to reduce current drain.

The output of the amplifier is fed to the miniature transmitter, which converts the time-varying voltage to radio frequency on the commercial FM band (88 MHz). The whole telemetry system is powered by four nickel-cadmium rechargeable cells with a capacity of 20 mAH. This power supply allows the operation of the system for eight continuous hours before recharging. The system, with its protective case and mounting hardware, has a total mass of 27 grams.

3. THE DESIGN OF MOUNTING HARDWARE FOR THE TELEMETRY

With so much effort being put into the elimination of trailing wires, the effect of an arbitrary telemetry mount and location had to be considered. Since the general form of the vibration was expected to be in bending, the mount had to allow bending without restriction. Other desirable qualities would be sturdiness, light weight, and ease of positioning. With these qualities in mind, we set out to design the best possible mounting hardware.

From any strength of materials textbook, one finds that a pin joint permits unrestricted bending. The problem, then, was to design a support which included pin joint(s). From here one seems to be on his own, and a trial and error scheme eventually led to the final support geometry, shown in Figure 3. A countersunk aluminum plate with a screw inserted is bonded to the telemetry case using cyanoacrylate adhesives (otherwise known as Super Glue). Then, a round brass or steel sphere is bored out to clear the screw threads and placed on the screw. Next, a hole is drilled through the specimen to be tested, and the assembly is placed on the specimen. Finally, another sphere and lock nut complete the assembly. One can see that the mount adds little mass to the system, and provides no restrictions to bending in any direction.

So far nothing has been said about the location of the telemetry unit. Only two locations seem desirable -- a center mount, which provides symmetry, and a location at a vibration node, which should cause the least disturbance to the system. A possible drawback to the nodal location is the necessity of an identical mass being placed to provide symmetry of the mass distribution. At the time of this writing, it is planned that both locations will be tested, and the one with the least influence will be used for all of the subsequent testing.

4. THE DESIGN OF A REMOTELY CONTROLLED LAUNCHER

For the purpose of general vibration testing, it is necessary to provide some sort of excitation to the model. In addition, for the task of measuring damping in a simulated space environment, one needs a launcher that will both excite the model and project it into free-fall. Fortunately, this is not in itself a difficult requirement; however, to facilitate experimentation it is desirable to have a mechanism that can be reset remotely. Otherwise, one is faced with the time-consuming procedure of breaking the vacuum, manually resetting the launcher, and then restoring the vacuum.

Quite a few methods were considered to power the launching mechanism: among them springs, compressed air, hydraulics, falling weights, and powerful electromagnets. After much consideration, the first method was chosen because of two major reasons: first, the author's familiarity with standard hardware, and secondly, because of the success with the system reported in references [1] - [3]. However, it was decided to modify that system considerably for ease of construction and resetting.

The first method chosen to recompress the springs was an electric motor powered winch which pulled on a cable. The electric motor shaft was coupled to a planetary gearbox to provide adequate torque for the compression. The case of the gearbox could be released, after which the springs were free to extend and launch the specimen. Unfortunately, the inertia and friction in the gearbox was enough to prevent adequate launch velocities.

The next iteration employed an electromagnetic clutch as a release mechanism. This modification proved successful until the surface of the clutch wore with continued usage. This wear caused slippage which made it impossible to reset the system.

The final resetting mechanism is based on that used by the MIT group [1] - [3], and is shown in Figure 4. Here, the mechanism is reset as follows: first, a small DC motor raises an electromagnet up to an iron plate underneath the spring-loaded model support. Upon contact, the electromagnet is energized. The DC motor's rotation is reversed to pull the model support down, which compresses the springs. The motor is stopped when the proper spring compression is reached. Switching off the current to the electromagnet releases the model support, which rapidly accelerates under the spring forces. When the model support impacts the rubber stops at the top of the vertical rods, the instrumented model continues vibrating in free-fall. Changing the horizontal location of the model supports and the stroke of the launcher offers the experimenter a choice of stress levels. All commands are operated by a standard hobby radio-control transmitter.

5. REMOTELY RESETTING THE EXPERIMENT

A large amount of time was spent in the design and construction of the launcher. But one might ask how the instrumented specimen will be returned to the model supports once it has completed its free-fall. In addition, whatever system is chosen must be able to function in a vacuum. With this in mind, the author and an associate, Mr. Brian Chan, designed and built a unique radio-controlled mechanism for the resetting of the experiment. The mechanism is shown in Figure 5. It is simply a miniature forklift, operated by the same transmitter as the launcher.

The forklift performs any task that its bigger brothers can do. Battery powered, it can move forward and reverse and can steer right or left. In addition, the lift can raise 1 Kg from the ground to a height of 45 cm, which is the height of the top of the launcher. Finally, the forklift can "kneel" to get its lift arms underneath any object.

Permission has been obtained to use the Heat Transfer vacuum chamber in NASA Ames Research Center's Arc Jet Testing Facility. The 2.5 meter ceiling permits free-fall test periods of approximately 1.4 seconds. Its 2.5 m x 3 m floor can easily accommodate larger models for testing, as well as the maneuvering of the forklift resetting mechanism, which can reset the model in less than three minutes (in the worst case). This is considerably faster than the five minutes required to break the vacuum combined with a ten minute evacuation time. Figure 6 shows a view of the apparatus through a 50 cm window in the vacuum chamber. It is quite easy to control the mechanisms visually through the window.

6. THE EXPERIMENTAL SETUP

Figure 7 shows a sketch of the experimental setup. The FM vibrational signals are picked up by a folded dipole antenna inside the vacuum chamber. The signals are amplified by an RF amplifier, and passed through the vacuum chamber wall by RG-59 coaxial cable. The cable connects to an impedance matching transformer coupled to a standard home FM receiver. The receiver is modified for DC output from its "detector", which then is input to a differential DC amplifier. The resulting signals are recorded by an analog instrumentation tape recorder, for subsequent analysis. The signals are monitored by an oscilloscope in parallel with the tape recorder. Later, the signals are analyzed by a Fast-Fourier-Transform routine to extract the damping ratio for any desired mode or frequency range. Figure 8 shows an overall view of the test equipment outside of the vacuum chamber.

Planned testing includes aluminum beams, for verification of the telemetry system by comparison with references [1] - [3]. In addition, various specimens of fiberglass/epoxy, graphite/epoxy, and Kevlar®/epoxy are expected to be fabricated by the Boeing Aerospace Company in a variety of shapes, sizes, and ply orientations. Also, testing will include plates of the above specimens, and if time permits, a simple truss specimen will be fabricated and tested.

7. RESULTS

The reader of this paper probably has already noted the presence of what is commonly called "Murphy's Law" in the number of iterations and redesigns already mentioned (many more are not mentioned here). The latest occurrence of such presence was the failure of a motor in the tape recorder. Naturally, this failure came at just the right time to preclude any computational analysis of the vibrational data taken up to this point.

In order to foil Murphy, at least temporarily, a camera was strapped onto the oscilloscope and photos were taken of the transmitted signal. Eleven reject photos later, the author succeeded in capturing a waveform which is shown in Figure 9. A "back of the envelope" analysis yields a damping ratio of about 0.005, which is the right order of magnitude. It should be noted that this test took place at atmospheric pressure, and the repetition of the test in vacuum will yield a considerably lower value [1]. In addition, this test model was not symmetrical, and in fact has received considerable abuse in all the testing of the experimental apparatus. It is clear that the procedure reported in this paper can accurately measure material damping.

REFERENCES

[1] Vorlicek, P. L. "Material Damping of Aluminum and Graphite/Epoxy in a Simulated Zero-Gravity Environment," M.I.T. Space Systems Laboratory Report, SSL #13-81, January 1981.

[2] Mohr, David G. and Crawley, Edward F., "Experimental Measurements of Material Damping of Aluminum and Graphite/Epoxy in Free-Fall With Tunable Excitation," M.I.T. Space Systems Laboratory Report, SSL #11-82, June 1982.

[3] Sheen, Raymond L., and Crawley, Edward F., "Experimental Measurement of Material Damping for Space Structures in Simulated Zero-G," M.I.T. Space Systems Laboratory Report, SSL #1-84, December 1983.

Figure 1. Miniature Telemetry Transmitter
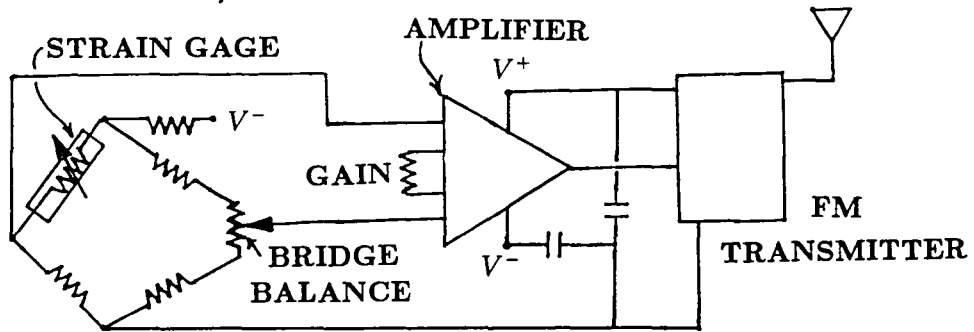
Figure 2. Telemetry Schematic
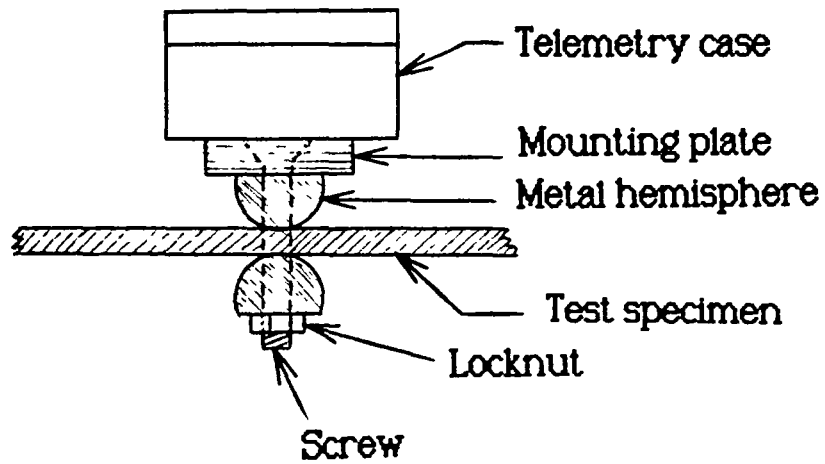
Figure 3. Telemetry Support Geometry
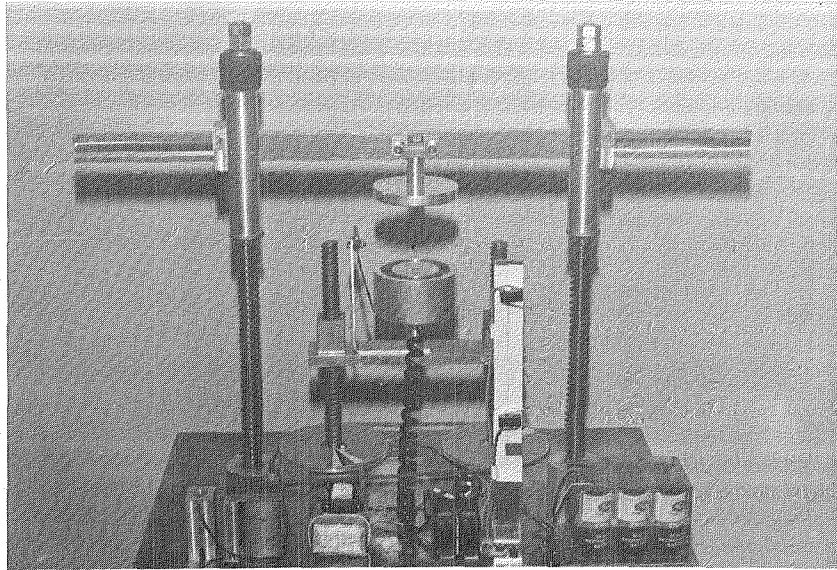
Figure 4. Remotely Resettable Spring-Powered Launcher
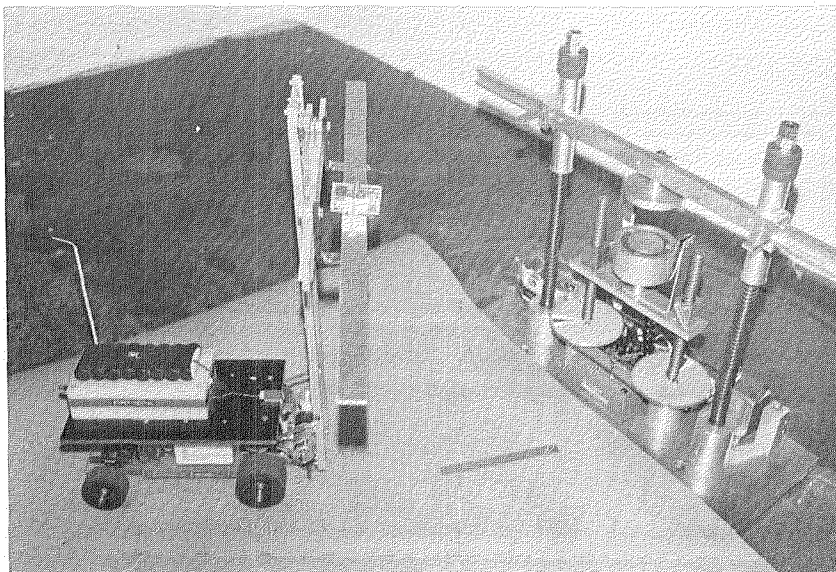
Figure 5. Radio-Controlled Forklift, carrying test specimen to launching
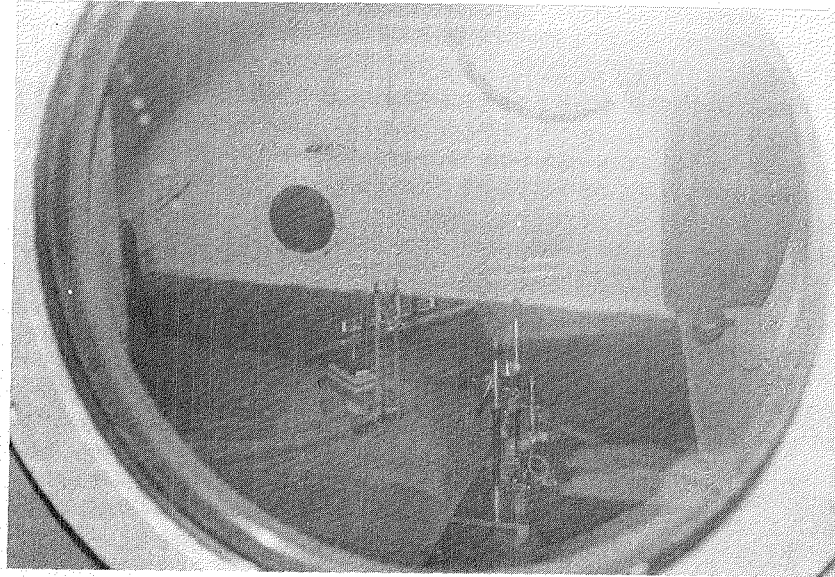device(note six-inch ruler in foreground)

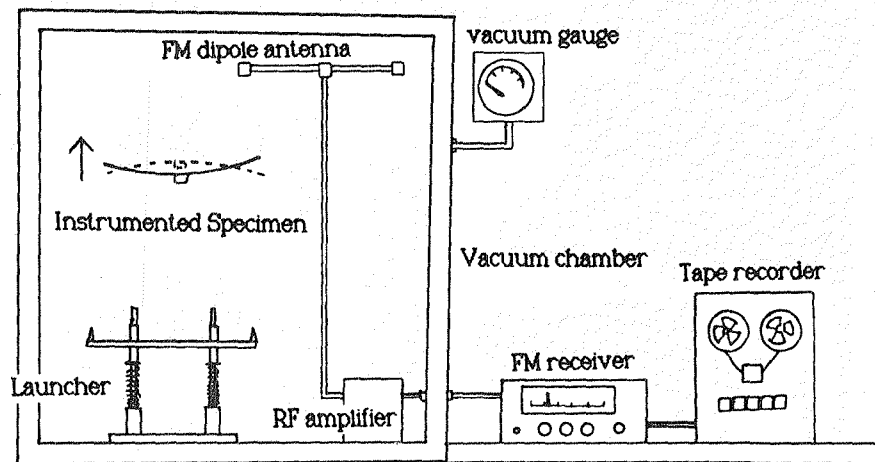Figure 6. View of Test Apparatus through vacuum chamber window
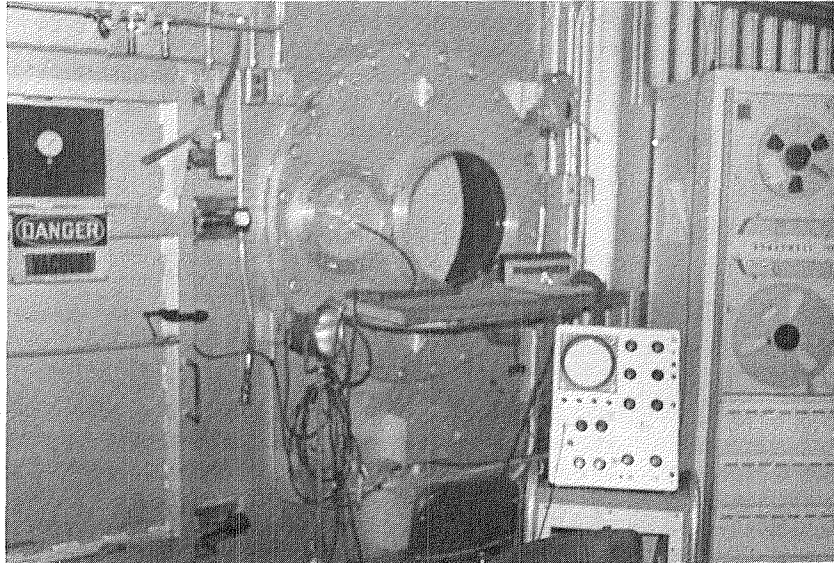

Figure 7. Experimental Setup
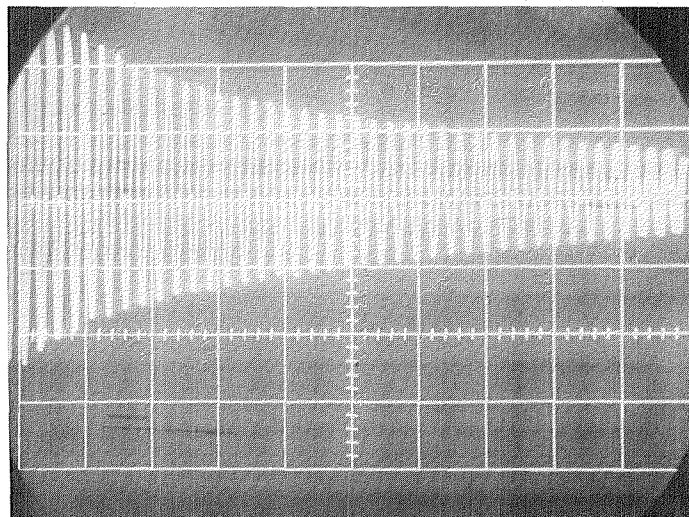
Figure 8. View of Test Setup and Vacuum Chamber

Figure 9. Oscilloscope Trace of Damping Test Waveform

End of Document